UNIVERSITY OF NOVI SAD
FACULTY OF TECHNOLOGY
NOVI SAD

# ACTA PERIODICA TECHNOLOGICA

APTEFF, Vol. 54, 1-335 (2023)

ACTA PERIODICA TECHNOLOGICA (formerly Zbornik radova Tehnološkog fakulteta and Proceedings of Faculty of Technology) publishes articles from all branches of technology (food, chemical, biochemical, pharmaceutical), process engineering and related scientific fields.

Articles in Acta Periodica Technologica are abstracted by: Chemical Abstracts Service – Columbus, Ohio; Referativnyi zhurnal – Khimija, VINITI, Moscow; listed in Ulrich's International Periodical Directory, and indexed in the Elsevier Bibliographic databases – SCOPUS.

ISSN 1450-7188 (Print)
ISSN 2406-095X (Online)

CODEN: APTEFF
UDC 54:66:664:615

***Publisher***
University of Novi Sad, Faculty of Technology Novi Sad
Bulevar cara Lazara 1, 21000 Novi Sad, Serbia

***For Publisher***
Prof. Dr. Biljana Pajin, Dean

# CONTENT

APTEFF, Vol. 54, 1-335 (2023)
DOI: https://doi.org/10.2298/APT2354001Z

UDC: 678.82:547.424:661.728
BIBLID: 1450-7188 (2023) 54, 1-19

Original scientific paper

# BLEND MICROSPHERES OF POLY (GLYCOLIDE-CO-ε-CAPROLACTONE) AND ETHYL CELLULOSE FOR THE CONTROLLED RELEASE OF 5-FLUOROURACIL

*Asma ZIANE*, Hichem BAKOURI, Oum El kheir KHOUKHI, Kaddour GUEMRA*

Physical and Organic Macromolecular Chemistry Laboratory (LCOPM), Faculty of Exact Sciences,
University of Djillali Liabes, BP 089, Sidi Bel Abbes, Algeria

**Received: 05 October 2022** **Revised: 24 October 2022** **Accepted: 27 October 2022**

*In this present study, a series of copolymers with diverse compositions were produced using bulk ring-opening polymerization of glycolide and ε-caprolactone, using stannous(II) octoate as initiator.* $^1H$, $^{13}C$ *NMR, and FTIR spectroscopy were used to characterize the resultant copolymers. Afterwards, the oil/water emulsion evaporation technique was used to create blend microspheres of poly (glycolide-co-ε-caprolactone) and ethylcellulose in order to investigate the controlled release of 5-fluorouracil, an anticancer drug. The size distribution of the microspheres was studied by optical microscope, which confirmed their spherical nature with sizes ranging from 112 to 186µm, FTIR and X-ray diffraction were used to confirm the polymer blend compatibility and to confirm the absence of drug-polymer interactions. Moreover, in vitro release experiments were performed at 37 °C in simulated buffer medium of the stomach (pH=1.2) for 2h, and simulated intestinal medium (pH=7.4). It was found that the release of 5-fluorouracil from blend microspheres followed pH-independent release as compared to that of plain poly(ε−caprolactone) and ethylcellulose microspheres for more than 10h. Furthermore, to better understand the nature of the drug release profiles, release data was fitted to empirical models.*

**Keywords**: 5-Fluorouracil, poly(glycolide-co-caprolactone), ethylcellulose, microparticles, polymer blends, solvent evaporation method, controlled release, kinetic study.

## INTRODUCTION

Microencapsulation is based on fabricating materials with interesting new properties in the pharmaceutical industry and so many other fields (1), in the area of pharmaceutics, drug delivery system (DDS) has been the most promising and convenient route for inducing drug to the body as needed to safely achieve its desired therapeutic effect (2). Nowadays controlled drug release methods received more attention due to their advantages such as prolonged release time, drug effectiveness, decreasing unnecessary poisoning effect of the drug, biocompatibility, and helps to avoid the multi-drug resistance (3).

Biodegradable polymers have been used either alone or in combination with other polymers for several biomedical and pharmaceutical applications because of their inherent properties such as biocompatibility, predictability of degradation kinetics, and ease of fabrication (4-6). The commonly studied biodegradable polymers for controlled drug delivery are the aliphatic polyesters; poly(lactide), poly(glycolide) (PGL), poly(ε−caprolactone) (PCL) and their copolymers (7).Various materials with a broad range of properties can be

---

* Corresponding author: Asma ZIANE, Physical and Organic Macromolecular Chemistry Laboratory (LCOPM), Faculty of Exact Sciences, University of Djillali Liabes, BP 089, Sidi Bel Abbes, Algeria.
e-mail: asmaziane.chem@gmail.com

obtained by copolymerization of different co-monomers and modulation of their ratio in the copolymer, such as the reported poly(lactide-*co*-glycolide) (PLGA) (8), poly(lactide-*co*-caprolactone) (PLC), and poly(glycolide-*co*-ε-caprolactone) (PGC) (9, 10). The interest of PCL has been highlighted as platform for oral delivery. Microparticles can be prepared either by PCL alone, or by using copolymers with PCL or PCL blends in order to obtain the desired release characteristics (11–13). In the recent years the copolymers of glycolide with caprolactone began to attract considerable interest, they had been applied as implants and surgical suture with satisfactory results (14–16), for the controlled release, to prepare microspheres, the copolymers should first of all be soluble in common solvents. However, PGA is a rigid, highly crystalline material, insoluble in most organic solvents, PCL, a biocompatible semi-crystalline polymer with a low glass transition temperature. The advantages of PCL include its high permeability to small drug molecules, its failure to generate an acidic environment during degradation when compared to polylactides and glycolides, its exceptional ability to form blends with other polymers and its slow degradation when compared to PLGA making it more suitable for long term delivery systems lasting up to a year. Thus, to improve solubility, the material used to make microspheres should have high caproyl unit content (17).

Cancer is a dangerous disease-causing death worldwide. Both the incidence and mortality of cancer are rising day by day. At present, the cancer treatment relies on surgery, radiofrequency, ablation, cryosurgery, chemotherapy, radiation therapy and targeted therapy, among which chemotherapy is a successful cancer therapy, but it comes with many challenges due to toxicity towards normal cells. Among the various chemotherapeutic agents available, 5-fluorouracil (5-FU) is considered to be the standard first-line treatment (18), which is an effective drug used for the treatment of variety of cancers like lungs, abdomen, carcinomas of the colon or rectum, breast cancer and precancerous dermatoses. However like other drugs used for chemotherapy, 5-FU is found to cause severe side effects when the concentration is too high (19). Also, it causes bone-marrow disorders and produce toxic effects on the gastro intestinal tract (20). For the convenient treatment, biodegradable drug carriers are developed to encapsulate such drugs (21).

Recently, many polymeric, controlled release (CR) systems have been developed, by using suitable drug delivery carriers (22), the side effects can be decreased by keeping the concentration 5-FU at low level (23), and the controlled release of the drug will not harm the healthy tissues (24).

To overcome this, the present study investigates the development and evaluation of an efficient CR polymer matrix for 5-FU, in the present work, biocompatible and biodegradable poly(glycolide-co-ε–caprolactone) at different ratios are synthesized and then blended with ethyl cellulose to entrap 5-FU by the oil/water emulsion-solvent evaporation method. Several analytical techniques were used to characterize the drug-loaded formulations in order to understand their size, shape, and morphology, as well as the chemical interactions between the polymers and drug.

The *in vitro* 5-FU release was investigated in pH=1.2 for the initial 2h, and in pH=7.4 phosphate buffer media for up to 10h, to study the effect of matrix, the blend composition, and initial drug loading drug release kinetics parameters have been estimated through empirical equations that are widely used in the literature, to understand the nature of drug release mechanism.

# EXPERIMENTAL

## MATERIALS AND METHOD

The reagents used in this study: Glycolide (purified by recrystallization from dry ethyl acetate), ε-caprolactone (dried and distilled under argon before use), stannous (II) octoate ($Sn(Oct)_2$), 5-fluorouracil (5-FU), chloroform (b. p. = 61.2 °C, formula $CHCl_3$, M =119. 38 g/mol), polyvinyl alcohol (PVA) 87%-89% hydrolysed ($M_W$=13000-23000), Dichloromethane (DCM) (≥ 99 of purity) and absolute ethanol (99.8 % of purity) were purchased from Sigma-Aldrich (USA), Ethylcellulose (EC) (10 m.pa/s) was purchased from Fluka analytical.

### *General procedure of polymerization and formulation*

### Synthesis of poly(glycolide-co-ε-caprolactone) (PGC)

PGC was synthesized using the previously described procedure (10, 25) by bulk ring-opening copolymerization of glycolide with ε-caprolactone at three different percentages: 50:50, 70:30, and 30:70, respectively. $Sn(Oct)_2$ was used as initiator with an I/M molar ratio of 1/800. Polymerization was performed under argon atmosphere at a high temperature of 140 °C for 24 hours. The reaction medium solidified as the polymerization proceeded. After dissolving in chloroform, the polymers were precipitated in methanol. The copolymers produced were dried under vacuum at ambient temperature up to constant weight. This is schematically illustrated in Scheme 1.

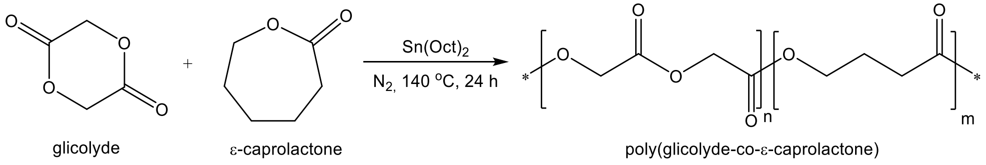

**Scheme 1**. Schematic representation of copolymerization of glycolide and ε-caprolactone by bulk ring-opening.

### Synthesis of Poly(ε-caprolactone)

Engelmann et al. (26) reported the reaction conditions for producing PCL by ring opening polymerization of ε-caprolactone by $FeCl_3 \cdot 6H_2O$.

### Preparation of 5-FU microspheres

5-FU microspheres were prepared using an o/w emulsification-solvent evaporation technique as reported by Woodruff and Hutmacher (27). Briefly, mixture of EC (1g) and PGC (1g) was dissolved in dichloromethane. The 5-FU solution was added to EC-PGC solution, and the mixture was suspended by ultra-sonication. This suspension was poured into an aqueous solution of PVA (1% w/vol).

The organic phase was emulsified with the continuous phase under mechanical stirring (600 rpm) for 4 hours at room temperature to allow solvent evaporation and microspheres formation. The microspheres were separated by vacuum filtration. The remaining loose drug and PVA was removed by washing microspheres 3 times. The microspheres were collected and dried then preserved in desiccators kept in refrigerator until use.

Secondly, a PCL and EC microspheres and the blend of polymers PCL (1g) with EC (1g) microspheres were prepared by the same procedure the o/w emulsion-solvent evaporation as described in Table 1.

**Table 1.** Operating conditions of the different formulations of 5-FU performed

| Code | Active agent | Polymer matrix | Emulsifier | Parameter of organic phase A (%) | Parameter of organic phase B (%) | Parameter of aqueous phase C (%) | Speed (rpm) | Organic solvent |
|---|---|---|---|---|---|---|---|---|
| F1 | 5-Fluorouracil (5FU) | EC-PGC 50/50 | PVA | 25 | 6.25 | 1 | 600 | DCM |
| F2 | | EC-PGC 70/30 | PVA | 25 | 6.25 | 1 | 600 | DCM |
| F3 | | EC-PGC 30/70 | PVA | 25 | 6.25 | 1 | 600 | DCM |
| F4 | | EC-PCL | PVA | 25 | 6.25 | 1 | 600 | DCM |
| F5 | | EC | PVA | 25 | 6.25 | 1 | 600 | DCM |
| F6 | | PCL | PVA | 25 | 6.25 | 1 | 600 | DCM |

$$A\%=\frac{active\ agent}{polymer},\ B\%=\frac{polymer}{solvent},\ C\%=\frac{surfactant}{water}$$

### Characterization of copolyesters/microparticles

The structures of the obtained PGC and PCL copolymers were confirmed using $^{1}$H, $^{13}$C-NMR, and FTIR spectroscopy. The NMR analysis ($^{1}$H, $^{13}$C-NMR) of PGC is described in section Results and Discussion, and confirmed the structure of both obtained copolymers. The spectra of PCL are given in Figure 1. In addition, the obtained copolymers were analysed by FTIR, X-Ray diffraction and particle size analysis.

### NMR measurements

The NMR analysis includes $^{1}$H-NMR (500 MHz) and$^{13}$C-NMR (125.75 MHz), spectra were recorded by using Bruker DRX 500 MHz spectrometer. The chemical shifts (δ) are given in ppm and referenced to the internal solvent signal namely TMS and $CDCl_3$, respectively.

### Fourier Transform Infrared Spectroscopy (FTIR) measurements

To confirm the effective 5-FU encapsulation, microspheres were characterized by infrared spectroscopy. The FTIR spectra were recorded from 400 to 4000 cm$^{-1}$ using a Bruker-ATR spectrometer. The infrared spectra of pure 5-FU and the obtained formulations on powder form were compared.

Original scientific paper

**$^1$H-NMR-PCL (a)**

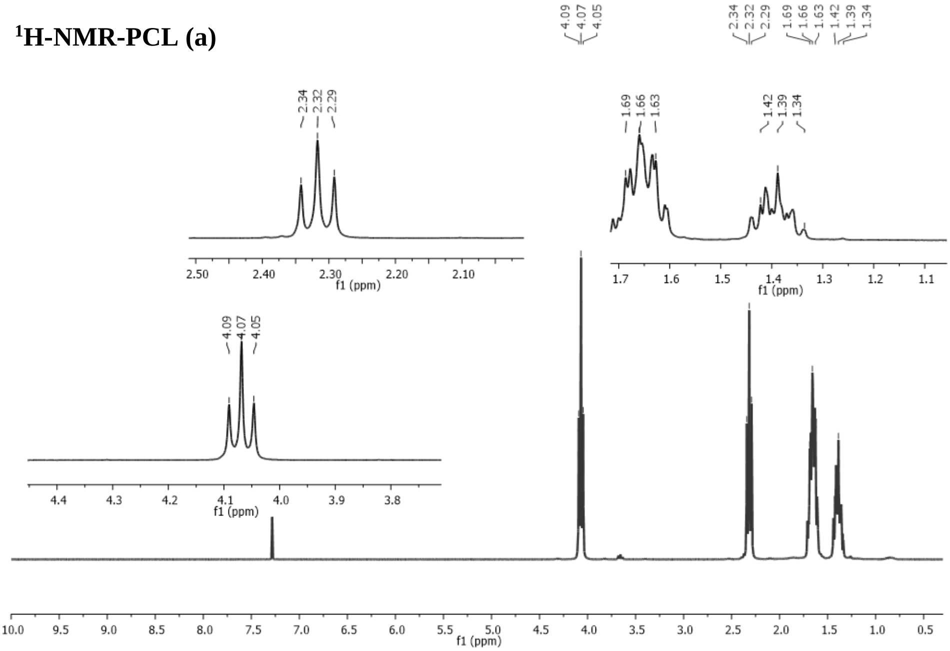

**$^{13}$C-NMR-PCL (b)**

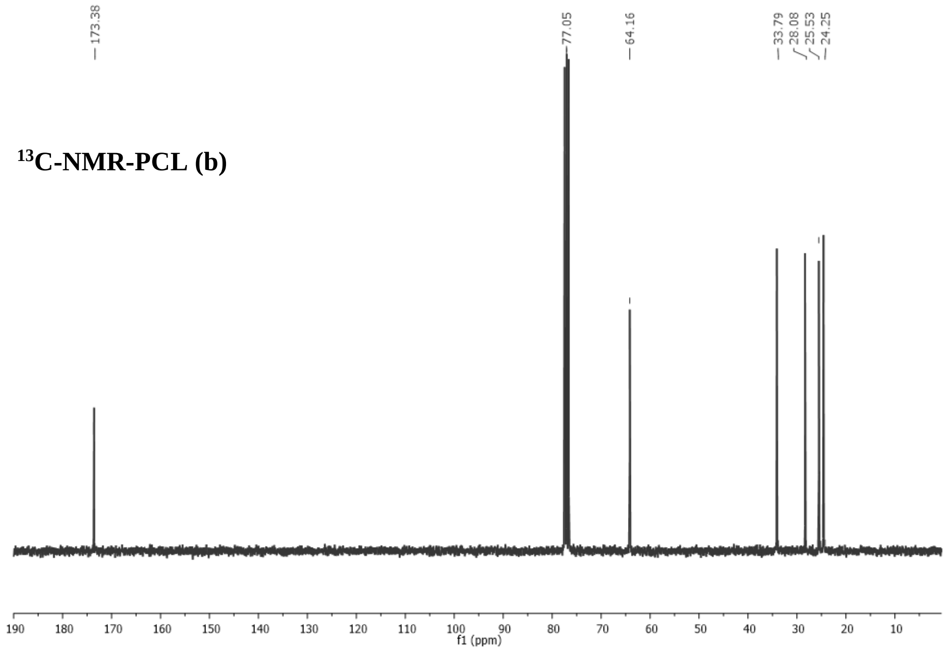

**Figure 1**. $^1$H-NMR (a) and $^{13}$C-NMR (b) spectra of poly (ε-Caprolactone).

### X-Ray Diffraction measurements

The X-ray diffraction patterns were traced employing X-Ray Diffractometer using nickel-filtered CuKα; data was collected in the continuous scan using step size 0,002°/23s, the scanning range was 0-70 °C. The X-ray diffractograms of pure 5-FU and the obtained formulations on powder form were compared.

### Particle size analysis

The mean diameters ($d_{10}$, $d_{32}$, $d_{43}$) and size distribution (δ) of microparticles were calculated from the results of optical microscopy (Optika Via Rigla, 32 24010 Ponteranica Optika B1, Digital camera Assembled in Italy), by applying the following equations and using Excel worksheet. More than 500 microspheres were taken on a glass slide and the particle size was measured using appropriate lenses.

$$d_{10}=\sum n_i d_i/\sum n_i, \qquad [1]$$

$$d_{32}=\sum n_i d_i^3/\sum n_i d_i^2, \qquad [2]$$

$$d_{43}=\sum n_i d_i^4/\sum n_i d_i^3, \qquad [3]$$

$$\delta=d_{43}/d_{10} \qquad [4]$$

where $d_{10}$, $d_{32}$ and $d_{43}$ are respectively the number, surface and volume mean diameters.

### Entrapment Efficiency and Drug Loading

The loading efficiency (5-FU$_{\text{loaded}}$, %) and the encapsulation efficiency (yield, %) were determined after extraction in an appropriate solvent, according to the following equations:

$$\text{5-FU}_{\text{loaded}}\ \% = \frac{\text{mass of 5-FU}_{\text{extracted}}}{\text{mass of microparticles}}\cdot 100 \qquad [5]$$

$$\text{Yield}\ \% = \frac{\text{mass of 5-FU}_{\text{extracted}}}{\text{initial mass of PRX}}\cdot 100 \qquad [6]$$

Extractions of drug from microparticles were performed in triplicate. 50 mg of dried microparticles was soaked in 50 mL of absolute ethanol under stirring in a sealed bottle for 24 hours. The resulting solution was analysed by UV-VIS spectroscopy (Shimadzu UV-2401 PC, Shimadzu, Japan) after an appropriate dilution with ethanol, at the wavelength ($\lambda_{max}$) of 266 nm where a molar extinction coefficient (ε) was equal to 7055 $L\cdot mol^{-1}\cdot cm^{-1}$.

### *In Vitro* Release Study

The 5-FU release kinetics from the obtained formulations were followed in an appropriate dissolution reactor plunged in a bath regulated at 37±1 °C. This reactor (Erlenmeyer flask) is equipped by filter tube which permits us to withdraw solution without microparticles.

At initial time, 100 mg of microparticles were soaked in the reactor containing 900mL of buffered solution at pH = 1.2 ± 0.1 and pH = 7.4 ± 0.1 obtained with a classical preparation and under a stirring rate of 250 rpm.

At predetermined time, 3mL of solution are withdrawn, analysed by UV spectroscopy (Shimadzu UV-2401 PC, Shimadzu, Japan) without dilution, 3mL of fresh buffered solution replaced in the Erlenmeyer flask.

The 5-fluorouracil released was analysed in acidic solution (pH=1.2) at a wavelength ($\lambda_{max}$) of 265.8 nm where $\varepsilon$ =7380.6 L mol$^{-1}$ cm$^{-1}$, and basic solution (pH= 7.4) at a wavelength ($\lambda_{max}$) of 265 nm where $\varepsilon$ = 5957.7 L mol$^{-1}$ cm$^{-1}$. The kinetic experiments were established in duplicate.

## RESULTS AND DISCUSSION

### MICROPARTICLES CHARACTERIZATION

### NMR spectroscopic characterization

In the order to obtain more information about the purity of PGC and PCL, both, experimental $^1$H and $^{13}$C-NMR are used as preeminent technique for confirmation of the structure of PGC and PCL. Hence, Figures 2a and 2b depict the NMR spectra versus chemical shift dissolved in $CDCl_3$ over the scan ranges 0 to 8 ppm for $^1$H-NMR and 0 to 190 ppm for $^{13}$C-NMR. The spectroscopic data are given below.

**$^1$H-NMR**-[PGC], ($CDCl_3$) $\delta_H$(ppm) = 1.43 (m, $CH_2$), 1.66-1.74 (m, $CH_2$), 2.23-2.48 (m, $CH_2$), 4.06-4.19(m, $CH_2$), 4.67-4.83 (m, $CH_2$).
**$^{13}$C-NMR**-[PGC], ($CDCl_3$) $\delta_C$(ppm) = 24.51, 25.16, 28.26, 33.27, 34.22, 60.39, 63.88, 65.06, 167.80, 172.72, 173.48.

As mentioned above and based on the corresponding structure of PGC, the $^1$H-NMR spectrum of PGC displayed four singlets at $\delta_H$=4.67-4.83 ppm corresponding to the methylene protons of the glycolide unit (Figure 2a ($H_6$)) resulting from the sequence distribution of the glycolyl and caproyl units. Those $\delta_H$ = 4.06-4.19 (Figure 2a($H_1$)) $\delta_H$ = 2.23-2.48, and $\delta_H$ = 1.66-1.74, $\delta_H$ = 1.43 ppm (Figure 2a($H_{3-5}$)), respectively, were assigned to the methylene protons of the caproyl unit adjacent the ester group. On the other hand, the $^{13}$C-NMR spectrum of PGC (Figure 2b) shows very clearly eleven signals between $\delta_C$ = 173.48 and 24.51 ppm confirm the appropriate structure of the resultant copolymer PGC. Therefore, both spectra clearly confirm that PGC has been synthesized successfully. Our NMR spectra results are consistent with those of previous studies (28).

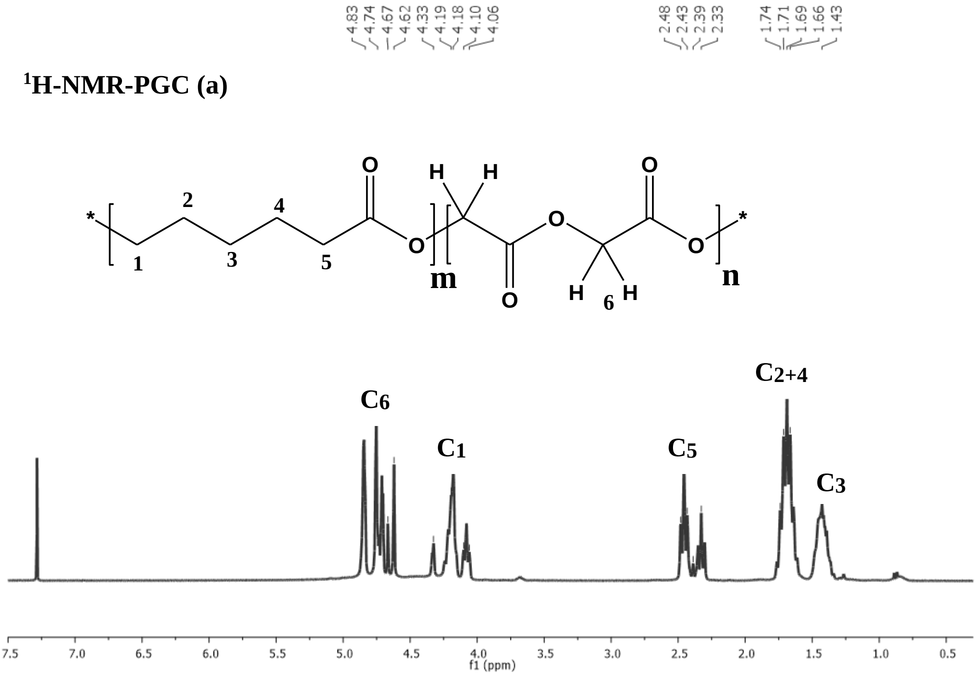

$^1$H-NMR-PGC (a)

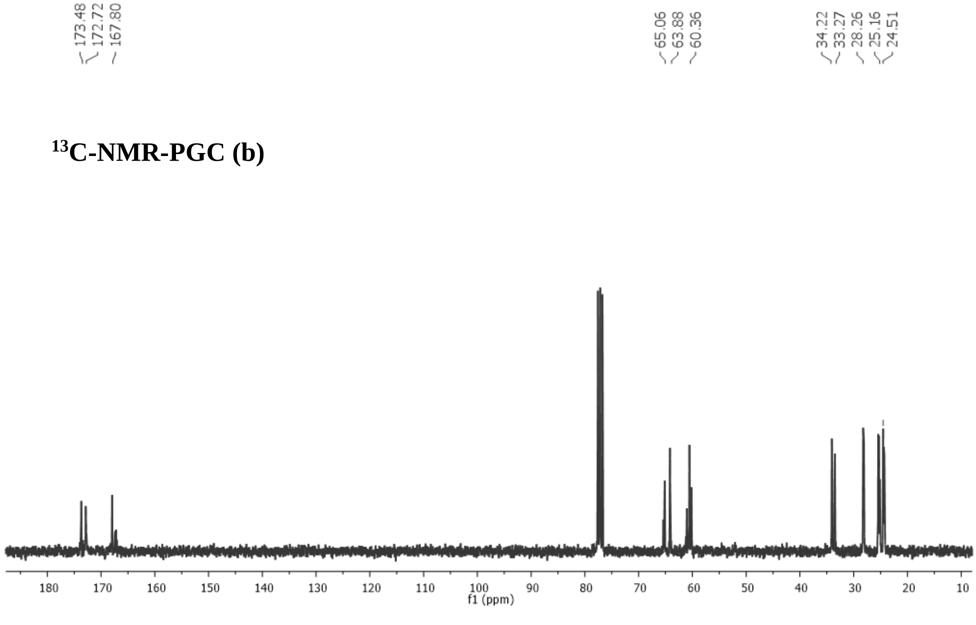

$^{13}$C-NMR-PGC (b)

**Figure 2**. $^1$H-NMR (500 MHz) (a) and $^{13}$C-NMR (125.75 MHz) (b) spectra of PGC copolymer.

### X-Ray diffraction analysis

The XRD spectra recorded for nascent 5-FU, and 5-FU$_{\text{loaded}}$ microspheres, are presented in Figure 3 and 4, to investigate the physical state of 5-FU in the matrix. The 5-FU exhibits characteristic intense peaks between 2θ of 28° and 30°, but in the case of 5-FU$_{\text{loaded}}$ microspheres F1, F2, F3, no sharp peaks are observed between 2θ of 20° and 35°, this revealed to the presence of the drug in the amorphous part of the matrix. However, with 5-FU$_{\text{loaded}}$ microspheres F4, F5, F6, the characteristic peaks of 5-FU are observed along with the broad peak of the polymer matrix, indicating the crystalline nature of 5-FU in the microspheres.

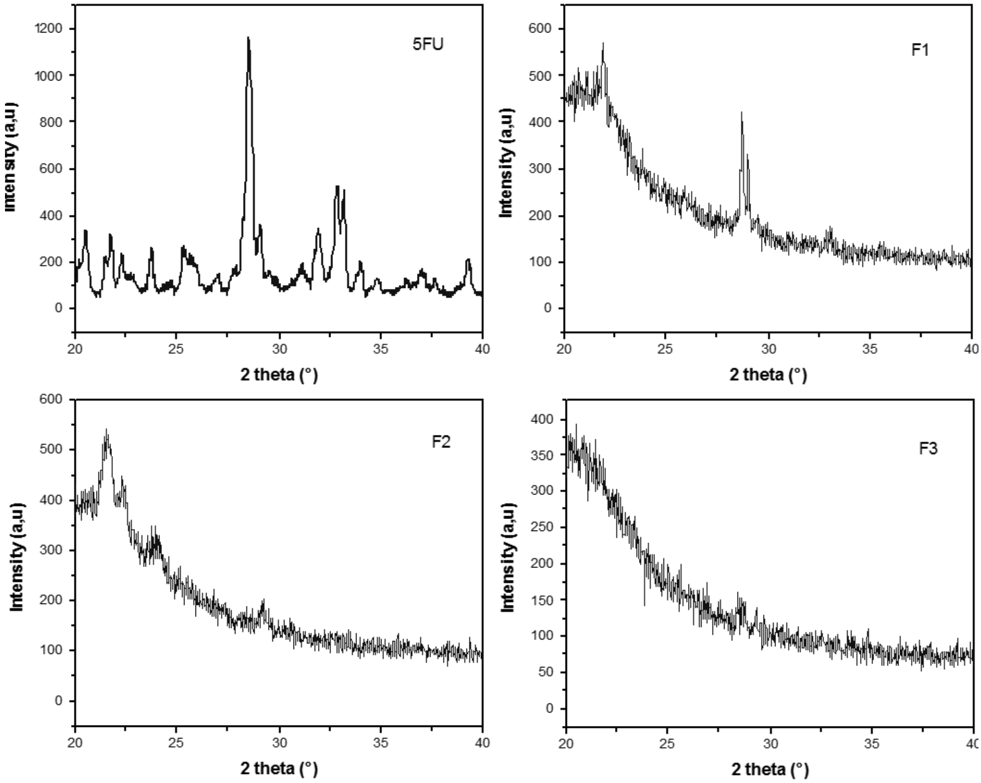

**Figure 3.** XRD diffraction analysis (nascent 5-FU, F1, F2 and F3 microspheres).

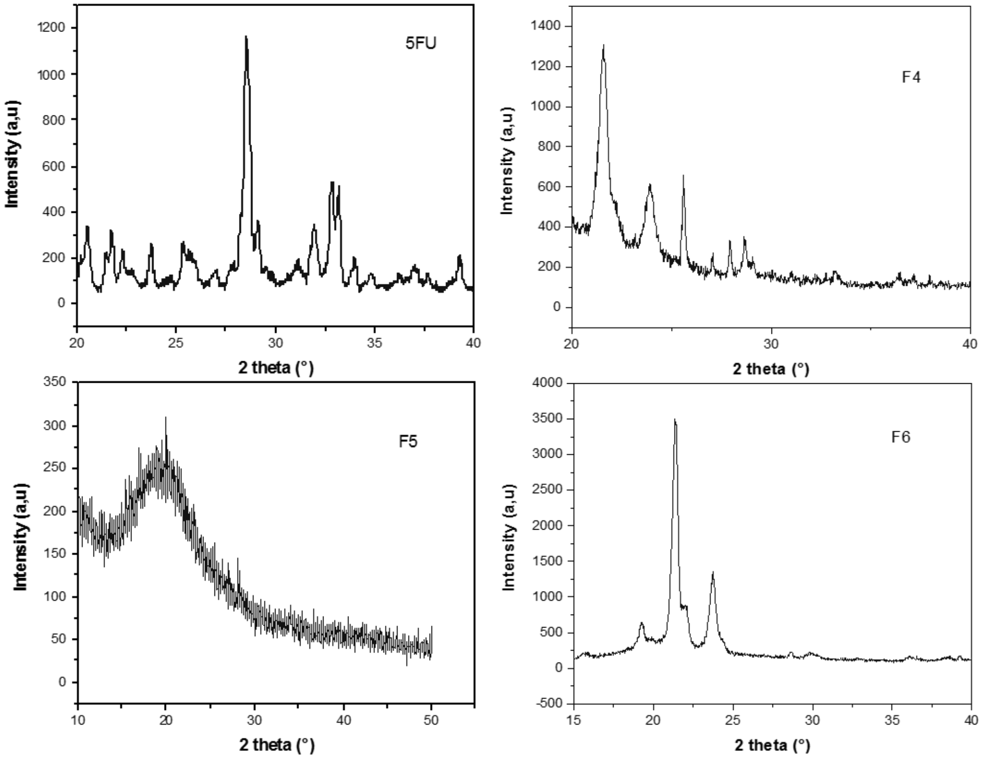

**Figure 4**.XRD diffraction analysis (nascent 5-FU, F4, F5 and F6 microspheres).

## FTIR spectroscopy study

Figures 5-8 shows FTIR spectra of the six 5-FU$_{\text{loaded}}$ formulations compared with pure 5-FU. The characteristic bands of pure 5-FU are detected at 1720, 1427, 1246, 803, and 548 cm$^{-1}$ resulting from the vibration of imides stretch (amide II and amide III) and aromatic ring. Furthermore, the IR band observed at 1347 cm$^{-1}$ is assigned to the vibration of the pyrimidine ring, also, the peak at 1179 cm$^{-1}$is assigned to the C=O vibrations, and at 1243 cm$^{-1}$ is associated to C-N vibrations. These stretching frequencies are similar to those observed by Haddad et al. (29-30). Moreover, the spectra of 5-FU microspheres have shown the amide group bands in the range between 1470 and 1760 cm$^{-1}$. While the carbonyl band is observed at 1736 cm$^{-1}$. It also depicts -CH$_2$ stretching bands in the range of 2668–2996 cm$^{-1}$ and C=O stretching in the range of 1063–1252 cm$^{-1}$. The C-H stretching band was demonstrated as a characteristic peak in the range of 3496–2830 cm$^{-1}$ (31). Generally, the spectrum of microspheres kept the sharpest characteristic peaks of 5-FU with slight shifting.

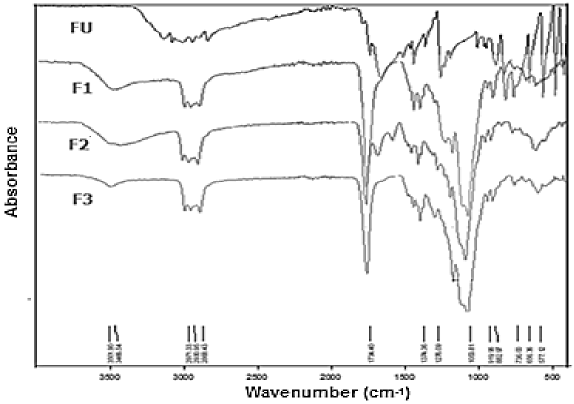

**Figure 5.** FT-IR spectra of: pure 5-FU, F1, F2 and F3 blended microparticles.

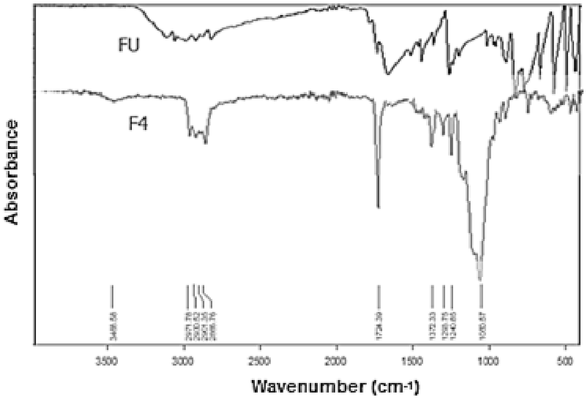

**Figure 6**. FT-IR spectra of pure 5-FU and F4 microparticles.

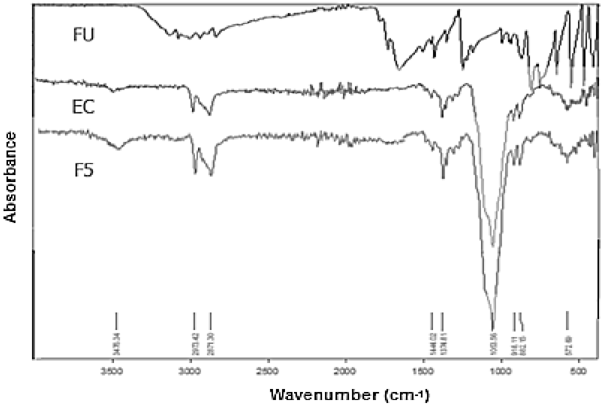

**Figure 7.** FT-IR spectra of pure 5-FU, EC and F5 microparticles.

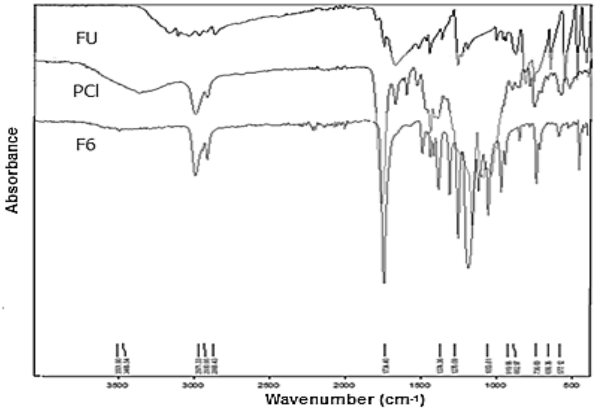

**Figure 8.** FT-IR spectra of pure 5-FU, PCL and F6 microparticles.

### Yield, drug loading and particle size analysis

The microparticles were characterized in terms of shape and size (mean diameter). As reported in Table 2, six batches of microparticles were prepared by emulsion-solvent evaporation at several experimental conditions. The results of the drug loading (5-FU$_{\text{loaded}}$, %) and the encapsulation efficiency (Yield, %) are mentioned in table 1. As reported, the percentage of 5-FU$_{\text{loaded}}$ varied from 11.95 % to 23.37 % and the yield varied from 21.27 % to 56.56%.

**Table 2**. Microencapsulation results.

| N° Lot | Composition (Matrix-Drug*) | Stirring speed (rpm) | 5-FU $_{\text{loaded}}$, % n=3 mean ± Sd | Yield, % n=3 mean ± Sd |
|---|---|---|---|---|
| F1 | EC/PGC (50/50) - 5-FU | 600 | 22.04 ± 1.80 | 51.58 ± 4.21 |
| F2 | EC/PGC (70/30) - 5-FU | 600 | 23.37 ± 1.09 | 56.56 ± 2.64 |
| F3 | EC/PGC (30/70) - 5-FU | 600 | 19.12 ± 1.46 | 34.81 ± 2.66 |
| F4 | EC/PCL - 5-FU | 600 | 17.70 ± 0.92 | 29.03 ± 1.50 |
| F5 | EC - 5-FU | 600 | 11.95 ± 1.88 | 21.27 ± 3.35 |
| F6 | PCL - 5-FU | 600 | 15.08 ± 0.58 | 27.75 ± 1.06 |

The loading efficiency (% 5-FU$_{\text{loaded}}$) were close to 24% in some cases however the yield didn't exceed 57%; it was not excellent because we used an oil in water (o/w) emulsion to prepare the microparticles and the low value of yield can be due to the water solubility of 5-fluorouracil and its possible transfer in the external phase (water). However, by choosing this technique, we tried to minimize the employment of organic and toxic solvents in the microparticles preparation.

The loading efficiency and yield were found to be dependent on the nature of polymer used in the formulation. In general, an increase in DL % from 19.12 to 22.04 and 23.37 and yield % from 34.81 to 51.58 and 56.56 were recorded for F3, F2 and F1, respectively. These results revealed that F1, F2 and F3 exhibited a significant higher yield % and DL % than other formulations. They are both composed of different ratios of CL and GL. Increasing the polymers portion in the formulation ratio, particularly PCL, was found to significantly improve both the % yield and the % DL, as evidenced by the higher % yield (56.56%) and drug loading (23.37) achieved with the formulation F2 (70/30) compared with lower values (21.27 % in % yield and 11.95% in % DL) obtained with the formulation F5 (with EC only). However, 5-FU being high solubility drug with low dose required high concentration of polymer and/or excipients in dosage form for better formulation development.

Table 3 resumed the size distribution and the mean diameters ($d_{10}$, $d_{32}$ and $d_{43}$) of microparticles which were calculated from counting more than 500 microparticles. Depending on the microparticles composition, the number mean diameter ($d_{10}$) of microparticles batches ranged between 112 to 186 μm.

**Table 3**. Size and size distribution of microparticles

| N° Lot | $d_{10}$ (μm) | $d_{32}$ (μm) | $d_{43}$ (μm) | Dispersion δ |
|---|---|---|---|---|
| F1 | 112.89 | 137.8 | 144.7 | 1.28 |
| F2 | 186.06 | 214.9 | 227.2 | 1.22 |
| F3 | 178.8 | 222.3 | 245.6 | 1.37 |
| F4 | 185.7 | 223.3 | 236.0 | 1.27 |
| F5 | 145.34 | 159.8 | 166.5 | 1.14 |
| F6 | 155.1 | 215.9 | 233.9 | 1.50 |

The results of microparticles size showed that the mean diameter increased by modifying the PGC concentration (ε-CL % and GL %) and the EC blend, this result is due to molecular weight of ethyl cellulose and hydrophobicity of PCL. A bigger droplet was formed and mean particle size increase when the viscosity of dispersed phase present high viscosity. We noted the effect of the size of 5-fluorouracil crystals, when we use it in its raw state, he has a mean size of 247±95 μm, they cannot be correctly incorporated into the polymeric matrix which was reflected the low of loading formulation and the mean size of microspheres. When the active agent is not soluble in the dispersed phase, the use of a commented drug is a prerequisite to assuring adequate distribution of the particles within the matrix, ensuring significant loadings. However, in the classical emulsion-solvent evaporation method, when the drug pulverization processed, it favouring their dissolution in water. This might explain the use of 5-fluorouracil crystals to minimize the loss of drug in the aqueous phase (32, 33).

### Drug dissolution results

The dissolution of 5-FU from microparticle samples was investigated in simulated gastric liquid at 37 °C for 2h, followed by the simulated intestinal medium for 48h. All drug release profiles are drawn in Figures 9 and 10. As well, the release kinetics of 5-FU from these formulations were evaluated according to the following models in the earlier stage.

Hixson-Crowell model:

$$\boldsymbol{M}t^{1/3} = \boldsymbol{Ks(t)} \quad [7]$$

Higuchi model:

$$\frac{\boldsymbol{M_t}}{\boldsymbol{M_i}} = \boldsymbol{K_H(t)^{\frac{1}{2}} + a} \quad [8]$$

Korsmeyer–Peppas model:

$$\frac{\boldsymbol{M_t}}{\boldsymbol{M_i}} = \boldsymbol{K_K(t)^n} \quad [9]$$

where $M_t$ is the weight of drug dissolved in time t, $Mt/M_i$ = is the fractional drug release; $K_S$, $K_H$ and $K_K$ are, respectively the Hixson-Crowell's, Higuchi's and the Korsmeyer's release constants; and n is an exponent which characterizes the drug release mechanism (34, 35); the results of data analysis are regrouped in Table 4.

$n \leq 0.5$ corresponds to a Fickien diffusion mechanism,
$0.5 < n < 1$ non-Fickien material transport,
n = 1: Transport II (Relaxation) case,
n > 1: Super-II Transport Case II.

**Table 4.** Results of data analysis of the drug release kinetics.

| **N° Lot** | **pH** | **Hixson-Crowell** | | **Higuchi** | | **Korsmeyer-Peppas** | | |
|---|---|---|---|---|---|---|---|---|
| | | K | $R^2$ | K | $R^2$ | K | N | $R^2$ |
| **$F_1$** | 1.2 | 00001 | 0.817 | 1.864 | 0.997 | 0.00019 | 1.39 | 0.988 |
| | 7.4 | 0000 | 0.985 | 0.183 | 0.970 | 0.0026 | 1.709 | 0.971 |
| **$F_2$** | 1.2 | 00001 | 0.927 | 1.831 | 0.990 | 0.00002 | 2.02 | 0.977 |
| | 7.4 | 0000 | 0.959 | 0.154 | 0.985 | 0.0038 | 1.36 | 0.989 |
| **$F_3$** | 1.2 | 00001 | 0.841 | 2.204 | 0.996 | 0.00003 | 1.9 | 0.992 |
| | 7.4 | 0000 | 0.890 | 0.253 | 0.993 | 0.0011 | 2.35 | 0.983 |
| **$F_4$** | 1.2 | 00001 | 0.992 | 1.794 | 0.987 | 0.000015 | 2.32 | 0.985 |
| | 7.4 | 0000 | 0.906 | 0.291 | 0.996 | 0.001 | 2.206 | 0.994 |
| **$F_5$** | 1.2 | 00001 | 0.977 | 0.947 | 0.992 | 0.0002 | 1.45 | 0.996 |
| | 7.4 | 0001 | 0.887 | 0.422 | 0.994 | 0.0006 | 1.96 | 0.997 |
| **$F_6$** | 1.2 | 00001 | 0.935 | 1.190 | 0.980 | 0.0004 | 1.28 | 0.998 |
| | 7.4 | 00001 | 0.941 | 0.478 | 0.980 | 0.00189 | 1.76 | 0.959 |

A number of factors influenced the drug release when 5-FU was encapsulated, including crystal size, morphology, the nature of matrix, dissolution media and the drug formulation.

*In vitro* drug release studies showed that approximately 4 % to 11 % of drug was released at acidic pH (pH = 1.2) from the polymer blends, however higher releases were obtained from the pure polymers (F5 and F6), this is explained by the greater swelling with these formulations. This result is consistent with the morphology of the microspheres, where the drug is uniformly dispersed in the polymer matrix.

At pH = 7.4, 27% to 99% of the drug is released (alkaline pH), previous studies have been performed on 5-FU loaded microspheres using a variety of different types of polymers

(36,37). The results showed that the release half-life of 5-FU is quite short in the colon (10-20 min).

In the same medium, formulations F2, prepared with (70% GL and 30% ε-CL), F1 prepared with (50% GL and 50% ε-CL), released 99% and 90% of 5-FU respectively after 24h, while the F3 formulation, prepared with (30% GL and 70% ε-CL), shows a value of 70% 5-FU after 36 h. Here, addition of EC to PGC makes the microspheres more porous upon exposure to alkaline pH.

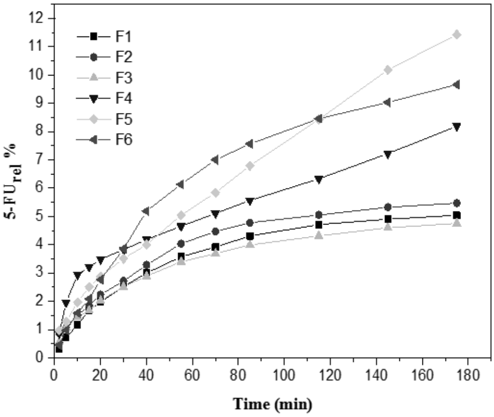

**Figure 9**. 5-FU release profiles from microparticles batches in buffer pH=1.2.

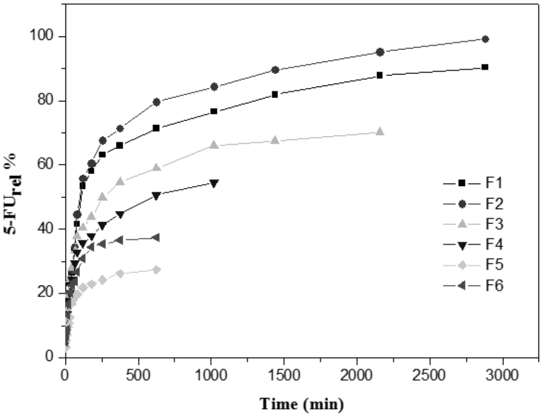

**Figure 10**. 5-FU release profiles from microparticles batches in pH=7.4.

Thus, the formulations prepared with a high content of GL polymer have a lower water absorption capacity, these highly cross-linked matrices are more rigid, and therefore a lower delayed release of 5-FU in an alkaline medium, on the other hand, those prepared with a lower content of GL, better facilitate the release of 5-FU.

Similarly, the F4 formulations from (EC/PCL) released 54% 5-FU after 24 hours following the release experiment. However, formulations F5 (from EC) and F6 (from PCL) released 27% and 37% of 5-FU after 10 h.

The study showed that higher release is observed for formulations loaded with more drug, and that increasing the polymer concentration also promotes drug release (Figure 10). The microspheres obtained with the polymer blend (EC/PCL) showed more delayed release in an alkaline medium, in agreement with the literature (38).

### Release data analysis

As mentioned previously, three mathematical models have been tested in order to identify the mechanism of drug dissolution from these formulations. The models tested for established kinetics are respectively: Hixson-Crowell's model and the two mathematical models most used by pharmacists: Higuchi's and Korsmeyer-Peppas model (39). As seen from table 4, according to the correlation values, release data fitted to the Higuchi's model on all pH values evaluated which indicates that 5-FU is released by diffusion. Except the formulation F1 at pH=7.4 and formulation F4 at pH=1.2 where the highest $R^2$ values were obtained with Hixson-Crowell model.

Higuchi kinetics is based on the release of drug molecules from polymer matrix, as the microspheres interact with release medium active ingredient on the surface or near surface will be expected to release following a burst effect, then the release of active ingredient within the polymer matrix will be realized. Compliance of 5-FU's release profile with Higuchi kinetics showed that the release was mainly diffusion controlled.

However, The Hixson–Crowell model assumes that the drug release is limited by the dissolution rate of the particles, and not by diffusion through the polymer matrix.

By applying the Korsmeyer–Peppas model the diffusion type can be discussed. In fact, the $n$ exponent from Korsmeyer–Peppas model can be used to characterize the drug release mechanisms as Fick diffusion, when $n = 0.5$ and as a non-Fickian model if $n$ is higher than 0.5.

From the kinetic results, the exponent $n$ was higher than 1 (Table 4). We concluded that the drug release follows super case II transport (40).

## CONCLUSION

Through the bulk ring-opening polymerization of glycolide and ε-caprolactone and using stannous(II) octoate as initiator, a series of copolymers with diverse compositions were produced and characterized by FT-IR and by $^1$H and $^{13}$C-NMR spectroscopies. These copolymers were blended with EC to prepare the 5-FU microspheres following the o/w emulsion method.

The matrices were used to study 5-FU controlled release. The encapsulation efficiency of microspheres ranged from 11 to 23%, and FTIR and DRX confirmed the absence of drug-polymer interaction, indicating molecular level dispersion of 5-FU in the formulations. The result of *in vitro* release profiles of 5-FU from the blended formulation have been compared with those unblended microspheres. Higher controlled release of 5-FU occurred in alkaline pH over in acidic pH, suggesting that blended PGC microspheres are able to bypass the gastric environment, while at the same time maintaining its slow-release characteristics in intestinal conditions due to its pH-independent swelling behaviour. The developed devices may be useful as well-suited matrices for colon delivery of 5-FU. The release profiles when analysed by empirical equations suggested the presence of super case II transport mechanism.

## Acknowledgements

This work was supported with grants from financial support by The Ministry of Higher Education and Scientific Research (MESRS) of Algeria in PRFU project code: B00L01UN220120200. A. Ziane would like to thank Dr H. BRAA for their fruitful support.

## REFERENCES

1. Venkatesan, P.; Manavalan, R.; Valliappan, K. Microencapsulation: a vital technique in novel drug delivery system. *J. Pharm. Sci*. **2009**, *1(4)*, 26-35.
2. Jyothi, N. V. N.; Prasanna, P. M.; Sakarkar, S. N.; Prabha, K. S.; Ramaiah, P. S. and Srawan, G.Y. Microencapsulation techniques, factors influencing encapsulation efficiency. *J. Microenc*. **2010**, *27 (3)*, 187-197.
3. Anirudhan, T. S.; Vasantha, C. S.; Sasidharan, A. V. Layer-by-layer assembly of hyaluronic acid/carboxymethylchitosan polyelectrolytes on the surface of aminated mesoporous silica for the oral delivery of 5-fluorouracil. *Eur. Polym. J*. **2017**, *93*, 572-589.
4. Jana, P.; Shyam, M.; Singh, S.; Jayaprakash, V.; Dev, A. Biodegradable polymers in drug delivery and oral vaccination. *Eur. Polym. J*. **2021**, *142*, 110155.
5. Gagliardi, A.; Giuliano, E.; Venkateswararao, E.; Fresta, M.; Bulotta, S.; Awasthi, V.; Cosco, D. Biodegradable polymeric nanoparticles for drug delivery to solid tumors. *Front. pharmac*. **2021**, *12*, 601626.
6. Daniel, S. Biodegradable Polymeric Materials for Medicinal Applications. In *Green Composites.* **2021**, 351-372. Springer, Singapore.
7. Begines, B.; Ortiz, T.; Pérez-Aranda, M.; Martínez, G.; Merinero, M.; Argüelles-Arias, F.; Alcudia, A. Polymeric nanoparticles for drug delivery: Recent developments and future prospects. *Nanomaterials*. **2020**, *10(7)*, 1403.
8. Barakat, N. S.; G, Al-Shazli.; Almedany, A. H. Development of Novel Controlled Release Gliclazide-Loaded poly (ε- caprolactone) Microparticles: Effect of Polymer Blends. *Pharm. Anal. Acta*. **2012**, *03*(03), 2153-2435.
9. D’Avila, C.; Carvalho, E. Synthesis and Characterization of Poly (D, L-Lactide-co-Glycolide) Copolymer. *JBNB*. **2012**, *03(02)*, 208-225.
10. Kasperczyk, J.; Li, S.; Jaworska, J.; Dobrzyński, P.; Vert, M. Degradation of copolymers obtained by ring-opening polymerization of glycolide and ε-caprolactone: A high resolution NMR and ESI-MS study. *Polym. Deg. Stab*. **2008**, *93(5)*,990-999.
11. Park, J. H.; Kang, H. J.; Kwon, D. Y.; Lee, B. K.; Lee, B.; Jang, J. W.; Chun, H. J.; Kim, J. H.; Kim, M.S. Biodegradable poly (lactide-co-glycolide-co-ε-caprolactone) block copolymers – evaluation as drug carriers for a localized and sustained delivery system. *J. Mater. Chem. B*. **2015**, *3 (41)*, 8143-8153.
12. Bennabi, L.; Abiras, H. W.; Belarbi, L.; Bennabi, F.; Chaibi, W.; Guemra, K. Effect of polymer blends and evaluation from controlled release procaine hcl loaded poly (ε- caprolactone) microsphers. *Biointer. Res. App. Chem*. **2016**, *6(5)*, 1483-1490.
13. Dash,T. K.; Konkimalla, V. B. Poly-ϵ-caprolactone based formulations for drug delivery and tissue engineering: A review. *J. Contr. Rel*. **2012**, *158 (1)*,15-33.
14. Campos, J. M.; Ribeiro, M. R.; Ribeiro, M. F.; Deffieux, A.; Peruch, F. Copolymerisation of ε-caprolactone and trimethylene carbonate catalysed by methanesulfonic acid. *Eur.Polym. J*. **2013**, *49 (12)*, 4025-4034.

Original scientific paper

15. Pamula, E.; Dobrzynski, P.; Szot, B.; Kretek, M.; Krawciow, J.; Plytycz, B.; Chadzinska, M. Cytocompatibility of aliphatic polyesters - *In vitro* study on fibroblasts and macrophages. *J. Biomed. Mater. Res*. **2008**, *87(2)*, 524-535.
16. Salerno, A.; Saurina, J.; Domingo, C. Supercritical $CO_2$ foamed polycaprolactone scaffolds for controlled delivery of 5-fluorouracil, nicotinamide and triflusal. *Int. J. Pharm*. **2015**, *496(2)*, 654-663.
17. Serrano, M. C.; Chung, E. J.; Ameer, G. A. Advances and Applications of Biodegradable Elastomers in Regenerative Medicine. *Adv. Funct. Mater*. **2010**, *20 (2)*,192-208.
18. Cai, Q.; Bei, J.; Wang, S. Synthesis and properties of ABA-type triblock copolymers of poly(glycolide-co-caprolactone) (A) and poly (ethylene glycol) (B). *Polym*. **2002**, *43(13)*,3585-3591.
19. Pasban, S.; Raissi, H.; Pakdel, M.; Farzad, F. Enhance the efficiency of 5-fluorouracil targeted delivery by using a prodrug approach as a novel strategy for prolonged circulation time and improved permeation. *Int. J. Pharm*. **2019**, *568*, 118491.
20. Zhang, X.; Wang, W.; Yu, W.; Xie, Y.; Zhang, X.; Zhang, Y.; Ma, X. Development of an in vitro Multicellular Tumor Spheroid Model Using Microencapsulation and Its Application in Anticancer Drug Screening and Testing, *Biotech. Progress*. **2008**, *21(4)*, 1289-1296.
21. Potikanond, S.; Chiranthanut, N.; Khonsung, P.; Teekachunhatean, S. Cytotoxic Effect of *Coscinium fenestratum* on Human Head and Neck Cancer Cell Line (HN31). *Evid. Comp. and Altern. Med*. **2015**, 1-8.
22. Zhang, X.; Wang, W.; Yu, W.; Xie, Y.; Zhang, X.; Zhang, Y.; Ma, X. Preparation and Characterization of Poly (L -lactide-co-glycolide-co-ε-caprolactone) Porous Microspheres. *J. Macro. Sci, PartB*. **2021**, *60(5)*,313-323.
23. Ganguly, K.; Aminabhavi, T. M.; Kulkarni, A. R. Colon Targeting of 5-Fluorouracil Using Polyethylene Glycol Cross-linked Chitosan Microspheres Enteric Coated with Cellulose Acetate Phthalate. *Ind. Eng. Chem. Res*. **2011**, *50(21)*,11797-11807.
24. Kanth, V.; Kajjari, P.; Madalageri, P.;Ravindra, S.; Manjeshwar, L.; Aminabhavi, T. Blend Hydrogel Microspheres of Carboxymethyl Chitosan and Gelatin for the Controlled Release of 5-Fluorouracil. *Pharmaceutics*. **2017**, *9(4)*, 13.
25. Su, M.; Xie, J.; Zeng, Q.; Shu, M.; Liu, J.; Jiang, Z. Enzymatic synthesis of PEGylated lactide-diester-diol copolyesters for highly efficient targeted anticancer drug delivery. *Mat. Sci. Eng: C*. **2020**, *115*, 111125.
26. Engelmann, G.; Jugelt, W.; Kossmehl, G.; Welzel, H. P.; Tschuncky, P.; Heinze, J. Doped Polymers by Oxidative Polymerization. 4. Oxidative Coupling of Methylated Oligothiophenes by $FeCl_3{\cdot}6H_2O$ as a Model Reaction for the Oxidative Polymerization of Thiophene Derivatives. *Macromolecules.* **1996**, *29(10)*, 3370-3375.
27. Woodruff, M. A.; Hutmacher, D. W. The return of a forgotten polymer-Polycaprolactone in the 21st century. *Prog. Pol. Sci*. **2010**, *35(10)*,1217-1256.
28. Lee, S-H.; Kim, B-S.; Kim, S. H.; Choi, S. W.; Jeong, S.I.; Kwon, I. K.; Kang, S.W.; Nikolovski, J.; Mooney, D. J.; Han, Y-K.; Kim, Y. H. Elastic biodegradable poly (glycolide-co-caprolactone) scaffold for tissue engineering. *J. Biomed. Mater. Res.***2003**, *66A (1)*, 29-37.
29. Boumediene, M.; Haddad, B.; Paolone, A.; Drai, M.; Villemin, D.; Rahmouni, M.; Abbas, O. Synthesis, thermal stability, vibrational spectra and conformational studies of novel dicationic meta-xylyl linked bis-1-methylimidazolium ionic liquids. *J. Mol. Struc*. **2019**, *1186*, 68-79.
30. Assenine, M. A.; Haddad, B.; Paolone, A.; Brandán, S. A.; Goussem, M.; Villemin, D.; Bresson, S. Synthesis, thermal properties, vibrational spectra and computational studies of Trioctylmethylammonium bis(trifluoromethylsulfonyl) imide ionic liquid. *J. Mol. Struc*. **2021**, *1232*, 130085.
31. Haddad, B.; Brandán, S. A.; Fetouhi, B.; Boumediene, M.; Paolone, A.; Villemin, D.; Bresson, S. Synthesis, NMR, vibrational spectroscopy, thermal and DFT studies of new DABCO hexafluorophosphate based ionic liquid. *J. Mol .Struc.* **2022**, *1258*, 132682.
32. Lamprecht, A.; Yamamoto, H.; Takeuchi, H.; Kawashima, Y. Microsphere design for the colonic delivery of 5-fluorouracil. *J. Contr. Rel.* **2003**, *90(3)*, 313-322.

33. Boisdron-Celle, M.; Menei, P.; Benoit, J. P. Preparation and Characterization of 5-Fluorouracil-loaded Microparticles as Biodegradable Anticancer Drug Carriers. *J. Pharm. Pharmacol.* **2011**, *47(2),*108-114.
34. Higuchi, T. Mechanism of sustained-action medication. Theoretical analysis of rate of release of solid drugs dispersed in solid matrices. *J. Pharm. Sci*. **1963**, *52(12),*1145-1149.
35. Korsmeyer, R. W.; Lustig, S. R.; Peppas, N. A. Solute and penetrant diffusion in swellable polymers. I. Mathematical modeling. *J. Polym. Sci. B Polym. Phys*. **1986**, *24(2),*395-408.
36. Dhawale, S. C.; Bankar, A.S.; Patro, M. N. Formulation and Evaluation Porous Microspheres of 5- Fluorouracil for Colon Targeting. *Int. J. Pharmatech Res*. **2010**, *2 (2),* 1112-1118.
37. Obayemi, J. D.; Jusu, S. M.; Salifu, A. A.; Ghahremani, S.; Tadesse, M.; Uzonwanne, V. O.; Soboyejo,W. O. Degradable porous drug-loaded polymer scaffolds for localized cancer drug delivery and breast cell/tissue growth. *Mat. Sci. Eng: C.* **2020**, *112,* 110794.
38. Chaturvedi, K.; Kulkarni, A. R.; Aminabhavi, T. M. Blend Microspheres of Poly(3-hydroxybutyrate) and Cellulose Acetate Phthalate for Colon Delivery of 5-Fluorouracil. *Ind. Eng. Chem. Res*. **2011**, *50(18),* 10414-10423.
39. Dash, S.; Murthy, P. N.; Nath, L.; Chowdhury, P. Kinetic Modeling on Drug Release from Controlled Drug Delivery Systems. *Polish. Pharm. Societ*. **2010**, *67(3),* 217-223.
40. Olukman, M.; Şanlı, O.; Solak, E. K.Release of Anticancer Drug 5-Fluorouracil from Different Ionically Crosslinked Alginate Beads. *JBNB*. **2012**, *03(04),* 469-479.

APTEFF, Vol. 54, 1-335 (2023) UDC: 543.573:519.23:[636.32/.38+637.64
DOI: https://doi.org/10.2298/APT2354021P BIBLID: 1450-7188 (2023) 54, 21-35

Original scientific paper

# THERMO GRAVIMETRIC ANALYSIS STUDY OF KINEMATIC PARAMETERS AND STATISTICAL ANALYSIS FOR BIG SHEEP HORN/SCAPULA BONE OF INDIAN ORIGIN

*Arun Y. PATIL[1]*, Tajammul H. M. MYSORE[1], Akshay B. KULKARNI[2], Shridhar N. MATHAD[3], Mallikarjunagouda B. PATIL[4]*

[1] School of Mechanical Engineering, K.L.E Technological University, Hubballi, India
[2] Department of Physics, S.K.E. S's Govindram Seksaria Science College, Belagavi, India
[3] Department of Physics, K.L.E. Institute of Technology, Hubballi, India
[4] Bharat Ratna Prof. CNR Rao Research Centre, Basaveshwar Science College, Bagalkot, India

**Received: 07 October 2022 Revised: 16 December 2022 Accepted: 21 December 2022**

*The current work focus on a novel biomaterial extracted from Indian origin Deccani-Big sheep horn/scapula bone for exhaustive thermal property study using Thermo gravimetric analysis (TGA) and statistical analysis study using log normal to determine the failure rate of brittle material. The TGA shows four regions, first region in the water reduction range, second region is plateau with no change in weight, third regionfor decomposition and last plateau showing stable final product. Broido, Coats-Redfern, Chang and Horowitz-Metzger approximations are employed to compute the activation energy (Ea) of samples during decomposition. The observed average mean tensile strength is 63.38MPa whereas with the help of Weibull distribution shows 64.55MPa with $R^2$ as 0.94.*

**Keywords**: Big sheep horn, Kinetic parameter, TGA, DSC, Statistical analysis.

## INTRODUCTION

Biomaterials have come a long way in today's world and they are making inroads in to unimaginable domains such as bio-medical, high temperature applications to further get accommodated as exotic materials in aerospace, satellite, and agricultural applications (1-5). Micro characterization studies have supported equally in identifying the surface behaviour and in depth understanding of material properties (6-10). Thermo gravimetric analysis has been a critical to decide its thermal aspects for decomposition (11-13). In the past lot many scientists and researchers have worked on the statistical analysis and kinematic parameters to determine the influence by empirical formulas (14). The well-known surface characterization and thermal behaviour studies are based on the models such as Coats-Redfern (15, 16), Broido (17), Horowitz-Metzger (18), Freeman (19), and Chang (20).

The Current work proposes about the chemical steps of the investigated degradation and the evaluation of the kinetic and thermodynamic parameters by using Coats-Redfern, Horowitz-Metzger and Broido methods. The frequency factor (A), entropy change (ΔS), enthalpy change (ΔH) and changes in internal energy (ΔG) of decani sheep horn breed of Indian continent is reported for the first time.

---

* Corresponding author: Arun Y. PATIL, School of Mechanical Engineering, K.L.E. Technological University, Hubballi, India, e-mail: patilarun7@gmail.com

## MATERIAL AND METHODS

Sheep horn has been in the research since last two decades. The current breed Deccani as shown in Fig.1 has been extracted from Haveri district, Karnataka, India. The sheep horn comprising of α keratin and β keratin having lower stiffness and strength than later. Considering the parameters of impact resistive and high temperature conditions this is one of the prominent breed population wise in the middle region of Karnataka, Maharashtra, and Andhra Pradesh. The horns collected from slaughter house are subjected to cleaning the outer skin or scale to make a compatible material for the purpose of kinetic parameter study. The entire horn further, subjected to grinding in clean abrasive blade and the extracted powder subjected to sieve analysis before its send to testing.

**Figure 1.** Big Sheep Horn - Deccani breed

## EXPERIMENTAL

### THERMO GRAVIMETRIC ANALYSIS

TGA is carried out for three forms of sheep horn/scapula bone material. The sheep scapula bone/shoulder bone extraction is of dark brown color in nature (Sample 1 - Dark brown). The sheep horn is extracted in fiber form, is of white color in nature (Sample 2 – White fiber). The sheep horn after extraction dried, heated and powdered (Sample 3 – Powder). Figure 2a illustrate about the dark brown form, figure 2b explains about white fiber form and figure 2c elaborates about the powder form.

The figures show 4 regions, region-I: room temperature to ~90 °C is a continuous decaying phase, where water molecules are lost. Region-II: from ~90 °C to ~250 °C is a plateau region showing no reaction/decomposition/decay. Region-III: from ~250 °C to ~400 °C where a continuous decay in weight is observed, which is decomposition region. Region-IV: above 400˚C where plateau with a continuous slow decay is observed due to oxidation.

Original scientific paper

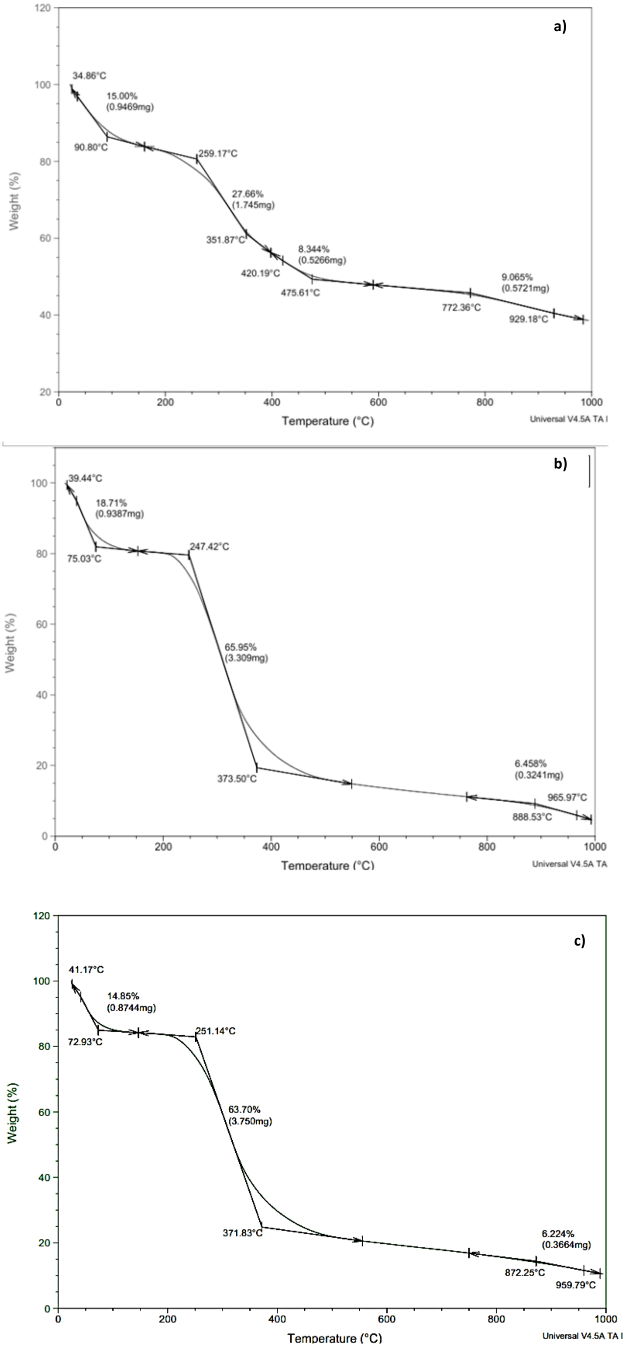

**Figure 2.** TGA for: a) Dark Brown, b) White fiber, and c) Powder samples

## METHODS FOR KINEMATIC PARAMETERS

### Coats and Redfern method

From the Coats and Redfern explanation, the mathematical relation for reaction is given by eq. 1 and 2.

$$\log\left[\frac{-\log(1-\alpha)}{T^2}\right]=\log\frac{AR}{\beta E_a}\left[1-\frac{2RT}{E_a}\right]-\frac{E_a}{2.303RT}\quad \text{For order of reaction n=1} \qquad [1]$$

$$\log\left[\frac{1-(1-\alpha)^{1-n}}{T^2(1-n)}\right]=\log\frac{AR}{\beta E_a}\left[1-\frac{2RT}{E_a}\right]-\frac{E_a}{2.303RT}\quad \text{For order of reaction n}\neq 1 \qquad [2]$$

where, T - Absolute temperature (in Kelvin), A - Frequency factor, Arrhenius constant, Pre-exponential factor (min$^{-1}$), $E_a$ - Activation energy (kJ/mol), R - Universal gas constant (JK -1mol$^{-1}$), n - Order of reaction, β - Rate of heating (20 °C/min), the fraction of sample (α) decomposed $\alpha=\frac{W_0-W_t}{W_0-W_f}$ , $W_t$ - weight of sample at any given temperature T (mg),

$W_o$ – Initial weight of the sample before start of reaction (mg), $W_f$ - final weight of the sample after completion of reaction (mg), W - $W_t$-$W_f$ (mg),

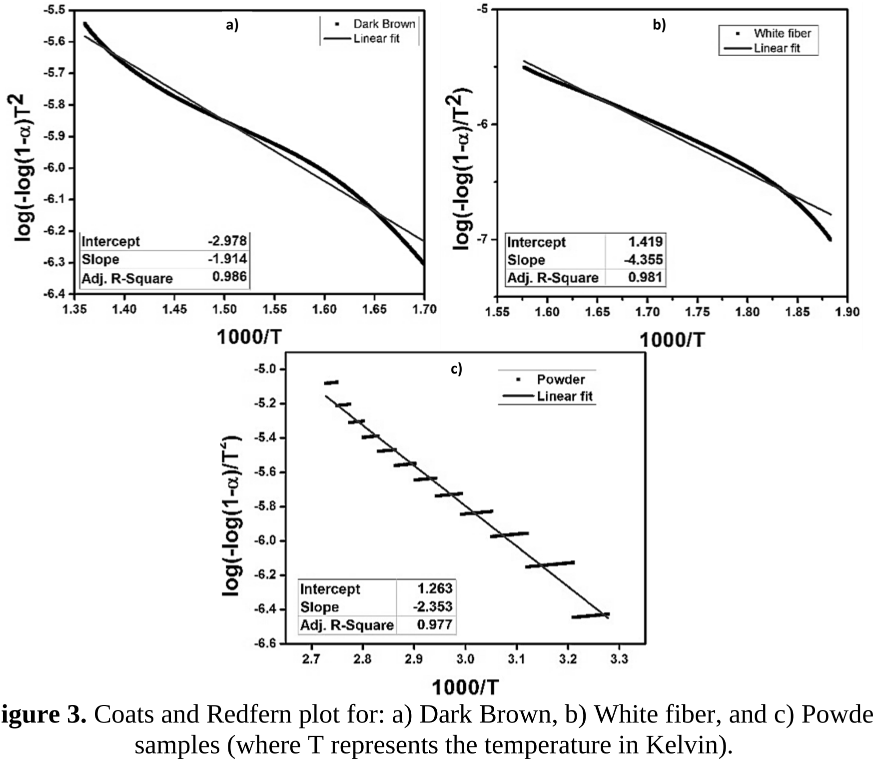

**Figure 3.** Coats and Redfern plot for: a) Dark Brown, b) White fiber, and c) Powder samples (where T represents the temperature in Kelvin).

Assuming n=1 a graph of $log\left[\frac{-log(1-\alpha)}{T^2}\right]$ vs 1000/T is plotted is plotted as shown in Fig. 3 considering $log\frac{AR}{\beta E_a}\left[1-\frac{2RT}{E_a}\right]$ for the vast majority of $E_a$ values and the temperature range in which reactions typically occur, stay remarkably stable. The straight line's slope is $-E_a/2.303R$, and the intercept can be used to calculate the frequency factor A. Table 1 displays the computed activation energy. According to the literature (15-16, 21), the graph deviates from the straight line in the following instances.

## Broido method

Broido employed various approximations in his method (17, 21) and came up with three equivalent following equations [3-5].

$$ln\,ln(1/y)=\left(\frac{E_a}{RT_M}+1\right)ln\,T+Constant \quad [3]$$

$$ln\,ln(1/y)=\left(\frac{E_a}{RT_M^2}\right)T+Constant \quad [4]$$

$$ln\,ln(1/y)=-\left(\frac{E_a}{R}\right)\frac{1}{T}+Constant \quad [5]$$

where, fraction of sample not yet decomposed (y) $y=\frac{W_t-W_f}{W_0-W_f}$, t - Temperature (°C), T – Absolute temperature (K), TM - Temperature at which the rate of sample decomposition is maximum (K).

All three equations produce a linear graph, as seen in Figs. 4, 5, and 6, but the last one, Fig. 6, is believed to be the most accurate according to Broido approximations. After introducing the correction factor S(z), the final equation [6] for determining activation energy for Fig. 4 is:

$$E_a= -S(z)R\frac{\Delta[ln\,ln(1/y)]}{\Delta 1/T} \quad [6]$$

S(z) is assumed to be 0.96 for the full temperature range. The mistake generated by the constant slope assumption over the common heating range is safely less than 10%. The TM value of 557K (dark brown), 550K (white), and 369K is used in the calculation (Powder). Table 1 displays the computed activation energy.

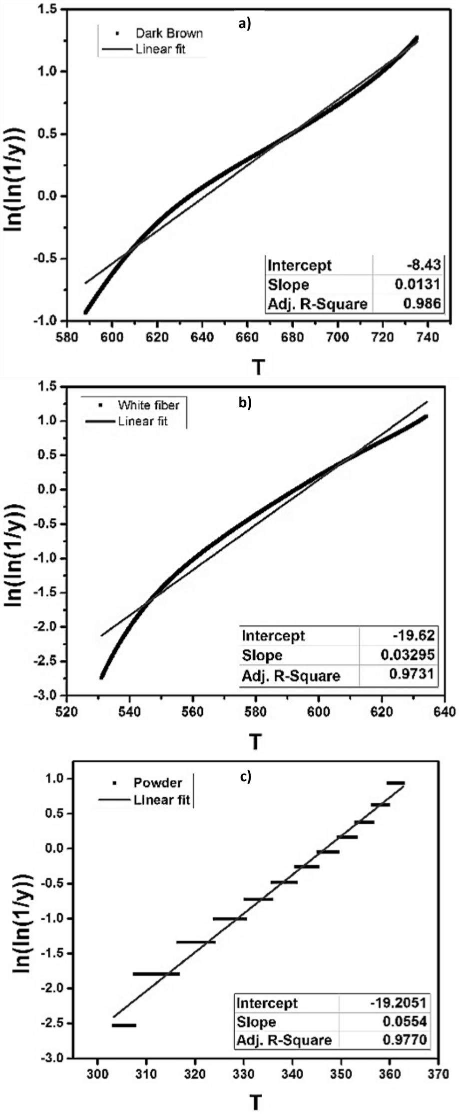

**Figure 4.** Broido plot of *lnln*(1/y) vs. T for a) Dark brown, b) White fiber, and c) Powder samples

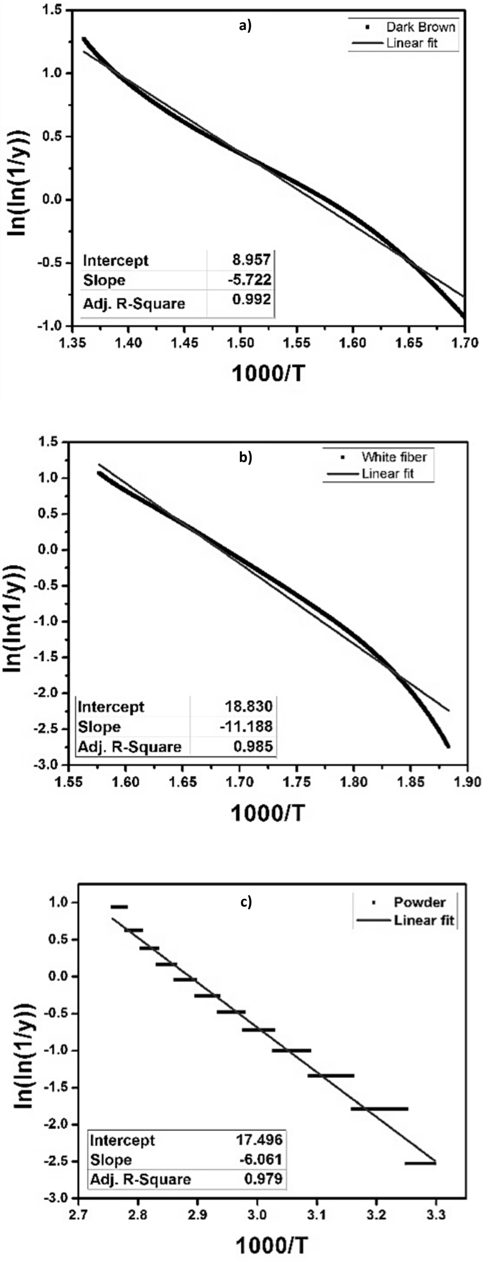

**Figure 5.** Broido plot of *lnln*(1/y) vs. 1000/T for: a) Dark brown, b) White fiber, and c) Powder samples

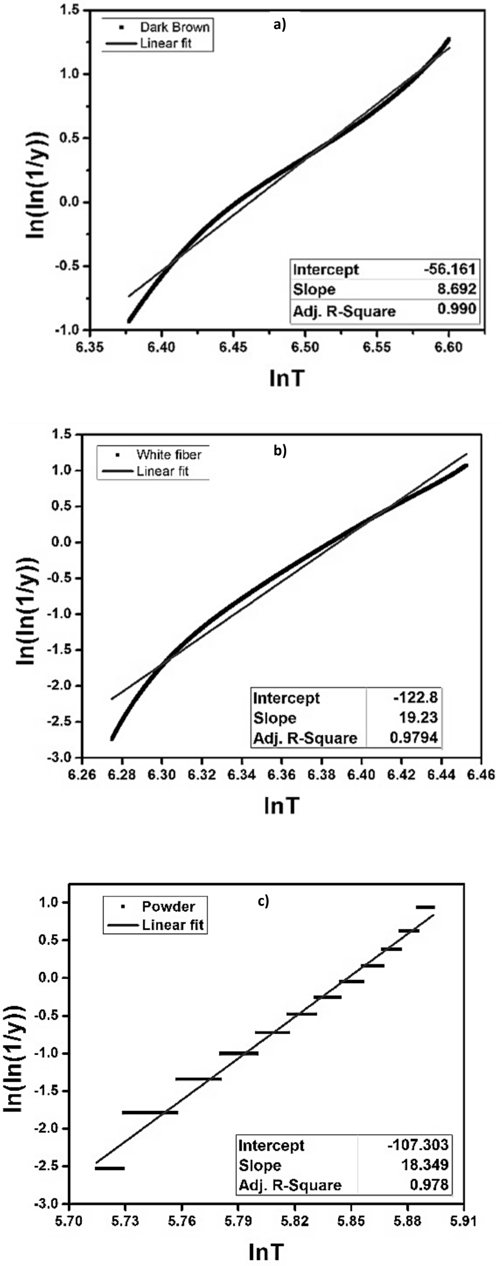

**Figure 6.** Broido plot of *lnln*(1/y) vs. lnT for: a) Dark brown, b) White fiber, and c) Powder samples

### Horowitz-Metzger method

In Horowitz and Metzger method (18, 21), Horowitz and Metzger derived equation [7, 8] assuming θ/Ts<<1 the graph is plotted as shown in Fig. 7.

$$-1 = -\frac{A}{\beta}\frac{RT_S^2}{E_a}e^{-\frac{E_a}{RT_S}} \qquad [7]$$

$$lnln(1/\mathrm{y}) = \frac{\mathrm{E_a}\theta}{\mathrm{RT_S^2}} \qquad [8]$$

where, θ=T-Ts (K), Ts- Temperature defined such that at Ts, W/Wo = l/e. When T=Ts, θ=0 and $W_0$=-1

Activation energy is calculated by taking Ts as634K (Dark brown), 593K (White fiber), 368K (Powder) for decomposition and tabulated in Table 1.

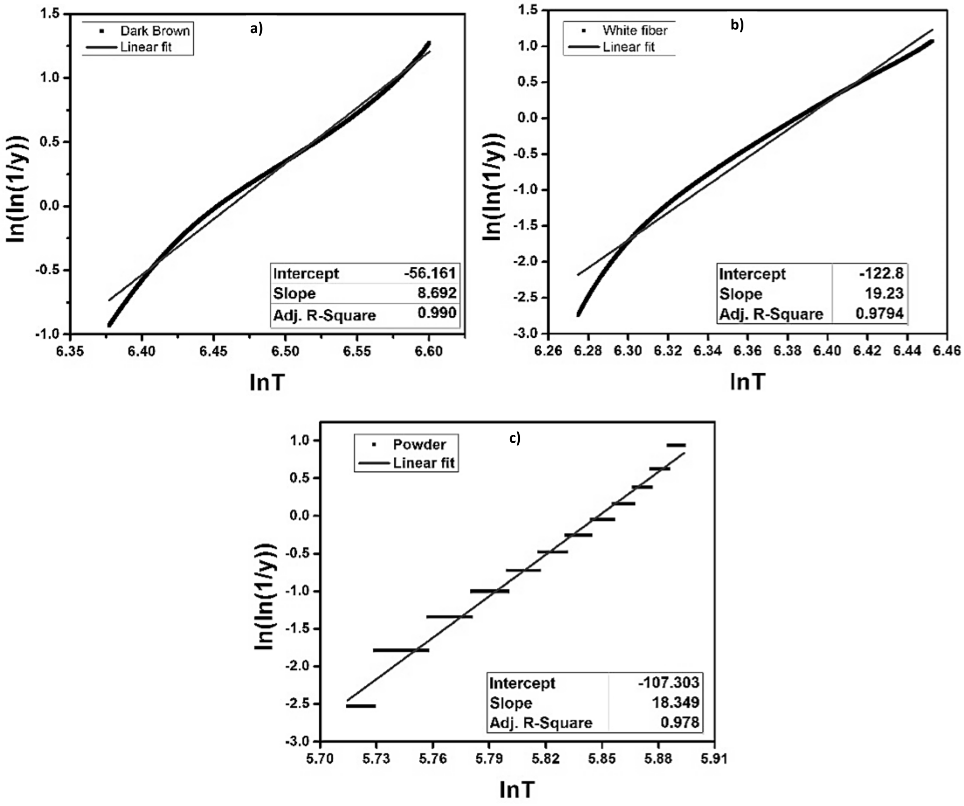

**Figure 7.** Horowitz and Metzger plot of vs. θ for: a) Dark brown, b) White fiber, and c) Powder samples

**Table 1.** Activation energy values from Coats-Redfern, Broido and Horowitz-Metzger methods

| Description | Coats and Redfern | Broido lnln(1/y) vs. lnT | Broido lnln(1/y) vs. T | Broido lnln(1/y) vs. 1000/T | Horowitz and Metzger | Average Activation energy |
|---|---|---|---|---|---|---|
| Activation energy (kJ/mol) Dark Brown sample | 36.66 | 35.62 | 33.92 | 47.59 | 43.94 | 39.55 |
| Activation energy (kJ/mol) White fiber sample | 83.38 | 83.34 | 82.87 | 93.01 | 96.33 | 87.78 |
| Activation energy (kJ/mol) Powder sample | 45.05 | 62.71 | 50.39 | 53.22 | 61.36 | 54.55 |

## STATISTICAL METHODS

### LOG NORMAL DISTRIBUTION

To characterise failure of brittle materials, the logarithmic normal distribution approach is introduced, and the cumulative probability function (22) is given by equation [9]:

$$P_f^{LN} = \frac{1}{2}\left[1 + erf\left(\frac{ln(\sigma)-\mu}{s\sqrt{2}}\right)\right] \qquad [9]$$

where, σ - given uni axial stress, μ - mean= ln (σ_0), σ_0 is geometric mean of fracture strength, s - standard deviation of the natural logarithms of the fracture strength, $P_f^{LN}$- the probability of failure behaviour under the given stress

The probability of failure ($P_f^{LN}$) at a uni axial stress σ, can be calculated using the equation [10] (median rank value),

$$P_f^{LN} = \frac{i\text{-}0.3}{N+0.4} \qquad [10]$$

where i is the rank for the $i^{th}$ sample, and N is the total number of samples tested.

The value of μ can be obtained by plotting the in (failure stress MPa) versus ($2P_f^{LN}$-1) as shown in the Fig. 7 (a-d) below.

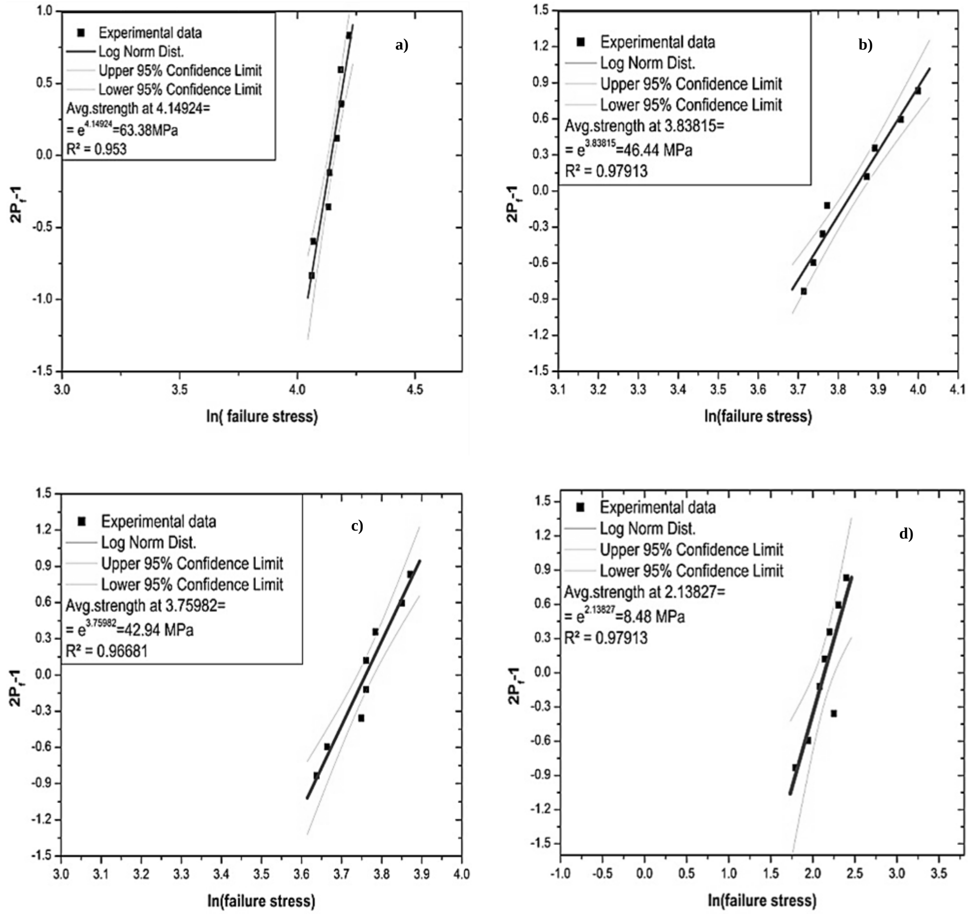

**Figure 7.** Logarithmic normal distribution fitting curve: **a)** for the dry longitudinal specimen of sheep horn’s at the fracture strengths; **b)** for the dry transverse specimen of sheep horn’s at the fracture strengths; **c)** for the wet longitudinal specimen of sheep horn’s at the fracture strengths; and **d)** for the wet transverse specimen of sheep horn’s at the fracture strengths.

According to the above logarithmic normal distribution fitting results, the geometric average strength at μ is extremely close to the arithmetic average stress values which are tabulated below Table 2.

**Table 2.** Strength values of dry longitudinal, dry transverse, wet longitudinal and wet transverse specimens.

| Type of the specimens | Arithmetic mean value of strength MPa | Fitted mean (μ) | Geometric average strength at fitted mean value MPa |
|---|---|---|---|
| Dry Longitudinal | 63.51 | 4.149 | 63.38 |
| Dry Transverse | 46.67 | 3.818 | 46.44 |
| Wet Longitudinal | 43.06 | 3.759 | 42.94 |
| Wet transverse | 8.62 | 2.138 | 8.48 |

## WEIBULL ANALYSIS

The strength (23, 24) of sheep horn is discovered to be statistically dispersed because to the variable severity of defects throughout the keratin fibre. As a result, the typical Weibull model is used to characterize the distribution of failure strength of sheep horn under tension. Equation [11] is used to express the cumulative probability distribution function (25).

$$P_f^{WB} = \left[1\text{-}exp\left(\text{-}V\left(\frac{\sigma\text{-}\sigma_\mu}{\sigma_p}\right)^m\right)\right] \qquad [11]$$

where, $P_f^{WB} = P_f$ - Weibull cumulative distribution/failure probability of horn keratin fiber, V - Volume of the wire specimen, $\sigma_\mu$ - fracture strength threshold value, $\sigma_p$ - Weibull scale parameter that represents the stress when $P_f^{WB} = 63.2$ %, m - Weibull modulus, which depicts fracture strength variability; a lower 'm' indicates a broad distribution of fracture strength, while a higher 'm' indicates a narrow distribution.

Table 3 summarizes the Weibull parameters of Deccani breed sheep horn based on the two-parameter Weibull model. In comparison with all the type of specimen dry longitudinal specimen has high value of Weibull modulus. This indicates that the material is more consistent means its uniform and defects are evenly distributed in longitudinal direction as compared to transverse direction and narrower is probability distribution curve for failure strength. McCabe (27) stated that “it would appear that Weibull modulus of at least 10 is necessary in order that a test to be acceptable for multicenter testing”.

**Table 3.** Shape factor and scale factor of dry longitudinal, dry transverse, wet longitudinal and wet transverse specimens.

| Type of the specimen | No of samples | Shape factor (Weibull modulus m) | Scale factor ($\sigma_p$) MPa | $R^2$ |
|---|---|---|---|---|
| Dry Longitudinal | 8 | 18.620 | 64.555 | 0.94 |
| Dry Transverse | 8 | 9.552 | 48.618 | 0.93 |
| Wet Longitudinal | 8 | 13.130 | 44.656 | 0.97 |
| Wet transverse | 8 | 5.079 | 9.388 | 0.91 |

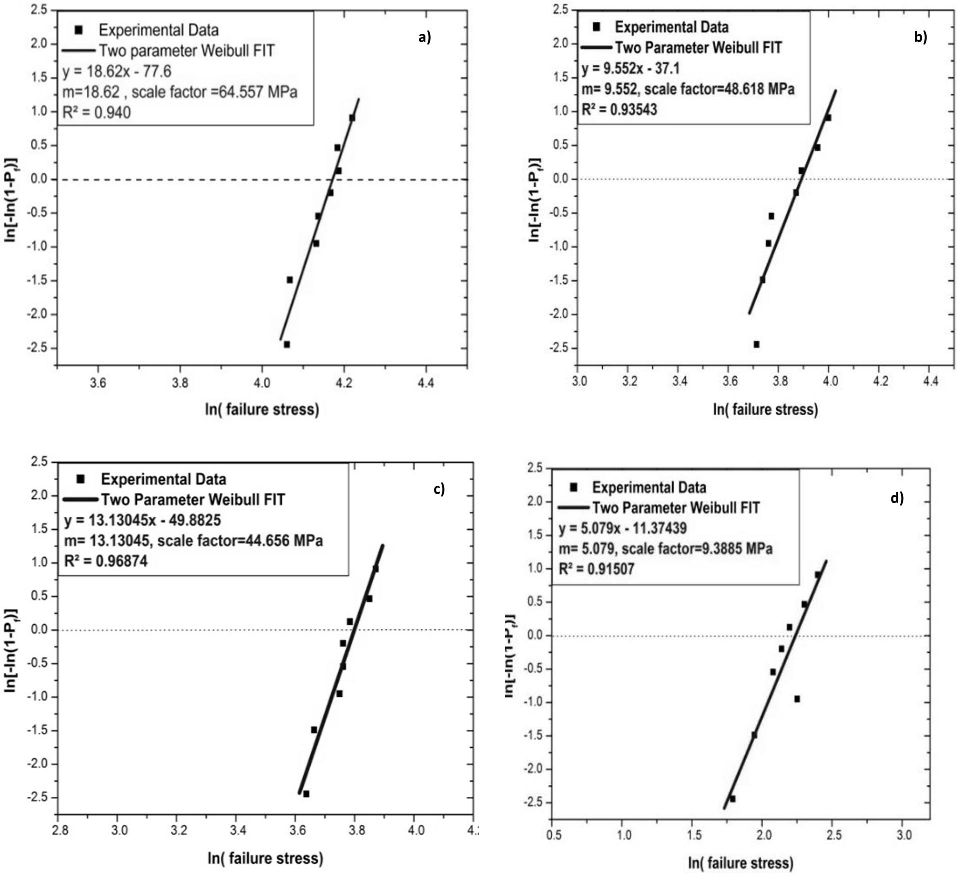

**Figure 8.** Two parameter Weibull distribution fitting curve for: **a)** the dry longitudinal specimen at the failure strengths; **b)** the dry transverse specimen at the failure strengths; **c)** the wet longitudinal specimen at the failure strengths; and **d)** the wet transverse specimen at the failure strengths.

## CONCLUSION

The sheep scapula bone/shoulder bone extraction is of dark brown color in nature, the sheep horn is extracted in fiber form, is of white color in nature, the sheep horn after extraction dried, heated and powdered. The TGA of extracted samples is taken showing a similar nature for all three samples. The activation energy of decomposition of material is calculated using different approximations like, Coats &Redfern, Broido and Horowitz methods. The average activation energy is observed to be 39.55 kJ/mol (Dark Brown), 87.78 kJ/mol (White Fiber) and 54.55 kJ/mol (Powder). The strength values of the samples calculated using logarithmic normal distribution and Weibull distribution. The geometric and arithmetic average strength and shape factors are also in good agreement.

APTEFF, Vol. 54, 1-335 (2023) UDC: 543.573:519.23:[636.32/.38+637.64
DOI: https://doi.org/10.2298/APT2354021P BIBLID: 1450-7188 (2023) 54, 21-35

Original scientific paper

## REFERENCES

1. Meyers, M.A.; Chen, P.-Y.; Lin, A.Y.-M.; Seki, Y. Biological materials: Structure and Mechanical properties. *Prog. Mater. Sci.* **2008**, *53*, 1–206.
2. McKittrick, J.; Chen, P.Y.; Tombolato, L.; Novitskaya, E.E.; Trim, M.W.; Hirata, G.A.; Olevsky, E.A.; Horstemeyer, M.F.; Meyers, M.A. Energy absorbent natural materials and bioinspired design stratergies: A review. *Mater. Sci. Eng. C,* **2010**, *30*, 331.
3. Tombolato, L.; Novitskaya, E.E.; Chen, P.Y.; Sheppardd, F.A.; McKittrick, J. Microstructure, elastic properties and deformation mechanisms of horn keratin. *Acta Biomater*. **2010**, *6*, 319–330.
4. Mysore, T.H.M.; Patil, A.Y.; Raju, G.U.; Banapurmath, N.R.; Bhovi, P.M.; Afzal, A.; Alamri, S.; Saleel, C.A. Investigation of Mechanical and Physical Properties of Big Sheep Horn As an Alternative Biomaterial for Structural Applications. *Materials*, **2021**, *14*, 4039. https:// doi.org/10.3390/ma14144039.
5. Srivastava, B.; Khatri, M.; Singh, G.; Arya, S.K. Microbial keratinases: An overview of biochemical characterization and itseco-friendly approach for industrial applications. *J. Clean. Prod.* **2020**, *252*, 119847.
6. Patil, A. Y.; Naik, A.; Vakani, B.; Kundu, R.; Banapurmath, N. R.; Roseline, M.; Krishnapillai, L.; Mathad, S. N. Next Generation material for dental teeth and denture base material: Limpet Teeth (LT) as an alternative reinforcement in Polymethylmethacrylate (PMMA), *Journal of nano- and electronic physics*, **2021**, *13* (2), 02033, 6 pp. DOI: 10.21272/jnep.13(2).02033
7. Liu, S.; Xu, S.; Song, J.; Zhou, J.; Xu, L.; Li, X.; Zou, M. Mechanical properties and failure deformation mechanisms of yak hornunder quasi-static compression and dynamic impact. *J. Mech. Behav. Biomed. Mater*. **2020**, *107*, 103753.
8. Patil, A.Y.; Banapurmath, N.R.; EP, S.; Chitawadagi, M.V.; Khan, T.M.; Badruddin, I.A.; Kamangar, S. Multi-Scale Study on Mechanical Property and Strength of New Green Sand (Poly Lactic Acid) as Replacement of Fine Aggregate in Concrete Mix. *Symmetry*, **2020**, *12*, 1823.
9. Dhaduti, S.C.; Sarganachari, S.G.; Patil, A.Y.; Khan, T.Y. Prediction of injection molding parameters for symmetric spur gear. *J.Mol. Model*. **2020**, *26*, 302.
10. Kumar, N.V.; Banapurmath, N. R.; Sajjan, A. M.; Patil, A. Y.; Ganachari, S.V. Studies on Hybrid Bio-nanocomposites for Structural applications, *J. of Materi. Eng. and Perform.* **2021**, *30,* 6461–6480. https://doi.org/10.1007/s11665-021-05843-9.
11. Patil, V.S.; Banoo, F.; Kurahatti, R.V.; Patil, A. Y., Raju, G.U.; Afzal, A.; Soudagar, M. E. M.; Kumar, R.; Ahamed Saleel, C. A study of sound pressure level (SPL) inside the truck cabin for new acoustic materials: An experimental and FEA approach, *Alexandria Engineering Journal*, **2021**, 60(6), 5949-5976. https://doi.org/10.1016/j.aej.2021.03.074.
12. Król, P. Synthesis methods, chemical structures and phase structures of linear polyurethanes. Properties and applications of linear polyurethanes in polyurethane elastomers, copolymers and ionomers. *Prog Mater Sci*. **2007**, *52*(6), 915-1015.
13. Madhusudhana, H. K.; Kumar, M. P.; Patil, A. Y.; Keshavamurthy, R.; Khan, T. M. Y.; Badruddin, I. A.; Kamangar, S. Analysis of the Effect of Parameters on Fracture Toughness of Hemp Fiber Reinforced Hybrid Composites Using the ANOVA Method. *Polymers*, **2021**, *13*, 3013. https://doi.org/10.3390/polym13173013
14. Keshavamurthy, R.; Tambrallimath, V.; Rajhi, A. A.; R. M, S. A.; Patil, A.Y.; Yunus Khan, T.M.; Makannavar, R. Influence of Solid Lubricant Addition on Friction and Wear Response of 3D Printed Polymer Composites. *Polymers*, **2021**, *13*, 2905. https://doi.org/10.3390/polym13172905.
15. Coats, A.W.; Redfern, J. P. Kinetic Parameters from Thermogravimetric Data, *Nature*, **1964**, *201*, 68-69.
16. Coats, A.W., Redfern, J. P., Thermogravimetric Analysis. A review. *Analyst*, **1963**, *88,* 906-924.
17. Broido, A. A simple, sensitive graphical method of treating thermogravimetric analysis data. *Journal of Polymer Science,* **1969**, *7,* 1761-1773. https://doi.org/10.1002/pol.1969.160071012

18. Horowitz, H. H.; Metzger, G. A New Analysis of Thermogravimetric Traces. *Analytical Chemistry*, **1963**, *35* (10), 1464-1468. https://doi.org/10.1021/ac60203a013.
19. Freeman, E.S.; Carroll, B. The Application of Thermoanalytical Techniques to Reaction Kinetics: The Thermogravimetric Evaluation of the Kinetics of the Decomposition of Calcium Oxalate Monohydrate. *The Journal of Physical Chemistry*, **1958**, *62*, 394-397. http://dx.doi.org/10.1021/j150562a003
20. Chang, W. L. Decomposition behavior of polyurethanes via mathematical simulation. *Journal of Applied Polymer Science*, **1994**, *53* (13), 1759-1769.
21. Kulkarni A.B.; Mathad, S.N.; Bakale, R.P. The evaluation of kinetic parameters for cadmium doped Co-Zn ferrite using thermogravimetric analysis. *Ovidius University Annals of Chemistry*, **2019**, *30* (1), 60-64.
22. Sharpe, W. N.; Pulskamp, J.; Gianola, D. S.; Eberl, C.; Polcawich, R. G.; Thompson, R. J. Strain measurements of silicon dioxide microspecimens by digital imaging processing. *Exp. Mech*. **2007**, *47*, 649–658. DOI:10.1007/s11340-006-9010-z.
23. Amornsakchai, T.; Cansfield, D.L.M.; Jawad, S.A.; Pollard, G.; Ward, I.M. The relation between filament diameter and fracture strength for ultra-high-modulus polyethylene fibres. *J. Mater. Sci.* **1993**, *28*, 1689–1698.
24. Thomason, J.L. On the application of Weibull analysis to experimentally determined single fibre strength distributions. *Compos. Sci. Technol.* **2013**, *77*, 74–80.
25. Weibull, W.A. Statistical distribution function of wide applicability. *J. Appl. Mech*. **1951**, 3, 293-297.
26. Sullivan, J. D.; Lauzon, P. H. Experimental probability estimators for Weibull plots. *J. Mater. Sci. Lett.*, **1986**, *5*, 1245-1247.
27. McCabe, J. F.; Watts, D. C.; Wilson, H. J.; Worthington, H. V. An investigation of test house variability in the mechanical testing of dental materials and the statistical treatment of results. *J. Dent.* **1990**, *18* (2), 90-97. doi: 10.1016/0300-5712(90)90091-r

APTEFF, Vol. 54, 1-335 (2023)
DOI: https://doi.org/10.2298/APT2354037N
UDC: 678.7:691.771:678.029.4:67.017
BIBLID: 1450-7188 (2023) 54, 37-50

Review paper

# REVIEW OF POLYMER-MATRIX COMPOSITES WELDED TO ALUMINIUM ALLOYS

*Agha Inya NDUKWE*, Chukwudike ONUOHA, Chioma Emmanuella NJOKU,*
*Nsikan Etim DAN, Justus Uchenna ANAELE*

Materials & Metallurgical Engineering Department, Federal University of Technology, Owerri, Imo State, Nigeria

**Received: 21 November 2022** **Revised: 10 January 2023** **Accepted: 16 January 2023**

*This review covers previous work by different scholars on welding polymer-matrix composites to aluminium alloys between 2015 and 2021. The highest tensile shear stress measured for the joint between polymer-matrix composite and aluminium (AA7075) alloy was 59.9 MPa. Welding using top-thermic friction stir was the method that produced the desired outcome. Additionally, the aluminium (AA2024) alloy and fibre-reinforced polymer composite were joined using an ultrasonic metal welding procedure, which produced a weld with a high tensile shear strength of roughly 58 MPa. The friction-aided joining of carbon fibre-reinforced polyphenylene sulphide composites and aluminium (AA7075) alloy has been studied by researchers. A laser treatment was applied to the aluminium surface to enhance the interlocking between the two materials being combined. This development was reported to cause inadequate bonding between the polymer-matrix composite and the metal. Despite this, the joints demonstrated significant load-bearing capacities of up to 10.7 kN.*

**Keywords**: polymer-matrix composites, mechanical properties, reinforcements, welding, aluminium alloys.

## INTRODUCTION

Composites are joined to metals to exploit their distinctive characteristics and considerably improve the metal's isotropic behaviour (1). Several welding methods have been employed in the joining of composites to metals (2). When welding thermoplastic composites to metals, the interface at the joint is heated above the melting point (for semicrystalline polymers) or beyond the glass transition temperature (for amorphous polymers) and is then compressed to consolidate (3). Thermosetting and thermoplastic polymers are often used as matrices for polymer matrix composites for various technical applications due to their low melting points (4), lightness in weight, and ease of processing amongst others. Nonetheless, thermoplastic-based composites are mostly utilized because they can be recycled, have shorter times of processing, have high resistance to impact (3, 5), and can be applied from microelectronics to large wind turbine blades (6).

Two or more components (phases) are combined to form a composite material (7, 8, 9). The overall composite will have qualities that are distinct from those of its constituent parts while maintaining the characteristics of each. Rice and Sparks (8) reported that the matrix and one or more scattered phases are the two distinct and separate phases that must be present in a composite material. When compared to any of the components, its bulk characteristics are different. The scattered phase is held in place by and shares a load with the

---

* Corresponding author: Agha Inya NDUKWE, Materials & Metallurgical Engineering Department, Federal University of Technology, Owerri, Imo State, Nigeria, e-mail: agha.ndukwe@futo.edu.ng

UDC: 678.7:691.771:678.029.4:67.017
BIBLID: 1450-7188 (2023) 54, 37-50

Review paper

matrix, the principal continuous phase. Typically, it is a softer phase and is more ductile. The secondary phases that are incorporated into the matrix are called dispersed phases. The reinforcing phase is frequently used to describe this phase since it is often stronger (8).

Numerous metallic components have been replaced with composite materials, particularly in the sectors of aircraft, avionics, civil structures, automobiles, and sports equipment (8). Future use of these materials is anticipated to see a patronage increase of roughly 5% on average annually. Their high strength and stiffness-to-weight ratio are factors contributing to this increase. Some advanced composite materials can be as strong and rigid as some structural metal alloys while having a much lower density and total component weight (10). Advanced composites are very appealing in circumstances where the component's weight is important because of these features. The fundamental drawback of most composite materials, similar to ceramic materials, is their fragility and low fracture toughness. By carefully choosing the matrix material, some of these flaws may be remedied in specific circumstances (7, 8).

Polymer-matrix composites (PMCs) have lower strength and heat resistance compared to the metal matrix and ceramic matrix composites (8). The maximum service temperature is typically determined by the polymer matrix since it frequently softens, melts, or degrades at a much lower temperature than the fibre (7). The least expensive polymer resins are polyesters and vinyl esters. Glass fibre-reinforced composites are the primary end-uses for these matrix materials (11). Several resin compositions offer a variety of properties for these polymers. Epoxies are widely used in PMCs for aerospace applications because they are more moisture-resistant and have better mechanical qualities than polyester and vinyl resins. The highest temperature for continuous use of polyimide resins, which are employed in high-temperature applications, is about 230 °C. Lastly, high-temperature thermoplastic resins with promise for use in aerospace applications include polyether-ether-ketone (PEEK), poly (phenylene sulphide), and polyetherimide (7).

The joining of thermoplastic composites is a crucial step in the construction of thermoplastic composite aeroplane structures. Researchers have studied and developed a few joining methods for thermoplastic composite components. The main types of attachment for thermoplastic composites are mechanical fastening, welding, or fusion bonding, solvent bonding, and adhesive bonding. Welding offers a lot of potential for joining, assembling, and repairing thermoplastic composite components and has several advantages over other joining techniques. Fusion-bonding includes melting the polymer on the component bond surfaces, forcing those surfaces together, and then allowing the polymer to solidify and consolidate (12).

## COMPOSITES MADE OF POLYMER-MATRIX THAT CAN BE WELDED TO ALUMINIUM ALLOYS

### POLYMER-MATRIX COMPOSITES (PMCS)

In polymer-matrix composites (PMCs), which feature a polymer resin matrix, fibres act as the reinforcing medium. These materials are used in the biggest variety of composite applications and in, the highest quantities because of their room-temperature properties, ease of manufacture, and low cost (7). Future developments are required to boost mechanical characteristics even more and create quick and affordable processing techniques. Finding reinforcements and processing settings that can meet these demands are therefore heavily prioritized (6, 13).

## COMPOSITES MADE OF GLASS FIBRE-REINFORCED POLYMERS

Fibres enclosed in a polymer matrix make up the composite material known as fibreglass (7). Typically, fibre diameters fall between 3 and 20 μm. Several factors make glass an attractive material for fibre reinforcement. When combined with other polymers, it produces a composite with a very high specific strength, which makes the composite useful in a variety of hostile environments (14). It can be produced into an affordable glass-reinforced plastic using a wide range of composite production processes, and it is widely available.

Numerous manufacturing processes are used to produce glass fibre-reinforced polymer composites, which are extensively used in a wide range of industries. Glass fibre-reinforced composites have received a great deal of investigation in recent years (15) because of their exceptional mechanical properties. They have been used often in advanced technical applications. But because composites are anisotropic, it can be very difficult to detect damage and failure when they are subjected to real-time loads (16).

## COMPOSITES MADE OF CARBON FIBRE-REINFORCED POLYMER

Composites made of carbon fibre-reinforced polymer (CFRP) are incredibly strong and light fibre-reinforced polymers. They are widely employed in an expanding variety of consumer and technical applications that call for materials with a high strength-to-weight ratio and stiffness (rigidity) (7, 17). Although other thermoset or thermoplastic polymers, such as polyester, vinyl ester, or nylon, are sometimes utilised, the binding polymer is often a thermoset resin like epoxy. However, it is occasionally necessary to manually process CFRP composites to get the desired design (18).

## ARAMID FIBRE–REINFORCED POLYMER COMPOSITES

A long-chain synthetic polyamide fibre with at least 85% of the amide linkages directly connected to two aromatic rings is known as an "aramid fibre" (41). Because they beat metals in terms of strength-to-weight ratios, aramid fibres are frequently used. Since the fibres are ductile and relatively flexible, they may be processed using the most common textile methods. The most important trade names for aramid textiles include Nomex and Kevlar (7). These aramid composites are often employed in ballistic products (bulletproof jackets and armour), sports equipment, tires, ropes, missile casings, and pressure vessels, and as an asbestos substitute in brake and clutch linings and gaskets for vehicles (7).

## WELDING POLYMER-MATRIX COMPOSITES TO ALUMINIUM ALLOYS

In the production process of welding, components are melted together and then cooled to create fusion, thereby joining the materials. Welding can take place between a thermoplastic and a metal. The parent metal (base metal) is melted during welding, unlike lower-temperature processes like brazing and soldering (20, 21). When the polymer chains on the surface of one component are sufficiently mobile to entangle with chains on the surface of the other component, polymer welding occurs (22).

Not all welding techniques are appropriate for connecting composites made of polymer-matrix materials with aluminium alloys. Abrasive stir welding, according to Huang et al. (23), is a potential production technique for combining aluminium and polymer-matrix materials because it joins the materials below their melting temperatures (23, 24). The two components may be fused - a technique known as fusion welding - or they may be joined together under pressure and maybe with the addition of heat to form a metallic connection across the interface.

## STIR-WELDING USING FRICTION FOR POLYMER-MATRIX COMPOSITES AND ALUMINIUM ALLOYS JOINTS

Since its invention in 1991, friction stir welding has been utilised to combine thermoplastics as well as aluminium alloys (25).

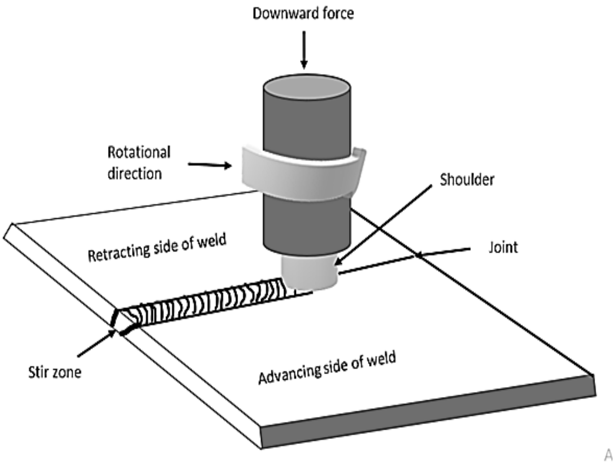

**Figure 1.** The friction stir welding method (26, 27)

Contrary to conventional friction welding techniques, which rely on relative motion between the two elements to be fused, friction stir welding involves driving a rotating or reciprocating tool down the joint line between two stationary components. As a result of frictional contact between the material and the moving tool, the polymer at the junction melts (25), and when the tool has passed, the material solidifies to form a weld (25), as seen in Figure 1 (26, 27).

## ULTRASONIC WELDING OF POLYMER-MATRIX COMPOSITES TO METALS

High-frequency mechanical sound energy is used in ultrasonic welding to soften or melt the thermoplastic at the connecting line. Under pressure, ultrasonic vibrations at a frequency of 20 or 40 kHz are then applied to the pieces that need to be joined through the welding horn (25). Figure 2 (28, 29) depicts the ultrasonic welding setup.

Review paper

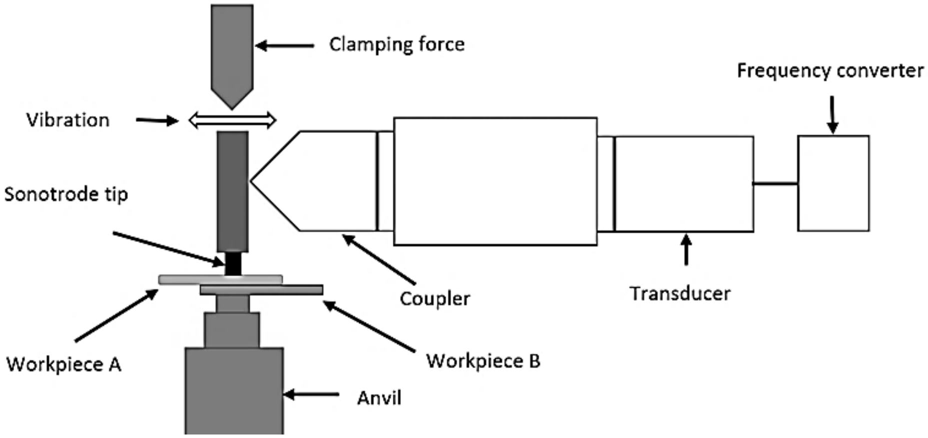

**Figure 2.** Set-up for the ultrasonic welding (28, 29)

The ultrasonic welding method has a varying heating effect depending on the type of material being welded. The mechanical properties of the material to be welded, the component design, and the welding equipment design all have an impact on how successfully a component can be welded (25). The thermoplastic composite structures may be joined quickly and with high bonding strength using the ultrasonic welding (UW) process (30).

Due to the significant difference in the thermal expansion coefficients of metal and composite, ultrasonic welding is currently only possible at very small polymer matrix composite-metal junctions (31). This variation in coefficients of thermal expansion, according to Melentiev et al. (31), might lead to thermal cycling wear.

## LASER WELDING OF METALS TO POLYMER-MATRIX COMPOSITES

During laser welding, a strong beam of light, frequently in the infrared portion of the electromagnetic spectrum, is directed towards the material to be connected (32). This causes a resonance frequency in the molecule to be excited, which heats the substance in the vicinity.

The use of laser welding in the industry has just recently emerged after being originally tested on thermoplastics in the 1970s (25). The two types of laser welding that are frequently used are transmission, and carbon dioxide laser welding techniques. Plastics easily absorb $CO_2$ laser radiation, but they also restrict the depth to which the beam may penetrate, making film applications the only feasible use for the method. The Nd: YAG and diode lasers have less of a tendency to absorb their radiation than other types of lasers and are appropriate for transmission laser welding. To guarantee that the laser beam concentrates on the joint region during welding, one of the polymers must transmit laser light while the other must absorb laser energy (25).

APTEFF, Vol. 54, 1-335 (2023)
DOI: https://doi.org/10.2298/APT2354037N

UDC: 678.7:691.771:678.029.4:67.017
BIBLID: 1450-7188 (2023) 54, 37-50

Review paper

# OVERVIEW OF CURRENT LITERATURE RELATED TO THE JOINING OF POLYMER-MATRIX COMPOSITES (PMC) TO METALS

## TRENDS IN ACADEMIC RESEARCH ON COMPOSITES WITH POLYMER-MATRIX WELDED TO METALS (2015 – 2021)

Discussions in the previous sections have mentioned the various techniques which have been used successfully to join polymer-matrix composites (PMCs) to metals. PMCs – metal joints have recently attracted several research interests from various authors across the globe. For instance, up to 9,083 papers have been published on PMCs welded to metal between 2015 to 2021 as presented in Table 1.

**Table 1.** Polymer-matrix composites that are welded to metals: trends in academic publications (2015 – 2021)

| Year | Publications on polymer-matrix composites welded to metals | Ref. |
|---|---|---|
| 2015 | 796 | (33) |
| 2016 | 927 | [34) |
| 2017 | 1,090 | (35) |
| 2018 | 1,220 | (36) |
| 2019 | 1,400 | (37) |
| 2020 | 1,630 | (38) |
| 2021 | 2,020 | (39) |
| Total | 9,083 | |

As can be seen from Table 1, there is a progressive growth in research about joining PMCs to metals. This can be attributed to the recent demand for metal-composite structures in several engineering applications, especially in aircraft industries (40). The overview of the findings of some of these studies on the welding of PMC to metals is presented in Table 2.

## PREVIOUS STUDIES ON POLYMER-MATRIX COMPOSITES WELDED TO METALS

Table 2 provides a summary of several studies that have looked at the welding of polymer-matrix composites to metals.

Meng et al. (41) studied joints composed of PMCs and metals using the friction self-riveting welding method. The PMCs were softened and squeezed into the pre-fabricated holes and porous oxide structures under the frictional heat and forging force, mimicking the squeezing behaviour of the joining process to cause mechanical interlocking. The resulting joints were evaluated to ascertain their strength. It was observed that the joint attained maximum tensile shear strength of 27 MPa. In another study conducted by Li et al. (42), in which a PMC was joined to AA7075 aluminium alloy using a top-thermic friction stir lap welding technique. The tensile shear strength of the joint was found to be 59.9 MPa. Al-Obaidi (61) investigated the influence of prominent bonding factors (metal thickness, vibration amplitude, and bonding forces) on the ultrasonic joining of an amorphous thermoplastic polymer (ABS 750 SW) to an aluminium alloy (Al 6082-T6). He concluded that increasing bonding pressures, oscillation amplitude, and bonding duration resulted in increased lap shear strength (> 2.31 MPa), and pre-treatment of Al alloy resulted in improved mechanical interlocking between the polymer and metal alloy surfaces.

**Table 2.** A summary of prior research on metal-welded polymer-matrix composites

| Welded materials | Welding technique | The strongest possible tensile shear (load) attained | Ref. |
|---|---|---|---|
| Metal + polymer-matrix composite | Friction self-riveting welding | 27 MPa | (41) |
| 7075 aluminium alloy + polymer-matrix composite | Welding using top-thermic friction stir | 59.9 MPa | (42) |
| Aluminium alloy 6014 with carbon fibre-reinforced polymer composite | Spot welding with regenerated friction | (1.6 kN) | (43) |
| Short carbon fibre reinforced polyether-ether ketone composite with aluminium alloy AA2060-T8 | Friction stir welding with joint performance and shape control | 33 MPa | (44) |
| Composite made of carbon fibre-reinforced polymer and aluminium alloy | An innovative static shoulder design for friction stir spot welding | (0.26 kN) | (45) |
| Aluminium alloy + polymer composite | Electromagnetic pulse welding | - | (46) |
| AA5754 aluminium alloy + poly methyl methacrylate composite | Stir-welding using friction | 50 MPa | (47) |
| Metal + thermoplastic composite | Welding using resistance elements | - | (48) |
| Composite made of polyether ether ketone reinforced with carbon fibre and aluminium alloy | Spot weld using the friction-stir process | (2.69 kN) | (49) |
| Composite material reinforced with extra carbon fibre and aluminium alloy (AA5052) | Spot weld using the friction-stir process | (1.78 kN) | (50) |
| Aluminium alloy AA7075 with carbon-reinforced polyphenylene sulphide | Joining with friction. | (10.7 kN) | (51) |
| SS304 stainless steel + glass fibre reinforced plastic composite | YAG Continuous wave laser welding | (4 kN) | (52) |
| Composite material made of carbon fibre and 6061 aluminium alloy | Hybrid laser-arc welding | (4.65 kN) | (53) |
| Aluminium alloy (AA5754) + composite made of carbon fibre-reinforced epoxy | Spot welding with ultrasound | 34.8 MPa | (54) |
| Aluminium alloy (AA2024) + composite of fibre reinforced polymer | Spot welding with ultrasound | 58 MPa | (55) |
| Composite made of carbon fibre reinforced polymer + aluminium sheet | Spot welding with ultrasound | 30 MPa | (56) |
| aluminium (AA5052) alloy and Composite made of polypropylene and short carbon fibres (PP-SCF) | A new refill friction spot welding | 28 MPa | (57) |
| Composite made of carbon fibre-reinforced poly (phenylene sulphide) and aluminium AA2024-T3 (alclad and bare) | Friction Spot welding | 43 MPa and 27 MPa | (58) |
| Carbon fibre reinforced polymer composite [CFRPC] with metal (steel DC01 and aluminium AlMg3) (CF-PEEK and organic sheets CF-PA66) | Induction Spot Welding | $AlMg_3$/CF-PA66 is 14.5 MPa, while DC01/CF-PEEK is 20 MPa. | (59) |
| Stainless steel + polymer-matrix composite | Dynamic joining | (4.99 kN) | (60) |
| Amorphous thermoplastic polymer (ABS 750 SW) + aluminum alloy (Al 6082-T6) | ultrasonic welding | > 2.31 MPa | (61) |

Ashong et al. (43), studied the refill friction stir spot welding of dissimilar AA6014 Al alloy and carbon-fibre-reinforced polymer composite. The joint was found to support a maximum load of 1.6 kN. Huang et al. (44) investigated the use of friction stir welding to link AA2060 aluminium alloy to short fibre-reinforced poly-ether-ether ketone while simultaneously managing shape and performance. It was observed that the joint provided high-quality surface integrity and maximum tensile shear strength of 33 MPa. In addition, it was found that reducing the heat input made it easier to get rid of welding flaws while also enhancing the joint's capacity to bear weight. Bolouri et al. (45) designed a unique static method for friction stir spot joining of Al alloys and carbon fibre-reinforced composites. To examine their impacts on the joining temperature, the interaction of the materials, and the strength of joints, the primary joining parameters, including pin rotational speed, pin feed rate, and pin plunge depth, were modified. It was found that the pin rotational speed had the greatest impact on the joining temperature, and a lap shear force of 230 to 260 N was observed. In a related study, Derazkola et al. (47) joined AA5754 aluminium alloy with poly methyl methacrylate via friction stir spot welding. It was observed that fewer flaws emerged as the interaction layer's thickness increased when the heat input into the stir zone was controlled by speeding up the rotation. Joint strength of 50 MPa was attained. Dong et al. (49) improved the welding parameters of the friction stir spot welding technique. With a plunge speed of 10 mm/min and an 8sec dwell period, it was found that the ultimate tensile shear force was 2690 N. Khalil et al. (46) studied the magnetic pulse hybrid joining of polymer composites to AA5052 aluminium alloy. The joint was found to support a maximum tensile shear load of 1779.6 N. The study noted two ways of establishing the joint namely: the employment of a metallic insert in a polymer composite and the use of an exterior patch. The mechanical tests indicated a negligible reduction in tensile strength when using magnetic pulse welding on the insert whenever the juxtaposition of the hole weld was avoided.

Troschitz et al. (48) carried out a study on the joining of thermoplastic composites with metals using resistance element welding. Metal (weld) inserts were employed to interact with the composite material, thereby giving rise to a top-notch joint. Lambiase et al. (51) studied the mechanism of bonding of AA7075 aluminium alloy and carbon fibre-reinforced polyphenylene sulphide (CFRP) during friction-assisted joining. The aluminium surface was given a laser texture to encourage interlocking between the two materials being put together. However, it was observed that there was poor contact between the metal and reinforced plastic substrates. Despite this, the joints had significant load-carrying capacities of up to 10.7 kN. In a related study, Kuzu et al. (52) used continuous wave laser welding technology to combine SS304 stainless steel and glass fibre-reinforced plastic composite. The results of the mechanical strength test (53) showed that the strongest joint could withstand a force of roughly 4000 N before breaking. On the other hand, the joint created by fusing AA6061 aluminium alloy and carbon fibre plastic composite with the help of a laser-arc hybrid welding technique yielded a maximum tensile shear load of 4650 N with a welding current of 90 Amperes (53).

The use of ultrasonic spot welding to join AA5754 aluminium sheet and carbon fibre-reinforced epoxy composite has been successfully carried out (54). The carbon fibre epoxy stack was coated with a thermoplastic polyamide film before curing, generating a functional surface on the thermoset matrix that made welding go more quickly. Average adhesive joint strength of 34.8 MPa was realized (54). Aluminium sheet and carbon-reinforced polymer composite were joined using an ultrasonic spot-welding procedure (56), resulting in a joint with a tensile strength of about 30MPa. When aluminium alloy and fibre-reinforced polymer composite were joined by ultrasonic metal welding, a greater tensile strength of 58MPa was obtained (55). Threaded Hole Friction Spot Welding (THFSW) which is a novel infill friction spot welding procedure, was developed by Pabandi et al. (57) to weld sheets of composite material made of short carbon fibre-reinforced polypropylene (PP-SCF) and AA5052 aluminium alloy. The method involved adding melted and then resolidified polymer to the pre-threaded hole. The findings showed that THFSW was effective in joining aluminium to polymer sheets, and the hole was filled with melted polymer. The joint's maximum shear strength was 28 MPa. Alclad and bare aluminium AA2024-T3 were joined together with carbon fibre-reinforced poly using the THFSW welding procedure. By employing aluminium bare specimens, lap-shear tensile strength as high as 27 MPa was reportedly attained. On aluminium surfaces, sandblasting was also used as an efficient mechanical surface pre-treatment. This increased surface roughness, which in turn enhanced the mechanical interlock and performance of the joint. The alclad specimens also had lap shear strengths of 43 MPa.

Mitschang et al. (59) studied induction spot welding of metal/CFRPC hybrid joints. Metal (steel DC01 and aluminium $AlMg_3$) and carbon fibre-reinforced polymer composite [CFRPC] (organic sheets CF-PA66 and CF-PEEK) were joined using induction spot welding (59). $AlMg_3$/CF-PA66 and DC01/CF-PEEK joints were observed to have shear tensile strengths of 14.5 MPa and 20 MPa, respectively. The study noted that for structural loading, joining polymer matrix composites to metal (like stainless steel) requires resolving intrinsic variations in the joining properties of each material. A substance that would act as a bridge between the metal and the composite is therefore required. A weldable, hard steel intermediate material that can also pick up the composite fibre stress would be suitable. It was explained that expanded mesh or shear studs that interact with and press on the crossovers of the composite's woven-reinforcement design serve as the intermediary in the "dynamic joining" idea. An ideal PMC-metal joint is one with the ability to absorb energy from the joint’s plastic behaviour. Strong structural stress transfer, scalable joint stiffness (based on the number of studs and their material properties), fabrication accuracy and use of commercial off-the-shelf processes to build the metallic portion of the joint are among the potential benefits of the dissimilar material joining concept. The greatest shear load of the dynamic joint between polymer matrix composites and metals according to Whitney & Bettinger (60), was around 4.99 kN. However, further study to investigate the mechanical behaviour of the welded joint using the diametral compression strength test (62) is advised.

## CONCLUSIONS

In the present study that reviewed the welding of polymer-matrix composites and aluminium alloys, the following conclusions can be made:

(1) The maximum tensile shear stress obtained for the joint between 7075 aluminium alloy and polymer-matrix composite was 59.9 MPa (42), using top-thermic friction stir lap welding.
(2) Researchers have explored the friction-aided joining of AA7075 aluminium alloy and carbon fibre-reinforced polyphenylene sulphide composites (51). It was observed

that despite the processing circumstances involving the use of a laser to texturize the surface of the aluminium alloy, there was inadequate contact between the metal and reinforced plastic substrates. The joints did, however, possess excellent 10.7 kN load-bearing capacity.

(3) The ultrasonic metal welding process used in joining AA2024 aluminium alloy and fibre-reinforced polymer composite gave a high tensile shear strength joint of about 58 MPa.

The results above provide invaluable information that welding polymer-matrix composites to aluminium alloys utilizing friction stir welding and ultrasonic welding methods can result in a robust joint.

## RECOMMENDATIONS TO FILL UP THE KNOWLEDGE GAPS FOUND AFTER REVIEWING EARLIER RESEARCH ON POLYMER-MATRIX COMPOSITES JOINED WITH ALUMINIUM ALLOYS.

After reviewing past studies on polymer-matrix composites welded to aluminium alloys, the following suggestions have been made to fill up the knowledge gaps found:

(i) There is limited knowledge about the optimum methods to prepare the interfaces (between the polymer-matrix composite and aluminium alloy) for welding. Future research into the appropriateness of the surface textures for welding from a metallurgical standpoint is advised.

(ii) The majority of the reviewed study focused on tensile and shear strengths. Investigations should be conducted into other crucial mechanical qualities such as ductility, impact resistance, compressive strength, and flexural strength.

(iii) Prior research largely concentrated on joints between aluminium alloys and polymer-matrix. It is recommended that research be done into the possibility of joining various metals and alloys to polymer-matrix composites.

## REFERENCES

1. Reddy, K. M.; Vardhan, D. H.; Reddy, Y. S. K.; Raghavendra, G.; Rudrapati, R. Experimental Study of Thermal and Mechanical Behaviour of Graphite-Filled UJF Composite. *Advances in Materials Science and Engineering*. **2021**, 1-7. DOI: https://doi.org/10.1155/2021/3739573
2. Kumar, S.; Roy, B. S. A Comparative Analysis between Conventional Tool and Double-Step Shoulder Tool for Joining of Acrylonitrile Butadiene Styrene and Polycarbonate Plate by Using Friction Stir Welding. Materials Today: *Proceedings*. **2020**. https://doi.10.1016/j.matpr.2020.02.48.
3. Rohart, V.; Laberge-Lebel, L.; Dubé, M. Improved adhesion between stainless steel heating element and PPS polymer in resistance welding of thermoplastic composites. *Composites Part B: Engineering*. **2020**. doi:10.1016/j.compositesb.2020.107876
4. Rudrapati, R.; Pal, P. K.; Ojha, J. On the Relationship Between Laser Welding Process Variables in Through-transmission Laser Welding (TTLW) of Polycarbonate Plastics. *Lasers in Engineering*, **2019**, 3 (44), 51–65.
5. Kropka, M.; Muehlbacher, M.; Neumeyer, T.; Altstaedt, V.; From UD-tape to Final Part – A Comprehensive Approach Towards Thermoplastic Composites. *Procedia CIRP*. **2017**, 96–100. doi:10.1016/j.procir.2017.03.371

6. Kessler, M. R. Polymer Matrix Composites: A Perspective for a Special Issue of Polymer Reviews. *Polymer Reviews.* **2012**, *52*(3), 229–233. https://doi:10.1080/15583724.2012.708004
7. Smith, W. F.; Hashemi, J.; Presuel-Moreno, F. Foundations of Materials Science and Engineering. McGill Hill: New York. **2019**; pp 656-667.
8. Rice, E.; Sparks, B. Polymer-matrix Composites: Materials, Mechanics and Applications. Nova Science Publishers Inc.: New York. **2018**.
9. Ndukwe, A. I.; Umoh, S.; Ugwochi, C.; Ogbuji, C.; Ngolube, C.; Aliegu, F.; Izuegbu, L. Prediction of Compression Strength of Bamboo Reinforced Low-density Polyethylene Waste (LDPEw) Composites. *Composites Theory and Practice*. **2022**, *22* (3), 142-149.
10. Chebolu, R.; Nallu, R.; Chanamala, R.; Sharma, S. K.; Rudrapati, R. Influence of SiC/TiB2 Particles Addition on Corrosion Behavior of As-Cast Zn-Al-Cu Alloy Hybrid Composites. *Journal of Engineering*. **2022**, 1-5. https://doi.org/10.1155/2022/3669584
11. Vardhan, D. H.; Kishore, D. S. C.; Reddy, Y. S. K.; Reddy, K. M.; Raghavendra, G.; Rudrapati, R. Effect of Grey and White Portland Cement Fillers on Flexural and Shear Strength of GFRP Composite Material. *Journal of Engineering*. **2022**, 1-5. https://doi.org/10.1155/2022/3669584
12. Yousefpour, A.; Hojjati, M.; Immarigeon, J. P. Fusion Bonding/Welding of Thermoplastic Composites. Journal of Thermoplastic Composite Materials. **2004**, 17(4), 303–341. doi:10.1177/0892705704045187
13. Gupta, N.; Doddamani, M. Polymer Matrix Composites. *JOM.* **2018**, *70*(7), 1282–1283. doi:10.1007/s11837-018-2917-x
14. Rudrapati, R. Effects of welding process conditions on friction stir welding of polymer composites: A review. *Composites Part C: Open Access*. **2022**, 1-7. https://doi.org/10.1016/j.jcomc.2022.100269
15. Morampudi, P.; Namala, K. K.; Gajjela, Y. K.; Barath, M.; Prudhvi, G. Review on Glass Fibre Reinforced Polymer Composites. *Materials Today: Proceedings*. **2021**, 314–319. doi:10.1016/j.matpr.2020.11.669
16. Shahbaz, S. R.; Berkalp, Ö. B.; Zameer U. l.; Hassan, S.; Siddiqui, M. S.; Bangash, M. K. Fabrication and analysis of integrated multifunctional MWCNTS Sensors In Glass Fibre Reinforced Polymer Composites. *Composite Structures*. **2021**, 260, 113527. doi:10.1016/j.compstruct.2020.113527
17. Nguyen, D.; Bin Abdullah, M. S., Khawarizmi, R., Kim, D.; Kwon, P. The Effect of Fiber Orientation on Tool Wear in Edge-Trimming of Carbon Fiber Reinforced Plastics (CFRP) Laminates. *Wear*. **2020**. doi:10.1016/j.wear.2020.203213
18. Geier, N.; Paulo Davim, J.; Szalay, T. Advanced Cutting Tools and Technologies for Drilling Carbon Fibre Reinforced Polymer (CFRP) Composites: A Review. *Composites Part A: Applied Science and Manufacturing*. **2019**. doi:10.1016/j.compositesa.2019.105552
19. Chawla, K. K.; Chawla, N. Fibrous Reinforcements for Composites. *Comprehensive Composite Materials II*. **2018**, 1–12. doi:10.1016/b978-0-12-803581-8.09874-x
20. Mathers, G. The welding of aluminium and its alloys. Woodhead Publishing: England. 2002.
21. Welding. Retrieved November 12, **2022**, from https://en.wikipedia.org/wiki/Welding
22. Solvent Cementing of Plastics. Adhesives Technology Handbook. **2009**, 209–229. doi:10.1016/b978-0-8155-1533-3.50012-8
23. Huang, Y.; Meng, X.; Xie, Y.; Wan, L.; Lv, Z; Cao, J.; Feng, J. Friction Stir Welding/Processing of Polymers And Polymer Matrix Composites. *Composites Part A: Applied Science and Manufacturing*. **2018**, 235–257. doi:10.1016/j.compositesa.2017.12
24. Shankar, S.; Kaushal, A.; Chattopadhyaya, S.; Vilaça, P.; Bennis, F. Joining of aluminium to the polymer by friction stir welding: An overview. *IOP Conference Series: Materials Science and Engineering*. **2021**, 1104(1). doi:10.1088/1757-899x/1104/1/012005
25. Buxton, A. L. The Joining of Plastics and Polymer Composite Materials. Polymer Technology Group, TWI Ltd. Paper presented at the I Mech E seminar (2002). Accessed, October 20, **2022**,

from https://www.twi-global.com/technical-knowledge/published-papers/welding-technologies-for-polymers-and-composites
26. Thomas, W. Nicholas, E. Friction Stir Welding for The Transportation Industries. *Materials & Design*. **1997**, *18*(4-6), 269–273. doi:10.1016/s0261-3069(97)00062-9
27. EWI.: Interested in Friction Stir Welding, Check this out! **2012**. Retrieved from https://ewi.org/ interested-in- friction-stir-welding-check-this-out/
28. Selvaraj, S. K.; Srinivasan, K.; Chadha, U.; Mishra, R.; Arpit, K.; Apurb, K.; Hu, Y. C. Contemporary Progresses in Ultrasonic Welding of Aluminum Metal Matrix Composites. *Front. Mater.* **2021**. doi: 10.3389/fmats.2021.647112
29. Electrical Workbook.: What are Ultrasonic Welding Process, Diagram, and Advantages? **2022**. Retrieved from https://electricalworkbook.com/ultrasonic-welding/
30. Bhudolia, S. K.; Gohel, G.; Leong, K. F.; Islam, A. Advances in Ultrasonic Welding of Thermoplastic Composites: A Review. *Materials*. **2020**, *13*(6), 1284. doi:10.3390/ma13061284
31. Melentiev, R.; Yudhanto, A.; Tao, R.; Vuchkov, T.; Lubineau, G. Metallization of polymers and Composites: State-of-the-art approaches. Materials & Design. **2022**. https://doi.org/10.1016/j.matdes.2022.110958.
32. Rudrapati, R.; Kumar, N.; Pal, P. K. Application of Taguchi Method for Parametric Optimization of through Transmission Laser Welding of Acrylic Plastics. **2019**, https://doi.org/10.1063/1.5085584
33. Scholar, G. Polymer Matrix Composites Welded to Metals: Published papers. **2015**. Accessed, October 20, 2022, from https://scholar.google.com/scholar?q=polymer-matrix+composites+welded+to+metals&hl=en&as_sdt=0%2C5&as_ylo=2015&as_yhi=2015
34. Scholar, G. Polymer Matrix Composites Welded to Metals: Published papers. **2016**. Accessed, October 20, 2022, from https://scholar.google.com/scholar?q=polymer-matrix+composites+welded+ to+metals&hl=en&as_sdt=0%2C5&as_ylo=2016&as_yhi=2016
35. Scholar, G. Polymer Matrix Composites Welded to Metals: Published papers. **2017**. Accessed, October 20, 2022, from https://scholar.google.com/scholar?q=polymer-matrix+composites+welded+to+metals&hl=en&as_sdt=0%2C5&as_ylo=2017&as_yhi=2017
36. Scholar, G. Polymer Matrix Composites Welded to Metals: Published papers. **2018**. Accessed, October 20, 2022, from https://scholar.google.com/scholar?q=polymer-matrix+composites+welded+to+metals&hl=en&as_sdt=0%2C5&as_ylo=2018&as_yhi=2018
37. Scholar, G. Polymer Matrix Composites Welded to Metals: Published papers. **2019**. Accessed, October 20, 2022, from https://scholar.google.com/scholar?q=polymer-matrix+composites+welded+to+metals&hl=en&as_sdt=0%2C5&as_ylo=2019&as_yhi=2019
38. Scholar, G. Polymer Matrix Composites Welded to Metals: Published papers. **2020**. Accessed, October 20, 2022, from https://scholar.google.com/scholar?q=polymer-matrix+composites+welded+to+metals&hl=en&as_sdt=0%2C5&as_ylo=2020&as_yhi=2020
39. Scholar, G. Polymer Matrix Composites Welded to Metals: Published papers. **2021**. Accessed, October 20, 2022, from https://scholar.google.com/scholar?q=polymer-matrix+composites+welded+to+metals&hl=en&as_sdt=0%2C5&as_ylo=2021&as_yhi=2021
40. Kumar-Sharma, A.; Bhandari, R.; Aherwar, A.; Rimašauskienė, R.; Pinca-Bretotean, C. A study of advancement in application opportunities of aluminium metal matrix composites. *Materials Today: Proceedings*. **2020**. doi:10.1016/j.matpr.2020.02.516
41. Meng, X.; Huang, Y.; Xie, Y.; Li, J.; Guan, M.; Wan, L.; Dong, J.; Cao, J. Friction Self-Riveting Welding between Polymer Matrix Composites and Metals. *Composites Part A: Applied Science and Manufacturing*. **2019**. doi:10.1016/j.compositesa.2019.105
42. M. Li, X. Xiong, S. Ji, W. Hu, Y. Yue, Achieving high-quality metal to polymer-matrix composites joint via top-thermic solid-state lap joining. *Composites Part B: Engineering*. **2021**. doi:10.1016/j.compositesb.2021.108941

43. Ashong, A. N.; Lee, M.; Hong, S.-T.; Lee, Y. S.; Kim, J. H. Refill Friction Stir Spot Welding of Dissimilar AA6014 Al Alloy and Carbon-Fiber-Reinforced Polymer Composite. *Metals and Materials International*. **2020**. doi:10.1007/s12540-020-00788-5
44. Huang, Y.; Meng, X.; Xie, Y.; Li, J.; Wan, L. Joining of carbon fibre reinforced thermoplastic and metal via friction stir welding with co-controlling shape and performance. *Composites Part A: Applied Science and Manufacturing.* **2018**, *112*, 328-336. doi:10.1016/j.compositesa.2018.06.027
45. Bolouri, A.; Fotouhi, M.; Moseley, W. A New Design for Friction Stir Spot Joining of Al Alloys and Carbon Fiber-Reinforced Composites. *Journal of Materials Engineering and Performance.* **2020**, *29*(8), 4913–4921. doi:10.1007/s11665-020-04998-1
46. Khalil, C.; Marya, S.; Racineux, G. Magnetic Pulse Hybrid Joining of Polymer Composites to Metals. **2021**. https://doi.org/10.3390/met11122001
47. Derazkola, H. A.; Simchi, A. An Investigation on the Dissimilar Friction Stir Welding of T-Joints Between AA5754 Aluminum Alloy and Poly (Methyl Methacrylate). Thin-Walled Structures. **2019**, 376–384. doi:10.1016/j.tws.2018.11.027
48. Troschitz, J.; Vorderbrüggen, J.; Kupfer, R.; Gude, M.; Meschut, G. Joining of Thermoplastic Composites with Metals Using Resistance Element Welding. *Applied Sciences*. **2020**, *10*(20). doi:10.3390/app10207251
49. Dong, H.; Tang, Z.; Li, P.; Wu, B.; Hao, X.; Ma, C. Friction Stir Spot Welding of 5052 Aluminum Alloy to Carbon Fiber Reinforced Polyether Ether Ketone Composites. *Materials & Design.* **2021**. doi:10.1016/j.matdes.2021.109495
50. Kalaf, O.; Nasir, T.; Asmael, M.; Safaei, B.; Zeeshan, Q.; Motallebzadeh, A.; Hussain, G. Friction stir spot welding of AA5052 with Additional Carbon Fiber-Reinforced Polymer Composite Interlayer. *Nanotechnology Reviews*. **2021**, *10*(1), 201-209. doi:10.1515/ntrev-2021-0017
51. Lambiase, F.; Paoletti, A.; Durante, M. Mechanism of Bonding of AA7075 Aluminum Alloy and CFRP during Friction assisted Joining. *Composite Structures*. **2021**. doi:10.1016/j.compstruct.2021.113
52. Kuzu, A. T.; Karaguzel, U.; Erbay, B.; Bakkal, M. Effect of scanning strategies and laser parameters on metal-composite joining. *Materials and Manufacturing Processes*. **2021**, 1–9. doi:10.1080/10426914.2021.1905827
53. Wang, H.; Huang, B.; Li, J.; Li, N.; Liu, L. Welding and Riveting Hybrid Bonding of 6061 Al and Carbon Fiber Reinforced Composites. *Polymers.* **2022**, *14*(1), 99. https://doi.org/10.3390/polym14010099
54. Lionetto, F.; Balle, F.; Maffezzoli, A. Hybrid ultrasonic spot welding of aluminium to carbon fibre reinforced epoxy composites. *Journal of Materials Processing Technology.* **2017**, 289-295. doi:10.1016/j.jmatprotec.2017.05.002
55. Wagner, G.; Balle, F.; Eifler, D. Ultrasonic Welding of Aluminum Alloys to Fiber Reinforced Polymers. *Advanced Engineering Materials.* **2013**, *15*(9), 792–803. doi:10.1002/adem.201300043
56. Balle, F., Wagner, G., & Eifler, D. Ultrasonic Spot Welding of Aluminum Sheet/Carbon Fiber Reinforced Polymer – Joints. *Materialwissenschaft Und Werkstofftechnik.* **2007**, *38*(11), 934–938. doi:10.1002/mawe.200700212
57. Pabandi, H. K.; Movahedi, M.; Kokabi, A. H. A New Refill Friction Spot Welding Process for Aluminum/Polymer Composite Hybrid Structures. Composite Structures. **2017**, 59–69. https://doi.org/10.1016/j.compstruct.2017.04.053
58. Goushegir, S. M.; dos Santos, J. F.; Amancio-Filho, S. T. Friction Spot Joining of aluminium AA2024/carbon-fibre reinforced poly(phenylene sulfide) composite single lap joints: Microstructure and mechanical performance. *Materials & Design* (1980-2015). ***2014***, 196–206. doi:10.1016/j.matdes.2013.08.034
59. Mitschang, P.; Velthuis, R.; Didi, M. Induction Spot Welding of Metal/CFRPC Hybrid Joints. *Advanced Engineering Materials*. **2013**, *15*(9), 804–813. doi:10.1002/adem.201200273

60. Whitney, T. J.; Bettinger, D. Dynamic Joining of Polymer Composites to Metals. Volume 4: Design and Manufacturing. **2008**. doi:10.1115/imece2008-68818
61. Al-Obaidi, A. Ultrasonic Joining of Metal-polymer Surfaces. PhD. Thesis. The University of Sheffield. 2017, 190-192.
62. Ovri, J. E. O.; Ndukwe, A. I. The Densification and Diametral Compression Strength of Isi-Ogwuta Clay. *AJER*. **2014**, 3(1), 18–26. http://www.ajer.org/papers/v3(1)/D0311826.pdf

APTEFF, Vol. 54, 1-335 (2023)
DOI: https://doi.org/10.2298/APT2354051N

UDC: 677.31:667.24:547.265
BIBLID: 1450-7188 (2023) 54, 51-58

Original scientific paper

# EFFECT OF PRETREATMENT WITH PENTANOL FOR DYEING WOOL FIBERS AT LOW TEMPERATURE

*Milena M. NIKODIJEVIĆ**, Dragan M. ĐORĐEVIĆ*

University of Niš, Faculty of Technology, Bulevar oslobođenja 124, 16000 Leskovac, Serbia

**Received: 13 December 2022 Revised: 27 December 2022 Accepted: 16 January 2023**

*This paper describes the influence of pre-treatment with pentanol for the dyeing of wool fibers at low temperatures. Wool fiber is expensive to produce and process; accordingly, it must be economically viable and meet consumer demands. Acid dyes are the most important class of commercial dyes and account for more than half of the dyes in the industry. Isomers of pentanol and alcohols with a longer carbon chain have higher reactivity at low temperatures and lower impact resistance. In the experimental part, the 100% wool fiber was treated in pentanol at a temperature of 20 °C for 30 minutes. After pretreatment, samples were dried and relaxed at room temperature for 24 hours. This is followed by dyeing the treated fibers with Supramin blau acid dye. The used dye concentrations were 100, 200, 300, 400, and 500 mg/dm$^3$. The time of dyeing was 5, 10, 20, 30, 40, 50, and 60 minutes. Pretreated wool fibers with pentanol give good results at low temperatures i.e. 40 °C. A constant increase in the degree of dye exhaustion on the pretreated wool fiber was observed during the increase in the initial concentration of the dye. A longer dyeing time for pretreated wool results in a higher degree of exhaustion. A pseudo-first-order adsorption model can be used to describe the adsorption process because there is very little deviation around the ideal curve and functional straight lines cover most points.*

**Keywords**: wool, dyeing, pentanol, pseudo-first-order, pseudo-second-order.

## INTRODUCTION

Wool represents less than 5% of the world's fiber consumption. Wool is an expensive fiber to produce and process; accordingly, it must be economically viable and meet consumer demands. Wool manufacturers must understand basic wool technology to identify mill needs and the range of wool prices offered. A better understanding of wool and its grades will enable the producer to recognize and address two major areas of concern: genetic uniformity and wool management and preparation techniques. Wools with finer diameter fibers will produce lighter materials, while larger diameter fibers produce heavier textiles (1).

It has been estimated that wool contains more than 170 different proteins. Heterogeneous protein composition is responsible for different physical and chemical properties of different regions of wool. Proteins in wool are composed of amino acids and contain a basic amino (-$NH_2$) and acidic carboxylic (-COOH) groups. Most acid dyes are derivatives of sulfonic acid azo dyes. Usually, these dyes are isolated as sodium salts (2, 3).

Acid dyes are the most important class of commercial dyes and account for more than half of the dyes in the industry, which contain various intermediates. They are usually highly dyed compounds that can be intensely yellow, red, orange, blue, or even green, depending on the exact structure of the molecule. These dyes are widely used in analytical

---

* Corresponding author: Milena M. NIKODIJEVIĆ, University of Niš, Faculty of technology, Bulevar oslobođenja 124, 16000 Leskovac, Serbia, e-mail: nikmilena94@gmail.com

chemistry, metallurgy, the textile industry, optical data storage, photo switching, and nonlinear optical materials (4-8).

Alcohols are considered good alternatives to conventional petroleum fuels or fuel additives because they can be obtained from a variety of renewable raw materials, and more importantly, they have similar physicochemical properties to fossil fuels. Isomers of pentanol and alcohols with a longer carbon chain have stronger reactivity at low temperatures and lower impact resistance (9).

The paper presents news from research in laboratory conditions of dyeing wool fibers with acid dyes. The goal of the research is the development of a procedure for dyeing wool fiber previously treated with alcohol at a lower temperature.

## EXPERIMENTAL

100% wool fiber was used in the experimental part. Wool fibers were washed in detergent for 30 minutes at 40 °C and then dried and processed in solvent - pentanol alcohol at a temperature of 20 °C for 30 minutes at a bath ratio of 1:50. After pretreatment, it was dried and relaxed at room temperature for 24 hours. This is followed by dyeing the treated fibers with Supramin blau acid dye.

The chemical structure of the dye used is shown in Figure 1. The initial concentrations of the dye were 100, 200, 300, 400, and 500 mg/l. The addition is the acid HCOOH, at pH=3. The ratio of the dyeing bath is 1:50, the dyeing temperature is 40 °C, while the dyeing time is varied, 5, 10, 20, 30, 40, 50, and 60 minutes. After the dyeing was finished, the absorbance at the maximum wavelength (590 nm) for the dye used was measured using a spectrophotometer (Cary 100 Conc UV-VIS, Varian). Also, a calibration curve was created to determine the unknown dye concentration in the solution during dyeing.

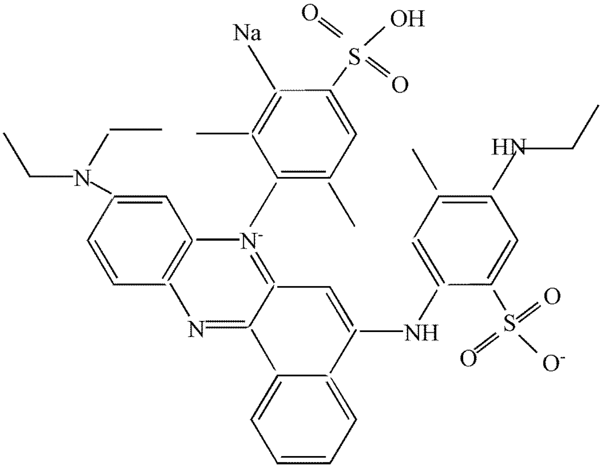

**Figure 1.** Chemical structure of Supramin Blau acid dye

The degree of dye exhaustion during dyeing was calculated using the formula [1] (10):

$$E = \frac{C_0 - C_t}{C_0} \times 100\ (\%) \qquad [1]$$

where are: $C_0$ and $C_t$ (mg/l), initial and dye concentration in time *t*.

The amount of absorbed dye per unit mass of adsorbent (adsorption capacity) was obtained using the equation [2] (10):

$$q_t = \frac{C_0 - C_t}{w} \times V \quad \text{i} \quad q_e = \frac{C_0 - C_e}{w} \times V \qquad [2]$$

here are $q_t$ (mg/g), a mass of absorbed dye per unit mass of fiber during dyeing time *t;* $q_e$ (mg/g), a mass of absorbed dye per unit mass of fibers at equilibrium, $C_o$ (mg/l), initial dye concentration; $C_t$ (mg/l), the concentration of the dye in the solution at the time of dyeing *t*, $C_e$ (mg/l), the equilibrium concentration of the dye in the solution; *w* (g), a mass of fiber and *V* (dm$^3$), volume of dyeing solution.

To define the sorption mechanism, characteristic sorption constants were determined using Lagergren's equation for pseudo-first-order based on full capacity and pseudo-second-order equation based on full phase sorption (11).

Adsorption kinetic data described by Lagergren's pseudo-first-order model represent the earliest known equation describing the rate of adsorption based on adsorption capacity.

Lagergren equation is usually expressed as follows in equation [3] (11):

$$log\ (q_e - q_t) = log\ (qe) - \frac{k_1}{2{,}303} \cdot t \qquad [3]$$

where are: $q_e$ and $q_t$ (mg/g) - adsorption capacities at equilibrium and after time t, respectively, $k_1$ (1/min) - pseudo-first-order adsorption rate constant.

The pseudo-second-order model is presented as equation [4] (11):

$$\left(\frac{t}{q_t}\right) = \frac{1}{k_2 \cdot q_e^2} + \frac{1}{q_e} \cdot t \qquad [4]$$

where are: $q_e$ and $q_t$ (mg/g) - adsorption capacities at equilibrium and after time *t*, respectively, $k_2$ (1/min) - pseudo-second-order adsorption rate constant.

## RESULTS AND DISCUSSION

Raw wool fibers contain significant amounts of surface impurities that interfere with dyeing. These impurities must be removed before mechanical and chemical pre-treatment, as well as before dyeing the wool, which is done by washing and carbonizing the wool. It is known that raw pure wool has a lower affinity for dye. Pre-treatment with pentanol changes the surface morphology and affinity of wool to dye, i.e. the increase in affinity towards dye will be somewhat more pronounced (12-14).

In this research, pre-treatment of wool with pentanol at 20 °C and then dyeing at 40 °C showed excellent results, even better than standard raw fiber dyeing at the same temperature. A higher degree of dye exhaustion was observed, as well as a greater amount of adsorbed dye by the modified wool compared to the raw sample without prior treatment with pentanol. Because of this, pre-treatment (modification) of raw wool allows dyeing at lower temperatures and with a smaller amount of dye and additives.

The advantages of dyeing wool at lower temperatures include less yellowing, less fiber damage, less structural and relaxation changes, preservation of properties, etc. High dyeing temperatures can weaken the fiber structure when the chemical and mechanical properties of the textile deteriorate. As a rule, dyes at low temperatures do not penetrate sufficiently into the fibers, which leads to uneven coloring. Pretreatment with alcohol causes structural and chemical changes in the fibers, which results in a greater degree of exhaustion and a greater amount of adsorbed dye per unit of fiber mass.

The results of the influence of the initial concentration of dye ($C_o$) on the degree of exhaustion and adsorption capacity of acid dye during the dyeing of raw wool and pre-treated - modified wool with pentanol at 40 °C for 60 minutes are shown in Table 1. As the initial concentration of the dye increases, there is a noticeable continuity in the changes in the analyzed properties. With the increase in concentration, the degree of dye exhaustion increases as well as the amount of adsorbed dye per unit mass of adsorbent-fiber. The values of the degree of exhaustion for raw wool are around 68-82%, while for wool treated with pentanol, these values are around 92-95%. An increase in the acid dye adsorption capacity during wool dyeing at 40 °C was observed in wool pretreated with pentanol.

**Table 1**. Influence of the initial dye concentration on the degree of exhaustion and adsorption capacity of the acid dye during the dyeing of raw wool and wool pretreated with pentanol (40 °C, $t$=60 min)

| **$C_o$, mg/l** | **$E$, %** | | **$q_e$, mg/g** | |
|---|---|---|---|---|
| | **Raw wool** | **Treated wool** | **Raw wool** | **Treated wool** |
| 100 | 68.84 | 92.37 | 3.44 | 4.62 |
| 200 | 77.57 | 94.22 | 7.76 | 9.42 |
| 300 | 79.16 | 94.83 | 11.87 | 14.23 |
| 400 | 81.43 | 95.15 | 16.28 | 19.03 |
| 500 | 82.79 | 95.73 | 20.70 | 23.93 |

The effect of dyeing time on the degree of exhaustion and acid dye adsorption capacity for raw and pentanol-treated wool at 40 °C at the lowest initial dye concentration of 100 mg/l is shown in table 2. Continuity in changes during increasing dyeing time is visible. With increasing time, the degree of dye exhaustion per unit mass of adsorbent-fiber increases. As time increases, so does the degree of dye exhaustion. At the longest dyeing time, i.e. At 60 minutes, the highest degree of exhaustion occurs (68.84% for raw wool and 92.37% for pentanol-treated wool). Higher values of acid dye adsorption capacity during wool dyeing at 40 °C at an initial concentration of 100 mg/l were observed for wool pretreated with pentanol. Longer dyeing time means higher values of the adsorbed amount of adsorbate (dye) on the adsorbent (fiber) for both raw and pentanol-treated wool.

**Table 2.** Change in degree of exhaustion and adsorption capacity of acid dye during dyeing of raw wool and wool pretreated with pentanol (40 °C, $C_o$=100 mg/l)

| Dyeing time, min | *E*, % | | $q_e$, mg/g | |
|---|---|---|---|---|
| | Raw wool | Treated wool | Raw wool | Treated wool |
| 5 | 11.98 | 35.51 | 0.6 | 1.77 |
| 10 | 17.86 | 45.31 | 0.89 | 2.26 |
| 20 | 27.67 | 57.08 | 1.38 | 2.85 |
| 30 | 39.43 | 66.88 | 1.97 | 3.34 |
| 40 | 51.2 | 78.65 | 2.56 | 3.93 |
| 50 | 62.96 | 86.49 | 3.15 | 4.32 |
| 60 | 68.84 | 92.37 | 3.44 | 4.62 |

Figure 2 shows the results of the sorption kinetics research (pseudo-first-order model) of acid dye on wool fiber for different initial dye concentrations. The pseudo-first-order model, according to the diagram, is applicable to describe the sorption flow because there is very little scatter around the ideal curve, so functional straight lines cover most points very well. Since the reaction takes place in the adsorbed layer on the surface of the adsorbent, its speed depends on the concentration of the reactant in the layer on the surface of the adsorbent. This kinetic equation significantly covers the experimental points, there is little scattering, so it can be concluded that the pseudo-first-order model is suitable for describing the kinetics of the adsorption of Supramin blau acid dye on the wool fiber.

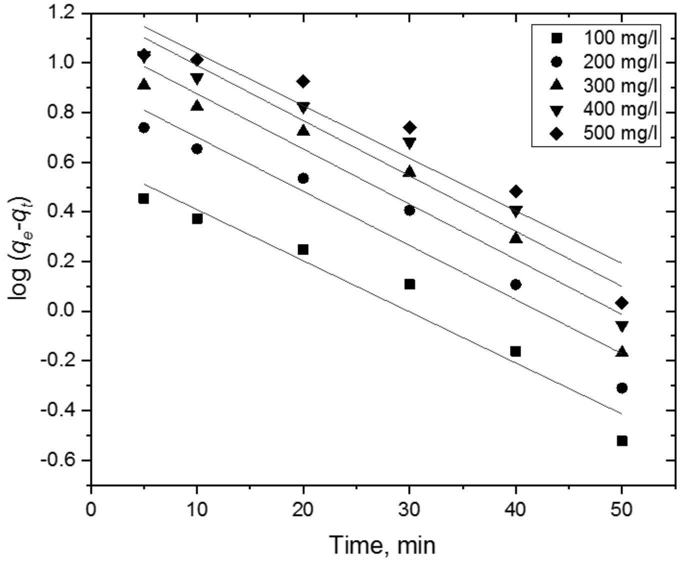

**Figure 2.** Kinetics of acid dye adsorption on the modified wool fiber during dyeing at 40 °C (pseudo-first-order model)

Table 3 gives the values of the kinetic parameters of the acid dye adsorption process on the adsorbent (pseudo-first-order model) for all initial dye concentrations, operating temperature, as well as the model validity parameter, as well as the values for the $q_e$ parameter (calculated - $q_{e,cal}$, and experimental - $q_{e,exp}$). The pseudo-first-order kinetic model has a coefficient of determination over $R^2 > 0.91$ for all dye concentrations, thus achieving high functionality. Accordingly, it is concluded that the initial rate of adsorption does not depend on the chemical reaction, the good fit of the pseudo-first-order model to the experimental data should be considered an empirical correlation without any hints regarding the actual adsorption mechanism.

The value of the rate constant $k_1$ varies less with the change in the initial dye concentration, which means that it does not depend on the concentration of the reactants. Larger numerical values of $k_1$ indicate that a shorter adsorption time is required to achieve the same fractional uptake.

**Table 3.** Kinetic parameters of the dyeing process of modified wool (pseudo-first-order model)

| $C_0$ (mg/l) | $q_{e,exp}$ | $q_{e,cal}$ | $k_1$ (1/min) | $R^2$ |
|---|---|---|---|---|
| 100 | 4.11 | 4.62 | 0.047 | 0.952 |
| 200 | 8.29 | 9.62 | 0.050 | 0.932 |
| 300 | 12.52 | 14.23 | 0.051 | 0.926 |
| 400 | 16.34 | 19.03 | 0.051 | 0.926 |
| 500 | 17.86 | 23.93 | 0.049 | 0.912 |

The kinetics of acid dye adsorption on wool fiber, according to the pseudo-second-order model (Figure 3), is represented by a diagram of the dependence of $t/q_t$ in relation to time. By fitting the data, functional straight lines were obtained for all initial dye concentrations and operating temperature. This model includes all phases of adsorption, such as external diffusion, adsorption and internal diffusion in particles, since it is a pseudo model. By comparing the appearance of the fitted curves from the diagram, as well as the appearance and scattering of points around the ideal fitting line, it was determined that the adsorption kinetics of Supramin blau dye on the adsorbent-fiber is perfectly described by the pseudo-second-order model. The coefficient of determination at all values of the initial dye concentration is $R^2 > 0.97$, which confirms the very high functionality of the variables.

Table 4 gives the values of the kinetic parameters of the acid dye adsorption process on the wool fiber (pseudo-second-order model) for all initial dye concentrations at temperature of 40 °C, as well as the values for the $q_e$ parameter. The validity parameter ($R^2$) has very high numerous values, which proves the applicability of the pseudo-second-order model. No significant differences in numerous values between the parameters $q_{e,cal}$ and $q_{e,exp}$ were observed, which highlights the suitability of the model. The coefficients of determination have higher values compared to the pseudo-first-order model, which all together favors and gives an advantage to the pseudo-second-order model. The pseudo-second-order rate constant ($k_2$) is generally independent of the initial dye concentration. Based on the value of the constant rate $k_2$, it is determined that the limiting rate step can be attributed to chemical adsorption, where the formation of a covalent bond is caused by the exchange of electrons between metal ions and the adsorbent binding site.

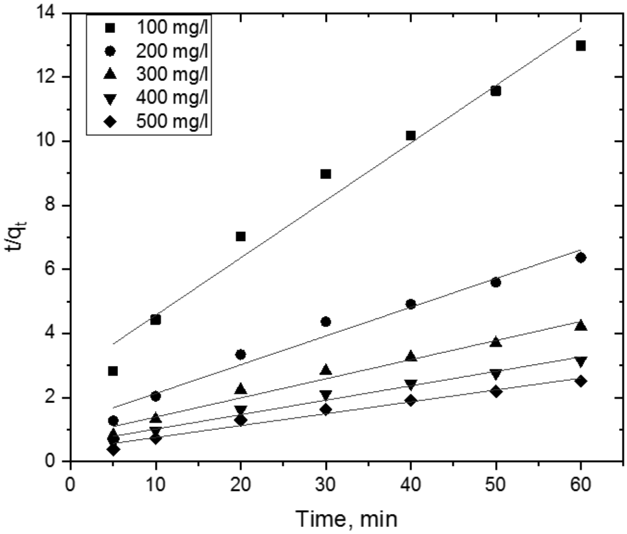

**Figure 3.** Kinetics of acid dye adsorption on the modified wool fiber during the dyeing at 40 °C (pseudo-second-order model)

**Table 4.** Kinetic parameters of the dyeing process of modified wool (pseudo-second-order model)

| $C_0$ (mg/l) | $q_{e,exp}$ | $q_{e,cal}$ | $k_2$ g/(mg·min) | $R^2$ |
|---|---|---|---|---|
| 100 | 4.62 | 5.58 | 0.0116 | 0.973 |
| 200 | 9.62 | 11.14 | 0.0065 | 0.973 |
| 300 | 14.23 | 16.75 | 0.0045 | 0.974 |
| 400 | 19.03 | 22.19 | 0.0036 | 0.978 |
| 500 | 23.93 | 26.98 | 0.0036 | 0.973 |

## CONCLUSION

Based on the obtained experimental results, the following conclusions were made:

Comparing the results of dyeing wool with an acid dye without and with pretreatment, the fact is that pretreatment with pentanol increased the degree of exhaustion and the adsorbed amount of dye in relation to the dyeing of raw wool fiber.

A constant increase in the degree of dye exhaustion on the pretreated wool fiber was observed during the increase in the initial concentration of the dye. As the initial concentration increases, the degree of dye exhaustion per unit mass of adsorbent-fiber increases.

A longer dyeing time for pretreated wool results in a higher degree of exhaustion. At lower initial dye concentrations, initially, a higher percentage of exhaustion occurs and this trend is maintained mostly throughout the dyeing process.

The change in the adsorbed amount of adsorbate (dye) on the pretreated adsorbent (fiber), for different initial concentrations and dyeing time, increases during the increase of the initial concentration and over time, i.e. a larger amount of dye in the solution or a longer dyeing time results in a slightly larger amount of adsorbed dye per unit mass of the adsorbent.

The pseudo-first-order model, according to the diagrams, is applicable to describe the adsorption flow because there is very little scatter around the ideal curve, so functional straight lines cover most points very well.

The appearance and scattering of points around the ideal fitting line in the interpretation of the pseudo-second-order model, it was determined that the adsorption kinetics of the Supramin blue dye on the adsorbent-fiber is perfectly described by this model. The coefficient of determination at all values of the initial dye concentration was over $R^2 > 0.97$, which is why this model was preferred over the pseudo-first-order model.

## REFERENCES

1. Popescu, C.; Wortmann, F. J. Wool–structure, mechanical properties and technical products based on animal fibres. *Industrial Applications of Natural Fibres: Structure, properties and technical applications*, **2010**, *10*, 255.
2. Hameed, N.; Guo, Q. Blend films of natural wool and cellulose prepared from an ionic liquid. *Cellulose*, **2010**, *17*(4), 803-813.
3. Wadia, D. N.; Patel, P. M. Synthesis and Application of Acid Dyes Based on 3-(4-Aminophenyl)-5-benzylidene-2-substituted phenyl-3, 5-dihydroimidazol-4-one, *E-Journal of Chemistry*, **2008**, *5*(1), 987-996.
4. Amin, A. S. Determination of molybdenum in human urine by spectrophotometric method using thiazolylazo compounds as chromogenic reagents, *Analytical Letters*, **1999,** *32*(8), 1575-1587.
5. Santra, P. K.; Das, D.; Misra, T. K.; Roy, R.; Sinha, C.; Peng, S. M. Chemistry of azopyrimidines: Synthesis, spectral characterization, electrochemistry and X-ray crystal structure of bis [2-(arylazo) pyrimidine] complexes of copper (I), *Polyhedron*, **1999**, *18*(14), 1909-1915.
6. Omar, M. Spectroscopic, spectrophotometric and potentiometric studies on 3-(naphthylazo)-5-phenylpyrazole dye and its metal chelates, *Annali di chimica.* **2002**, *92*(5-6), 601-614.
7. Khoo, I. C.; Shih, M. Y.; Shishido, A.; Chen, P. H.; Wood, M. V. Liquid crystal photorefractivity-towards supra-optical nonlinearity, *Optical Materials,* **2001**, *18*(1), 85-90.
8. Kandil, S. S. Cobalt (II), nickel (II) and copper (II) complexes of 4-(sulfonylazido) phenylazopyrazolones, *Transition Metal Chemistry*, **1998**, *23*(4), 461-465.
9. Heufer, K. A.; Sarathy, S. M.; Curran, H. J.; Davis, A. C.; Westbrook, C. K.; Pitz, W. J. Detailed kinetic modeling study of n-pentanol oxidation, *Energy & Fuels.* **2012**, *26*(11), 6678-6685.
10. Tayebi, H. A.; Yazdanshenas, M. E.; Rashidi, A.; Khajavi, R.; Montazer, M. The isotherms, kinetics, and thermodynamics of acid dye on nylon6 with different amounts of titania and fiber cross sectional shape, *Journal of Engineered Fibers and Fabrics.* **2015**, *10*(1), 97-108.
11. Ismail, L. F. M.; Sallam, H. B.; Farha, S. A.; Gamal, A. M.; Mahmoud, G. E. Adsorption behaviour of direct yellow 50 onto cotton fiber: equilibrium, kinetic and thermodynamic profile, *Spectrochimica Acta Part A: Molecular and Biomolecular Spectroscopy*, **2014**, *131*, 657-666.
12. Datyner, A. Surfactants in Textile Processing, *Surfactant Science Series*, **1983**, *10*, 55–65.
13. Lewis, D. M. The colouration of wool, *Handbook of Textile and Industrial Dyeing*, **2011**, 33-39.
14. Anderson, C. A. Mechanisms of Raw Wool Scouring - The Role of the Protein Contaminant Layer, *Textile Research Journal*, **1983**, *53*(12), 741-750.

APTEFF, Vol. 54, 1-335 (2023)
DOI: https://doi.org/10.2298/APT2354059H

UDC: 66-911.33:621.182.1:536(65)
BIBLID: 1450-7188 (2023) 54, 59-80

Original scientific paper

# THERMODYNAMIC EXPERIMENTAL STUDY OF AN ALGERIAN CONDENSATE GAS

*Rima HARCHE*, Abdelkader MOUHEB, Merhoune Ilhem REZIG, Imane BEKKOUCHE*

Transfer Phenomena Laboratory (LPDT) , Department of Chemical Engineering and Cryogenics,
FGMGP- University of Sciences and Technology Houari Boumediene USTHB
BP 32 Bab Ezzouar, 16111 – ALGIERS

**Received: 09 December 2022 Revised: 26 January 2023 Accepted: 01 February 2023**

*When a gas field is discovered, the gas condensate is often in a gaseous single-phase state in the reservoir under pressures and at temperatures which are higher the greater the depth. During operation, the pressure drop in the repository results in liquid deposits in both the repository and surface facilities. These liquid deposits are composed for the most part of heavy constituents of great importance for the producer. They are usually unrecoverable.*

*For this, we carry out a thermodynamic study, called the PVT study, the object of our current work concerning the condensate gas coming from a newly discovered deposit in southern Algeria.*

*A series of experiments was carried out, making it possible to experimentally determine physical-chemical and thermodynamic properties. A GPC analysis was then performed to determine the gas condensate composition under study.*

**Keywords**: condensate gas, PVT, bottom pressure, hydrocarbon mixtures.

## INTRODUCTION

A deposit is made up of one or more reservoirs superimposed or close laterally, underground rock. Some deposits consist of several dozen or even several hundred reservoirs. They are called multipliers. Containing liquid or gaseous hydrocarbons of sedimentary origin. The reservoir rock is porous and permeable, and the structure is bounded by impermeable barriers that trap hydrocarbons. A tank can contain either oil or gas, or even the two superposed fluids. The most important characteristic of these tanks is their porosity: the fluids are stored and move in very small pores (1).

When a gas field is discovered, the gas condensate is often in a gaseous single-phase state in the reservoir under pressures and at temperatures which are higher the greater the depth. During its operation, the pressure decreases in the latter by causing liquid deposits as well as in the deposition or in the surface installations. These liquid deposits are composed for the most part of heavy constituents of great importance for the producer. They generally remain unrecoverable (2), (3).

Algeria has an important gas industry and a major global gas producer.

The international market requires rigorous processing, so the transmission and distribution is done by pipeline is characterized by certain specifications, including calorific value, C5+ content.

---

* Corresponding author: Rima HARCHE, Transfer Phenomena Laboratory (LPDT), Department of Chemical Engineering and Cryogenics, FGMGP- University of Sciences and Technology Houari Boumediene USTHB BP 32 Bab Ezzouar, 16111 – ALGIERS, e-mail: s_r_harche@yahoo.fr

APTEFF, Vol. 54, 1-335 (2023)
DOI: https://doi.org/10.2298/APT2354059H
UDC: 66-911.33:621.182.1:536(65)
BIBLID: 1450-7188 (2023) 54, 59-80

Original scientific paper

The analysis and design of natural gas and crude oil production plans and equipment requires knowledge of the thermal and physical properties of hydrocarbons (4).

However, it is impossible to measure all of its properties for all hydrocarbon fluids under all conditions. For this reason, alternative methods of estimating thermodynamic properties are frequently used, such as empirical correlations or state equations (5).

In order to remedy this, we are concerned with determining the volumetric characteristics of this raw gas and the changes of state that affect it during its movement in the reservoir and even in the surface production facilities. This information guides the selection of an operating mode for optimal retrieval. Thus, the dimensioning of the exploitation and treatment and storage units of this gas will be based on the availability of reliable and precise data on phase equilibrium and volumetric properties (6).

For this, an in-depth thermodynamic study has been carried out on the physico-chemical characteristics of the Algerian condensed gas, coming from a new deposit in the south of Algeria;

This study is being conducted at one of SONATRACH's research centres, which is called the Centre for Research and Sustainable Development (CRD).

Our present study is aimed at extending to the points below:

- Determination of the volumetric characteristics and the changes of state of the fluid;
- Simulate fluid transformations in the reservoir and even in production plants.

## EXPERIMENTAL

### SAMPLE COLLECTION

Sampling occurs at the deposition level, but certain precautions need to be taken during sampling.

When the ambient temperature is higher than the temperature of the separator, there is a risk of producing a flash in the sample bottle (Figure 1), which would make the sample unrepresentative. In this case, the cylinder must be cooled below the separator temperature.

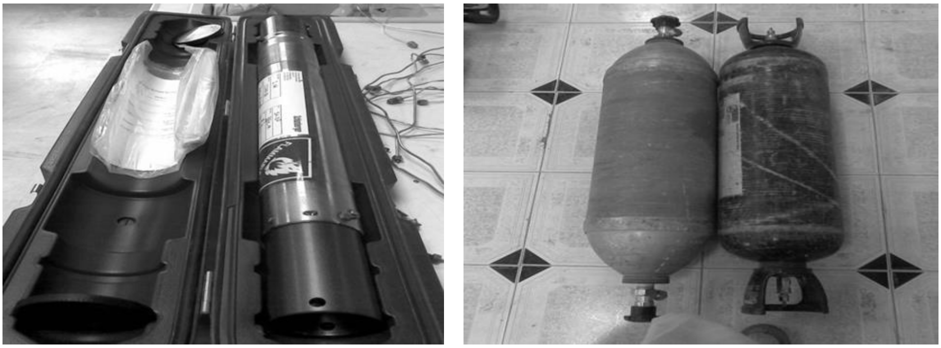

**Figure 1.** Gas and separator liquid sampling bottles (6)

Before taking the samples, the bottle must be cleaned with a non-corrosive liquid (Gasoline Safety and Repair Automotive), it must also be filled with water, and the piston placed at the end of the race (the upper part of the bottle). The bottle is connected to the upper valve by a tube, as short as possible, a tapping placed either on the lower connection of the separator level indicator, or on the oil outlet pipe, as close as possible to the separator before the automatic valve.

The tube is filled by creating a leak at the junction of the bottle. The leakage is eliminated when the tube is bled 2 to 5 times its volume.

A manometer will be attached to the valve opposite that of the inlet of the fluid to be sampled (the lower valve), which allowed to control the pressure inside the cylinder, equipped with a flexible hose ending in a graduated cylinder to collect and count the volume of water.

The top valve is open and, following pressure stabilization, the bottom valve is open very slowly. The movement (of water) of the piston shall be carried out at reduced speed so as not to create a pressure difference between the cylinder inlet and outlet, the fluid is admitted until the pressure in the cylinder is that of the separator. We stop refilling when we fail ¾ of the volume of the bottle (the remaining volume of water takes up approximately ¼ of the volume of the bottle), Our first close the lower valve (water side) and after stabilization of pressure, the upper valve is closed, then the valve on the separating outlet (Figure 2).

**Figure 2**. Separator Sampling

## Description of apparatus required for a thermodynamic study (7)

PVT material for thermodynamic analysis of hydrocarbon mixtures includes:

### a) DBR type oven

The oven is made up of finned immersion heaters, electrically powered and providing uniform air mixing and efficient heat distribution within the enclosure. The refrigeration system completes the assembly, thus making it possible to carry out the test under ambient conditions and even at low temperatures (Figure 3):

- Maximum operating temperature = +200 ºC.
- Minimum operating temperature = -35 °C.

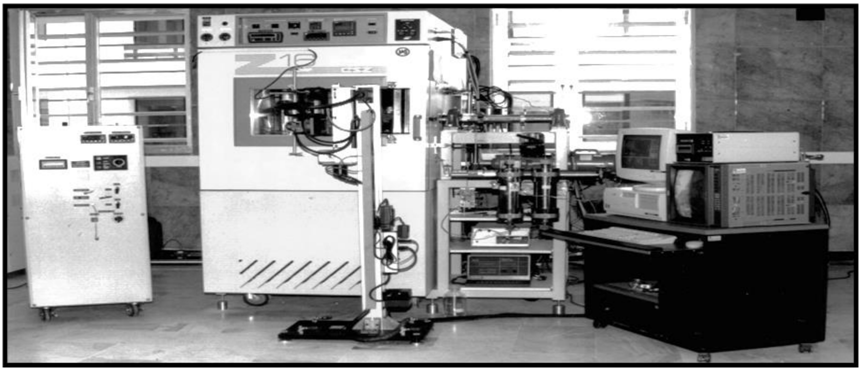

**Figure 3.** D.B ROBINSON brand PVT study equipment

### b) A PVT-DBR cell with total visibility

The PVT-DBR cell is a high precision stainless steel instrument for determining physical properties balances (liquid / vapour) (Figure 4).

The maximum operating pressure is at 10,000 psi ±10 psi with a total volume of 132 $cm^3$, with an accuracy of volume reading of 0.01 $cm^3$. Maximum operating temperature is 200 °C ± 0.1°C.

The PVT-DBR cell has many advantages such as:

- Direct measures of contact phase volumes;
- Easy to care for and disassemble during cleaning;
- High thermal mass ensuring temperature stability;
- Total visibility of the sample throughout the windows.

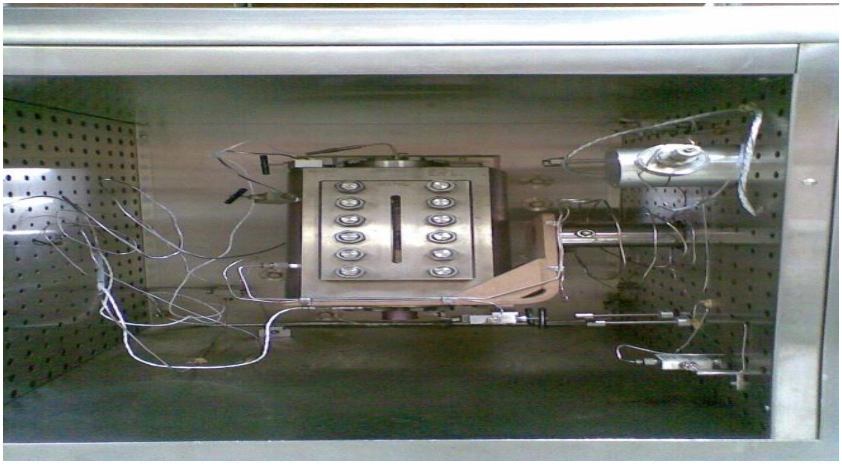

**Figure 4.** A PVT-DBR cell with total visibility

*** A high pressure DBR volumetric pump**

The volumetric pump is software driven and offers maximum flexibility in operating modes.

- Maximum operating pressure : 10,000 Psi ;
- Total volume = 500 $cm^3$ ;
- Maximum movement rate= 100 $cm^3$ /h;
- Minimal flow of movement= 1 $cm^3$ /h.

*** A high resolution CCD video system**

This system is composed by:

- A high magnification telescopic lens;
- An optical extension tube, which acts as a microscope at a long distance from the porthole of the PVT-DBR cell;
- A high-resolution color screen makes it possible to view and accurately measure the volumes of the phases present. The reading of the volumes is presented on a calibration table of the cathetometer.

The equipment is entirely controlled by computer, once the sample has been transferred, the manipulation is summarized in instructions, the pump and the temperature probe as well as other organs are completely and automatically controlled.

## CALCULATION METHODOLOGY

### Validation of samples (8)

As the validity of a "PVT" thermodynamic study depends a lot on the representativeness of the sampling, which is the first and most important operation for the realization of a PVT study, it is therefore essential to control and validate the samples taken either at the bottom or at the level of the separator before undertaking the experiment.

Validation of background samples includes:

- Bottle opening pressure ;
- Determination of saturation pressure at tank temperature.

Validation of surface samples includes:

A. **For liquids**

- Bottle opening pressure ;
- The determination of the saturation pressure has the separation temperature which must be identical to the separation pressure.

B. **For gases**

The validation is done by chromatographic analysis and the opening pressure must be close if not equal to the separation pressure, in addition the chromatographic composition of the gas all the bottles sampled must be identical.

### Validation of the separator gas

The separated gas is analyzed by gas phase chromatography, the purpose of this study is to correct the gas-oil ratio of the site (gas oil Ratio "GOR") and to determine:

### a) The Chemical Composition

It indicates hydrocarbon compounds and other gas constituents and their relative importance in the mixture through their volume and molecular fraction. The chemical composition of a gas is used for recovery studies.

It is also used to calculate certain properties as a function of pressure and temperature (compressibility factor, density) and to define the conditions for its treatment during operation (extraction of the liquid product). B

### b) The average molar mass

The average molar mass of a separator gas is calculated from its composition according to the following formula:

$$\mathrm{M} = \sum_{i=0}^{n} Yi \cdot Mi \qquad [1]$$

### c) The density

The density of the bottom effluent during the isothermal expansion process is determined in the conventional manner:

$$\rho = \frac{m}{V} \qquad [2]$$

### d) The compressibility factor

To describe the behavior of gas mixtures, the petroleum industry introduced into the ideal gas equation a dimensionless coefficient (Z) called the compressibility factor. With the usual notations, the equation of state of natural gases is written in the form:

$$PV = Z\, n\, RT \qquad [3]$$

The compressibility factor depends on the compressibility of the gas, the pressure and the temperature. When the pressure tends towards 0, the molecular interactions decrease; the behavior of the gas tends towards that of an ideal gas and Z tends towards 1

n: number of moles of the effluent = m/M;

## Preliminary study on separator oil (5)

### a) The pressure -volume relationship or constant composition study

- ❖ Study procedure: Before each PVT study, the study cell is cleaned, the seals are changed if necessary, the assembly is placed under vacuum, the pressure and temperature sensors are checked, the adjustment cathetometer and control of fluid transfer and release tubing.

A volume of 70 $cm^3$ (sufficient for a so-called CCE study) is then introduced into the study cell adjusted to the temperature and pressure conditions of the study. It is subject to exhaustion, which entails:

- The application of a series of thermodynamics balances at various pressure levels;
- The volumes used for mixing equilibrium conditions.

At each pressure level, the values of total volume (liquid-gas below the bubble pressure) of the fluid in the cell and of the corresponding pressure are recorded and noted, the equilibrium from one level to another is easier to reach thanks to the magnetic stirrer.

That no fluid is injected or released from the study cell during the experiment, hence the name constant mass study or Flash behavior.

This experiment makes it possible to determine the following parameters:

### 1) Oil saturation pressure (bubble point)

By definition, it is the pressure during which the first bubble of dissolved gas emerges from the oil. The value of the saturation pressure noted, "Pb".

### 2) The relative volume

The total relative volume denoted « $V_r$ » is the volume of the single-phase or two-phase fluid relative to the volume of oil at the bubble point.

$$V_r = \frac{oil\ Volume\ \ (P\ \&\ T)}{oil\ Volume\ (P_S\ \&T_S\ )}\ \ [vol/vol] \qquad [4]$$

### b) The flash separation (5)

Separation tests consist in simulating the crude separation process used in the field by bringing the oil from an initial state (reservoir pressure and temperature) to a final state (standard conditions), and this through 'a separator where the liquid/vapor balance is achieved perfectly thanks to a built-in circulation pump which continues to circulate the gas by bubbling in the liquid until all the condensable contained in the gas are deposited in the liquid (Figure 5).

The purpose of this step is to calculate the parameters and determine the composition of the separated liquid.

**Figure 5.** Flash separation equipment and DBROBINSON brand gasometer

### 1. The oil contraction factor ( $F_c$) or shrinkage (sh)

The difference between the volume of (pressure, temperature) given and the volume of the storage tank represents the contraction of the liquid, this contraction is due both to the release of the dissolved gas caused by the expansion to atmospheric pressure and to the decrease in temperature. The major factor that affects liquidity contraction is the release of dissolved gas. This factor is determined according to the following equation:

$$F_c = \frac{\text{volume of oil under standard conditions}}{\text{Volume of oil at P and T}} \qquad [5]$$

It is also given by:

$$F_c = \frac{1}{Bo} \qquad [6]$$

## 2. The gas-oil ratio (GOR)

The gas-oil ratio is defined by the ratio of the volume of gas released to the volume of separator liquid measured under standard conditions (see equation [7]).

$$GOR = \frac{\text{gas volume (Cs)}}{\text{liquid volume (Cstock)}} \ (m^3 / m^3) \qquad [7]$$

## 3. The volume factor of the liquid ($B_o$)

It is the volume of the liquid at a given pressure and temperature that leads to the unit volume of liquid in the storage tank. Its value is greater than unity, it is a function of the pressure, the temperature and the dissolved gas content and the surface oil treatment conditions (see equation [8]).

$$Bo = \frac{\text{oil volume (P\&T)}}{\text{oil volume (Cs)}} \qquad [8]$$

## 4. The density of a flashed liquid

The measurement of the density of a flashed liquid (storage oil at 15 °C.) is done using a DMA-48 electronic densitometer of the Arton Paar type (Figure 6).

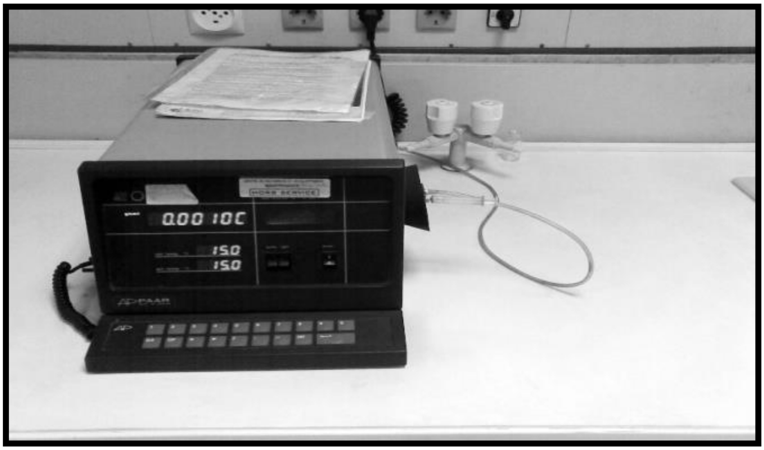

**Figure 6.** DMA-48 electronic densitometer of the Arton Paar type

## 5. Effluent compositions

The oil and the gas after the flash expansion are analyzed by gas phase chromatography to determine the chemical composition of the respective constituents which will be used for a mathematical recombination, which is done on “PVT sim” calculation software.

## 6. The composition of the separated liquid

Mathematical recombination makes it possible to reach the molar composition of the separating liquid from the chromatographic analysis of the effluents obtained by expanding at atmospheric pressure, of the storage density, of the GOR and of the molar masses of the constituents. The calculations are performed by a program in BASIC language.

### Recombination (6)

The purpose of the recombination of separator fluids is to reconstitute the bottom or reservoir fluid from the validated surface samples.

There are two types of recombination:

### A. Mathematical recombination

- Calculation of the molar mass of the gas

$$Mg = \frac{\sum(\mathrm{yi}*\mathrm{Mi})}{100} \qquad [9]$$

- Calculation of the mass concentration of the constituents in the gas

$$\mathrm{yi} = \frac{\mathrm{Yi}*\mathrm{MMi}}{\sum \mathrm{Yi}*\mathrm{MMi}} \qquad [10]$$

- Calculation of the molar mass of the liquid

$$\mathrm{Mh} = \frac{100}{\sum \mathrm{Xi}/\mathrm{MMi}} \qquad [11]$$

- Calculation of the molar concentration of the constituents in the liquid

$$\mathrm{Xi} = \frac{\mathrm{Xi}/\mathrm{MMi}}{\sum \mathrm{Xi}/\mathrm{MMi}} \qquad [12]$$

### B. Physical recombination of surface effluents

The recombined fluid is obtained by mixing the surface samples, separating oil and separating gas in well-defined proportions.

Corrected GOR must be calculated. The physical parameters provided by the study of the gas and the separator, oil will be used to correct the site GOR to obtain the initial fluid. The recombination GOR is calculated from site and laboratory data using the following formula:

$$\text{GOR corrected} = \text{GOR site} \cdot \text{Fc} \cdot \sqrt{\frac{(d.Z)site}{(d.Z)laboratory}} \qquad [13]$$

APTEFF, Vol. 54, 1-335 (2023) UDC: 66-911.33:621.182.1:536(65)
DOI: https://doi.org/10.2298/APT2354059H BIBLID: 1450-7188 (2023) 54, 59-80

Original scientific paper

## Thermodynamic study of the recombinant (of the representative sample of the background fluid) (10)

### Study (CCE)

Its purpose is to reproduce at the temperature of the formation the process of gas expansion in the areas of the reservoir where there is no fluid flow (flash expansion occurring at the limit of the zone of influence of the well).

The isotherm in PV variables is plotted point by point by performing gas equilibria at the temperature of the reservoir in a measuring cell.

### *The amount of gasoline deposited in the cell*

The exploitation of a gas condensate field is characterized by the deposit in the pores of the rock of the liquid resulting from the isothermal decline of the pressure.

These deposits are not recoverable because they form at low pressures. To be able to recover them, it takes a great energy input to increase the pressure and make them rise to the surface, so they represent the losses. The percentage of liquid deposits is given by:

$$\%\ liquid\ deposit = \frac{V}{V_r}.100 \qquad [14]$$

where: V: volume corresponding to a given pressure lower than the dew pressure;
$V_r$: volume at dew point.

### Constant Volume Study (CVD)

This involves simulating isothermal expansion of the well, when it is in production by releasing gas, in order to monitor the evolution of the different thermodynamic parameters of the down hole fluid and the composition during the decompression process of the deposit.

This study is carried out by conservation of the volume of the deposit effluent. It allows us to perform the following operations:

- Of the compressibility factor of the released gas (Z) ;
- Of the volume factor of the gas released (Bg) ;
- Of the molar composition of the gaseous complex recovered at the surface ;
- Of the quantity of gasoline produced ;
- Of C3+, C4+, and C5+.

### A. The volumetric factor (Bg) of the released gas

$$B_g = \frac{volume\ of\ gas\ released\ under\ cell\ conditions}{volume\ of\ gas\ under\ standard\ conditions} \qquad [15]$$

### B. The content of condensable

The condensable content of a gas is expressed as the mass of recoverable products in the liquid state per unit volume of gas under standard conditions. It is calculated from the composition of the gas.

Compounds considered condensable include propane and higher homolog (C3+, C4+, C5+).

Note: The C3+ compound includes all homolog higher than propane.

$$C_n^+(g/cc)=\frac{\sum_{i=n}^{m}(Y_i.M_i)}{23,63}\cdot 1000 \qquad [16]$$

## RESULTS AND DISCUSSION

### PRELIMINARY STUDY ON SEPARATOR SAMPLES

### Study of the separator gas

The composition of the separator gas and the molar mass of each constituent are given in the Table 1.

**Table 1**. Molar composition of the separator gas

| Constituents | Yi (%Molar) | Mi (g/mol) |
|---|---|---|
| **$N_2$** | 0.820 | 28.014 |
| **$CO_2$** | 3,200 | 44.010 |
| **C1** | 75.310 | 16.043 |
| **C2** | 11,150 | 30.070 |
| **C3** | 4.410 | 44.097 |
| **$iC_4$** | 1,480 | 58.124 |
| **$nC_4$** | 1,460 | 58.124 |
| **$iC_5$** | 0.920 | 72.151 |
| **$nC_5$** | 0.420 | 72.151 |
| **C6** | 0.530 | 86.178 |
| **C7** | 0.220 | 96,000 |
| **C8** | 0.080 | 107,000 |
| **TOTAL** | 1 | 22.45 |
| **The density of the separator gas** | d= 0.774 | |
| **Separator gas compressibility factor** | Z(P,T)= 0.983 at (T=29°C, P=73 psia) | |

### Study of oil separator

The results of this study are summarized in the Table 2.

***Density determination for different pressures***

It is recalled that the CCE is done at constant mass.

The density of separator liquid is determined gravimetrically at 3000 psia at the separation temperature T=29 °C.

$$P_{(3000\ psia)}=\frac{\textit{filled pycnometer mass -empty pycnometer mass}}{\textit{Volume of liquid transferred}}=0.700\ g/cm^3 \qquad [17]$$

We have: $\rho = m/V$ from where: $m = \rho\cdot V$ we calculate the initial mass which remains constant:

$$M = 0.700 \cdot 40.01 = 28.01g$$

**NB:** To determine the density for the different pressures, it suffices to calculate the *m/V* ratio each time. The mass is determined, and it remains constant, and the volume is obtained for each pressure.

**Table 2.** Behavior at constant mass of the separator oil

| **Pressure (psia)** | **Pressure (MPa)** | **volume ( $cm^3$ )** | **Relative Volume $V/V_{sat}$ ($m^3/m^3$)** | **Volumic mass (g/ $cm^3$)** |
|---|---|---|---|---|
| 5000 | 34.48 | 29.15 | 0.916 | 0.710 |
| 3000 | 20.69 | 40.01 | 0.974 | 0.700 |
| 2500 | 17.24 | 40.16 | 0.978 | 0.697 |
| 2000 | 13.79 | 40.32 | 0.982 | 0.695 |
| 1500 | 10.34 | 40.49 | 0.986 | 0.692 |
| 1000 | 6.90 | 40.68 | 0.991 | 0.688 |
| 500 | 3.45 | 40.88 | 0.996 | 0.685 |
| **73** | **0.50** | **41.06** | **1.000** | **0.682** |
| 60 | 0.41 | 43.24 | 1.053 | - |
| 55 | 0.38 | 45.6 | 1.111 | - |
| 50 | 0.34 | 51.66 | 1.258 | - |

### A. Bubble pressure

As shown in the Table 2, the bubble pressure is equal to 73 psia, and it corresponds to the opening pressure, so this sample is valid.

### B. Flash separation

- Contraction factor (Fc): Fc= 0.987;
- The gas-to-oil ratio (GOR): $GOR_{LABO}$ = 5.36 cc/cc;
- Liquid volume factor (Bo): Bo= 1.013;
- Density of the storage liquid: $D_{15}$ = 0.742 g/$cm^3$;
- The density of the storage liquid is determined using a DMA-48 electronic densimeter of the Artoo Paar type.
- Composition of flash effluents (Table 3)

**Table 3.** Molar composition of flash gas

| Constituents | % molar |
|---|---|
| Nitrogen | 0.950 |
| Carbon dioxide | 1,740 |
| Methane | 42,440 |
| Ethane | 20.410 |
| Propane | 9.910 |
| i-butane | 4,550 |
| n-butane | 3.580 |
| i-pentane | 1,340 |
| n-pentane | 1.020 |
| i-hexane | 3.370 |
| n-hexane | 5,500 |
| i-heptane | 5.190 |
| n-heptane | 0.950 |

## Recombination

### A. Composition of the separator liquid

The mathematical recombination of the flash effluents allows us to have the composition of the separator liquid (Table 4).

$$\mathbf{GOR_{LABO} = 5.\ 36\ m^3/m^3} \quad \text{and} \quad \boldsymbol{\rho} \mathbf{= 0.\ 742\ Kg/\ m^3}$$

**Table 4.** Composition of the separator liquid

| Constituents | % molar |
|---|---|
| $N_2$ | 0.030 |
| $CO_2$ | 0.054 |
| C1 | 1.323 |
| C2 | 1.192 |
| C3 | 2.629 |
| $iC_4$ | 2.739 |
| $nC_4$ | 4.269 |
| $iC_5$ | 6.807 |
| $nC_5$ | 4.478 |
| C6 | 14.617 |
| C7 | 19.482 |
| C8 | 12.634 |
| C9 | 10.396 |
| C10 | 0.053 |
| C11 | 6.307 |
| $C12_+$ | 12.990 |

### B. Physical recombination

All the parameters for calculating the GOR and the results of the physical recombination are grouped in (Table 5) and (Table 6) respectively:

**Table 5.** Parameters for GOR calculation

| | |
|---|---|
| Separation pressure (psia) | 73 |
| Separation temperature (°C) | 29 |
| Density of "site" separating gas | 0.780 |
| Density of the "laboratory" separating gas | 0.774 |
| "site" compressibility factor Z | 0.980 |
| compressibility factor Z "lab" | 0.983 |
| GOR "site" ($Sm^3/m^3$) | 2585 |
| Contraction factor "Fc" ($m^3/m^3$) | 0.987 |

GOG recombination= S557.357 $m^3/m$

Table 6. Physical recombination

| | |
|---|---|
| $P_1$ ( psia) | 5000 |
| $V_1$ ( $cm^3$ ) | 70 |
| $T_0$ ( K ) | 288.15 |
| $Z_0$ | 1 |
| $T_1$ ( K) | 300.85 |
| $P_0$ ( psia ) | 14.7 |
| $Z_1$ to $T_0$ and $P_1$ | 0.96 |
| $V_r$ at 5000 Psia | 0.97 |
| $V_0$ (cm $^3$) | 23754.62 |
| $V_{liq}$ (cm $^3$) | 9.29 |
| $V_{liq}$ (5000 psia) (cm $^3$) | 8.93 |

70 $cm^3$ of separator gas are therefore mixed with 8.93 $cm^3$ of separator liquid to obtain the representative sample of the deposit fluid.

### C. Bottom fluid composition

The composition of the bottom fluid is obtained from the mathematical recombination of the separator gas and separator liquid (corrected **GOR = 2557.354 $m^3/m^3$**, **$\rho$ = 0.682 $kg/m^3$**).

The composition is given in the Table 7.

**Table 7.** Composition of the bottom fluid (reservoir)

| Constituents | %Molar |
|---|---|
| **$N_2$** | 0.776 |
| **$CO_2$** | 3.023 |
| **C1** | 71.15 |
| **C2** | 10.59 |
| **C3** | 4.31 |
| **$iC_4$** | 1.551 |
| **$nC_4$** | 1.618 |
| **$iC_5$** | 1.251 |
| **$nC_5$** | 0.648 |
| **C6** | 1.322 |
| **C7** | 1.303 |
| **C8** | 0.786 |
| **C9** | 0.584 |
| **C10** | 0.003 |
| **C11** | 0.355 |
| **C12 +** | 0.730 |

## Thermodynamic study of the bottom sample

### A. Constant mass study (CCE) at 125 °C

All results are grouped in Table 8.

**Table 8.** Evolution of relative volume, density and compressibility factor, % Liquid deposits as a function of pressure at T=125 °C. (*) *Saturation pressure*

| Pressure (psia) | Pressure (Mpa) | Volume Complex (CC) | Deposits Liquid (cc) | Percentage (%) of Liquid Deposits | V/Vr (dc) | Mass volume (cc/g) | Compressi-bility factor Z | ρ Mass volume |
|---|---|---|---|---|---|---|---|---|
| 7000 | 48.28 | 28.83 | - | - | 0.858 | 3.125 | 1.236 | 0.320 |
| 6500 | 44.83 | 29.77 | - | - | 0.886 | 3.227 | 1.186 | 0.310 |
| 6000 | 41.38 | 30.65 | - | - | 0.912 | 3.322 | 1.127 | 0.301 |
| 5500 | 37.93 | 32 | - | - | 0.953 | 3.469 | 1.078 | 0.288 |
| ***5021** | **34.63** | **33.7** | **0.00** | **0.00** | **1.000** | **3.641** | **1.033** | **0.275** |
| 4800 | 33.10 | 34.51 | 0.10 | 0.30 | 1.027 | 3.741 | 1.015 | 0.267 |
| 4500 | 31.03 | 35.95 | 0.29 | 0.86 | 1.070 | 3.897 | 0.991 | 0.257 |
| 4000 | 27.59 | 39.17 | 0.80 | 2.38 | 1.166 | 4.246 | 0.960 | 0.236 |
| 3000 | 20.69 | 49.45 | 1.83 | 5.45 | 1.472 | 5.360 | 0.909 | 0.187 |
| 2200 | 15.17 | 66.88 | 2.47 | 7.35 | 1.991 | 7.249 | 0.902 | 0.138 |
| 1800 | 12.41 | 82.92 | 2.46 | 7.32 | 2.469 | 8.988 | 0.914 | 0.111 |
| 1600 | 11.03 | 94.41 | 2.36 | 7.03 | 2.811 | 10.233 | 0.926 | 0.098 |

### B. Constant volume study (CVD) at 125 °C

All the results are grouped in Tables 9 and 10, respectively:

**Table 9.** Evolution of the compressibility factor (Z), volumetric factor (Bg) and % liquid deposits as a function of pressure. (*) Saturation pressure.

| **Pressure (psia)** | **Pressure (mpa)** | **Volume Complex (CC)** | **V Deposits Liquid (CC)** | **% of the Deposits liquid** | **Vgas released in the cell (cc) at P and T** | **Vgas (cc) at 15°C** | **Z** | **Bg*100 $m^3/m^3$** |
|---|---|---|---|---|---|---|---|---|
| 5021 | 34.63 | 33.73 | - | - | - | - | 1.033 | - |
| 4000 | 27.59 | 38.46 | 0.83 | 2.46 | 4.4 | 951.19 | 0.929 | 0.463 |
| 3500 | 24.14 | 37.24 | 1.09 | 3.23 | 3.3 | 643.02 | 0.902 | 0.513 |
| 3000 | 20.69 | 38.5 | 1.24 | 3.68 | 4.49 | 765.77 | 0.884 | 0.586 |
| 2500 | 17.24 | 39.56 | 1.3 | 3.85 | 5.66 | 814.17 | 0.874 | 0.700 |
| 2200 | 15.17 | 38.29 | 1.31 | 3.88 | 4.12 | 521.99 | 0.874 | 0.789 |
| 1500 | 10.34 | 49.42 | 1.24 | 3.68 | 15.69 | 1288.44 | 0.922 | 1.218 |

**Table 10.** Molar composition of the gaseous complex released gases produced at the surface, and evolution of the content of condensable products as a function of the pressure

| **Pressure (psia)** | 4000 | 3500 | 3000 | 2500 | 2200 | **1500** |
|---|---|---|---|---|---|---|
| **Constituents** | **Zi (%)** | | | | | |
| **Nitrogen $N_2$** | 0.79 | 0.79 | 0.79 | 0.80 | 0.80 | 0.80 |
| **Carbon dioxide $CO_2$** | 3.04 | 3.05 | 3.06 | 3.06 | 3.07 | 3.08 |
| **Methane $C_1$** | 71.76 | 72.08 | 72.59 | 72.59 | 72.69 | 71.77 |
| **Ethane $C_2$** | 10.61 | 10.62 | 10.66 | 10.66 | 10.68 | 10.74 |
| **Propane $C_3$** | 4.29 | 4.28 | 4.28 | 4.28 | 4.28 | 4.31 |
| **Butane $C_4$** | 3.14 | 3.12 | 3.10 | 3.09 | 3.08 | 3.10 |
| **Pentane $C_5$** | 1.86 | 1.84 | 1.82 | 1.80 | 1.79 | 1.78 |
| **Hexanes $C_6$** | 1.28 | 1.26 | 1.23 | 1.20 | 1.18 | 1.65 |
| **Heptanes plus $C_{7+}$** | 3.24 | 2.96 | 2.73 | 2.52 | 2.42 | 2.77 |
| **Total** | 100.00 | 100.00 | 100.00 | 100.00 | 100.00 | 100.00 |
| **Molar mass (g/mole)** | 25.53 | 25.28 | 25.10 | 24.86 | 24.76 | 25.39 |
| **Density / air** | 0.880 | 0.872 | 0.866 | 0.857 | 0.854 | 0.876 |
| **$C3_+$ (g/ $cm^3$)** | 392.90 | 379.48 | 367.93 | 357.43 | 352.08 | 384.23 |
| **$C4_+$ (g/ $cm^3$)** | 312.74 | 299.51 | 287.96 | 277.46 | 272.11 | 303.70 |
| **$C5_+$ (g/ $cm^3$)** | 235.40 | 222.67 | 211.61 | 201.36 | 196.25 | 227.35 |

### Flashing behavior of the separator liquid

During the lighted expansion, the volume of the gasoline increases substantially until there is a sudden change in the bubble point (Figure 7). This is explained by the phase change of the gasoline, which passes from the liquid state to the gaseous state. And the bubble pressure which is equal to 73 psia is the separation pressure, hence the validity of the sample.

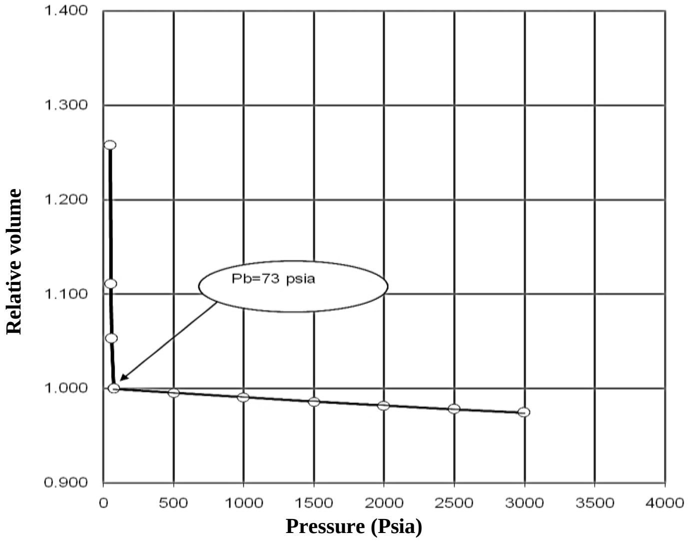

**Figure 7.** Variation of relative volume ($V_R$) as a function of pressure at ($T_S$ =29 °C) CCE

### Study of recombinant fluid

#### A. Variation of relative volume as a function of pressure

The evolution of the volume of recombinant fluid during expansion shows that a greater increase takes place from the dew pressure, because the recombined is relieved of its heavy components (Figure 8).

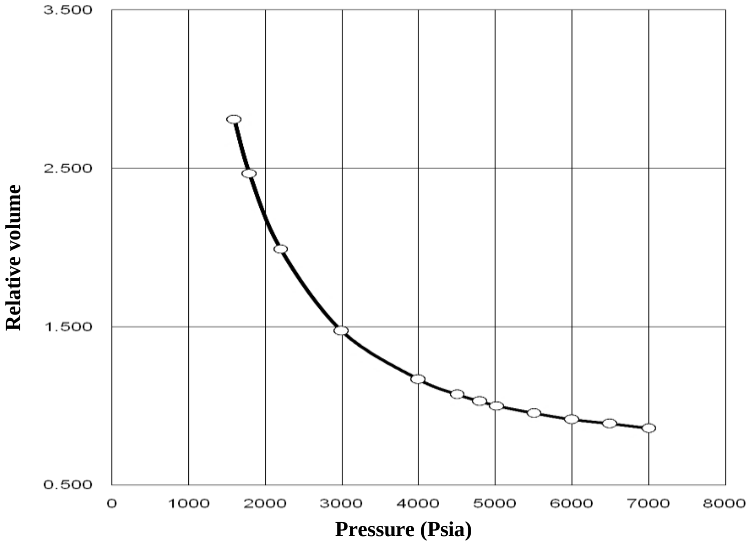

**Figure 8.** variation of relative volume as a function of pressure at (Tg=125 °C) CCE

### B. Density variation with pressure

The density increases as the pressure increases, which corresponds to the theory (Figure 9). The density is in proportion to the pressure. $\rho = \frac{M.P}{R.T.Z}$

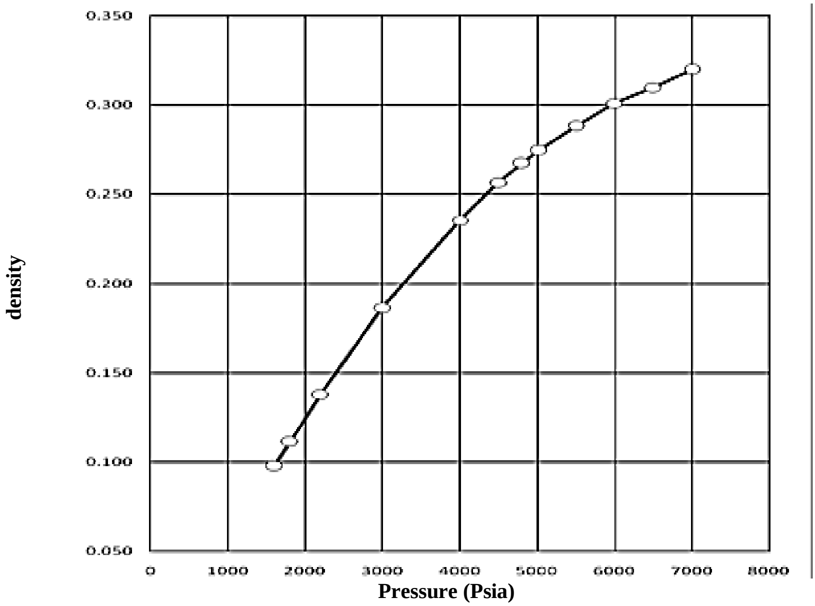

**Figure 9.** variation of density as a function of pressure at (Tg=125 °C) CCE

### C. Variation of the compressibility factor (Z) as a function of pressure

The compression factor decreases as a minimum with increasing pressure. This is the typical form for all real gases. This minimum increases with increasing pressure and tends to disappear in the event of high pressure (Figure 10).

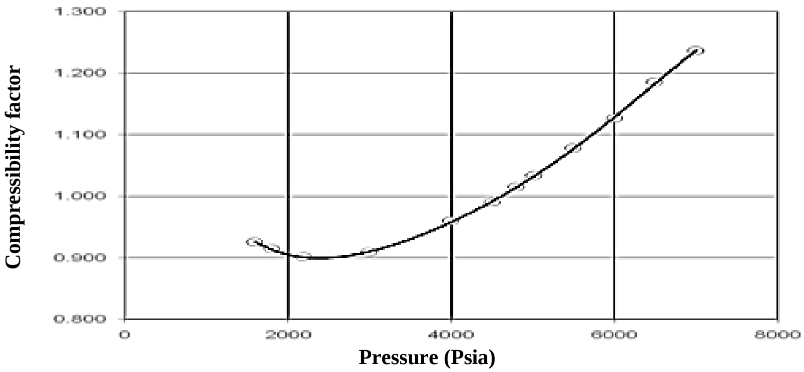

**Figure 10.** Compressibility factor “Z” as a function of pressure at (Tg=125 °C) CCE

We note that Z tends to one when the pressure tends to zero, which is consistent with the ideal gas theory.

### D. Liquid deposition curves as a function of pressure

The liquid deposition curves bring to light the phenomenon of retrograde condensation. They represent what happens within a gas condensate field.

Keep the pressure down, the volume of liquid deposits increases up to a pressure of (1800 psia) which corresponds to Pmax after which the volume of liquid deposits begins to decrease (Figure 11).

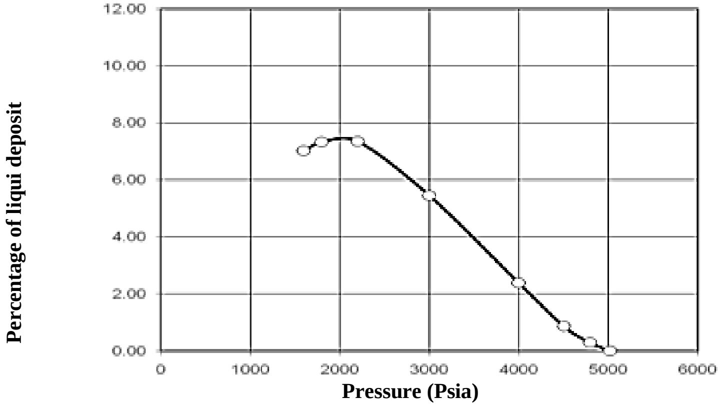

**Figure 11.** percentage of liquid deposits as a function of pressure at (Tg=125 °C) CCE

### E. Curve of volumetric factor (Bg)

The volume factor for the gases released (Bg) increases with the pressure drop, which is due to the release of gas which is always larger during the expansion process, this is a perfect fit with the theory (Figure 12).

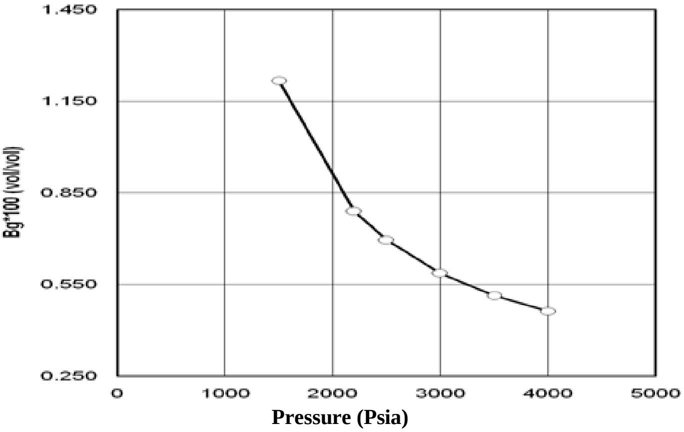

**Figure 12.** Variation of volumetric factor (Bg) as a function of pressure at (Tg=125 °C) CVD

### F. Curve of the composition of the gas complex recovered at the surface

A very small change that results in a slight decrease is observed for methane and its superior equivalents (C1, C2, C3, C4) during expansion (Figure 13).

With respect to heavy constituents (C5, C6, C7+), the reduction is very noticeable during expansion.

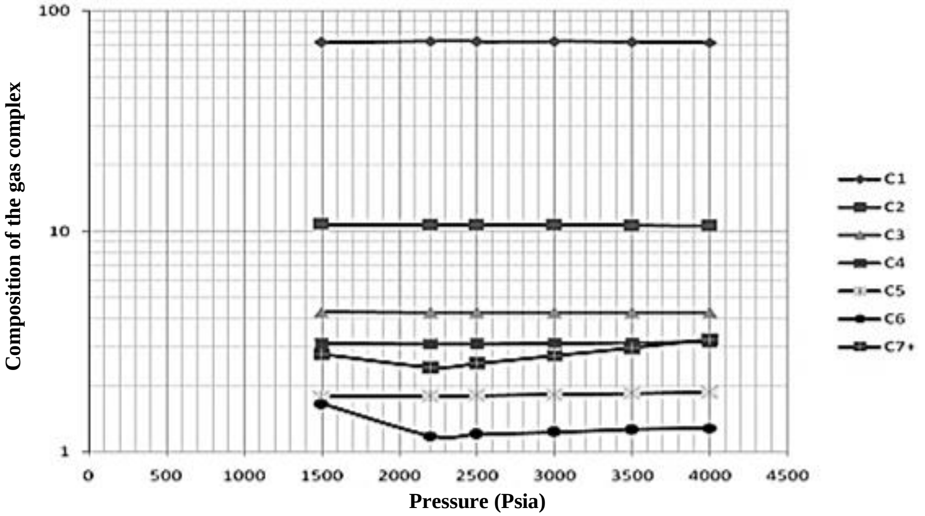

**Figure 13**. Evolution of the composition of the gas complex as a function of pressure at (Tg=125 °C) CVD

### G. Condensable product content curve

We can see that the amount of C 3 +, C 4 + and C5+ increases as the pressure increases (Figure 14).

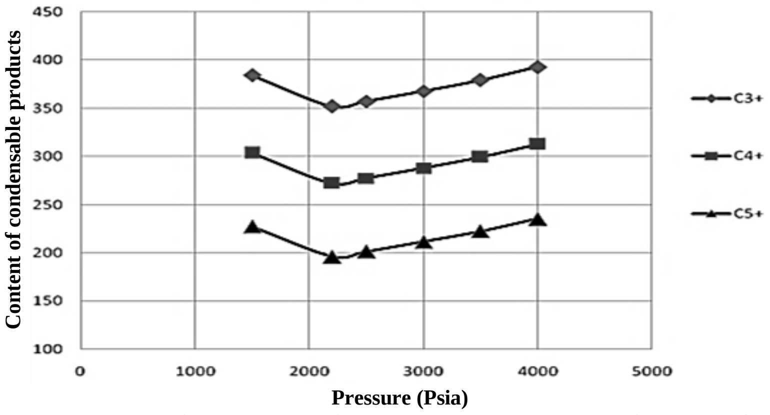

**Figure 14.** Evolution of the content of condensable products as a function of pressure at (Tg=125°C) CVD

APTEFF, Vol. 54, 1-335 (2023) UDC: 66-911.33:621.182.1:536(65)
DOI: https://doi.org/10.2298/APT2354059H BIBLID: 1450-7188 (2023) 54, 59-80

Original scientific paper

## CONCLUSIONS

Our work was carried out at the PVT laboratory, the work was devoted to the thermodynamic study of the PVT status variables of Algerian condensate gas.

The results of our work demonstrated the reliability of the devices used and the growing advantage of often inaccessible data; otherwise very costly in terms of time and money experientially.

As our results show, the computational methods used in the PVT laboratory have greatly improved, to obtain results with the right accuracy, and this was confirmed and compared with the results obtained at the site level. and this was confirmed and compared to the results obtained on the website. after the site and depot data.

In the experimental part, the bubble pressure of the separation liquid was determined, which was compared to the separation pressure, and the value was the same.

After obtaining the fluid composition from the tank, the thermodynamic study has allowed us to determine the dew pressure and thermodynamic parameters and to observe the behaviour of this fluid.

Liquid deposition containing heavy compounds ($C_5$, $C_6$, $C_7$+) , this head forms at low pressure at the deposit temperature but after a certain pressure this volume begins to decrease and which highlights the phenomenon of retrograde condensation.

The condensate content C3+, C4+, and C5+ increases as the pressure increases.

### List of symbols

$M_i$ : the molar mass of component *i* in the gas mixture;
$Y_i$ : the molar fraction of component *i* in the gas mixture;
n: number of gas constituents;
$d_g$ : gas density;
$M_g$ : molar mass of gas;
Vr : _ relative volume [$m^3/m^3$];
$P_s$ and $T_s$ : pressure and temperature at saturation point;
$d_{site}$ : Density of gas (air) determined on site ;
$Z_{site}$: Gas compressibility factor determined on site ;
$d_{laboratory}$: Density of the gas (air) determined in the laboratory;
$Z_{laboratory}$: Gas compressibility factor determined in the laboratory;
Fc: Separating liquid contraction factor (vol/vol).;
m: mass of the effluent;
v: volume of the recombinant during isothermal expansion at a given *p*;
m': the mass introduced initially;
M: the molar mass of the effluent known from its composition;
$Y_i$: molar fraction of the gas complex;
$M_i$: molar mass of component *i* of the gas complex;
v= 23.63: molar volume (in liters) occupied by one mole under standard conditions,
and n= 3, 4, 5.

## REFERENCES

1. Sidrouhou, H.M; Korichi, M; Dada. S. Evaluation of Correlations of Compressibility Factor (z) of Natural Gas for Algerian Gas Reservoirs. *Energy Procedia*. **2019**, *157*, 655-669.
2. Metallaoui, N. Thermodynamic study of the MS7001EA gas turbine at the Skikda GNL1K complex. M.S Thesis. University of Badji mokhtar annaba, Algiers, 2017.
3. Jmai, S; Bagane, M.; Queneudec-T'Kint, M. Physico-chemical, thermal, thermodynamic and kinetic characterization of a porous material (Di-calcium phosphate). *Heat and Mass Transfer*. **2019**, *55*, 3589-3602.
4. Eilert, S; Kenneth, C. Phase Relations of Gas-Condensate Fluids: Test Results, Apparatus, and Techniques, Volume 1 of Two Volumes. American Gas Association. 3 September 1957, p 430-439.
5. Danesh, A. PVT and Phase Behavior of Petroleum Reservoir Fluids. Elsevier Science.7 May 1998, *47*, 33-45.
6. Jacoby, R. H.; Koeller, R.C. and BERRY, V.J. Effect of composition and temperature on phase Behavior and Depletion performance of rich gas-condensate systems. *J. Pet. Technol.* ***1959**, 11* (07), 58-63.
7. Sidrouhou, H. M.; Korichi, M. Emprirical and correlative study of PVT proprietier of Algerian oil. *Energy procedia*. **2013**, *36*, 738-745.
8. Zanochuev, S. A; Shabarov, A. B; Podorozhnikov, S. Yu; Zakharov, A. A. Thermodynamic properties of gas-condensate system with abnormally high content of heavy hydrocarbons. *Materials Science and Engineering*. **2018**, *357*, 12-24.
9. Uribe-Vargas, V; Carreón-Calderón. B; Ramírez-Jaramillo, E. Thermodynamic Characterization of Undefined Petroleum Fractions of Gas Condensate using Group Contribution. Oil & Gas Science and Technology. *IFP Energies nouvelles*. **2016**, *71*(5), 2-12.
10. Sutton, R. P. Fundamental PVT Calculations for Associated and Gas/Condensate Natural-Gas Systems. *SPE Res Eval & Eng.* ***2007**, 10* (03), 270-284.

APTEFF, Vol. 54, 1-335 (2023) UDC: 664.696:633.18:581.48+635.615]:664.64.016.3
DOI: https://doi.org/10.2298/APT2354081S BIBLID: 1450-7188 (2023) 54, 81-91

Original scientific paper

# INFLUENCE OF EXTRUSION CONDITIONS ON FUNCTIONAL AND TEXTURAL PROPERTIES OF BROWN RICE-WATERMELON SEEDS EXTRUDED SNACKS

*Mayowa Saheed SANUSI*, Musliu Olushola SUNMONU, Sodiq Oladimeji ALASI*

Department of Food Engineering, Faculty of Engineering and Technology, University of Ilorin, Nigeria

**Received: 14 January 2023 Revised: 28 February 2023 Accepted: 01 March 2023**

*This study aims to evaluate and model the effect of extrusion conditions on the functional and textural properties of brown rice-watermelon seeds extruded snacks. Taguchi was used in designing the experiment and Response Surface Methodology was used to evaluate and model the effect of exit barrel temperature (120 – 140 °C), barrel screw speed (300 – 420 rpm), and feed moisture content (16-18%) on water absorption index (WAI), water solubility index (WSI), hardness, chewiness, gumminess, and springiness of the extruded snacks. The Pareto plot was used to evaluate the significant extrusion parameters on the functional and textural properties. The WAI and WSI of the extruded snacks ranged between 2.09 and 2.87 (g/g), and 2.12 and 2.59% respectively. The hardness, chewiness, gumminess, and springiness of the extruded snacks ranged between 118.92 and 4054.40 N, 0.06 and 326.00 N, 2.41 and 1509.17 N, and 0.02 and 0.21, respectively. The Pareto plot showed that exit barrel temperature had the most significant influence on WAI and WSI whereas, the quadratic interaction effect of feed moisture content had the most significant influence on the hardness, chewiness, gumminess, and springiness of the extruded snacks. Polynomial regression models were developed for the functional and textural properties with an adequate coefficient of determination (R2) that ranged from 0.74 to 0.99, thus indicating their ability to predict the properties. Conclusively, a hybrid of Taguchi and Response Surface Methodology (RSM) technique was used to establish and predict the influence of extrusion conditions on the functional and textural properties of brown rice-watermelon seeds extruded snacks.*

**Keywords**: Taguchi, Response Surface Methodology, extrusion, textural, functional properties.

## INTRODUCTION

Extrusion cooking is a novel technology that has been adopted in many food processing industries due to its versatility, low cost, and efficiency. Extrusion technology can be used to produce different types of food products with varying shapes and sizes. Food products such as ready-to-eat snacks, breakfast cereals, and texturized vegetable protein are produced through mixing, continuous cooking, and forming processes (1). In the extrusion of raw materials, transformations such as protein denaturation, starch gelatinization, inactivation of anti-nutrients and enzymes, degradation of pigments and vitamins, and complex formation of amylose and lipids occur (2, 3). Functional and textural properties are among consumers' key indicators for product acceptability (3, 4). Extrusion cooking has been used to develop novel extruded products from blends of different raw materials and agricultural by-products. However, little has been reported in the literature about the utilization of broken

---

* Corresponding author: Mayowa Saheed SANUSI, Department of Food Engineering, Faculty of Engineering and Technology, University of Ilorin, Nigeria, e-mail: sanusi.ms@unilorin.edu.ng

APTEFF, Vol. 54, 1-335 (2023) UDC: 664.696:633.18:581.48+635.615]:664.64.016.3
DOI: https://doi.org/10.2298/APT2354081S BIBLID: 1450-7188 (2023) 54, 81-91

brown rice and watermelon seeds to produce extruded snacks. Brown rice is a rich source of fibre, antioxidants, phytoestrogens, minerals (iron, phosphorus, magnesium, potassium, zinc, and copper) and B vitamins (5, 6). In addition, its protein content is higher than in white rice. Watermelon seeds are a rich source of protein, as well as phytochemicals (7). In developing countries, broken brown rice is believed to have a low market value, while watermelon seeds are usually discarded as a waste product. However whole brown rice and broken brown rice have the same nutritional composition and can be exploited as a starch-rich ingredient to produce extruded snacks. Also, watermelon seeds can be converted to flour and used as a protein source to enrich extruded snacks. Therefore, the effect of extrusion parameters on the blends of brown rice flour and watermelon seeds flour on the functional (water absorption index and water solubility index) and textural properties (hardness, springiness, chewiness, and gumminess) needed to be established. Oke et al. (8) and Sahu (9) reported that the final product quality, beside mixture composition, could be affected by extrusion parameters such as extruder screw speed, barrel temperature, feed moisture content, and diameter of the die. Thus, this suggests a proper adjustment of extrusion conditions to produce desired quality products is needed. Many researchers have found that feed moisture content, extruder temperature, and screw speed had a significant effect on the textural and functional properties of extrudates (3, 4, 8, 9). However, there is a paucity of information on the effect of extrusion parameters on the functional and textural properties of brown rice-watermelon seeds extruded snacks. Response Surface Methodology (RSM) and Taguchi design have been separately used to evaluate, model and optimize the effect of process parameters on product quality characteristics by several researchers (3, 4, 10-13). In spite of this, little has been reported about the integration of Taguchi design and response surface methodology to evaluate and model the effect of extrusion conditions on product quality parameters. Therefore, this study aimed to evaluate and model the effect of extrusion conditions on the functional and textural properties of brown rice-watermelon seeds extruded snacks using a hybrid of Taguchi design and response surface methodology approach.

## METHODOLOGY

### MATERIALS

Broken brown rice and watermelon seeds were obtained from Saris-Sodiq rice mill and Fruits glow store, Ilorin, Nigeria and were both processed into brown rice flour (0.30 mm) and watermelon seed flour (65 μm) using a Hammer mill (Nukor, Model: SG 30, South Africa) and an electric blender (Geepas Mixer Grinder, Model: 550w, India), respectively.

### BLENDS PREPARATION

A preliminary experiment was conducted to select the best blends of brown rice flour and watermelon seed flour using mixture design in Minitab Statistical Software version 20.3. Mixture of brown rice flour (90%) and watermelon seeds flour (10%) was selected based on the highest protein content (12%) obtained from the preliminary experiment as shown in Figure 1.

DOI: https://doi.org/10.2298/APT2354081S BIBLID: 1450-7188 (2023) 54, 81-91

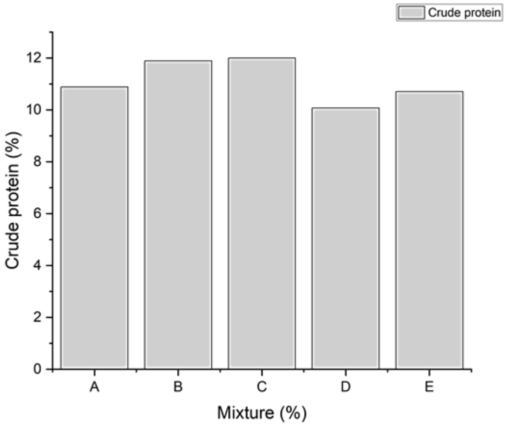

**Figure 1.** Effect of different mixture of brown rice flour and watermelon seeds flour on crude protein

where A is the mixture of 80% brown rice flour and 20% watermelon seeds flour, B is 100% brown rice, C is 90% brown rice flour and 10% watermelon seeds flour, D is 85% brown rice flour and 15% watermelon seeds flour, and E is 95% brown rice flour and 5% watermelon seeds flour.

## EXPERIMENTAL DESIGN

A hybrid of Taguchi and response surface methodology was used to design and evaluate the effect of extrusion parameters on functional and textural properties of brown rice-watermelon seeds extruded snacks. Taguchi Orthogonal Array Design which is $L_9(^{3**3})$ was generated using Minitab Software Version 20 UK. The $L_9$ implies nine runs, while 3**3 implies 3 factors with 3 levels. The factors are Exit Barrel Temperature (EBT), Barrel Screw Speed (BSS) and Feed Moisture Content (FMC) while the levels ranged from 16-18%, 300– 420 rpm and 120 - 140 °C, respectively as shown in Table 1. Response surface methodology (RSM) was used to analyze the results obtained from the Taguchi design by using the second-order polynomial regression model of RSM that has linear, quadratic, and interaction relationships as shown in Equation [1].

$$Y = \beta_o + \sum_{i=1}^{3} \beta_i X_i + \sum_{j=1}^{3} \beta_{ii} X_i^2 + \sum_{i=1}^{2} \sum_{j=1}^{3} \beta_{ij} X_i X_j + \varepsilon \quad [1]$$

where $\beta_o$ is the coefficients of the model constant, $\beta_i X_i$ is the linear terms, $\beta_{ii} X_i^2$ is the quadratic terms and $\beta_{ij} X_i X_j$ is the interaction terms, Y is the responses (water absorption index, water solubility index, hardness, springiness, chewiness and gumminess), $X_i$ and $X_j$ are the independent variables (exit barrel temperature, barrel screw speed and feed moisture content). The fitness of the models for water absorption index, water solubility index, hardness, springiness, chewiness, and gumminess were determined by the coefficient of determination $R^2$, $R^2_{\text{adjusted}}$ and $R^2_{\text{predicted}}$. Analysis of variance (ANOVA) was used to determine the p-values at 95% confidence level and Fischer values (F value) of water absorption index, water solubility index, hardness, springiness, chewiness, and gumminess. Pareto plot in Minitab software version 20.3 was used to determine the most significant extrusion parameters. In the Pareto plot, a reference line is drawn on the chart to indicate the P=0.05 threshold for a statistically significant effect.

**Table 1.** Taguchi experimental design

| Extrusion Parameters | Units | Low | Medium | High |
|---|---|---|---|---|
| Exit Barrel Temperature (EBT) | °C | 120 | 130 | 140 |
| Barrel Screw Speed (BSS) | rpm | 300 | 360 | 420 |
| Feed Moisture Content (FMC) | % | 16 | 17 | 18 |

## EXTRUSION PROCEDURE

Figure 2 shows the schematic illustration of the extrusion of brown rice-watermelon seed blends using a twin-screw extruder. The co-rotating twin-screw extruder (Model: HN-65, Zhuoheng Product, Jinan City, Shandong Province, China) was used to extrude the mixture of brown rice flour and watermelon seeds flour in a ratio of 90:10. The blend was mixed with potable water at 16%, 17%, and 18% moisture content of the entire mixture mass using a mixer (Sokany Stand Mixer, Model: Cx-6612, China). The extruder was set at a temperature of 80 °C and 100 °C in the first and second heating bands, while the last heating band temperature was varied from 120 °C, 130 °C, and 140 °C. The samples were fed through the hopper at a constant speed of 120 rpm which was conveyed into the barrel, where the cooking took place. From the barrel, the samples passed through the three heating zones at various barrel screw speeds of 300, 360 and 420 rpm. The cooked sample within the barrel was passed through the orifice die of 4 mm and the extrudates were cut at a speed of 1500 rpm. The extrudates were collected, dried using a fabricated forced-air dryer and packed in a zip-lock container at room temperature for proper storage.

## WATER ABSORPTION INDEX (WAI) AND WATER SOLUBILITY INDEX (WSI)

The determination of WAI and WSI was performed by employing the approach outlined by Stojceska et al. (14) and Sahu and Patel (15). Three samples of each run were analyzed where extrudate of 2 g of powdered form from each run was poured into a centrifuge tube where 20 ml of distilled water was also added to dissolve the products for 30 mins under room temperature, and gently stirred for 5 mins. Centrifugation was completed by rotating at a very high speed of 3000 rpm for 15 mins. Equations [2] and [3] were used for the evaluation of the WAI and WSI.

$$\text{WAI (g/g)} = \frac{WS}{WDS} \quad [2]$$

$$\text{WSI (\%)} = \frac{WDSS}{WDS} \times 100 \quad [3]$$

where WS is the weight of sediment, WDS is the weight of dry solids, WDSS is the weight of dissolved solids in the supernatant.

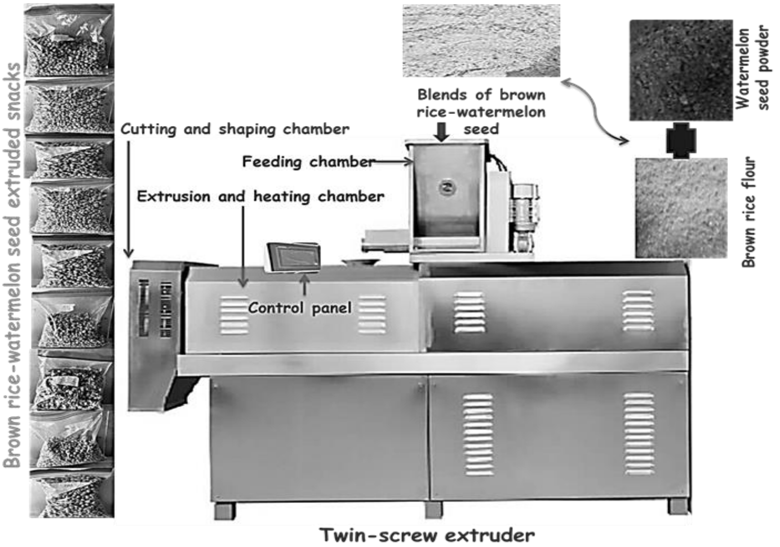

**Figure 2.** Schematic illustration of extrusion of brown rice-watermelon seeds blends using a twin-screw extruder

### TEXTURAL PROFILE ANALYSIS

Texture profile analysis (TPA) of the extruded snacks samples was conducted with a texture analyser (Stable Micro Systems, England, UK). For the TPA, a 36 mm cylindrical aluminium probe and 30 kg load capacity were used in two compression cycles. The test speed was 200 mm/min, compression was at 50% and the recovery period between the strokes was 5 s. The recorded parameters were hardness, chewiness, gumminess, and springiness. Measurements were done in triplicates per sample.

### STATISTICAL ANALYSIS

The experiments were conducted in triplicate and analysis of variance (ANOVA) of the data was performed using the SPSS package (SPSS 20.0, SPSS Inc., and Chicago, IL, USA). Duncan multiple tests with a confidence interval of 95% were used to determine significant differences between means.

## RESULTS AND DISCUSSION

### WATER ABSORPTION INDEX (WAI)

WAI is a measure of the degree of gelatinization index and dextrinization of starch by determination of water absorption and retention by starch (16, 17). The WAI of the brown rice-watermelon seeds extruded snacks ranged between 2.09 and 2.87 (g/g) as shown in

Table 2. The snacks' maximum WAI was recorded at 17% FMC, 120°C EBT and 300 rpm BSS whereas, the minimum was recorded at 18% FMC, 140°C EBT and 420 rpm BSS. It was observed that all the linear, quadratic, and interaction effects of the extrusion parameters have a significant influence on the WAI (Figure 3a). However, it was observed that EBT had the most significant influence on the WAI of the snacks. The developed model is significant for WAI prediction and is presented in Table 3. The $R^2$ presents its close adequacy. The predicted $R^2$ of the model strongly agrees with the adjusted $R^2$ and shows its adequacy to predict the effect of extrusion parameters on WAI. The negative linear coefficient of EBT, BSS, and FMC implies that an increase in WAI would occur as a result of a decrease in EBT, BSS, and FMC. Figure 3c&d showed that lower EBT, BSS and FMC lead to an increase in WAI of the extrudates. These results could be traced to the extrusion process as lower FMC led to excess shearing by the barrel screw which ultimately maximizes the WAI retained (18, 19). Also, Samyor et al. (20) similarly reported an inverse relationship between BSS and WSI from passion fruit-rice flour-based extrudates, which was traced to the reduction in the polymeric chain length from high screw speed. Likewise, the negative coefficient of EBT indicated dextrinization of starch takes place at lower EBT and thus increased the WAI. This could be attributed to the decomposition of starch at a lower temperature. Our results have a relative connection with the study of Beigh *et al.* (17) and Sahu *et al.* (3) on the production of extrudates from barley and chestnut flour and soy protein enriched maize-based extruded snacks.

## WATER SOLUBILITY INDEX (WSI)

The WSI defines the water-soluble components liberated during extrusion which is the measure of starch degradation and digestibility (16, 17). The WSI of brown rice-water melon seeds snacks ranged between 2.12 and 2.59% as shown in Table 2.

**Table 2.** Effect of extrusion conditions on functional and textural properties of brown rice-watermelon seeds extruded snacks

| **Samples** | **FMC (%)** | **EBT (°C)** | **BSS (rpm)** | **WAI** | **WSI** | **Hardness (N)** | **Chewiness (N)** | **Gumminess (N)** | **Springiness** |
|---|---|---|---|---|---|---|---|---|---|
| AA1 | 17 | 120 | 300 | 2.87$^{a}$ | 2.56$^{a}$ | 136.05$^{a}$ | 0.07$^{a}$ | 3.68$^{a}$ | 0.02$^{a}$ |
| AA2 | 18 | 120 | 360 | 2.45$^{b}$ | 2.59$^{b}$ | 193.53$^{a}$ | 0.07$^{a}$ | 6.25$^{a}$ | 0.03$^{a}$ |
| AA3 | 16 | 120 | 420 | 2.38$^{c}$ | 2.14$^{f}$ | 167.58$^{a}$ | 0.26$^{a}$ | 6.64$^{a}$ | 0.07$^{a}$ |
| BB1 | 18 | 130 | 300 | 2.16$^{d}$ | 2.15$^{f}$ | 158.12$^{a}$ | 0.46$^{a}$ | 10.61$^{a}$ | 0.06$^{a}$ |
| BB2 | 16 | 130 | 360 | 2.54$^{e}$ | 2.30$^{c}$ | 118.92$^{a}$ | 0.56$^{a}$ | 4.35$^{a}$ | 0.03$^{a}$ |
| BB3 | 17 | 130 | 420 | 2.14$^{f}$ | 2.12$^{g}$ | 184.94$^{a}$ | 0.16$^{a}$ | 14.45$^{a}$ | 0.04$^{a}$ |
| CC1 | 16 | 140 | 300 | 2.32$^{g}$ | 2.23$^{d}$ | 135.98$^{a}$ | 0.41$^{a}$ | 2.69$^{a}$ | 0.02$^{a}$ |
| CC2 | 17 | 140 | 360 | 2.21$^{h}$ | 2.22$^{e}$ | 133.15$^{a}$ | 0.06$^{a}$ | 2.41$^{a}$ | 0.02$^{a}$ |
| CC3 | 18 | 140 | 420 | 2.09$^{i}$ | 2.21$^{e}$ | 4054.40$^{b}$ | 326.00$^{b}$ | 1509.17$^{b}$ | 0.21$^{b}$ |

Means value and superscript with dissimilar letters along the same column are significantly different at $P < 0.05$.

The snacks maximum WSI was recorded at 18% FMC, 120 °C EBT and 360 rpm BSS whereas, the minimum was recorded at 17% FMC, 130 °C EBT and 420 rpm BSS. It was observed that the linear, quadratic and interaction effects of the extrusion parameters have a significant influence on the WSI (Figure 3b). However, it was observed that EBT had the most significant influence on the WSI of the extrudates. Table 3 showed the developed regression model for WSI with a high F-value. The value of $R^2$ presents its close adequacy.

The predicted $R^2$ of the model strongly agrees with the adjusted $R^2$ showing the adequacy to predict the effect of extrusion parameters on WSI. Figures 4a&b showed that higher EBT and lower BSS are desirable for lower WSI while higher EBT and FMC lead to a decrease in WSI of the extrudates.

**Table 3.** Regression equations and statistical analysis for the responses of brown rice-watermelon seeds extruded snacks

| Response | Model | $R^2$ | $R^2$ Adj | $R^2$ Pred | F-value |
|---|---|---|---|---|---|
| WAI | $3.06 - 0.3439X_1 - 0.0455X_2 - 0.8198X_3 + 0.0010X_1^2 - 0.0001X_2^2 + 0.0383X_3^2 - 0.0004X_1X_2 - 0.0053X_1X_3$ | 0.99 | 0.99 | 0.99 | 6018.65 |
| WSI | $26.173 - 0.223X_1 - 0.028X_2 - 0.375X_3 + 0.0013X_1^2 - 0.0001X_2^2 + 0.0641X_3^2 - 0.0003X_1X_2 - 0.0143X_1X_3$ | 0.99 | 0.99 | 0.99 | 2933.25 |
| Hardness | $59022 - 2363X_1 - 400.3X_2 + 6.495X_1^2 + 0.185X_2^2 + 1295X_3^2 + 2.139X_1X_2$ | 0.97 | 0.96 | 0.94 | 94.20 |
| Chewiness | $49831 - 200.5X_1 - 33.5X_2 + 108.6X_3^2 + 0.1807X_1X_2$ | 0.74 | 0.62 | 0.42 | 6.44 |
| Springiness | $26.83 - 0.0958X_1 - 0.0133X_2 + 0.0001X_2^2 + 0.0576X_3^2 + 0.00001X_1X_2$ | 0.83 | 0.76 | 0.62 | 11.09 |
| Gumminess | $228292 - 910X_1 - 154.8X_2 + 2.45X_1^2 + 499X_3^2 + 0.832X_1X_2$ | 0.82 | 0.74 | 0.60 | 10.41 |

where WAI is the water absorption index and WSI is the water solubility index, $X_1$ is the exit barrel temperature (EBT), $X_2$ is the Barrel Screw Speed (BSS) and $X_3$ is the Feed Moisture Content.

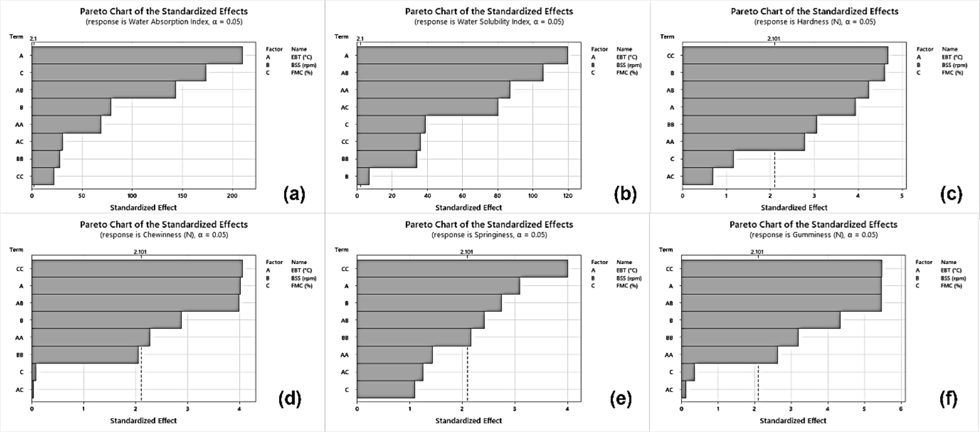

**Figure 3.** Influence of extrusion parameters on (a) water absorption index (b) water solubility index (c) hardness (d), chewiness (e) gumminess and (f) springiness content of brown rice-water melon seeds extruded snacks. EBT- Exit barrel temperature, BSS- Barrel screw speed, FMC- Feed moisture content

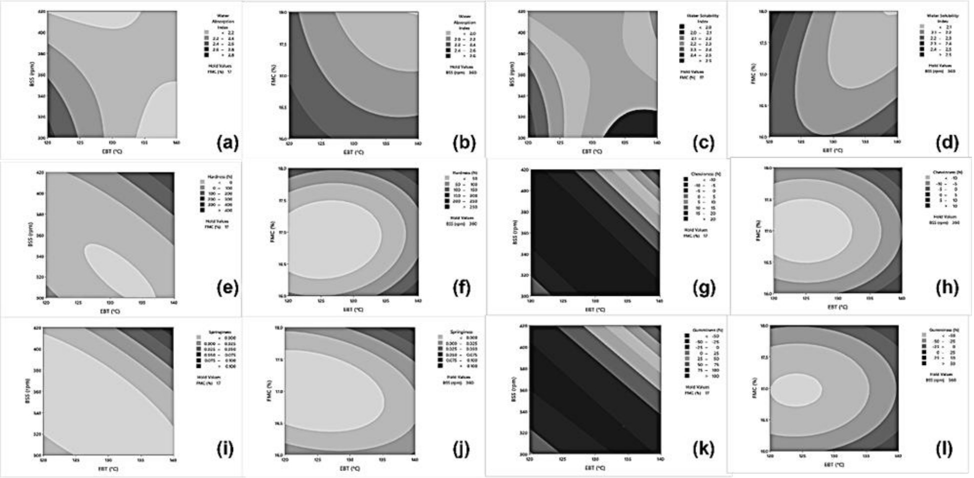

**Figure 4.** Effect of extrusion parameters on water solubility index (a&b), water absorption index (c&d), hardness (e&f), chewiness (g&h), springiness (i&j) and gumminess (k&j) of brown rice-watermelon seeds extruded snacks.

This supports the report by Gopirajah and Muthukumarappan (21), as the increase in temperature decreased the water solubility due to the release of numerous soluble materials from c. The negative linear coefficient of EBT, BSS and FMC imply that an increase in WSI would occur as a result of a decrease in EBT, BSS and FMC. The reduction in the WSI with an increase in feed moisture content could be due to a reduction in lateral expansion of starch because of the plasticization. An increase in EBT with a decrease in water solubility may also be due to the lateral expansion of the extrudates as a result of incomplete starch gelatinization. This study agrees with Kebede *et al.* (22) and Nargis *et al.* (23) findings during the production of extruded products from rice and carrot blend.

## TEXTURAL ANALYSIS

The hardness, chewiness, gumminess, and springiness of the brown rice-water melon seeds extruded snacks ranged between 118.92 and 4054.40 (N), 0.06 and 326.00 (N), 2.41 and 1509.17 (N), and 0.02 and 0.21, respectively (Table 2). The hardness measured the highest penetration force required to collapse an extrudate and has a direct implication on product expansion and its structure (24). Chewiness defined how extrudates behave through the process of biting. Gumminess is a sensory property of snacks that defines the energy needed to crumble a semi-solid food material into a condition prepared for consumption, while springiness is a sensory property of snacks that defines their ability to leap back after initial distortion. This property is lower in crispy snacks (24). The quadratic effect of FMC was observed to have the most significant influence on the hardness, chewiness, gumminess and springiness of the extruded snacks as shown in Figures 3 c, d, e & f. At higher FMC, the dough elasticity reduces through plasticization which invariably affected the hardness, chewiness, gumminess and springiness (Yağcı *et al.* (25); Sahu *et al.* (3)). Table 3 showed the developed regression models for hardness, chewiness, gumminess and springiness. All the models were significant at $P<0.05$ with F-values ranging from 10.41 - 94.20 (Table 3). The combined values of $R^2$, adjusted $R^2$ and predicted $R^2$ present strong adequacy for the prediction of the hardness of the extruded snacks under different extrusion parameters. For chewiness, the values of $R^2$, adjusted $R^2$, and predicted $R^2$ also present strong sufficiency for its prediction. The $R^2$ of gumminess presents close adequacy with adjusted and predicted values. The model strongly agrees with adjusted showing its adequacy for the prediction of gumminess. The predictive model between springiness and extrusion parameters gave an $R^2$ close to unity while the adjusted $R^2$ and predicted $R^2$ also showed a close agreement. The springiness, chewiness and gumminess of the extruded snacks were observed to increase as the EBT and FMC increased (Figures 4 f, g, h, i, j & k). Inversely, the hardness increased with lowered barrel screw speed and increased barrel temperature (Figures 4 e). The results corroborate with the findings of Yağcı *et al.* (25) that low barrel screw speed and high extrusion temperature and extrusion temperature increase the hardness of chickpea extrudates while Neder-Su´arez *et al.* (26) also reported that increasing feed moisture content and barrel screw speed increases the hardness of extrudates. Wang *et al.* (27) reported that chewiness reduces at lower screw speed and extrusion temperature which thus correlates with the obtained result. This could be attributed to the destruction of starch network continuity at lower screw speed and extrusion temperature, and at high pressure and thus causing lower chewiness.

## CONCLUSIONS

A hybrid of Taguchi and response surface methodology technique was successfully used to depict the effect of extrusion conditions on the functional and textural properties of brown rice-watermelon seeds extruded snacks. Extrusion process parameters significantly influenced the functional and textural properties of the extruded snacks. Pareto plot showed that exit barrel temperature had the most significant effect on water absorption index and water solubility index, whereas quadratic interaction of feed moisture content had the most significant effect on hardness, chewiness, gumminess and springiness of the extruded snacks. The exit barrel temperature negatively influenced the water absorption index and water solubility index, whereas the quadratic interaction of feed moisture content positively influences hardness, chewiness, gumminess, and springiness. The second-order polynomial regression models developed for functional and textural properties showed their adequacy to predict the effect of extrusion conditions on the functional and textural properties with the coefficient of determination ($R^2$) that ranged between 0.74 and 0.99. Therefore, with minimum experimental runs using Taguchi design, the effect and model of extrusion conditions on functional and textural properties of brown rice-watermelon seeds extruded snacks can be established using response surface methodology. Also, blends of broken brown rice flour and watermelon seeds flour can also be used to produce an extruded product with good functional and textural properties, thus valorize by-products.

### Acknowledgements

Authors are grateful to the Department of Food Engineering, University of Ilorin for providing facilities support for this study.

## REFERENCES

1. Ananthanarayan, L.; Gat. Y.; Panghal, A.; Chhikara, N.; Sharma, P.; Kumar, V.; Singh, B. Effect of extrusion on thermal, textural and rheological properties of legume-based snack. *J. of Food Sci. and Techn.*, **2018**, *55*(9), 3749-3756.
2. Ding, Q.B.; Ainsworth, P.; Tucker, G.; Marson, H. The effect of extrusion conditions on the physicochemical properties and sensory characteristics of rice-based expanded snacks. *J. of Food Engr.*, **2005**, *66*(3), 283-289.
3. Sahu, C.; Patel, S.; Tripathi, A.K. Effect of extrusion parameters on physical and functional quality of soy protein enriched maize based extruded snack. *Applied Food Resear.*, **2022**, *2*(1), 100072.
4. Nidhi, K.; Mohan, S. Effect of Extrusion Parameters on Textural Properties of Parboiled Rice based Bittergourd and Water Chestnut Blended Extrudates. *Intern. J. of Current Microb. Applied Sci.*, **2019**, *8*(7), 2021-2029.
5. Upadhiyay, A.; Karn, S. K. Brown Rice: Nutritional Composition and Health Benefits, *J. of Food Sci. and* Techn. *Nepal*, **2018**, *10*, 47-52.
   Retrieved from https://doi.org/10.3126/ jfstn.v10i0.191711
6. Sanusi, M.S.; Akinoso, R. Modelling and optimising the impact of process variables on brown rice quality and overall energy consumption. *Intern. J. of Postharvest Techn. and Innovation*, **2021**, *8*(1), 70-88.
7. Lopusiewicz, L. Antioxidant, antibacterial properties and the light barrier assessment of raw and purified melanins isolated from *Citrullus lanatus* (watermelon) seeds. *Herba Polonica*, **2018**, *64*(2).
8. Oke, M.O.; Awonorin, S.O.; Sanni, L.O.; Asiedu, R.; Aiyedun, P.O. Effect of extrusion variables on extrudates Properties of water yam flour–a response Surface analysis. *J. of Food Processing and Preserv.*, **2013**, *37*(5), 456-473.
9. Sahu, C. Effect of Extrusion Process Parameters on Textural Properties of Maize-Millet Based Soy Fortified Extruded Product. *Intern. J. of Current Microbiol. and Applied Sci.*, **2020**, *9*(6), 2098-2107.
10. Hussein, J.B.; Oke, M.O.; Adeyanju, J.A.; Sanusi, M.S. Optimisation of Microwave Drying of Tomatoes (*Solanum lycopersicum* L.) Slices Using Taguchi Method. *Nigerian Food J.*, **2019**, *37*(2), 57-71.
11. Sanusi, M.S.; Sunmonu, M.O.; Adepoju, A.L.; Abodunrin, T.O.; Ajibade, H. A. Development and Evaluation of the Operational Parameters of a Rotary Oven. *Nigerian J. of Techn. Development*, **2020**, *17*(4), 239-249.
12. Sanusi, M.S.; Akinoso, R. Evaluation of Energy Consumption Pattern in Rice Processing Using Taguchi and Artificial Neural Network Approaches. *Agricultural Engr. International: CIGR Jour.*, **2022**, *24*(2).
13. Wu, J.; Jiang, Z.; Wan, L.; Song, H.; Abbass, K. Robust Optimization for Precision Product using Taguchi-RSM and Desirability Function. *Arabian J. for Sci. and Engineering*, **2021**, *46*(3), 2803-2814.
14. Stojceska, V.; Ainsworth, P.; Plunkett, A.; İbano ğlu, E.; İbano ğlu, S. Cauliflower by-products as a new source of dietary fibre, antioxidants and proteins in cereal based ready-to-eat expanded snacks. *J. of Food Engr.*, **2008**, *87* (4), 554–563, 10.1016/j.jfoodeng.2008.01.009.
15. Sahu, C.; Patel, S. Optimization of maize–millet-based soy fortified composite flour for preparation of RTE extruded products using D-optimal mixture design. *J. of Food Sci. and Techn.*, **2021**, *58* (7), 2651–2660.
16. Lucas, B.F.; de Morais, M.G.; Santos, T.D.; Costa, J.A.V. Spirulina for snack enrichment: Nutritional, physical and sensory evaluations. *LWT-Food Sci. and Techn.*, **2018**, *90*, 270-276.

17. Beigh, M.; Hussain, S.Z.; Qadri, T.; Naseer, B.; Raja, T.; Naik, H. Investigation of process and product parameters for physico-chemical properties of low Glycemic Index water chestnut and barley flour-based extruded snacks. *British Food J.*, **2019**, *122* (1), 227-241.
18. Sandrin, R.; Caon, T.; Zibetti, A.W.; de Francisco, A. Effect of extrusion temperature and screw speed on properties of oat and rice flour extrudates. *J. of the Sci. of Food and Agric*., **2018**, *98*(9), 3427–3436.
19. Dalbhagat, C.G.; Mahato, D.K.; Mishra, H.N. Effect of extrusion processing on physicochemical, functional and nutritional characteristics of rice and rice-based products: A review. *Trends in Food Sci. & Techn*., **2019**, *85*, 226-240.
20. Samyor, D.; Deka, S. C.; Das, A. B. Effect of extrusion conditions on the physicochemical phytochemical properties of red rice and passion fruit powder based extrudates. *J. of Food Sci. and Techn.*, **2018**, *55*, 5003-5013.
21. Gopirajah, R.; Muthukumarappan, K. Effect of extrusion process conditions on the physical properties of tef-oat healthy snack extrudates. *J. of Food Process. and Preser.*, **2018**, *42*(3), e13559.
22. Kebede, L.; Worku, S.; Bultosa, G.; Yetneberek, S. Effect of extrusion operating conditions on the physical and sensory propertiesof tef (Eragrostis tef [Zucc.] Trotter) flour extrudates. *Ethiopian J. of Applied Sci. and Techn.*, **2010**, *1*, 27–38.
23. Nargis, T.; Krishna, K.; Amrit Raj, G.; Amit, S.; Dipayan, R.; Debrup, S.; Saikat, C.; Satinath, M.; Dipyaman, G.; Partha, C. KLK5 induces shedding of DPP4 from circulatory Th17 cells in type 2 diabetes. *Molec. Metabolism*, **2017**, *6* (11) 1529-1539.
24. Shah, F.U.H.; Sharif, M.K.; Butt, M.S.; Shahid, M. Development of protein, dietary fiber, and micronutrient enriched extruded corn snacks. *J. of Texture Studies*, **2017**, *48*(3), 221-230.
25. Yağcı, S.; Altan, A.; Doğan, F. Effects of extrusion processing and gum content on physicochemical, microstructural and nutritional properties of fermented chickpea-based extrudates. *LWT-Food Sci. and Techn*., **2020**, *124*, 109150.
26. Neder-Suárez, D.; Quintero-Ramos, A.; Meléndez-Pizarro, C.O.; de Jesús Zazueta-Morales, J; Paraguay-Delgado F.; Ruiz-Gutiérrez, M.G. Evaluation of the physicochemical properties of third-generation snacks made from blue corn, black beans, and sweet chard produced by extrusion. *LWT- Food Sci. and Techn*. **2021**, *146*, 111414.
27. Wang, L.; Duan, W.; Zhou, S.; Qian, H.; Zhang, H.; Qi, X. Effects of extrusion conditions on the extrusion responses and the quality of brown rice pasta. *Food Chem.*, **2016**, *204,* 320-325.

APTEFF, Vol. 54, 1-335 (2023) UDC: 677.31:677.027.423.1
DOI: https://doi.org/10.2298/APT2354093K BIBLID: 1450-7188 (2023) 54, 93-103

Original scientific paper

# DYEING OF THE WOOLEN KNITWEAR WITH ACID DYE

*Slađana KAPUŠI*, Milena M. NIKODIJEVIĆ, Dragan M. ĐORĐEVIĆ*

[1] University of Niš, Faculty of Technology, Bulevar oslobođenja 124, 16000 Leskovac, Serbia

**Received: 24 January 2023 Revised: 09 February 2023 Accepted: 20 February 2023**

*The process of woolen knitwear dyeing using acid dye is investigated in this paper. Wool, as a natural protein fiber, is quite costly to produce and process, and thus it is crucial to ensure its economic viability and meet consumer demands. Acid dyes are a popular choice for woolen knitwear dyeing because of their strong coloring properties and ability to bind to the protein fibers in wool. They are usually strongly dyed compounds whose colouring depends on the molecular structure. A woolen knitwear made of 100% extra fine merino wool was used. In this specific study, was used a brand of acid dye called Supramin Blau GW and tested different concentrations and dyeing times to see how they affected the final color of the wool fibers. The dye concentrations were 100, 200, 300, 400, and 500 mg/l. The dyeing time were 5, 10, 15, 25, 35 and 45 minutes. The aqueous dye solution had an electrolyte concentration of 2 g/l of sodium acetate and acetic acid for a pH of 5, while the dyeing temperature was 98 °C. The results showed that initial dye concentration and dyeing time increased, resulting in a corresponding increase in the degree of dye exaustion on the wool fibers. A longer dyeing time resulted in a higher degree of dye exhaustion. The Freundlich's and Langmuir's models were used to describe the adsorption process, which gives the relationship between the amount of dye adsorbed on the woolen knitwear and the concentration of dye in the solution. Freundlich's model was better that Langmuir's model for describing the adsorption process because there was very little scatter around the ideal curve and functional straight lines covered most points well. Overall, this study highlights the importance of understanding the factors that influence the dyeing process of woolen knitwear with acid dyes, as it can help ensure that the final product is economically sustainability and meets consumer demands.*

**Keywords**: wool, dyeing, Freundlich model, Langmuir model, acid dye.

## INTRODUCTION

Wool is a protein fiber that has special qualities like wrinkle resistance, rapid drying, and heat retention. Wool's fundamental molecular structure is made up of amide-bonded macromolecular chains of amino acid residues with a $\alpha$ helical shape (1).

The relative hydrophobicity of wool fabric surfaces, which is brought on by the presence of methyl groups from the side chains along the amino acid structure with a significant amount of disulfide cross-links (-S-S-), makes it difficult to dye and wet the fabric surface. Wool is a common fiber used in textile processing (1, 2).

Textile finishing and dyeing both fall under the category of textile refining. It is a procedure that can be used at any point in the textile production process and finalizes the fiber (textile product). Chemical structure, fabric structure, and dye type are all crucial factors in dyeing (3).

Dyes can be absorbed by or adhered to the substrate through covalent bonding, complexation with salts or metals, chemical retention, or physical adsorption. Dyes are applied to

---

* Corresponding author: Slađana Kapuši, University of Niš, Faculty of technology, Bulevar oslobođenja 124, 16000 Leskovac, Serbia, e-mail: sladjana.kapusi@gmail.com

textiles made of various fibers in a variety of ways and have varying origins and compositions (4, 5).

The arrangement of fibrils, the supramolecular structure, and the interior keratin structure all affect the characteristics of wool. Due to all of this, wool fibers are materials with extraordinary qualities, which vary in intensity depending on the breed of sheep and the environment in which they are raised (6).

Acid dyes are a broad category of dyes that includes various subcategories. Most notably, sulfonic acid derivatives of azo dyes are what acid dyes are. The ability of these dyes to colorize protein and/or polyamide fibers defines their practical utility. They are anionic in nature and have the general formula -$RSO_3Na$, just like direct dyes. However, unlike direct dyes, they cannot dye cellulose fibers. Acid dyes are soluble in water, produce vivid colors, and hold up well through washing. They have an acidic and chromophoric group in the form of a sodium salt, most frequently -$SO_3H$, which makes them water soluble (7).

A smaller acid bath is required to exhaust the dye sufficiently as its molecular weight rises. In terms of application properties, degree of exhaustion, leveling, and durability properties, the chosen colors should be as similar as feasible (8).

The aim of this study is to develop a comprehensive model for the dyeing of wool knitwear with acid dye at 98 °C. This research endeavors to identify and understand the critical elements involved in the acid dyeing process, and to use this understanding to formulate an optimized, cost-effective, and environmentally friendly strategy. The ultimate goal is to improve the quality of the dyeing results, increase process efficiency, and reduce production costs, thereby promoting sustainability in the wool knitwear industry.

## MATERIALS AND METHODS

In the experimental part, a woolen knitwear made of 100% extra fine merino wool was used. Figure 1 shows the knitting pattern of the woolen fabric used. The basic characteristics of woolen knitwear are given in table 1.

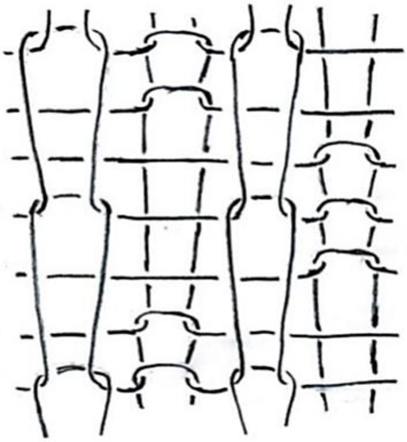

**Figure 1.** Right-right knitting pattern of woolen knitwear

**Table 1.** Basic characteristics of the used woolen knitwear

| Analysed properties | Unit | Measured value |
|---|---|---|
| Longitudinal mass | tex | 48×2 |
| Metric track | Nm | 320/1 |
| Mass per unit area | g/m$^2$ | 434 |
| Thickness | mm | 2.33 |
| Interlacement | - | Tvil Reljef Nec i Flot |
| Direcetion of twist | - | S |

Figure 2 shows images of woolen knitwear raw and dyed samples at different dye concentrations. There are considerable shade variations across the samples, which are related to various dying circumstances, i.e. variations in the initial acid dye concentration used to dye woolen knitwear.

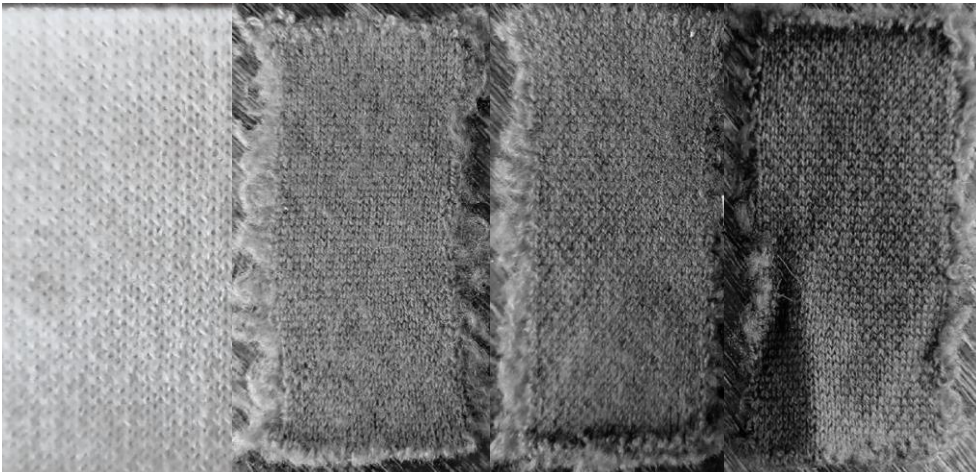
a b c d

**Figure 2.** Appearance of raw and dyed samples of woolen knitwear (a - raw sample; b - $C_o$=100 mg/l, c - $C_o$=300 mg/l, d - $C_o$=500 mg/l)

Wool knitwear was dyed using an acid dye known by the brand name Supramin blau GW. The dye concentrations were 100, 200, 300, 400, and 500 mg/l, respectively. In order to conduct the dyeing-adsorption test, a sample of woolen knitwear weighing 1 g was dyed in a solution with a constant volume of 40 cm$^3$. In every dyeing instance, distilled water was used. While the other intervals were 5, 10, 15, 25, and 35 minutes, the maximum dyeing time was 45 minutes. The equilibrium period of 45 minutes demonstrates that no substantial changes occur with prolonged dyeing.

The equilibrium period of 45 minutes demonstrates that there are no appreciable changes in the level of dye fatigue with extended dyeing. The aqueous dye solution had an electrolyte concentration of 2 g/l of sodium acetate and acetic acid for a pH of 5, while the dyeing temperature was 98 °C. The chemical composition of Supramin Blau GW acid dye is depicted in Figure 3.

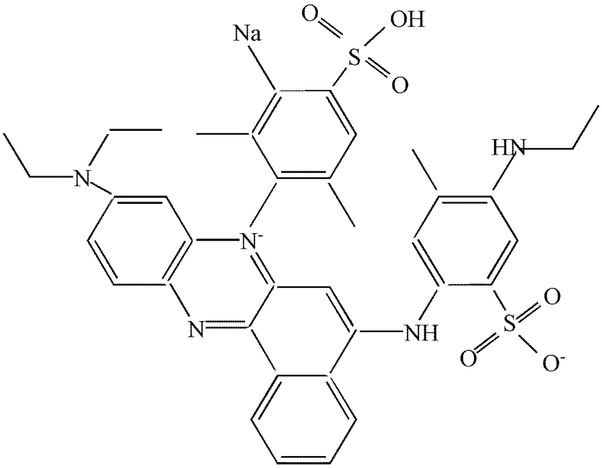

**Figure 3**. Chemical structure of Supramin Blau GW acid dye

Colorimeter model CO7500 (United Kingdom) was used to determine the concentration of dye in the solution. Absorption was measured at the maximum wavelength of 680 nm. The degree of dye exhaustion was calculated using the equation [1] (9):

$$Degree\ of\ dye\ exhaustion=\frac{C_0\text{-}C_t}{C_0}\cdot 100\ \ (\%) \qquad [1]$$

where: $C_o$ and $C_t$ (mg/dm$^3$) - initial and dye concentration at time t.

The amount of adsorbed dye was obtained using the formulas [2] (9):

$$q_t=\frac{C_0-C_t}{w}\cdot V \qquad \text{i} \qquad q_e=\frac{C_0-C_e}{w}\cdot V \qquad [2]$$

where: $q_t$ (mg/g) - the amount of adsorbed dye per unit mass of knitted fabric in the dyeing time $t$; $q_e$ (mg/g) - the mass of adsorbed dye per unit mass of knitted fabric in equilibrium; $C_0$ (mg/dm$^3$) - initial dye concentration; $C_t$ (mg/dm$^3$) - concentration of the dye in the solution during the dyeing time $t$; $C_e$ (mg/dm$^3$) - equilibrium concentration of the dye in the solution; $w$ (g) - the mass of knitted fabric and $V$ (dm$^3$) - the volume of dyeing solution.

The *Freundlich's* model is represented by the following linear equation [3] (9):

$$lnq_e=lnK_F+\frac{1}{n}ln\ \ C_e \qquad [3]$$

where: $K_F$ (mg/g)·(dm$^3$/mg)(1/n) and $n$ - constants characteristic of the observed system: adsorbent (knitting), adsorbate (dye) and solvent (water).

*Langmuir*'s adsorption isotherm is based on two assumptions that the forces of interaction between adsorbed molecules are negligible and when a molecule occupies a place, no

DOI: https://doi.org/10.2298/APT2354093K
BIBLID: 1450-7188 (2023) 54, 93-103

further adsorption occurs. The *Langmuir's* isotherm refers to homogeneous adsorption, without transmigration of adsorbate in the plane of the surface.

This isotherm can be expressed in linear form as:

$$\frac{C_e}{q_e} = \frac{1}{Q^o \cdot b} + \frac{C_e}{Q^o} \qquad [4]$$

where $C_e$ (mg/dm$^3$) is the equilibrium concentration of the dye in the solution; $q_e$ (mg/g) - adsorption capacity; $Q_o$ (mg/g) - constant related to the heat of adsorption; $b$ (dm$^3$/mg) - variable adsorption energy.

## RESULTS AND DISCUSSION

The graph in figure 4 demonstrates the relationship between initial dye concentration and dye adsorption-exhaustion during normal equilibrium dyeing for various dye concentrations and time intervals. It can be observed that as the initial dye concentration increases, the amount of dye exhaustion per unit mass of the adsorbent decreases. This observation aligns with theoretical expectations and suggests that a higher initial dye concentration results in a more efficient utilization of the dye. The graph also shows that as the dyeing time increases, the degree of dye exhaustion increases as well. This finding indicates that longer dyeing times result in higher degrees of dye exhaustion, implying that extended dyeing time is necessary to achieve a desired degree of exhaustion. Overall, the graph provides important insights into the dynamics of the dyeing process and highlights the importance of controlling initial dye concentration and dyeing time for optimal results.

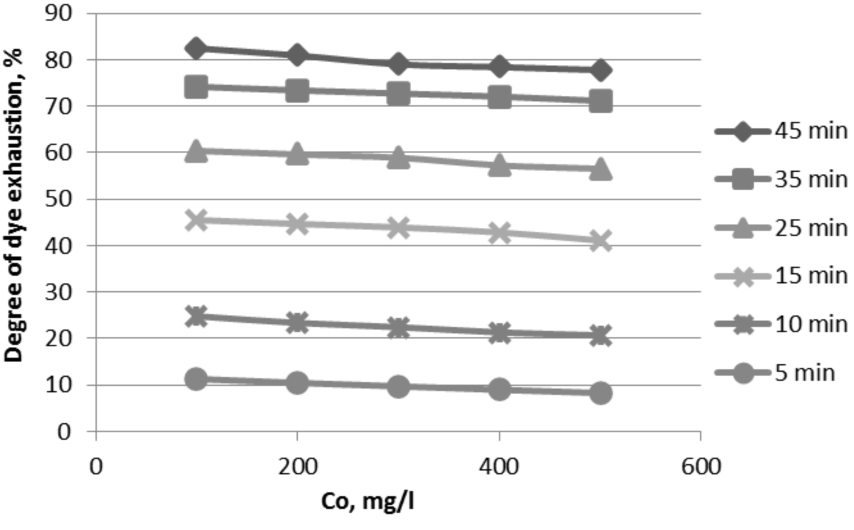

**Figure 4.** The initial concentration of acid dye like an impact on the degree of exhaustion achieved during the dyeing process of woolen knitwear.

Figure 5 illustrates the relationship between the initial dye concentration and the amount of dye absorbed per unit of fiber mass. The graph clearly shows that as the initial dye concentration increases, the amount of dye absorbed per unit of fiber mass also increases in a consistent and proportional manner. This relationship can be described as nearly linear, which suggests that the dye absorption process is characterized by a simple functional relationship between the initial dye concentration and the amount of dye absorbed. The graph highlights the importance of controlling the initial dye concentration in order to achieve a desired degree of dye absorption. Additionally, the graph indicates that longer dyeing times result in higher degree of dye absorption, with a corresponding increase in the amount of dye absorbed per unit of fiber mass. This finding suggests that extended dyeing time is necessary to achieve a desired level of dye absorption and highlights the importance of considering both the initial dye concentration and dyeing time in the dyeing process.

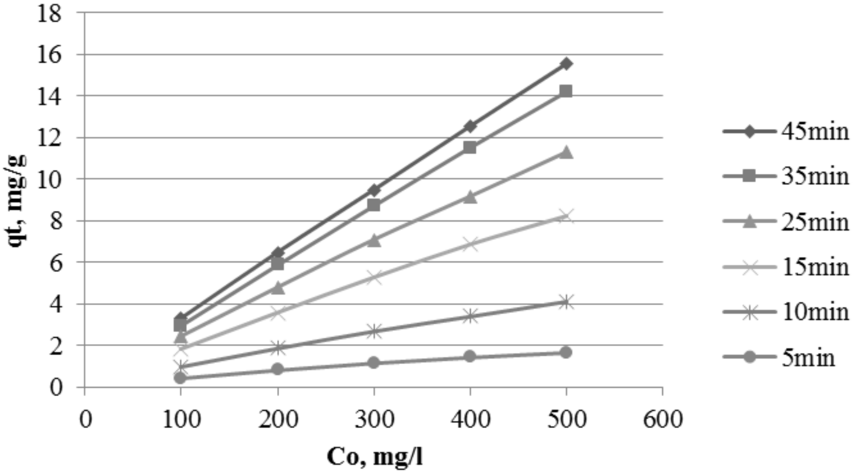

**Figure 5.** The effect of the initial acid dye concentration on the amount of dye absorbed per mass of woolen knitted fabric.

Figure 6 presents the relationship between the length of contact between the adsorbate (acid dye) and the adsorbent (wool) and the adsorption-exhaustion of the acid dye during wool dyeing, for various initial dye concentrations. The graph demonstrates a clear continuity in the changes through time, with longer contact times resulting in higher degree of dye exhaustion. It can also be observed that a higher percentage of dye exhaustion occurs at lower initial dye concentrations, and this pattern is largely maintained throughout the dyeing process. These findings highlight the importance of considering the length of contact time in the dyeing process and suggest that extending the dyeing time is necessary to achieve a higher level of dye exhaustion. Additionally, the graph indicates that the initial dye concentration also plays a critical role in determining the degree of dye exhaustion, with lower concentrations resulting in higher levels of exhaustion. Overall, figure 6 provides important insights into the dynamics of the dyeing process and the interplay between initial concentration and contact time in determining the degree of dye exhaustion.

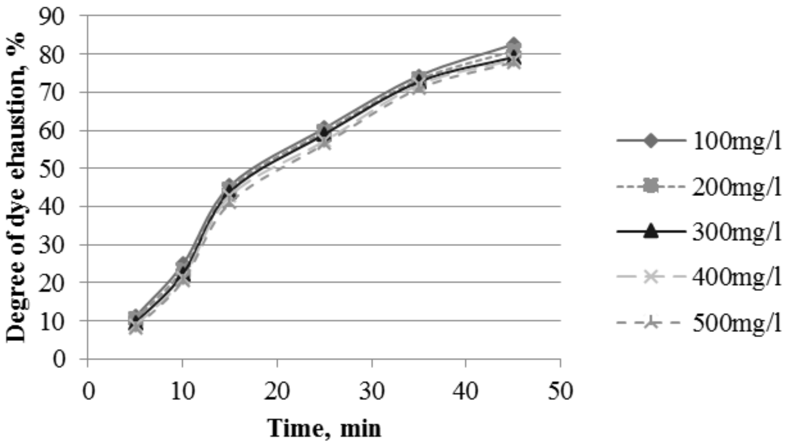

**Figure 6.** The impact of time on acid dye exhaustion during dyeing for various beginning dye concentrations.

Figure 7 presents the results of the variations in the amount of dye absorbed on the woolen knitwear over time for different initial dye concentrations. The graph clearly shows the consistency in the changes as the initial concentration increases, with higher initial concentrations resulting in a higher amount of dye being adsorbed per unit mass of the wool. This relationship between initial concentration and adsorption highlights the importance of controlling the initial dye concentration in order to achieve a desired level of dye absorption. Additionally, the graph indicates that the highest levels of dye absorption occur at the highest initial concentrations, further emphasizing the critical role of initial concentration in the dyeing process. Moreover, the graph suggests that the dye molecules adsorb more quickly onto the wool fibers during dyeing compared to the additives because of the greater overall surface area of the fibers. This finding highlights the significance of considering the fiber surface area in the dyeing process and the relative adsorption rates of different components of the dye solution. Overall, Figure 7 provides important insights into the dynamics of the dyeing process and the interplay between initial concentration, fiber surface area, and adsorption rate in determining the level of dye absorption.

The dye aggregates will disintegrate into molecules as a result of this disrupting the solution's dynamic equilibrium, which will then allow the solution to return to equilibrium. Up until a balance is reached between the dye concentration in the solution and the dye concentration on the fiber, the adsorption process will continue. Given that dye molecules in aqueous solutions tend to clump, applying a higher temperature and agitating the solution will induce the aggregates to break down and the size of the dye particles to decrease, which is the first requirement for greater adsorption on the adsorbent (9).

For the study of dyeing processes, isothermal adsorption is crucial. It is crucial to analyze isothermal data by fitting it through several isothermal equations in order to establish an equilibrium model that can be used to regulate the dyeing process. Using Microsoft Excel (USA) software, *Freundlich's* and *Langmuir's* isotherm models were utilized in this study to fit experimental points.

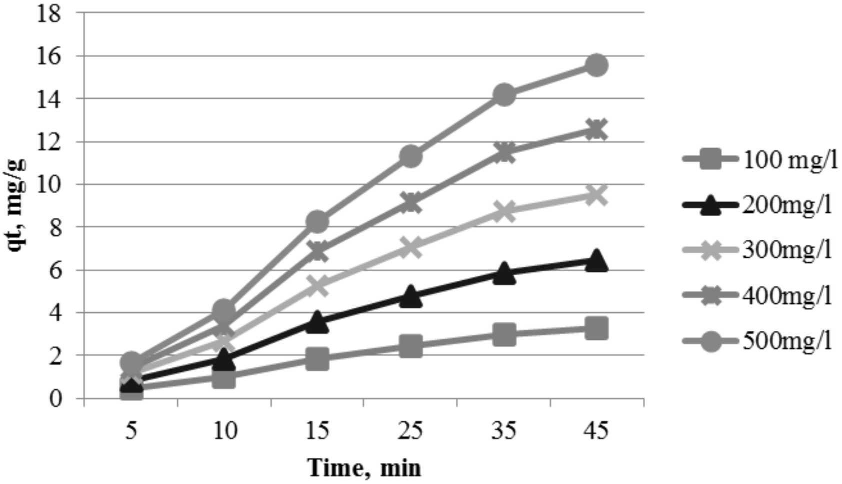

**Figure 7**. The amount of acid dye adsorbs per mass of woolen knit fabric in proportion to the amount of time needed to dye the sample pf woolen knitwear for various initial dye concentrations.

Figures 8 and 9 present the results of fitting the experimental data to *Freundlich*'s and *Langmuir*'s isotherm models, respectively, for all initial dye concentrations in the solution. The diagrams show the linear regression lines of the models, which were generated by fitting the experimental data to the models. A visual evaluation of the regression lines reveals that the *Langmuir*'s model deviates more from the experimental points, as the position of the regression line is slightly farther away from the experimental points. This deviation indicates that the *Langmuir*'s model may not accurately represent the adsorption behavior of the dye onto the wool knitted fabric in this particular system.

On the other hand, the *Freundlich*'s model appears to better capture the experimental points, as the regression line is closer to the experimental points. This suggests that the *Freundlich*'s model may be a more appropriate representation of the adsorption behavior of the dye onto the woolen knitwear in this system. The comparison of the two models provides important insights into the effectiveness of different isotherm models in representing the adsorption behavior of dyes onto wool knitted fabrics and highlights the importance of selecting the appropriate model to better understand the underlying mechanisms of the adsorption process. Overall, the results of the fitting of the experimental data to the Freundlich's and Langmuir's isotherm models provide a more detailed understanding of the adsorption behavior of the acid dyes onto wool knitted fabrics and support the development of more efficient and effective dyeing processes.

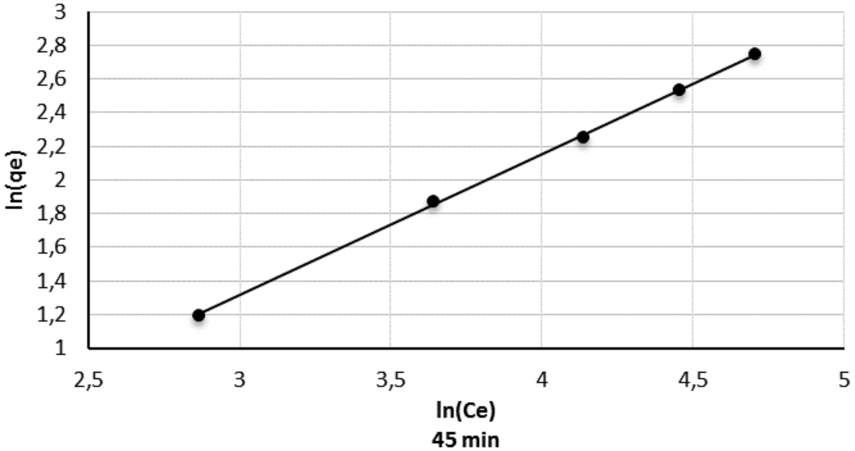

**Figure 8**. *Freundlich's* isotherm for dyeing of woolen knitwear with acid dye

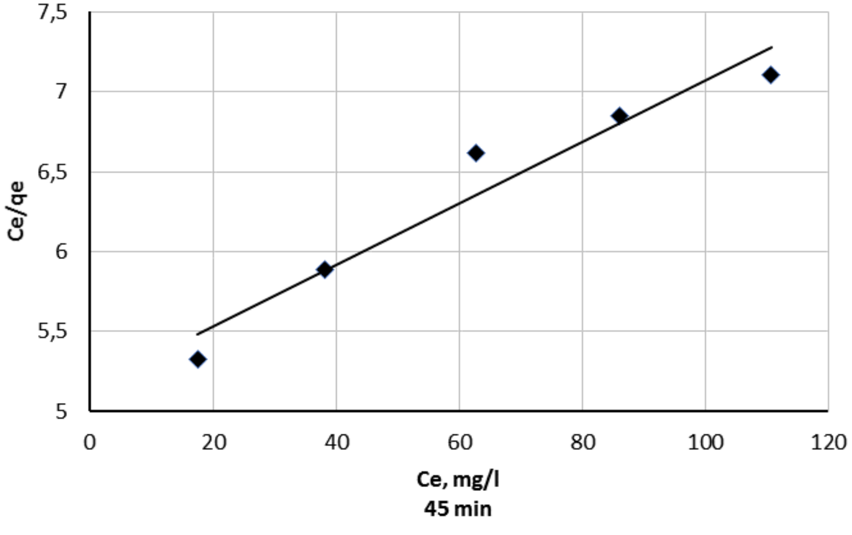

Figure 9 *Langmuir's* isotherm for dyeing of woolen knitwear with acid dye

The information in table 2 indicates that the *Freundlich* isotherm's coefficient of determination ($R^2$=0.999) is the highest of the two models, indicating that this isotherm is the best at linearly replicating the isothermal adsorption of acid dye on woolen knitted fabric. Additionally, this table displays analytical equations for linear adsorption isotherms, adsorption parameter values, and $R^2$ coefficient values.

It should be emphasized that this equation provides a connection that describes non-ideal and reversible adsorption, which is not confined to the development of a monolayer, and that the *Freundlich*'s isotherm is a better model for describing the dyeing of woolen knitwear with an acid dye.

This empirical model thus supports the reality of multilayer adsorption in the particular scenario, with a non-uniform distribution of adsorption heat and affinity over a heterogeneous surface. According to this definition, the amount of dye adsorbed is the total of the adsorptions at each site, each of which has a different binding energy, where the stronger binding sites are occupied first. After the adsorption process is complete, the adsorption energy is exponentially reduced.

**Table 2.** Analytical expression of the *Freundlich's* and *Langmuir's* linear isotherms for the acid dye–wool knitwear system

| **Models** | **Equations** | **Model parameters** | | |
|---|---|---|---|---|
| ***Freundlich*** | $ln(q_e) = -1.2 + 0.84 \cdot ln(C_e)$ | $K_F$ (mg/g)·(dm$^3$/mg)(1/n) | ***n*** | $R^2$ |
| | | 0.3 | 1.19 | 0.999 |
| ***Langmuir*** | $C_e/q_e = 5.142 + 0.019 \cdot C_e$ | $Q_o$ (mg/g) | ***b*** (dm$^3$/mg) | $R^2$ |
| | | 51.81 | 0.0037 | 0.943 |

## CONCLUSION

According to the results of the research in the laboratory, some specificities were singled out in the dyeing of woolen knitwear, which can also be transferred in industrial conditions.

By modeling the dyeing process, data is obtained that connect the concentration of dye, temperature, the presence of electrolytes and the efficiency of dyeing achieved on the knitted fabric, that is, the amount of waste dye that remains in the spa after dyeing.

Based on the obtained experimental results, the following conclusions were made:

- According to visual inspection, acid dyeing of woolen knitwear in laboratory conditions gives excellent results at a temperature of 98 °C.
- With the increase in dye concentration when dyeing woolen knitwear with acid dye, the degree of exhaustion decreases, longer dyeing time gives a higher degree of dye exhaustion, and this is maintained throughout the dyeing process.
- The change in the adsorbed amount of adsorbate (dye) on the adsorbent (knit), for different initial concentrations and dyeing time, increases during the increase of the initial concentration and time, i.e. a larger amount of dye or a longer period of dyeing brings a larger amount of adsorbed dye per unit mass of knitwear.
- The *Freundlich*'s adsorption isotherm model best covers the experimental points, while the *Langmuir*'s isotherm is a somewhat weaker model for describing a specific coloring system.

The results of this work suggest the possibility of a more economical approach in the process of refining woolen knitwear, all in favor of better effects, savings and environmental protection.

DOI: https://doi.org/10.2298/APT2354093K BIBLID: 1450-7188 (2023) 54, 93-103

Original scientific paper

## REFERENCES

1. Kan, C. W.; Yuen, C. W. M.; Hung, O. N. Improving the pilling property of knitted wool fabric with atmospheric pressure plasma treatment. *Surface and Coatings Technology*, **2013**, *228*, 588-592.
2. Panda, P. K.; Rastogi, D.; Jassal, M.; Agrawal, A. K. Effect of atmospheric pressure helium plasma on felting and low temperature dyeing of wool. *Journal of applied polymer science*, **2012**, *124*(5), 4289-4297.
3. Choudhury, A. R. Textile preparation and dyeing. Science publishers, **2006**.
4. Scheibel, J. J. The evolution of anionic surfactant technology to meet the requirements of the laundry detergent industry. *Journal of surfactants and detergents*, **2004**, *7*(4), 319-328.
5. Ayadi, I.; Souissi, Y.; Jlassi, I.; Peixoto, F.; Mnif, W. Chemical synonyms, molecular structure and toxicological risk assessment of synthetic textile dyes: a critical review. *Journal of Developing Drugs*, **2016**, *5*(151), 2.
6. Lasic, D. D.; Barenholz, Y. Handbook of nonmedical applications of liposomes: *Theory and basic sciences*, **1996**, (Vol. 1). CRC Press.
7. Akhtar, Z.; Farooq, M.; Kazimi, M. R.; Parveen, R.; Ali, S. I.; Karim, A.; Khan, K. M. Syntheses and Application of Sulfonic Acid Dyes on Wool Fabric. *Journal of the Chemical Society of Pakistan*, **2016**, 38(1), 127-132.
8. Fisher, A. Dyeing methods for wool, *CSIRO*, **1995**, p. 27.
9. Shahbeig, H., Bagheri, N., Ghorbanian, S. A., Hallajisani, A., & Poorkarimi, S. A new adsorption isotherm model of aqueous solutions on granular activated carbon. *World Journal of Modelling and Simulation*, **2013**, *9*(4), 243-254.

APTEFF, Vol. 54, 1-335 (2023) UDC: 546.214:541.128:621.577]:614.712
DOI: https://doi.org/10.2298/APT2354105C BIBLID: 1450-7188 (2023) 54, 105-114

Original scientific paper

# INCREASING THE EFFICIENCY OF OZONE TECHNOLOGY IN AIR PURIFICATION HVAC SYSTEMS

*Dzhamalutdin CHALAEV*[1], *Tatiana HRABOVA*[1]*, *Vitalii SYDORENKO*[1],
*Pavlo HONCHAROV*[2], *Rostyslav BAZIEIEV*[1]

[1] Institute of Engineering Thermophysics of the National Academy of Sciences of Ukraine 2, Akademika Bulakhovskoho St., Kyiv, Ukraine, 03164
[2] E.O. Paton Electric Welding Institute of the National Academy of Sciences of Ukraine 11, Kazymyr Malevych St., Kyiv, Ukraine, 03150

**Received: 17 January 2023** **Revised: 02 March 2023** **Accepted: 06 March 2023**

*The global problem of air pollution is exacerbated by large-scale pandemics and the catastrophic consequences of the war in Ukraine. To solve the problems of air purification, a technological scheme and equipment for plasma-chemical air treatment with a module for combined catalytic and thermal decomposition of excess ozone are proposed. Approbation of the scheme with the combined method of ozone destruction on oxide-cement catalysts showed an increase in ozone conversion by 10 - 15%. At the same time, the energy consumption for the implementation of the combined method of ozone destruction using heat pump recovery is 7-10 times less compared to the direct method of air heating.*

**Keywords**: ozone, decomposition, plasma, catalysis, heat pump.

## INTRODUCTION

One of the effective methods of air disinfection in centralized ventilation systems of public buildings can be the treatment of airflow with ozone. Ozone is an extremely powerful disinfectant capable of oxidizing a wide range of organic and inorganic compounds.

Ozone technologies are based on the generating of ozone in high concentrations in the air (over 0.4 mg/m$^3$), at which the active oxidation of high-molecular and toxic substances begins, destruction of cell walls of microorganisms, oxidation of aromatic and heterocyclic compounds. The effectiveness of technologies is due to the high chemical activity of ozone with its ecological purity (1, 2).

On the one hand, ozone is a powerful oxidizer, and on the other hand, it can be harmful to living things depending on the concentration, place, and duration of exposure (Figure 1) (3). At the same time, the ozone molecule is unstable, and the period of its decay depends significantly on temperature, humidity, and the composition of the ozone-air mixture. The half-life period is quite long at 10-40 °C is 0.2-3 days, and at 120 °C it is reduced to 1.5 hours (1, 4).

The above mentioned factors are imposing restrictions on the application of ozone technologies for air purification in central heating, ventilation, and air-conditioning (HVAC) without additional actions for excess ozone neutralizing. Therefore, for the safe operation of air purification units in the supply and exhaust ventilation systems of buildings and during their design, it is necessary to take into account the ozone threshold value in the air

---

* Corresponding author: Tatiana HRABOVA, Institute of Engineering Thermophysics of the National Academy of Sciences of Ukraine 2, Akademika Bulakhovskoho St., Kyiv, Ukraine, 03164, e-mail: gtln@ukr.net

after purification: the average daily maximum permissible concentration in atmospheric air (MPC) should not exceed 0.03 mg/ $m^3$ (7, 8).

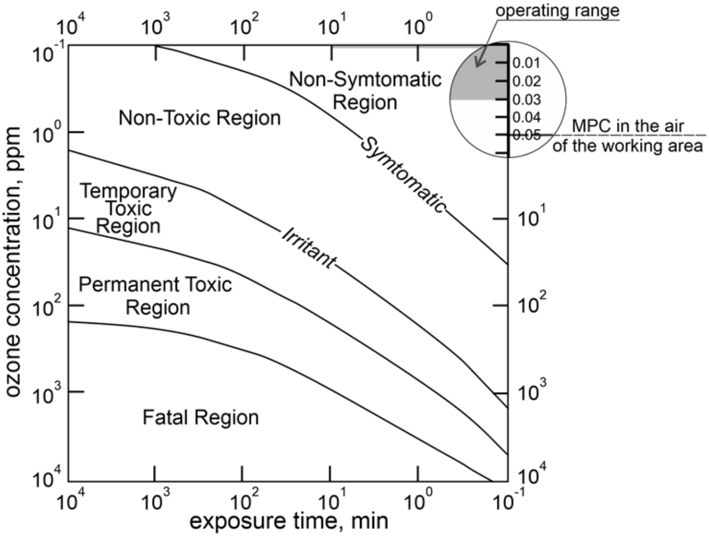

**Figure 1.** Regions of ozone toxicity (5, 6)

An effective and economical method of air disinfection in ventilation systems is the inactivation of airborne pathogenic microbial flora and the degradation of molecular pollutants by treating the airflow with low-temperature atmospheric pressure plasma.

Under the action of an electric field, electrons fly out of the cathode and are accelerated to ionization energies. Collisions of these electrons with nitrogen, oxygen, and water molecules in the air cause their excitation, ionization, and dissociation.

Inactivation of pollutants is carried out by oxidation of organic impurities under the action of active forms of oxygen, such as OH, $O_3$, $H_2O_2$, NO (9). Plasma chemical air treatment technology has a great potential for use as an effective method of inactivating airborne pathogens, including SARS-CoV-2 (10).

One of the ways to the safe use of ozone technologies in centralized HVAC systems is the use of devices for excess ozone decomposition. A comparative analysis of the main groups of available methods of ozone decomposition was carried out, namely photochemical, thermal, and catalytic (Table 1).

Currently, the method of catalytic decomposition of ozone using adsorbents with active catalytic components, such as oxides of noble and transition metals, is the most widely used. The mechanism of the catalytic decomposition of ozone is following. Firstly, the ozone molecule is adsorbed on the surface of the catalyst, and then it dissociates into an oxygen molecule and atomic oxygen. At the same time, pollutants remaining after the plasma chemical reactor are destroyed on the catalyst due to an intense reaction with atomic oxygen. At the same time, an effective and technically simple way of decomposing concentrated excess ozone is the thermal method. However, this method has limited application due to high energy costs for the process of heating and subsequent air cooling.

UDC: 546.214:541.128:621.577]:614.712
BIBLID: 1450-7188 (2023) 54, 105-114

**Table 1.** Analysis of ozone decomposition methods

| Ozone decomposition method | Main characteristics and parameters | Advantages | Disadvantages and limiting parameters | Source |
|---|---|---|---|---|
| photochemical | decomposition under the influence of laser or ultraviolet radiation | selective decomposition of ozone | - sensitive to the parameters and composition of the gas-ozone mixture;<br>- complex hardware equipment of the technology;<br>- expensive | (1,11) |
| thermal | the beginning of the decomposition process from 50 ºC | - does not pollute the air with decomposition products;<br>- is relatively simple from the point of view of technological equipment | - effective at high temperatures (350-400 ºC);<br>- above the critical temperature, detonation of the gas-ozone mixture is observed (above 105 °C, the kinetic decomposition of ozone can transform into an explosion);<br>- energy-consuming method | (1,11) |
| catalytic | - decomposition on highly developed surfaces with active catalytic components:<br>- precious metals;<br>- oxides of transition metals;<br>- mixed catalysts, which include oxides of d-elements and metals of the platinum group | - for a wide range of air-gas mixtures;<br>- a cost-effective method | - at certain temperatures and velocity of wet gas flow, the method is not effective;<br>- catalyst poisoning (complicated desorption of ozone decomposition products);<br>- high aerodynamic resistance, strength, and erosive resistance of catalytic granules in aerodynamic flows;<br>- the activity of modes (kinetic and diffusion) of ozone destruction depends on the development and accessibility of the contact surface of the catalyst | (9,12) |

Taking into account the above, the issue of choosing an effective method of ozone decomposition in dynamic air flows and the method of its implementation is relevant.

The aim of the work is to develop and create an effective module for decomposition of excess ozone in plasma-chemical air purification technologies in centralized HVAC systems.

## EXPERIMENTAL

Specialists of the Institute of Engineering Thermophysics of the National Academy of Sciences of Ukraine and E.O. Paton Electric Welding Institute of the National Academy of Sciences of Ukraine developed and made a modular experimental setup (13). The following units and modules are installed in the air duct system: a ventilation unit with an air productivity regulator, a G-class filter for coarse air purification, an ozone synthesis module, an adsorption-catalytic module, and a recuperative plate heat exchanger. Autonomous modules have been made, which makes it possible to easily install them in the duct system and vary the sequence of their location. Monitoring of air quality parameters according to the Air Quality Index (PM 2.5 particulate matter content, ozone concentration, relative humidity, %, temperature, carbon dioxide concentration, and air flow rate) was carried out online in the air duct after the MP1 ozone generator and after adsorption-catalytic module MP2.

The developed ozone synthesis module is based on the technology of active oxygen (ozone) generation from atmospheric air by the method of low-temperature (or cold) plasma corona discharge. According to the results of actual tests, the best results in terms of the degree of ionization and the intensity of the electric field in the air gap of the ozone generator were shown by the saw-blade corona electrodes.

Also, it was found that varying the values of the high voltage supplied to the plasma generator allows for regulating the ozone concentration in air streams.

The dependence of ozone generation in the voltage range of 5...25 kV with a high probability of approximation ($R^2$=0.98) is described by a second-degree polynomial with an inflection point in the region of 20...23 kV, i.e., after 20 kV, ozone generation declines (1, Fig. 2).

A plasma-chemical module with the following technical characteristics and operating conditions has been developed:

- Dimensions - 320x260x260, mm;
- The distance between the electrodes is 20...25 mm;
- The voltage supplied to the low-temperature plasma unit is up to 20 kV;
- The intensity of the electric field between the electrodes is up to $8 \cdot 10^3$ V/cm;
- Air exchange - up to700 $m^3$ /h;
- Operating temperature range - 17... 30 °C;
- Relative air humidity - 45...70% at 25 °C.

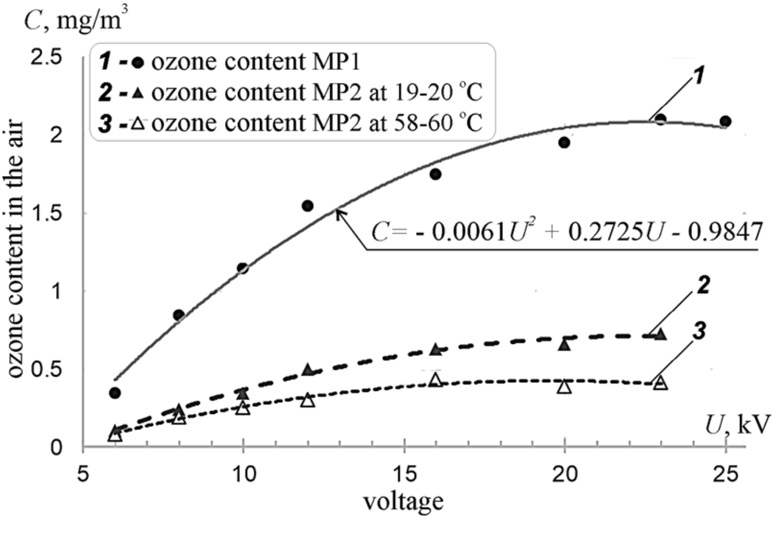

**Figure 2.** Dependencies on the voltage supplied to the ozone generator at an air speed of 1.2 m/s: *1* – ozone synthesis (after the generator in MP1); *2-3* – ozone content (after the adsorption and catalytic module in MP2)

The air flow with dispersed particles, which were electrified in the corona discharge zone, enters the adsorption-catalytic module of the flow type, which consists of a set of cartridges (Fig. 3). Every cartridge consists of two cylinders of different diameters, which are formed from filter material made of fibrous polypropylene of class G, the space between them is filled with granules of an oxide cement-containing adsorbent-catalyst.

Porous granules were obtained by extrusion technology from a mixture of oxides of transition metals and thallium (up to 40 wt. %) with a maximum specific surface of 180 $m^2/g$ (according to the BET method).

The efficiency of the adsorption-catalytic module was evaluated by indicators of the change in ozone concentration compared to the initial 1 (Fig. 2). Thus, ozone destruction was 64-71% by means of heterogeneous catalysis at an air flow speed in the duct of 1.2 m/s.

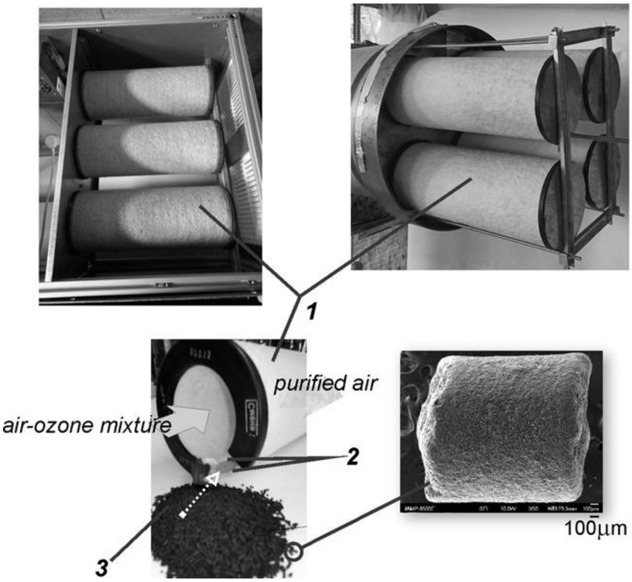

**Figure 3.** Types of the adsorption-catalytic module:
*1* – cartridge, *2* – filter layers, *3* – adsorption-catalytic granular layer (granule at x50 magnification, JAMP 9500F, Japan)

## RESULTS AND DISCUSSION

In order to increase the efficiency of the unit for the destruction of excess ozone, a technological scheme of the plasma-chemical air purification module in supply and exhaust ventilation systems of buildings with an energy-efficient system for the destruction of excess ozone, which uses a combined thermal and catalytic treatment of the air flow, has been proposed and developed (Fig. 4).

Original scientific paper

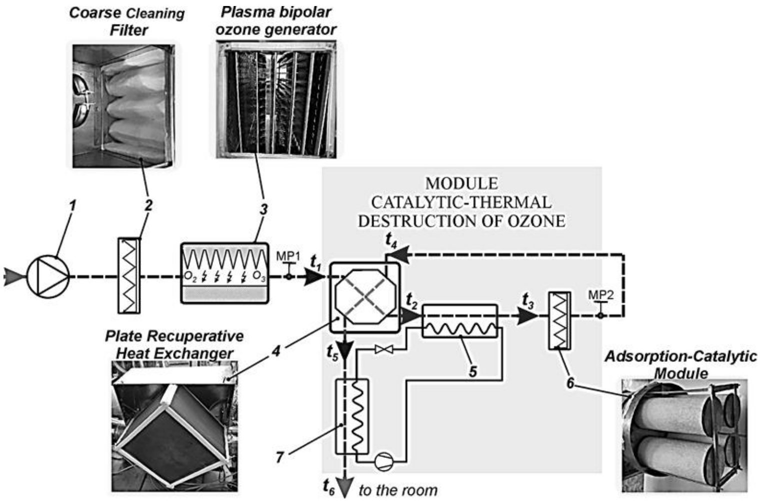

**Figure 4.** Technological scheme of energy-efficient air cleaning technology: *1* – discharge fan; *2* – coarse filter; *3* – ozone generator; *4* – heat exchanger (recuperator); *5* – heat pump evaporator; 6 – adsorption-catalytic module; *7* – heat pump capacitor; MP1-MP2 – air quality monitoring points; $t_1 ... t_6$ - air temperature monitoring points

The principle of operation of the proposed system for air purification is as follows.

The contaminated airflow is forced by fan 1 and passed through a mechanical coarse filter 2, which captures dispersed particles larger than 10 μm. Further, the contaminated air enters the ozone generator 3 and passes through a non-uniform electric field created by corona discharges. In the zone of the corona discharge, free radicals and ozone are intensively formed, which start the process of destruction of molecular pollutants and pathogenic microflora in the air flow. Air saturated with ozone with temperature $t_1$ passes through the heating channel of the recuperative heat exchanger 4 and is heated to temperature $t_2$ due to heat exchange with the flow of hot purified air, which is fed into the cooling channel of the recuperative heat exchanger after passing through the adsorption-catalytic module 6.

The air heated in the recuperative heat exchanger is additionally heated in the heat pump condenser 5 to the temperature $t_3$ of the beginning of the catalytic decomposition of ozone and enters the catalytic module 6. On the surface of the adsorbent-catalyst, pollutants and intermediate products of their decomposition enter into an oxidation reaction and decompose. Also, in module 6, the destruction of excess ozone takes place.

As can be seen from Fig. 2, a comparison of dependence 3 with 1 shows that the use of the combined thermal-catalytic method allows for increasing the speed and depth of the ozone destruction process in the adsorption-catalytic module to 75-80%.

This makes it possible to increase the ozone generation in the ionization chamber, which contributes to an increase in the number of active radicals in the air, and as a result, intensifies the destruction of molecular pollutants and increases the efficiency of air disinfection. In addition, the increase in air temperature in the adsorption-catalytic module contributes to the decomposition of organic impurities accumulated on the surface of the catalytic filter.

At this stage of development, experimental studies have determined that the resource of effective operation of the adsorption-catalytic module is 4-5 months. The evaluation was carried out in a non-production room with a short-term mode of operation with a total duration of up to 1020 hours, air exchange was 200...500 m$^3$/h, the air temperature was 17...60 °C, relative air humidity was up to 70%, the average concentration of PM10 and PM2.5 in the air stream was 5...25 mg/m$^3$.

## ESTIMATION OF ENERGY CONSUMPTION

As mentioned above, the thermal method of ozone decomposition requires additional energy consumption. Therefore, as part of the work, an estimation of the energy efficiency of the proposed heat pump heat recovery scheme for the implementation of the combined thermal-catalytic method was carried out (Fig. 4).

$$Q_{heating} = c_p \cdot G \cdot (t_3 - t_1)$$

In the case of using a recuperative heat exchanger, the energy consumption for air heating is equal to:

$$Q_{heatong}^{P} = c_p \cdot G \cdot \left[t_3 - t_1 - E \cdot (t_4 - t_1)\right],$$

where, *E* is the temperature efficiency of the recuperator, the value of which depends on the speed of air movement in the channels; *G* is the air mass flow rate; $c_p$ is the specific heat capacity of air.

The graphical dependence of the efficiency of the recuperator on the speed of air at equal mass flows in the supply and exhaust channels is shown in Figure 5.

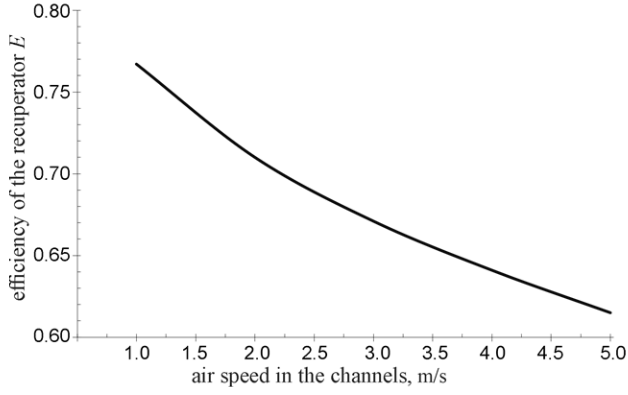

**Figure 5.** Dependence of the efficiency of the cross-flow recuperator on the air speed in the channels

The heat exchange unit of the cross flow recuperator was made of plates of cellular polycarbonate with a distance between the plates of 4 mm. The design of the heat exchange unit is hermetic and excludes overflowing from one air stream to another.

When using a recuperative heat exchanger and a heat pump, the energy consumption for the operation of the heat pump is:

$$Q_{heating}^{HP} = \frac{c_p \cdot G \cdot \left[t_3 - t_1 - E \cdot (t_4 - t_1)\right]}{COP_{HP}}$$

where $COP_{HP}$ is the heat pump conversion factor.

Figure 6 shows the influence of the temperature of the heated air stream on the value of the conversion factor of the air-to-air heat pump. The temperature of the cooling air flow is constant and equal to 20 °C.

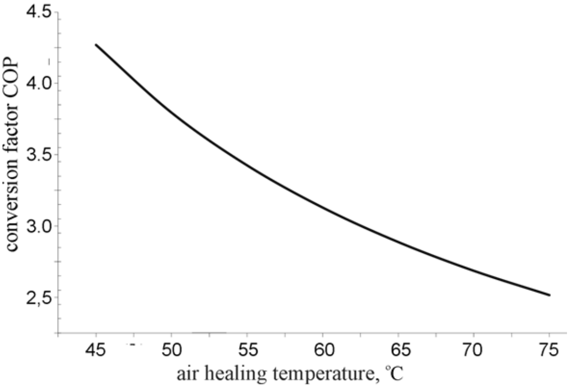

**Figure 6.** Dependence of the air-to-air heat pump conversion factor on the temperature regime of its operation

The combination of heat recovery using an air-to-air heat exchanger with thermodynamic recovery using a heat pump makes it possible to significantly reduce the energy consumption of the air cleaning system. Figure 7 presents the results of calculating the energy consumption for air heating using the experimental data shown in Figures 5 and 6. As can be seen from the graphs, the implementation of the proposed air heating scheme leads to an almost tenfold decrease in energy consumption.

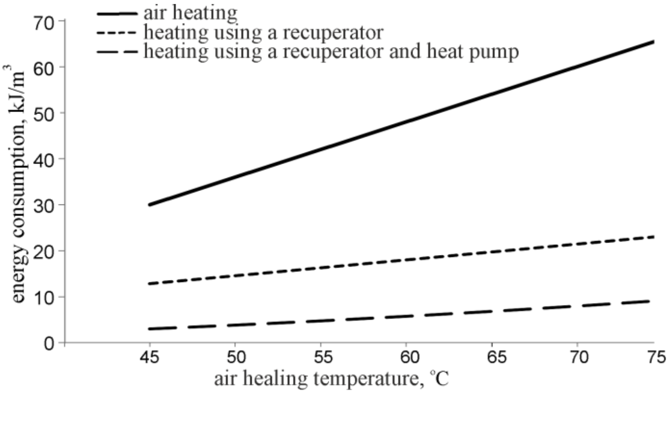

**Figure 7.** Comparison of energy consumption for air heating according to different airflow heating schemes

## CONCLUSIONS

According to the results of the work, the possibility of increasing the efficiency and safety of the ozone technology of air disinfection by destroying excess ozone through combined catalytic and thermal effects is shown.

The use of a catalytic-thermal ozone decomposition system ensures a reduction of the concentration of ozone in the airflow by 75-80%, which shows the prospects of using this air disinfection technology in buildings with a centralized supply and exhaust ventilation system. The implementation of the thermo-catalytic ozone decomposition scheme with the use of thermal and thermodynamic heat recovery makes it possible to reduce the energy consumption of the air purification system by almost 10 times. The average efficiency of the recuperative heat exchanger was 0.65-0.70, and the conversion factor of the heat pump was 2.7-3.2.

## Acknowledgements

The authors express their gratitude to junior researcher T.M. Nabok (E.O. Paton Institute of Electric Welding of the NAS of Ukraine) for the development of equipment for a high-voltage plasma chemistry unit, and to chief mechanical engineer V. I. Kovalov (Institute of Engineering Thermophysics of the NAS of Ukraine) for the development of the technology for the production of catalytic filters.

## REFERENCES

1. Batakliev, T.; Georgiev, V.; Anachkov, M.; Rakovsky, S.; Zaikov, G. Ozone decomposition. *Interdiscip Toxicol*. **2014**, *7*(2), 47–59. https://doi.org/10.2478/intox-2014-0008
2. Epelle, E.I.; Macfarlane, A.; Cusack, M. Bacterial and fungal disinfection via ozonation in air. *Journal of Microbiological Methods*. **2022**, *194*, 106431. https://doi.org/10.1016/j.mimet.2022.106431
3. Swanson, T. J.; Jamal, Z.; Chapman, J. Ozone Toxicity. In StatPearls. StatPearls Publishing, 2022. Available from: https://www.ncbi.nlm.nih.gov/books/NBK430685/
4. Taran, V.S.; Krasnyj, V.V.; Lozina, A.S. Investigation of ozone decay half-life in dependence of temperature and humidity as well as $H_2S$ and $NH_3$ oxidation mechanism. *Problems of atomic science and technology. Series: Plasma Physics*. **2017**, *1*(107), 244-246. Available from: https://vant.kipt.kharkov.ua/
5. International Ozone Association, Pan American Group (IOA-PAG). (Copyright 2021). Ozone Safety. Available from: https://ioa-pag.org/guidance
6. National Research Council. 1984. Emergency and Continuous Exposure Limits for Selected Airborne Contaminants: Volume 1. Washington, DC: The National Academies Press. https://doi.org/10.17226/689
7. Ministry of health of Ukraine. Order, Regulation No. 1596 dated 14.07.2020 On the approval of hygienic regulations on the permissible content of chemical and biological substances in the air of the working area. *Official Gazette of Ukraine*. **2020**, *64*, 111, article 2085. Available from: https://zakon.rada.gov.ua/
8. Guidelines of the WHO European Center for Environment and Health. (2021). New WHO Global Air Quality Guidelines. Available from: https://www.who.int/news/item/22-09-2021
9. Laroussi, M. Low temperature plasma-based sterilization: overview and state-of-the-art. *Plasma Processes and Polymers*. **2005**, *2*, 391-400. https://doi.org/10.1002/ppap.200400078

10. Bisag, A.; Isabelli, P.; Laurita, R. Cold atmospheric plasma inactivation of aerosolized micro-droplets containing bacteria and purified SARS-CoV-2 RNA to contrast airborne indoor transmission. *Plasma Processes and Polymers*. **2020**. https://doi.org/10.1002/ppap.202000154
11. Tkachenko, S. N. Homogeneous and heterogeneous ozone decomposition. Doctor of Sciences. Thesis, Lomonosov Moscow State University, 2004. Available from: https://fizmathim.com/
12. Li, X.; Ma, J.; He, H. Recent advances in catalytic decomposition of ozone. *Journal of Environmental Sciences*. **2020**, *94*, 14-31. https://doi.org/10.1016/j.jes.2020.03.058
13. Lobanov, L. M.; Chalaev, D. M.; Goncharov, P. V. Development of Equipment for Air Decontamination in the Ventilation and Air Conditioning Systems of Public Buildings with the Use of the Photocatalysis and Plasmochemistry Methods. *Sci. innov.* **2023**, *19*(1), 57-71. https://doi.org/doi:10.15407/scine19.01.057

APTEFF, Vol. 54, 1-335 (2023)　　UDC: 621.565:532.54:628.19
DOI: https://doi.org/10.2298/APT2354115K　　BIBLID: 1450-7188 (2023) 54, 115-127

Original scientific paper

# EXPERIMENTAL AND STATISTICAL ANALYSIS ON THE EFFECTS OF FOULING AND EFFECTIVE PARAMETERS ON PERFORMANCE OF HEAT EXCHANGER

*Ikram KOUIDRI[1]*, Djilali KAIDAMEUR[1], Mehdi ZAHRAOUI[2,3]*

[1] Department of Mechanical Engineering, GIDD Industrial Engineering and Sustainable Development Laboratory, Faculty of Science and Technology, University of Relizane, Bourmadia 48000, Algeria
[2] Department of Process Engineering, University of Relizane, Bourmadia 48000, Algeria
[3] Material Chemistry Laboratory (LCM), Université Oran1, BP.1524 Oran El Menaouer, 31100 Oran, Algeria

**Received: 4 March 2023**　**Revised: 26 March 2023**　**Accepted: 28 March 2023**

*Increasing the performance of heat exchangers is one of the main objectives of researchers and engineers in the industry. In this paper an experimental work is carried out aiming at modeling the efficiency of shell and tube heat exchanger under the influence of the most contributing factors on performance as fouling resistance, the inlet temperatures and the flow rate of the fluids. An experimental design method of type $3^1.2^4$ was used for the studies, requiring 48 tests with three repeats. The following factors are taken into account: the inlet temperature and flow rate of crude oil fluid and TEG fluid on two levels, and the fouling resistance on three levels. Regression analysis was produced a mathematical model for the efficiency based on the influential variables. The response surface and contour plots were allowed the selected from the optimum and predicted the behaviors of parameters. The effectiveness decreases considerably with the increase in fouling resistance and the decrease of inlet temperatures and flow rates.*

**Keywords**: heat exchanger, fouling, efficiency, experimental design, regression.

## INTRODUCTION

In the petroleum industry, heat exchangers are an essential component, especially for the treatment of crude oil or the atmospheric distillation of the latter. There are several types and sizes of heat exchangers: shell and tube, plate frame, double pipe heat exchanger (1, 2), but the basic principle remains relatively simple: a heat exchange makes it possible to transfer thermal energy from one fluid to another, without mixing them (3). The thermal and pressure drop performance of heat exchangers is greatly influenced by the inlet temperatures, the tube diameter, the fluid velocity and the presence of fouling on the heat transfer surface, which requires special attention (4). Fouling remains one of the major concerns of the industrialists of the thermal transfers' equipment sector; it is created by the accumulation of unwanted or undesirable deposits on a heat transfer surface in different forms: sediments, crystals, biological residues, products of a chemical reaction or even be the combination of several of these elements. The basic fouling process is divided into primary steps: incubation, transport, deposition, removal, and aging (5).The main factors influencing the deposition mechanism of solid matter are the temperature and pH of the solution, the temperature of the heat exchange surface, the solution velocity and in some cases pressure(6).

---

* Corresponding author: Ikram KOUIDRI, Department of Mechanical Engineering, GIDD Industrial Engineering and Sustainable Development Laboratory, Faculty of Science and Technology University of Relizane, Bourmadia 48000, Algeria, e-mail: kouidri.ikram@univ-relizane.dz

Fouling of crude oil heat exchangers is complex phenomena and the cause of many technical, financial and environmental problems .It has two massive consequences on the efficiency of shell-and-tube heat exchangers: (i)Thermal impact: as fouling accumulates, the resistance to heat transfer increases in the exchangers and impairs heat recovery, resulting in a gradual decrease in inlet temperature to the furnace, which must be compensated for by burning more fuel or decreasing throughput; (ii) hydraulic impact: fouling causes a progressive obstruction of the tubes, reducing the cross sectional area, restricting flow and increasing pressure drop, resulting in operational issues and even lower throughput (7).

Fouling research has been an essential part of heat exchanger research for many years. Lebele-Alawa et al. (8) analyzed the performance of the three heat exchangers (Pump around the cooler, first stage condenser, and preheated) in a polyethylene plant by comparing design data with direct measurements to predict the effect of degradation from fouling. They found an increase in fouling factor, which also affected the efficiency of heat exchangers. Cremaschi and Wu (9) realized an experimental study of the high and medium potential water fouling effect on the thermal and hydraulic performance of two brazed heat exchangers with a wave angle of 30° and 63° (BPHE) and one tube heat exchanger in the smooth tube (TTHE) and water consumption of cooling tower systems. They found that the resistance of fouling increases asymptotically. Ibrahim and Attia (10) analyzed the effect of fouling on the thermal performance of a pressurized nuclear power plant (PWR NPP) project. They concluded that efficiency is decreased with an increase in the fouling factor of seawater in the range of 0.00015-0.00035 $m^2K/W$. Jaglarz et Taler (11) presented an experimental study of the thermal resistance of fouling in plate heat exchangers that are part of the district heating system in Cracow, and the analysis was carried out. The additional studies make it possible to observe the evolution of fouling resistance over time and program temporary cleaning stops to optimize the thermal stations' efficiency. Sulaiman et al. (12) studied the effect of fouling on the performance of the shell and tube heat exchanger of a $CO_2$ fertilizer production company in Nigeria, two different heat exchanger units (cold gas heater and $CO_2$ water cooler in the washing process) were taken into account for the analysis of this study. They found that the fouling factor was 31.58% higher than the design value over a 47-day operational period. Fguiri et al. (13) conducted a theoretical and experimental study of the fouling of the three heat exchangers phosphoric acid/steam (stainless steel tubular, graphite from the two suppliers in a phosphoric acid concentration unit of the Tunisian chemical group for seeing the effect of the type of heat exchanger on fouling.

From the literature review, we found that various analytical, numerical, and hybrid models have been created and utilized to predict fouling or heat exchanger efficiency throughout the years (13, 14, 15, 16), but there is no model that combines the effect of fouling and other factors, as well as the interaction between them on the efficiency heat exchanger .

In this paper, we present an experimental research followed by modeling of the heat exchanger’s efficiency based on five factors.

## EXPERIMENTAL

### MATERIALS

The study was carried out in the EL GASSI OOS (crude optimization system). The objective of this unit is to maintain the outlet temperature of the oil from the BP separation at 50 °C. The LP separation outlet temperature range should ensure that the oil entering storage meets the crude shipping specification, including ried vapor pressure (RVP). The crude is heated by circulating a heat transfer fluid, composed of 50% Tri ethylene glycol (TEG) and 50% water in shell and tube heat exchanger (Figure1).

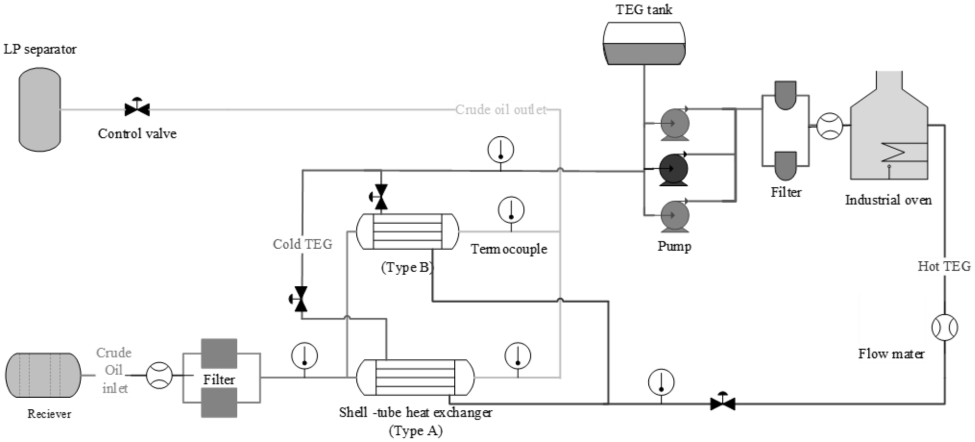

**Figure 1.** EL GASSI OOS

The essential components of the experimental installation are two shell and tube heat exchangers (Type A, Type B) of identical design, one in service, and the other in the stand-by. Two fluids pass through the test sections in counter flow with crude oil on the shell side and the triethylene glycol solution with water on the tube side. The crude oil circulation system consists of a receiver, gate valves, two filters (one in service and the other in stand-by), thermocouples, flow meter, and control valves. The solution circulation system consists of a TEG tank, three pumps (two in service and one in standby), tow filters, industrial oven, thermocouples, flow meters and control valves. Fluid temperature and flow rate are controlled by the data acquisition system, and the data can be transferred to a computer.

The table 1 provides the characteristics of shell-tube heat exchanger

**Table 1.** Characteristics of shell and heat exchanger (type A)

| **Characteristics** | **Symbol** | **Shell-tube heat exchanger** | |
|---|---|---|---|
| | | **Tubes side $_{(t)}$** | **Calendars side $_{(c)}$** |
| Fluid circulating | / | Crude oil | Tri ethylene glycol(TEG) |
| Flow rate ($m^3$/h) | q | 180 | 75 |
| Input temperature(°C) | $T_i$ | 26 | 140.7 |
| Output temperature(°C) | $T_o$ | 76.1 | 73.4 |
| Density (kg/$m^3$) | ρ | 730 | 1020 |
| A number of master keys | / | 2 | 1 |
| Fouling resistance ($m^2$ °C/W) | $R_f$ | 0.0005 | 0.00035 |

## Experimental design method

To examine the influence of effective parameters including the crude oil inlet temperature "$T_t$", the TEG inlet temperature "$T_c$", the flow rate crude oil "$q_t$", the flow rate TEG "$q_c$" and the fouling resistance "$R_f$" on the efficiency of shell-tube heat exchanger "ε". The response surface methodology (RSM), based on the composite design of experiments method of the type $3^1.2^4=48$, was used (17, 18). The numbers 3 and 2 represent the level of each factor and the powers 1 and 4 represent the number of factors used. This type is used when predicting quadratic effects of some parameter among others.

As shown in Table 1, the $T_{ti}$, $T_{ci}$, $q_t$ and $q_c$ parameters are chosen in two levels for each parameter and $R_f$ is chosen in three levels.

**Table 2.** Levels matrix

| Parameters | Unit | Code | High level+1 | Intermediate level 0 | Low level-1 |
|---|---|---|---|---|---|
| $T_{ti}$ | °C | $X_1$ | 38.6 | / | 15 |
| $T_{ci}$ | °C | $X_2$ | 146 | / | 124 |
| $q_t$ | $m^3/h$ | $X_3$ | 165 | / | 98 |
| $q_c$ | $m^3/h$ | $X_4$ | 78 | / | 63 |
| $R_f$ | $m^2$ °C/W | $X_5$ | 0,0031076 | 0,00189 | 0,00067 |

The value of variable coded was via Equation [1]:

$$X_i = \frac{x_i - x_{i0}}{\Delta x} \qquad i=1, 2\ldots k \qquad [1]$$

where $X_i$ represents the coded level, $x_i$ represents the real value of an independent variable, $x_{i0}$ represents the real value of an independent variable at the central point, and $\Delta x$ represents the step change of variable *i*.

The real functional connection between the independent variables and their responses was ascertained by the RSM using a quadratic polynomial. The real response surface was calculated using the equation below (19, 20):

$$Y\,(X_1, X_2, \ldots\ldots\ldots, X_k) = \beta_0 + \sum_{i=1}^{k} \beta_i X_i\, X_j + \sum_{i,j=1}^{k} \beta_{ij}\, X_i\, X_j + \sum_{i=1}^{k} \beta_{ii} X_i^2 \qquad (i \neq j) \qquad [2]$$

where Y is the expected response (the efficiency); $X_1$, $X_2$, …, $X_k$ are coded independent variables; $\beta_0$ is the free term, and $\beta_i$, $\beta_{ii}$, $\beta_{ij}$ and e are the first-order effect, quadratic effect, interaction effect.

## STATISTICAL ANALYSIS

Once the mathematical model obtained (regression equation), we proceed to the statistical analysis of results in order to verify the significance of these regression coefficients and the adequacy of the model, following the algorithm of BOX WILSON (21).

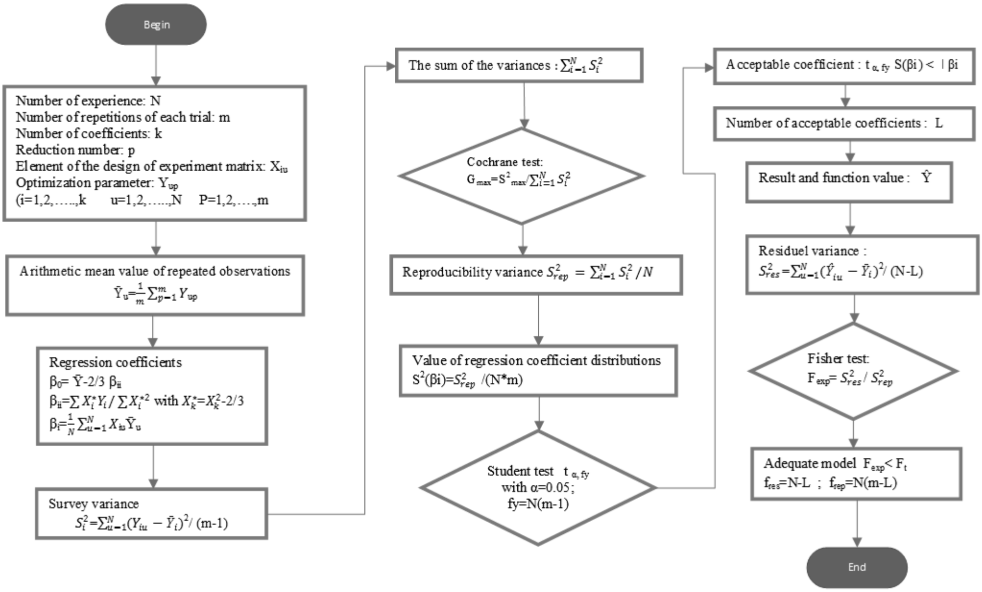

**Figure2.** Statistical analysis flowchart

## RESULTS AND DISCUSSION

### EXPERIMENTAL RESULTS

The experimental values for each experimental run are presented in Table 3. Each efficiency value is repeated three times to obtain the average value which is $\bar{\varepsilon}$. These results can prove that the increasing of fouling resistance reduces the efficiency. According to this data, the optimal value of efficiency can be observed when $T_t$ = 15 °C, $T_c$=124 °C, $q_t$=98m$^3$/h, $q_c$=78m$^3$/h et $R_f$= 0.00067 m$^2$ °C/W. The interaction between these parameters has significant influence on the obtained response and can be described by equation [3], which can be used for calculation of optimal parameters.

### MATHEMATICAL MODEL

The coefficients' confidence interval for t (0.05; 96)= 1.6645 and S(βi)=0.00073. Regression analysis will be used to validate the student's test condition, and the model will take the following form after only taking into account significant regression coefficients:

$$Y (X_i, \beta_i)= 0.428 + 0.0242X_1\, 0.0095\, X_2 + 0.0753\, X_3 - 0.0055\, X_4 - 0.0346\, X_4 - \\ - 0.0062X_{12} + + 0.0042\, X_{13} - 0.0076\, X_{15} + 0.0017\, X_{23} - 0.003\, X_{25} - 0.0148\, X_{35} \\ - 0.0011\, X_{123} + 0.0019\, X_{125} + 0.031\, X_{45} + 0.05186X_5^2 \qquad [3]$$

Fischer's criteria has an experimental value of $F_{exp}$ = 0.15, which means that the model [3] adequately captured the phenomena.

**Table 3.** Experimental data

| N° | te | Te | qv | qv | R | ε1 | ε2 | ε3 | ε̄ |
|---|---|---|---|---|---|---|---|---|---|
| 1 | 38,6 | 146 | 165 | 78 | 0,0031 | 0,213752 | 0,211145 | 0,216358 | 0,213752 |
| 2 | 15 | 146 | 165 | 78 | 0,0031 | 0,247146 | 0,244306 | 0,249987 | 0,247146 |
| 3 | 38,6 | 124 | 165 | 78 | 0,0031 | 0,231063 | 0,228376 | 0,233750 | 0,231063 |
| 4 | 15 | 124 | 165 | 78 | 0,0031 | 0,250833 | 0,247983 | 0,253684 | 0,250833 |
| 5 | 38,6 | 146 | 98 | 78 | 0,0031 | 0,324037 | 0,320086 | 0,327989 | 0,324037 |
| 6 | 15 | 146 | 98 | 78 | 0,0031 | 0,374664 | 0,370357 | 0,378970 | 0,374664 |
| 7 | 38,6 | 124 | 98 | 78 | 0,0031 | 0,350281 | 0,346208 | 0,354354 | 0,350281 |
| 8 | 15 | 124 | 98 | 78 | 0,0031 | 0,380253 | 0,375932 | 0,384574 | 0,380253 |
| 9 | 38,6 | 146 | 165 | 63 | 0,0031 | 0,210147 | 0,207584 | 0,212710 | 0,210147 |
| 10 | 15 | 146 | 165 | 63 | 0,0031 | 0,242978 | 0,240185 | 0,245771 | 0,242978 |
| 11 | 38,6 | 124 | 165 | 63 | 0,0031 | 0,227166 | 0,224525 | 0,229808 | 0,227166 |
| 12 | 15 | 124 | 165 | 63 | 0,0031 | 0,246602 | 0,243800 | 0,249405 | 0,246602 |
| 13 | 38,6 | 146 | 98 | 63 | 0,0031 | 0,319110 | 0,315219 | 0,323002 | 0,319110 |
| 14 | 15 | 146 | 98 | 63 | 0,0031 | 0,368966 | 0,364725 | 0,373207 | 0,368966 |
| 15 | 38,6 | 124 | 98 | 63 | 0,0031 | 0,344954 | 0,340942 | 0,348965 | 0,344954 |
| 16 | 15 | 124 | 98 | 63 | 0,0031 | 0,374469 | 0,370214 | 0,378725 | 0,374469 |
| 17 | 38,6 | 146 | 165 | 78 | 0,0018 | 0,293375 | 0,289797 | 0,296953 | 0,293375 |
| 18 | 15 | 146 | 165 | 78 | 0,0018 | 0,339208 | 0,335309 | 0,343107 | 0,339208 |
| 19 | 38,6 | 124 | 165 | 78 | 0,0018 | 0,317133 | 0,313445 | 0,320820 | 0,317133 |
| 20 | 15 | 124 | 165 | 78 | 0,0018 | 0,344266 | 0,340354 | 0,348178 | 0,344266 |
| 21 | 38,6 | 146 | 98 | 78 | 0,0018 | 0,428830 | 0,423600 | 0,434059 | 0,428830 |
| 22 | 15 | 146 | 98 | 78 | 0,0018 | 0,495827 | 0,490128 | 0,501527 | 0,495827 |
| 23 | 38,6 | 124 | 98 | 78 | 0,0018 | 0,463557 | 0,458167 | 0,468948 | 0,463557 |
| 24 | 15 | 124 | 98 | 78 | 0,0018 | 0,503222 | 0,497503 | 0,508940 | 0,503222 |
| 25 | 38,6 | 146 | 165 | 63 | 0,0018 | 0,286628 | 0,283132 | 0,290123 | 0,286628 |
| 26 | 15 | 146 | 165 | 63 | 0,0018 | 0,331405 | 0,327596 | 0,335214 | 0,331405 |
| 27 | 38,6 | 124 | 165 | 63 | 0,0018 | 0,309838 | 0,306235 | 0,313441 | 0,309838 |
| 28 | 15 | 124 | 165 | 63 | 0,0018 | 0,336346 | 0,332524 | 0,340168 | 0,336346 |
| 29 | 38,6 | 146 | 98 | 63 | 0,0018 | 0,420243 | 0,415118 | 0,425368 | 0,420243 |
| 30 | 15 | 146 | 98 | 63 | 0,0018 | 0,485897 | 0,480312 | 0,491482 | 0,485897 |
| 31 | 38,6 | 124 | 98 | 63 | 0,0018 | 0,454273 | 0,448991 | 0,459556 | 0,454273 |
| 32 | 15 | 124 | 98 | 63 | 0,0018 | 0,493142 | 0,487538 | 0,498746 | 0,493142 |
| 33 | 38,6 | 146 | 165 | 78 | 0,00067 | 0,467534 | 0,461832 | 0,473235 | 0,467534 |
| 34 | 15 | 146 | 165 | 78 | 0,00067 | 0,540571 | 0,534357 | 0,546784 | 0,540571 |
| 35 | 38,6 | 124 | 165 | 78 | 0,00067 | 0,505387 | 0,499511 | 0,511264 | 0,505387 |
| 36 | 15 | 124 | 165 | 78 | 0,00067 | 0,548623 | 0,542389 | 0,554857 | 0,548623 |
| 37 | 38,6 | 146 | 98 | 78 | 0,00067 | 0,633798 | 0,626069 | 0,641528 | 0,633798 |
| 38 | 15 | 146 | 98 | 78 | 0,00067 | 0,732816 | 0,724393 | 0,741239 | 0,732816 |
| 39 | 38,6 | 124 | 98 | 78 | 0,00067 | 0,685117 | 0,677151 | 0,693083 | 0,685117 |
| 40 | 15 | 124 | 98 | 78 | 0,00067 | 0,743736 | 0,735284 | 0,752187 | 0,743736 |
| 41 | 38,6 | 146 | 165 | 63 | 0,00067 | 0,450628 | 0,445133 | 0,456124 | 0,450628 |
| 42 | 15 | 146 | 165 | 63 | 0,00067 | 0,521021 | 0,515032 | 0,527009 | 0,521021 |
| 43 | 38,6 | 124 | 165 | 63 | 0,00067 | 0,487111 | 0,481447 | 0,492776 | 0,487111 |
| 44 | 15 | 124 | 165 | 63 | 0,00067 | 0,528780 | 0,522771 | 0,534789 | 0,528780 |
| 45 | 38,6 | 146 | 98 | 63 | 0,00067 | 0,615218 | 0,607716 | 0,622721 | 0,615218 |
| 46 | 15 | 146 | 98 | 63 | 0,00067 | 0,711330 | 0,703154 | 0,719506 | 0,711330 |
| 47 | 38,6 | 124 | 98 | 63 | 0,00067 | 0,665030 | 0,657297 | 0,672763 | 0,665030 |
| 48 | 15 | 124 | 98 | 63 | 0,00067 | 0,721927 | 0,713723 | 0,730130 | 0,721927 |

## ANALYSIS WITH TWO VARIABLES FACTORS

### Effect of inlet temperatures of crude oil and TEG fluids on the efficiency

This configuration describes the mathematical model where the flow rates of the fluids (TEG and crude oil) and the fouling resistance are fixed at real average values $X_3$=131.5 $m^3$/h; $X_4$=70.5 $m^3$/h; $X_5$=0.00067 $m^2$ °C/W. The model will therefore have the form:

$$Y(X_1, X_2) =0.4+0.0242\ X_1+0.0095X_2-0.0062\ X_1X_2 \qquad [4]$$

Its response surface and contour plot are represented in Figure 3. For a temperature variation of the cold fluid (tube) from 16.77 °C to 22.08 °C and the temperature of the hot fluid (shell) from 79.31 °C to 80.86 °C, the efficiency increases linearly and rapidly. Beyond these values, it grows non-linearly and slowly.

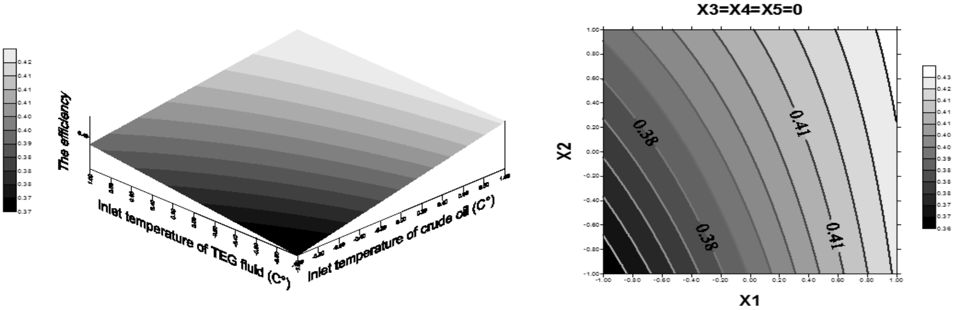

**Figure 3.** Effect of inlet temperatures of crude oil and TEG fluids on the efficiency

### Effect of inlet temperature of crude oil and flow rate of TEG fluid on the efficiency

If the TEG fluid enters with an average temperature and flow rate of $X_2$= 80.55 °C and $X_4$= 70.5 $m^3$/h respectively, and the fouling resistance fixed at $X_5$= 0.0018 $m^2$ °C/W, the model will have the form:

$$Y(X_1, X_3) =0.4+0.0242\ X_1+0.0753\ X_3+0.0042\ X_1X_3 \qquad [5]$$

With an increase in the inlet temperature and the flow rate of the cold fluid, the efficiency increases in a linear and rapid manner (Figure 4).

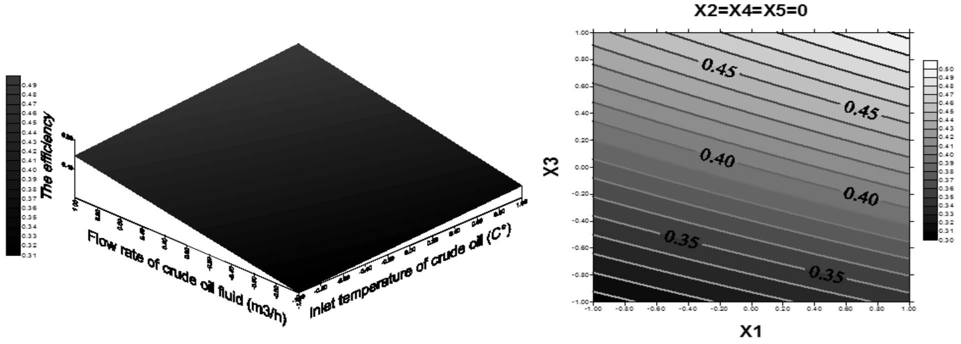

**Figure 4.** Effect of inlet temperature of crude oil and flow rate of TEG fluid on the efficiency

## Effect of inlet temperature of crude oil and fouling resistance on the efficiency

If the parameters $T_t$, $q_t$ and $q_c$ are kept constant for the average values respectively $X_2$= 135 °C; $X_3$= 131.5 $m^3/h$; $X_4$= 70.5 $m^3/h$, we obtain a model of the form:

$$Y(X_1, X_5) = 0.4+0.0242X_1-0.0346X_5-0.0076 X_1X_5+0.051 X_5^2 \qquad [6]$$

With an increasing variation of the crude oil inlet temperature and a decreasing variation of the fouling resistance from 0.003 $m^2$ °C/W to 0.001 $m^2$ °C/W, the efficiency increases non-linearly and slowly, then linear and quickly up to the 0.5 value (Figure 5).

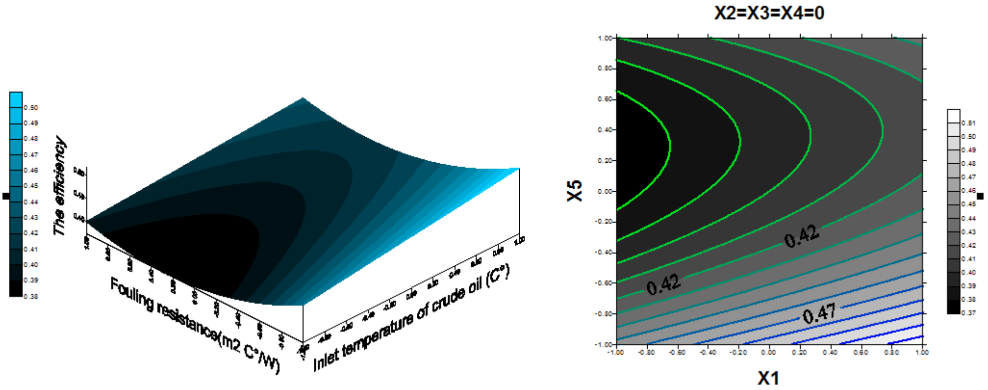

**Figure 5.** Effect of inlet temperature of crude oil and fouling resistance on the efficiency

### Effect of inlet temperature of TEG fluid and flow rate of crude oil on the efficiency

For average and constant values: $X_1$= 26.8 °C, $X_4$=70.5 m$^3$/h and $X_5$= 0.0018 m$^2$ °C/W. The model will take the following form:

$$Y(X_2, X_3) = 0.4+0.0095\ X_2+0.0753\ X_3+0.0017\ X_2X_3 \qquad [7]$$

The model is represented in the Figure (6), where the efficiency increases in a linear and slow way with the increase of the inlet temperature of the TEG fluid and the mass flow of the crude brut fluid.

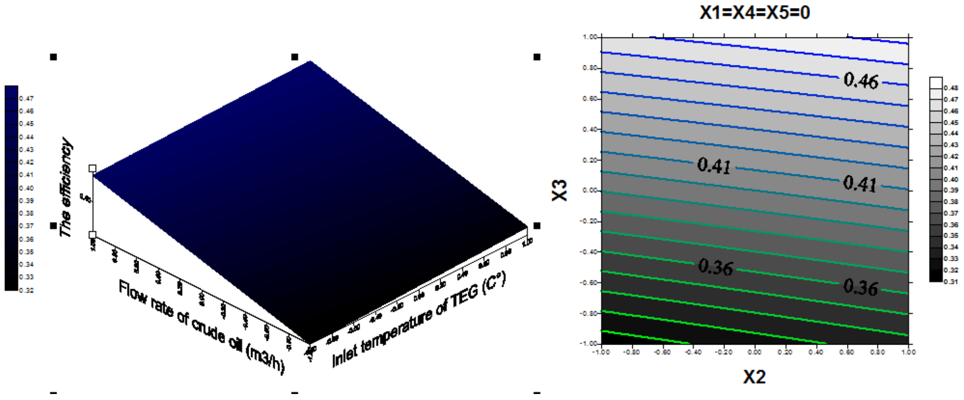

**Figure 6.** Effect of inlet temperature of TEG fluid and flow rate of crude oil on the efficiency

### Effect of flow rate of crude oil and fouling resistance on the efficiency

If we maintain the three parameters $X_1$, $X_2$, $X_4$ at their average values, the model will have the following form:

$$Y\ (X_3, X_5) = 0.4+0.0753\ X_3-0.0346X_5-0.0148X_3X_5+0.051X_5^2 \qquad [8]$$

From figure (7), for a decreasing variation of the fouling resistance from 0, 0031 m$^2$ °C/W to 0.0006769 m$^2$ °C/W, the efficiency varies according to two domains:

1 - when the flow rate of the crude oil fluid varies from 98m$^3$/h to 126.8 m$^3$/h, the efficiency increases slowly with a non-linear pace.

2 - when the flow rate of the cold fluid exceeds the value of 126.8 m$^3$/h, the efficiency increases linearly and rapidly.

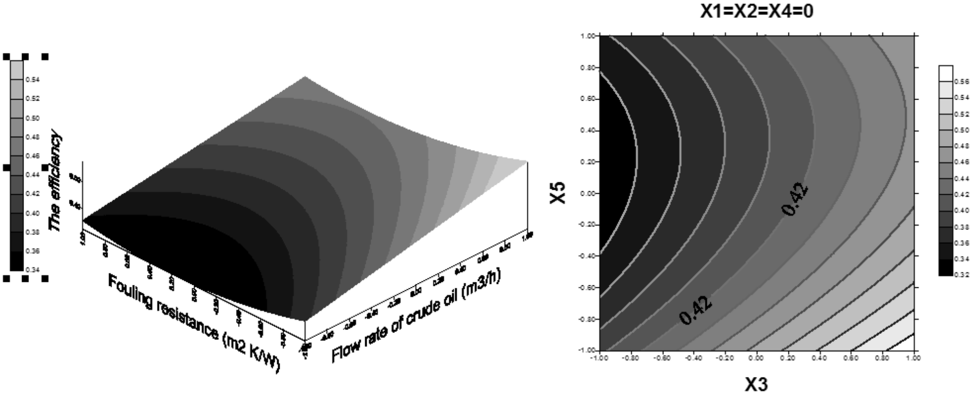

**Figure 7.** Effect of flow rate of crude oil and fouling resistance on the efficiency

## Effect of flow rate of TEG fluid and fouling resistance on the efficiency

For average values of the parameters $T_t$, $T_c$ and $q_t$, the mathematical model will have the form:

$$Y(X_4, X_5) =0.4-0.0055 X_4-0.0346X_5+0.031X4X_5+0.0051X_5^2 \quad [9]$$

When the flow rate of TEG fluid varies from 78 $m^3$/h to 63 $m^3$/h, the efficiency decreases non-linearly and rapidly under the effect of the increasing variation in the fouling resistance $R_f$ of 0.0029 $m^2$ °C/ W to 0.0011 $m^2$ °C/W. For $R_f$ varying from 0.00067 $m^2$ °C/W to 0.0029 $m^2$ °C/W the efficiency decreases linearly and rapidly.

This representation shows that the efficiency has an optimum point of real coordinates: $q_c$ =74.475 $m^3$/h and $R_f$=0.0021 $m^2$ C°/W, which is a mini-max where its value is 43% (Figure 8).

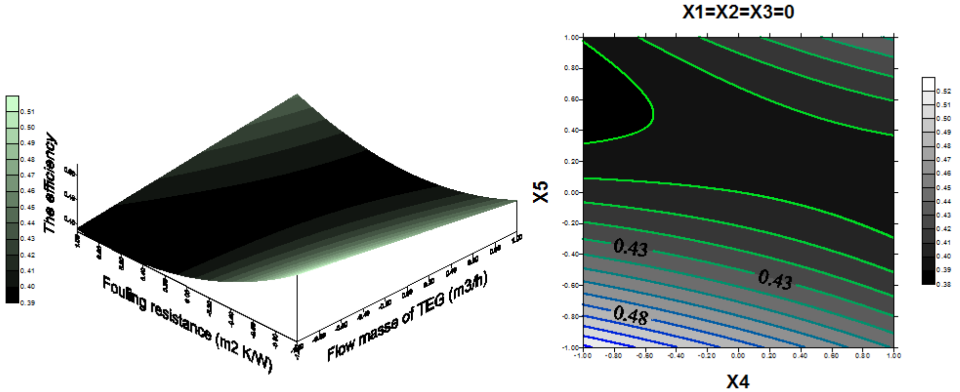

**Figure 8.** Effect of flow rate of TEG fluid and fouling resistance on the efficiency

### Effect of inlet temperature of TEG fluid and fouling resistance on the efficiency

If now, the TEG fluid enters with a temperature $X_2$= 80.55 °C and the crude oil fluid enters with an average flow of $X_3$=131.5 $m^3$/h respectively, and the flow rate of the TEG fluid fixed at $X_4$=70.5 $m^3$/h. The model will have the form:

$$Y(X_2, X_5) = 0.4+0.0095 X_2-0.0346 X_5-0.003 X_2X_5+0.051 X_5^2 \qquad [10]$$

With an increase in the TEG inlet temperature, the efficiency varies according to 3 domains:

1 - When the fouling resistance goes from 0.00067 $m^2$ °C/W to 0.000913 $m^2$ °C/W, the efficiency decreases linearly and rapidly.

2 - for a fouling resistance between 0.000913 $m^2$ °C/W and 0.001277 $m^2$ °C/W, the efficiency decreases linearly and slowly.

3 - When $R_f$ exceeds the value 0.001399 $m^2$ K/W, the efficiency decreases non-linearly and slowly.

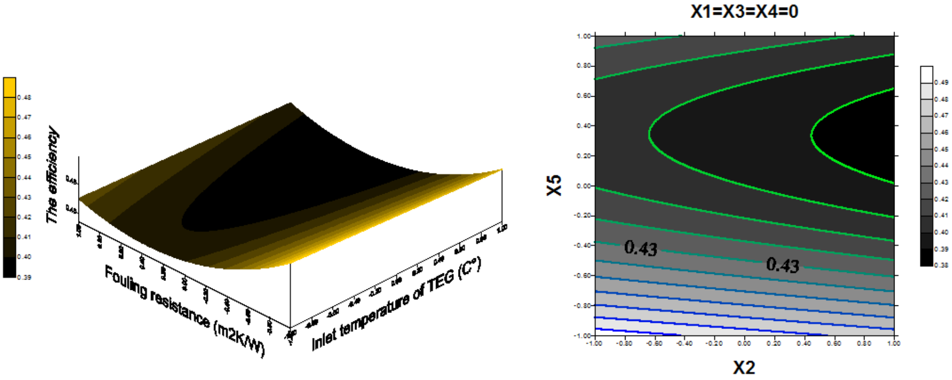

**Figure 9.** Effect of inlet temperature of TEG fluid and fouling resistance on the efficiency

## CONCLUSION

Maintaining high efficiency of heat exchanger is one of the biggest challenges engineers face in industry but it is very possible to improve it by providing some optimal regulations on parameters influencing this performance such as the inlet temperatures, the flow rate of crude oil and TEG fluids, and the fouling resistance. The experimental study allowed us to establish the relationship of these parameters with the efficiency of the shell-tube exchanger by a mathematical model resulting from a statistical method for planning experiments. This model is represented graphically by fixing in each case three parameters among the five considered at their average value in order to allow us the visualization of the effect which can apply the two other unfixed parameters. This operation offered seven responses surfaces and contour plots allowing us to observe the following:

- In one of the seven cases observed, efficiency has an optimum point which is a "Min-max".

- The actual values of the factors influencing performance equivalent to the coordinates "coded" of the "Mini-Max" make it possible to indicate that the efficiency of the exchanger is the most important in the vicinity of the average values of the various factors.
- The efficiency of shell and tube heat exchanger is proportional to the inlet temperature and flow rate of fluids but inversely proportional to fouling resistance.

## Acknowledgements

The authors acknowledge the engineers of Gassi El Agreb OOS (optimization oil system), SonaHess, Hassi Massoud, Algeria.

## REFERENCES

1. Faes, W.; Lecompte, S.; Ahmed, Z.Y.; Van Bael, J. Salenbien, R.; Verbeken, K.; De Paepe, M. Corrosion and corrosion prevention in heat exchangers. *Corros Rev*. **2019**, *37*:131–155.
2. Davoudi, E.; Vaferi, B. Applying artificial neural networks for systematic estimation of degree of fouling in heat exchangers. *Chem Eng Res Des.* **2018,** *130*, 138–153.
3. Ajayi, O.; Ogbonnaya, S. Fouling phenomenon and its effect on heat exchanger: a review. *FHMT.* **2017**, *1*, 9-31.
4. Awais, M.; Bhuiyan, A.A. Recent advancements in impedance of fouling resistance and particulate depositions in heat exchangers. *Int J Heat Mass Transf.* **2019**, *141*, 580–603.
5. Arsenyeva, O.; Matsegora,O.; Kapustenko, P.; Yuzbashyan, A.; Klemeš, J. J. The water fouling development in plate heat exchangers with plates of different corrugations geometry. *Therm Sci Eng Prog.* **2022**, *32*, 101310.
6. Kazi, S.N.; Teng, K.H.; Zakaria, M.S.; Sadeghinezhad, E.; Bakar, M. A. Study of mineral fouling mitigation on heat exchanger surface. *Desalination.* **2015**, *367*, 248–254.
7. Diaz-Bejarano, E.; Behranvand, E.; Coletti, F. Organic and inorganic fouling in heat exchangers–Industrial case study: Analysis of fouling state. *Appl Energy.* **2017**, *206*, 1250–1266.
8. Lebele-Alawa, B.T.; Ohia I.O. Influence of fouling on heat exchanger effectiveness in a polyethylene plant. *Energy and Power.* **2014** ,*4*(2), 29–34.
9. Cremaschi, L.; Wu, X. Effect of fouling on the thermal performance of condensers and on the water consumption in cooling tower systems. *Heat Transf Eng.* **2015**, *36* (7,8), 663–675.
10. Ibrahim, S. M. A.; Attia, S.I. The influence of condenser cooling seawater fouling on the thermal performance of a nuclear power plant. *Ann Nucl Energy.* **2015**, *76*, 421–430.
11. Jaglarz, G.A.; Taler, D. Experimental study of fouling in plate heat exchangers in district heating systems. *J Power Technol.* **2015**, *95*(5),42.
12. Sulaiman, M.A.; Kuye, S.I.; Owolabi, S.A.Investigation of fouling effect on overall performance of shell and tube heat exchanger in a urea fertilizer production company in Nigeria. *Niger J Technol.* **2016**, *35*(1), 129–136.
13. Fguiri, A.; Jradi, R.; Marvillet, C.; Jeday,M.R. Heat exchangers fouling in phosphoric acid concentration. *Heat Mass Transf.* **2020**, *56*, 2313–2324.
14. Fguiri, A.; Daouas, N.; Radhouani, M. S.; Aissia, H. B. Inverse analysis for the determination of heat transfer coefficient. *Can. J. Phys.* **2013**, *91*(12), 1034-1043.
15. Lokk, R.; Alsadaie, S.M.; Mujtaba, I.M. Dynamic simulation of once-through multistage flash (MSF-OT) desalination process: Effect of seawater temperature on the fouling mechanism in the heat exchangers. *Comput Chem Eng.* **2021**, *155*, 107515.
16. Aguel, S.; Meddeb, Z.; Jeday, M.R. Parametric study and modeling of cross-flow heat exchanger fouling in phosphoric acid concentration plant using artificial neural network. *J Process Control.* **2019**, *84*, 133–145.

17. Torkaman, R.; Rovais, M.R.A.; Heydari, M.; Torab-Mostaedi, M.; Asadollahzadeh; M. Effects of the presence and absence of nanoparticles in the hold-up and hydrodynamic velocities in the pulsed disc and doughnut column by using central composite design method. *Prog Nucl Energy.* **2022**, *147*:104217.
18. Meslameni, W.; Kamoun, T.; Hbaieb, M. Experimental modeling of EDM process using the experimental design method Modélisation expérimentale du processus EDM par la méthode des plans d’expériences **2019**. https://researchegate.net (accessed July 2019).
19. Vidović, S.S.; Zeković, Z.P.; Lepojević, Ž.D.; Radojković, M. M.; Jokić, S. D.; Anačkov, G. T. Optimization of the Ocimum basilicum L. extraction process regarding the antioxidant activity. *Acta Period Technol.* **2012**, 315–323.
20. Zahović, I.E; Dodić, J.M; Trivunović, Z.Z. Xanthan production on crude glycerol-based medium by local Xanthomonas isolate: Optimization of inoculum incubation time. *Acta Period Technol.* **2022**, 147–157.
21. Kaidameur, D.; Serrier, M. Experimental method of tribological modelling of different coatings of stainless steel. *Mech Mech Eng.* **2018**, *22*,1273–1285.

APTEFF, Vol. 54, 1-335 (2023)
DOI: https://doi.org/10.2298/APT2354129B

UDC: 546.62:546.281'261:661.183.8]:539.375
BIBLID: 1450-7188 (2023) 54, 129-136

Original scientific paper

# OPTIMIZATION STUDY ON WEAR BEHAVIOUR OF ALUMINIUM 7075 HYBRID COMPOSITE CONTAINING SILICON CARBIDE AND ALUMINIUM OXIDE USING TAGUCHI METHOD

*Shridhar H. BUDAPANAHALLI*[1], *S. B. MALLUR*[2], *Arun Y. PATIL*[3]*, *Raman KUMAR*[4]

[1] Department of Mechanical Engineering, KLE institute of Technology, Hubballi, Karnataka, India
[2] Department of Mechanical Engineering, UBDT College of Engineering, Davanagere, Karnataka, India
[3] Department of Mechanical Engineering, KLE Technological University, Vidya Nagar, Hubballi, India
[4] Department of Mechanical Engineering and University Centre for Research and Development, Chandigarh University, Mohali-140413, Punjab, India

**Received: 24 February 2023** **Revised: 11 March 2023** **Accepted: 30 March 2023**

*Due to light weight, high strength to weight ratio, higher wear resistance aluminium and its alloy have got greater consideration as a matrix material in most of the composite applications. Al MMCs is used in preparation of pistons, cylinder barrel, break discs, gears, valves etc. Use of Al-Si alloys are increasing in areas of automobile and aerospace industries. Present study aims to investigate about wear behaviour of aluminium 7075 hybird composite with silicon carbide (SiC) and aluminium oxide ($Al_2O_3$) as reinforcements. Hybird composite material were processed through stir casting process. Addition of SiC is 3,6 and 9 wt.% whereas $Al_2O_3$ is fixed 5 wt.%. Wear test was conducted through unlubricated conditions. Wear rate was been recorded after each set of experiment carried through wear test. To optimize the control parameters Taguchi method was used as a statistical tool. L9 orthogonal array was utilized and investigational design was based on control factors namely SiC wt.%, load, sliding distance and response factor was wear rate to study the wear performance. Empirical relation was established for wear rate in relations of control variables by multiple regression analysis. Finally, analysis of variance (ANOVA) was used to evaluate the impact of specific factors on wear rate. MINITAB V.17.1.0 was used to analyse the results. It was observed that load and SiC wt.% were significant factor affecting response variable. Higher values of SiC wt.% increased the wear resistance.*

**Keywords**: Aluminium 7075, Silicon carbide (SiC), Aluminium oxide ($Al_2O_3$), Wear analysis, Taguchi method.

## INTRODUCTION

Composite material is a material which is made from at least two constituent materials. These constituent materials have especially dissimilar chemical or physical properties and are converged to make a material with properties better than their singular partner (1). Al 7075 is extensively used in a variety of applications due to its low density (2). Due to its greater resistance to corrosion when encountered with salt water, Al 7075 is used in US Navy’s aircrafts (3). However, Al 7075 has some limitations such as less wear resistance, low strength etc which makes it unsuitable for many of the applications. Therefore, aluminium should be added with some of the reinforcement so that its mechanical and tribological properties can be increased and it can be suited for required applications. Experimental results showed that addition of SiC as reinforcement in Al 7075 increases wear rate (4-5). Aluminium Hybrid composites have got greater wear resistance when compared to sing-

---

* Corresponding author: Arun Y. PATIL, Department of Mechanical Engineering, KLE Technological University, Vidya Nagar, Hubballi, India, 580031, e-mail: patilarun7@gmail.com

UDC: 546.62:546.281'261:661.183.8]:539.375
BIBLID: 1450-7188 (2023) 54, 129-136

Original scientific paper

le reinforced composites (6-7). Combination of SiC and Gr as hybrid reinforcements yielded in better wear resistance rather using them separately (6). Al 7075 with hybrid combination of $B_4N$ and BN provided higher tensile strength and wear resistance (7). Increase in addition of Gr in Al 356 along with SiC decreased the wear rate (8). Al 7075 with SiC and $Al_2O_3$ as reinforcement has got higher hardness of 98 VHN, higher tensile strength of 366.45MPa compared to unreinforced Al 7075 (9). Load is an influential parameter in occurrence of wear as realized during experimentation and even ANOVA results reflected the same (10-11). Wear rate decreases as wt.% of $Al_2O_3$ was increased, but it was only 5 wt.%. Further addition of $Al_2O_3$ wear rate got increased (12) and same results were show cased even in Al 7075 hybrid composites with SiC and $Al_2O_3$ as reinforcements (13). Experimental results show that strength of composite material improved with increase in reinforcement percentage and also by squeeze pressure. Because pressure decreases porosity. Optimum wear rate is observed for Al 7075 with 5 wt.% of $Al_2O_3$ for different pressure in squeeze casting (14). Aluminium based composite and aluminium hybrid composite can be processed through stir casting method in an effective way and comparable in an economic manner (15-19), vacuum casting (20), friction stir process (21), powder metallurgy (6).

The objective of the present work is to determine wear rate through pin on disc wear test. Three different hybrid combinations were used for testing, aluminium 7075 with varying wt.% (3%, 6%, 9%) SiC and fixed wt.% of 5% $Al_2O_3$. For this combination of hybrid composite there is wide potential in gear application (9). Whenever a material is suggested in preparation of gear, its wear study need to be studied, but wear study has got wide number of factors affecting the material. Therefore, an optimizing study is required to check the influence of each factor on wear rate and even which factor affects more and which affects least should also be determined. So, Taguchi method is used to find out optimal parameter to determine wear rate and analysis of variance (ANOVA) is accomplished to identify the impact of individual factor on wear rate.

## MATERIALS AND METHODS

### ALUMINIUM 7075 HYBRID COMPOSITE PROCESSING

Aluminium 7075 basically have more content of zinc in them. Chemical composition of aluminium 7075 is shown in Table 1 and mechanical properties of unreinforced and hybrid reinforced aluminium 7075 is shown in Table 2. The aluminium 7075 hybrid composite material is processed through stir casting process. Reinforcements added were Silicon carbide with changing wt.% of 3%, 6%, 9% and aluminium oxide with fixed weight percentage of 5%. Commercial grades aluminium 7075 ingots were used as a matrix material. Bharat Aerospace Metals, Mumbai supplied Aluminium 7075 ingots. The average particle size of aluminium oxide is 0.191 microns and silicon carbide is 1.04 microns. At a temperature of around 750 °C Aluminium 7075 alloy ingot was melted in a mild steel crucible. Succeeding to melting, degassing was carried by adding hexachloroethane tablets. The mixture was stirred by using zirconium coated mild steel stirrer at about 400rpm for 15 min. Simultaneously during the time of stirring aluminium oxide and silicon carbide will be added which were earlier heated at 250 °C. Finally, the molten hybrid composite material was poured into preheated metal mould and allowed to solidify. Once solidified Aluminium

7075 with various weight percentage of hybrid composites were ready to prepare test specimens. Test specimens were machined in accordance to ASTM standards.

Wear test for dry sliding conditions were carried with pin on disc apparatus (Magnum, Bengaluru, India) as per ASTM G99 standard. Disc material is EN 31 with hardness of 58-60 HRC and diameter of 165mm. The specimens were tested for different loads and disc radius at constant sliding speed of 450rpm under unlubricated conditions with real time data acquisition of wear rate. The wear test specimen has got diameter 8mm and length 28mm.

**Table 1.** Chemical composition of aluminium 7075 (22)

| Elements | % By wt. |
|---|---|
| Zinc | 5.1 |
| Magnesium | 2.185 |
| Copper | 1.69 |
| Chromium | 0.193 |
| Aluminium | Remaining |

**Table 2.** Mechanical Properties of reinforced and unreinforced hybrid aluminium 7075 (9)

| Material | Hardness (VHN) | Tensile Strength (MPa) |
|---|---|---|
| Unreinforced Al 7075 | 51 | 118 |
| Al 7075 + 3 % SiC + 5% $Al_2O_3$ | 66 | 166 |
| Al 7075 + 6 % SiC + 5% $Al_2O_3$ | 73 | 366.45 |
| Al 7075 + 9 % SiC + 5% $Al_2O_3$ | 98 | 228.6 |

## TAGUCHI METHOD

Taguchi method uses set of statistical techniques and is usually used in experimental design. Greater advantage of this technique is that it uses special orthogonal arrays to determine all design factors with a smaller number of experiments (23-24). Optimization of factors affecting wear rate is done through Taguchi method since it is effective, simple and systematic approach. Different control variables and their levels to conduct the experiment were listed in Table 3. Here 3 factors and 3 levels were considered in this study, which counts to 9 degrees of freedom, therefore L9 orthogonal array was selected for conducting experiments and experimental design as shown in table 4.

**Table 3.** Factors and Levels in the experimental plan

| Level | SiC wt% | Load in N | Sliding Distance in m |
|---|---|---|---|
| 1 | 3 | 10 | 154 |
| 2 | 6 | 15 | 503 |
| 3 | 9 | 20 | 754 |

UDC: 546.62:546.281'261:661.183.8]:539.375
BIBLID: 1450-7188 (2023) 54, 129-136

Original scientific paper

**Table 4.** Taguchi $L_9$ experimental design for wear rate of Al 7075 hybrid composite

| Run No. | SiC wt.% | Load in N | Sliding distance in m | Specific wear rate in mm$^3$/N-m X $10^{-4}$ |
|---|---|---|---|---|
| 1 | 3 | 10 | 154 | 0.298 |
| 2 | 3 | 15 | 503 | 1.682 |
| 3 | 3 | 20 | 754 | 4.696 |
| 4 | 6 | 10 | 503 | 0.402 |
| 5 | 6 | 15 | 754 | 1.814 |
| 6 | 6 | 20 | 154 | 2.185 |
| 7 | 9 | 10 | 754 | 0.558 |
| 8 | 9 | 15 | 154 | 0.771 |
| 9 | 9 | 20 | 503 | 2.603 |

## RESULTS AND DISCUSSION

Minitab V.17.1.0 was used as a statistical tool for analysis of data collected from the experiments. Taguchi method stresses upon the importance of studying the response variable using signal-to-voice ratio. Here the term signal refers to desirable value(mean) whereas the term noise refers to undesirable value (standard deviation) for output quality characteristics. Noise can be defined as the effect of external factors on the outcome of quality characteristic under test. In this work S/N ratio for “smaller the better” is used to predict the optimum values since lesser wear rate is preferred. Here firstly mathematical relation for wear rate as a response variable was developed in terms of control variables by using regression analysis. Secondly ANOVA was carried to find the significant factors which affect the wear rate of Al 7075 hybrid composite reinforced by SiC and $Al_2O_3$. Finally optimum values for control variables were identified using Taguchi technique.

Before arriving into conclusions model adequacy needs to be ensured by checking the assumptions of ANOVA. Here one of the assumptions states that, when the distribution of residuals is normal, they follow a straight line in normal probability plot (25). Figure 1 reflects normal probability plot, where it indicates points closely aligned to the line. This ensures normal distribution is valid (25). Table 5 gives ANOVA results for wear rate of Al 7075 with SiC and $Al_2O_3$ as reinforcements. The results show that load is significant factor as its P-value is less than 0.05 (25).

**Table 5.** ANOVA results for wear rate of Al 7075 with SiC and $Al_2O_3$ as reinforcements.

| Source | DF | Adj SS | Adj MS | F-Value | P-Value |
|---|---|---|---|---|---|
| % of SiC | 1 | 0.000001 | 0.000001 | 2.74 | 0.159 |
| Load in N | 1 | 0.000010 | 0.000007 | 24.64 | 0.004 |
| Sliding distance in m | 1 | 0.000002 | 0.000010 | 3.14 | 0.137 |
| Error | 5 | 0.000002 | 0.000000 | | |

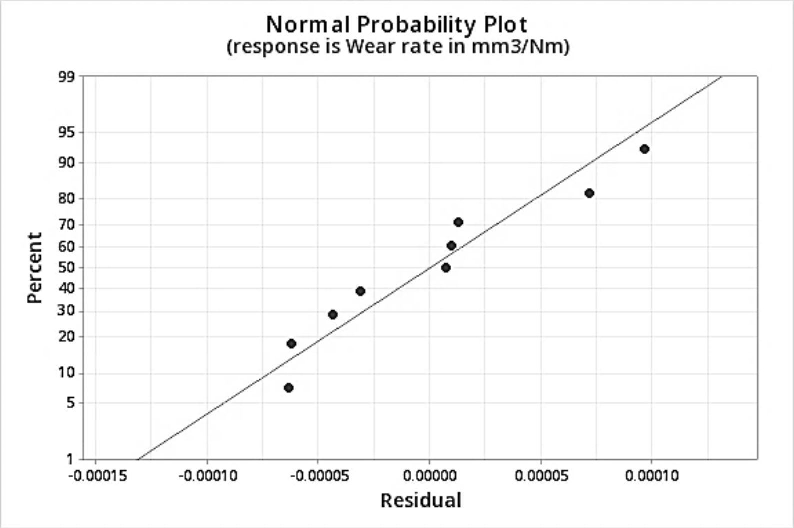

**Figure 1.** Normal probability plot of residuals

In experimentation of investigation for wear rate of Al 7075 with SiC and $Al_2O_3$ as reinforcements, load shows higher influence on wear rate of hybrid composite followed by reinforcement percentage and sliding distance. These are based on ranks given in Table 6.

**Table 6.** Response table for mean (smaller the better)

| Level | Wt % of SiC | Load | Sliding distance |
|---|---|---|---|
| 1 | 72.47 | 81.56 | 75.72 |
| 2 | 78.65 | 77.52 | 78.36 |
| 3 | 79.67 | 71.71 | 76.71 |
| Delta | 7.20 | 9.84 | 2.64 |
| Rank | 2 | 1 | 3 |

These ranks denote the amount of influence of input factor on response variable based on delta values. The delta values are the difference between highest and lowest value in the column (25). Obtained F value and P value for SiC wt.% were 3.56 and 0.11 (26) whereas in this current work F value and P value are 2.74 and 0.159 respectively. Figure 2 shows the main effects plot of SNR values for wear rate. This plot shows that least wear is observed for 6 wt.% Silicon carbide, 10N of load and 154m sliding distance.

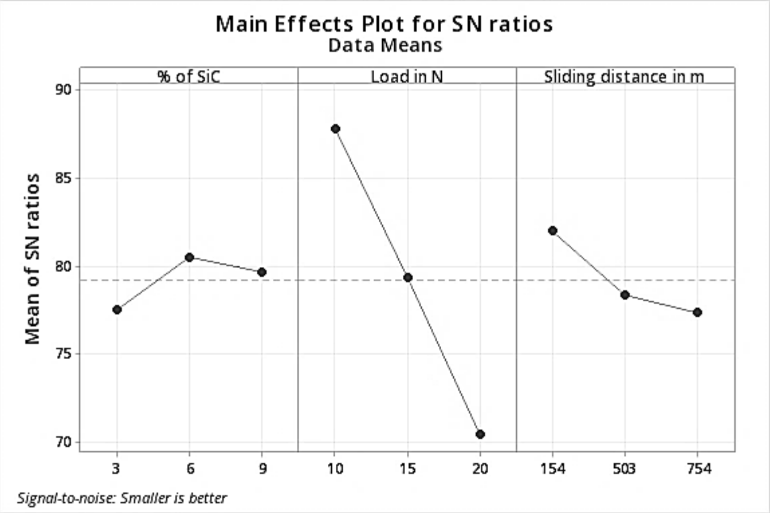

**Figure 2.** Main effects plot for SN ratios

## ANALYSIS OF WORN SURFACES:

Worn out surfaces can be seen in Figure 3. Figure 3-A shows wear specimen of Al 7075+3%SiC+5%$Al_2O_3$, here it can be seen that complete tip of the specimen has been worn out due to wear. Figure 3-B,C shows wear specimen of wear specimen of Al 7075+ 6%SiC+5%$Al_2O_3$ and wear specimen of Al 7075+9%SiC+5%$Al_2O_3$ respecitively. Here groove can be seen rather than complete wear of the tip. Less wear in both these cases is due to presence of the reinforcement, which increases the hardness which inturn increases load bearing capacity along with increase in wear resistance. Here mainly there is abrasive wear which leads to removal of material from the pin due high contact pressure.

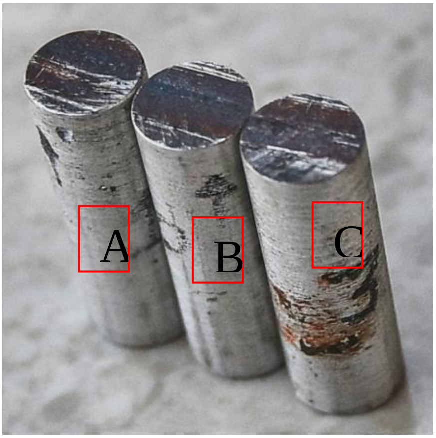

**Figure 3.** Wear specimens after Testing. A- Al 7075+3%SiC+5%$Al_2O_3$, B- Al 7075+6%SiC+5%$Al_2O_3$, C- Al 7075+9%SiC+5%$Al_2O_3$

## CONCLUSION

Wear behaviour is observed for Al 7075 reinforced with varying 3,6,9 wt.% of silicon carbide and 5 wt.% of $Al_2O_3$ fixed by conducting unlubricated wear test for 9 sets of experimentation as per L9 orthogonal array. There is abrasive wear mechanism and by looking into images of specimen pins after testing which indicates that Al 7075+3%SiC+5%$Al_2O_3$ has got higher wear with larger groove formation on the face of the pin, which not the same for Al 7075+6%SiC+5%$Al_2O_3$ and Al 7075+9%SiC+5%$Al_2O_3$ where formation of groove is comparatively smaller. The influencing parameters identified for the test were wt.% of SiC, load applied and sliding distance travelled by the pin. The output parameter was wear-rate. Based on experimentation and Taguchi optimization technique following conclusions were drawn:

i) For 6 wt.% SiC, 10N and 154m sliding distance minimum wear rate was been observed.
ii) As per ranks load is the most influential factor on wear rate followed by wt.% of SiC and sliding distance.

## REFERENCES

1. Ogundiji, O.E.; Oyatogun, G.M. Tensile and flexural properties of polyester composites reinforced by iron filings. *Tribology and Materials*. **2022**, *1*, 157-162.
2. Olawalec, O.J.; Shittuc, M.D. Effect of Heat Treatment on Some Mechanical Properties of 7075 Aluminium Alloy. *Materials Research*. **2013**, *16* (1). 190-194.
3. Pao, P.S.; Feng, C.R.; Gill, S.J. Corrosion Fatigue Crack Initiation in Aluminum Alloys 7075 and 7050. *Corrosion*, **2000**, *56* (10), NACE-00101022.
4. Suresh, S.; Harinath Gowd, G.; Deva Kumar, M. L. S. Wear behaviour of Al 7075/SiC/Mg metal matrix nano composite by liquid state process. *Advanced Composites and Hybrid Materials*. **2018**, *1*, 1-7.
5. Veeresh Kumar, G.B.; Rao, C.S.P.; Selvaraj, N. Mechanical and Dry Sliding Wear Behavior of Al7075 Alloy-Reinforced with SiC Particles. *Journal of Composite Material*. **2012**, *46*(10), 1201-1209.
6. Sridhar, A.; Prasanna Lakshmi, K. Evaluation of Mechanical and Wear Properties of Aluminum 7075 Alloy Hybrid Nanocomposites with the Additions of Sic/Graphite. *Materials Today: Proceedings*. **2021**, *44* (1), 2653–2657.
7. Vignesh Kumar V.; Raja, K.; Ramkumar, T.; Selvakumar, M.; Senthil Kumar, T.S. Studies on Mechanical Property and Wear Behaviour of AA7075 Hybrid Composites Prepared by a Conventional Casting Method. *Journal of Process Mechanical Engineering*. **2021**, *235* (6), 2180-2188.
8. Vencl, A.; Vučetić, F.; Bobić, B.; Pitel, J.; Bobić, I. Tribological characterisation in dry sliding conditions of compocasted hybrid A356/SiCp/Grp composites with graphite macroparticles. *The International Journal of Advanced Manufacturing Technology*. **2019**, *100*, 2135-2146.
9. Budapanahalli, S.H.; Mallur, S.B., Patil, A.Y., Mohamed, A.; Khan A.A.; Hussein M.A.; Asiri, A.M. A Tribological Study on the Effect of Reinforcing SiC and Al2O3 in Al7075: Applications for Spur Gears. *Metals,* **2022**, *12* (6), https://doi.org/10.3390/met12061028.
10. Girish, G.; Anandakrishnan, V. Optimization of Dry Sliding Wear Parameters of Recursive Friction Stir Processed Aluminium 7075 Alloy. *Journal of Engineering Tribology*. **2020**, *235* (6), 1222-1231, https://doi.org/10.1177/1350650120941615
11. Ekka, K. K.; Chauhan, S.R.; Varun. Study on the Sliding Wear Behaviour of Hybrid Aluminium Matrix Composites using Taguchi Design and Neural Network. *Journal of Materials: Design and Applications*. **2015**, *230* (2), 537-549. https://doi.org/10.1177/1464420715581393

12. Bai, Y.; Guo, Y.; Li, J.; Yang, Z.; Tian, J. Effect Of Al2O3 Nanoparticle Reinforcement on The Mechanical and High-Temperature Tribological Behavior of Al-7075 Alloy. *Journal of Engineering Tribology*. **2016**, *231* (7), 900-909. https://doi.org/10.1177/1350650116683627
13. Suryakumari, T.S.A.; Ranganathan, S. Preparation and Study the Wear Behaviour of Aluminium Hybrid Composite. *Materials Today: Proceedings.* **2018**, *5* (2)2, 8104–8111.
14. Daoud, A.; Abou El-Khair, M.T.; Abdel-Azim, A.N. Effect of Al2O3 Particles on the Microstructure and Sliding Wear of 7075 Al Alloy Manufactured by Squeeze Casting Method. *Journal of Materials Engineering and Performance*. **2004**, *13*(2), 135-143.
15. Bhushan, R.K., Kumar, S. Influence of SiC Particles Distribution and Their Weight Percentage on 7075 Al Alloy. *Journal of Materials Engineering and Performance*. **2011**, *20,* 317–323.
16. Al-Salihi, H.A., Mahmood, A.A.; Alalkawi, H.J. Mechanical and Wear Behavior of AA7075 Aluminum Matrix Composites Reinforced by Al2O3 nanoparticles. *Nanocomposites*. **2019**, *5* (3), 67–73.
17. Rajeswari, B.; Amirthagadeswaran, K. S.; Anbarasu, K.G. Investigation on Mechanical Properties of Aluminium 7075-Silicon Carbide-Alumina Hybrid Composite using Taguchi method. *Australian Journal of Mechanical Engineering*. **2015**, *13* (2), 127-135.
18. Suresh, S.; Harinath Gowd, G.; Devakumar, M. L. S. Corrosion Behaviour of Al 7075/Al2O3/SiC MMNCs by Weight Loss Method. *Journal of Bio- and Tribo-Corrosion*. **2018**, *4* (62). https://doi.org/10.1007/s40735-018-0182-8
19. Roy, P.; Singh, S.; Pal, K. Enhancement of Mechanical and Tribological Properties of SiC- and CB-Reinforced Aluminium 7075 Hybrid Composites Through Friction Stir Processing. *Advanced Composite Materials,* **2019**, 28 (1), 1-18. DOI: 10.1080/09243046.2017. 1405596
20. Al-Furjan, M.S.H.; Hajmohammad, M.H.; Shen, X., Rajak, D.K.; Kolahchi, R. Evaluation of tensile strength and elastic modulus of 7075-T6 aluminum alloy by adding SiC reinforcing particles using vortex casting method. *Journal of Alloys and Compounds*. **2021**, *886* (19), 161261.
21. Ande, R.; Gulati, P.; Shukla, D.K.; Dhingra, H. Microstructural and Wear Characteristics of Friction Stir Processed Al-7075/SiC Reinforced Aluminium Composite. *Materials Today: Proceedings*. **2019**, *18*, 4092–4101.
22. Pugalenthi,P.; Jayaraman, M.; Subburam, V. Study of The Microstructures and Mechanical Properties of Aluminium Hybrid Composites with SiC and Al2O3, *Materials and technology*. **2019**, *53*(1), 49-55. DOI:10.17222/mit.2018.118
23. Vencl, A.; Stojanović, B.; Gojković, R.; Klančnik, S.; Czifra, Á.; Jakimovska, K.; Harničárová, M. Enhancing of ZA-27 alloy wear characteristics by addition of small amount of SiC nanoparticles and its optimisation applying Taguchi method. *Tribology and Materials*. **2022**, *1*(3), 96-105.
24. Miloradović, N.; Vujanac, R.; Stojanović, B.; Pavlović, A. Dry sliding wear behaviour of ZA27/SiC/Gr hybrid composites with Taguchi optimization. *Composite Structures*. **2021**, *264*, 113658, https://doi.org/10.1016/j.compstruct.2021.113658
25. Shankar, B.L., Nagaraj, P.M., Anil, K C. Optimization of Wear Behaviour of AA8011-Gr Composite using Taguchi Technique. *Materials Today: Proceedings.* **2017**, *4,* 10739–10745.
26. RaviKumar, M.; Reddappa, H.N.; Suresh, R.; Gangadharappa, M. Investigation on Hardness of Al 7075/Al2O3/SiCp Hybrid Composite Using Taguchi Technique. *Materials Today: Proceedings.* **2018**, *5*, 22447–22453. DOI:10.1016/j.matpr.2018.06.614

APTEFF, Vol. 54, 1-335 (2023)
UDC: 547.565.2:665.587:634.63
DOI: https://doi.org/10.2298/APT2354137C
BIBLID: 1450-7188 (2023) 54, 137-150

Original scientific paper

# KINETIC AND ISOTHERM EVALUATION OF *O*-CRESOL ADSORPTION ON ACTIVATED CARBON PROCURED FROM OLIVE POMACE

*Salima CHOUKCHOU BRAHAM, Zoubida TALEB, Soumia DJEZIRI,*
*Hadja Mebarka DJELLOULI**

Laboratory of Materials & Catalysis, Faculty of Exact Sciences, Djillali Liabes University, BP 89, Sidi Bel Abbes, Algeria

**Received: 18 March 2023** **Revised: 02 May 2023** **Accepted: 04 May 2023**

*This article aims to apply an activated carbon on the adsorption of o-cresol in an aqueous medium. Our work presents a double environmental aspect: On one hand, a valorization of under-natural products, which is the olive pomace and on the other hand, the study of the adsorbent efficiency of the activated carbon resulting from these cores. Activated carbon is prepared with chemical activation of olive pomace using $H_3PO_4$. The characterization of this porous material has shown a specific surface area equal to 651 $m^2/g$ with the presence of mesopores. Various parameters influencing the adsorption were optimized, mainly the effect of the contact time, initial concentration of o-cresol and pH of the solution were studied. The experimental results show that the sorption equilibrium is reached within 60 min with an adsorption yields of 83.66%. Indeed, the experimental adsorbed quantity of adsorbent is 3.82 mg/g with o-cresol concentration of 50 mg/L, T = 30 °C and pH 2.6 for the better adsorption.*

*The adsorption process was also studied by examining Langmuir, Freundlich, Temkin isotherm, and Dubinin–Radushkevich (D-R) isotherm models. The results revealed that the adsorption system followed the pseudo-second order model and the Freundlich model. Several thermodynamic factors, namely, the standard free energy ($\Delta G_{ads}$), enthalpy ($\Delta H_{ads}$), and entropy ($\Delta S_{ads}$) changes, were also calculated. The results demonstrated that the adsorption process is a physical and endothermic. The obtained results are interesting, and applications on other pollutants, in wastewater are in progress.*

**Keywords**: *o*-Cresol, Olive Pomace, Removal, Activated carbon, Isotherm.

## INTRODUCTION

The adsorption process with low cost natural minerals is an attractive option because of their efficient removal rate for organic pollutants at even trace levels. Well-designed adsorption processes provide high-quality effluent after treatment. In recent years, considerable attention has been focused on the utilization of pomace such as from deoiled red raspberry pomace (1), cranberry pomace (2) and apple pomace (3-6). Also, the grape pomace mainly composed of seeds, skins and stalks, all containing high amounts of valuable phytochemicals, is the main solid residue of wine industry and is also used (7). In the other hand, olive production is one of the important human activities through the transformation of olive into olive oil and olive table. The olive oil production in Mediterranean countries is more than 94% of world olive oil production (8, 9). Olive dry cake olive pomace also

---

* Corresponding author: Hadja Mebarka DJELLOULI, Laboratory of Materials & Catalysis, Djilali Liabes University, Faculty of Exact Sciences, Djillali Liabes University, BP 89, Sidi Bel Abbs, Algeria.
e-mail: mebarkad@yahoo.fr

referred to as olive pomace is generated from the extraction of olive oil. Olive pomace contains, in addition to its content, fruit components such as crushed olive stone pieces, olive pulp with residual oil, and 65% water from olive oil extraction (10, 11). Nieto et al. (12) studied the adsorption of Fe by olive stones in agricultural wastewaters. The percentage of iron adsorption increased from 30 to 70% when the initial biomass concentration rose from 25 to 125 g dm$^{-3}$. Bohli et al. (13) examined adsorption of phenol on a prepared activated carbon activated chemically (by $H_3PO_4$). Authors tested effect of pH, initial concentration ($C_0$: 25-300 mg/L) and equilibrium time. The results show that activated carbon from olive stone can be used for adsorption of phenol from aqueous solution.

Cresol compounds are substituted phenols which are generated by petroleum and petrochemical, coal conversion, cresols producing industries, and other chemical processes, are common contaminants in wastewater. Cresols are widely used for the commercial production of a wide variety of resins including phenolic resins, which are used as construction materials for epoxy resins and adhesives. Cresols as a class of organics that are resistant to biodegradation. Cresols are previously eliminated from wastewaters using different methods such as adsorption, chemical precipitation, ozonation, ion exchange, filtration, membrane separation, and reverse osmosis (14, 15). Gracioso et al. studied removal of phenolic *o*-cresol from raw industrial wastewater containing a mixture of phenols, *m*-cresol, *o*-cresol, 90% biodegradation was achieved after 80 h of inoculation (16).

The aims of this work were as follows: first, to study the *o*-cresol adsorption kinetics on activated carbon from olive pomace; second, to assess the initial *o*-cresol concentration and adsorbent amount effect on matter transfer rate. Eventually, to find a simple mathematical model suitable for a better understanding of the physical phenomena involved in a more appropriate design, operation, optimization, and control of the industrial process separation. Simplified isotherm models are tested to describe the adsorption process. Kinetics are determined using different models and then correlated with the experimental variables.

## EXPERIMENTAL

### ACTIVATED CARBON

Activated carbon (AC) was prepared from olive pomace by chemical activation with orthophosphoric acid ($H_3PO_4$) according to the method developed by Gharib and *al.* (17): Initially, the precursor was washed thoroughly with hot water, dried and then impregnated with a dilute phosphoric acid solution for 6 hours at 110 °C. The resulting material was washed with distilled water to remove all leachable impurities. The dried solid was carbonized in a muffle furnace (NaberTherm B180). The optimized carbonization time and temperature were 1 h and 600 °C, respectively. The producer of carbon was washed with distilled water and then dried to be ready for use.

Specific surface area of prepared activated carbon was determined by nitrogen adsorption and desorption isotherms at 77.7 K with an automatic Sorptiometer Autosorbe-1C Quantachrome apparatus. The specific surface area and pore volumes were calculated by applying Brunauer-Emmett-Teller (BET) analysis method. The point of zero charge ($pH_{PZC}$), pH at which the adsorbent is neutral in aqueous suspension, was determined following the procedure of Altenor (18) et al. In this method, 50 mL of 0.01M NaCl solution was filled in closed

Erlenmeyer flasks at room temperature. Then, the pH of the solutions was modified to values from 2 and 12 by adding 0.1M HCl or 0.1M NaOH solutions. These pHs were mentioned as the initial pH ($pH_{initial}$). Finaly, 0.1g of solid adsorbent (AC) was added to each flask and the final pH ($pH_{final}$) was measured after 24 h. The $pH_{final}$ was plotted against the $pH_{initial}$ and the $pH_{PZC}$ is the point where the curve $pH_{final}$ versus $pH_{initial}$ intersects the first bisector.

### *O*-CRESOL

Analytical-reagent grade *o*-cresol (purity > 99%), was used as the adsorbate. A stock solution was prepared by dissolving required amount of o-Cresol in double distilled water. Different initial concentrations ($C_0$) of *o*-cresol, in the range of 25-100 mg/L, were obtained by successive dilutions. *o*-Cresol concentration was determined by UV absorption at 270 nm wave-length using a calibrated UV-Visible Perkin Elmer spectrophotometer.

### ADSORPTION EXPERIMENTAL PROCEDURE

Adsorption process was performed as a function of contact time, pH, initial concentrations of the *o*-cresol and temperature using an AC adsorbent amount of 1g and adsorbate volume of 100 mL (0.1 L) of *o*-cresol determined concentrations (cited in the previous paragraph). The contact time between solid–liquid were from 0 to 120 min; pH was varied from 2 to 12 and the temperature from 20 to 80 °C. The removal yield (%) and the of equilibrium adsorption $q_e$ (mg/g) were calculated from the following Equations 1 and 2, respectively:

$$\text{Yield (\%)} = \frac{(C_i - C_{eq})}{C_i} \times 100 \qquad [1]$$

$$q_e\ (\text{mg/g}) = \frac{X}{m} = \frac{(C_i - C_{eq})}{m} \times V \qquad [2]$$

where $C_i$ is the initial concentration (mol/L) and $C_{eq}$ is the equilibrium concentration (mol/L). V is the volume of the solution (L), m is the mass of adsorbent (g) and X is mass of *o*-cresol adsorbed (mg).

### KINETICS STUDY

In order to understand the mechanism and dynamism of adsorption, five kinetic models have been chosen pseudo, first-order (Equation 3), pseudo second-order (Equation 4) and Elovich (Equation 5) (19). In addition, intra-particle diffusion (Equation 6) (20) and external diffusion (Equation 7) (21) were studied, too:

$$ln\left(q_e - q_t\right) = ln\, q_e - K_1 \cdot t \qquad [3]$$

$$\frac{1}{(q_e - q_t)} = \frac{1}{q_e} + K_2 \cdot t \qquad [4]$$

where, $K_1$ ($min^{-1}$) is pseudo-first-order kinetic constant, and $K_2$ represents pseudo-second-order kinetic constant.

$$q_t = \frac{\ln(\alpha_E \times \beta_E)}{\beta_E} + \frac{1}{\beta_E} \cdot \ln t \qquad [5]$$

where $\beta_E$ (g/mg) parameter related to the extent of surface coverage and activation energy, and $\alpha_E$ (mg/g.min) represents initial adsorption rate.

$$q_t = K_i\, t^{\frac{1}{2}} \qquad [6]$$

where $q_t$ is amount of adsorbate on the surface of the adsorbent at time $t$, mg/g; $K_i$ is the intra-particle rate constant, mg/(g·min$^{1/2}$).

$$\ln\left(\frac{C_o - C_e}{C_t - C_e}\right) = k\left(\frac{a}{V}\right)t = k' t \qquad [7]$$

$k'$ is the external rate constant (min$^{-1}$) and $a$ is the solid/liquid interface area.

## ISOTHERM STUDY

Adsorption isotherms have an important role in the determination of adsorbent capacity. The obtained results of the influence of the initial *o*-cresol concentration on AC adsorption during this study were used to draw them. There are many theoretical models that have been developed to describe adsorption isotherms. However, the models of Freundlich (Equation 8) and also of Langmuir (Equation 9), Elovich (Equation 10) and Temkin (Equation 11) (19), Dubinin Radushkevich (Equation 12) (22), Kiselev (Equation 13) (23) and Fowler Guggenheim (Equation 14) (24) allowed to deduce the main parameters characterizing each model as shown below:

$$\log(q_e) = \log(K_F) + n \log(C_e) \qquad [8]$$

where $K_F$ (mg/L) and n are Freundlich constants related to the adsorption capacity and adsorption intensity, respectively.

$$\frac{1}{q_e} = \frac{1}{C_e}\frac{1}{q_m K_L} + \frac{1}{q_m} \qquad [9]$$

$K_L$ (L/mg) is Langmuir constant and $q_m$ theoretical maximum adsorption capacity (mg/g).

$$\ln\frac{q_e}{C_e} = \ln(q_m K_E) - \frac{q_e}{q_m} \qquad [10]$$

$K_E$ (L/mg) is the Elovich constant.

$$q_e = B_T \ln K_T + B_T \ln C_e \qquad [11]$$

where $K_T$ (L/mg) is Temkin constant, $T$ (K) is temperature and $B_T$ (J/mol) is related to the activation energy.

$$\ln(qe) = \ln(q_{mDR}) - K_D\, \varepsilon^2 \qquad [12]$$

where $K_D$ is is Dubinin-Radushkevich constant, ε (kJ.kmol$^{-1}$) is potential of Polanyi $= RTln(1+\frac{1}{C_e})$; $R$ is the universal gas constant (8.314 J/mol.K) and E is mean adsorption energy $E = \frac{1}{\sqrt{K_D}}$.

$$\frac{1}{C_e(1-\theta)} = \frac{K_1}{\theta} + K_i K_n \qquad [13]$$

where $K_i$ is Kiselev equilibrium constant (L/mg) and $K_n$ is equilibrium constant of the formation of complex between adsorbed molecules, $\theta$ the fractional coverage.

$$ln\left(\frac{C_e(1-\theta)}{\theta}\right) = -lnK_{FG} + \frac{2W\theta}{RT} \qquad [14]$$

where $K_{FG}$ is the Fowler–Guggenheim equilibrium constant (L/mg) and $W$ (kJ mol$^{-1}$) is the interaction energy between adsorbed molecules.

## THERMODYNAMIC STUDY

Thermodynamic properties such as standard enthalpy ($\Delta H_{ads}$), entropy ($\Delta S_{ads}$) and Gibbs free energy ($\Delta G_{ads}$) are essential for the study of any adsorption system. These properties determine the nature of adsorption and spontaneity. These thermodynamic parameters of adsorption were carried out at four different temperatures: 25, 45, 60, 80 °C and were calculated using the following equations (19, 24):

$$ln\, K_P = \frac{\Delta S_{ads}}{R} - \frac{\Delta H_{ads}}{RT} \qquad [15]$$

$$\Delta G = \Delta H_{ads} - T\,\Delta S_{ads} \qquad [16]$$

The apparent equilibrium constant ($K_d$) of adsorption is defined as:

$$K_d = \frac{C_{ads}}{C_{eq}} \qquad [17]$$

where, $K_P$ is the thermodynamic equilibrium constant and it is the ratio of concentration of adsorbate in the solid and liquid phases. $\Delta H_{ads}$ and $\Delta S_{ads}$ were derived from the slope and intercept of the linear plot (i.e., Van't Hoff plot) of $lnKp$ versus $1/T$, respectively.

## RESULTS AND DISCUSSION

### CHARACTERIZATION OF ADSORBENT

The adsorption/desorption curve of the AC prepared from olive pomace (Figure 1a) shows a hysteresis for which desorption branch joins the adsorption branch for a relative pressure equal to 0.42 at 77 K. This hysteresis is significant of the presence of constituent mesopores of a stable structure (type IV isotherm) (25). In addition, the obtained results show that the AC has a surface area equal to 651 m$^2$/g, a pore volume of 0.280385 cm$^3$/g.

A large specific surface area permits high adsorption. The pHpzc is an important parameter based on the determination of the range of pH sensibility and allows the active surface and adsorption capacities to be predicted (26). The pHpzc value of AC found was equal to 3.01 (Figure 1b).

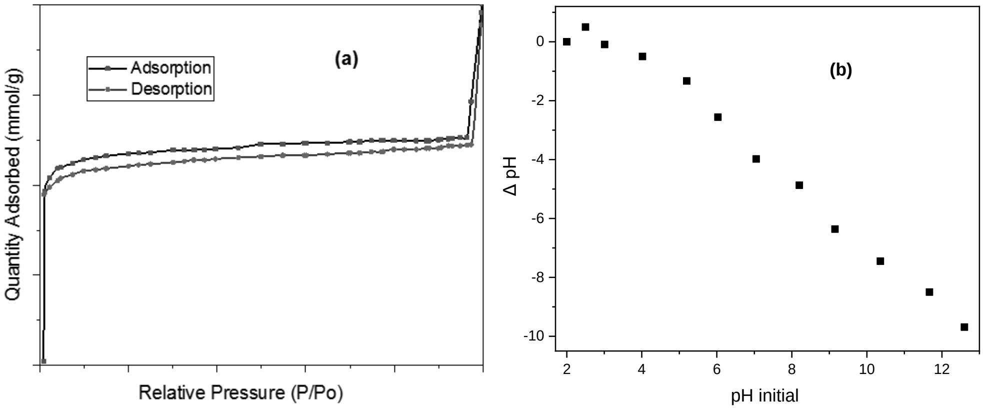

**Figure 1.** $N_2$ adsorption-desorption isotherm of AC (a) and the pH point of zero charge ($pH_{pzc}$) (b)

## ADSORPTION STUDIES

### Effect of adsorbent amount

To investigate the effect of the adsorbent dose on the efficiency of the adsorption process, a series of experiments were conducted with various adsorbent amounts of AC from 0.25 to 3 g in 100 mL of 50 mg/L *o*-cresol solution.

The effect of adsorption amount on adsorption is shown in Figure 2.

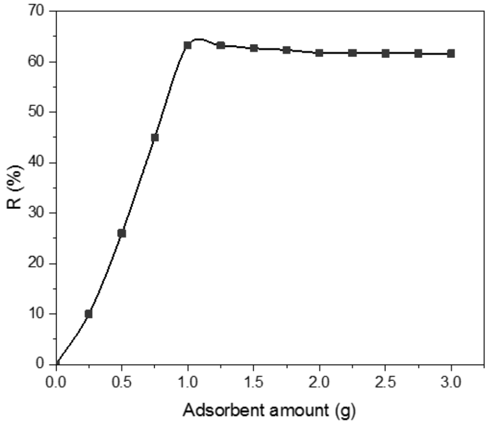

**Figure 2.** Effect of adsorbent amount on *o*-cresol adsorption (pH = 6.8, Time = 120 min, T = 25 °C and $C_i$ = 50 mg/L)

As the mass of the adsorbent increased, the adsorption yields also increased to 63.25%. This is due to the presence of more active sites on the surface (27). The maximum adsorption efficiency of *o*-cresol was achieved with 1 g of AC. In addition, it is clear that an increase in the adsorbent mass above 1 g saturates the surface of the AC adsorbent and stops the adsorption phenomenon. In this case, it can be said that the adsorption equilibrium of *o*-cresol on AC is reached.

## Effect of initial pH on the adsorption

The pH of the solution is one of the most important parameters affecting adsorption processes because it affects the surface charge of the adsorbent, the degree of ionization and speciation of the pollutants (28). The effect of initial pH on adsorption of *o*-cresol was studied with 50 mg/L initial concentration and 1 g optimum AC amount.

Figure 3 shows the influence of solution pH on *o*-cresol removal by AC in the pH range of 2 to 12. The *o*-cresol adsorption decreases with the increase of pH. The maximum *o*-cresol removal obtained at pH lower than $pH_{pzc}$ ($pH_{pzc}$=3.01) can be explained by the fact that at this pH range the AC surface is charged positively and *o*-cresol was protonated (29). This creates a strong electrostatic interaction between *o*-cresol molecule carbon surface. However, with the increase of pH solution up to pHpzc, *o*-cresol becomes more dissociated and AC surface is charged negatively leading to increased electrostatic repulsion force between the anionic *o*-cresol form and $OH^-$ groups on AC surface and between phenolate-phenolate anions in solution (30) resulting in a decrease of *o*-cresol adsorption yields. Taking into account the obtained results, the rest of experiments were carried out at pH 2.6.

## Effect of contact time and initial concentration

The effect of *o*-cresol initial concentration on the adsorption yield is reported in Figure 4. When initial *o*-cresol concentration increased from 25 to 100 mg/L, the adsorption yields on AC increased from 19.33 to 75.15%. The time evolution of the amount adsorbed *o*-cresol indicates that the equilibrium time was reached at about 60 min for all the initial concentrations. Two kinetics regions were observed: the first one is characterized by a high adsorption rate due to the high initial number of free sites in activated carbon available and the driving force for the mass transfer is greater. Therefore, *o*-cresol reaches easily the adsorption sites of AC. As time progresses, the number of free sites in AC decreases and the non-adsorbate molecules are assembled at the surface thus limiting the capacity of adsorption. The increase of loading capacities of AC with increasing *o*-cresol concentration is may be due to the higher π-π interaction between *o*-cresol and the surface function of activated carbon. The π-π interaction is usually the mean involved mechanism of *o*-cresol adsorption (31, 32).

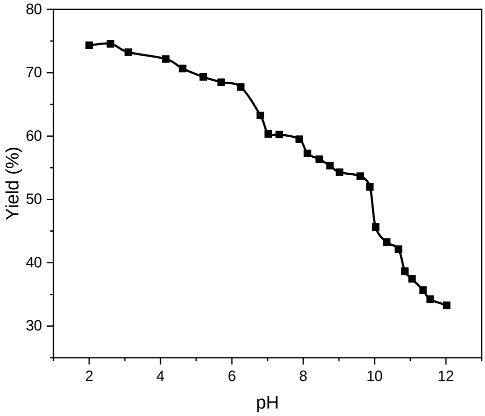

**Figure 3.** Effect of pH on *o*-cresol adsorption (m = 1 g, Time = 120 min, T = 25 °C and $C_i$ = 50 mg/L)

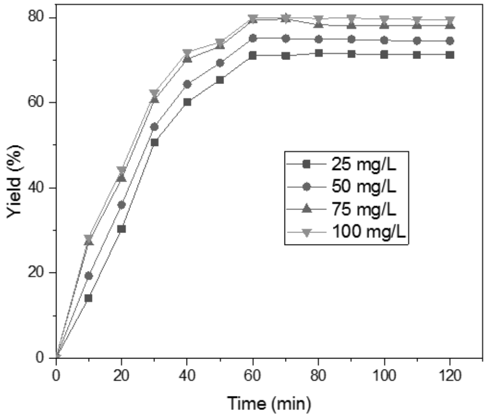

**Figure 4.** Effect of initial concentration *o*-cresol adsorption

## Effect of the temperature

The temperature effect on adsorption of *o*-cresol on AC was examined at a range from 20 °C to 80 °C and shown in Figure 5. The yield of adsorbed *o*-cresol increased until it reaches the maximum adsorption of 83.66% at 30 °C. Then, yield of *o*-cresol adsorption decreased gradually with the increase in temperature. This can be attributed to the possible damage of adsorption sites at elevated temperatures.

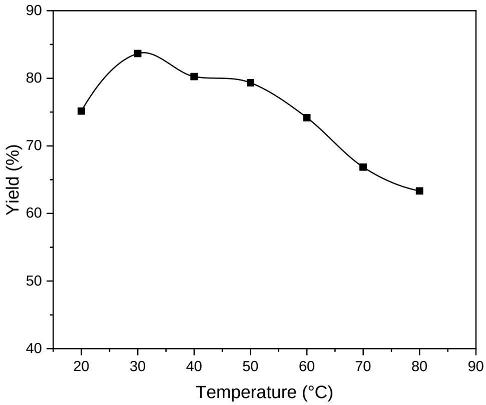

**Figure 5.** Effect of the temperature on the *o*-cresol adsorption

## KINETIC STUDY

Adsorption *o*-cresol kinetics on AC was studied by fitting experimental data. The obtained parameters, the experimental adsorbed quantity ($q_e$) and correlation coefficients were calculated from the equations cited previously (See section 2.4) and regrouped in Table 1.

**Table 1.** Parameters and correlation coefficients of adsorption kinetic models applied to experimental data of o-Cresol adsorption on AC

| **Kinetic models** | **Constants** | **Results** |
|---|---|---|
| Pseudo first-order | $K_1$ (min$^{-1}$)<br>$q_e$ (mg.g$^{-1}$)<br>$R^2$ | 0.045<br>3.420<br>0.830 |
| Pseudo second-order | $K_2$ (min$^{-1}$)<br>$q_e$(mg.g$^{-1}$)<br>$R^2$ | 0.028<br>4.040<br>0.995 |
| Elovich | $\alpha_E$(mg.g$^{-1}$.min)<br>$\beta_E$ (g/mg.min$^{-1}$).<br>$R^2$ | 3.460<br>0.614<br>0.922 |
| Intra-particle diffusion | $K_i$ (mg/(g·min$^{1/2}$))<br>$R^2$ | 0.366<br>0.821 |
| External diffusion | $K_f$ (min$^{-1}$)<br>$R^2$ | 0.011<br>0.632 |

According to these values, the pseudo second order and Elovich models present very significant regression coefficient values ($R^2 > 0.90$), but the pseudo-second order model presents a correlation coefficient value the highest ($R^2 = 0.995$). It can therefore deduce that the pseudo-second order model is the best model describes the adsorption process of *o*-cresol on the prepared activated carbon. Also, the value of the quantity adsorbed calculated by the kinetic model of pseudo-second order 4.04 mg/g is very close to the value of experimental quantity adsorbed (3.82 mg/g).

## ISOTHERM STUDY

The values of the calculated constants of isotherms are shown in Table 2. From these modeling results, it can be observed that most of the linear models represent well the adsorption isotherms of *o*-cresol on the prepared AC with non-negligible correlation coefficients. The values of the regression coefficients indicate that the adsorption process of *o*-cresol is described in a favorable way by the Freundlich isotherm with excellent linear regression coefficients ($R^2$ = 0.996) which is very close to unity.

**Table 2.** Parameters and correlation coefficients of isotherms models applied to experimental data of o-Cresol adsorption on AC

| Isotherm models | Constants | Results |
|---|---|---|
| Freundlich | $K_F$ (mg.g$^{-1}$) (L.mg$^{-1}$)<br>n<br>$R^2$ | 0.090<br>1.510<br>0.996 |
| Langmuir | $K_L$(L.mg$^{-1}$)<br>$q_m$(mg.g$^{-1}$)<br>$R^2$ | 0.023<br>8.400<br>0.974 |
| Elovich | $q_m$ (mg.g$^{-1}$)<br>$k_E$ (L.mg$^{-1}$)<br>$R^2$ | 12.500<br>0.017<br>0.929 |
| Temkin | $B_T$ (Kj.mol$^{-1}$)<br>$K_T$ (L.mol$^{-1}$)<br>$R^2$ | -10.490<br>0.174<br>0.943 |
| Dubinin Radushkevich | $K_D$ (mol.j$^2$)<br>$R^2$ | 6.10$^{-5}$<br>0.796 |
| Kiselev | $K_1$ (L.mg$^{-1}$)<br>$K_n$ (L.mg$^{-1}$)<br>$R^2$ | -0.022<br>-10.810<br>0.500 |
| Fowler Guggenheim | $K_{FG}$ (L.mg$^{-1}$)<br>W (Kj.mol$^{-1}$)<br>$R^2$ | 0.020<br>-3702<br>0.990 |

In addition, the value of *n* (Freundlich constant) is greater than 1, it means that the adsorption is favorable (the intensity of the adsorption is high) with the formation of strong bonds between the adsorbate and the adsorbent in the studied temperature range. The adsorption is an endothermic process; it can be explained by the increase of the temperature with the value of $K_F$ (33). Indeed, the value of the regression coefficient shows that the Fowler Guggenheim model ($R^2$=0.99) is adequate for a good description of this adsorption of o-Cresol on the prepared AC. The regression coefficients were not satisfactory for the isotherm of Elovich, Kiselev and Dubinin Radushkevich, so they do not model the isotherm of adsorption of o-Cresol on activated carbon.

## THERMODYNAMIC STUDY

The thermodynamic parameters: free energy ($\Delta G_{ads}$), enthalpy ($\Delta H_{ads}$) and entropy ($\Delta S_{ads}$) are regrouped in Table 3. The enthalpy ($\Delta H_{ads}$) is positive, which implies that the adsorption process is endothermic. It is also noticed that $\Delta G_{ads}$ increases with the increase in the temperature of the solution. The result can be explained by the fact that adsorption becomes very difficult and disadvantaged when the temperature becomes very high (33). Positive values of $\Delta G_{ads}$ and its increase with temperature indicate an increase in disorder during adsorption, the randomness increases at the solid-solution interface during this fixation process. This can be explained by the redistribution of energy between the adsorbent and the adsorbate. The *o*-cresol adsorption process is a physical adsorption type when the $\Delta G_{ads}$ values are less than 40 KJ/mol. The negative value of $\Delta S_{ads}$ shows that the adsorption takes place with an increase in the order at the solid-solution interface.

**Table 3.** Thermodynamic parameters of o-Cresol adsorption on AC

| **Parameters** | **T (K)** | **$\Delta G_{ads}$ (KJ/mol)** | **$\Delta H_{ads}$ (KJ/mol)** | **$\Delta S_{ads}$ (J/mol)** |
|---|---|---|---|---|
| Results | 293 | 2.204 | 16.279 | -60.240 |
| | 301 | 1.675 | | |
| | 312 | 2.489 | | |
| | 333 | 3.763 | | |
| | 333 | 3.874 | | |
| | 345 | 4.587 | | |
| | 357 | 5.192 | | |

## CONCLUSION

In this study, the removal of *o*-cresol from aqueous solution by adsorption on olive pomace activated carbon (AC) was developed. This is in order to protect the environment by using the waste from olive oils production (olive pomace) in the elimination of another type of industrial waste (*o*-cresol, a toxic phenolic derivative). The characterization of the activated carbon prepared with chemical activation from olive pomace showed a specific surface area equal to 651 $m^2/g$ with the presence of mesopores.

The obtained results show that the equilibrium of sorption is reached within 60 min with a removal yield of 83.66%. Indeed, the experimental adsorbed quantity of adsorbent is 3.82 mg/g with *o*-cresol concentration of 50 mg/L, T = 30 °C and pH 2.6 for a good adsorption. Some kinetics, isotherms and thermodynamics adsorption studies were investigated: The kinetics of *o*-cresol adsorption on AC follows the pseudo-second order model and fitted the

Freundlich model. The results demonstrated that the adsorption is a physical and endothermic process.

In the end, prepared AC from olive pomace is a promising material for *o*-cresol elimination and may also be effective in removing other pollutants.

## Acknowledgements

The Algerian Directorate General of Scientific Research and Technological Development (DGRSDT), and the Algerian Ministry of Higher Education and Scientific Research (MESRS) are greatly thanked.

## REFERENCES

1. Li, M.; Liu, Y.; Yang, G.; Sun, L.; Song, X.; Chen, Q.; Bao, Y.; Luo T.; Wang, J. Microstructure, physicochemical properties, and adsorption capacity of deoiled red raspberry pomace and its total dietary fiber, LWT, **2022**, *153*, 112478. Doi: 10.1016/j.lwt.2021.112478
2. Gao, C.; Zhao, S.; Yagiz, Y.; Gu, L. Static, Kinetic, and Isotherm Adsorption Performances of Macroporous Adsorbent Resins for Recovery and Enrichment of Bioactive Procyanidins from Cranberry Pomace. *Journal of food Sci*. **2018**, *83*(5), 1249-1257. Doi: 10.1111/1750-3841.14142
3. Chand, P.; Pakade, Y.B. Synthesis and characterization of hydroxyapatite nanoparticles impregnated on apple pomace to enhanced adsorption of Pb (II), Cd (II), and Ni (II) ions from aqueous solution. *Environ. Sci. Pollut Res*. **2015**, *22*(14), 10919-10929. Doi: 10.1007/s11356-015-4276-2
4. Wu, L.; Melton, L.D.; Sanguansri L.; Augustin, M. A. The batch adsorption of the epigallocatechin gallate onto apple pomace. *Food chemistry*. **2014**, *160*, 260-265. Doi: 10.1016/j.foodchem.2014.03.098
5. Wu, L.Y. ; Guo, Y.L.; Cao, L.L.; Jin, S.; Lin, H.Z.; Wu, M.Y.; Lin J.K.; Ye, J.H. Application of NaOH-HCl-Modified Apple Pomace to Binding Epigallocatechin Gallate. *Food Bioprocess Technol*. **2016**, *9*, 917-923. Doi: 10.1007/s11947-016-1683-4
6. Singh, R.J.; Martin, C.E.; Barr D.; Rosengren, R.J. Immobilised apple peel bead biosorbent for the simultaneous removal of heavy metals from cocktail solution. *Cogent Environ Sci*. **2019**, *5*, 1673116. Doi: 10.1080/23311843.2019.1673116
7. Perra, M.; Bacchetta, G.; Muntoni, A.; De Gioannis, G.; Castangia, I.; Rajha, H.N.; Manca, M. L.; Manconi, M. J. An outlook on modern and sustainable approaches to the management of grape pomace by integrating green processes, biotechnologies and advanced biomedical approaches. *Funct. Foods.* **2022**, *98*, 105276. Doi: 10.1016/j.jff.2022.105276
8. Sbai, G.; Loukli, M. Traitement Electrochimique Des Margines Et Identification Des Composes Avant Et Apres Traitement Par Chromatographie En Phase Gazeuse Couplee Par Spectroscopie De Masse. *Larhyss Journal*. **2015**, *22*, 139-152.
9. Bekri, I.; Taleb, Z.; Taleb, S.; Tlemsani, S.; Hodaifa, G.; Abdelkader, B. High adsorption capacity of thermally treated solid olive wastes to treat olive mill wastewater. *Environ Qual Manage.* **2022**, *31*(4), 391-402. Doi: 10.1002/tqem.21823
10. Marrakchi, F.; Bouaziz, M.; Hameedc, B.H. Adsorption of acid blue 29 and methylene blue on mesoporous $K_2CO_3$-activated olive pomace boiler ash. *Colloids and Surfaces A*. **2017**, *535*, 157-165. http://dx.doi.org/10.1016/j.colsurfa.2017.09.014
11. Alburquerque, J.A.; Gonzálvez, J.; Garcıá, D.; Cegarra, J. Agrochemical characterisation of alperujo, a solid by-product of the two-phase centrifugation method for olive oil extraction. *Bioresour. Technol.* **2004**, *91*, 195-200.
12. Nieto, L.M.; Alami, S.B.D.; Hodaifa, G.; Faur, C.; Rodriguez, S.; Gimenez, J.A.; Ochando, J. Adsorption of iron on crude olive stones. *Ind Crops Prod.* **2010**, *32*(3), 467-471.

UDC: 547.565.2:665.587:634.63
BIBLID: 1450-7188 (2023) 54, 137-150

Original scientific paper

13. Bohli, T.; Ouederni, A.; Fiol, N.; Villaescusa, I. Evaluation of an activated carbon from olive stones used as an adsorbent for heavy metal removal from aqueous phases. *C. R. Chimie*. **2015**, *18*(1), 88-99. http://dx.doi.org/10.1016/j.crci.2014.05.009
14. Kandah, M.I.; Meunier, J.-L. Removal of Nickel Ions from Water by Multi-Walled Carbon Nanotubes. *Journal of Hazardous Materials*. **2007**, *146*, 283-288.
15. Taleb, Z.; Ramdani, A.; Berenguer, R.; Ramdani, N.; Adjir, M.; Taleb, S.; Morallón, E.; Nemmich S.;Tilmatine, A. Combined ozonation process and adsorption onto bentonite natural adsorbent for the o-cresol elimination. *Int. J. Environ. Anal. Chem.* **2021**, *103*(5), 977-994. Doi: 10.1080/03067319.2020.1865335
16. Gracioso, L. H.; Vieira, P. B.; Baltazar, M. P. G.; Avanzi, I. R.; Karolski, B.; Nascimento, C. A. O.; Perpetuo, E. A. Removal of phenolic compounds from raw industrial wastewater by Achromobacter sp. isolated from a hydrocarboncontaminated area. *Wat. and Environ. J.* **2019**, *33*(1), 40-50. Doi: 10.1111/wej.12367
17. Gharib, H.; Ouederni, A. Transformation du grignon d’olive Tunisien en charbon actif par voie chimique à l’acide phosphorique- Processing olive pomace Tunisian activated carbon chemically with phosphoric acid. Recent Advances in Process Engineering, SFGP, Paris, France, 2005, 92.
18. Altenor, S.; Carene, B.; Emmanuel, E.; Lambert, J.; Ehrhardt, J. J. and Gaspard, S. Adsorption studies of methylene blue and phenol onto vetiver roots activated carbon prepared by chemical activation. *J. Hazard. Mater.* **2009**, *165*, 1029. Doi: 10.1016/j.jhazmat.2008.10.133
19. Tlemsani, S.; Taleb, Z.; Piraúlt-Roy L. and Taleb, S. Temperature and pH influence on Diuron Adsorption by Algerian Mont-Na Clay. *Int. J. Environ. Anal. Chem.* **2022**. Doi: 10.1080/03067319.2022.2060093
20. Soenmezay, A.; Öncel, M.S.; Bektaş, N. Adsorption of lead and cadmium ions from aqueous solutions using manganoxide minerals, *Trans. Nonferrous Met. Soc. China*. **2012**, *22*(12), 3131-3139. Doi: 10.1016/S1003-6326(12)61765-8
21. Belaid, K.; Kacha, S. Study of the kinetics and thermodynamics of the adsorption of a basic dye on sawdust. *J. Wat Sci.* **2011**, *24*(2), 131-144.
22. Ayawei, N.; Ebelegi, A.N.; Wankasi, D. Modelling and Interpretation of Adsorption Isotherms. *J. chem.*, **2017**. 3039817. Doi: 10.1155/2017/3039817
23. Hamdaoui O.; Naffrechoux, E. Modeling of adsorption isotherms of phenol and chlorophenols onto granular activated carbon Part I. Two-parameter models and equations allowing determination of thermodynamic parameters *J. Hazard. Mater.* **2007**, *147*, 381-394. Doi: 10.1016/j.jhazmat.2007.01.021
24. Lu, M.; Zhang, Y. M.; Guan, X. H.; Xu, X. H.; Gao, T. T. Thermodynamics and kinetics of adsorption for heavy metal ions from aqueous solutions onto surface amino-bacterial cellulose. *Trans. Nonferrous Met. Soc. China*. **2014**, *24,* 1912-1917. Doi: 10.1016/S1003-6326(14)63271-4
25. Thommes, M.; Kaneko, K.; Neimark, A.V.; Olivier, J.P.; Rodriguez-Reinoso, F.; Rouquerol, J.; Sing, K.S. Physisorption of gases, with special reference to the evaluation of surface area and pore size distribution (IUPAC Technical Report). *Pure Appl. Chem.* **2015**, *87*(9-10), 1051-1069. Doi: 10.1515/pac-2014-1117
26. Pintor, M.J.; Jean-Marius, C.; Jeanne-Rose, V.; Taberna, P.L.; Simon, P.; Gamby, J.; Gadiou, R.; Gaspard, S. Preparation of activated carbon from Turbinaria turbinata seaweeds and its use as supercapacitor electrode materials. *C. R. Chimie*. **2013**, *16*, 73-79.
27. Boudia, R.; Mimanne, G.; Benhabib, K.; Pirault-Roy, L. Preparation of mesoporous activated carbon from date stones for the adsorption of bemacid red. *Water Sci. Technol.* **2019**, *79*(7), 1357-1366. Doi: 10.2166/wst.2019.135 28.
28. Maleki, A.; Mahvi, A.H.; Ebrahimi, R.; Khan, J. Evolution of Barley straw and its Ash in Removal of Phenol from Aqueous System. *Word Appl. Sci. J.* **2010**, *8*(3), 369-373.
29. Lü, G.; Hao, J.; Liu, L.; Ma, H.; Fang, Q.; Wu, L.; Wei, M.; Zhang, Y. The Adsorption of Phenol by Lignite Activated Carbon. *Chin. J. Chem. Eng.* **2011**, *19*(3), 380-385.

30. Mareno-Castilla, C. Adsorption of organic molecules from aqueous solutions on carbon materials. *Carbon*. **2004**, *42*, 83-94.
31. Li, D.; Wu, Y.; Feng, L.; Zhang, L. Surface properties of SAC and its adsorption mechanisms for phenol and nitrobenzene. *Bioresour. Technol.* **2012**, *113*, 121-126. Doi: 10.1016/j.biortech.2012.02.130
32. Li, Y.; Du, Q.; Liu, T.; Peng, X.; Wang, J.; Sun, J.; Wang, Y.; Wu, S.; Wang, Z.; Xia Y.; Xia, L. Comparative study of methylene blue dye adsorption onto activated carbon, graphene oxide, and carbon nanotubes. *Chem. Eng. Res. Des*. **2013**, *91*(2), 361-368. Doi: doi.org/10.1016/j.cherd.2012.07.007
33. He, J. Hong, S. Zhang, L. Gan F.; Ho, Y.S. Equilibrium and thermodynamic parameters of adsorption of methylene blue onto rectorite. *Fresenius Environ. Bull.* **2010**, *19*(11), 2651-2656.

APTEFF, Vol. 54, 1-335 (2023)
DOI: https://doi.org/10.2298/APT2354151K
UDC: 663.424:665.52(65)
BIBLID: 1450-7188 (2023) 54, 151-163

Original scientific paper

# COMPOSITION, ANTIMICROBIAL AND ANTIOXIDANT ACTIVITY OF *ARTEMISIA HERBA-ALBA* ESSENTIAL OIL FROM NORTHEAST ALGERIA (KHENCHELA REGION)

*Mounira KADRI[1]*, Aicha MOUANE[2], Sana GOUBI[1], Farah RAMDAN[1],*
*Abdelouhab YAHIA[3]*

[1] Laboratory of Biology, Environment and Health, Faculty of Natural Sciences and Life, El Oued University, PO Box 789, 39000 Algeria.
[2] Laboratory of biodiversity and application of biotechnology in agriculture field, Faculty of Natural Sciences and Life, El Oued University, PO Box 789, 39000 Algeria.
[3] Laboratory of Natural Sciences and Materials (LSNM), Institute of Sciences and Technology, Abdelhafid Boussouf University Center in Mila, BP No. 26, RP Mila 43000, Algeria.

**Received: 18 March 2023** **Revised: 02 May 2023** **Accepted: 08 May 2023**

*Plants are traditionally utilized in Algeria to treat many disorders, such as Artemisia herba-alba (Asteraceae family), which is a North African species. In Algeria, it is characterized by an excellent fodder fee and by a composition of essential oils having antiseptic, vermifuge, and antispasmodic properties. The present study aims to investigate the antioxidant and antimicrobial activities and chemical composition of the essential oil of Artemisia herba-alba found in northeast Algeria (Khenchela region).*

*Artemisia herba-alba essential oil was extracted by hydrodistillation and its chemical composition was identified by GC/MS. In addition, the antioxidant activity of the extracted essential oil was determined using the DPPH assay. The agar disc diffusion method was used to determine how well the essential oil killed germs.*

*The essential oil was analyzed by GC/MS, revealing 35 constituents, of which the major ones were identified as Thujone (10.55%), borneol (5.98%), and eucalyptol (1.63%). The observed IC50 values for the DPPH assay were 18.44 ± 0.006 mg/mL. On the other hand, this oil proved effective against all tested strains in the 22.67 ± 3.215 mm range, including Listeria innocua CIP 74915.*

**Keywords**: Khenchela (Algeria), *Artemisia herba-alba*, GC/MS, antioxidant activity, antibacterial activity.

## INTRODUCTION

Algeria is renowned for its wealth of medicinal plants, which are utilized to treat various diseases (1,2). The country's flora is diverse, owing to its size and climatic variations, with a Mediterranean climate in the north, the Atlas Mountains in the center, and the Sahara in the south (3). According to WHO statistics, around 80% of the African population use traditional medicine as their primary healthcare. Recently, the use of medicinal plants has increased significantly, perhaps due to their local abundance, cultural significance, and low cost of acquisition (4). Essential oils are rich sources of biologically active compounds, and there has been growing interest in their antimicrobial properties (5). Many essential oils have also been shown to possess antioxidant activity (6). As part of the evaluation of the biological effectiveness of medicinal plants, *Artemisia herba-alba* Asso (Aste-

---

* Corresponding author: Mounira KADRI, Faculty of Nature Sciences and Life, El Oued University, PO Box 789, 39000 Algeria, e-mail: mounira-kadri@univ-eloued.dz

raceae family) is widely found in semi-arid and arid steppes of North Africa, Spain, the Middle East, and the Northwest Himalayas (7). This plant is used to treat stomach ailments such as diarrhea, abdominal pain, and to heal external wounds. The terpenoid sesquiterpene lactone dehydroleucodine, which is mainly found in the aerial parts of Artemisia herba-alba, is responsible for its medicinal properties (8). The essential oil of this plant is known for its disinfectant, anthelmintic, and antispasmodic therapeutic properties (9). Consumers are becoming increasingly aware of the dangers posed by the use of synthetic antioxidants and antimicrobials in the food industry and are seeking safer and more sustainable alternatives. This study analyzes the antioxidant activity of essential oils using the DPPH method, their antimicrobial effects against bacterial strains, and the chemical composition of the essential oil extracted from the aerial parts of *Artemisia herba-alba* originating from northeast Algeria (Khenchela region).

## EXPERIMENTAL

### STUDY AREA

We collected the aerial parts of *Artemisia herba-alba* during the flowering phase from Khenchela, which is located in the northeast Algeria in the Aurès region between 35°25'50" N and 07°8'44" E (Figure 1). Khenchela has a semi-arid climate with cool winters and torrid summers with an average temperature of 26.97 °C (Figure 2). The relative humidity is low, except for the winter months when it reaches 71% (Figure 3). The area receives high precipitation throughout the year, with 481mm on average (Figure 4). The ombrothermic diagram of Bagnouls and Gaussen shows that Khenchela has a dry summer period and three dry months. The ombrothermic diagram indicates that Khenchela is in conditions of permanent drought (Figure 5).

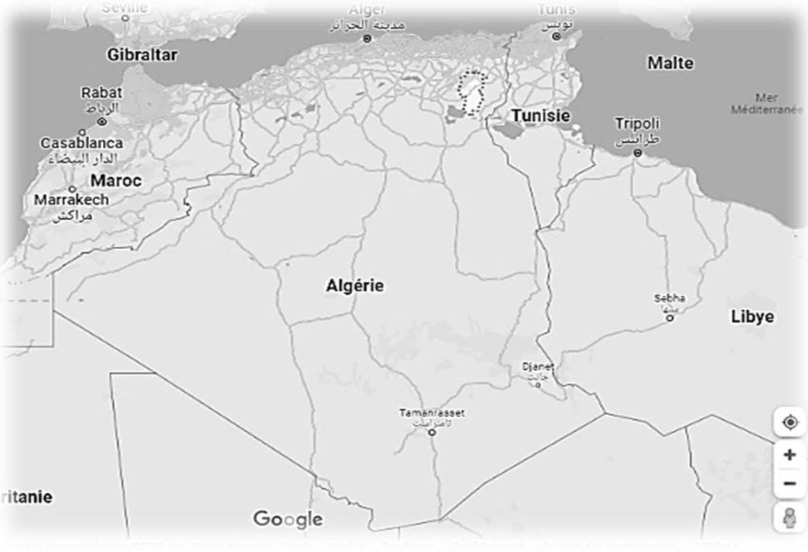

**Figure 1.** Location of the Khenchela

UDC: 663.424:665.52(65)
BIBLID: 1450-7188 (2023) 54, 151-163

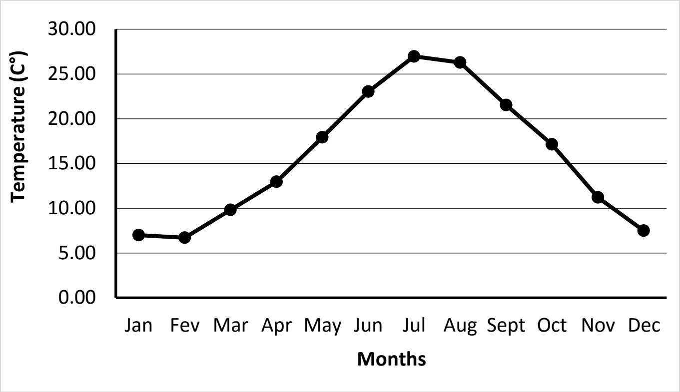

**Figure 2**. Annual monthly change in average temperature of Khenchela during the period (2007-2016).

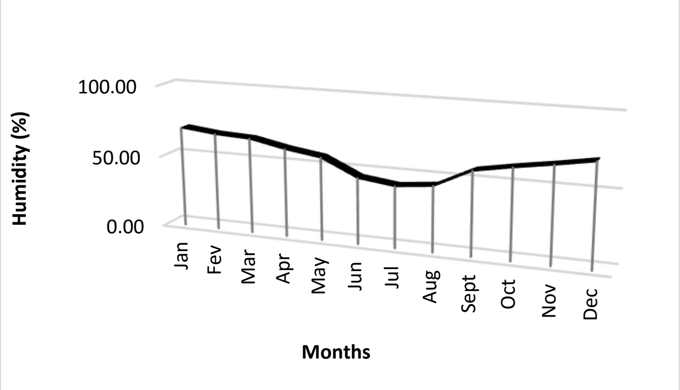

**Figure 3**. Annual monthly change in average Humidity of Khenchela during the period (2007-2016).

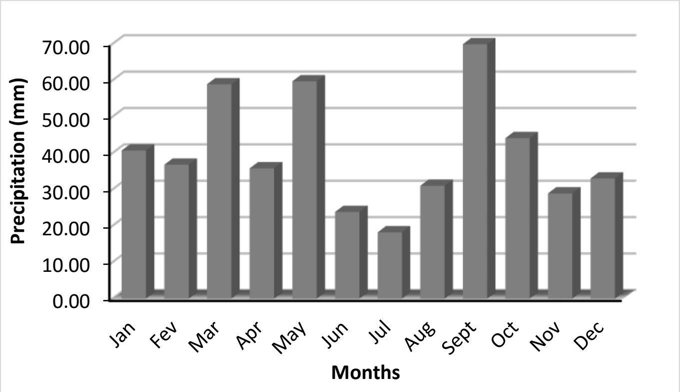

**Figure 4**. Annual monthly change in average Precipitation of Khenchela during the period (2007-2016).

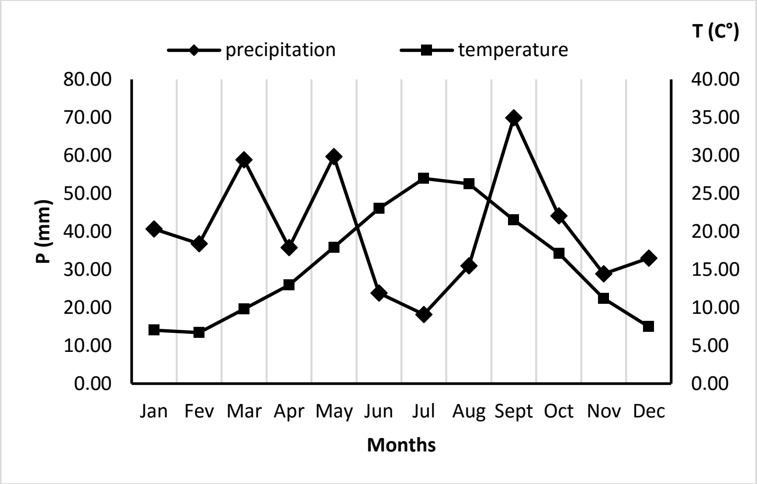

**Figure 5.** Ombrothermic diagrams of BAGNOULS and GAUSSEN the Khenchela

## HYDRODISTILLATION OF ESSENTIAL OIL

The essential oil was obtained by hydrodistillation from air-dried *Artemisia herba-alba* parts using a Clevenger apparatus for 3 hours. The average yield of each essential oil across the three replicates was calculated. The oils were stored at 4 °C until they were analyzed (10). The essential oil yield (Y) was calculated as the weight of the essential oil (wEO) divided by the weight of the Plant material utilized (wPM) (11):

$$Y(\%) = (wEO / wPM) \times 100$$

## ANTIOXIDANT ACTIVITY

The antioxidant assay is based on measuring the loss of color of DPPH solution through the change of absorbance at 517 nm caused by the reaction of DPPH with the tested sample. The reaction was monitored using a UV-VIS spectrophotometer (12).

The radical scavenging activity of the essential oil was determined using 2,2-diphenyl-1-picrylhydrazyl (DPPH) and evaluated using the methodology described by Blois (13), as elaborated by Elmastas et al. (14). In dry test tubes, 200 µL of various essential oil dilutions (EO methanolic solutions) were mixed with 800 µL of 0.004% (w/v) DPPH methanol solution. The reaction mixture was vigorously stirred and incubated at room temperature and in the dark for 30 minutes. Absorbance was measured at 517 nm. The negative control contained 200 µL of methanol and 800 µL of DPPH.

The DPPH radical scavenging capacity was calculated using the following formula: A control (Ac) is the absorbance of the control reaction, and A sample (As) is the absorbance when all extract samples and references are present. All tests were run in triplicate, and the results were averaged. Ascorbic acid was used as a standard.

$$\text{Inhibition }\%=\frac{(\text{Ac-As})\times 100}{\text{Ac}}$$

The graph of the scavenging effect percentage against extract concentrations allowed for the calculation of the oil concentration that offers 50% inhibition ($IC_{50}$) (15).

## GAS CHROMATOGRAPHY-MASS SPECTROMETRY (GC-MS)

Analysis by GC/MS was carried out using a Varian GC 3800 equipped with an SPB1 capillary column (30m ×0,25 mm × 0,20 µm) and a "Mass Selective MS Saturn Series 2200, column SPB-1." The temperature of the detector was 250 °C and that of the injector was 210 °C. The oven temperature was programmed as before, and the transfer line temperature was 280 °C. Operating under the GC condition, programmed heating at 55 °C for 1 min to 150 °C for 3 min to 250 °C for 8 min. The injector temperature was 250°C. Helium was the GC carrier gas.

## EVALUATION OF ANTIBACTERIAL ACTIVITY

In the current study, one strain of gram-positive bacteria, *Klebsiella pneumonia* ATCC7000603, and four strains of gram-negative bacteria, *Pseudomonas aeruginosa* ATCC 25922, *Salmonella enterica* CIP 81-3, *Listeria innocua* CIP 74915, and *Escherichia coli* ATCC 25922, were donated by the hospital Elhakim Saadan Biskra (Algeria). With a small modification, the disc agar diffusion method was used to complete the research for this publication (16). After growing on Müller-Hinton agar for 18 hours at 37 °C, the bacteria strains were suspended in a saline solution (0.9 % NaCl). The turbidity was then corrected to 0.5 MacFarland standards (108 CFU/mL). The medium mentioned above was present in 90 mm diameter Petri plates that were inoculated with the suspension. After being sterilized, sterile paper disc No. 1 (6 mm in diameter) was put onto the surface of agar plates and soaked with 10 mL of essential oil. The incubation conditions for bacteria were 37 °C for 24 hours prior to incubation. The widths of the inhibition zones were measured in order to assess antimicrobial activity. Chloramphenicol (C30), Cefixime (CFM), Gentamycin (GEN), Ofloxacin (OF), and Co-Trimoxazole Sulfamethoxazole (COT) were employed as positive controls to assess the sensitivity of gram-positive and gram-negative bacteria, respectively. The study was completed in aseptic circumstances (17). The results of the inhibitory zone measured in millimeters were averaged across all tests carried out in triplicate for each strain of microorganism.

## DATA ANALYSIS

The Co Stat-Statistics Software version 6.4 was used to perform an analysis of variance (ANOVA) on the data. The significance of differences between treated samples was assessed using the LSD test for mean and standard deviation (SD) of inhibition diameter comparisons and yield. Each experiment had three replicates and three determinations, with the significance level for all measurements set at $p \leq 0.05$.

## RESULTS AND DISCUSSION

### OIL YIELD

A Clevenger-type apparatus was used for hydrodistillation of air-dried *Artemisia herba-alba* parts. The resulting essential oil was liquid, gilded yellow in color, and had a strong penetrating odor. The yield of the essential oil was 1.07 ± 0.0681% (w/w) based on the dry weight of the plants. In another study conducted in Bousaada (Algeria) (20), the yield of the essential oil was 0.72% and, in another study, 0.33±0.029 (21). In Tunisia, the yield was reported to be between 0.68% and 1.93% (22). In Morocco, it was 1.2% (23), and in Biskra (Algeria), it was 0.95% (24) and 1.02% in M'sila (Algeria) (25), In Ghardaïa) Algeria), the yield reached 1.5±0.093% (26).

### CHEMICAL COMPOSITION OF ESSENTIAL OILS

GC/MS was used to analyze the chemical composition of essential oil extracted from the aerial parts of *Artemisia herba-alba* via hydrodistillation. 35 constituents were identified, with the major ones being Thujone (10.555%), Borneol (5.978%), and Eucalyptol (1.628%) (Table 1), (Figure 6). Haouari and Ferchichi (22), Kadri et al. (26), and Kadri el al. (21) reported that the major compounds are Thujone (34.32%), (12.759%), (9.875%) Respectively. Zaim et al. (23) also concluded that the major compound is Chrysanthenone (28.10%). According to Dahmani-Hamzaoui and Baaliouamer (27), the major compounds are composed of Cischrysanthenyl acetate (25.12%) (24).

**Table 1.** The composition of *Artemisia herba-alba* aerial part's essential oil.

| RT (min) | Constituent | % | RT (min) | Constituent | % |
|---|---|---|---|---|---|
| 5.031 | Camphene | 0.88 | 15.205 | Humulen-(v1) | 0.027 |
| 5.292 | β -Phellandrene | 0.472 | 16.394 | Limonen-6-ol, pivalate | 0.082 |
| 5.935 | 1,3,5-Trimethylbenzene | 0.195 | 16.802 | ɣ -Elemene | 0.096 |
| 6.420 | Benzene | 0.319 | 16.927 | Isobornyl propionate | 0.09 |
| 6.513 | 4-Isopropyltoluene | 0.628 | 17.140 | Butanoic acid | 0.016 |
| 6.560 | Eucalyptol | 1.628 | 17.219 | Naphthalene | 0.073 |
| 7.185 | 1,4-Cyclohexadiene | 0.097 | 17.269 | Azulene | 0.019 |
| 7.584 | Terpineol | 0.152 | 17.960 | Neoclovene oxide | 0.087 |
| 7.885 | 3,5-Heptadienal | 0.063 | 18.053 | 1,5-Cyclodecadiene | 0.121 |
| 8.635 | Thujone | 10.555 | 18.588 | (-)-Spathulenol | 0.93 |
| 10.017 | Borneol | 5.978 | 18.913 | Cubenol | 0.167 |
| 11.105 | Acetic acid | 0.161 | 19.535 | 5α -Pregnan-20-one | 0.082 |
| 11.414 | D-Verbenone | 0.119 | 19.645 | Longipinocarvone | 0.223 |
| 11.602 | Benzaldehyde | 0.187 | 20.091 | 2-Naphthalenemethanol | 0.033 |
| 12.508 | trans-2-Caren-4-ol | 0.08 | 20.160 | ɣ -Himachalene | 0.056 |
| 12.997 | Ascaridole epoxide | 0.115 | 20.280 | 1H-Indene | 0.025 |
| 14.254 | α -Cadinol | 0.167 | 22.151 | Alfaxalone | 0.039 |
| 14.604 | Cyclohexene | 0.097 |  | NI | 0.728 |

Note: a RT: Retention time of the compound in minutes

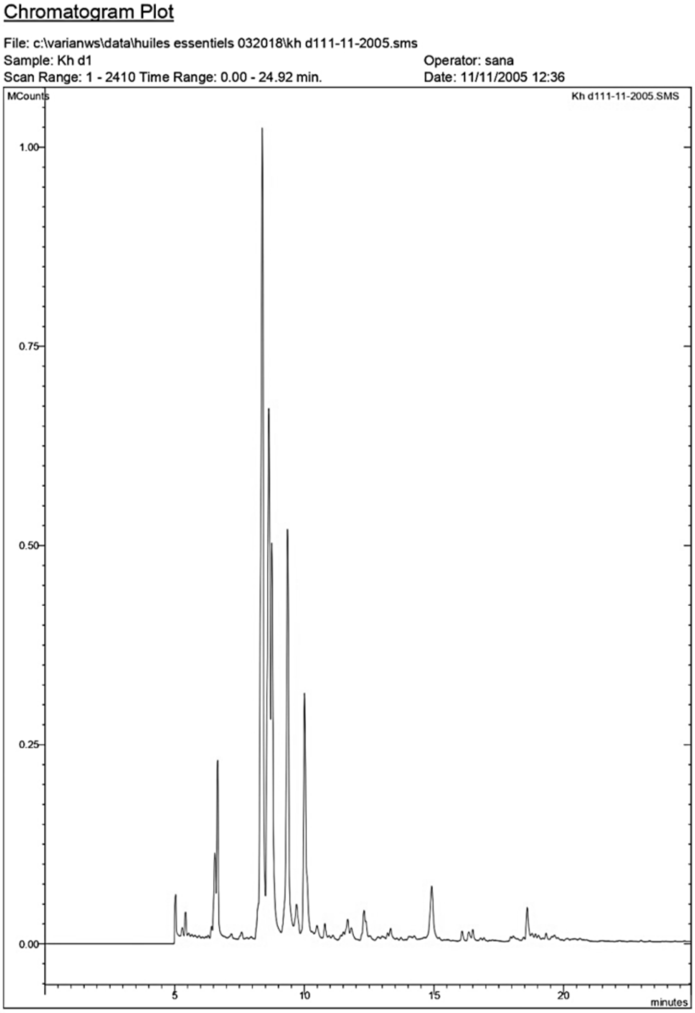

Chromatogram Plot

File: c:\varianws\data\huiles essentiels 032018\kh d111-11-2005.sms
Sample: Kh d1
Operator: sana
Scan Range: 1 - 2410 Time Range: 0.00 - 24.92 min.
Date: 11/11/2005 12:36

**Figure 6**. Chromatogram *Artemisia herba-alba* essential oil (GC/MS)

## ANTIOXIDANT ACTIVITY

It is believed that the ability of antioxidants to donate hydrogen is what causes them to affect DPPH (29). Activities that neutralize free radicals are crucial in preventing their harmful effects in conditions like cancer. Antioxidants are known to function to reduce lipid peroxidation by scavenging DPPH free radicals. The $IC_{50}$ for the activity to scavenge DPPH radicals was 18.44 ± 0.006 mg/mL. The $IC_{50}$ values for ascorbic acid were 2.82 ± 0.06 µg/mL (Figure 7, 8). In previous studies, $IC_{50}$ was estimated 20.27 ± 0.76 mg/mL (26), and 7.31 ± 0.88mg/mL (21).

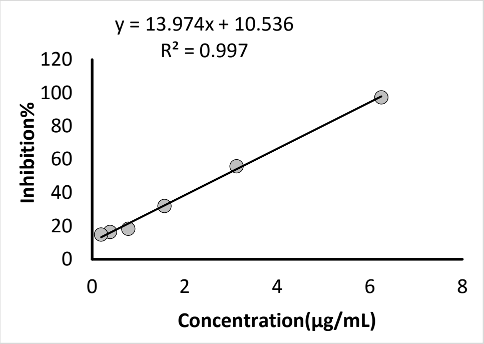

**Figure 7**. Reducing power of antioxidant activity of Ascorbic acid

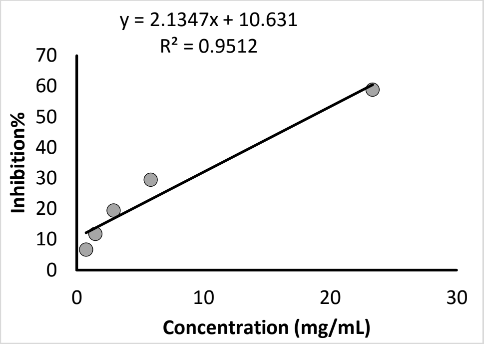

**Figure 8.** Reducing power of antioxidant activity of essential oil of *Artemisia herba-alba*

Regarding antioxidant activity, Akrout et al. (36) found that, when compared to *Thymus capitatus*, the anti-free radical activity of essential oils from *Artemisia campestris* of the thujone (α+β) type was relatively poor. However, in contrast, they conducted a study on four Artemisia species using DPPH, ABTS, and linoleic acid and found that *Artemisia herba-alba* had low activity, and the activity of all essential oils investigated remained lower than that of controls. This was confirmed in studies on a few Artemisia species (37). Numerous studies have shown, however, that the major compounds in essential oils are responsible for their antioxidant properties (38), with essential oils rich in oxygenated compounds (such as linalool, eugenol, geraniol, borneol, and terpineol) having stronger antioxidant properties than those with hydrocarbon terpenes (39). Based on this theory, we can explain the variation in antioxidant activity by examining the chemical composition, which can be influenced by various variables such as edaphic, climatic, and others, as well as by the extraction temperature, solvent type, and extraction method (40, 41).

## ANTIBACTERIAL ACTIVITY

The antibacterial activity of essential oil components is largely dependent on the lipophilic nature of the hydrocarbon skeleton and the hydrophilic nature of their functional groups (30). Due to these data, we were interested in studying the antimicrobial activity of the essential oil. The results were summarized in Table 3, which showed that essential oil obtained from *Artemisia herba-alba* prevented the growth of some tested microorganisms with an inhibition zone medium diameter. The highest inhibition zone recorded was for *Listeria innocua*, with a diameter of 22.67 ± 3.215 mm. The essential oil obtained from *Artemisia herba-alba* growing in other regions of Algeria (Boussaada and Ghardaïa) had the same effect on the *Listeria innocua* strain with a difference in the diameter of inhibition only if estimated by 12.77 ± 0.51 mm and 15.67 ± 1.53 mm Respectively (21, 26). It should be mentioned that there are no background antibacterial studies on *Artemisia herba-alba*. Some studies on *Artemisia herba-alba* have reported that the essential oil exhibited much higher antibacterial activity, with a diameter of 31.3 mm against *Klebsiella oxytoca* (31).

**Table 3**. Zone of Inhibition of bacterial strains against of essential oil *Artemisia herba-alba* and positive control.

| Bacteria strain | Zone inhibition(mm) | | | | | | P |
|---|---|---|---|---|---|---|---|
| | Essential oil | C30 | GEN | CFM | OF | COT | |
| ***E. coli*** | $10.22 \pm 0.381^{d}$ | $20 \pm 1^{c}$ | $18 \pm 1^{c}$ | $24 \pm 0.5^{b}$ | $30 \pm 1^{a}$ | $25 \pm 0.79^{b}$ | 0.000 |
| ***L. innocua*** | $22.67 \pm 3.215^{d}$ | $26 \pm 0.\ 7^{bc}$ | $30 \pm 3.46^{ab}$ | $20^{d}$ | $28^{\pm}0.23^{ab}$ | $32 \pm 0.6^{a}$ | 0.000 |
| ***K. pneumoniae*** | $6^{c}$ | $30 \pm 2.46^{a}$ | $30 \pm 1.78^{a}$ | $20 \pm 1^{b}$ | $27 \pm 0.4^{a}$ | $28^{a}$ | 0.000 |
| ***P. aeruginosa*** | $6^{d}$ | $12 \pm 0.56^{c}$ | $26 \pm 0.66^{b}$ | $8^{d}$ | $30 \pm 1.77^{a}$ | $6^{d}$ | 0.000 |
| ***S. enterica*** | $6^{e}$ | $20 \pm 0.87^{b}$ | $18^{c}$ | $20 \pm 0.4^{b}$ | $15.30 \pm 1.13^{d}$ | $29 \pm 0.50^{a}$ | 0.000 |

Note: Means of three replicates ± SD (standard deviation) followed by at least one same letter are not significantly different according to LSD test at $p < 0.05$.

This study focused on investigating the bioactivity of *Artemisia herba-alba* oil in northeast Algeria (Khenchela region). The variation in the chemical composition of essential oils of the *Artemisia herba-alba* species can be attributed to geographical, genetic (32), seasonal, or even environmental factors such as soil and humidity (33). The age of the plant and the part of the plant studied could also explain the differences in the chemical analysis of *Artemisia herba-alba* essential oils, depending on the type of oil (34). The chemical composition of essential oils can be affected by storage conditions. During storage, volatile oil components can come into contact with oxygen and react with it, evaporate, and undergo other changes that may not be beneficial (35).

*Artemisia herba-alba essential* oil had a strong antimicrobial effect. The limited activity of essential oils may be due to their chemical composition. Studies on the antimicrobial properties of specific essential oil compounds have revealed that phenolic compounds like thymol and carvacrol have antibacterial properties (42, 43). In contrast, pulegone, menthone, 1,8-cineole, *p*-cymene, *iso*-menthone, myrcene, pinene, piperitone, limonene, linalool, terpinene, sesquiterpenes, and terpenic acid are constituents with low antibacterial activity (44, 45, 46).

All of the essential oils and their main constituents' modes of action appear to have an impact on the cytoplasmic wall or membrane. However, the variety of chemicals found in essential oils demonstrates the presence of substances that can work through novel biological mechanisms (47, 48). The primary quality of the molecules found in essential oils is their hydrophobicity, which allows them to be solubilized in the membranes, leading to the structure becoming unstable and the membrane permeability increasing (49). Therefore, we can explain the variance in antibacterial activity by examining the type of essential oils, which can vary based on edapho-climatic conditions (50).

## CONCLUSION

In conclusion, a phytochemical analysis was conducted, and the antioxidant and antibacterial properties of *Artemisia herba-alba* growing in Algeria were reported. A Clevenger-type apparatus was used for hydrodistillation of air-dried *Artemisia herba-alba* parts, and 1.07 ± 0.0681% (w/w) of a liquid, golden-yellow, strong-smelling essential oil was produced based on the plant's dry weight. GC/MS was used to analyze the chemical composition of the essential oil extracted from the aerial parts of *Artemisia herba-alba* via hydrodistillation, Thujone (10.555%), Borneol (5.978%), and Eucalyptol (1.628%) were identified as constituents. The $IC_{50}$ for DPPH radical-scavenging activity was $18.44 \pm 0.006$ mg/mL for antioxidant activity, while ascorbic acid had an $IC_{50}$ value of $2.82 \pm 0.06$ µg/ml. On the other hand, this oil was effective against all the strains that were tested, with its activity ranging from $22.67 \pm 3.215$ mm with *Listeria innocua* CIP 74915.

These interesting results show that *Artemisia herba-alba* growing in the northeast of Algeria has significant antioxidant and antimicrobial activity, which makes us want to learn more about their pharmacological properties.

## Acknowledgements

The authors gratefully thank the University Hamma Lakhder, Eloued (Algeria), for giving the opportunity to perform the analysis as well as Laboratory of Biology, Environment and Health Laboratory, faculty of Nature Sciences and Life, Eloued, Algeria.

## REFERENCES

1. Benarba, B.; Belabid, L.; Riqhi, K.; Bekkar, A.A.; Elouissi, M.; Khaldi, A.; Hamimed, A. Ethnobotanical study of medicinal plants used by traditional healers in Mascara (North West of Algeria). *J Ethnopharmacol*. **2015**, *175*, 626-636. https://doi.org/10.1016/j.jep.2015.09.030
2. Sarri, M.; Mouyeta, F.Z.; Benzianea, M.; Cherieta, A. Traditional use of medicinal plants in a city at steppic character (M'sila, Algeria). *J Pharmacol Pharmacogn Res*. **2014**, *2*, 31-35.
3. Hamza, N.; Berke, B.; Umar, A.; Cheze, C.; Gin, H.; Moore, N. A review of Algerian medicinal plants used in the treatment of diabetes. *J Ethnopharmacol*. **2019**, *238*, 111841. https://doi.org/10.1016/j.jep.2019.111841
4. Thomford, N.E.; Dzobo, K.; Chopera, D.; Wonkam, A.; Skelton, M.; Blackhurst, D.; Chirikure, S.; Dandara, C. Pharmacogenomics implications of using herbal medicinal plants on African populations in health transition. *Pharmaceuticals (Basel)*. **2015,** *8*(3), 637-663. https://doi.org/10.3390/ph8030637
5. Lis-Balchin, M.; Deans, S.G.; Bioactivity of selected plant essential oils against *Listeria monocytogenes*. *J Appl Bacteriol*. **1997**, *82*(6), 759-762. http://dx.doi.org/10.1046/j.1365-2672.1997.00153.x
6. Zhang, H.; Chen, F.; Wang, X.; Yao, H.Y. Evaluation of antioxidant activity of parsley (*Petroselinum crispum*) essential oil and identification of its antioxidant constituents. *Food Res Int*. **2006**, *39*, 833-839. http://dx.doi.org/10.1016/j.foodres.2006.03.007
7. Wang, W.M. On the origin and development of Artemisia (Asteraceae) in the geological past. *Bot J Linn Soc*. **2004**, *145*(3), 331-336. https://doi.org/10.1111/j.1095-8339.2004.00287.
8. Abood, S.; Eichelbaum, S.; Mustafi, S., Veisaga, M.L.; López, L.A.; Barbieri, M. Biomedical properties and origins of sesquiterpene lactones, with a focus on dehydroleucodine. *Nat Prod Commun*. **2017**, *12*(6), 995-1005. https://doi.org/10.1177%2F1934578X1701200638
9. Hatimi, S.; Boudouma, M.; Bichichi, M.; Chaib, N.; Idrissi, N.G. In vitro evaluation of antileishmania activity of *Artemisia herba alba* Asso. *Bull Soc Pathol Exot*. **2001**, *94*(1), 29-31.
10. Bruneton, J. Pharmacognosie. Phytochimie. Plantes médicinales. TEC et DOC. Paris. 3ème édition, Lavoisier, **1999**, 1120 p.

11. Benfares, R.; Kord, A.; Boudjema, K.; Bouarab, M.; Benrabah, S.; Boudjemaa, K.; Švarc-Gajić, J. Chemical characterization of essential oils and antioxidant activity of *Dictyota dichotoma* and *Dictyopteris membranacea*. *APTEFF* **2019**, 50, 33-42. https://doi.org/10.2298/APT1950033B
12. Dimitrijević, D.; Kostić, D.; Paunović D.; Mitić, M.; Krstić, J.; Ivana, Rašić Mišić, B.; Arsić, B: Antimicrobial activity and the quantitative analyses of phenolic compounds and heavy metals of red mulberry extracts (Morus rubra L.) from Serbia. *Studia UBB Chemia*. **2022**, LXVII, *1*, 195-207. DOI: 10.24193/Subbchem.2022.1.13
13. Blois, M. S. Antioxidant determination by the use of a stable free radical. *Nature*. **1958**, *181*, 1199-1200. https://doi.org/10.1038/1811199a0.
14. Elmastas, M.; Isildak, O.; Turkekul, I.; Temur, N. Determination of antioxidant activity and antioxidant compounds in wild edible mushrooms. *J. Food Compos. Anal.* **2007**, *20*, 337-345. https://doi.org/10.1016/j.jfca.2006.07.003.
15. Shimada, K.; Fujikawa, K.; Yahara, K.; Nakamura, T. Antioxidative properties of xanthone on the auto-oxidation of soybean oil in cyclodextrin emulsion. *J. Agric. Food Chem*. **1992**, *40*, 945-948. https://doi.org/10.1021/jf00018a005.
16. Phaiphan, A.; Baharin, B. S.; Tan, C. P.; Abdul Rahman, R.; Ganesan, P. Antioxidant and antibacterial activities of different solvent extractions from Cassia siamea (Lamk.) leaves. *J. Chem. Pharm. Res*. **2014**, *6* (4), 655-662.
17. Schinor, E. C.; Salvador, M. J.; Ito, I. Y.; Dias, D. A. Evaluation of the antimicrobial activity of crude extracts and isolated constituents from Chresta scapigera. Braz. *J. Microbiol*. **2007**, *38*, 145-149. https://doi.org/10.1590/S1517-83822007000100030.
18. Trease, E.; Evans, W. C. Pharmacognosie. Bailliare Tindall, *London, 13th edition*, **1987**, pp. 61-62.
19. Harborne, J. B. Phytochemical methods: a guide to modern techniques of plant analysis, *Third Edition*, **1998**, ISBN 0-412-57260-5.
20. Belhattab, R.; Amor, L.; Barroso, J.G.; Pedro, L.G.; Figueiredo, A.C.;. Essential oil from *Artemisia herba-alba* Asso grown wild in Algeria: Variability assessment and comparison with an updated literature survey. *Arabian Journal of Chemistry*. **2014**, *7*(2): 243-251. http://dx.doi.org/10.1016/j.arabjc.2012.04.042
21. Kadri, M.; Yahia, A.; Goubi, S.; Mekhedmi, N.E.; Selmane, M.; Chemsa, A.E. Chromatography analysis, in vitro antioxidant and antibacterial activities of essential oil of *Artemisia herba-alba* Asso of Boussaâda, Algeria. *Biodiversitas*. **2022**, *23*(9), 4424-4431. http://dx.doi.org/10.13057/biodiv/d230907
22. Haouari, M.; Ferchichi, A. Essential Oil Composition of *Artemisia herba-alba* from Southern Tunisia. *Molecules*. **2009**, *14*(4), 1585-1594. https://doi.org/10.3390/molecules14041585
23. Zaim, A.; El Ghadraoui, L.; Farah, A. Effets des huiles essentielles *d'Artemisia herba-alba* sur la survie des criquets adultes *d'Euchorthippus albolineatus* (Lucas, 1849). *Bulletin de l'Institut Scientifique*. **2012**, *34*(2), 127-133.
24. Bezza, L.; Mannarino, A.; Fattarsi, K.; Mikail, C.; Abou, L.; Hadj- Minaglou, F.; Kaloustian, J. Chemical composition of the essential oil of *Artemisia herba-alba* issued from the district of Biskra (Algeria). *Phytothérapie*. **2010**, *8*(5), 277-281. http://doi.org/10.1007/s10298-010-0576-3
25. Dob, T.; Ben Abdelkader, T. Chemical composition of the essential oil of *Artemisia herba-alba* Asso grown in Algeria. *Journal of Essential Oil Research*. **2006**, *18,* 685-690. https://doi.org/10.1080/10412905.2006.9699206
26. Kadri, M.; Goubi, S.; Salhi, N. GC/MS analysis and in vitro antioxidant and antibacterial activity of essential oil of Artemisia herba-alba Asso of Algeria. *International Journal of Biosciences* **2022**, *20*(3): 99-109. http://dx.doi.org/10.12692/ijb/20.3.99-109
27. Dahmani-Hamzaoui, N.; Baaliouamer, A. Chemical composition of Algerian *Artemisia herba-alba* essential oils isolated by microwave and hydrodistillation. *Journal of Essential Oil Research* **2010**, *22*(6), 514-517. https://doi.org/10.1080/10412905.2010.9700386

28. Abou El-Hamd, M.; Magdi, A.E.; Mohamed, E.H.; Soleiman, E.H.; Abeer, M.E.; Naglaa, S.M. Chemical Constituents and Biological Activities of *Artemisia herba-alba*. *Records of Natural Products*, **2010**, *4*(1), 1-25.
29. Shirwaikar, A.; Prabhu, K.S.; Punitha, I.S.R. In vitro antioxidant studies of *Phaeranthus indicus*. *Indian Journal of Experimental Biology*, **2006**, *44*, 993-996.
30. Griffin, S.G.; Wyllie, S.G.; Markham, J.L.; Leach, D.N. The role of structure and molecular properties of terpenoids in determining their antimicrobial activity. *Flavour and Fragrance Journal*. **1999**, *14*, 322-332. http://doi.org/10.1002/(SICI)1099-1026(199909/10)14:5%3C322::AID-FFJ837%3E3.0.CO;2-4
31. Bertella, A.; Benlahcen, K.H.; Abouamama, S.; Diana, C.G.A.P.; Karim, M.K.; Kihal, M.; Artur, M.S.S. *Artemisia herba-alba* Asso. essential oil antibacterial activity and acute toxicity. *Industrial Crops and Products*. **2018**, *116*, 137-143. https://doi.org/10.1016/j.indcrop.2018.02.064
32. Karousou, R.; Koureas, D.N.; Kokkini, S. Essential oil composition is related to the natural habitats: *Coridothymus capitatus* and *Satureja thymbra* in NATURA 2000 sites of Crete. *Phytochemistry*. **2005**, *66*(22), 2668-2673. https://doi.org/10.1016/j.phytochem.2005.09.020
33. Ghanmi, M.; Satrani, B.; Aafi, A.; Ismaili, M.R.; Houtia, H.; Manfalouti, H.; Benchakroun, K.; Abarchane, M.; Harki, L.; Boukir, A.; Chaouch, A.; Charrouf, Z. Effet de la date de récolte sur le rendement, la composition chimique et la bioactivité des huiles essentielles de l'armoise blanche (*Artemisia herba-alba*) de la région de Guercif (Maroc oriental). Phytothérapie, **2010**, *8*(5), 295-301. http://dx.doi.org/10.1007/s10298-010-0578-1
34. El-massry, K.F.; El-ghorab, A.H.; Farouk, A. Antioxidant activity and volatile components of Egyptian Artemisia judaica L. Food Chemistry, **2002,** *79*, 331-336. http://dx.doi.org/10.1016/S0308-8146(02)00164-4
35. Jain, N.; Sharma, M. Comparative Analysis of Antidermatophytic Potential of Cymbopogon citratus Essential Oil Stored in Different Temperature Condition for Two Years. *Pharmacognosy Research*, **2022**, *14*(3), 241-245. https://doi.org/10.5530/pres.14.3.34
36. Akrout, A. Essential Oil Study of Some Pastoral Plants from Matmata (South Tunisia). *Cahiers Options Méditerranéennes (CIHEAM)*. **2004,** *62*, 289-292.
37. Lopes-Lutz, D.; Alviano, D.; Alviono, C.S.; Kolodziejczyk, P.P. Screening of Chemical Composition, Antimicrobial and Antioxidant Activities of Artemisia Essential Oils. *Phytochemistry*. **2008**, *69*, 1732-1738. https://doi.org/10.1016/j.phytochem.2008.02.014
38. Ramdane, F.; Medjour, O.; Ben Aoun, A.K.; Hadjadj, S.; Guemouda, M.; Kadri, M.; Hadj Mahammed, M. Essential Oil and Ethanolic Extract Composition from *Myrtus nivellei* Batt. & Trab. and their Biological Evaluations. *APTEFF*. **2021**, 1450-7188 52, 111-121. https://doi.org/10.2298/APT2152111R
39. Falleh, H.; Ksouri, R.; Chaieb, K.; Karray-Bouraoui, N.; Trabelsi, N.; Boulaaba, M.; Abdelly, C. Phenolic Composition of *Cynara cardunculus* L. Organs, and Their Biological Activities. *Comptes Rendus Biologies*, **2008,** *331*(5), 372-379. https://doi.org/10.1016/j.crvi.2008.02.008
40. Teffane, M.; Boudries, H.; Bachir Bey, M.; Kadi, A.; Boukhalfa, F. Effect of Solvent Type, Extraction Temperature, Agitation Speed and Microwave Power on Phenolic Compound Extraction and Antioxidant Activity of Apricot Kernels (Prunus armeniaca L.). *Current Bioactive Compounds*, **2021,** *17*(2), 209-218. http://dx.doi.org/10.2174/1573407217666210215085507
41. Djousse, B.M.K.; Ngoune, N.F.; Djoukeng, H.G.; Nono, L.W.; Sogang, H.S.; Tangka, J.K. Extraction et Caractérisation des Huiles Essentielles de Trois Plantes Aromatiques Cultivées à l'Ouest-Cameroun: *Rosmarinus officinalis, Salvia officinalis* et *Cymbopogon citratus*. *Cameroon Journal of Biological and Biochemical Sciences*, **2022**. *30*(2), 121-133.
42. Cosentino, S.; Tuberoso, C.I.G.; Pisano, B.; Satta, M.; Mascia, V.; Arzedi, E.; Palmas, F. In-vitro Antimicrobial Activity and Chemical Composition of *Sardinia Thymus* Essential Oils. *Letters in Applied Microbiology* ,**1999**, *29*, 130-135. https://doi.org/10.1046/j.1365-2672.1999.00626.x
43. Gergis, V.; Spilotis, V.; Poulos, C. Antimicrobial activity of essential oils from Greek Sideritis species. *Pharmazie*, **1990**, *45*, 70-75.

44. Lattaoui, N.; Tantaoui-elaraki, A. Individual and combined antibacterial activity of the main components of three thyme essential oils. *Revista Italiana Eppos.* **1994**, *13*, 13-19.
45. Lim, X. Y.; Teh, B. P.; Tan, T. Y. C. Medicinal Plants in COVID-19: Potential and Limitations. *Front Pharmacol*. **2021**, *12*, 355. http://doi.org/10.3389/fphar.2021.611408
46. Carson, C. F.; Hammer, K. A.; Riley, T. V. Broth micro-dilution method for determining the susceptibility of *Escherichia coli* and *Staphylococcus aureus* to the essential oil of *Melaleuca alternifolia* (tea tree oil). *Microbios* ,**1995**, *82*, 181-185.
47. Guinoiseau, E. Molécules antibactériennes issues d'huiles essentielles : séparation, identification et mode d'action. [Dissertation]. **2010**. Thesis presented for obtaining the degree of doctor of the university of corse.
48. Arab, Y.; Sahin, B.; Ceylan, O.; Zellagui, A.; Olmez, O.; Kucukaydin, S.; Tamfu, A. N.; Ozturk, M.; Gherraf, N. Assessment of in vitro activities and chemical profiling of Senecio hoggariensis growing in Algerian Sahara. *Biodiversitas* **2022**, *23*(7), 3498-3506. http://DOI.org/10.13057/biodiv/d230724
49. Sikkema, J.; De Bont, J. A. M.; Poolman, B. Interactions of cyclic hydrocarbons with biological membranes. *J. Biol. Chem*. **1994**, *269*(11), 8022-8028.
50. Kadri, M.; Salhi, N.; Yahia, A.; Amiar, K.; Gnabzia, H. Chemical composition, antioxidant and antimicrobial activities from extracts of *Cymbopogon schoenanthus* L. (spreng) of Algeria. *Int. J. Biosci*. **2017**, *10*(1), 318-326. http://dx.doi.org/10.12692/ijb/10.1.318-326

APTEFF, Vol. 54, 1-335 (2023)
DOI: https://doi.org/10.2298/APT2354165O

UDC: 664.683.6:664.236]:633.492+637.25
BIBLID: 1450-7188 (2023) 54, 165-175

Original scientific paper

# PHYSICAL PROPERTIES, PROXIMATE COMPOSITION AND SENSORY ACCEPTABILITY OF GLUTEN-FREE COOKIES FROM SWEET POTATO USING SHEA BUTTER AS SHORTENING

*Oludolapo Akinyemi OSUNRINADE*, Anuoluwapo Arike PHILLIPS,*
*Abosede O. ALABI*

The Oke-Ogun Polytechnic Saki, Oyo State, Nigeria

**Received: 27 March 2023** **Revised: 12 May 2023** **Accepted: 20 May 2023**

*Sweet potato and shea butter remain underutilized crops. Their potential in the production of ready-to-eat snacks could enhance food security. Hence, this study evaluated cookies from sweet potato flour using shea butter as a shortening. Cookies samples were produced from 100% sweet potato flour with margarine (SPM); 100% sweet potato flour with shea butter (SPS); 100% wheat flour with shea butter (WCS); 100% wheat flour with margarine (WMC), 50% wheat, 50% sweet potato flour with shea butter (WSS); 50% wheat, 50% sweet potato flour with margarine (WSM). Cookies samples were analysed for physical properties, colour, proximate composition and sensory acceptability. The physical properties of the cookies samples had the weight, diameter, thickness and spread ratio ranging from 5.99 to 7.7 g, 3.76 to 4.27 cm, 0.54 to 0.64 cm, and 10.59 to 13.86, respectively. The colour properties of the cookies sample had the L*, a* and b* values ranging from 33.99 to 61.08, -6.03 to 0.72 and 10.87 to 22.51, respectively. The proximate composition of the cookies sample was moisture content (2.39-4.98%), fat (11.74-14.41%), protein (2.71-3.54%), fibre (2.26-2.83%), ash (1.92-1.99%), carbohydrate (74.28-78.66%), while the energy value ranged from 340.77 to 356.34 kCal. The use of shea butter as shortening led to a lower value of fat and spread ratio of cookies. In the sensorial acceptability ranking, the texture, crunchiness and aroma of cookies samples were not significantly different ($p < 0.05$). Sensory panellists adjudged cookies produced with sweet potato using shea butter shortening as liked moderately. Hence, the production of gluten-free cookies using sweet potato flour with shea butter shortening could serve as a low-cost, nutrient-dense, ready-to-eat snack.*

**Keywords**: Cookies, sweet potato, shea butter, proximate, gluten-free.

## INTRODUCTION

Cookies have been mostly patronized due to their ready-to-eat nature, affordability, and availability. Cookies consumption, although mostly by children is fast becoming a snack for all age groups (1). This is due to the improvement in its dietary composition which included making it cholesterol (2) and gluten-free (3) alongside the presence of numerous functional properties (4,5). One such improvement is the production of gluten-free cookies (3,4,6,7). Numerous researchers have successfully reduced or eliminated the use of wheat flour in the production of acceptable cookies (2,3,8,9). This need arose from consumers' interest in gluten-free foods and products with higher nutritional potential.

Sweet potato flour is gluten-free flour from the root of the sweet potato plant (*Ipomoea batatas* L. Lam) (10). Even though on the global and production scale, sweet potato is

---

* Corresponding author: Oludolapo Akinyemi OSUNRINADE, The Oke-Ogun Polytechnic Saki, Oyo State, Nigeria, e-mail: dolaps2004@yahoo.com

seventh among food crops, it is still of low economic value (11). Considering its potential for the production of functional foods (12), sweet potato is important for national food security in both developing and underdeveloped worlds (8). Sweet potato cultivation to harvest is a short period of about four months and the dry matter yield is high (9). Nutritional profiling of sweet potato showed that it is rich in vitamins B6 and C, beta carotene and dietary fibre (8). Its importance for food security worldwide stemmed from its short growing cycle, high dry matter yield and nutritional content (13,14). Sweet potato has found its use as fries, puff, mash and wedges among others (15). Sweet potato utilization for the composite formulation of pastry products has severally been reported (9,13,16,17).

The use of shortenings is unavoidable in most pastry products, as such, there have been researches focused on alternative shortenings (18–22). Commercially available shortenings such as margarine and butter are commonly used for pastries (23,24). However, the developing world requires a cheaper source of shortening for its baked products to ensure affordability. Shea butter from the seed of the tree of *Paradoxical vitelllara* is both underutilized and a cheap source of fat in the developing world (25,26). To reduce shea butter reported postharvest losses (27,28) and its export at low prices (29), the discovery of its use as edible fat and oil in ready-to-eat, fast-moving foods is important.

The work of Osunrinade et al. (30) produced acceptable cake samples from the use of shea butter as a shortening. Researchers have produced cookies from sweet potatoes using other types of shortening aside from shea butter (8,16). The use of underutilized crops and low-cost raw materials for food production is important for food security and combating malnutrition in developing countries (31). The present work studied the physical properties, proximate composition and sensory acceptability of cookies produced from sweet potatoes using shea butter as a shortening.

## MATERIALS AND METHODS

### SOURCE OF RAW MATERIALS

Orange fleshed sweet potato root, refined wheat flour (Golden Penny®), shea butter, Simas® baking fat (Margarine), granulated sugar, egg, salt, vanilla flavour and sodium bicarbonate were purchased from Sango market in Saki, Oyo State, Nigeria. All chemicals used were of laboratory standard.

### Production of Sweet Potato Flour

Sweet potato flour was produced according to the method described by Adeyeye and Akingabala (8). Briefly, the sweet potato tubers were thoroughly washed with running water in the laboratory to remove all extraneous materials before sorting and thereafter peeling. The peeled roots were washed and sliced to a thickness of about 1 mm to aid drying. The sweet potato strips were steeped in clean water containing 1 % sodium metabisulphite for 30 minutes. The sweet potato strip was drained on a mesh before drying on a thin layer in a forced draught oven (Thermostat oven DHG-9053A, Medifield Equipment & Scientific, England) operated at 70 °C. The dried sweet potato strips were milled using an attrition mill and passed through a sieve of 200 μm mesh size to obtain sweet potato flour.

## Production of Cookies

The formulation presented in Table 1 was used to prepare cookies samples (WMC, SPM, WSM, WCS, SPS and WSS). Cookies were produced by mixing the ingredients (Table 1) using a stand mixer (Rohnson stand mixer, SC-623, Italy), while the dough kneading was done for 12 minutes. The dough was smoothened by a rolling pin and cut using a circular shape before baking at 205 °C for about 45 minutes. Cookies produced were allowed to cool before packaging in high-density polyethene packs. The packaged cookies were kept in an air-tight container placed on the shelf at ambient temperature until further analysis.

## Determination of physical properties of cookies

### *Cookies diameter*

The diameter of cookies was measured by using a ruler placed edge to edge of the cookies samples. This was done for ten cookies taken from each sample.

**Table 1.** Ingredient Formulation for Cookies Production

| S/N | Sample code | Wheat flour (g) | Sweet potatoes (g) | Margarine (g) | Shea butter (g) | Sugar (g) | Egg (g) | Salt (g) | Sodium bicarbonate (g) | Vanilla essence (g) |
|---|---|---|---|---|---|---|---|---|---|---|
| 1 | WMC | 300 | 0 | 105 | 0 | 165 | 60 | 0.5 | 3.42 | 14.5 |
| 2 | SPM | 0 | 300 | 105 | 0 | 165 | 60 | 0.5 | 3.42 | 14.5 |
| 3 | WSM | 150 | 150 | 105 | 0 | 165 | 60 | 0.5 | 3.42 | 14.5 |
| 4 | WCM | 300 | 0 | 0 | 105 | 165 | 60 | 0.5 | 3.42 | 14.5 |
| 5 | SPS | 0 | 300 | 0 | 105 | 165 | 60 | 0.5 | 3.42 | 14.5 |
| 6 | WSS | 150 | 150 | 0 | 105 | 165 | 60 | 0.5 | 3.42 | 14.5 |

SPM= 100% sweet potato flour with margarine: SPS= 100% sweet potato flour with shea butter: WCS= 100% wheat flour with shea butter: WMC= 100% wheat flour with margarine: WSS= 50% wheat and sweet potato flour with shea butter: WSM= 50% wheat flour and 50% sweet potato with margarine.

## Cookies thickness

The thickness (*T*) of the cookies was measured by placing five cookies stacked on one another. The thickness was measured in centimetres by the use of the meter rule.

## Cookies weight

The weight (W) of the cookies was determined by placing ten cookie samples on a weighing scale immediately after cooling.

## Cookies spread ratio

The spread ratio was estimated as the ratio of the diameter of the cookies to their thickness (16).

### Colour of the cookies samples

The colour intensity of the surface of cookies samples in terms of lightness (L*), redness (a*), and yellowness (b*) were taken by the use of Chroma meter CR 410 Konica Minolta, sensing Inc; Japan. Triplicate readings for each cookie formulation sample were read and the average value was reported.

### PROXIMATE COMPOSITION OF COOKIES

The moisture, ash, crude fibre, fat and protein contents were determined by AOAC (32) methods. Briefly, a Force draught oven operating at 105 °C was used to determine the moisture content, while a muffle furnace operated at 600 °C for 3 hours was used to determine cookies ash content. Cookies' crude fibre was determined by sequential acid and alkaline hydrolysis. The soxhlet apparatus and Kjeldhal method determined the fat and protein contents, respectively. The carbohydrate content of cookies was estimated by difference (subtracting moisture, ash, crude fibre, fat and protein contents from hundred), while the Atwater factor (4, 4, 9) was used to estimate the energy value of cookies.

### SENSORY EVALUATION

A panel of (30) thirty consumers was recruited from the student of the Oke-Ogun Polytechnics, Saki to evaluate the sensory acceptability of the cookies on a 9-point hedonic scale, with 1= dislike extremely, 5= neither like nor dislike and 9= like extremely. Cookie samples were coded and presented in random sequence to the panellist for the assessment of appearance, texture, crunchiness, colour, taste, aroma and overall acceptability.

### STATISTICAL ANALYSIS

All data obtained were statistically analysed using the analysis of variance (ANOVA) and the Duncan Multiple range test with a significance level of $p<0.05$.

## RESULTS AND DISCUSSION

### PHYSICAL PROPERTIES OF COOKIES PRODUCED FROM THE COMPOSITE FLOUR

The weight, diameter, thickness and spread ratio of cookies (Table 2) ranged from 5.99-7.7 g, 3.76-4.27 cm, 0.54-0.64 cm and 10.59-13.86, respectively. The lowest diameter was from cookies baked from 100% sweet potato and shea butter, while the highest was from samples produced from 50% wheat flour, 50% sweet potato and shea butter. There was no significant difference in the diameter of samples WMC, SPM and SPS. The control cookies sample (WMC) had the highest weight, while the lowest was from sample SPS (100% sweet potato with shea butter). The use of sweet potato for cookies production by Chopra et al. (17), also reported a significantly reduced value for diameter as the percentage of sweet potato flour increased in the composite with wheat flour. This decrease in cookies diameter could be attributed to the rich fibre property of sweet potato flour (16).

**Table 2.** Physical properties of cookies produced from wheat-sweet potato composite

| Sample | Weight(g) | Diameter(cm) | Thickness(cm) | Spread ratio |
|---|---|---|---|---|
| SPM | 7.52±0.35$^{b}$ | 3.82±0.03$^{a}$ | 0.58±0.03$^{ab}$ | 13.26±0.81$^{ab}$ |
| SPS | 5.99±0.19$^{a}$ | 3.76±0.03$^{a}$ | 0.56±0.02$^{a}$ | 10.78±0.47$^{c}$ |
| WCS | 6.64±0.29$^{a}$ | 4.11±0.02$^{bc}$ | 0.57±0.02$^{a}$ | 11.70±0.52$^{bc}$ |
| WMC | 7.7±0.23$^{b}$ | 3.88±0.12$^{a}$ | 0.64±0.03$^{b}$ | 12.27±0.73$^{abc}$ |
| WSS | 6.13±0.22$^{a}$ | 4.27±0.03$^{c}$ | 0.58±0.01$^{ab}$ | 10.59±0.35$^{c}$ |
| WSM | 7.43±0.19$^{b}$ | 4.06±0.02$^{b}$ | 0.54±0.02$^{a}$ | 13.86±0.53$^{a}$ |

Values are means ± SD duplicate determinations. Value with the same superscript letter in each column was not significantly different ($p<0.05$). SPM= 100% sweet potato flour with margarine: SPS= 100% sweet potato flour with shea butter: WCS= 100% wheat flour with shea butter: WMC= 100% wheat flour with margarine: WSS= 50% wheat and sweet potato flour with shea butter: WSM= 50% wheat flour and 50% sweet potato with margarine.

The weight of the control sample (WMC) was significantly higher than that of cookies produced from the use of shea butter as a shortening. The total elimination of wheat flour and margarine in cookies sample production caused a significant reduction in the weight of cookies samples. The use of shea butter as a shortening and sweet potato also caused a significant decline in the thickness of cookies samples. This pattern of lower thickness was observed by Saeed et al. (11), and Chopra et al. (17), that reported a significant decrease in the thickness of cookies from 68.9 to 65.00 mm and 0.87 to 1.12 cm respectively, as the percentage of sweet potato increase.

However, the spread ratio of cookies sample produced was not significantly different ($p<0.05$) for all samples. It is worthy of note that the lowest spread ratio was obtained from cookies produced from shea butter as shortening. Also, the use of shea butter led to a lower value of the spread ratio of cookies, irrespective of the flour samples used. Although the water absorption capacity of the flour used was reported to correlate strongly to cookies spread (17), the present study observed that the type of shortening used caused variation in the spread ratio. This could be linked to the influence of shortening on the viscosity of the batter formed, thus causing a reduction in the spread ratio of the cookies (17).

## COLOUR PROPERTIES OF COOKIES SAMPLES

The result of the cookies instrumental measurement of colour is presented in Table 3. The cookies' lightness ranged from 33.99 to 61.08, while redness and yellowness were from -6.03 to 0.72 and 10.87 to 22.51, respectively. The sample produced from 100% wheat flour with margarine recorded the highest L-value while the sample from 100% sweet potato with shea butter had the lowest L-value among the sample produced. Generally, cookies samples produced with the inclusion of wheat flour had significantly higher lightness, lower redness and higher yellowness. There was a significantly lower value for yellowness in cookies produced from sweet potatoes irrespective of the shortening type. This is an indication of the strong dependence of the colour of cookies on the flour and not shortening. This result agrees with the research output of Shazia et al. (11) on the effect of the inclusion of sweet potatoes in cookies preparation. Shazia et al. (11) reported a continuous significant decline in the lightness and yellowness properties of cookies as the percentage of sweet potatoes increased.

The significant variation in the colour parameters of cookies showed that the type of raw materials (33) and the extent to which the flours supported caramelisation and Maillard reaction are major factors to consider for cookies production. For example, the higher reducing sugar in sweet potato could have led to reduced lightness emanating from the browning occurrence during baking above 150 °C. Reduction in the quantity of sugar and lower baking temperature could be considered for cookies production when using sweet potato flour, especially if lightness is a major quality parameter.

**Table 3.** Instrumental Colour Properties of Cookies Samples

| Sample | L | a | b | ΔL | Δa | Δb | ΔE |
|---|---|---|---|---|---|---|---|
| SPM | $39.43\pm0.09^{b}$ | 0.2±0.04d | $13.33\pm0.08^{b}$ | $21.49\pm0.09^{b}$ | $-3.4\pm0.05^{d}$ | $11.64\pm0.08^{b}$ | $24.7\pm0.04^{b}$ |
| SPS | $33.99\pm0.06^{a}$ | $0.72\pm0.02^{e}$ | $10.87\pm0.02^{a}$ | $16.07\pm0.06^{a}$ | $-2.87\pm0.02^{e}$ | $9.18\pm0.02^{a}$ | $18.73\pm0.04^{a}$ |
| WCS | $60\pm0.08^{d}$ | $-5.1\pm0.01^{b}$ | $22.51\pm0.02^{e}$ | $42.07\pm0.08^{d}$ | $-8.67\pm0.01^{b}$ | $20.83\pm0.02^{e}$ | $47.74\pm0.08^{d}$ |
| WMC | $61.08\pm0.05^{e}$ | -6.03±0.02a | $21.1\pm0.16^{d}$ | $43.16\pm0.05^{e}$ | $-9.61\pm0.02^{a}$ | $19.42\pm0.16^{d}$ | $48.29\pm0.02^{e}$ |
| WSS | $60\pm0.08^{d}$ | $-5.1\pm0.01^{b}$ | $22.51\pm0.02^{e}$ | $42.07\pm0.08^{d}$ | $-8.67\pm0.01^{b}$ | $20.83\pm0.02^{e}$ | $47.74\pm0.08^{d}$ |
| WSM | $44.47\pm0.04^{c}$ | $-1.04\pm0.01^{c}$ | $15.96\pm0.01^{c}$ | $26.54\pm0.04^{c}$ | $-4.61\pm0.01^{c}$ | $14.28\pm0.01^{c}$ | $30.49\pm0.04^{c}$ |

Values are means ± SD duplicate determinations. Value with the same superscript letter in each column was not significantly different ($p<0.05$). SPM= 100% sweet potato flour with margarine; SPS= 100% sweet potato flour with shea butter: WCS= 100% wheat flour with shea butter: WMC= 100% wheat flour with margarine: WSS= 50% wheat and sweet potato flour with shea butter: WSM= 50% wheat flour and 50% sweet potato with margarine. L represents the lightness; a represents redness); b represents yellowness.

## PROXIMATE COMPOSITION OF COOKIES SAMPLES

The proximate composition of cookies produced is presented in Table 4. Cookies produced had a moisture content ranging from 2.39 to 4.99%. Cookies samples from 100% sweet potato with margarine had the highest moisture content, and the lowest was from 100% wheat flour with shea butter. Cookies samples prepared with margarine as shortening had significantly higher moisture than cookies from shea butter. This could be due to the higher moisture and emulsification strength of margarine.

**Table 4.** Result of Proximate Composition of Cookies

| | Moisture(%) | Fat (%) | Protein(%) | Fibre (%) | Ash (%) | Carbohydrate(%) | Energy(Kcal) |
|---|---|---|---|---|---|---|---|
| SPM | $4.99\pm0.03^{a}$ | $13.19\pm1.03^{c}$ | $2.95\pm0.15^{c}$ | $2.26\pm0.04^{f}$ | $1.95\pm0.01^{b}$ | $74.66\pm1.16^{d}$ | $340.77\pm4.37^{f}$ |
| SPS | $2.89\pm0.01^{e}$ | $11.74\pm0.14^{f}$ | $2.71\pm0.03^{f}$ | $2.47\pm0.03^{e}$ | $1.99\pm0.02^{a}$ | $78.21\pm0.07^{a}$ | $356.34\pm0.48^{a}$ |
| WCS | $2.39\pm0.06^{f}$ | $13.08\pm0.15^{d}$ | $2.93\pm0.13^{d}$ | $2.78\pm0.03^{b}$ | $1.93\pm0.02^{c}$ | $76.91\pm0.27^{c}$ | $354.34\pm0.61^{c}$ |
| WMC | $3.34\pm0.37^{d}$ | $14.41\pm0.51^{a}$ | $3.53\pm0.68^{a}$ | $2.83\pm0.02^{a}$ | $1.92\pm0.01^{c}$ | $73.99\pm1.57^{f}$ | $344.91\pm0.27^{d}$ |
| WSS | $2.64\pm0.03^{e}$ | $12.41\pm0.07^{e}$ | $2.82\pm0.02^{e}$ | $2.63\pm0.04^{c}$ | $1.96\pm0.03^{b}$ | $77.56\pm1.22^{b}$ | $355.35\pm1.45^{b}$ |
| WSM | $4.16\pm0.05^{b}$ | $13.8\pm0.11^{b}$ | $3.24\pm0.05^{b}$ | $2.54\pm0.2^{d}$ | $1.93\pm0.01^{c}$ | $74.28\pm1.11^{e}$ | $342.42\pm2.14^{e}$ |

Values are means ± SD duplicate determinations. Value with the same superscript letter in each column was not significantly different ($p<0.05$). SPM= 100% sweet potato flour with margarine: SPS= 100% sweet potato flour with shea butter: WCS= 100% wheat flour with shea butter: WMC= 100% wheat flour with margarine: WSS= 50% wheat and sweet potato flour with shea butter: WSM= 50% wheat flour and 50% sweet potato with margarine.

Although, low moisture content supports longer shelf life, by preventing microbial proliferation, however, an intermediate moisture content could enhance the palatability and chewiness of cookies. On the other hand, the moisture content decreased as the percentage of wheat inclusion increases, whereas, a decrease in the percentage of sweet potato flour caused a decrease in the moisture content of cookies.

The fat, protein, crude fibre, ash and carbohydrate ranged from 11.74 to 14.41, 2.71 to 3.54, 2.26 to 2.83, 1.92 to 1.99, and 74.28 to 78.66%, respectively. The cookies sample from 100% wheat flour with margarine had the highest value of fat and the sample from 100% sweet potato with shea butter had the least value. More generally, Cookies sample prepared by using margarine as shortening had higher fat content compared to samples from shea butter. This was contrary to the work of Osunrinade et al. (30) which reported higher fat content for cakes produced from shea butter. This could be due to different treatments given to the shea butter used to produce the cake samples.

The highest protein and fibre content was obtained from cookies sample WMC (100% wheat flour with margarine), while the lowest was obtained from sample SPS (100% sweet potato with shea butter. On the contrary, the percentage of ash was higher in cookies produced from sweet potato flour when compared with wheat flour. Also, the carbohydrate content of sweet potato cookies was higher than cookies from wheat flour. Adeyeye and Akingbala (8) reported lower values for moisture, crude fibre, fat and protein of cookies sample produced with the inclusion of sweet potato flour. On the contrary, the present study had lower protein and crude fibre content only for cookies samples from sweet potato flour.

The calorific value of cookies samples ranged from 340.77 to 356.34 kCal. The highest energy value (356.34 Kcal) was obtained from cookies baked with sweet potato flour and shea butter. The range of energy value from this study was slightly lower than the 397 Kcal obtained by Adeyeye and Akingbala (8) for cookies from sweet potato flour.

## SENSORY PROPERTIES OF COOKIES PRODUCED FROM THE COMPOSITE FLOUR.

The result of the sensory evaluation of cookies is presented in Table 5. Sensorial assessment of the cookies sample showed that all parameters assessed based on a 9-point hedonic scale had values that indicated moderate, very much and extreme likeness for all the samples. However, aside from cookies texture and crunchiness, cookies produced from wheat and margarine were most liked by the sensory panellists.

**Table 5.** Sensory Acceptability of Cookies Samples

| Sample | Appearance | Texture | Crunchiness | Colour | Taste | Aroma | Overall acceptability |
|---|---|---|---|---|---|---|---|
| WMC | $8.48\pm0.18^{c}$ | $11.28\pm3.24^{a}$ | $7.8\pm0.27^{a}$ | $8.16\pm0.23^{c}$ | $8.28\pm0.22^{c}$ | $8.08\pm0.26^{a}$ | $8.88\pm0.07^{c}$ |
| SPM | $7.56\pm0.25^{ab}$ | $7.64\pm0.22^{a}$ | $7.68\pm0.29^{a}$ | $7.84\pm0.18^{ab}$ | $7.72\pm0.31^{bc}$ | $7.68\pm0.21^{a}$ | $7.76\pm0.25^{b}$ |
| WCS | $7.92\pm0.18b^{c}$ | $7.44\pm0.22^{a}$ | $7.68\pm0.26^{a}$ | $7.36\pm0.28^{ab}$ | $7.24\pm0.31^{ab}$ | $7.4\pm0.26^{a}$ | $6.96\pm0.27^{a}$ |
| WSM | $7\pm0.29^{a}$ | $7.6\pm0.28^{a}$ | $7.84\pm0.28^{a}$ | $7.12\pm0.27^{a}$ | $6.72\pm0.31^{a}$ | $7.88\pm0.24^{a}$ | $7.52\pm0.19^{ab}$ |
| SPS | $7.56\pm0.25^{ab}$ | $7.16\pm0.29^{a}$ | $7.36\pm0.28^{a}$ | $7.68\pm0.21^{ab}$ | $7.04\pm0.28^{ab}$ | $7.8\pm0.20^{a}$ | $7.8\pm0.16^{b}$ |
| WSS | $7.36\pm0.22^{ab}$ | $7.44\pm0.27^{a}$ | $7.64\pm0.26^{a}$ | $7.52\pm0.26^{ab}$ | $7.6\pm0.24^{bc}$ | $7.8\pm0.22^{a}$ | $8\pm0.20^{b}$ |

Values are means ± Standard deviation. Value with the same superscript letter in each column was not significantly different ($p<0.05$). SPM= 100% sweet potato flour with margarine; SPS= 100% sweet potato flour with shea butter: WCS= 100% wheat flour with shea butter: WMC= 100% wheat flour with margarine: WSS= 50% wheat and sweet potato flour with shea butter: WSM= 50% wheat flour and 50% sweet potato with margarine.

There was no significant difference in cookies samples that were produced either from using shea butter or margarine in appearance assessment. Although there was significant variation in colour and overall acceptability of cookies samples. Cookies produced using sweet potato and shea butter were not significantly different from the control sample ($p<0.05$) in sensorial assessment concerning texture, crunchiness and aroma.

## MULTIVARIATE ANALYSIS OF COOKIES' PHYSICAL, PROXIMATE AND SENSORY COMPONENTS

Multivariate analysis carried out using Principal Component Analysis (PCA) showed that two components accounted for 98.57% of the data variation (Table 6.0). The Variation had the first and second components as 75.69 and 22.87% respectively. As presented in Figure 1, samples produced from 100% sweet potato flour (SPM and SPS) and sample from a composite containing 50% Sweet potato using margarine as shortening (WSM) lies at the negative side of the first principal component. Whereas, samples produced from 100% Wheat flour (WCS and WMC) and the sample from composite flour using shea butter as shortening (WSS) are on the positive side of the first principal component.

The first principal component had a positive correlation with the cookies' diameter, thickness, lightness (L), yellowness (b), Fat content, protein content, ash content, energy value and all sensory parameters except aroma. This is an indication of the positive correlation of samples WCS, WMC and WSS with these parameters (34). On the other hand, cookies spread ratio, moisture, crude fibre, carbohydrate and aroma showed a negative correlation with the first principal component and thus have a correlation with samples SPM, SPS and WSM.

The cookies' hierarchical clustering analysis based on Euclidean distance (Figure 2) classified the cookies samples into four (4) groups. Samples WSM and SPM were in the same group, while samples WCS and WSS also fell into the same group. Cookies produced from sweet potato using shea butter (SPS) and wheat flour using margarine (WMC) have distinguished groups.

**Table 6.** Summary of Principal Component Analysis Value

| PC | Eigenvalue | % variance |
|---|---|---|
| 1 | 181.767 | 75.692 |
| 2 | 54.9082 | 22.865 |
| 3 | 2.7692 | 1.1532 |
| 4 | 0.508726 | 0.21185 |
| 5 | 0.186591 | 0.077701 |

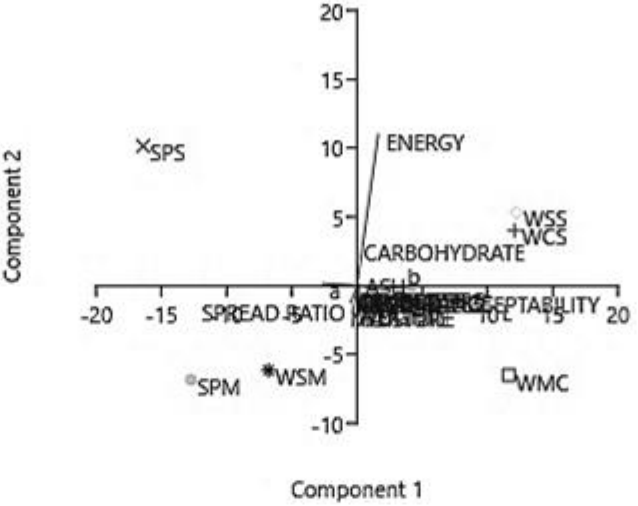

**Figure 1.** Biplot of Cookies' Physical, Proximate and Sensory Component

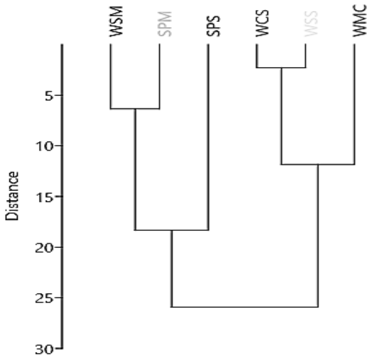

**Figure 2.** Hierarchical clustering of Cookies Samples

## CONCLUSION

This work established the possibility of producing gluten-free cookies from sweet potato flour using shea butter as shortening. Irrespective of the flour sample used, the use of shea butter as shortening led to a lower value of spread ratio of cookies. Cookies samples produced with the inclusion of wheat flour had significantly higher lightness, lower redness and higher yellowness. There was a significantly lower value for yellowness in cookies produced from sweet potatoes. Cookies samples prepared with margarine as shortening had higher fat content compared to samples produced with shea butter as shortening. For all sensory parameters assessed by the panellist, consumers moderately liked cookies produced with sweet potato using shea butter as a shortening. Hence, the production of gluten-free cookies using sweet potato flour with shea butter shortening could serve as a low-cost, nutrient-dense ready-to-eat snack.

## Conflict of Interest

There is no known conflict of interest by the author.

## REFERENCES

1. Vatanparast, H.; Islam, N.; Masoodi, H.; Shafiee, M.; Patil, R.P.; Smith, J. Time, location and frequency of snack consumption in different age groups of Canadians. *Nutr J.* **2020**, *19*(1), 85.
2. Zhao, J.; Liu, X.; Bai, X.; Wang, F. Production of biscuits by substitution with different ratios of yellow pea flour. *Grain & Oil Science and Technology*. **2019**, *2*(4), 91–96.
3. Xu, J.; Zhang, Y.; Wang, W.; Li, Y. Advanced properties of gluten-free cookies, cakes, and crackers: A review. *Trends in Food Science & Technology*. **2020**, *103*, 200–213.
4. Jan, K.N.; Panesar, P.S.; Singh, S. Optimization of antioxidant activity, textural and sensory characteristics of gluten-free cookies made from whole Indian quinoa flour. *LWT*. **2018**, *93*, 573–582.
5. Handa, C.; Goomer, S.; Siddhu, A. Physicochemical properties and sensory evaluation of fructoligosaccharide enriched cookies. *J Food Sci Technol.* **2012**, *49*(2), 192–199.
6. Chung, H.J.; Cho, A.; Lim, S.T. Utilization of germinated and heat-moisture treated brown rices in sugar-snap cookies. *LWT - Food Science and Technology*. **2014**, *57*(1), 260–266.
7. Duta, D.E.; Culetu A. Evaluation of rheological, physicochemical, thermal, mechanical and sensory properties of oat-based gluten-free cookies. *Journal of Food Engineering*. **2015**, *162*, 1–8.
8. Adeyeye, S.A.; Akingbala, J.O. Quality characteristics and acceptability of cookies from sweet potato – maize flour blends. *Nutrition & Food Science*. **2015**, *45*(5), 703–715.
9. Singh, S.; Riar, C.S.; Saxena, D.C. Effect of incorporating sweetpotato flour to wheat flour on the quality characteristics of cookies. *Afr J Food Sci.* **2008**, *2*, 65-72.
10. Giri, N.A.; Sakhale, B.K. Development of sweet potato flour based high protein and low calorie gluten free cookies. *Curr Res Nutr Food Sci.* **2019**, *30*;7(2), 427–435.
11. Saeed, S.; Ahmad, M.M.; Humaira, K.; Parveen, S.; Sharoon, M.; Abdus S. Effect of sweet potato flour on quality of cookies, *J. Agric Res.* **2012**, *50*(4), 525-538. http://rgdoi.net/10.13140/RG.2.2.28963.30249
12. Moreno-Ochoa, M.F.; Calderón de la Barca, A.M.; Cárdenas-López, J.L.; Robles-Sánchez, R.M.; Rouzaud-Sández, O. Technological Properties of Orange Sweet Potato Flour Intended for Functional Food Products as Affected by Conventional Drying and Milling Methods. *ACS Food Sci Technol.* **2023**, *17*; 3(2), 283–291.
13. Mu, T.H.; Zhang, M.; Sun, H.N.; Pérez, I.C. Chapter 10: Sweet potato staple foods. In: Sweet Potato – Chemistry, Processing and Nutrition. Thai-Hua Mu, Jaspreet Singh,. Eds.; Elsevier; 2019; pp. 273–302. https://linkinghub.elsevier.com/retrieve/pii/B9780128136379000107
14. Hossain, M.M.; Rahim, M.A.; Moutosi H.N.; Das, L. Evaluation of the growth, storage root yield, proximate composition, and mineral content of colored sweet potato genotypes. *Journal of Agriculture and Food Research*. **2022,** *8*,100289.
15. Haverkort, A.J.; Linnemann, A.R.; Struik, P.C.; Wiskerke, J.S.C. On Processing Potato 2. Survey of Products, Processes and Operations in Manufacturing. *Potato Res*. **2023**, *66*, 339-383. https://doi.org/10.1007/s11540-022-09563-y
16. Korese, J.K.; Chikpah, S.K.; Hensel, O.; Pawelzik, E.; Sturm, B. Effect of orange-fleshed sweet potato flour particle size and degree of wheat flour substitution on physical, nutritional, textural and sensory properties of cookies. *Eur Food Res Technol*. **2021**, *247*(4), 889–905.

17. Chopra, N.; Dhillon, B.; Rani, R.; Singh A. Physico-Nutritional and Sensory Properties of Cookies Formulated with Quinoa, Sweet Potato and Wheat Flour Blends. *Curr Res Nutr Food Sci.* **2018**, *6*(3), 798–806.
18. Yazar, G.; Rosell, C.M. Fat replacers in baked products: their impact on rheological properties and final product quality. *Critical Reviews in Food Science and Nutrition*. **2022**, *14*, 1–24.
19. Dapčević Hadnađev, T.; Hadnađev, M.; Pojić, M.; Rakita, S.; Krstonošić, V. Functionality of OSA starch stabilized emulsions as fat replacers in cookies. *Journal of Food Engineering*. **2015** *167*, 133–138.
20. Zuin, J.C.; Gandra, R. L. de P.; Ribeiro, A.P.B.; Ract, J.N.R.; Macedo, J.A.; Macedo, G.A. Comparing chemical and enzymatic synthesis of rich behenic lipids products: technological and nutritional potential. *Food Sci Technol*. **2022**, *42*, e105821.
21. Gruczyńska, E.; Majewska, E.; Tarnowska, K. Development of Zero Trans Baking Shortenings By Enzymatic Interesterification. *Zeszyty Problemowe Postępów Nauk Rolniczych*. **2018**, 592, 27–35.
22. Yu, D.; Qi, X.; Jiang, Y.; Zou, D.; Wang, L.; Jiang, L. Preparation of Margarine Stock Rich in Naturally Bioactive Components by Enzymatic Interesterification. *J Oleo Sci.* **2018**, *67*(1), 29–37.
23. Gharaie, Z.; Azizi, M.H.; Barzegar, M.; Ahmadi Gavlighi H. Gum tragacanth oil/gels as an alternative to shortening in cookies: Rheological, chemical and textural properties. *LWT*. **2019**, 105, 265–271.
24. Marcus, J.B. Chapter 2 - Food Science Basics: Healthy Cooking and Baking Demystified. The Science behind Healthy Foods, Cooking and Baking. In *Culinary Nutrition*; Marcus, J.B. Ed. Academic Press, 2013. p. 51–97. https://doi.org/10.1016/B978-0-12-391882-6.00002-9
25. Choungo Nguekeng, P.B.; Hendre, P.; Tchoundjeu, Z.; Kalousová, M.; Tchanou Tchapda, A.V.; Kyereh, D. The Current State of Knowledge of Shea Butter Tree (Vitellaria paradoxa C.F. Gaertner) for Nutritional Value and Tree Improvement in West and Central Africa. *Forests*. **2021**, *12*(12), 1740.
26. Nahm, H.S.; Juliani, H.R.; Simon, J.E. Chapter 12 - Quality Characteristics of Shea Butter, *Vitellaria paradoxa*. In: *African Natural Plant Products Volume II: New Discoveries in Chemistry, Health and Nutrition*, Edition: Symposium Series 1127, Juliani, H.R.; Simon, J.E.; Ho C.T. Eds. ACS, Washington, D.C. 2013, p. 167–184. pubs.acs.org/doi/abs/10.1021/bk-2013-1127.ch012
27. Aneni, T.I.; Adaigbe, V.C.; Eziashi, E.I.; Esiegbuya, O.D. Insect Pest Management of Post Harvest Shea Fruits in Storage. *IJFSA*. **2020**, *4*(3), 330–337.
28. Tsado, E.K.; Adesina, O.A.; Adediran, O.A.; Saidu, A.; Jiya, M.J.; Lawal, L.T. Effect of using Vegetable Oils - Shea Butter (Vitellaria paradoxa) Oil and Coconut Oil as Waxing Material for Cucumber (Cucumis sativus L.) Fruits. *Direct Research Journal of Agriculture and Food Science*, **2019**, 7(6), 122-130. http://doi.org/10.5281/zenodo.3236134
29. Rousseau, K.; Gautier, D.; Wardell, D.A. Coping with the Upheavals of Globalization in the Shea Value Chain: The Maintenance and Relevance of Upstream Shea Nut Supply Chain Organization in Western Burkina Faso. *World Development*. **2015**, *66*, 413–427.
30. Osunrinade, O.A.; Azeez, A.O.; Babalola, K.A.; Bamisaye, Y.O. Physical, Proximate and Sensory Properties of Cake Produced using Shea Butter as Shortening. *TOFSJ*. **2020**, *12*(1), 18–23.
31. Herforth, A.; Bai, Y.; Venkat, A.; Mahrt, K.; Ebel, A.; Masters, W.A. Cost and affordability of healthy diets across and within countries. FAO Agricultural Development Economics Technical Study No. 9. Rome, FAO. 2020. https://www.fao.org/3/cb2431en/cb2431en.pdf
32. AOAC. Official method of Analysis. 18th ed. Association of Officiating Analytical Chemists, Washington DC; 2005.
33. Pereira, D.; Correia, P.M.R.; Guiné, R.P.F. Analysis of the physical-chemical and sensorial properties of Maria type cookies. *Acta Chimica Slovaca*. **2013**, *6*(2), 269–280.
34. Olawoye, B.; Gbadamosi, S.O. Influence of processing on the physiochemical, functional and pasting properties of Nigerian Amaranthus viridis seed flour: a multivariate analysis approach. *SN Appl Sci*. **2020**, *2*(4), 607. https://doi.org/10.1007/s42452-020-2418-8

APTEFF, Vol. 54, 1-335 (2023)
DOI: https://doi.org/10.2298/APT2354177K
UDC: 633.822+615.451.1:615.212:616.155.18
BIBLID: 1450-7188 (2023) 54, 177-186

Original scientific paper

# BIOLOGICAL ACTIVITIES OF *MENTHA SPICATA* L. EXTRACTS GROWING IN DIFFERENT GEOGRAPHICAL REGIONS OF ALGERIA

*Abdelbasset KADDOUR[1]*, Ahmed Elkhalifa CHEMSA[1,2], Hacen LAOUEDJ[1,3], Djilani Ghemam AMARA[1,3], Younes MOUSSAOUI[4,5], Nezar CHERRADA[1,2], Abdelmalek ZAATER[6]*

[1] El Oued University, Faculty of Life and Natural Sciences, Department of Biology, Algeria.
[2] El Oued University, Laboratory of Biodiversity and Application of Biotechnology in Agriculture, Algeria.
[3] El Oued University, Laboratory of Biology, Environment and Health, Algeria.
[4] Laboratory of Organic Chemistry (LR17ES08), Faculty of Sciences of Sfax, University of Sfax, Tunis.
[5] Faculty of Sciences of Gafsa, University of Gafsa, Tunis.
[6] El Oued University, Faculty of Life and Natural Sciences, Department of Agronomy, Algeria.

**Received: 19 April 2023** **Revised: 04 May 2023** **Accepted: 07 May 2023**

*By understanding all the components of plants, especially medicinal ones, our goal is to discover plant-derived alternatives to antibiotics. This research aims to contribute to the knowledge of the biological activities Mentha spicata (MS) extracts and their effects under different environmental conditions. Hemolysis, analgesic, anti-inflammatory and antimicrobial activities were estimated of aqueous extracts of Mentha spicata. The results showed that MS El Oued extract protected the erythrocytes from hemolysis, while MS El Taref extract showed a lower protection capability. The results showed high levels of anti-inflammatory activity from plants found in the northeastern region (Tebessa and El Taref) compared to the southeast region (El Oued). They showed that MS El Oued extract exhibited higher analgesic activity (32.46%) compared to MS Tebessa, and MS El Taref extracts (19.48 and 12.97%, respectively). The results showed the antimicrobial activity, the inhibition diameter was between 17.4 - 25mm, and the largest diameter of all extracts was recorded against Aspergillus niger from the MS El Taref extract and the lowest against Staphylococcus aureus from the MS El Oued extract. The MS El Taref extract had the highest levels of activity against Aspergillus niger and Staphylococcus aureus and the MS Tebessa extract had the highest levels against Pseudomonas aeruginosa and Escherichia coli. The activity levels against Candida lipolytica, were found to be equal. In conclusion, the environmental conditions had an influence on the bioactive substances present in the plants. These bioactive substances directly influenced the biological activities of the plant extracts.*

**Keywords**: *Mentha spicata*, antimicrobial activity, analgesic, hemolysis, anti-inflammatory.

## INTRODUCTION

*Mentha spicata* L. commonly known as spearmint (1) is an aromatic and medicinal plant of the *Lamiaceae* family, genus *Mentha* (2). Spearmint is spread across North America, Australia, Europe, and Africa (3). Nowadays, spearmint is widely distributed, including eighteen species, with eleven naturally occurring and grown in most regions of the world (4,5). *M. spicata* is a perennial herb with a creeping rhizome, its leaves have a characteristic aromatic odor and a pungent taste (5). They are used as a carminative and to treat flatulence, in food preparation, as confectionery, and as chewing gum (6). Additionally, they are

---

* Corresponding author: Abdelbasset KADDOUR, El Oued University, Faculty of Life and Natural Sciences, Department of Biology, Algeria. E-mail: bastitourek@gmail.com

used as a flavoring agent in tea (1). Daniela et al. (7) indicated that the *Lamiaceae* family could have the antioxidant properties because its richness of the phenolic compounds. According to Tawaha et al. (8) who demonstrated that *M. spicata* has high antioxidant activity due to its flavonoid content. Additionally, spearmint has many biological uses, such as in insecticides, antimicrobials (2), and anti-inflammatory applications (9). The biological properties of spearmint extracts can be influenced by climatic conditions and soil type (10, 11). According to Kaddour et al. (12) who demonstrated that soil type and climatic factors can strongly influence on bioactive substances of *M. spicata* plants. Algeria is characterized by a great diversity in terrain, climate, and soil, encompassing multiple climatic ranges. It boasts a significant vegetation cover, which includes numerous types of medicinal plants. The economic potential of spearmint is considerable, and the influence of climatic and soil factors on the plant's compounds is of utmost importance. Many studies have shown that the production of secondary metabolites and different biological activities in the plants depends on factors such as the harvest season, soil fertility, and geographic location (13, 14, 15). The aforementioned factors can have an impact on the content of secondary metabolites in *M. spicata*. Consequently, variations in temperature and precipitation throughout different seasons can be attributed to the marked variations in the activity of active substances observed in various species of medicinal plants. In this context, temperature and the amount of sunlight are significant factors that greatly influence the phytochemical and rate of secondary metabolite production in mints. Therefore, our study aimed to investigate and evaluate the diverse biological activities exhibited by extracts of *M. spicata* grown in various geographical regions of Algeria.

## EXPERIMENTAL

### MATERIALS AND INSTRUMENTS

The following compounds were used in the study: carrageenan, paracetamol, gentamicin, chloride sodium (NaCl), phosphate buffer solution (PBS), EDTA, acetic acid, dimethyl sulfoxide (DMSO), and hydrogen peroxide ($H_2O_2$). These compounds were obtained from Sigma-Aldrich.

### PLANT SAMPLING AND EXTRACT PREPARATION

*Mentha spicata* leaves were collected in the spring from three regions of Algeria: El Oued in the southeast (Sahara), Tebessa in the northeast of Algeria, and El Taref region in the far northeast. The plant material was rinsed several times to remove sand and impurities. It was dried at room temperature and converted to a fine-texture powder. To obtain the extract, 10g of the powdered plant material was mixed with 100mL of distilled water. The mixture was subjected to magnetic stirring for 12 hours at a temperature of 25 °C (±2 °C). Afterward, the mixture was filtered using Whatman paper, and the resulting filtrate was concentrated using a rotavapor. The aqueous extract obtained was stored in brown bottles at temperature of 4 °C.

## DETERMINATION OF HEMOLYSIS ACTIVITY

The effect of the *M. spicata* extracts on the erythrocytes hemolysis was determined according to method Rjeibi et al. (16) using $H_2O_2$ as an oxidative stress inducer. The erythrocytes were obtained by centrifugation of 15mL of fresh blood in EDTA (1000 rpm). Then, they were suspended in the phosphate buffer solution (PBS;10 mM, pH 7.4). The erythrocytes were centrifuged at 4500 rpm in temperature of 4 °C during 10 min. After, the erythrocytes were washed three times and diluted in PBS to give a 2% (w/v) solution. Different concentrations of aqueous extracts of *M. spicata* were used (0.25 to 2 mg/mL) in the PBS and were mixed with 500 µL of $H_2O_2$ (7.5 mM) to induced hemolysis. After 60 minutes of incubation at 37 °C, the absorbance of the solution was measured at 540 nm. Vitamin C was used as a positive control. Hemolysis inhibition was evaluated with the following equation:

$$\text{Inhibition } (\%) = [(1 - (\text{Absorbance of sample} / \text{Absorbance of control})] \times 100$$

## DETERMINATION OF ANALGESIC ACTIVITY

According to study of Florentino et al. (17), the analgesic activity was evaluated using six groups of rats as tested subjects. The first group served as a negative control and received an injection of 0.1% acetic acid in a saline solution at a dose of 10 mL/kg body weight. Four groups of tested rats were orally administered the aqueous extracts of *M. spicata* harvested from the three different regions at doses ranging from 50 to 100 mg/kg body weight. After one hour, all groups received an intraperitoneal injection of 0.1% acetic acid in saline at a dose of 10 mL/kg body weight. The sixth group, which served as the positive control, received a dose of paracetamol (10 mg/kg body weight) one hour prior to the acetic acid injection.

$$\text{Inhibition\%} = [(\text{Nte} - \text{Nt}) / \text{Nte}] \times 100$$

where: Nte means the writhing number of the negative control and Nt means the writhing number of the test lot or the positive control.

## DETERMINATION OF ANTI-INFLAMMATORY ACTIVITY

The anti-inflammatory activity was evaluated using carrageenan-induced paw edema. The rats were divided into four groups. The first group received an injection of 50 µL of carrageenan (1% carrageenan in 0.9% NaCl) in the plantar hind legs. The other groups (II, III, IV) were orally administered the aqueous extracts of *M. spicata* (100 mg/kg body weight in 0.9% NaCl) 60 minutes prior to the carrageenan injection.

The paw volumes (in mm) were measured using a digital caliper at 60, 120, 180, 240, and 300 minutes after the carrageenan injection (18). The percentage of inhibition was evaluated using the following equation:

$$\text{Inhibition\%} = [(P_0 - P_1) / P_0)]$$

where P1 represents the size of paw edema obtained at different time intervals, and P0 represents the size of paw edema obtained before the injection.

### DETERMINATION OF ANTIMICROBIAL ACTIVITY

The antimicrobial activity was assessed using the disc diffusion method. For this, 100 mg of the aqueous extracts of *M. spicata* were dissolved in 1000 µL of dimethyl sulfoxide (100%). A suspension of microorganisms was prepared with 200 µL of the culture: $10^6$ CFU/mL of bacterial cells and $10^8$ spores/mL of fungal strains (measured using a Malassez slide). The bacterial culture was placed on PCA medium, while the fungal strains were placed on PDA medium.

Wells with a diameter of 7 mm were filled with 100 µL of the *M. spicata* extracts (100 mg/mL). Additionally, one well containing 100 µL of dimethyl sulfoxide (without extract) was used as a negative control. Gentamicin was used as a positive control. The Petri dishes were stored at 4 °C for one hour, followed by incubation at 37 °C for 24 hours for the bacterial cells and at 30 °C for 72 hours for the fungal strains.

The antimicrobial activity was evaluated by measuring the diameter of the inhibition zones (in mm). The values were obtained from three replicate measurements.

### MICROORGANISMS USED

Antimicrobial activity of the aqueous extracts of *M. spicata* harvested from three regions (Tebessa, El Taref, and El Oued) was tested against three strains of the bacterial cells: the gram-negative bacilli were *Escherichia coli* (*CTM 50 227*) and *Pseudomonas aeruginosa* (*CTM 50 238*), while the gram-positive cocci was *Staphylococcus aureus* (*CTM 50 041*). The fungal strains tested were *Candida lipolytica* (*CTM 30 027*) and *Aspergillus niger (CTM 10 099*).

### STATISTICAL ANALYSIS

A statistical analysis was conducted on the average of three repetitions to assess the dispersion of the data using the standard deviation (SD) as a measure. To compare the means, the data obtained from the study on antibacterial activities underwent variance analysis (ONE-Way ANOVA) in Excel. Additionally, a least significant difference (LSD) multiple comparison test was performed to determine the significance levels of these differences, with a confidence level of $P < 0.05$.

## RESULTS AND DISCUSSIONS

### HEMOLYSIS INHIBITION ACTIVITY

The hemolysis effects increased in direct proportion to the concentration of *M. spicata* extracts. At concentration 400 ug/mL, the hemolysis activity of aqueous extracts of *M. spicata* extracts was classified as follows: *M. spicata* extract harvested from El Oued region > *M. spicata* extract harvested from Tebessa region > *M. spicata* extract harvested from El Taref region. In addition, the results were consistent to previous researchers published studies (19, 20). Moreover, the difference of hemolysis activity of aqueous extracts of *M. spicata* harvested from different regions may be related to the contents of the chemical compounds present in the plants (21). Study by Ebrahimzadeh et al. (22) demonstrated that the difference of the hemolysis activity is due to geographic location and environmental conditions.

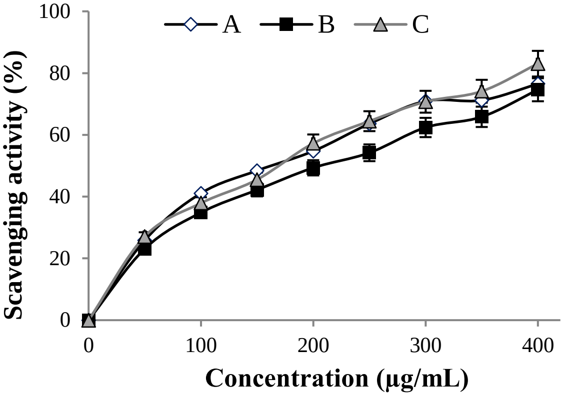

**Figure 1.** Profile of hemolysis inhibition test of aqueous extracts of *M. spicata* harvested from the different regions in Algeria.
(A: Tebessa, B: El Taref, C: El Oued). Results are expressed as Mean ± Standard Deviation (SD).

### ANALGESIC ACTIVITY

Injection of acetic acid in rats causes local irritation and leads to the secretion of several chemical mediators, resulting in inflammation. The researchers Park et al. (23) explained that injection of acetic acid in rats may cause abdominal contortions and the release of chemical mediators such as prostaglandins (PGE2α, PGF2α), histamine, and serotonin. Paracetamol appears to act on pain mechanisms by intervening in the biosynthesis of prostaglandins (24).

**Table1**. Analgesic activity of aqueous extracts *of M. spicata* harvested from three regions in Algeria (Tebessa, El Taref and El Oued)

| Treatment | Dose | Number of contortions (30min) | Inhibition (%) |
|---|---|---|---|
| Control (0.1% acetic acid) | 10 mL/kg | 30.8± 3.85 | - |
| Paracetamol | 1 mg/kg | 17.2±1.83* | 44.15 |
| *MS* extract of Tebessa | 150 µg/kg | 24.8±2.49* | 19.48 |
| *MS* extract of El Taref | 150 µg/kg | 26.8±0.69 * | 12.97 |
| *MS* extract of El Oued | 150 µg/kg | 20.8±1.83* | 32.46 |

Values are expressed as the mean ± SD. * $p < 0.05$, indicates a significant difference compared to the control group.

The obtained results demonstrated that aqueous extracts of *M. spicata* reduced the number of abdominal contortions in a dose-dependent and significant manner. This suggests that the analgesic effect of aqueous extracts of *M. spicata* could be linked to the prevention of the release of chemical mediators, specifically by inhibiting the synthesis of prostaglandins. Additionally, the extract harvested from the El Oued region showed the highest analgesic activity. The researchers (25) demonstrated that flavonoids present in plants can reduce inflammation by inhibiting prostaglandin secretion or by competitively binding with ATP at catalytic sites on enzymes, resulting in the inhibition of kinases. Additionally, a study by Correa et al. (26) showed that plants containing saponins have the ability to inhibit prostaglandins.

## ANTI-INFLAMMATORY ACTIVITY

Inflammation is an innate physiological defense mechanism employed by the immune system to expel toxins and pathogens. To investigate the potential anti-inflammatory effect of plant extracts, a model of acute inflammation known as carrageenan-induced foot edema in rats was utilized (27). Figure 2 presents the anti-inflammatory activity of aqueous extracts of *M. spicata* harvested from different regions in Algeria (Tebessa, El Taref, and El Oued).

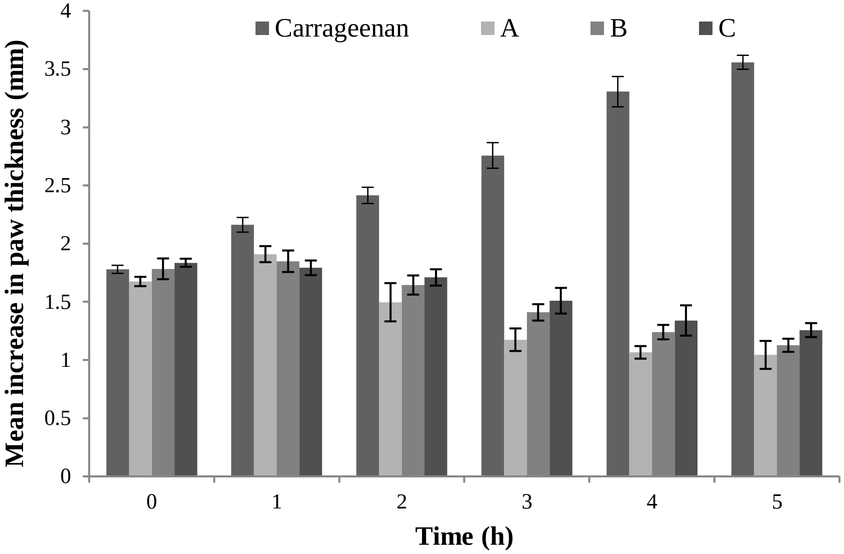

**Figure 2.** Profile of the anti-inflammatory activity of aqueous extracts of *M. spicata* harvested from different regions in Algeria: Tebessa (A), El Taref (B), and El Oued (C).

The obtained results demonstrate that *M. spicata* plants show promising potential as a source of bioactive components with significant anti-inflammatory activity. Initially, the percentage of inhibition by the aqueous extracts from the three regions was similar, but it increased after one hour. Furthermore, the anti-inflammatory activity was higher for the extracts of *M. spicata* harvested from the Tebessa and El Taref regions, with a percentage of inhibition of 70.78% and 68.54%, respectively. Actually, the appearance of edema was due to the injection of carrageenan, which leads to an acute and local response that stimulates the production of several immune elements acting as inflammatory mediators, such as histamine, bradykinin, and serotonin (28). As a result, there is an expansion and increased permeability of blood vessels, as well as infiltration of inflammatory cells into the tissue. Additionally, at a later stage, prostaglandins, cytokines (such as TNF-α and IL-6), chemokines, and enzymes (such as COX-2 and iNOS) may be formed and secreted (29). Study by Lin et al. (30) declared that the cytokines are influenced by the inhibition of inflammatory cells, induction of several proteins, and cytotoxicity. Other researchers (31) confirmed that the phytochemicals are produced in plants under stress. Also, an inverse relationship between the anti-inflammatory, the antioxidant activities and the content of phenols of the plants, was found by Correa et al. (26).

## ANTIMICROBIAL ACTIVITY

The results of the antimicrobial activity are presented in Table 2, and the values shown are the averages of three measurements. The antimicrobial activities of aqueous extracts of *M. spicata* harvested from three regions were estimated by measuring the diameter of the zone of inhibition around the wells containing the extracts, which were tested against the microorganisms. Additionally, the diameters of the zone of inhibition varied depending on the type of bacteria and the extracts used. Although there are discrepancies in the average inhibition disc values, the results of the ANOVA statistical analysis and the least significant difference test (LSD) indicate that there are no significant differences between the extracts from the different regions.

**Table 2**. Diameters of inhibition of the antimicrobial activity of aqueous extracts of *Mentha spicata* harvested from different regions in Algeria.

| **Microorganisms** | **Diameter of inhibition** | | | | | |
|---|---|---|---|---|---|---|
| | Tebessa | El Taref | El Oued | Gentamicin | LSD | DMSO |
| *Pseudomonas aeruginosa* | $23\pm1.3^{b}$ | $20\pm0.3^{b}$ | $20\pm3.2^{b}$ | $28\pm2.1^{a}$ | 4.34 | No inhibition |
| *Escherichiacoli* | $20\pm1.2^{b}$ | $17.5\pm0.4^{b}$ | $18.7\pm3.3^{b}$ | $29\pm2.2^{a}$ | 6.02 | No inhibition |
| *Staphylococcus aureus* | 21±3.3 | 21.4±2.4 | 17.4±1.5 | 21±3.3 | / | No inhibition |
| *Aspergillus niger* | $22\pm0.1^{b}$ | $25\pm2.4^{b}$ | $24\pm1.5^{b}$ | $31\pm4.3^{a}$ | 4.45 | No inhibition |
| *Candida lipolytica* | $20\pm1.7^{b}$ | $20\pm2.2^{b}$ | $19.4\pm0.6^{b}$ | $28\pm1.3^{a}$ | 4.72 | No inhibition |

According to Chalker Scott (32), it has been confirmed that plants from the *Lamiaceae* family have demonstrated protective properties against a variety of microorganisms due to their rich content of phenolic compounds. The significant antimicrobial effect of *M. spicata* extracts is attributed to their high antimicrobial activity, primarily due to the presence of essential oils (33, 34). Furthermore, the results indicated that the aqueous extract of *M. spicata* harvested from the El Taref region exhibited higher antifungal activity compared to the other extracts. Some researchers suggested that the variation in anti-fungal activity can be attributed to the flavonoid content (35, 36). Also, several studies have confirmed that antimicrobial activity can be influenced by meteorological factors and external environmental changes, such as temperature (37, 38, 39).

In addition, the results indicate that the aqueous extract of *M. spicata* harvested from the Tebessa region has a higher antibacterial activity against *P. aeruginosa*, *E. coli*, and *S. aureus* bacteria compared to the extracts from El Oued and El Taref. Tebessa is a high-altitude area, 1040 m above sea level, with a very dry and warm climate, and weather conditions play a crucial role in the production of official substances (40). A study by Ullah et al. (41) explained that the increased antibacterial activity of *M. spicata* plants is associated with higher altitudes of the harvested plant areas, where temperatures decrease and the production of secondary metabolites increases. Another study by Fenghour et al. (40) reported that the essential oil of *Eucalyptus camaldulensis* and *Artemisia herba alba*, harvested from the Tebessa region, exhibits the highest antibacterial activity against *E. coli* and *S. aureus*.

## CONCLUSION

Algeria is rich in climatic and soil diversity. This diversity is seen and represented by great vitality at the species level. The study reflects this vitality with the results indicating great biochemical diversity in *M. spicata* harvested from different regions in Algeria (El Oued, El Taref, and Tebessa) as confirmed by the obtained results. The extracts showed high degrees of efficacy in the tested activities. Extracts of *M. spicata* harvested from El Oued region achieved superiority in analgesic and hemolysis activities, while the extracts of *M. spicata* harvested from El Taref and Tebessa regions achieved superiority in both anti-inflammatory and antimicrobial activities. These results confirm the significant role of climate and soil factors in biodiversity at the molecular level used in medical and functional foods applications.

## REFERENCES

1. Mahendran, G.; Verma, S.K.; Rahman, L.U. The traditional uses, phytochemistry and pharmacology of spearmint (*Mentha spicata* L.). *J. Ethnopharmacol*. **2021**, *278*, 114266.
2. Scherer, R.; Lemos, M.F.; Martinelli, G.C.; Martins, J.D.L.; da Silva, A.G. Antioxidant and antibacterial activities and composition of Brazilian spearmint (*Mentha spicata* L.). *Indus. Cro. Prod*. **2013**, *50*, 408-413.
3. Mahboubi, M. *Mentha spicata* as natural analgesia for treatment of pain in osteoarthritis patients. *Ther. Clin. Pract.* **2017**, *26*, 1-4.
4. Aprotosoaie, A.C.; Ciocarlan, N.; Brebu, M.; Trifan, A.; Grădinaru, A.C.; Miron, A. Chemical composition, antioxidant and antimicrobial activities of Mentha gatte fosseimaire essential oil. *Farmacia*. **2018**, *66*(5), 778-782.
5. Kee, L.A.; Shori, A.B.; Baba, A.S. Bioactivity and health effects of *Mentha spicata*. *Food NutrMetab*. **2017**, *5*(1), 1-2.
6. Mahboubi, M. *Mentha spicata* L. essential oil, phytochemistry and its effectiveness in flatulence. *J. Tradit. Complement. Med*. **2018**, 1-7.
7. Vlase, L.; Benedec, D.; Hanganu, D.; Damian, G.; Csillag, I.; Sevastre, B.; Tilea, I. Evaluation of antioxidant and antimicrobial activities and phenolic profile for *Hyssopus officinalis*, *Ocimum basilicum* and *Teucrium chamaedrys*. *Molecules*. **2014**, *19*(5), 5490-5507.
8. Tawaha, K.A.; Hudaib, M.M. Chemical composition of the essential oil from flowers, flower buds and leaves of *Thymus capitatus Hoffmanns*. & Link from Jordan. *J. Essent. Oil-Bear. Plants.* **2012**, *15*(6), 988-996.

9. Kiselova, Y.; Ivanova, D.; Chervenkov, T.; Gerova, D.; Galunska, B. Correlation between the in vitro antioxidant activity and polyphenol content of aqueous extracts from Bulgarian herbs. *Phytother Res*, **2006**, *20*, 961-965.
10. Shanjani, P.S.; Mirza, M.; Calagari, M.; Adams, R.P. Effects drying and harvest season on the essential oil composition from foliage and berries of *Juniperusexcelsa*. *Ind. Crops Prod*. **2010**, *32*(2), 83-87.
11. Butkiene, R.; Mockute, D. The variability of the essential oil composition of wild *Ledum palustre* L. shoots during vegetation period. *J. Essent. Oil. Res*. **2011**, *23*(1), 9-13.
12. Kaddour, A.; Ghemam-Amara, D.; Moussaoui, Y.; Chemsa, A.E.; Alia, Z.; Kamarchou, A.Total phenolic and flavonoid contents of *Mentha spicata* leaves aqueous extracts in different regions of Algeria and their antioxidant, and antidiabetic activities. *TJPR*. **2022**, *21*(9), 1907-1913.
13. Ahmed, S.; Griffin, T.S.; Kraner, D.; Schaffner, M.K.; Sharma, D.; Hazel, M.; Cash, S.B. Environmental factors variably impact tea secondary metabolites in the context of climate change. *Front. Plant. Sci*. **2019**, *10*, 939.
14. Li, Y.; Kong, D.; Fu,Y.; Sussman, M.R.; Wu, H. The effect of developmental and environmental factors on secondary metabolites in medicinal plants. *Plant Physiol. Biochem*. **2020**, *148*, 80-89.
15. Liu, W.;Yin, D.; Li, N.; Hou, X.;Wang, D.; Li, D.; Liu, J. Influence of environmental factors on the active substance production and antioxidant activity in *Potentilla fruticosa* L. and its quality assessment. *Scientific reports*. **2016**, *6*(1), 1-18.
16. Rjeibi, I.; Feriani, A.; Hentati, F.; Hfaiedh, N.; Michaud, P.; Pierre, G. Structural characterization of water-soluble polysaccharides from *Nitraria retusa* fruits and their antioxidant and hypolipidemic activities. *Int. J. Biol. Macromol*. **2019**, *129*, 422-432.
17. Florentino, I.F.; Nascimento, M.V.M.; Galdino, P.M.; Brito, A.F.; Rocha, F.F.; Tonussi, C.R.; Costa, E.A. Evaluation of analgesic and anti-inflammatory activities of *Hydrocotyle umbellata* L., Araliaceae (acariçoba) in mice. *An. Acad. Bras. Cienc*. **2013**, *85*, 987-997.
18. Khalid, A.; Khan, I.; Khan, A.; Shafie, S.; Tlili, I. Case study of MHD blood flow in a porous medium with CNTS and thermal analysis. *Case Stud. Therm. Eng*. **2018**, *12*, 374-380.
19. Hajji, M.; Jarraya, R.; Lassoued, I.; Masmoudi, O.; Damak, M.; Nasri, M. GC/MS and LC/MS analysis and antioxidant and antimicrobial activities of various solvent extracts from *Mirabilis jalapa* tubers. *Process Biochem*. **2010**, *45*(9), 1486-1493.
20. Louerrad, Y.; Haddi, R.; Kaid, H.M. Etude de la peroxydation lipidique chez une plante médicinale *Haloxylon scoparium Pomel*. *J. Biores,* **2016**, *1*, 28-33.
21. Rocha, S.; Costa, E.; Coimbra, S.; Nascimento, H.; Catarino, C.; Rocha-Pereira, P.; Santos-Silva, A. Linkage of cytosolic peroxiredoxin 2 to erythrocyte membrane imposed by hydrogen peroxide-induced oxidative stress. *Blood Cells Mol Dis*. **2009**, *43*(1), 68-73.
22. Ebrahimzadeh, M.A.; Pourmorad, F.; Hafezi, S.; Antioxidant activities of Iranian corn silk. *Turk. J. Biol.* **2008**, *32*(1), 43-49.
23. Park, H.J.; Cha, H.C. Flavonoids from leaves and exocarps of the grape Kyoho. *KJBS*. **2003**, *7*(4), 327-330.
24. Yougbaré-Ziébrou, M.N.; Ouédraogo, N.; Lompo, M.; Bationo, H.; Yaro, B.; Gnoula, C.; Guissou, I P. Anti-inflammatory, analgesic and antioxidant activities of an aqueous extract of *Saba senegalensis Pichon* stems with leaves (Apocynaceae). *Phytothérapie*. **2016**, *14*, 213-219.
25. Muley, M.M.; Krustev, E.; Mc Dougall, J.J. Preclinical assessment of inflammatory pain. *CNS Neurosci. Ther*. **2016**, *22*(2), 88-101.
26. Correa , A.S.; ALMEIDA, V.L.; Lopes, B.; Franco, A.; MATOS, F.R.; Quintans-Junior, L.J.; Paranhos, L.R. The influence of non-steroidal anti-inflammatory drugs and paracetamol used for pain control of orthodontic tooth movement: a systematic review. *An. Acad. Bras. Cienc.* **2017**, *89*, 2851-2863.
27. Soro, T.Y.; Traore, F.; Sakande, J. Activité analgésique de l'extrait aqueux de *Ximenia americana* (Linné)(Olacaceae). *C. R. Biol.* **2009**, *332*(4), 371-377.

28. Tamokou, J.D.D.; Mbaveng, A.T.; Kuete, V. Antimicrobial Activities of African medicinal Spices and Vegetables, Medicinal Spices and Vegetables from Africa: *Therapeutic Potential against Metabolic, Inflammatory, Infectious and Systemic Diseases. Academic Press.* **2017**, 207-237.
29. Coura, C.O.; Souza, R.B.; Rodrigues, J.A.G.; Vanderlei, E.D.S.O.; de Araújo, I.W.F.; Ribeiro, N.A.; Benevides, N.M.B. Mechanisms involved in the anti-inflammatory action of a polysulfated fraction from Gracilaria cornea in rats. *PLoS One*. **2015**, *10*(3), e0119319.
30. Lin, Y.Y.; Lin, S.C.; Feng, C.W.; Chen, P.C.; Su, Y.D.; Li, C.M.; Wen, Z.H. Anti-inflammatory and analgesic effects of the marine-derived compound excavatolide B isolated from the culture-type Formosan gorgonian *Briareum excavatum*. *Mar. Drugs.* **2015**, *13*(5), 2559-2579.
31. Jin, Q.; Lee, C.; Lee, J.W.; Yeon, E.T.; Lee, D.; Han, S.B.; Hwang, B.Y. 2-Phenoxychromones and prenylflavonoids from *Epimedium koreanum* and their inhibitory effects on LPS-induced nitric oxide and interleukin-1β production. *J. Nat. Prod.* **2014**, *77*(7),1724-1728.
32. Chalker Scott, L. Environmental significance of anthocyanins in plant stress responses. *Photochem. Photobiol.* **1999**, *70*(1), 1-9.
33. Kumar, S.; Yadav, A.; Yadav, M.; Yadav, J.P. Effect of climate change on phytochemical diversity, total phenolic content and in vitro antioxidant activity of *Aloe vera* (L.) Burm. f. *BMC Res. Notes.* **2017**, *10*(1), 1-12.
34. Gortzi, O.; Lala, S.; Chinou, I.; Tsaknis, J. Evaluation of the antimicrobial and antioxidant activities of *Origanum dictamnus* extracts before and after encapsulation in liposomes. *Molecules.* **2007**, *12*(5), 932-945.
35. Giordani, R.; Hadef, Y.; Kaloustian, J. Compositions and antifungal activities of essential oils of some Algerian aromatic plants. *Fitoterapia*. **2008**, *79*(3), 199-203.
36. Yakhlef, G.; Laroui, S.; Hambaba, L.; Aberkane, M.C.; Ayachi, A. Évaluation de l’activité antimicrobienne de *Thymus vulgaris* et de *Laurus nobilis*, plantes utilisées en médecine traditionnelle. *Phytothérapie*. **2011**, *9*(4), 209-218.
37. Merghache, D.; Boucherit-Atmani, Z.; Boucherit, K. Évaluation de l’activité antifongique de différents extraits de la cannelle de Chine (*Cinnamomum cassia*). *Phytothérapie*. **2012**, *10*(4), 215-221
38. Yala, J.F.; Ntsameso-Mve-Mba, V.; Issembe, Y.A.; Lepengue, N.A.; Souza, A. Évaluation in vitro de l’activité antimicrobienne de l’extrait aqueux d’*Eryngium foetidium* récolté dans la ville de Franceville. *J. Appl. Biosci*. **2016**, *103*, 9886-9893.
39. Lusby, P.E.; Coombes, A.; Wilkinson, J.M .Honey : A potent agent for wound activity. *Asian Pac. J. Trop. Biomed.* **2002**, *1*, 154-160
40. Fenghour, H.; Bouabida, H.; Dris, D.; Houhamdi, M. Antibacterial effect of essential oils of two plants *Eucalyptus camaldulensis* and *Artemisia herba alba* on some bacterial strains. *Biosyst. Divers.* **2021**, *29(2)*,73-77.
41. Ullah, N.; Khurram, M.; Amin, M.U.; Khan, T.A.; Khayyam, S.U.; Khan, F.A.; Ullah, S. Impact of geographical locations on *Mentha spicata* antibacterial activities.*J. Med. Plant Res.* **2012**, *6(7)*, 1201-1206.

APTEFF, Vol. 54, 1-335 (2023) UDC: 582.628+631.576.4]:628.35
DOI: https://doi.org/10.2298/APT2354187N BIBLID: 1450-7188 (2023) 54, 187-196

Original scientific paper

# WALNUT SHELLS AS A POTENTIAL BIOSORBENT FOR Cu(II), Pb(II) AND As(III)/(V) IONS REMOVAL FROM RIVER WATERS

*Maja M. NUJKIĆ*, Žaklina Z. TASIĆ, Dragana V. MEDIĆ, Snežana M. MILIĆ, Sonja S. STANKOVIĆ*

University of Belgrade, Technical Faculty in Bor, Vojske Jugoslavije 12, 19210 Bor, Serbia

**Received: 07 April 2023** **Revised: 06 June 2023** **Accepted: 09 June 2023**

*In this study, the potential of the walnut shell as a biosorbent for biosorption of Cu(II), Pb(II), and As(III)/(V) ions from river water samples was investigated. The effects of various conditions of water samples such as the initial ion concentration, sample pH, and contact time at a constant temperature and biosorbent dosage, on biosorption of Cu(II), Pb(II), and As(III)/(V) were investigated. Walnut shells, as the material with a high potential for removal of investigated ions, have biosorption efficiency of up to 99.6%, under the applied experimental conditions. The best adsorption time was obtained at 4 h for Cu(II), Pb(II), and As(III)/(V) ions. The maximum removal of 97.6% (Cu(II)), 82.9% (Pb(II)), and 99.6% (As(III)/(V)) was obtained at pH=4.43, pH=8.55, and pH=7.84, respectively. Hence, the walnut shell shows potential of a cost-effective biosorbent that could be used for the treatment of contaminated rivers. However, further investigation is needed to fully explore this potential.*

**Keywords**: biosorption, walnut shell, metal/oids, natural material, wastewater.

## INTRODUCTION

Worldwide, the extensive growth of industrialization and agricultural activities, along with the lack of enforcement of environmental protection laws, has contributed to the production of large amounts of wastewater (1). In Serbia, wastewater containing both organic and inorganic compounds has become almost ubiquitous and is the most commonly encountered. In South and Eastern Serbia, only 4.9% of industrial and sewage wastewaters are treated before being discharged into the environment (2). Therefore, potential issues related to the discharge of untreated wastewater into natural watercourses are identified in Serbia. For over 100 years, Eastern Serbia has been the most important center of copper mining and metallurgy, which lead to serious environmental issues in the region. Numerous studies were published about copper smelter impact on surface waters in Eastern Serbia (3-5) showing that they have been contaminated with heavy metals, especially Cu, As, and Pb.

Cu, Pb, and As are among the most commonly heavy metals found in wastewater originating from mining industries, metal plating, coal combustion, herbicide use, paints, electronic devices, battery production, and fossil fuel burning (6, 7). In Eastern Serbia, the primary factor contributing to surface water pollution stems from the oxidation of sulfide ores in copper mines and their surrounding areas. This process generates acid mine drainage, resulting in the deposition of pollutants from the air into the water, leaching of acid water enriched with heavy metal ions from mining and metallurgy facilities, as well as the dis-

---

* Corresponding author: Maja M. NUJKIĆ, University of Belgrade, Technical Faculty in Bor, Vojske Jugoslavije 12, 19210 Bor, Serbia, e-mail: mnujkic@tfbor.bg.ac.rs

charge of overburden dumps and flotation tailings (8). The effective removal of those elements from surface waters is of the great importance, considering environmental regulations and human health.

One of the most commonly used methods is adsorption with activated carbon, but its application is limited due to the high cost of production and regeneration of activated carbon. In recent years, efforts have been made to find new, cheaper, and more efficient materials for wastewater treatment (9). The main focus is natural materials, especially agroindustrial waste that is readily available in large quantities. Biosorption as a method for removing heavy metals from water has been studied for more than twenty years (10). The advantages of this method compared to traditional methods are low cost, high efficiency, minimization of chemical or biological sludge, the ability to regenerate biosorbent, and extract metals.

Walnut shell is considered as hard-shell and non-perishable material that possesses properties such as high mechanical strength, chemical stability, and non-toxicity. The walnut shell is rich in lignin and cellulose, which contain many functional groups with a strong affinity for heavy metal ions. As a result, it is widely examined for the removal of heavy metals in contaminated waters (7, 11, 12).

This study aims to investigate the potential of the walnut shell for the removal of metal/oid ions (Cu (II), Pb (II), and As (III)/(V)) from river water samples contaminated with wastewater from Mining and Smelting Complex Bor, ZiJin Bor Copper.

## EXPERIMENTAL

### SAMPLING LOCATION

The city of Bor is located in the eastern part of the Republic of Serbia and covers an area of 856 km$^2$. It borders the municipalities of Majdanpek, Negotin, Zaječar, Boljevac, and Žagubica. Bor is a mining and industrial city located approximately 245 km southeast of Belgrade. The metallurgical complex of ZiJin Bor Copper, formerly known as the Mining and Metallurgical Basin Bor (RTB Bor) is located on the northeastern outskirts of the city. Within the industrial complex of ZiJin Bor Copper, during the copper production process, significant amounts of wastewater are generated, which negatively impacts the environment and leads to the long-term contamination of surface water, land, and underground water (8). The most directly threatened are the Bor River, Krivelj River, and other local rivers. These rivers belong to the catchment area of the Timok River, which flows further into the Danube and therefore represents an international ecological problem (13). Into the Bor River flows all the wastewater as a result of the drainage of tailings, flotation, and other plants for the production and processing of copper and copper ores. Therefore, Bor River is one of the most polluted rivers in the world (14).

### Biosorbate sampling

Seven different water samples were collected from rivers at locations Jaruga (J), Krivelj (K), spring of Bor River (I), Timok (T), Slatina (S), Robule (R), and Bor River at Oštrelj (O). The selection of the representative water samples was based on the assumed contamination of rivers located in the area of mining and metallurgical activities. The control zone was Jaruga (J), a possibly unpolluted area of the rural settlement Podgorac. The grab samples were collected according to procedure The Official Gazette of the Republic of Serbia, no. 33/2016 (15).

### Biosorbent preparation

Walnut shell as biosorbent was collected from rural households. Biosorbents were previously air-dried to constant mass and then grounded in a vibrating mill with Mesh-Tyler rings. Subsequently, the ground walnut shell samples were dried in a laboratory oven at 105 °C for approximately 1 hour and passed through a 200 mm sieve, and sealed in the paper bags until biosorption experiments.

### Biosorption experiments

The biosorption of Cu(II), Pb(II), and As(III)/(V) ions using walnut shells dispersed in river water samples was examined. The effects of contact time (1-4 h), sample pH (3–9), and initial Cu(II), Pb(II), and As(III)/(V) concentrations (0.04–76.7 mg/L) at a constant temperature and biosorbent dosage on biosorption were investigated. A mass of 20 g/L of the walnut shell was added to each water sample ($J_0$, $K_0$, $I_0$, $T_0$, $S_0$, $R_0$, $O_0$) and stirred with a magnetic stirrer (600 rpm, Rotamix SHP-10, Tehtnica) for 1h, 2h, and 4h at room temperature. After filtration, the concentration of Cu (II), Pb (II), and As (III)/(V), ions before and after biosorption was determined using inductively coupled plasma optical emission spectrometer (ICP-OES Optima 8300; Perkin Elmer, USA). Before biosorption, pH values of the real water samples ($J_0$, $K_0$, $I_0$, $T_0$, $S_0$, $R_0$, $O_0$) and initial concentrations of Cu(II), Pb(II), and As(III)/(V) ions (mg/L) in real water samples were measured. pH values of the real water samples were measured using a pH meter Jenway, 3510 (Jenway, UK).

The biosorption efficiency (E, %) of the walnut shell was calculated using Eqs. 1 (16):

$$E(\%) = \frac{C_o - C_e}{C_o} \times 100 \qquad [1]$$

where $C_o$ and $C_e$ are initial and equilibrium Cu(II), Pb (II), and As (III)/(V) concentrations in the water sample (mg/L).

All biosorption experiments were carried out in triplicate.

## RESULTS AND DISCUSSION

Concentrations of Cu(II), Pb(II), and As(III)/(V) ions in analyzed water samples before and after biosorption are given in Table 1. High concentrations of Cu(II), Pb(II) and As(III)/(V) ions in water samples collected downstream of Bor River at site S were 76.68 mg/L, 1.62 mg/L, and 4.44 mg/L, respectively. It can be noticed that the content of these ions in water samples collected from the city of Bor and surrounding areas, were higher than the World Health Organization's 2017 provisional guideline values for heavy metal ions (0.01 mg/L for As, 2 mg/L for Cu, and 0.01 mg/L for Pb) in drinking water (17), except for Cu(II) ions determined at sampling site J, K, I and T. According to Adamović et al. (13), and Đorđievski et al. (4), results of the geochemical analysis show that mining activities and metallurgical wastewater in Bor area have a significant environmental impact on river water.

Overall, the results from this study showed that the investigated rivers were highly contaminated with Cu, As, and Pb, which amplified the need for the urgent removal of these toxic elements from surface waters.

This study investigated the effectiveness of walnut shells for the removal of Cu(II), Pb(II), and As(III)/(V) ions from river water samples. The concentrations of the investigated metal ions and pH values in the river water samples varied depending on the sampling location (as shown in Table 1. and Figure 1.).

**Table 1.** Initial concentrations of Cu(II), Pb(II), and As(III)/(V) ions (mg/L) in tested water samples ($J_0$, $K_0$, $I_0$, $T_0$, $S_0$, $R_0$, $O_0$) and concentrations of Cu(II), Pb(II), and As(III)/(V) ions after biosorption time of 1h ($J_1$, $K_1$, $I_1$, $T_1$, $S_1$, $R_1$, $O_1$), 2h ($J_2$, $K_2$, $I_2$, $T_2$, $S_2$, $R_2$, $O_2$), and 4 h ($J_4$, $K_4$, $I_4$, $T_4$, $S_4$, $R_4$, $O_4$) at biosorbent dosage 20 g/L, and temperature of 25°C.

| **Water sample** | **Pb(II)** | **As (III)/(V)** | **Cu(II)** |
|---|---|---|---|
| **$J_o$** | **0.080** | **0.213** | **0.893** |
| $J_1$ | 0.057 | 0.133 | 0.555 |
| $J_2$ | 0.039 | 0.006 | 0.200 |
| $J_4$ | 0.027 | 0.001 | 0.186 |
| **$K_o$** | **0.090** | **0.039** | **0.795** |
| $K_1$ | 0.070 | 0.032 | 0.501 |
| $K_2$ | 0.042 | 0.019 | 0.247 |
| $K_4$ | 0.025 | 0.012 | 0.186 |
| **$I_0$** | **0.089** | **0.062** | **0.688** |
| $I_1$ | 0.052 | 0.045 | 0.584 |
| $I_2$ | 0.023 | 0.002 | 0.283 |
| $I_4$ | 0.017 | 0.001 | 0.255 |
| **$T_o$** | **0.123** | **0.076** | **0.886** |
| $T_1$ | 0.075 | 0.054 | 0.712 |
| $T_2$ | 0.036 | 0.036 | 0.336 |
| $T_4$ | 0.021 | 0.030 | 0.261 |
| **$S_o$** | **1.619** | **4.436** | **76.68** |
| $S_1$ | 0.078 | 3.026 | 7.522 |
| $S_2$ | 0.058 | 2.700 | 5.342 |
| $S_4$ | 0.045 | 2.300 | 5.096 |
| **$R_o$** | **0.040** | **0.047** | **7.352** |
| $R_1$ | 0.037 | 0.037 | 1.357 |
| $R_2$ | 0.014 | 0.002 | 0.667 |
| $R_4$ | 0.009 | 0.001 | 0.178 |
| **$O_o$** | **0.088** | **0.058** | **40.08** |
| $O_1$ | 0.031 | 0.043 | 3.345 |
| $O_2$ | 0.029 | 0.021 | 3.180 |
| $O_4$ | 0.021 | 0.009 | 2.781 |

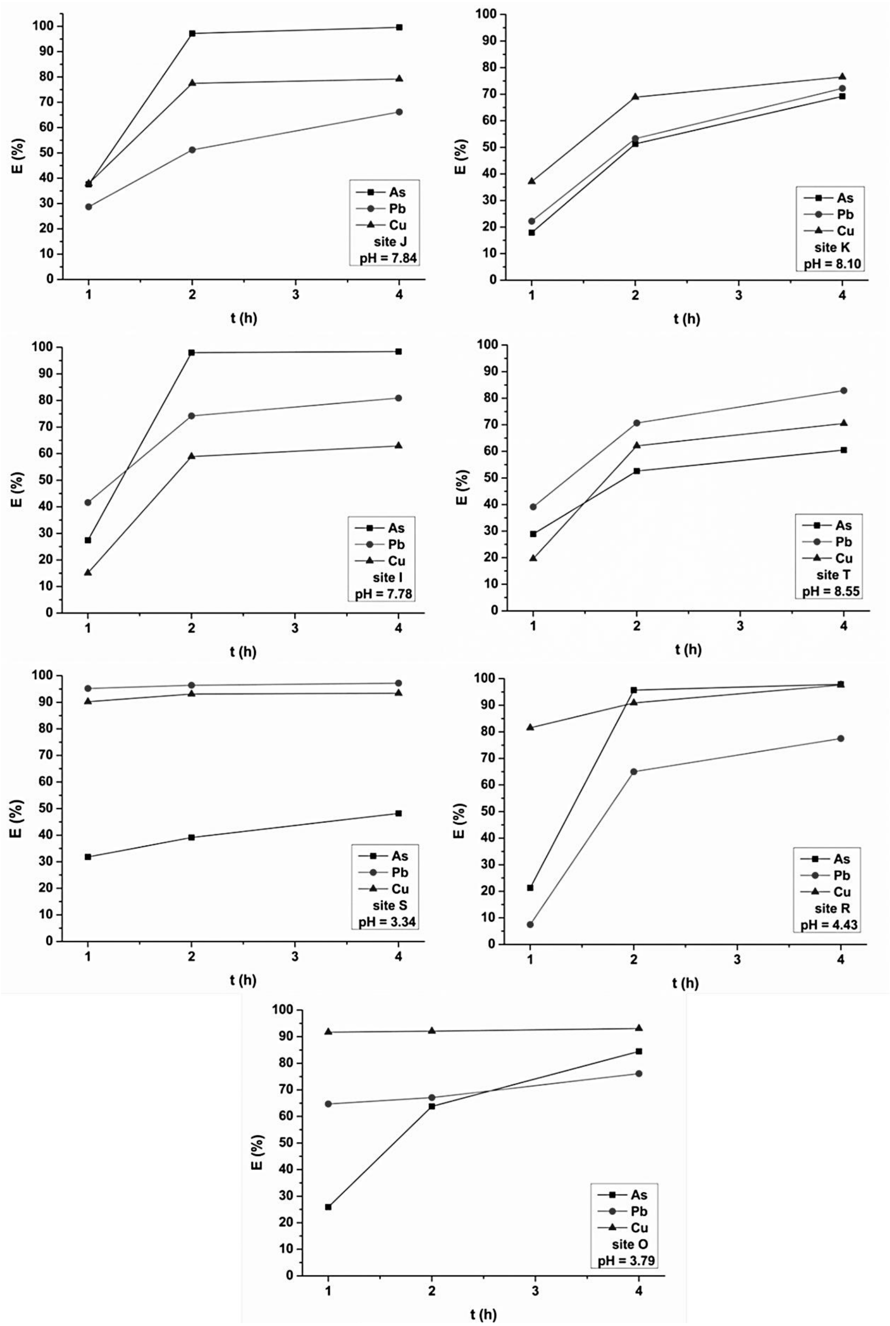

**Figure 1.** Efects of contact time on biosorption efficiency (%) of walnut shells in removing Cu(II), Pb(II), and As(III)/(V) ions from different water samples ($J_0$, $K_0$, $I_0$, $T_0$, $S_0$, $R_0$, $O_0$).

The initial concentrations of Cu(II), Pb(II), and As(III)/(V) ions decreased with time at a constant temperature. The most significant reduction in Cu(II), Pb(II), and As(III)/(V) ion concentrations were observed in the sample collected from Bor River at Slatina (S) where the initial concentration of Cu (II) ions, 76.7 mg/L was reduced to 5.1 mg/L after 4 h of biosorption. In the same sample and contact time, the concentrations of Pb(II), and As(III)/(V) ions decreased from 1.62 mg/L to 0.05 mg/L and from 4.44 mg/L to 2.30 mg/L, respectively. The examined biosorbent showed high affinity for Cu(II), Pb(II), and As(III)/(V) ions in all tested water samples (Table 1.). In the case of Cu(II), Pb(II), and As(III)/(V) ions, the differences between 1h and other contact times (2 and 4h) were above 30%, meaning that 1h of exposure to the walnut shell is insufficient. On the other hand, in some investigated samples, the biosorption efficiency during 2h was relatively high (51.3-98.0%), but the highest biosorption efficiency of the walnut shell for investigated ions was determined after 4h of contact in all water samples. These results indicate that 4h of contact time between investigated biosorbent and treated water was the best and accepted for the next biosorption experiments. Kamar and Nechifor (18) suggested optimal time for biosorption with walnut shells to be longer than 2 h.

Using 20 g/L of walnut shell, the removal of As(III)/(V) ions from sites J, I, T, R, O, and K ranged from 60.5 to 99.6% (Figure 1.). The removal of Cu(II) and Pb(II) ions by a walnut shell was very high (62.9-97.6%), with the highest biosorption efficiency (97.6%) for Cu (II) detected at site R, followed by Pb(II) ions (97.2%) at the site S. According to the obtained results, walnut shell showed a more efficient removal of Cu(II) and Pb(II) ions at site S than As(III)/(V) ions, which may also be influenced by other factors and conditions. Similar results were obtained by other researchers in synthetic solutions. Sepúlveda et al. (19) obtained a biosorption efficiency of 88% for Cu(II) ions from a synthetic solution at 30 min, pH=5, and an optimum agitation speed of 400 rpm. Also, the walnut shell was found to be effective in removing 90% of Pb(II) ions from the synthetic solution till 2h, when the pH of the solution was adjusted to 4 (20). Moreover, Saqib et al. (21) reported that walnut shells could remove up to 70% and 85% of arsenic ions from synthetic solution after optimal contacting time of 20 and 40 min at pH= 8.

The pH values of analyzed water samples ranged from 3.34 to 8.55, depending on the sampling site. Water samples from the sites S (pH=3.34), R (pH=4.43), and O (pH=3.79) are extremely acidic, due to the release of sulfide mineral oxidation products into the environment which potentially contaminates local surface water and lowers the pH of water (22). Other sampling locations, J (pH=7.84), I (pH=7.78), K (pH=8.10), and T (pH= 8.55), showed neutral to slightly alkaline pH values. This can be explained by the impact of the bedrock on rivers of Eastern Serbia which are predominantly carbonates that keeps the pH of the river near neutral (23).

Figure 2. shows the effect of river water pH on biosorption of Cu(II), Pb(II), and As(III)/(V) ions by walnut shells. The highest biosorption efficiency (99.6%, 98.4%, and 97.9%) of As(III)/(V) ions was achieved at pH=7.84, pH= 7.78, and pH =4.43 at sites J, I, and R respectively, indicating that the biosorption is favored in slightly alkaline and acidic river water. Similarly, Shakoor et al. (24) investigated the influence of pH on biosorption efficiency of watermelon rind for the removal of As(III)/(V) ions in the range of pH=3-10. It was shown that both As(III)/(V) ions removal depends on sample pH, and maximum biosorption (85% and 98%) was achieved at pH=7.2 and pH= 4.6, respectively. The authors explained the influence of alkaline pH on the removal of As(III) ions through the interaction of monoanionic $H_2AsO_3$ and $H_3AsO_3$ species with biosorbent where substitution of –OH groups or water mo-

lecules occurs. For predominant As(V) species ($H_2AsO_4^-$ and $HAsO_4^{2-}$) in acidic conditions, sorption on the surface of the biosorbent can occur through the substitution of –OH and –COOH groups or coordination of –OH groups with As(V) ions. (24).

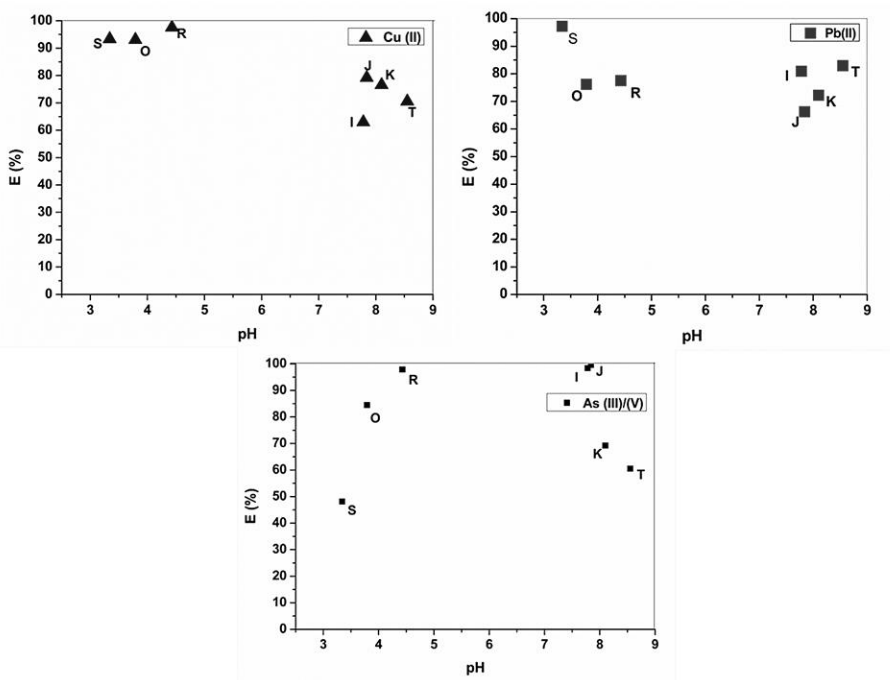

**Figure 2.** Effects of river water pH on biosorption efficiency (%) of walnut shells in removing Cu(II), Pb(II), and As(III)/(V) ions from different water samples ($J_4$, $K_4$, $I_4$, $T_4$, $S_4$, $R_4$, $O_4$).

The maximum Pb(II) biosorption efficiency (97.2%) occurred at pH=3.34 (S) by walnut shells. However, in the pH range of 6-8, high Pb(II) biosorption efficiency (72.2-82.9%, Fig. 2) due to the more negatively-charged active sites on the walnut shell was observed. Formation of $Pb(OH)^+$ and $Pb(OH)_2$ precipitates could decrease the biosorption process (6). For this reason, other authors (25, 26) showed that solution pH near a neutral state is an optimal condition for further Pb (II) adsorption studies and data from site S does not provide a reproducible and characteristic impression of true adsorption.

The highest biosorption efficiencies (93.4%, 97.6%, and 93.1%) were detected for Cu (II) at site S (pH=3.34), R (pH=4.43), and O (pH=3.79), respectively. According to Nujkić et al. (27) the optimal pH value for the removal of Cu(II) ions by walnut shell is 4. This can be explained by the active binding sites on the biosorbent surface that become negatively charged in acidic solutions, which enhances Cu(II) biosorption. Bamisaye et al. (28) have observed similar findings on the effects of pH on Cu(II) removal using walnut shell.

## CONCLUSION

In this research, possibility of using walnut shells for biosorption of Cu(II), Pb(II), and As(III)/(V) ions from river water samples were investigated. Considering obtained results it can be concluded that walnut shell has a good potential as a biosorbent due to the high removal efficiency of Cu(II), Pb(II), and As(III)/(V) ions under different conditions, such as pH, initial concentration and contact time at a constant temperature and biosorbent dosage. The maximum efficiency of 93.41%, 97.25 and 99.6% were achieved at Cu(II), Pb(II) and As(III)/(V) concentration of 76.7, 1.62 and 0.21 mg/L, respectively. Water pH values of pH=4.43, pH=8.55, and pH=7.84, indicated the best removal for Cu(II) (97.6%), Pb(II) (82.9%), and As(III)/(V) (99.6%) ions, respectively. The highest values of biosorption efficiency were achieved at a contact time of 4h in all water samples. The highest efficiency removal of Cu(II), Pb(II), and As(III)/(V) ions with the walnut shell occurred in the sample S which contained the highest initial ions concentration. Therefore, the walnut shell can be used as an eco-friendly and low-cost adsorbent, in those areas where this material is abundant. For further investigations, the walnut shell could be applied to multielement synthetic systems and modified for similar examination.

## Acknowledgements

The authors are grateful to the Ministry of Science, Technological Development and Innovation of the Republic of Serbia, for the financial support of this work (project number 451-03-47/2023-01/ 200131).

## REFERENCES

1. Dey, P.; Mahapatra, B.S.; Juyal, V.K.; Pramanick, B.; Negi, M.S.; Paul, J.; Singh, S.P. Flax processing waste – a low-cost, potential biosorbent for treatment of heavy metal, dye and organic matter contaminated industrial wastewater. *Ind. Crops. Prod.* **2021**, *174*, 114195. https:// doi.org/10.1016/j.indcrop.2021.114195
2. Regions of the Republic of Serbia, Statistical Office of the Republic of Serbia, Belgrade, 2021. https://publikacije.stat.gov.rs/G2021/PdfE/G202126001.pdf
3. Adamovic, D.; Ishiyama, D.; Dordievski, S.; Ogawa, Y.; Stevanovic, Z.; Kawaraya, H.; Sato, H.; Obradovic, Lj.; Marinkovic, V.; Petrovic, J.; Gardic, V. Estimation and comparison of the environmental impacts of acid mine drainage-bearing river water in the Bor and Majdanpek porphyry copper mining areas in Eastern Serbia. *Resour. Geol.* **2021**, *71* (2), 123–143. https://doi.org/10.1111/rge.12254
4. Đorđievski, S.; Ishiyama, D.; Ogawa, Y.; Stevanovic, Z. Mobility and natural attenuation of metals and arsenic in acidic waters of the drainage system of Timok River from Bor copper mines (Serbia) to Danube River. *Environ. Sci. Pollut. Res.* **2018**, *25*, 25005–25019. https://doi.org/10.1007/s11356-018-2541-x
5. Šerbula, S.; Stanković, V.; Živković, D.; Kamberović, Ž.; Gorgievski, M.; Kalinović, T. Characteristics of Wastewater Streams Within the Bor Copper Mine and Their Influence on Pollution of the Timok River, Serbia. *Mine Water Environ.* **2016**, *35*, 480–485. https://doi.org/10.1007/s10230-016-0392-6

UDC: 582.628+631.576.4]:628.35
BIBLID: 1450-7188 (2023) 54, 187-196

Original scientific paper

6. Das, A.; Bar, N.; Das, S.K.; Pb(II) adsorption from aqueous solution by nutshells, green adsorbent: Adsorption studies, regeneration studies, scale-up design, its effect on biological indicator and MLR modeling. *J. Colloid Interface Sci.* **2020**, *580*, 245-255. https://doi.org/10.1016/j.jcis.2020.07.017
7. Figueira, P.; Henriques, B.; Teixeira, F. Afonso. N.; Pinto. J.; Tavares. D.; Vale. C.; Pereira. E. Potentialities of Agro-Based Wastes to Remove Cd, Hg, Pb, and As from Contaminated Waters. *Water Air Soil Pollut.* **2022**, *78*, 233. https://doi.org/10.1007/s11270-022-05543-7
8. Dimitrijević, M.; Kostov, A.; Tasić, V.; Milosević, N. Influence of pyrometallurgical copper production on the environment. *J. Hazard. Mater.* **2009**, *164* (2–3), 892-899. https://doi.org/10.1016/j.jhazmat.2008.08.099
9. Li, X.S.; Liu, S.L.; Na, Z.Y.; Lu, D.N.; Liu, Z. Adsorption, concentration, and recovery of aqueous heavy metal ions with the root powder of Eichhornia crassipes. *Ecol. Eng.* **2013**, *60*, 160–166. https://doi.org/10.1016/j.ecoleng.2013.07.039
10. Milojković, J.V.; Lopičić, Z.R.; Anastopoulos, I.P.; Petrović, J.T.; Milićević, S.Z.; Petrović, M.S.; Stojanović, M.D. Performance of aquatic weed - Waste Myriophyllum spicatum immobilized in alginate beads for the removal of Pb(II). *J. Environ. Manage.* **2019**, *232*, 97–109. https://doi.org/10.1016/j.jenvman.2018.10.075
11. Lu, Xg.; Guo, Yt. Removal of Pb (II) from aqueous solution by sulfur-functionalized walnut shell. *Environ. Sci. Pollut. Res.* **2019**, *26*, 12776–12787. https://doi.org/10.1007/s11356-019-04753-7
12. Dias, M.; Pinto, J.; Henriques, B.; Figueira, P.; Fabre, E.; Tavares, D.; Vale, C.; Pereira, E. Nutshells as Efficient Biosorbents to Remove Cadmium, Lead, and Mercury from Contaminated Solutions. *Int. J. Environ. Res. Public Health.* **2021**, *18*, 1580. https://doi.org/10.3390/ijerph18041580
13. Adamovic, D.; Ishiyama, D.; Kawaraya, H.; Ogawa, Y.; Stevanovic, Z. Geochemical characteristics and estimation of groundwater pollution in catchment areas of Timok and Pek Rivers, Eastern Serbia: Determination of early-stage groundwater pollution in mining areas. *Groundw. Sustain. Dev.* **2022**, *16*, 100719. https://doi.org/10.1016/j.gsd.2021.100719
14. Bugarin, M.; Jonović; R., Avramović, Lj. Tretman industrijskih otpadnih voda iz procesa proizvodnje bakra u RTB Bor. *Rudarski radovi*, Bor. **2012**, *4*, 67-78. https://scindeks.ceon.rs/article.aspx?artid=1451-01621204067B
15. The Official Gazette of Republic of Serbia, no. **33/2010**: The method and conditions for measuring the quantity and testing the quality of waste water and the content of the measurement report (in Serbian).
16. Sheikh, Z.; Amin, M.; Khan, N.; Khan, M.N.; Sami, S.K.; Khan, S.B.; Hafeez, I.; Khan, S. A.; Bakhsh, E. M.; Cheng, C. K. Potential application of Allium Cepa seeds as a novel biosorbent for efficient biosorption of heavy metals ions from aqueous solution. *Chemosphere.* **2012**, *279*, 130545. https://doi.org/10.1016/j.chemosphere.2021.130545
17. WHO, **2017**a. Guidelines for Drinking-Water Quality: Fourth Edition Incorporating the First Addendum. World Health Organization, Geneva.
18. Kamar, F.; Nechifor, A.C. Removal of copper ions from wastewater using walnut shells as a natural adsorbent material. *UPB Scientific Bulletin, Series B,* **2015**, *77* (3), 141–150.
19. Sepúlveda, P.; Pavez, O.; Tume, P.; Sepúlveda B. Biosorption of copper ions with olive pomace and walnut shell. *Environ. Geochem. Health,* **2022**. https://doi.org/10.1007/s10653-022-01303-y
20. Celebi, H.; Gok, O. Evaluation of Lead Adsorption Kinetics and Isotherms from Aqueous Solution Using Natural Walnut Shell. *Int. J. Environ. Res.* **2017**, *11*, 83–90. https://doi.org/10.1007/s41742-017-0009-3
21. Saqib, A.N.S.; Waseem, A.; Khan, A.F.; Mahmood, Q.; Khan, A.; Habib, A.; Khan, A.R. Arsenic bioremediation by low cost materials derived from Blue Pine (*Pinus wallichiana*) and Walnut (*Juglans regia*), *Ecol. Eng.* **2013**, *51*, 88-94. https://doi.org/10.1016/j.ecoleng.2012.12.063
22. Nujkić, M.; Milić, S.; Spalović, B.; Dardas, A.; Alagić, S.; Ljubić, D.; Papludis, A. Saponaria officinalis L. And Achillea millefolium L. as possible indicators of trace elements pollution cau-

sed by mining and metallurgical activities in Bor, Serbia. *Environ. Sci. Pollut. Res.* **2020**, *27*, 44969–44982. https://doi.org/10.1007/s11356-020-10371-5

23. Pešić, M.; Milić, S.; Nujkić, M.; Marić, M. Determination of Heavy Metal Concentration and Correlation Analysis of Turbidity: a Case Study of the Zlot Source (Bor, Serbia). *Water Air Soil Pollut.* **2020**, *231*, 98. https://doi.org/10.1007/s11270-020-4453-x
24. Shakoor, M.B.; Niazi, N.K.; Bibi, I.; Shahid, M.; Sharif, F.; Bashir, S.; Shaheen, S.M.; Wang, H.; Tsang, D.C.W.; Ok, Y.S.; Rinklebe, J. Arsenic removal by natural and chemically modified water melon rind in aqueous solutions and groundwater. *Sci. Total Environ.* **2018**, *645*, 1444–1455, https://doi.org/10.1016/j.scitotenv.2018.07.218
25. Cruz-Lopes, L.P.; Macena, M.; Esteves, B.; Guiné, R.P.F. Ideal pH for the adsorption of metal ions $Cr^{6+}$, $Ni^{2+}$, $Pb^{2+}$ in aqueous solution with different adsorbent materials, *Open Agric.*, 2021, *6* (1), 115-123. https://doi.org/10.1515/opag-2021-0225
26. Edathil, A.A.; Shittu, I.; Zain, J.H.; Banat, F.; Haija M.A. Novel magnetic coffee waste nano-composite as effective bioadsorbent for Pb(II) removal from aqueous solutions, *J. Environ. Chem. Eng.*, 2018, *6* (2), 2390-2400, https://doi.org/10.1016/j.jece.2018.03.041.
27. Nujkić, M.; Tasić, Ž.; Milić, S.; Medić, D.; Papludis, A.; Stiklić, V. Mullein leaf as potential bio-sorbent for copper(II) ions removal from synthetic solutions: optimization, kinetic and isotherm. *Int. J. Environ. Sci. Technol.* **2022**, *133*. https://doi.org/10.1007/s13762-022-04541-w
28. Bamisaye A.; Adesina M.O.; Alfred M.O.; Ige A.R.; Idowu M.A.; Adegoke K.A. Kinetic and mechanistic study of the biosorption of Copper(II) Ion from wastewater using porous Chitosan-Walnut shell composite, *CDC*, **2023**, *45*, 101024. https://doi.org/10.1016/j.cdc.2023.101024

APTEFF, Vol. 54, 1-335 (2023) UDC: 66.021.3.081.3:547.56]:628.3
DOI: https://doi.org/10.2298/APT2354197D BIBLID: 1450-7188 (2023) 54, 197-208

Original scientific paper

# KINETIC STUDY OF ADSORPTION OF PHENOLIC COMPOUNDS FROM OLIVE OIL MILL WASTEWATER ON ACTIVATED CARBON

*Soumia DJEZIRI, Zoubida TALEB, Hadja Mebarka DJELLOULI**

Laboratory of Materials & Catalysis, Faculty of Exact Sciences, Djillali Liabes University,
BP 89, Sidi Bel Abbes, Algeria.

**Received: 18 May 2023** **Revised: 08 July 2023** **Accepted: 10 July 2023**

*Olive oil Mill Wastewater (OMW) is not degradable due to the presence of substances (phenols, volatile fatty acids, etc.), which pose problems for the environment. In order to protect this environment, currently know various treatment methods of wastewater such as adsorption. We have studied in our work the adsorption capacity of phenolic compounds present in Olive Oil Mill Wastewater on activated carbon (AC). The phenolic compounds are known for their carcinogenicity and their high toxicity and the activated carbon is the most popular and widely used adsorbent material for OMW treatment. The AC was prepared by the valorization of agri-food waste that are olive leaves (calcination followed by chemical activation using phosphoric acid). A range of analyses was carried out for the characterization of the used adsorbent, among them: Infrared (IR) spectroscopy, which showed the main characteristic bands of activated carbons, X-ray diffractometry (XRD), iodine value, moisture content, ash content and pHzpc. The effect of several parameters such as contact time, amount of adsorbent and pH of the solution were studied. The best adsorption conditions are simple to achieve: Ambient temperature, direct use of the olive oil mill wastewater (V = 100 mL, pH = 1.95) with 4 g mass of AC adsorbent. The obtained adsorption kinetics showed that the adsorption of phenolic compounds from OMW on prepared activated carbon is well described by the Pseudo second order. The obtained results indicate the possibility of olive leaves valorization in the form of activated carbon with what all this implies as socio-economic impacts*

**Keywords**: kinetic adsorption, activated carbon, olive leaves, phenolic compounds, olive oil mill wastewater.

## INTRODUCTION

The olive oil industry is an important economic activity, concentrated mainly in the Mediterranean countries, which account for about 97% of world production (1). The production of this industry generates a number of residues, both liquid (olive oil mill wastewater OMW: margins) and solid (pomace and leaves) (2, 3). As a result, huge amounts of waste are generated. Annually, the volume of olive oil mill wastewater discharged exceeds 250,000 m$^3$ and the quantities of pomace and olive leaves reach some 400 thousand tons (4).

Olive oil mill wastewater is the main waste generated during the extraction of olive oil. It is a highly polluted discharge, in liquid form whose composition is variable. The quality and quantity of the Olive oil mill wastewater depend on the olive oil extraction operation. They are also influenced by the varieties of olives, harvesting season, ripening rate of fruits

---

* Corresponding author: Hadja Mebarka DJELLOULI, Laboratory of Materials & Catalysis, Djilali Liabes University, Faculty of Exact Sciences, Djillali Liabes University, BP 89, Sidi Bel Abbs, Algeria, e-mail: mebarkad@yahoo.fr

and climatic conditions (5). About 2.72 million tons of olive oil are produced each year in the world, the majority of which is concentrated in the Mediterranean basin (6).

The harmful effects of the effluents are largely due to their phenolic compounds (polyphenols) content. Phenols can indeed inhibit the microbial activity of the soil. Other compounds, such as acids, mineral elements and organic substances are responsible for the destruction of the cation exchange capacity of the soil and are also a source of pollution of groundwater and surface water (3). OMW contains phenolic compounds (with low biodegradation and high toxicity (7) as well as their high anticarcinogenic and antioxidant capacity (8) is a serious environmental problem, and it should not be released without treatment into the eco-system (7).

The transformation of olive leaves into activated carbon is very interesting, not only because of the considerable need for adsorbents in the industrial sector but also because bio-adsorbents have good efficiency at a lower cost (9). Activated carbons (ACs) provide economic and environmental advantages with high removal efficiency for biogas purification (10). In addition, the transformation of olive leaves into activated carbon is an opportunity to produce inexpensive adsorbents using local renewable resources.

This work aims to prepare from olive leaves an activated carbon chemically activated using phosphoric acid. The prepared AC was used for phenolic compound elimination from olive oil mill wastewater. Some parameters of adsorption were studied such as time contact, the used mass of AC and the initial pH of the solution. Kinetics models are also studied for more understanding of the phenolic compounds adsorption on AC prepared from olive leaves.

## EXPERIMENTAL

The sampling of olive oil mill wastewater and olive leaves were carried out in the region of Sidi Bel Abbes (West Algeria) from an oil mill extraction system by centrifugation in three phases during the olive campaign 2019-2020. The olive oil mill wastewater taken from the storage tank was homogenized and transported in bottles of 5 Liters. The bottles were stored away from light at 4 °C for later use.

### DETERMINATION OF THE POLYPHENOLS CONCENTRATION

The oil mill wastewater collected and studied in our research has a strong odor reminiscent of olive oil. It has a cloudy appearance with a dark brown to reddish brown color, which darkens during storage. Total phenolic compounds concentration was determined by using the Folin-Ciocalteu method (11, 12): For the polyphenol’s extraction, olive oil mill wastewater was mixed with ethyl acetate (1/1). The polyphenolic compounds and ethyl acetate are recovered after centrifugation for 10 minutes at a speed of 3200 rpm. The ethyl acetate was then evaporated at 37 °C. Finally, polyphenols were recovered in methanol and the spectrophotometry was used for reading the optical density at 760 nm.

The phenolic compounds can be either polyphenols which result from the polymerization of the simple phenols or flavonoids. The content of phenolic compounds is about 0.45 g/L. Phenolic composition of olive oil mill wastewaters depends on the variety and maturity of the fruit and on climatic conditions, as well as on the separating process of the aqueous phase (OMW) from the oily phase (13). However, these compounds are strong inhibitors of flora hence the high toxicity of these rejects, which make the treatment of OMW imperative (14). The color of OMW reflects the state of degradation of the phenolic compounds and the olives from which they are derived.

## ACTIVATED CARBON PREPARATION FROM OLIVE LEAVES

Firstly, the olive leaves are washed with distilled water several times, dried, crushed and sieved. The dried sample was carbonized at the temperature of 400 °C for 1 hour. The activation was carried out chemically by $H_3PO_4$ acid. Indeed, this agent has been widely used for the activation of carbons (15). Next, the sample was immersed in a volume of the acid under agitation. The liquid was then separated by simple filtration and dried at 105 °C for 24 h. After drying, the activated carbon was washed again with distilled water until a pH of 6 in the residual water. Finally, the activated carbon was put in the oven at 110 °C for 24 hours and packed in ready-to-use boxes.

## CHARACTERIZATION OF PREPARED ACTIVATED CARBON

**Structural analysis by Fourier transforms infrared spectroscopy:** The surface functional groups were studied by Fourier transforms infrared spectroscopy. The IR spectrum of the resulting activated carbon was recorded between 4000 and 550 $cm^{-1}$ in a Perkin Elmer spectrometer.

**X-ray diffractometry (XRD):** X-ray diffraction XRD was used to determine the amorphous or crystalline structure of our prepared material. The XRD was studied by Cu-Co with an energy source occupied on a 40 kV power voltage and 25 mA current, on the monochromatic copper radiation Kα1 (1.54178A&). The observed range of the angle 2θ was recorded between 2° and 70°.

**Determination of the zero-point charge ($pH_{zpc}$):** It is a pH for which activated carbon is electrically neutral in solution. It is the sum of the charges on the surface is zero. This pH is called pH at the point of zero charge ($pH_{zpc}$) (16,17). A quick and easy way to determine the isoelectric point is to place 50 mL of distilled water in beakers and adjust the pH of each (values between 2 and 12) by adding 0.1M NaOH or HCl solution. Then, add to each 1g of the adsorbent material. The suspensions must be kept under agitation, at room temperature for 24 h and the final pH was then measured. The value of $pH_{zpc}$ was read from the curve $\Delta pH = f(pH_i)$ with $\Delta pH = pH_{final} - pH_{initial}$.

**Moisture content:** The moisture content represents the amount of water physically not bound to the activated carbon. Moisture is a ratio expressed as a percentage; it is determined by drying the adsorbent in an oven at 105 °C until its weight remains constant. It is calculated using the Equation [1] (18):

$$H\% = \frac{m_0 - m_1}{m_0} \times 100 \qquad [1]$$

where *H* is moisture content (%), $m_0$ and $m_1$ (g)are the mass of the AC adsorbent before and after drying, respectively.

**Ash content:** This is the inorganic, inert, amorphous and unusable part present in the material (17, 18). A 1 g of adsorbent was placed in a crucible. This crucible is introduced

UDC: 66.021.3.081.3:547.56]:628.3
BIBLID: 1450-7188 (2023) 54, 197-208

into the oven and heated for one hour up to 1000 °C. After cooling, the crucible was weighed. The ash content is calculated by the following Equation [2]:

$$\%\text{Ash} = \frac{p_0 - p_1}{p_0} \times 100 \qquad [2]$$

where *%Ash* is the percentage of ash rate content (%), $P_0$ and $P_1$ (g) are the weight of the filled crucible before and after carbonization, respectively.

**Iodine value:** The iodine index (iodine number) is a microspore content measure of adsorbent material. The iodine number is an indicator of the porosity of an activated carbon (17-19).

The iodine adsorption capacity of AC material was determined according to the following procedure: 10 ml of a 0.01 N iodine solution was titrated with a 0.1 N sodium thiosulfate solution, in a few drops' presence of a starch solution as an indicator, until the color disappeared. In the second step, 0.05 g of activated carbon was added to 15 mL of a 0.1 N iodine solution with 5 min stirring. Then, the obtained iodine solution was filtered and titrated with 0.1 N sodium thiosulfate solution in the presence of two drops presence of starch solution. The iodine value (*Id*) was calculated by the following Equation [3]:

$$\text{Id} = \frac{(\text{Vb} - \text{Vs}).\text{N}.(126.9).15/10}{\text{M}} \qquad [3]$$

where ($V_b$ -$V_S$) in mL is the between the required volumes of sodium thiosulfate for the blank ($V_b$) and the sample ($V_s$), $N$ is the normality of the sodium thiosulfate solution in (mol/L), the *126.9* g/mol is the atomic mass of iodine and $M$ (g) is the mass of the AC adsorbent.

## ADSORPTION EXPERIMENTAL PROCEDURE

Adsorption experiments were carried out by varying the time of the solution, adsorbent mass and pH of the solution at ambient temperature by magnetic agitation. For each experiment, 100 mL of 450 mg/L initial concentration of OMW was treated with the prepared activated carbon. After stirring, the solution was filtered and the filtrate was analyzed to obtain the residual concentration of phenolic compounds using a UV/Vis spectrophotometer. Absorbance values were determined at a maximum wavelength ($\lambda_{max}$) of 760 nm. The removal yields (% Y), and the amount of the adsorbed phenolic compounds ($q_e$) were calculated using the following expressions:

$$Y\,(\%) = \frac{(C_i - C_{eq})}{C_i} \times 100 \qquad [4]$$

$$q_e\,(mg/g) = \frac{(C_0 - C_e)}{m} \times V \qquad [5]$$

where $C_0$ (mol/L) is the initial concentration and $C_e$ (mol/L) is the equilibrium concentration. V (L) is the volume of the solution, m (g) is the mass of the adsorbent (20-22).

## RESULTS AND DISCUSSION

### CHARACTERIZATION OF ADSORBENT

The infrared analysis spectrum of prepared activated carbon is shown in Figure 1. The fine band at about 3500 cm$^{-1}$ can be designated to the -OH stretching vibration mode of hydroxyl functional compound and this is due to the existence of cellulose (23). The existence of a small band located at 2924.38 cm$^{-1}$ is assigned to C–H vibration stretching of the alkane groups (24). The band located around 1605.80 cm$^{-1}$ can be attributed to aromatic carbon (stretch of C=C in pungent ring) and carboxyl group (C=O stretch). The peaks at 1315.51 cm$^{-1}$ and 1061 cm$^{-1}$ correspond to C–O stretching vibration modes (stretch (alcohols, ethers, acids, and esters) (23). The band at 779.9 cm$^{-1}$ is credited to -CH out-of-plane bending vibration on the aromatic rings. Overall, these functional groups are derived from main components such as pectin, hemicellulose, and lignin (23).

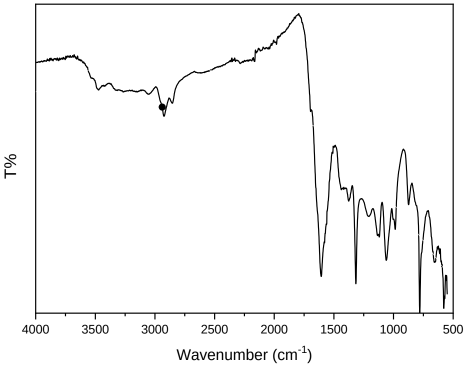

**Figure 1.** IR Spectrum of the activated carbon

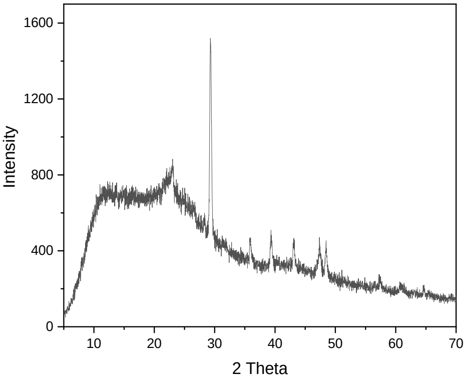

**Figure 2.** X-ray diffraction of the activated carbon

The XRD spectrum in Figure 2 shows the intensity versus 2 theta angle curve of the prepared activated carbon. As indicated, the large hill of the prepared activated carbon, less than 29° indicated the existence of amorphous compounds. The peak at $2\theta = 29°$ demonstrates the existence of a crystalline structure. This crystalline structure's existence is due to the chemical activation process cellulose (25).

The results of the moisture content, ash content, iodine value and pHzpc of the prepared activated carbon are shown in Table 1. The low ash content (0.06 %) implies that the activated carbon consists essentially of organic matter, therefore of the carbon element (16). The prepared activated carbon has also a low moisture content (0.0038%), which highlights a low water content conservation. For the iodine value, the prepared activated carbon gives a high iodine value 932.98 mg/g that clearly illustrates the microporosity of an activated carbon.

The found value of $pH_{zpc}$ of the prepared activated carbon is $pH_{zpc} = 8$. It means that the obtained AC material has a basic character. The surface of the activated carbon is positively charged at pH below 8 and negatively charged at pH above 8 (17).

**Table 1.** Activated carbon properties

| Characteristics | Value |
|---|---|
| Moisture content | 0.06 % |
| Ash content | 0.0038 % |
| Iodine value | 932.98 mg/g |
| $pH_{zpc}$ | 8 |

## ADSORPTION STUDIES

### Effect of time of contact

This study was carried out in order to determine the fixed quantities of the pollutant from its contact until a time t, in order to know the equilibrium time. For this, a solution for 100ml, with an initial concentration $C_i$ (450 mg/l) of the polyphenol of OMW was put in contact with a mass of activated carbon (1g) at pH of the solution (4.52). The mixture obtained was immediately agitated at different contact times varying from 1 to 6 h. The analysis of the initial or residual polyphenol concentration is carried out by UV-Visible adsorption spectroscopy at a wavelength $\lambda_{max}$=760 nm.

Figure 3 shows the time effect of phenolic adsorption on activated carbon. The adsorption yields (%) of polyphenol from olive oil mill wastewater increases exponentially with time, reaching its maximum value after 240 minutes. Beyond that comes the state of adsorption equilibrium. It thus becomes clear that activated carbon has an adsorption capacity (37.02 % of the initial concentration of OMW 450 mg/g).

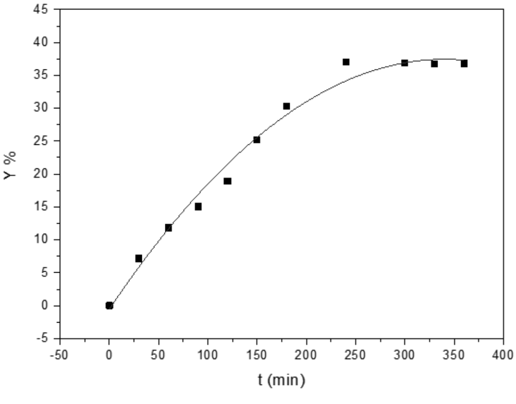

**Figure 3.** Effect of time effect on phenolic adsorption

### Modeling of adsorption kinetics

The kinetic study was conducted to analyze the effect of time on removing and possible mechanisms involved in the process (25). This uptake rate decides the retention time of adsorbate at the solid-liquid interface and thus determines the rate-controlling mechanism (26).

Several kinetic models were used to interpret the experimental data, giving essential information for using these activated carbons in the adsorption field (18). Five kinetic models were adopted: pseudo-first-order, pseudo-second order, Elovich, intraparticle and external diffusion models. The kinetics equations used are regrouped in Table 2 with the values of the constants. These last were calculated and deduced from the Figure 4. More this factor higher, more favorable the model is for the adsorption study process. When this coefficient is close to 1, the adsorption kinetics model is favorable for study. All the studied kinetic models had very close to 1 regression coefficient values ($R^2 > 0.900$), but the pseudo-second order model has the higher correlation coefficient value ($R^2 = 0.992$). It can be deduced that the pseudo-second order model is the best kinetic model that described the adsorption process of phenolic compounds from OMW on the prepared activated carbon. Also, the value of the adsorbed quantity calculated from the kinetic model of pseudo-second order is close to the experimental adsorbed quantity (17 mg·g$^{-1}$).

**Table 2.** Equations and constant values of kinetic models

| Kinetic models | Equation | Constants | AC results |
|---|---|---|---|
| **Pseudo-first order** | $\mathrm{Ln}\ (q_e - q_t) = \ln (q_e) - k_1 \cdot t$ | $K_1$ (min$^{-1}$)<br>$q_e$(mg·g$^{-1}$)<br>$R^2$ | 0.01645<br>1.298<br>0.964 |
| **Pseudo-second order** | $1/ q_t= 1/ k_2\, q_{e2} \cdot t + 1 / q_e$ | $K_2$ (min$^{-1}$)<br>$q_e$(mg·g$^{-1}$)<br>$\mathbf{R^2}$ | 0.004<br>25<br>**0.993** |
| **Elovich** | $q_t = \dfrac{\ln (\alpha_E . \beta_E)}{\beta_E} + \dfrac{1}{\beta_E} \ln t$ | $\alpha_E$(mg·g$^{-1}$min)<br>$\beta_E$ (g/mg·min$^{-1}$)<br>$R^2$ | 0.2641<br>0.1579<br>0.928 |
| **Intraparticule diffusion** | $q_t = k_i \cdot t^{1/2} + C$ | $K_i$(mg·g$^{-1}$min$^{-1/2}$)<br>$R^2$ | 1.16923<br>0.951 |
| **External diffusion** | $\mathrm{Ln}\ (1 - q_t/q_e) = -\ k_f\ t + C$ | $K_f$ (min$^{-1}$)<br>$R^2$ | -0.015<br>0.922 |

Where $q_e$ and $q_t$ are the adsorption capacities at equilibrium and at time $t$, respectively; $k_1$ and $k_2$ are the speed constants of the pseudo-first and second order, respectively; $\alpha_E$ is the initial adsorption rate and $\beta_E$ is the constant linked to the extent of surface coverage in Elovich kinetic; $k_i$ is the intraparticle diffusion rate and $K_f$ is the external diffusion rate constant in the liquid film.

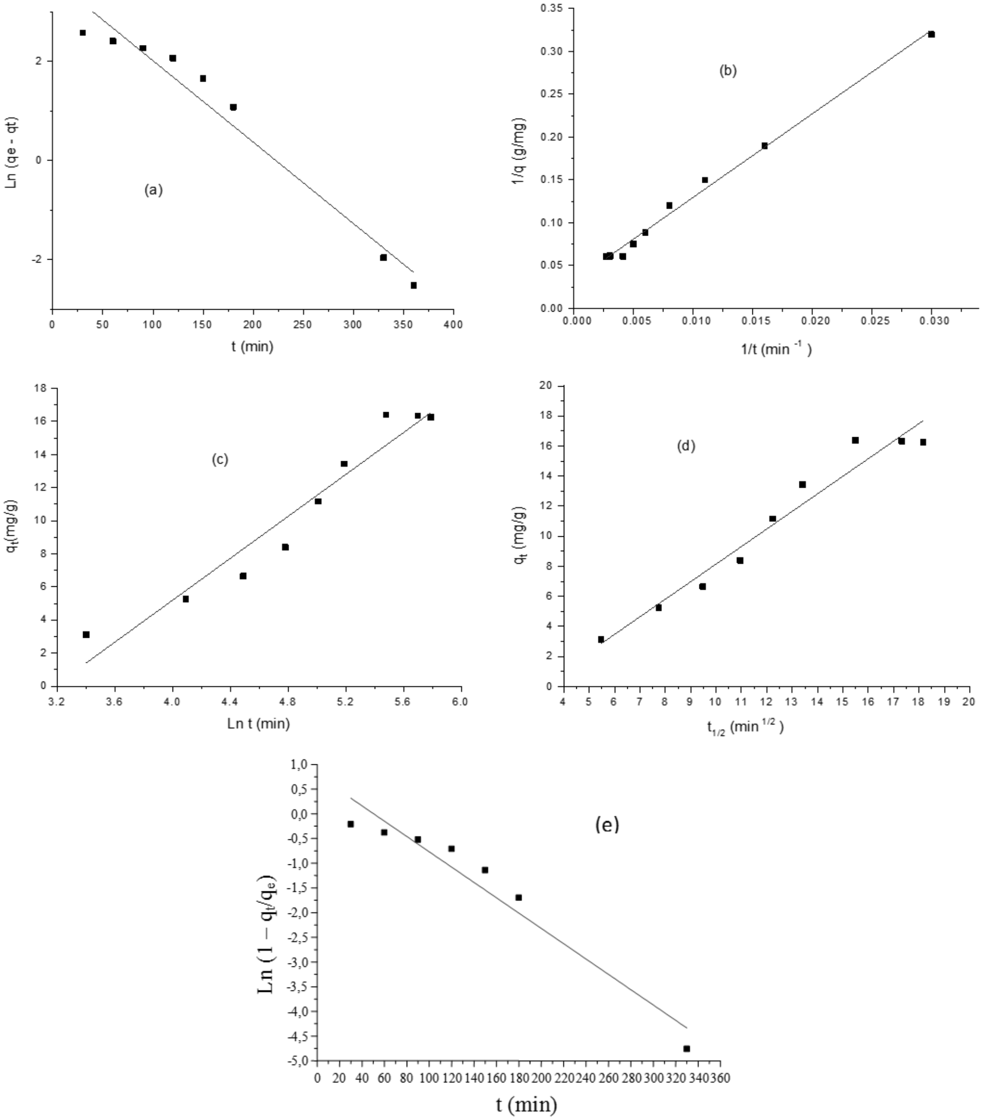

**Figure 4.** (a) Pseudo First order; (b) Pseudo Second order; (c) Elovich; (d) Intraparticle diffusion; **(e)** External diffusion kinetic adsorption

### Effect of AC mass on adsorption

In this set of experiments, different masses of the AC adsorbent chosen from 0.25 to 8 g were treated with 100 mL solution of 450 mg/L initial concentration of OMW at the optimum time obtained from the effect of contact time experiments (240 minutes). Figure 9 shows the percentage of phenolic compounds adsorption as a function of the AC adsorbent mass. In all cases, the percentage yield of this pollutant removal increases when the mass of the AC adsorbent increases until total saturation. This is due to the presence of large numbers of active sites on the surface (27). The curve in Figure 9 shows that 4 g of carbon mass is able to adsorbate a maximum of phenolic compound (62.32%) from OMW. In the next step, the optimal AC mass of 4 g will be taken to study the pH effect on phenolic compound adsorption from OMW.

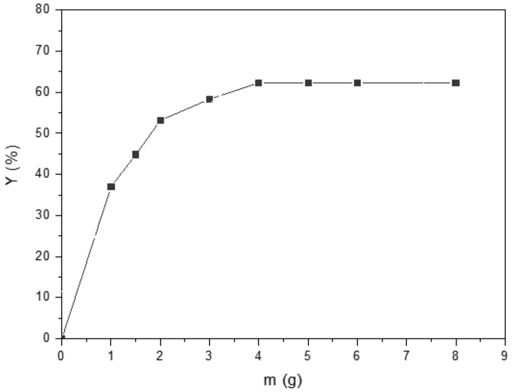

**Figure 5.** AC mass effect on phenolic adsorption

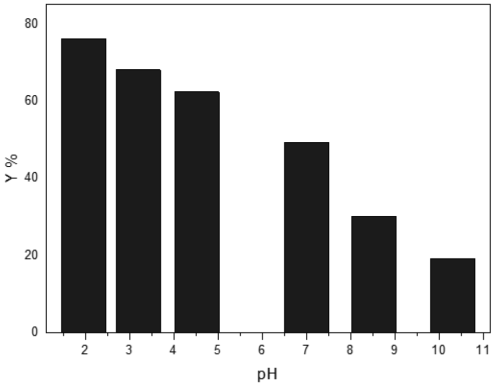

**Figure 6.** Effect of pH on phenolic adsorption

### Effect of pH on adsorption

The pH of the solution has a very significant role in the adsorption process (1). The pH of the OMW solution was chosen between 1.95 and 10.32 and a contact time was fixed from previous results at 240 min. The obtained results (Figure 10) show a considerable influence of the pH value on the retention of phenolic from vegetable water by the activated carbon: The adsorption yields decrease with the increase of the pH values. The lower adsorption yields in an alkaline medium can be explained by an excess of OH ions in the solution, which leads to competition with this effluent on the adsorption sites of the activated carbon. Indeed, the high concentration and high mobility of OH ions would promote their adsorption relative to the pollutant (28). The optimum pH allowing maximum adsorption of OMW on activated carbon **(**Y% = 76.19) is pH = 1.95 under the study conditions.

## CONCLUSION

The discharge of olive oil mill wastewater from olive oil-producing industries is a major problem, especially for countries in the Mediterranean basin. They contain a large organic fraction (phenolic compounds) and cause several types of pollution.

In this study, activated carbon was successfully used for the elimination of phenolic compounds from olive oil mill wastewater. The prepared activated carbon from olive leaves using carbonization and chemical activation process. The material was characterized using different technics: Ash content, moisture content, iodine value, $pH_{zpc}$, FTIR, and XRD. From the operating conditions, the results of phenolic compounds on activated carbon show that the prepared AC can adsorb close to 80 % of pollutant using 4 g and 100 mL volume of solution at 240 min and pH 1.95. The kinetics of phenolic compounds adsorption on the prepared activated carbon were studied. It can be deduced that the pseudo-second-order model described well this adsorption. The correlation coefficient was $R^2 = 0.992$ and the value of the calculated adsorbed quantity is close to the value of the experimental adsorbed quantity. The use of activated carbon prepared from olive leaves is an economical and environmental way to reduce the amount of waste from olive oil mills.

## Acknowledgements

The Algerian Directorate General of Scientific Research and Technological Development (DGRSDT), and the Algerian Ministry of Higher Education and Scientific Research (MESRS) are greatly thanked.

## REFERENCES

1. Philip, K.; Jacob, R. and Gopalakrishnan, J. Characterization of Cassava Root Husk Powder: Equilibrium, Kinetic and Modeling Studies as Bioadsorbent for Copper(II) and Lead(II). *Journal of Encapsulation and Adsorption Sciences.* **2021**, *11* (2), 69. doi: 10.4236/jeas.2021.112004
2. Achaka, M.; Hafidi, A., Ouazzani,N.; Sayadi, S. and Mandi, L. Low cost biosorbent "banana peel" for the removal of phenolic compounds from olive mill wastewater: Kinetic and equilibrium studies. *Journal of Hazardous Materials*. **2009**, *166*, 117–125.
3. Elboughdiri, N.; Jamoussi, B.; Hannachi, A.; Romdhane, M. and Ab-Derraba, A. Separation of phenolic compounds from olive oil mill wastewater. *Science and Technology Waste.* **2006**, *47*, 17.
4. Khdair, A. I.; Abu-Rumman, G.; Khdair, S. I. Pollution estimation from olive mills wastewater in Jordan. *Heliyon*, **2019**, **5** (8), e02386. doi: 10.1016/j.heliyon.2019.e02386
5. El Yamani, M.; Sakar, E.; Boussakouran, A.; Ghabbour, N.; Rharrabti, Y. Physicochemical and microbiological characterization of olive mill wastewater (OMW) from different regions of Northern Morocco. *Environmental Technology*. **2020**, *41*(23). Doi: 10.1080/09593330.2019.1597926

6. Ouabou, E.; Anouar, A.; Hilali, S. Elimination of organic pollutants in olive oil margin by filtration on a clay column and eucalyptus sawdust. *Journal of Applied Biosciences*. **2014**, *75*, 6232. http://dx.doi.org/10.4314/jab.v79i1.12
7. Papazi, A.; Pappas, I.; Kotzabasis, K. Combinational system for biodegradation of olive oil mill wastewater phenolics and high yield of bio-hydrogen production. *Journal of Biotechnology*. **2019**, 306, 47. https://doi .org/10.1016/j.jbiotec.2019.09.009
8. Grigalius, I.; Petrikaite, V. Relationship between Antioxidant and Anticancer Activity of Trihydroxyflavones. *Molecules.* **2017**, *22*(12), 2169. doi: 10.3390/molecules22122169.
9. Ukanwa, K. S.; Patchigolla, K.; Sakrabani, R.; Anthony, E.; Mandavgane, S. A Review of Chemicals to Produce Activated Carbon from Agricultural Waste Biomass. *Sustainability*. **2019**, *11* (22), 6204. doi:10.3390/su11226204.
10. Tuerhong, T. and Kuerban, Z. Preparation and characterization of cattle manure-based activated carbon for hydrogen sulfide removal at room temperature. *Journal of Environmental Chemical Engineering*. **2022**, *10* (2), 107177. doi: 10.1016/j.jece.2022.107177.
11. Chedeville, O.; Debacq, M.; Porte, C. Removal of phenolic compounds present in olive mill wastewaters by ozonation. *Journal of Desalination*. **2009**, *249*, 865.
12. Mouzaoui, K.; Yazzag, L.; Moulti-Mati, L. Phenolic compounds of olive pomace from traditional and modern oil mills: Purification test of oleuropein and hydroxytyrosol. *Sciences & Technologie C.* **2014**, *40*. http://revue.umc.edu.dz/index.php/c/issue/view/133
13. Caporaso, N.; Formisano, D.; Genovese, A.Use of phenolic compounds from olive mill wastewater as valuable ingredients for functional foods. *Critical Reviews In Food Science and Nutrition*. **2018**, *58*(16), 2829. doi: 10.1080/10408398.2017.1343797
14. Al-Qodah, Z.; Al-Zoubi, H.; Hudaib, B.; Omar, W.; Soleimani, M.; Abu-Romman, S.; Frontistis, Z. Sustainable vs. Conventional Approach for Olive Oil Wastewater Management: A Review of the State of the Art. *Water*. **2022**, *14*(11), 1695. https://doi.org/10.3390/w14111695.
15. Hakky Mohammad, A.; Radović, I.; Ivanović, M.; Kijevčanin, M. Adsorption of Metformin on Activated Carbon Produced from the Water Hyacinth Biowaste Using $H_3PO_4$ as a Chemical Activator. *Sustainability*. **2022**, *14*, 11144. https://doi.org/10.3390/su141811144
16. Siragi, D.; Maazou, B.; Hima, H. I.; Mousbahou, M.; Adamou, Z.; Natatou, I. Elimination of chromium by activated carbon produced and characterized from the shell of the kernel of Balanites Aegyptiaca. *Int. J. Biol. Chem. Sci.* **2017**, *11*(6), 3050. doi: https://dx.doi.org/10.4314/ijbcs.v11i6.39
17. Boudia, R.; Mimanne, G.; Benhabib, K.; Pirault-Roy, L. Preparation of mesoporous activated carbon from date stones for the adsorption of Bemacid Red. *Water Sci. Technol.* **2019**, 79(7), 1357. doi: 10.2166/wst.2019.135
18. Djeziri, S.; Djellouli, M. Enhancing the value of agro-food waste in the treatment of water laden with organic pollutants. Desalination and Water Treatment. 2022, 255, 34. doi: 10.5004/dwt.2022.28319
19. Dhidan, S. K. Removal of phenolic compunds from aqueous solutions by adsoption onto activted carbons prepared from date stones by chemical activation with $FeCl_3$. *J. Engineering.* **2012**, *18*, 63–77.
20. H.T. Kuete, I.; Tchuifon, D.R.; Ndifor-Angwafor, G.N.; Kamdem, A.T.; Anagho, S.G. Kinetic, isotherm and thermodynamic studies of the adsorption of Thymol blue onto powdered activated carbons from Garcinia cola nut shells impregnated with $H_3 PO_4$ and KOH: non-linear regression analysis. *J. Encapsulation Adsorpt. Sci*. **2020**, *10*. doi: 10.4236/jeas.2020.101001
21. Alorabi, A.Q. Effective Removal of Malachite Green from Aqueous Solutions Using Magnetic Nanocomposite: Synthesis, Characterization, and Equilibrium Study. *Adsorption Science & Technology*. **2021**, *6*, 1-15. doi: 10.1155/2021/2359110
22. Asrat, Y.; Adugna, A.T.; Kamaraj, M.; Beyan, S.M. Adsorption Phenomenon of Arundinaria alpine Stem-Based Activated Carbon for the Removal of Lead from Aqueous Solution. *Journal of Chemistry*. **2021**, Article ID 5554353. https://doi.org/10.1155/2021/5554353

UDC: 66.021.3.081.3:547.56]:628.3
BIBLID: 1450-7188 (2023) 54, 197-208

Original scientific paper

23. Beyan, S. M.; Prabhu, S. V.; Abeto Ambio, T.; Gomadurai, C. A Statistical Modeling and Optimization for Cr(VI) Adsorption from Aqueous Media via Teff Straw-Based Activated Carbon: Isotherm, Kinetics, and Thermodynamic Studies. *Adsorption Science & Technology*. **2022**, Article ID 7998069. doi: 10.1080/03067319.2022.2026942
24. Liu, L.; Rao, Y.; Tian, C. ; Huang, T.; Lu, J.; Zhang, M. and Han, M. Adsorption Performance of La(III) and Y(III) on Orange Peel: Impact of Experimental Variables, Isotherms, and Kinetics. *Adsorption Science & Technology*. **2021**, Article ID 7189639. https://doi.org/10.1155/2021/7189639
25. Villabona-Ortíz, A.; Kelly, J.; Lopez, F.; Ortega-Toro, R. Kinetics and Adsorption Equilibrium in the Removal of Azo-Anionic Dyes by Modified Cellulose. *Journal of Sustainability*. **2022**, *14*, 3640. https://doi.org/10.3390/su14063640
26. Prajapati, A.K.; Verma, P.; Singh, S.; Mondal, M.K. Adsorption-Desorption Surface Bindings, Kinetics, and Mass Transfer Behavior of Thermally and Chemically Treated Great Millet Husk towards Cr(VI) Removal from Synthetic Wastewater. *Journal of Adsorption Science & Technology*, **2022**, 1-16. https://doi.org/10.1155/2022/3956977
27. Kra, O.; Atheba, G.P.; Kouadio, N.A.; Drogui, P. and Trokourey, A. Activated Carbon Based on Acacia Wood (Auriculeaformis, Côte d'Ivoire) and Application to the Environment through the Elimination of $Pb^{2+}$ Ions in Industrial Effluents. *Journal of Encapsulation and Adsorption Sciences*, **2021**, *11* (1), 18-43. doi: 10.4236/jeas.2021.111002
28. Kyzas, G. Z.; Siafaka, P. I.; Bikiaris, D. N.; Koukaras, E. N.; Froudakis, G. E. Alternative use of cross-linked polyallylamine (known as Sevelamer pharmaceutical compound) as biosorbent. *J. Colloid Interface Sci.* **2015**, *442*, 49–59.

APTEFF, Vol. 54, 1-335 (2023) UDC: 621.642:634.12:550.34:504.06
DOI: https://doi.org/10.2298/APT2354209S BIBLID: 1450-7188 (2023) 54, 209-222

Original scientific paper

# MEMBRANE INSTALLATION IN STORAGE TANKS FOR SEISMIC LOADS IMPACT PROTECTION

*Olena SIERIKOVA*[1]*, *Elena STRELNIKOVA*[2], *Denys KRIUTCHENKO*[2]

[1] Applied Mechanics and Environmental Protection Technologies Department, National University of Civil Protection of Ukraine, Kharkiv, Ukraine
[2] A.M. Podgorny Institute for Mechanical Engineering Problems NAS of Ukraine, Kharkiv, Ukraine

**Received: 15 Januar 2023** **Revised: 20 August 2023** **Accepted: 01 September 2023**

*There are about 1 million earthquakes of varying intensity every year in the world. The research of seismic loads on the important technogenic objects remains the urgent issue both globally and regionally. The paper aim is to prevent emergencies and negative impact on the environment in case of damage, destruction and leakage of storage tanks for toxic and flammable liquids due to seismic loads of different strength. The liquid vibrations in rigid and elastic reservoirs have been considered. It has been established that level changing via time for reservoirs without covering membrane can be very large and lead to the appearance of excess pressure on the tank wall. The installation of the floating membrane leads to decreasing both the free surface level and the pressure on the tank walls. The results of the research will allow to reduce sloshing effects and pressure on the reservoir walls, and so to extend the service life, minimize the ecologically hazardous impact on the environment, and prevent emergencies.*

**Keywords**: storage tanks, environmental safety, earthquakes, seismic loads, free and forced vibrations, membrane cover.

## INTRODUCTION

In the modern world, natural disasters turn into social catastrophes, often due to the unpreparedness of society for the next manifestations of the elements. The first and most important step in reducing earthquake damage should be to study the "seismic climate" of the area, i.e. its zoning according to the degree of seismic hazard, and the corresponding seismic construction and preventive measures for objects that could dangerously affect the environment.

Every year there are about 1 million earthquakes of varying intensity in the world. Therefore, the study of seismic loads on important technogenic objects remains the urgent issue both globally and regionally (1).

It should be noted that strong subcortical earthquakes of the Vrancea zone (Romania) are felt throughout Ukraine. The last strong earthquakes occurred in 1940, 1977, 1986 and 1990. In general, up to 40% of the territory of Ukraine could be covered by the direct impact of dangerous seismic events and up to 70% - the joint impact of earthquakes with flooding, landslides, subsidence and other engineering and geological processes that adversely affect the stability of structures (2,3). Seismic areas of Ukraine, with the projected

---

* Corresponding author: Olena SIERIKOVA, Applied Mechanics and Environmental Protection Technologies Department, National University of Civil Protection of Ukraine, Kharkiv, Ukraine.
E-mail: elena.kharkov13@gmail.com

seismic intensity of 6-9 points, occupy about 20% of the territory (≈120 thousand km$^2$), inhabited by more than 10 million people. Areas with the intensity of 7–9 points occupy about 12% of the territory and include about 80 settlements inhabited by more than 7 million people (4,5).

Containers and tanks for oil storage, toxic and flammable liquids are widely used in various fields of engineering practice, such as aircraft, chemical, oil and gas industry, energy engineering and transport. These tanks operate under conditions of high technological loads and filled with oil, flammable or toxic substances. As a result of the sudden action of seismic loads, the liquid stored in the tanks begins to experience intense sloshing (6).

Sloshing is the phenomenon observed in the number of industrial facilities: in containers for storage of liquefied gas, oil, fuel tanks, in the tanks of cargo tanks. It is known that partially filled tanks are exposed to particularly intense sloshes. This could lead to high pressure on the tank walls, destruction of the structure or loss of stability and could cause the outflow of hazardous contents, which in turn could lead to serious environmental consequences. In case of tank accidents, oil products spill and pollute the surrounding areas and water basins. The ingress of toxic and flammable liquids from the tanks for their storage into the environment and their further spread to the territory of settlements could cause mass people and animals poisoning, and lead to environment pollution. Liquid spills could lead to explosions and fires that could spread to nearby reservoirs and surrounding areas. As the tanks store the huge supply of combustible substances, the fire could have serious consequences. Economic losses from oil leakage and fire accidents include not only direct losses, but also the cost of environmental restoration measures, as well as the cost of replenishing the stock of petroleum products (6-8).

The structural damage of reservoirs for the preservation of toxic and flammable liquids of strong winds has been calculated in (9).

Kendzera O.V. has treated the different seismic loads and responses in soils (4, 5).

Most of the research papers of Korgin A.V. (10), Qin F. (11), and Khalmuradov B. (12) devoted to assessing the significance of the effects of reservoirs for the preservation of toxic and flammable liquids on the environment and monitoring changes in the tightness of reservoirs, the rate of their destruction under technogenic and climatic factors, but such the significant impact on reservoir stability as earthquakes insufficiently studied.

Analysis of research on the sloshing issues of liquid in tanks, provided in the R.A. Ibrahim papers (13, 14). Note also the papers on the liquid sloshing in cylindrical tanks under the action of seismic loads (15-17).

A finite element model has been developed in (18) to study free vibration of a liquid in a tank of arbitrary geometry with a flexible membrane constraining the liquid free-surface. However, other papers have also considered the moving containers to prevent resonance and such different loads on the containers.

The membrane implementation in liquid containers has been investigated in (19).

Improving tank material characteristics has been studied in papers (20-23).

Dynamic testing of tanks and silos could be traced to the late 1960s, however, the development in the last 15-20 years is more interesting to the reader and it might allow him to better understand the work and locate it as a new contribution to this field (24-28).

The aim of the paper is to prevent emergencies and negative impact on the environment in case of damage, destruction and leakage of storage tanks of toxic and flammable liquids due to seismic loads of different strength.

DOI: https://doi.org/10.2298/APT2354209S
BIBLID: 1450-7188 (2023) 54, 209-222

## MATERIALS AND METHODS

Estimation of seismic strength has been carried out as follows. At the first stage, the frequencies and modes of the natural vibrations of the tank have been determined using the methods developed in papers (23, 29, 30).

Next, the model inertial seismic loads on the structure have been determined.

Analysis of experimental studies of seismic resistance in paper (31) have been shown that usually only the lowest natural frequencies of oscillations are located in the region of seismic resonance. The higher natural frequencies are significantly away from the region of seismic resonance. Usually, already the second natural frequency is higher than the upper limit of the spectrum.

As in paper (31), it has been established that the lower frequencies of oscillations of a tank with a liquid at given mechanical and geometric characteristics are the sloshing frequencies. The frequency spectra of free surface oscillations and elastic walls are separated.

Forced oscillations of the reservoir under a given seismic load have been studied.

Here liquid vibrations have been considered with and without covering the free surface.

In the paper the issue of fluid vibrations in the arbitrary shell of revolution has been considered.

First, the frequencies and modes of the natural vibrations of the tank have been determined using the Boundary Element Methods (BEM).

It has been denoted the wetted surface of the shell by $S_1$, and the free surface by $S_0$ (Figure 1). The cylindrical shell with the flat bottom, partially filled with liquid has been considered as the model of the oil storage.

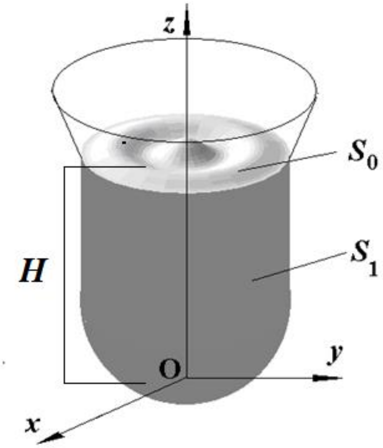

**Figure 1.** Shell of revolution

It has been assumed that the Cartesian coordinate system 0xyz connected to the shell, the free surface of the liquid $S_0$ coincides with the plane $z=H$ at rest. It has been presumed that the fluid is ideal, incompressible, and its motion, which began at rest, is vortex-free. Under these conditions, there is the potential for fluid velocities that satisfies the Laplace equation:

$$V_x = \frac{\partial \Phi}{\partial x};\ V_y = \frac{\partial \Phi}{\partial y};\ V_z = \frac{\partial \Phi}{\partial z}, \qquad [1]$$

The pressure $p$ value on the shell walls has been determined from the linearized Bernoulli’s integral by the formula:

$$p = -\rho_l\left(\frac{\partial \Phi}{\partial t} + gz\right) + p_0 + a_s(t)x, \qquad [2]$$

in which Φ is the velocity potential, $g$ is gravity acceleration, $z$ is the point coordinate of the fluid measured in the vertical direction, $\rho_l$ is the fluid density, $p_0$ is the atmospheric pressure, $a_s(t)$ is the function that characterizes the external influence (horizontal seismic acceleration). In equation [2] the value $gz$ is the gravitational potential, and so according to [14], at the free surface, the pressure is equivalent to the ambient pressure, i.e. $p = p_0$.

So, the following kinematic and dynamic conditions must be fulfilled on the free surface of the liquid:

$$\left.\frac{\partial \Phi}{\partial \mathbf{n}}\right|_{S_0} = \frac{\partial \zeta}{\partial t}; \quad p - p_0|_{S_0} = 0, \qquad [3]$$

where the function ζ describes the shape and position of the free surface.

Thus, for the velocity potential it has been obtained the following boundary value issue:

$$\nabla^2 \Phi = 0;\ \left.\frac{\partial \Phi}{\partial \mathbf{n}}\right|_{S_1} = 0; \left.\frac{\partial \Phi}{\partial \mathbf{n}}\right|_{S_0} = \frac{\partial \zeta}{\partial t}; \quad p - p_0|_{S_0} = 0;\ \left.\frac{\partial \Phi}{\partial t} + g\zeta + a_s(t)x\right|_{S_0} = 0. \qquad [4]$$

Determined the potential of velocities Φ and the function ζ, it has been set the height of the rise of the free surface and determined the pressure of the liquid on the shell walls.

It has been presented the potential Φ in the form:

$$\Phi = \sum_{k=1}^{M} \dot{d}_k \phi_k. \qquad [5]$$

For the functions $\varphi_k$, the following boundary value problems have been considered:

$$\nabla^2 \phi_k = 0, \left.\frac{\partial \phi_k}{\partial \boldsymbol{n}}\right|_{S_1} = 0, \qquad [6]$$

$$\left.\frac{\partial \phi_k}{\partial \boldsymbol{n}}\right|_{S_0} = \frac{\partial \zeta}{\partial t}; \quad \frac{\partial \phi_k}{\partial t} + g\zeta = 0. \qquad [7]$$

It has been differentiated the second ratio in equation [5] by $t$ and substitute in the obtained equality $\frac{\partial \zeta}{\partial t}$ from the first ratio.

Next, it has been presented as the functions $\phi_k$ as $\phi_k(x,y,z,t) = \exp(i\chi_k t)\phi_k(x,y,z)$. It has been gained the eigenvalues problem, and the following equality will be satisfied on the free surface:

$$\frac{\partial \phi_k}{\partial n} = \frac{\chi_k^2}{g}\phi_k. \qquad [8]$$

For the free surface level, the next expression has been obtained:

$$\zeta = \sum_{k=1}^{M} d_k \frac{\partial \phi_k}{\partial n}. \qquad [9]$$

In a cylindrical coordinate system, expressions for the required functions have been gained as follows:

$$\phi_k(r, z, \theta) = \phi_k(r, z) \cos \alpha\, \theta \qquad [10]$$

Here $\alpha$ is the harmonic number. Thus, the frequencies and modes of free oscillations for different $\alpha$ have been considered separately.

It has been represented $\varphi$ as the potentials sum of the simple and double layer (18):

$$2\pi\Phi(P_0) = \iint_S \frac{\partial\Phi}{\partial \mathbf{n}} \frac{1}{|P-P_0|} dS - \iint_S \Phi \frac{\partial}{\partial \mathbf{n}} \frac{1}{|P-P_0|} dS. \qquad [11]$$

Here $S = S_1 \cup S_0$; points P and $P_0$ belong to the surface S, and $|P - P_0|$ is the Cartesian distance between points $P$ and $P_0$. Equation [11] is a consequence of the third Green's identity in the case when the point $P_0$ belongs to the surface S (18) This is the integral form of Laplace's equation and it will be used here in numerical implementation of boundary element method (19).

Satisfying the boundary conditions in (6) and (7), it has been achieved the next system of integral equations:

$$\begin{cases} 2\pi\varphi_1 + \iint_{S_1} \varphi_1 \frac{\partial}{\partial n}\left(\frac{1}{r}\right) dS_1 - \frac{\chi^2}{g} \iint_{S_0} \varphi_0 \frac{1}{r} dS_0 + \iint_{S_0} \varphi_0 \frac{\partial}{\partial z}\left(\frac{1}{r}\right) dS_0 = 0, \\ - \iint_{S_1} \varphi_1 \frac{\partial}{\partial n}\left(\frac{1}{r}\right) dS_1 - 2\pi\varphi_0 + \frac{\chi^2}{g} \iint_{S_0} \varphi_0 \frac{1}{r} dS_0 = 0. \end{cases} \qquad [12]$$

Here, for convenience, it has been denoted the potential value on the free surface as $\varphi_0$, and as $\varphi_1$ on the shell walls.

The solution of system (12) in the form (10) has been found.

To solve this system of singular integral equations, it has been applied the boundary elements method described in papers (7, 8).

So, the modes and frequencies of own tank vibrations have been determined. These modes are hereinafter considered as basic functions.

Next stage of the research has been devoted to simulation of the forced vibrations. To determine the basic relations for $d_k$ in equation [9] it has been substituted basic functions into expressions for the velocity potential equation [5] and to the free surface shape equation [9]. The resulting series have been substituted into the boundary condition on the free surface:

$$\frac{\partial\Phi}{\partial t} + \left(g + a_z(t)\right)\zeta + a_x(t)x\Big|_{S_0} = 0.$$

Since in the cylindrical coordinate system, $x = r\cos\theta$, there will be only first harmonic, i.e. in formula [6] it has been considered only $\alpha$=1. Further, it has been performed correlation on the free surface $S_0$:

$$\sum_{k=1}^{M} \ddot{d}_k \phi_k + \left(g + a_z(t)\right) \sum_{k=1}^{M} d_k \frac{\partial \phi_k}{\partial n} + a_x(t) r = 0.$$

But on the surface S$_0$ the ratio [8] has also been fulfilled. Then the above equality will take the form:

$$\sum_{k=1}^{M} \ddot{d}_k \phi_k + \left(g + a_z(t)\right) \sum_{k=1}^{M} \frac{\chi_k^2}{g} d_k \phi_k + a_x(t) r = 0. \qquad [13]$$

Multiplying equation [9] scalarly on $\phi_l$ $\left(l = \overline{1, M}\right)$ and using the eigenforms orthogonality, it has been obtained the system of second-order ordinary differential equations:

$$\ddot{d}_k + \frac{\chi_k^2}{g}\left(g + a_z(t)\right) d_k + a_x(t) F_k = 0, \quad F_k = \frac{(r, \phi_k)}{(\phi_k, \phi_k)}, \quad k = \overline{1, M}. \qquad [14]$$

It has been assumed that before the horizontal load applied, the tank was at rest. Then equation [14] has been solved under zero initial conditions. To solve the system [14], the numerical method has been used as in papers (25, 26). This numerical solution allows us to receive the tie history for the free surface level ζ, ad well as the pressure *p*, obtained by the formula:

$$p = -\rho_l \left(\frac{\partial \Phi}{\partial t} + \left(g + a_z(t)\right)\zeta\right) + p_0 + a_x(t) x. \qquad [15]$$

It could be concluded from equation [15] that in the case of horizontal seism, the only first harmonic contributes to the studied values of ζ and *p*.

Considering nonlinear sloshing and coupled vertical and horizontal excitations, the Bernoulli equation has to be used:

$$p - p_0 = -\rho_l \left[\frac{\partial \Phi}{\partial t} + a_x(t) x + \left(g + a_z(t)\right)\zeta + \frac{1}{2}(\nabla\Phi, \nabla\Phi)\right] \qquad [16]$$

where $a_x(t)$ and $a_z(t)$ are vertical and horizontal driving force accelerations.

## RESULTS AND DISCUSSION

As an example, the elastic cylindrical shell with radius *R* = 1 m and the filling level *H* = 1 m under the action of seismic load with different parameters has been considered. It has been supposed that shell thickness *h* = 0.01 m, Young's modulus *E* = $2 \cdot 10^5$ MPa, Poisson's ratio ν = 0.3, shell material density ρ = 7800 kg/m3, liquid density ρ$_0$ = 1000 kg/m$^3$. It is assumed that the shell is rigidly fixed to the contour, that is, the boundary conditions are as follows: $u_r = u_z = u_\theta = 0$ at *z*=0 and *r*=*R*, Fig.1.

The linear formulation has been applied at the first stage. As it has been shown in paper (21), the non-linear effects associated with the sloshing of the filler have the greatest influence on the vibration damping. But to analyse the maximum level of liquid rise, there could be restricted ourselves to a linear formulation.

First of all, it is necessary to receive the own modes of the liquid vibrations, i.e. to obtain the system of basic functions. It has been done according to techniques, described in papers (12, 30). As it has been mentioned before, the first harmonic ($\alpha$=1) is a subject of interest. It should be noted that axially-symmetrical harmonic ($\alpha$=0) also will be involved in consideration, if even a very small vertical component of the seismic load has been observed. Fig. 2 demonstrates the first three vibration modes corresponding to these harmonics.

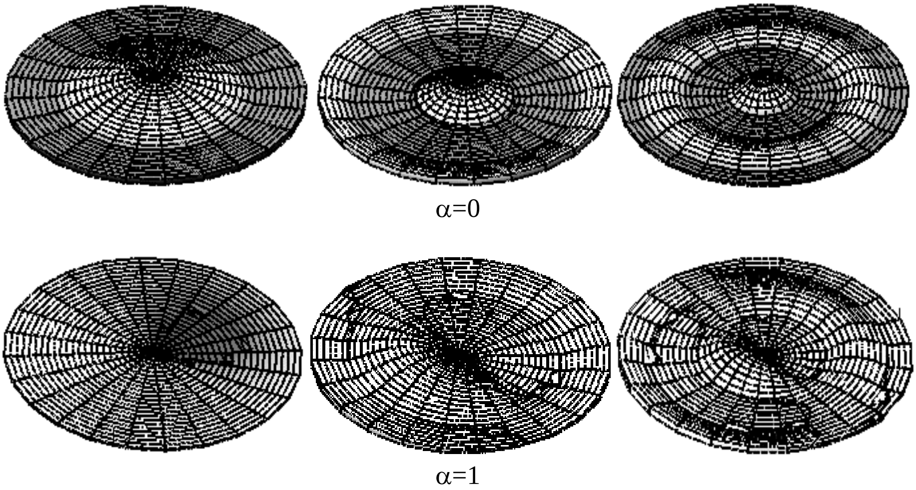

**Figure 2.** The first modes of axisymmetric and non-axisymmetric oscillations of the free surface

Table 1 shows the lowest vibration frequencies of the free liquid surface and the tank walls.

**Table 1.** Lowest vibration frequencies of cylindrical shell

| Frequency, Hz proposed BEM | Frequency, Hz analytical values (13) | Harmonics, frequency number | Vibration type |
|---|---|---|---|
| 0.6418 | 0.6418 | 1, 1 | sloshing |
| 0.9739 | 0.9739 | 0, 1 | sloshing |
| 1.1509 | 1.1510 | 1, 2 | sloshing |
| 1.3208 | 1.3209 | 0, 2 | sloshing |
| 1.4564 | 1.4566 | 1, 3 | sloshing |
| 1.7054 | 1.7058 | 1, 4 | sloshing |
| 1.7096 | - | 0, 1 | bottom vibration |
| 1.9212 | 1.9215 | 1, 5 | sloshing |

It has been established that the lower frequencies of vibrations of the liquid-filled tank with given mechanical and geometric characteristics are sloshing frequencies. The frequency spectra of free surface oscillations and elastic walls are separated. However, in supposition that the shell bottom is elastic, it could be found that for sufficiently thin shells, the bottom oscillation frequency is comparable (and even very close) to one of the fundamental frequencies. The results of Table 1 testify it, namely one could see that sloshing frequency $\omega_{14}$= 1.7054Hz is very close to the frequency of the axially-symmetric bottom vibration $\omega_{01}$= 1.7096Hz. So, these results reveal the necessity to consider first and zero harmonics at vibrations analysis taking into account the elasticity of the reservoir's walls (32,33). It leads to the next presentation of unknowns as in paper (34):

$$\mathbf{U} = \sum_{k=1}^{N} c_k \boldsymbol{u}_k,\ \Phi = \sum_{k=1}^{N} \dot{c_k} \varphi_{1k} + \sum_{k=1}^{N} \dot{d}_k \varphi_{2k}\boldsymbol{,}\ \zeta = \sum_{k=1}^{N} c_k \frac{\partial \varphi_{1k}}{\partial \mathbf{n}} + \sum_{k=1}^{N} d_k \frac{\partial \varphi_{2k}}{\partial \mathbf{n}} \quad [17]$$

Presentation [17] leads to the following system of second order ordinary differential equations has been received:

$$\ddot{c_l}(t) + \Omega_l^2 c_l(t) = +\sum_{k=1}^{M} \ddot{d}_k\,(t)(\varphi_{2k}, u_l) + a_x(t)(x, u_l) + +a_z(t)(z, u_l) = 0\boldsymbol{,} \quad [18]$$

$$\ddot{d}(\varphi_{2l}, \varphi(_{2l}) + (1 + a_z(t)/g)\chi_k^2(\varphi_{2l}, \varphi_{2l}) + \sum_{k=1}^{N} c_k \left(\frac{\partial \varphi_{1k}}{\partial \mathbf{n}}, \varphi_{2l}\right) + \ a_x(t)(x, \varphi_{2l}) = 0.$$

From equations [18], the unknown time dependent functions $c_k(t)$ and $d_k(t)$ will be received. For their unambiguous definition the initial conditions have been used in the form:

$$c_k(0) = c_k, \dot{c_k}(0) = c_{k1},\ d_k(0) = d_k, \dot{d_k}(0) = d_{k1} \quad [19]$$

Forced oscillations of the reservoir under a given seismic load have been studied.

Table 2 as in paper (33) provides accelerations for a given earthquake force.

**Table 2.** The level of acceleration via the seismicity

| Magnitude | 5 | 6 | 7 | 8 | 9 | 10 |
|---|---|---|---|---|---|---|
| Maximum acceleration level of (in fractions of g) | 0.025 | 0.050 | 0.100 | 0.200 | 0.400 | 0.800 |

The characteristic frequency of the seismic load at 6 points is equal to 2Hz.

The system of differential equations in the form [13], and initial data [14] has been obtained taking into account the entire frequency spectrum given in Table 1. Initial conditions are following:

$$c_k(0) = 0, \dot{c_k}(0) = 0,\ d_k(0) = 0, \dot{d_k}(0) = 0.$$

Furthermore, it has been supposed that before earthquake the liquid-filled the reservoir was in state of rest.

Next, the coupled problem of the liquid vibration in the rigid cylindrical shell with covering the free surface by thin elastic membrane has been considered. Assuming there is no gap between fluid and the elastic cover, the dynamic boundary condition on the interface of liquid domain and the elastic membrane could be given as follows:

$$\rho_m h_m \frac{\partial^2 w}{\partial t^2} + T\Delta^2 w = -\rho_l \frac{\partial \Phi}{\partial t} - \big(g + a_z(t)\big)w - a_x(t)x, \qquad [20]$$

where *w* is the deflection of the elastic plate, *t* is the time, and *T* is a tension, and $\rho_m$, $h_m$are, respectively, membrane's density and thickness. The right-hand side of [18] is the fluid pressure acting on the elastic cover, which is obtained from the linearized Bernoulli equation.

The linearized kinematic condition at the interface surface can be written as:

$$\left.\frac{\partial \Phi}{\partial \boldsymbol{n}}\right|_{S_0} = \frac{\partial w}{\partial t} \qquad [21]$$

On the rigid side walls and bottom of the tank the impermeable boundary condition has been applied:

$$\left.\frac{\partial \Phi}{\partial \boldsymbol{n}}\right|_{S_1} = 0 \qquad [22]$$

The potential Φ has been satisfied to the Laplace equation:

$$\nabla^2 \Phi = 0. \qquad [23]$$

In addition, the boundary conditions for membrane contour have been imposed. The most commonly used types have been clamped, free, and simply supported conditions. For clamped contour the Dirichlet condition is in use, namely $w(R) = 0$, and for free contour the Newman condition has been involved:

$$\left.\frac{\partial \mathrm{w}}{\partial \boldsymbol{r}}\right|_{r=R} = 0. \qquad [24]$$

It is namely condition [24] that should be chosen to adequately describe the floating cover.

Moreover, the following boundary value problem, described by equations [20], and [23] with boundary conditions [21], [22], and [24] has been gained.

For its numerical solution there have been used the mode superposition method as described in (27). First, the frequencies and modes of the membrane without interaction with the liquid have been obtained from the equation:

$$\rho_m h_m \frac{\partial^2 w}{\partial t^2} + T\Delta^2 w = 0 \qquad [25]$$

Then the presentation for *w* has been applied as:

$$w = \sum_{k=1}^{M} c_k w_k, \qquad [26]$$

where $w_k$ are their own membrane modes. For function Φ has been used the next presentation:

$$\Phi = \sum_{k=1}^{M} \dot{c}_k \phi_k, \qquad [27]$$

where functions $\phi_k$ are solutions of following boundary value problems:

$$\nabla^2 \phi_k = 0, \qquad \left.\frac{\partial \phi_k}{\partial \boldsymbol{n}}\right|_{S_0} = \frac{\partial w_k}{\partial t}, \qquad \left.\frac{\partial \phi_k}{\partial \boldsymbol{n}}\right|_{S_1} = 0. \qquad [28]$$

Substituting series [26] and [27] into [20] we come to the system of second order differential equations relative to time-dependent unknowns$[c_1, c_2, \dots . c_M]$.

According to papers (33, 34) the artificial accelerogram has been constructed for $a_x(t)$. Figure 2a demonstrates $a_x(t)$ for the earthquake with magnitude 6 points and characteristic frequency equals to 2Hz, and Figure 2b shows the free surface level via time. Here we consider the reservoir without covering the membrane.

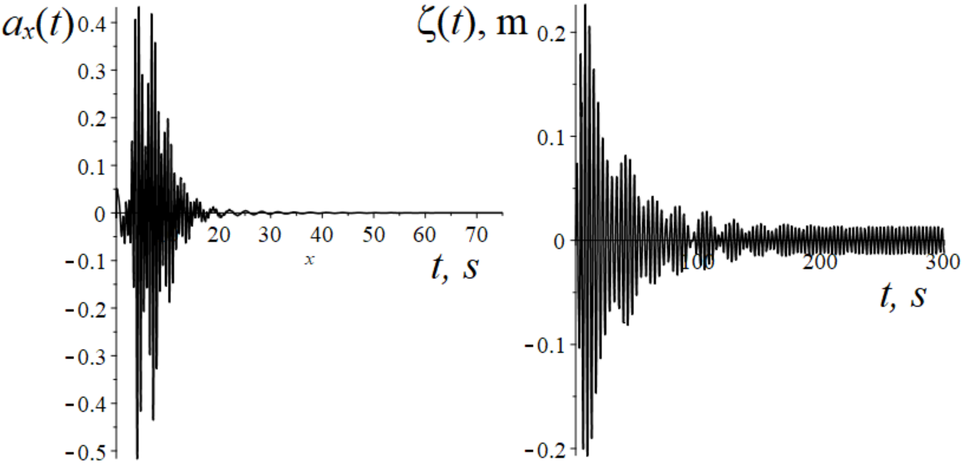

*a*) *b*)

**Figure 3.** Accelerogram and the free surface level via time.

As vertical acceleration we consider $a_z(t)$ =0.005 m/s$^2$. Figure 2b) shows time dependence of ζ in the point with coordinates $r=R$, $z=H$, θ=0.

From numerical results it has been concluded that change of the liquid level is near 0.4m. Such changing can lead to a large pressure on the tank walls. The normalized pressure $p_n$ has been calculated using equation [15]. Here $p_n=(p-p_0)/\rho_l$. The dependence of $p_n$ via time is plotted in Figure 3a. For comparison in Figure 3b one could see the dependence of $p_n$ via time when neglecting the effects of sloshing. The same point with coordinates $r=R$, $z=H$, θ=0 has been chosen for numerical simulation.

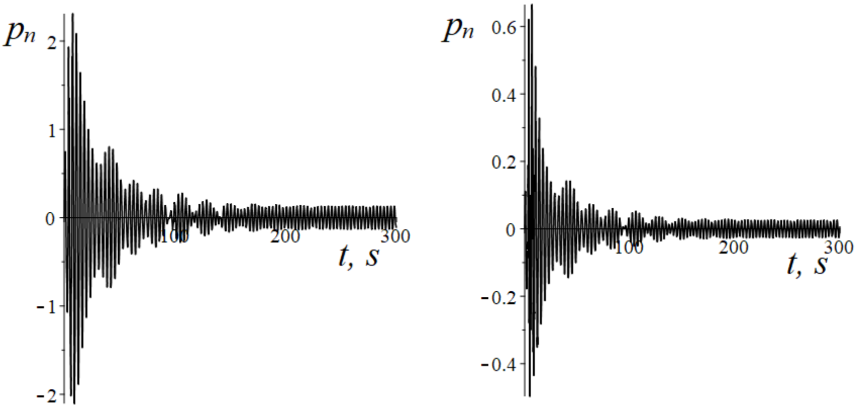

a) b)

Figure 3. Time histories of $p_n$

The results obtained indicate the need to reduce the level of sloshing. For this, various damping devices have been used. Among them there are horizontal and vertical partitions as suggested in paper (30). The installation of baffles leads to a shift in the frequency spectrum. But the frequencies of excitation forces as a result of artificial earthquakes, terrorist attacks could have a wide spectrum.

Paper (31) shows that the installation of a floating cover leads to a significant change in frequencies.

As reported in paper (31), the elastic membrane has been used to reduce sloshing. But here the time dependent solutions have been obtained. The clamped silicon membrane with radius $R = 1$ m, thickness $h_m = 0.001$ m, material density $\rho_m = 2800$ kg/m3, the Young modulus $E = 50$Mpa, Poisson's ratio $\nu = 0.49$ has been supposed to be applied.

Figure 4a demonstrates comparison of the free surface level changing with and without the membrane as a cover, and Figure 4b shows the dependence of $p_n$ via time. The black lines correspond to vibrations without cover, and by the grey lines the curves have been obtained assuming the presence of the elastic membrane installed at the level of the free surface have been marked.

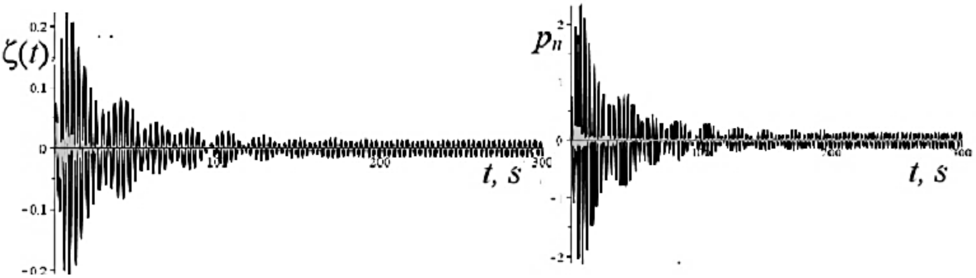

*a*) *b*)

**Figure 4.** Time histories of of $\zeta$ and $p_n$

The results obtained allow us to conclude that the installation of the membrane leads to a significant decrease in both the level of free surface rise and the pressure on the tank walls.

These data could be useful in assessing the stability of reservoirs under seismic loads.

## CONCLUSION

The liquid vibrations in rigid and elastic reservoirs have been considered. It has been established that level changing via time for reservoirs without covering membrane can be very large and lead to the appearance of excess pressure on the tank wall. The installation of the floating membrane leads to decreasing both the free surface level and the pressure on the tank walls.

These results allow us to prevent tanks destruction and to extend their service life using the floating membrane cover. It will increase the environmental safety level of the areas adjacent to the tanks and prevent emergencies.

## REFERENCES

1. Sierikova, O.; Strelnikova, E.; Degtyarev, K. Seismic Loads Influence Treatment on the Liquid Hydrocarbon Storage Tanks Made of Nanocomposite Materials. *WSEAS Transactions on Applied and Theoretical Mechanics,* **2022**. *17,* 62-70. DOI: 10.37394/232011.2022.17.9
2. Sierikova, E.; Strelnikova, E.; Pisnia, L.; Pozdnyakova, E. Flood risk management of Urban Territories. *Ecology, Environment and Conservation* India, **2020**, *26* (3), 1068-1077.
3. Sierikova, O.; Koloskov, V.; Strelnikova, E. The groundwater level changing processes modeling in 2d and 3d formulation. *Acta Periodica Technologica,* **2022,** 53, 36-47.
DOI: https://doi.org/10.2298/APT2253036S
4. Kendzera, O.V.; Mykulyak, S.V.; Semenova, Yu.V.; Skurativska, I.A.; Skurativskyi, S.I. Assessment of seismic response of a soil layer with the oscillating inclusions. *Geophysical journal*. **2020**, *42* (4), 47–58.
5. Kendzera O.V., Mykulyak S.V., Semenova Yu.V., Skurativska I.A., Skurativskyi S.I. Seismic response of a layered soil deposit with inclusions. *Geophysical journal*. 2021. 43 (2): 3–13.
6. Sierikova, O.; Strelnikova, E.; Gnitko, V.; Tonkonozhenko, A.; Pisnia L. Nanocomposites Implementation for Oil Storage Systems Electrostatic Protection. *Conf. Proc. of Integrated Computer Technologies in Mechanical Engineering – ICTM-2021.* Synergetic Engineering Springer Nature Switzerland AG 2022 M. Nechyporuk et al. (Eds.): ICTM 2021, 2022. LNNS 367: 573-585. https://doi.org/10.1007/978-3-030-94259-5_49
7. Dadashov, I.; Loboichenko, V.; Kireev, A. Analysis of the ecological characteristics of environment friendly fire fighting chemicals used in extinguishing oil products. *Pollution Research*. **2018**, *37* (1), 63-77.
8. Sierikova, O.; Koloskov, V.; Degtyarev, K.; Strelnikova, E. Improving the Mechanical Properties of Liquid Hydrocarbon Storage Tank Materials. *Materials Science Forum.* **2022**, *1068*, 223-229. doi:10.4028/p-888232
9. Ramirez, O.; Mesa, A.; Zuluaga, S.; Munoz, F.; Sanchez-Silva, M.; Salzano, E. Fragility Curves of Storage Tanks Impacted by Strong Winds. *Chemical Engineering Transactions.* **2019**, *77*, 91-96.
10. Korgin, A.V.; Kudishin, Y.I.; Ermakov, V.; Emelianov, M.V.; Zeyd-Kilani, L. Modeling of seismic impacts on the oil tanks. *International Journal of Applied Engineering Research.* **2016**, *11*(3), 680-1686.

11. Qin, F.; Chen, S.; Chen, R. Leakage detection of oil tank using terahertz spectroscopy. *Sci. China Technol. Sci.* **2021,** *64*, 1947-1952. https://doi.org/10.1007/s11431-021-1884-1
12. Khalmuradov, B.; Harbuz, S.; Ablieieva, I. Analysis of the technogenic load on the environment during Forced ventilation of tanks. *Technology audit and production reserves.* **2018**, *1/3* (39), 45-52. DOI: 10.15587/2312-8372.2018.124341
13. Ibrahim, R. A.; Pilipchuck, V. N.; Ikeda, T. Recent Advances In Liquid Sloshing Dynamics. *Applied Mechanics Reviews*. **2001**, *54* (2), 133-199.
14. Ibrahim, R. A. Liquid Sloshing Dynamics. Cambridge University Press, New York, 1948.
15. Gnitko, V.; Marchenko, U.; Naumenko, V.; Strelnikova, E. Forced vibrations of tanks partially filled with the liquid under seismic load, WIT Transaction on Modelling and Simulation, **2011**, *52,* 285-296. DOI: 10.2495/BE11025
16. Avramov, K.V.; Strelnikova, E.A.; Pierre, C. Resonant many-mode periodic and chaotic self-sustained aeroelastic vibrations of cantilever plates with geometrical non-linearities in incompressible flow. *Nonlinear Dyn.* **2012**, *70*, 1335-1354. https://doi.org/10.1007/s11071-012-0537-5
17. Gnitko, V.; Degtyariov, K.; Karaiev, A.; Strelnikova, E. Multi-domain boundary element method for axisymmetric problems in potential theory and linear isotropic elasticity. *WIT Transactions on Engineering Sciences*. **2019**, 13–25. DOI: 10.2495/BE410021
18. Kolaei, A.; Rakheja, S. Free vibration analysis of coupled sloshing-flexible membrane system in a liquid container. *Journal of Vibration and Control.* **2019**, *25*(1), 84-97. doi:10.1177/1077546318771221
19. Choudhary, N.; Strelnikova, E. Liquid vibrations in a container with a membrane at the free surface. *Vibroengineering PROCEDIA*, **2021**, *37*, 13-18. https://doi.org/10.21595/vp.2021.21996
20. Brebbia, C.A.; Telles, J.C.F.; Wrobel, L.C. Boundary element techniques: theory and applications in engineering. Springer-Verlag: Berlin and New York, 1984.
21. Sierikova, O.; Strelnikova, E.; Gnitko, V.; Degtyarev, K. Boundary Calculation Models for Elastic Properties Clarification of Three-dimensional Nanocomposites Based on the Combination of Finite and Boundary Element Methods. *2021 IEEE 2nd KhPI Week on Advanced Technology (KhPIWeek).* **2021**, 351-356. doi: 10.1109/KhPIWeek53812.2021.9570086.
22. Sierikova, O.; Koloskov, V.; Degtyarev, K.; Strelnikova, O. The Deformable and Strength Characteristics of Nanocomposites Improving. *Materials Science Forum.* **2021**, *1038*, 144-153.
23. Degtyariov, K.; Gnitko, V.; Kononenko, Y.; Kriutchenko, D.; Sierikova, O.; Strelnikova, E. Fuzzy Methods for Modelling Earthquake Induced Sloshing in Rigid Reservoirs. *2022 IEEE 3rd KhPI Week on Advanced Technology* (KhPIWeek), **2022**, 297-302. doi: 10.1109/KhPIWeek57572.2022.9916466
24. Silvestri, S.; Mansour, S.; Marra, M.; Distl, J.; Furinghetti, M.; Lanese, I. Shaking Table Tests of a Full-scale Flat-bottom Manufactured Steel Silo Filled with Wheat: Main Results on the Fixed-base Configuration. *Earthquake Eng Struct.* **2022**, *51*, 169–190. doi:10.1002/eqe.3561
25. Jing, H.; Chen, H.; Yang, J.; Li, P. Shaking table tests on a small-scale steel cylindrical silo model in different filling conditions. *Structures,* **2022**, *37*, 698–708.
26. Mansour, S.; Pieraccini, L.; Palermo, M.; Foti, D.; Gasparini, G.; Trombetti, T.; Silvestri, S. Comprehensive Review on the Dynamic and Seismic Behavior of Flat-Bottom Cylindrical Silos Filled with Granular Material. *Front. Built Environ*. **2022**, *7*. 805014.
27. Khalil, M.; Ruggieri, S.; Uva, G. Assessment of Structural Behavior, Vulnerability, and Risk of Industrial Silos: State-of-the-Art and Recent Research Trends. *Appl. Sci.* **2022**, 12, 3006. https://doi.org/10.3390/app12063006
28. Mansour, S.; Silvestri, S.; Sadowski, A.J. The ‘miniature silo’ test: A simple experimental setup to estimate the effective friction coefficient between the granular solid and a horizontally-corrugated cylindrical metal silo wall, *Powder Technol.* **2022**, *399*, 117212. https://doi.org/10.1016/j.powtec.2022.117212.

29. Sierikova, O.; Strelnikova, E.; Degtyarev, K. Srength Characteristics of Liquid Storage Tanks with Nanocomposites as Reservoir Materials. *2022 IEEE 3rd KhPI Week on Advanced Technol*ogy (KhPIWeek), **2022**, 151-157. DOI: 10.1109/KhPIWeek57572.2022.9916369
30. Gnitko, V.; Degtyariov, K.; Naumenko, V.; Strelnikova, E. BEM and FEM analysis of the fluid-structure interaction in tanks with baffles, *Int. Journal of Computational Methods and Experimental Measurements,* **2017**, *5* (3), 317–328. DOI:10.2495/CMEM-V5-N3-317-328.
31. Choudhary, N.; Kumar, N.; Strelnikova, E.; Gnitko, V.; Kriutchenko, D.; Degtyariov, K. Liquid vibrations in cylindrical tanks with flexible membranes. *Journal of King Saud University –* Science, **2021**, *33* (8), 101589. doi.org/10.1016/j.jksus.2021.101589
32. Shugaylo, O.; Bilyk, S. The Specifics of the Compilation of the Calculated Load Combinations in the Assessment of Seismic Resistance of Steel Supporting Structures of Nuclear Power Plant Equipment and Piping *J. of Mech. Eng.*, **2022**, *25* (3), 6-15. https://doi.org/10.15407/pmach2022.03.006
33. Akkar, S.; Moghimi, S.; Arici, Y. A study on major seismological and fault-site parameters affecting near-fault directivity ground-motion demands for strike-slip faulting for their possible inclusion in seismic design codes*, Soil Dyn Earthq Eng,* **2018**, 104, 88-105.
34. Strelnikova, E.; Choudhary, N.; Kriutchenko, D.; Gnitko V., Tonkonozhenko A, Liquid vibrations in circular cylindrical tanks with and without baffles under horizontal and vertical excitations, *Engineering Analysis with Boundary Element*s, **2020,** *120*, 13-27. DOI: 10.1016/j.enganabound.2020.07.02m

APTEFF, Vol. 54, 1-335 (2023)
DOI: https://doi.org/10.2298/APT2354223N

UDC: 66.017/.018:67.017]:669-14:546.62
BIBLID: 1450-7188 (2023) 54, 223-235

Review paper

# RECENT FINDINGS ON MECHANICAL BEHAVIOUR OF STIR CAST ALUMINIUM ALLOY-MATRIX COMPOSITES: AN OVERVIEW

*Agha Inya NDUKWE*

Department of Materials and Metallurgical Engineering, Federal University of Technology, Owerri, Nigeria.

**Received: 15 May 2023** **Revised: 02 September 2023** **Accepted: 04 September 2023**

*This study examined the previous research on the mechanical properties of reinforced composites of aluminium-matrix, manufactured by stir casting. Stir casting has been reported as the most economical fabrication method currently in use for producing Aluminum Matrix Composites because of its accessibility, portability, adaptability to be utilized for large-scale manufacture, and easy operation of the application to conventional shape casting foundry procedures. Apart from the minority report that recorded a reduction in ductility, yield strength, ultimate tensile strength, and modulus of elasticity but with an increase in hardness of the SiC particulate reinforced aluminium matrix composites following the increase in reinforcing material, the majority of work has shown that the mechanical properties increase with the increase in the addition of the reinforcing material. Reinforcing materials like silicon carbide, tungsten carbide, alumina, boron carbide, and multi-walled carbon nanotubes have been used in various compositions to manufacture aluminium-matrix composites. The highest reported ultimate tensile strength of 489 MPa was obtained after stir casting 10 vol% of SiC – aluminium matrix composite. The maximum tensile strength of 401 MPa was attained with 20% $B_4C$ – Al-matrix composite. Various uses of metal-matrix composites have been identified in the making of hypersonic aircraft, sporting equipment, and automobile engine parts.*

**Keywords**: Mechanical properties, nanocomposites, SiC, alumina, stir casting, metal-matrix composite.

## INTRODUCTION

A composite material is made up of at least two separate constituents that are mixed to provide unique material characteristics (1, 2). A novel family of materials called aluminium matrix composites (AMCs) has the potential to meet the requirements of sophisticated technical applications (3) where good rigidity, high strength, and low weight are required (4).

For the production of AMC materials, a variety of processing methods are available, including powder metallurgy (5), liquid metal infiltration, squeeze casting, stir casting, and spray deposition (6). Due to its simplicity, versatility, ability to be used in large-scale manufacturing, and ease of adaptation to traditional shape-casting foundry techniques, stir casting is the most cost-effective fabrication process currently being used to create aluminium matrix composites (6, 7). Stir casting refers to the technique that ensures the uniform dispersion of particles of the reinforcing materials during the casting process (8). The process parameters that are employed during the production process have a significant impact on the stir casting's efficacy. For the base metal, these factors include preheating time and

---

* Corresponding author: Agha Inya NDUKWE, Department of Materials and Metallurgical Engineering, Federal University of Technology, Owerri, Nigeria. E-mail: agha.ndukwe@futo.edu.ng

temperature, whereas the variables for the reinforcing particles include stirring speed, duration, temperature, and pouring (9).

The matrix metal's qualities are improved by the addition of reinforcement in terms of stiffness, specific strength, wear resistance, and corrosion resistance (10). According to the experimental findings of the A356/SiC composite, the inclusion of SiC ceramic particles significantly improves the base alloy’s impact resistance, hardness, and tensile strength (11). When compared to the source material, the generated titanium oxide reinforced Al-7075 matrix composite showed a noticeable improvement in hardness value, elongation, and ultimate tensile strength (12). A glass particle-reinforced aluminium matrix composite has been produced (13). The composite was developed utilizing a stir casting technique with reinforcement from 0 to 12 wt% glass particles with a 75 $\mu$m particle size. The tensile strength was observed to improve up to 8 wt% of reinforcement before decreasing with increase in the quantity of the reinforcing material.

## COMPOSITES MADE OF METAL-MATRIX MATERIALS (MMCS) BY STIR CASTING

Many novel high-strength-to-weight materials have been developed as a result of years of intensive study into metal-matrix composite materials. Although most of these materials were developed for the aircraft industry, several are also employed in other applications, such as car engines. The three basic varieties of MMCs are generally continuous fibre, discontinuous fibre, and particle-reinforced (14).

## MMCS WITH CONTINUOUS FIBRE REINFORCEMENT

The largest increase in stiffness (tensile modulus) and strength for MMCs comes from continuous filaments. The aluminium alloy matrix-boron fibre-reinforced system was among the earliest continuous-fibre MMCs to be manufactured. This composite's boron fibre is created via chemical vapour deposition of boron on tungsten-wire support. Al-Boron (B) composite is manufactured by sandwiching layers of B fibres between aluminium foils and applying heat to the mixture, which causes the foils to bend and adhere to one another. The axial tensile strength of aluminium alloy 6061 rose from 310 to 1417 MPa with the addition of 51 vol% B, while its tensile modulus increased from 69 to 231 GPa (14). Some of the structural components of the space shuttle orbiter's mid-fuselage are made of Al-B composites. Metal fibres are mostly utilized as reinforcement in concrete, tyres, and metal or metal foams (15).

Other continuous-fibre reinforcements that have been employed in MMCs include silicon carbide, graphite, alumina, and tungsten fibres. The vertical tail portion of an advanced fighter aircraft is being tested with a composite made of Al 6061 strengthened with SiC continuous fibres. Particularly intriguing is the planned application of SiC continuous fibre reinforcements in a titanium aluminium matrix for hypersonic aircraft like the NASA X-plane.

Particulate-reinforced MMCs are inexpensive aluminium alloy MMCs produced by utilizing irregularly shaped alumina and silicon carbide particles with a diameter of between 3 and 200 $\mu$m. The particulate, which occasionally receives a proprietary coating, can be combined with the molten aluminium alloy and cast into remelt ingots or extrusion billets for further manufacturing. Sports equipment and vehicle engine components are two examples of applications for this material (14).

## MMCS WITH DISCONTINUOUS FIBRE-REINFORCEMENT

The major methods for producing discontinuous fibre-reinforced composites MMCs are powder metallurgy and melt infiltration. In the powder metallurgy process, metal powders are combined with needle-like silicon carbide whiskers that range in size from 1 to 3 $\mu$m in diameter and 50 to 200 $\mu$m in length. The mixture is then hot-pressed into place before being extruded or forged into the required shape. With the addition of 20% SiC whiskers, the ultimate tensile strength of Al alloy 6061 may be boosted from 310 to 480 MPa while the tensile modulus can be increased from 69 to 115 GPa. The powder metallurgy and melt infiltration techniques are more expensive, even though whisker additions can yield larger gains in strength and stiffness than particulate material (14).

## STIR-CASTING OF COMPOSITES WITH AN ALUMINIUM MATRIX

A mechanical stirrer is used in the stir-casting process to create a vortex that mixes the reinforcement with the matrix material. Due to its affordability, suitability for mass production, simplicity, nearly net shaping, and ease of composite structure control, it is a good method for producing metal matrix composites (16). In this technique, motorized stirring is typically used to disperse powder from reinforcing phases into molten metals, as shown in Figure 1. The reinforcement is often distributed unevenly throughout the solidified composite due to the difference in density between the liquid metal and the reinforcement and the accompanying propensity for the reinforcement to sink or float (16).

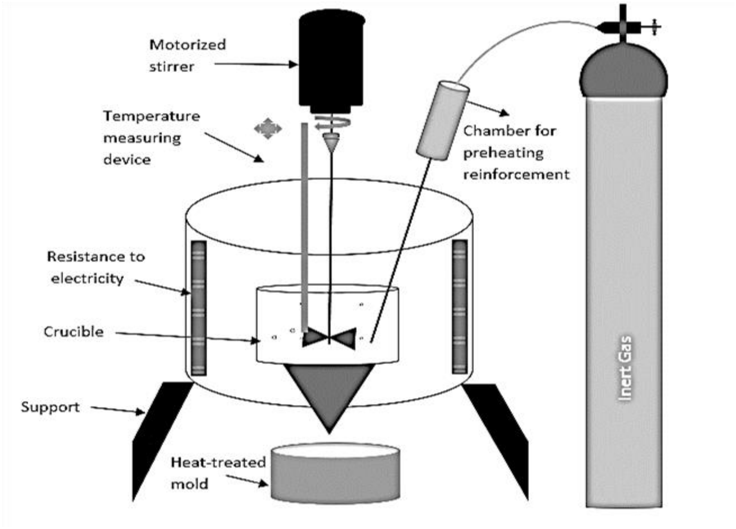

**Figure 1.** Motorized stirrer set up for stir casting (9)

To decrease oxidation, damping agents like magnesium and borax are added while the fluid composite in the heating system is stirred. As an oxygen scavenger, magnesium pulls oxygen from the air around the alumina particles. Magnesium promotes damping between

APTEFF, Vol. 54, 1-335 (2023) UDC: 66.017/.018:67.017]:669-14:546.62
DOI: https://doi.org/10.2298/APT2354223N BIBLID: 1450-7188 (2023) 54, 223-235

Review paper

the matrix and the reinforcing atoms. Reduced absorption and increased equivalent dispersion of TiC filling inside the Aluminium matrix are benefits of the stir casting process. It is crucial to choose the melt temperature at which to mix the supplement and melt the aluminium when using the stir-casting process (17).

According to earlier research (18), the aluminium alloy (Al 6061) was heated to 720 °C in a cast iron crucible during the stir-casting process to facilitate its phase shift from solid to liquid. Furthermore, to ensure adequate dispersion of the reinforcement particles in the matrix, Tungsten carbide particulates (5 μm) were initially heated to 700 °C, and a stainless-steel stirrer was used to stir the molten AA6061 at 450 °C. The molten metal was mixed with 1% of the reinforcement particles, and the stirrer's induced vortex in the crucible allowed the particles to disperse (18). The mixture from the crucible was transferred to a mild steel mould that had been heated to 450 °C and allowed to solidify at room temperature (18).

## REINFORCING MATERIALS FOR ALUMINIUM-MATRIX COMPOSITES

### Silicon carbide (SiC)

Silicon carbide's chemical expression is SiC. It is a silicon and carbon crystalline combination that is created synthetically, and it is extremely hard. In more recent times, it has been used for heating elements and refractory linings for industrial furnaces, wear-resistant components for pumps and rocket engines, and semiconducting substrates for light-emitting diodes (19).

In the current process of producing silicon carbide, a carbon conductor is encircled by a combination of pure silica sand and finely crushed coke within a brick electrical resistance-type furnace. A chemical reaction between the silicon in the sand and the carbon in the coke causes SiC and carbon monoxide gas to be produced when an electric current is sent through the conductor. Temperatures in a furnace run, which can last several days, range from 2200 to 2700 °C in the centre to around 1400 °C at the outside edge. Each run uses more than 100000 kilowatt-hours of electricity. The finished product is made up of a core of loosely interwoven green-to-black SiC crystals that are partially or surrounded by raw material that has not been transformed. The lump aggregate is broken down into different sizes according to the intended usage (19).

### Tungsten carbide (WC)

The inorganic compound of carbon known as tungsten carbide is used alone or in combination with 6 to 20 per cent of other metals to increase the hardness of cast iron, the cutting edges of saws and drills, and the penetrating cores of armour-piercing projectiles. It is a solid, metal-like material that is light grey with a blue tint that decomposes at 2600 °C as opposed to melting. To make tungsten carbide, powdered tungsten is heated at 1400–1600 °C with carbon black and hydrogen (20).

### Alumina ($Al_2SO_3$)

Aluminium oxide, which is also called alumina, is a white material that serves as a starting point for the production of aluminium metal. It also acts as an active substance in chemical mixtures and as a raw material for a variety of groundbreaking ceramic products. Bauxite, a naturally occurring mineral that contains varying proportions of hydrous (water-containing) aluminium oxides, is used to make alumina. Free $Al_2O_3$ may be developed synthetically but can be found in nature as the mineral corundum and its gemstone forms sapphire and ruby. However, the word "alumina" is more appropriately restricted to the substance used in aluminium metallurgy, industrial ceramics, and chemical processing (21).

### Boron carbide ($B_4C$)

A crystalline form of boron and carbon is called boron carbide ($B_4C$). It is a very tough, synthetic material that is employed in control rods for nuclear power plants, lightweight composite materials, abrasive and wear-resistant goods, and materials that are lightweight and composite. Boron carbide is among the toughest synthetic materials known to man, only being surpassed in hardness by cubic boron nitride and diamond, with a Mohs hardness between 9 and 10. Because of its hardness and extremely low density, it has been used to reinforce aluminium in military armour and high-performance bicycles. Its wear resistance has also led to its employment in pump seals and sandblasting nozzles (22).

During production in an electric furnace, boron oxide is heated to a high temperature and reduced with carbon to make boron carbide. After grinding, the black powder is pressed at temperatures above 2000 °C to solidify it (22).

### CARBON NANOTUBES WITH MANY WALLS (MWCNTS)

Multiple carbon nanotubes are nestled inside one another to form MWCNTs. There may be as few as three nanotubes or as many as twenty inside an MWCNT. The innermost nanotube's diameter can range from 2 nm to more than 50 nm, while the outermost nanotube's diameter can also change at the same time. They have remarkable mechanical, electrical, and thermal characteristics, just like single-walled nanotubes. However, compared to single-walled nanotubes, multi-walled nanotubes have a larger probability of having flaws, which leads to decreased performance. High volumes of MWCNTs can be manufactured, and they are simpler to purify (23).

## FINDINGS FROM STUDIES ON THE MECHANICAL BEHAVIOUR OF METAL-MATRIX COMPOSITES MADE THROUGH STIR-CASTING

### Mechanical behaviour of reinforced aluminium-matrix composites

The summary of the overview of previous studies on the mechanical characteristics of several reinforced aluminium-matrix composites is presented in Table 1.

The mechanical characteristics of the SiC-reinforced aluminium-matrix composite were examined by (24). The ultimate tensile strength of the composites was found to decrease from 176.75 to 167.64 MPa, while the ductility decreased from 13.7 to 10.1 MPa; the yield strength decreased from 91.68 to 100.44 MPa, and the modulus of elasticity decreased from 76.92 to 70.38 MPa. Only the composite's hardness, which went from 44.03 to 64.59 HV with an increase in SiC concentration from 8 to 15%, was discovered to rise (24). In contrast, it was found that when 9% of the SiC particles were stir cast with 6082 (Al)-matrix to produce MMCs, the tensile strength increased from 172.96 to 185.22 MPa (25).

**Table 1.** Summary of previous studies on the mechanical properties of reinforced aluminium-matrix composites

| Composite materials | Method of production (casting) | Reinforcement constituent that gave optimum strength | The highest mechanical properties reported | Ref. |
|---|---|---|---|---|
| AA (6101) and SiC | Stir 2-step | 8 % SiC | Ductility (13.7–10.1)<br>YS (91.68 – 100.44 MPa)<br>Hardness (44.03 – 64.59 Hv)<br>Modulus of elasticity (76.92 – 70.38 MPa)<br>UTS (176.75 – 167.64 MPa) | (24) |
| AA (6082) and SiC | Stir | 9 % SiC | TS (172.9 – 185.22 MPa) | (25) |
| AA (6061) and WC (Tungsten carbide) | Stir | 3 % WC | UTS (127.94 – 155.3 MPa) | (18) |
| AA (6061)–T6 and high entropy alloy (AlCoCrFeNi$_{2.1}$) | Stir (friction) | 15 % | Hardness (72 – 125 Hv)<br>TS (222.9 – 332.1 MPa) | (26) |
| AA (6082) and SiC nanoparticles | Stir | - | UTS (322.91 MPa)<br>YS (203.29 MPa) | (27) |
| SiC-Al$_2$O$_3$ and AA (6063) | Stir | 12 % SiC-Al$_2$SO$_4$ | UTS (134.63 MPa) | (28) |
| Aluminium alloy matrix and SiC (nano) – waste spent catalyst | Stir | Nano SiC (1.5 wt%) and spent catalyst (10 wt%) | UTS (134.53 MPa) | (29) |
| Aluminium matrix recycled composite | Stir | - | Compressive strength (433 MPa) | (30) |
| Al (5083) and SiC | Stir | 9 % | Tensile strength (172.96 – 185.22 MPa) | (31) |
| B$_4$C and AA (6082) | Stir | 20 % B$_4$C | Hardness (115 Hv)<br>Tensile stress (401 MPa) | (32) |
| SiC and AA (6082) | Stir | 20 % SiC | Hardness (113 Hv)<br>Tensile stress (379 MPa) | (32) |
| Multi-walled carbon nanotubes and Aluminium alloy matrix | Stir (Ultrasonic) | 3 % MWCNTs | Microhardness (175 HV) | (33) |
| SiC and AA (2024) | Stir (2 – step deformation) semi-solid | 10 vol% (10 $\mu$m) | UTS (489 MPa)<br>YS (295 MPa) | (34) |
| MoO$_3$ and AA7075 | Stir | 10 wt.% MoO$_3$ | Impact strength (126 MPa) | (35) |
| TiO$_2$ and AA2014 | Stir (Multi-step) | 4 wt.% TiO$_2$ | Optimal strength | (36) |
| Al6061, MoS$_2$, and B$_4$C | Stir | 4 wt.% MoS$_2$ and 12 wt.% B$_4$C | Hardness (114.03 Hv) | (37) |

Aluminium alloy (6061) has been reinforced with particles (5 $\mu$m) of tungsten carbide (WC) by stir casting (18). It was discovered that adding more reinforcement caused the mechanical properties such as tensile strength and hardness to increase. The basis for the increment was attributed to the even distribution of the tungsten carbide particles. The composite that consisted of 3 % WC gave the maximum tensile strength of 155.3 MPa. However, the clustering of WC particulates above 3 % indicated a lower tensile strength of 127.94 MPa. The reason for this development was linked to the presence of residual (internal) stresses in the material.

In an interesting study, a high entropy alloy ($AlCoCrFeNi_{2.1}$) was utilized to reinforce the aluminium (6061) – T6 matrix (26). It was discovered that after the T6 ageing heat treatment conducted on the composite, the hardness of the produced composite improved from 72 HV to 125 HV. In the same vein, the tensile strength also increased from 222.9 to 332.1 MPa. The reported increase in hardness and tensile strength was credited to the mismatched thermal strengthening and the Hall-Petch relationship.

The stir-casting process was used in the production of SiC-reinforced aluminium-matrix composites (27). The researchers observed that after conducting the T6 heat treatment on the composites, the highest yield and ultimate tensile strengths of 203.29 and 322.9 MPa respectively were attained (27). In another work, nano SiC (1.5 wt%) particles and spent catalyst (10 wt%) served as reinforcing materials for the manufacture of aluminium matrix composites (29). The ultimate tensile strength of 134.53 MPa was reported. On the other hand, the production of $SiC/Al_2O_3$-reinforced MMCs led to a maximum ultimate tensile strength of 134.63 MPa following the addition of the reinforcing material by 12 % (28).

The optimized stir-casting process was used to produce and evaluate the recycled aluminium-matrix composites *(30)*. The results of the optimized samples revealed the lowest porosity of about 5.29 % and maximum compressive strength of 433 MPa. The ultrasonic probe was used to study the mechanical behaviour of SiC-reinforced MMCs (31). They reported maximum tensile and compressive strengths of 254.9 and 350 MPa respectively.

The comparison of the mechanical behaviour of two aluminium alloy composites reinforced with $B_4C$ and SiC has been studied (32). The maximum hardness values obtained were 115 HV for the $B_4C$-reinforced Al-matrix composite and 113 HV for the SiC-reinforced Al-matrix composite. On the other hand, a higher tensile strength of 401 MPa was reported for the $B_4C$-Al composite in comparison with the 379 MPa for the SiC-Al composite. The even dispersion of the $B_4C$ and SiC particles during the manufacturing process was said to be responsible for the observed increase in tensile strength.

The ultrasonic aided stir casting has been used in the study of multi-walled carbon nanotube (MWCNT) reinforced aluminium-matrix (33). It was reported that the microhardness increased to a maximum of 175 HV with 3 % MWCNT reinforcing material. In another interesting study, Cao et al. *(34)* worked on how best to improve the ductility of SiC – 2024 (Al) composites produced by stir casting. At 10 $\mu$m particle size and 10 vol% SiC, the maximum yield and ultimate tensile strengths of 295 and 489 MPa were reported. The reason for the improved mechanical behaviour was ascribed to the enhanced bonding strength of the SiC – Al (2024) interface.

The mechanical and wear properties of molybdenum trioxide-reinforced aluminum alloy (AA7075) matrix composites produced through stir casting process were studied by Gopikrishnan et al. (35). In the investigation, stir casting was effectively used to manufacture AA7075-based composites with different weight percentages (wt.%) of molybdenum trioxide ($MoO_3$) ranging from 2.5 to 10 wt.%. A thorough examination was conducted to compare these innovative composites to the base-material and assess their mechanical and tribological characteristics. The cast components underwent testing for hardness, impact strength, and tensile. The 10-weight per cent $MoO_3$-reinforced Al7075 composite had the highest impact strength of all the composites, measuring 126 MPa, and the largest porosity of 3.9%. Additional testing was performed using a pin-on-disk wear tester with factors such as wt.% of $MoO_3$, applied stress (P), sliding distance (D), and sliding speed (V). This allowed the wear rate (WR) and friction coefficient (COF) to be calculated. According to the findings, the 10-weight per cent $MoO_3$ composite exhibited the maximum COF with a load application of 20 N and a sliding speed of 1 m/s. Furthermore, when the applied load was increased to 40 N and the sliding speed was increased to 4 m/s, the wear rate for the 10% $MoO_3$ composite was measured to be 0.00674 mm3/min. The findings of a statistical analysis using ANOVA revealed that the applied load, wt.% of $MoO_3$, sliding distance, and sliding speed, in that order, had the largest influence on the wear rate. It is interesting to note that the composite with 7.5 wt.% $MoO_3$ reinforcement outperformed those with 2.5, 5, and 10 wt.% $MoO_3$ in terms of wear resistance (35).

## WEAR BEHAVIOUR AND MICROSTRUCTURAL ANALYSIS OF REINFORCED ALUMINIUM-MATRIX COMPOSITES

The microstructures of $TiO_2$-reinforced aluminium composites produced through multi-step stir casting revealed that $TiO_2$ promoted grain refinement from dendritic to globular grains via nucleation across the AA2014 matrix owing to a high rate of solidification that increased with $TiO_2$ content (36). It was also found that $TiO_2$ interacted with Al in the matrix to generate $Al_2O_3$ in addition to $Al_2CuMg$ and $Al_2Cu$ secondary phases, providing extra strength to the composites. The composite sample supplemented with 4 wt% $TiO_2$ demonstrated the optimum mechanical property combination. However, mechanical property improvements above 3 wt% $TiO_2$ addition were found not to be substantial. On the other hand, Emiru et al. (37) researched hybrid aluminium Al6061 alloy metal matrix composites reinforced with $MoS_2$, SiC, and $B_4C$. Their tribology analysis revealed that mass loss increased dramatically as the applied load rose from 10 to 50 N. The wear performance of hybrid composites revealed that double- and triple-reinforced samples exhibited lower wear loss than non-reinforced specimens due to the solid $MoS_2$ lubricant and the creation of the $B_2O_3$ layer at the contact zone. The primary wear processes of the composites were found to be wear debris and delamination wear.

The stir-cast nano-$TiO_2$ reinforced AA7178 alloy revealed uniformly distributed reinforced particles within the matrix (38). Unlike other reinforcing materials that tend to disintegrate from the matrix, the nano-$TiO_2$ particles were not only found to be tenaciously bound to the AA7178 matrix but also enhanced the tribological performance of the composite. On the other hand, the applied load, sliding distance, and speed were reported to significantly influence the wear rate. The discovery was made when three specimens consisting of 3 wt.% nano-$TiO_2$ reinforced AA7178, 3 wt.% nano-SiC reinforced nanocomposites and AA7178 base alloy matrix were studied using the particle swarm optimization algorithm and the Taguchi optimization method (39). It was reported that the tribological behaviour was enhanced by the introduction of SiC and $TiO_2$ nanoparticles in comparison with the base-aluminium alloy. In another development, the introduction of different weight compositions of $TiB_2$ reinforcement in Al-7Si composites has been reported to improve wear performance (40). Their findings revealed that delamination and abrasion were the mechanisms of wear at increased sliding speeds and higher applied loads. Nonetheless, the wear rate of the $TiB_2$-reinforced Al-7Si composite was found to be less than that of the base alloy. Consequently, the microstructure of the produced composites indicated uniform dispersion of the $TiB_2$ particles within the grain refined aluminium, and the short rod-shaped eutectic silicon phase (40).

The image in Figure 2 is a scanning electron micrograph of a composite material made from $Si_3N_4$ and 2 wt.% granite powder reinforced Al7075 hybrid matrix. The wear test was conducted at 210°C working temperature, 50 N load, and 200 rpm disc speed, as reported by Shivaprakash et al. (41).

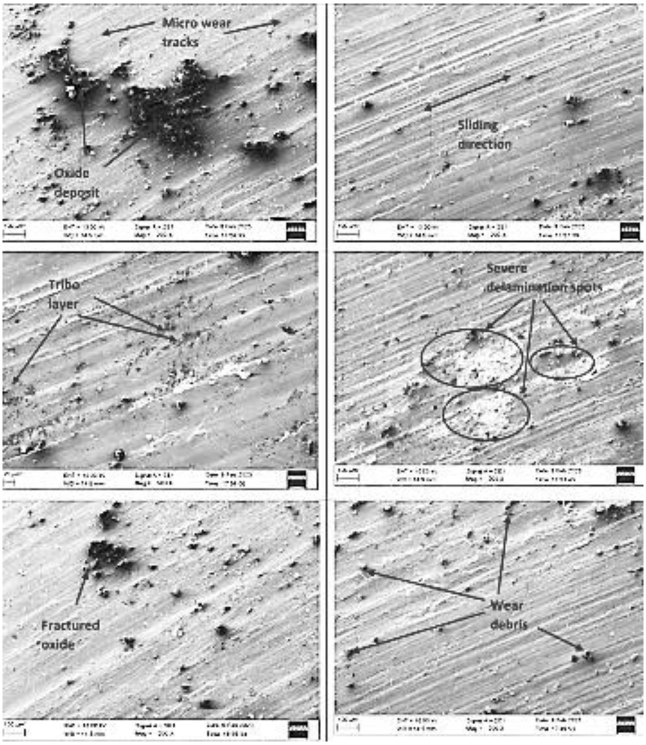

**Figure 2.** SEM micrographs of the composite's worn-out surface were taken at an operating temperature of 210 °C, 50 N load and 200 rpm disc speed (41)

The image shows multiple wear scratches which indicate abrasive wear. The worn surfaces of the composite material had fine grooves and minor plastic deformation along the groove edges. However, severe wear was observed at a few points on the surface, resulting in increased delamination. The surface damage was considerable, and there was a higher-scale material transfer to the counter face. Additionally, isolated oxide deposits were found on the surface, and their broken remains were also visible (41).

## IDENTIFIED GAPS IN KNOWLEDGE

Some gaps in knowledge were observed in the course of this study and they are itemized as follows:

1. In all the examined studies, the reinforcement of an aluminium-matrix composite with boron carbide ($B_4C$) produced the highest tensile strength, however, there is limited information available on the manufacturing of $B_4C$-Al-matrix composites utilizing the stir casting method. It is recommended that further studies be done to evaluate how process parameters and manufacturing conditions like the method of dispersion and particulate sizes can influence the mechanical characteristics of the composite.
2. It is important to acknowledge that many studies have been conducted to reveal different mechanical properties of the aluminium-matrix composite produced by stir casting, but there is limited knowledge regarding the impact, flexural and biaxial strength properties of the composite. It is advised that impact and biaxial strength tests be carried out on the composite to investigate the fracture toughness, plane stress and plane strain fracture conditions.

## CONCLUSIONS

From the review of previous studies on the mechanical properties of aluminium-matrix composites, the following conclusions can be made:

1. The majority of work has shown that the mechanical properties increase with an increase in the addition of the reinforcing material, except for a minority report that noted reductions in ductility, yield strength, ultimate tensile strength, and modulus of elasticity but with increases in hardness of the SiC particulate reinforced aluminium-matrix composites.
2. Aluminium-matrix composites have been produced using a variety of reinforcement elements, including multi-walled carbon nanotubes, tungsten carbide, alumina, silicon carbide, and boron carbide.
3. The greatest recorded ultimate tensile strength of 489 MPa was reached by stir-casting 10% SiC - aluminium matrix composite, whereas the highest tensile strength of 401 MPa was attained using 20% $B_4C$ - aluminium matrix composite.
4. It has been reported that metal-matrix composites have a variety of applications in the production of hypersonic aircraft, sporting goods, and vehicle engine components.

## REFERENCES

1. Mahesh Kumar, V.; Venkatesh, C. V. Effect of ceramic reinforcement on mechanical properties of aluminum matrix composites produced by stir casting process. *Materials Today: Proceedings* **2018**, *5*(1, Part 3), 2466–2473. doi:10.1016/j.matpr.2017.11.027.
2. Ndukwe, A. I.; Umoh, S.; Ugwochi, C.; Ogbuji, C.; Ngolube, C.; Aliegu, F.; et al. Prediction of compression strength of bamboo reinforced low-density polyethylene waste (LDPEw) composites. *Composites theory and practice* **2022**, *22*(3).

3. Lakshmi Narayana, K. S.; Benal, M. M.; Shivanand, H. K. Effect of graphite on aluminium matrix composites fabricated by stir casting route – A review. *Materials Today: Proceedings* **2021**, *45*, 327–331. doi:10.1016/j.matpr.2020.11.051.
4. Karthik, R.; Gopalakrishnan, K.; Venkatesh, R.; Mohana Krishnan, A.; Marimuthu, S. Influence of stir casting parameters in mechanical strength analysis of Aluminium Metal Matrix Composites (AMMCs). *Materials Today: Proceedings* **2022**, *62*, 1965–1968. doi:10.1016/j.matpr.2022.02.067.
5. Rathee, S.; Maheshwari, S.; Siddiquee, A. N.; Srivastava, M. Investigating Effects of Groove Dimensions on Microstructure and Mechanical Properties of AA6063/SiC Surface Composites Produced by Friction Stir Processing. *Transactions of the Indian Institute of Metals* **2017**, *70*(3), 809–816. doi:10.1007/s12666-017-1060-7.
6. Raei, M.; Panjepour, M.; Meratian, M. Effect of stirring speed and time on microstructure and mechanical properties of Cast Al–Ti–Zr–B4C composite produced by stir casting. *Russian Journal of Non-Ferrous Metals* **2016**, *57*(4), 347–360. doi:10.3103/S1067821216040088.
7. Jebeen Moses, J.; Joseph Sekhar, S. Investigation on the Tensile Strength and Microhardness of AA6061/TiC Composites by Stir Casting. *Transactions of the Indian Institute of Metals* **2017**, *70*(4), 1035–1046. doi:10.1007/s12666-016-0891-y.
8. Chakravarthy, M. P.; Santha Rao, D. Evaluation of mechanical properties of aluminium alloy (AA 6082) reinforced with Rice husk ash (RHA) and Boron carbide (B4C) hybrid metal matrix composites using stir casting method. *Materials Today: Proceedings* **2022**, *66*, 580–586. doi:10.1016/j.matpr.2022.06.293.
9. Kadam, M. S.; Shinde, V. D. Stir cast aluminium metal matrix composites with mechanical and micro-structural behavior: A review. *Materials Today: Proceedings* **2020**, *27*, 845–852. doi:10.1016/j.matpr.2020.01.017.
10. Pandian, V.; Kannan, S. Processing and preparation of aerospace-grade aluminium hybrid metal matrix composite in a modified stir casting furnace integrated with mechanical supersonic vibration squeeze infiltration method. *Materials Today Communications* **2021**, *26*, 101732. doi:10.1016/j.mtcomm.2020.101732.
11. Rawat, A.; Kumar, A.; Agrawal, A. P. Investigation of mechanical properties of heat-treated A356/SiC composite fabricated through stir casting technique. *Materials Today: Proceedings* **2022**, *62*, 203–208. doi:10.1016/j.matpr.2022.02.618.
12. Dhanabalakrishnan, K. P.; Mathan Kumar, N.; Mothilal, T.; Yatika, G.; Mohammed Ali, H.; Socrates, S. Influence of nano titanium oxide reinforced Al-7075 matrix composites in stir casting method. *Materials Today: Proceedings* **2022**, *69*, 1381–1386. doi:10.1016/j.matpr.2022.09.202.
13. Sinshaw, Y.; Y., B. S.; Palani, S.; J., U. P. Mechanical property analysis of glass particulates reinforced Aluminum matrix composites. *Materials Today: Proceedings* **2022**, *62*, 488–494. doi:10.1016/j.matpr.2022.03.572.
14. Smith, W.; Hashemi, J. *Foundations of Materials Science and Engineering*; 6th edition.; McGraw-Hill Education, 2018.
15. Akhil, M. G.; Arsha, A. G.; Manoj, V.; Rajan, T. P. D.; Pai, B. C.; Huber, P.; et al. 17 - Metal fiber reinforced composites. In *Fiber Reinforced Composites*. Joseph, K., Oksman, K., George, G., Wilson, R., Appukuttan, S., Eds.; Woodhead Publishing Series in Composites Science and Engineering; Woodhead Publishing, 2021; pp 479–513. doi:10.1016/B978-0-12-821090-1.00024-7.
16. Sahu, M. K.; Sahu, R. K. Fabrication of Aluminum Matrix Composites by Stir Casting Technique and Stirring Process Parameters Optimization. In *Advanced Casting Technologies*. Vijayaram, T. R., Ed.; InTech, 2018. doi:10.5772/intechopen.73485.
17. Bharti, C.; Singh, A.; Rahul, R.; Sharma, D.; Dwivedi, S. P. A critical review of aluminium based composite developed by various casting technique with different reinforcement particles to enhance tribo-mechanical behaviour. *Materials Today: Proceedings* **2021**, *47*, 4092–4097. doi:10.1016/j.matpr.2021.06.366.

18. Rajesh, D.; Anand, P.; Lenin, N.; Bupesh Raja, V. K.; Palanikumar, K.; Balaji, V. Investigations on the mechanical properties of tungsten carbide reinforced aluminium metal matrix composites by stir casting. *Materials Today: Proceedings* **2021**, *46*, 3618–3620. doi:10.1016/j.matpr.2021.01.634.
19. Britannica, T. *Silicon carbide | Discovery & Modern Uses | Britannica*. <https://www.britannica.com/science/silicon-carbide> Accessed 23.09.01.
20. Britiannica, T. *Tungsten carbide | hardness, strength, durability | Britannica*. <https://www.britannica.com/science/tungsten-carbide> Accessed 23.09.01.
21. Britannica, T. *Alumina | Properties, Uses & Production Process | Britannica*. <https://www.britannica.com/science/alumina> Accessed 23.09.01.
22. Britannica, T. *Boron carbide | Hardness, Abrasion Resistance, Refractory | Britannica*. <https://www.britannica.com/science/boron-carbide> Accessed 23.09.01.
23. Ossila, E. M. S. *Multi-Walled Carbon Nanotubes, MWCNT | Low Price*. Ossila. <https://www.ossila.com/products/multi-walled-carbon-nanotubes> Accessed 23.09.01.
24. Jain, P. K.; Baredar, P.; Soni, S. C. Microstructure and mechanical properties of silicon carbide particle reinforced aluminium 6101 metal matrix composite produced by two-step stir casting. *Materials Today: Proceedings* **2020**, *26*, 2740–2745. doi:10.1016/j.matpr.2020.02.573.
25. Mishra, D.; Kumar Nanda, A. Experimental investigation on mechanical properties of stir casted aluminum SiC metal matrix composites. *Materials Today: Proceedings* **2023**, *74*, 1023–1027. doi:10.1016/j.matpr.2022.11.412.
26. Li, P.; Tong, Y.; Wang, X.; Sato, Y. S.; Dong, H. Microstructures and mechanical properties of AlCoCrFeNi2.1/6061-T6 aluminum-matrix composites prepared by friction stir processing. *Materials Science and Engineering: A* **2023**, *863*, 144544. doi:10.1016/j.msea.2022.144544.
27. Zhu, J.; Jiang, W.; Li, G.; Guan, F.; Yu, Y.; Fan, Z. Microstructure and mechanical properties of SiCnp/Al6082 aluminum matrix composites prepared by squeeze casting combined with stir casting. *Journal of Materials Processing Technology* **2020**, *283*, 116699. doi:10.1016/j.jmatprotec.2020.116699.
28. Soni, S.; Verma, S. Double shear performance of the hybrid aluminium metal matrix composite Al6063-SiC/Al2O3 fabricated through electromagnetic stir casting process. *Materials Today: Proceedings* **2022**, *62*, 5942–5947. doi:10.1016/j.matpr.2022.04.639.
29. Pragathi, P.; Elansezhian, R. Studies on microstructural and mechanical properties of (Nano SiC + Waste Spent catalyst) reinforced aluminum matrix composites. *Materials Today Communications* **2022**, *30*, 103204. doi:10.1016/j.mtcomm.2022.103204.
30. Christy, J. V.; Arunachalam, R.; Mourad, A.-H. I.; Krishnan, P. K.; Piya, S.; Al-Maharbi, M. Processing, Properties, and Microstructure of Recycled Aluminum Alloy Composites Produced Through an Optimized Stir and Squeeze Casting Processes. *Journal of Manufacturing Processes* **2020**, *59*, 287–301. doi:10.1016/j.jmapro.2020.09.067.
31. Chaubey, A.; Dwivedi, R.; Purohit, R.; Rana, R. S.; Choudhary, K. Experimental inspection of aluminium matrix composites reinforced with SiC particles fabricated through ultrasonic assisted stir casting process. *Materials Today: Proceedings* **2020**, *26*, 3054–3057. doi:10.1016/j.matpr.2020.02.634.
32. Singh, G.; Sharma, N.; Goyal, S.; Sharma, R. C. Comparative Measurements of Physical and Mechanical Properties of AA6082 Based Composites Reinforced with B4C and SiC Particulates Produced via Stir Casting. *Metals and Materials International* **2021**, *27*(11), 4333–4345. doi:10.1007/s12540-020-00666-0.
33. Srinivas, V.; Jayaraj, A.; Venkataramana, V. S. N.; Avinash, T.; Dhanyakanth, P. Effect of Ultrasonic Stir Casting Technique on Mechanical and Tribological Properties of Aluminium–Multi-walled Carbon Nanotube Nanocomposites. *Journal of Bio- and Tribo-Corrosion* **2020**, *6*(2), 30. doi:10.1007/s40735-020-0331-8.

APTEFF, Vol. 54, 1-335 (2023)
DOI: https://doi.org/10.2298/APT2354223N
UDC: 66.017/.018:67.017]:669-14:546.62
BIBLID: 1450-7188 (2023) 54, 223-235

Review paper

34. Cao, F.; Deng, K.; Wang, C.; Nie, K.; Liang, W.; Fan, J. Synergistic Enhancement of the Strength-Ductility for Stir Casting SiCp/2024Al Composites by Two-Step Deformation. *Metals and Materials International* **2021**, *27*(12), 5450–5461. doi:10.1007/s12540-020-00928-x.
35. Gopikrishnan, C.; Ravichandran, M. Investigations on Mechanical and Wear Properties of Molybdenum Trioxide-Reinforced Aluminum Alloy (AA7075) Matrix Composites Produced via Stir Casting Process. *Arabian Journal for Science and Engineering* **2023**, *48*(3), 3021–3040. doi:10.1007/s13369-022-07059-y.
36. Khalkho, J. S.; Chevuri, S. V.; Dagarapu, B. K. Evaluation of Microstructure and Mechanical Properties of TiO2 Reinforced Aluminium Composites Developed Through Multi-Step Stir Casting. *International Journal of Metalcasting* **2023**, *17*(1), 272–283. doi:10.1007/s40962-022-00760-6.
37. Abebe Emiru, A.; Sinha, D. K.; Kumar, A.; Yadav, A. Fabrication and Characterization of Hybrid Aluminium (Al6061) Metal Matrix Composite Reinforced with SiC, B4C and MoS2 via Stir Casting. *International Journal of Metalcasting* **2023**, *17*(2), 801–812. doi:10.1007/s40962-022-00800-1.
38. Bharat, N.; Bose, P. Influence of nano-TiO2 particles on the microstructure, mechanical and wear behaviour of AA7178 alloy matrix fabricated by stir casting technique. *Proceedings of the Institution of Mechanical Engineers, Part L: Journal of Materials: Design and Applications* **2023**, *237*(4), 753–766. doi:10.1177/14644207221123520.
39. Bharat, N.; Bose, P. S. C. Optimizing the Wear Behaviour of AA7178 Metal Matrix Composites Reinforced with SiC and TiO2 Nanoparticles: A Comparative Study Using Evolutionary and Statistical Methods. *Silicon* **2023**, *15*(11), 4703–4719. doi:10.1007/s12633-023-02395-6.
40. Hullur, M. K.; Goudar, D. M.; Venkateshwaralu, K.; Kori, S. A. Sliding Wear Behaviour of In Situ TiB2 Reinforced Hypoeutectic Al-Si Alloy Composites. *International Journal of Metalcasting* **2023**, *17*(2), 1179–1190. doi:10.1007/s40962-022-00847-0.
41. Shivaprakash, Y. M.; Prabhu, S.; Anne, G.; Gurumurthy, B. M.; Hiremath, P.; Sharma, S.; et al. High-temperature dry sliding wear behaviour of pre-aged 3-step T6-treated Al7075 hybrid matrix composite. *Cogent Engineering* **2023**, *10*(1), 2235820. doi:10.1080/23311916.2023.2235820.

APTEFF, Vol. 54, 1-335 (2023)
DOI: https://doi.org/10.2298/APT2354237N

UDC: 66.069.84:532.5+620.193.16
BIBLID: 1450-7188 (2023) 54, 237-244

Original scientific paper

# EVALUATION OF THE EFFICIENCY OF LIQUID DEGASSING TECHNOLOGY BASED ON THE PRINCIPLE OF HYDRODYNAMIC CAVITATION

*Anna Ye. NEDBAILO* [1], *Georgy K. IVANITSKY* [1, 2], *Bogdan Ya. TSELEN* [1]*,
*Oleksandr M. OBODOVYCH* [1], *Natalia L. RADCHENKO* [1]*

[1] Institute of Engineering Thermophysics of the National Academy of Science of Ukraine, bld. 2,
Marii Kapnist str., Kyiv, Ukraine
[2] National technical University of Ukraine 'National Technical University of Ukraine "Igor Sikorsky Kyiv
Polytechnic Institute, bld. 37, Prospect Beresteiskyi (former Peremohy), Kyiv, Ukraine.

**Received: 11 July 2023** **Accepted: 04 September 2023**

*The article presents data on the evaluation of the effectiveness of liquid degassing in the conditions of hydrodynamic cavitation, which is implemented in a Venturi tube. Based on the conducted experimental studies and the obtained data on the change in pH of the liquid, a change in the carbonic acid-dissolved gas balance was observed. In the terms of the single bubble dynamics model, the potential different sizes growth of gas microbubbles of under pressure relief conditions for two treatment modes is determined. It was found that increasing the efficiency of degassing causes the pressure in the cavitator to decrease to the maximum possible negative pressure. This allows the growth of the smallest bubbles to be activated in the degasser equipment. It is shown that the theoretical assessment of the potential effectiveness of cavitation degassing is somewhat overestimated. This is explained by the difference in calculated pressure values and actually created pressures in the degassing equipment. Correlation of theoretical calculations of cavitation efficiency based on experimental data showed that in the proposed treatment modes it is possible to activate bubbles from 1.5 to 3.0 μm, which also ensures a high degree of degassing.*

**Keywords**: degassing, hydrodynamic cavitation, cavitation bubble, gas content, Venturi tube, pH.

## INTRODUCTION

The need for degassing processes in modern industry is widespread and concerns many and very different branches of production, from food to metallurgy (1–4). There is a wide range of methods that allow it to be carried out with varying degrees of efficiency. Modern requirements for degassing technologies, in addition to efficiency, are energy saving, environmental friendliness, cost-effectiveness, relative simplicity and versatility of equipment, etc. Currently, there are quite a few methods of degassing, which confirms the demand for such processes. Among them are chemical and physical methods, which are given greater preference.

Many modern scientific articles are devoted to degassing methods based on the process of acoustic cavitation, where the authors confirm the effectiveness of this process (1–5). Indeed, the use of acoustic methods is effective for processing small volumes of media. However, for large-scale production requiring continuity and low energy costs, this method may not be acceptable (6, 7). Technologies based on the use of hydrodynamic cavitation

---

* Corresponding author: Bogdan Ya. TSELEN, Institute of Engineering Thermophysics of the National Academy of Sciences of Ukraine 2, Akademika Bulakhovskoho St., Kyiv, Ukraine, e-mail: ittf_tds@ukr.net

APTEFF, Vol. 54, 1-335 (2023) UDC: 66.069.84:532.5+620.193.16
DOI: https://doi.org/10.2298/APT2354237N BIBLID: 1450-7188 (2023) 54, 237-244

Original scientific paper

can be quite promising, which eliminates the disadvantages of acoustic technologies. The Institute of Technical Thermophysics of the National Academy of Sciences of Ukraine conducts scientific research aimed at studying the thermo- and hydrodynamic characteristics of this process. As a result, a technology was developed, the principle of which is based on the use of the hydrodynamic cavitation process. The first version of the equipment, where the process of degassing by the cavitation method was implemented, was a technological scheme using a cavitator based on a rotary device. The technology proved its effectiveness in the extraction of carbon dioxide from exhaust gas condensate (8, 9) and was implemented at the thermal power plant of Ukraine. In the terms of this technological scheme, its modification was created, in which the Venturi tube is the cavitator. The implementation of such a process involves the creation of conditions for the growth of gas bubbles, their long-term existence and subsequent removal of uncondensed gas from them. A feature of the implementation of this process is the prevention of the bubble collapse and the subsequent removal of gas from it. Compared with the previous scheme, the use of a Venturi tube simplifies the design of the equipment, can ensure a constant flow rate, and reduce energy costs. However, compared to the previous version of the technological scheme, there will be no significant shear stress on the working environment, so the feasibility of using technology options should be decided according to the requirements for the target product. A number of experimental and analytical studies were conducted to assess the effectiveness of technology and mechanisms of impact on the working environment, the results of which are presented in the materials of this article. The processing efficiency was considered to be the ratio of the concentration of dissolved gases in the sample after degassing to the concentration of these gases in the sample before processing in percentage.

## EXPERIMENTAL

To study the processes of hydrodynamic cavitation the laboratory setup was designed, which can be regarded as a static type cavitation reactor. As a hydrodynamic cavitation reactor the profiled Venturi tubes have been used. Schematic diagram of the cavitation reactor is shown in Figure 1. The circulation loop includes a reservoir with a processing liquid, pipeline, centrifugal pump, Venturi nozzle, as well as measuring instruments (manometers, thermometer and flow rate meter).

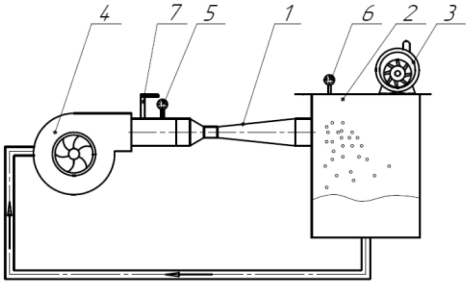

**Figure 1.** Scheme of a laboratory setup for liquid degassing: 1 – Venturi tube; 2 – container; 3 – vacuum pump; 4 – centrifugal pump; 5 – pressure gauge; 6 – vacuum gauge; 7 – supply control valve

The Venturi tube is directly connected to the vacuum chamber 2, in which a pressure lower than atmospheric is created by the vacuum pump 3 and the removal of dissolved gases is ensured. The pressure parameters in the chamber are controlled by a vacuum gauge 6, the supply of the working medium is carried out using a centrifugal pump 4, the supply modes are regulated by the valve 7. To control the pressure in the system, a pressure gauge 5 is installed, which displays the pressure readings in the system in front of the Venturi tube.

At the preliminary stage of the research, the optimal geometry of the Venturi nozzle was selected, which ensures high efficiency of cavitation effects with the lowest energy consumption when the liquid passes through the nozzle (10, 11).

The pipe cross section diameter $D_0$, which was the same at inlet and at outlet nozzle, is equal to 40 mm. The nozzle throat diameter $D_{thr}$ equals 16 mm, the nozzle throat length $L_{thr}$ equals 20 mm. Convergent angle $\beta_{con}$ is 60° and divergent angle of the diffuser $\beta_{dif}$ is 12°.

A model liquid, a solution of carbon in distilled water, was used as the working medium. To start the installation, the vacuum pump was first turned on, after setting the pressure in the vacuum chamber to 0.011 MPa, the centrifugal pump was turned on and the start time of the liquid treatment was fixed. Samples were taken after 2, 4 and 6 minutes of operation of the installation. The pH and temperature of the environment were determined in the samples. Experimental studies were carried out in two modes, the parameters of which are indicated in Table 1. The values of experimental data and carbon dioxide concentration from the conversion of pH units in the samples are indicated in Table 2.

Therefore, experiments were conducted in two modes of treatment of the working medium in conditions where the second mode provides a greater effect on its pH. The change in the temperature of the environment during the experiment was insignificant and amounted to 3 °C.

**Table 1**. Parameters of processing modes in the experimental setup

| Processing mode | Processing parameters | Value |
|---|---|---|
| I | Pressure in front of the Venturi tube, $P_0$ | 0,15 MPa |
| | Pressure in the vacuum chamber, $P_k$ | 0,011 MPa |
| | Mass rate, Q | $6{,}63 \cdot 10^{-3}$ m$^3$/s |
| II | Pressure in front of the Venturi tube, $P_0$ | 0,30 MPa |
| | Pressure in the vacuum chamber, $P_k$ | 0,011 MPa |
| | Mass rate, Q | $9{,}57 \cdot 10^{-3}$ m$^3$/s |

**Table 2.** Parameters of processing modes in the experimental unit

| **Processing mode** | | I | | | | II | | | |
|---|---|---|---|---|---|---|---|---|---|
| **Processing time, min** | | 0 | 2 | 4 | 6 | 0 | 2 | 4 | 6 |
| **Physicochemical parameters** | pH | 4.06 | 4.31 | 4.46 | 4.51 | 4.06 | 4.72 | 4.98 | 5.12 |
| | $CO_2$ concentration, mg/l | 1100.9 | 349.5 | 175.8 | 139.8 | 1100.9 | 53.6 | 16.5 | 8.8 |
| | Temperature, °C | 21.8 | 22.1 | 22.3 | 22.5 | 21.3 | 23.9 | 24.4 | 25.2 |

## RESULTS AND DISCUSSION

It is known that cavitation has an effect on the change in the pH value of solutions, which is associated with the removal of carbon dioxide, a change in the equilibrium in the solution due to the balance of carbon dioxide contained in the form of bubbles and dissolved carbon dioxide, hydrocarbonate and carbonate ions. Depending on the processing mode, the pH change was 0.45 units and 1.06 units, respectively, for the first and second modes during 6 minutes of processing. The most significant change in active acidity over time for the first mode was created after four minutes of processing, and was 0.4 units. At the same time, for the second processing regime, the pH difference after two minutes of processing was 0.66 units. The pH indicator of the final samples indicates a greater efficiency of degassing in the second processing mode. The change in the concentration of carbon dioxide in the model substance was 961.1 and 1092.1 mg/l during 6 minutes of processing, respectively, for the first and second treatment regimes. According to the obtained data, the efficiency of degassing is 99.2% for the second processing mode, and 87.3% for the first, the difference in the efficiency of degassing, in our opinion, is related to the hydrodynamic aspects of the processing modes.

To determine the hydrodynamic parameters of the treatment modes, analytical calculations of the pressure in the Venturi tube and its effect on the state of the microbubbles of dissolved gases in the liquid were performed. By solving the Bernoulli equation, the pressure change in the tube was determined (Figure 2). As can be seen from the figure, the first processing mode is characterized by a smaller value of the minimum tick and a smoother lowering / raising of it compared to the second. Thus, the pressure release time is 2.5 ms and 2 ms, and its rise time is 8 ms and 5 ms, respectively, for the first and second treatment modes. The minimum pressure was – 4.1 bar and – 9.2 bar in the first and second cases.

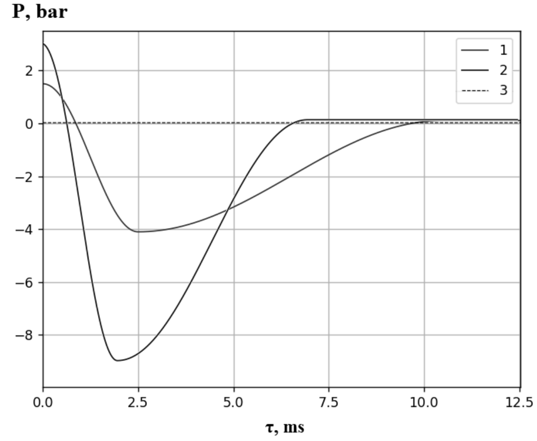

**Figure 2.** The dependence of the pressure change in the Venturi tube: 1 – the first processing mode; 2 – the second processing mode; 3 – saturation pressure

The obtained pressure curves made it possible to determine the behavior of the gas bubble. For this, the single bubble model was used (6, 10, 11). This model is based on the solution of the modified Rayleigh-Plesset equation. The conditions of bubble evolution were assumed to be isothermal. This is acceptable at the stage of bubble growth, which is of most interest to us in this study. Since bubbles with a radius of 5 μm or less are considered stable in the liquid, the graph shows the results for this range of their sizes.

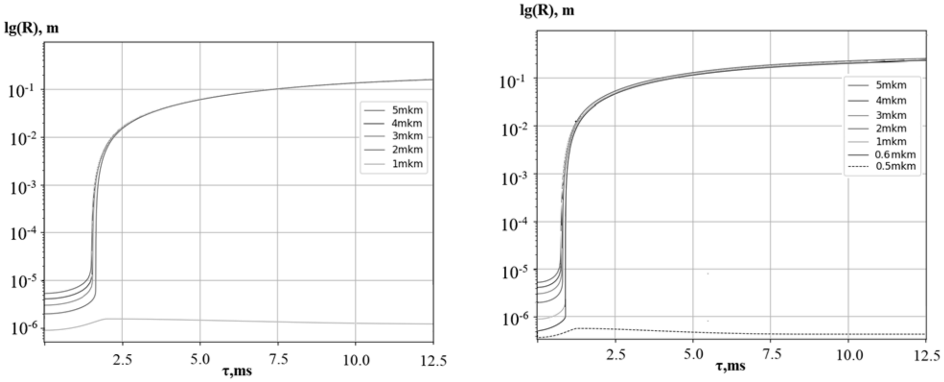

a) b)

**Figure 3.** The dependence of the bubbles radius changes over time from their initial size: a) – conditions of the first processing mode; b) – the conditions of the second processing mode

In the framework of degassing by physical methods, it is necessary to solve the problem of the abrupt release of pressure to values sufficient for the activation and growth of bubbles, the creation of a film flow, as well as the subsequent release of non-condensable gases. The results of the calculation show that the first processing mode allows the activation of bubbles with a radius of 2 μm and more, while the second mode allows the activation of bubbles from 0.6 μm, which is the garantee to removing a larger volume of gas. It should be noted here that the single bubble dynamics model does not take into account the conditions of mutual influence of bubbles growth and pressure changes in the cavitation cluster. However, these results show that the activation rate is higher for larger bubbles, so it can be assumed that gas in large bubbles will be removed first, and gas from smaller bubbles will be removed as larger fractions of bubbles are removed. The limiting condition for the removal of dissolved gases will be the largest negative pressure that can be achieved to activate bubbles of minimum size.

In the literature (12) there are data on the number of $N_b$ bubbles distributed in the liquid depending on their initial size (Figure 4, curve 1). Based on these data, curve 2 was constructed, which determines the dependence of the specific volume of gas occupied by the bubbles on their radius. Removal of larger bubbles allows removal of most of the dissolved gases. The presence of bubbles with a size of 1.5 μm and less does not significantly affect the content of dissolved gases, since they make up a small part of their total gas volume. The integration of curve 2 data made it possible to establish the volume of dissolved gases in bubbles in elements with a radius of 0.5 to 5 μm and to establish the volume of removed gases under the conditions of the first and second modes of operation, as well as to show the indicative efficiency of the degassing process. The data are shown in Table 3.

As can be seen from Table 3, the theoretical efficiency of degassing by the method of hydrodynamic cavitation has a fairly high potential efficiency. Estimates of possible gas removal are theoretical calculations. According to data (13–15), in practice, high values of negative pressures can be achieved in water free from impurities, which the authors of these works consider to be dissolved gases. However, the gradual removal of bubbles of dissolved gases allows you to reset the minimum pressure to lower values, which means that with each new cycle of liquid recirculation in the degassing unit, it is possible to remove the fraction with smaller bubbles.

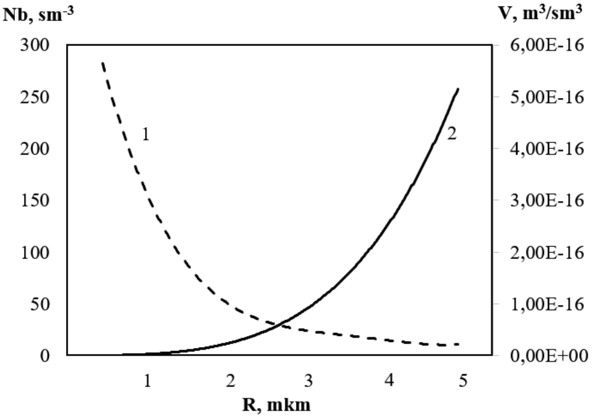

**Figure 4.** Distribution of the number of gas bubbles by size (curve 1) and their volumes (curve 2) contained in settled tap water

However, the gradual removal of bubbles of dissolved gases allows you to reset the minimum pressure to lower values, which means that with each new cycle of liquid recirculation in the degassing unit, it is possible to remove the fraction with smaller bubbles.

**Table 3.** Specific volume of dissolved gases in the liquid depending on the processing modes

| Sample | Specific volume of dissolved gases in the model liquid, μm$^3$/cm$^3$ | Degassing efficiency, % |
|---|---|---|
| Before processing | $6.5410 \cdot 10^{-4}$ | - |
| After processing (I-mode) | $0.1667 \cdot 10^{-4}$ | 97.5 |
| After processing (II- mode) | $0.0007 \cdot 10^{-4}$ | 99.9 |

The experimental data on the pH of the model substance and the efficiency of degassing based on them differ slightly from the theoretical calculations of this indicator when processing a liquid by the method of hydrodynamic cavitation. After adjusting the data of the degassing efficiency assessment based on pH and carbon dioxide concentration, it was determined that bubbles with a radius greater than 3.0 μm can be removed under the conditions of the first processing mode, and from 1.5 μm under the conditions of the second, which corresponds to 87.3% and 99.2% degassing efficiency, respectively.

## CONCLUSION

The paper presents an assessment of the efficiency of degassing technology, based on practical and analytical research of the process. It was established that it depends on the possibility of activation of the smallest gas bubbles. The theoretical and practical values of degassing efficiency differ somewhat, and this can be explained by the fact that in practice it is quite difficult to achieve low negative pressures in water containing impurities, and this has been described in a number of studies. The evaluation of the bubble sizes, based on practically obtained results, showed that in reality the radius of the bubbles that can be removed is greater than theoretical calculations give. At the same time, the efficiency of degassing by the method of hydrodynamic cavitation is quite high, and this is confirmed by experimental data. In the future, for more accurate forecasts of degassing efficiency, equipment development and processing modes, an interesting task will be the creation of a technique for calculating equipment parameters, in particular, a technique for determining real working pressures in technology.

For the practical use of this degassing technology, it is necessary to conduct additional research to determine the treatment modes and the duration of its exposure in accordance with the requirements for the target product. However, the promising use of this technology is confirmed by both analytical and experimental data.

## REFERENCES

1. Gogate, P.R. Hydrodynamic Cavitation for Food and Water Processing. *Food Bioprocess Technol.* **2011**, *4*, 996–1011. https://doi.org/10.1007/s11947-010-0418-1
2. Dolatowski, Z.J.; Stadnik, J.; Stasiak, D. Applications of Ultrasound in Food Technology. *Acta Sci. Pol., Technol. Aliment*. **2007**, *6*(3), 89–99. https://www.food.actapol.net/volume6/issue3/abstract-8.html
3. Villamiel, M.; Riera, E.; García-Pérez, J.V. The Use of Ultrasound for Drying, Degassing and Defoaming of Foods. *Innovative Food Processing Technologies*. **2021**, 415–438. https://doi.org/10.1016/B978-0-08-100596-5.22957-0
4. Eskin, D.G. Ultrasonic degassing of liquids. In Power Ultrasonics; Juan A. Gallego-Juárez and Karl F. Graff, Eds.; Woodhead Publishing, **2015**; pp 611–631. https://doi.org/10.1016/C2013-0-16435-5
5. Rozenberg, L.D. Physical Principles of Ultrasonic Technology; Springer New York: NY, **1973**; pp. 515. https://doi.org/10.1007/978-1-4684-8217-1
6. Dolinskiy, A.A.; Ivanitskiy, G.K. Heat and Mass Transfer and Hydrodynamics in Vapor-Liquid Dispersed Media; Naukova dumka: Kyiv, **2008**; pp 381.
7. Moholkar, V.S.; Senthil Kumar, P.; Pandit, A.B. Hydrodynamic cavitation for sonochemical effects. *Ultrasonic Sonochemestry*. **1999**, *6*(1-2), 53–65. https://doi.org/10.1016/S1350-4177(98)00030-3

8. Dolinskiy, A.A.; Tselen, B.Ya.; Gartvig, A.P.; Konyk, A.V.; Radchenko, N.L.; Shepkin, V.I. Formation of acid condensate during deep utilization of heat of combustion products of natural gas and equipment for its neutralization. *Scientific Works [Odessa national academy of food technologies]*. **2016**, *80*(1), 4–7. http://nbuv.gov.ua/UJRN/Np_2016_80_1_3
9. Obodovych O.M.; Tselen B.Ya.; Sydorenko V.V.; Ivanytskyi G.K.; Radchenko N.L. Application of the method of discrete-pulse energy input for water degassing in municipal and industrial boilers. *Acta periodica technologica*. **2022**, *53*, 123–130. https://doi.org/10.2298/APT2253123O
10. Ivanitsky, G.K. Numerical study of bubble cluster behavior in hydrodynamic cavitation processes. *Scientific Works [Odessa National Academy of Food Technologies]*. **2017**, *81*(1), 114–120. http://nbuv.gov.ua/UJRN/Np_2017_81_1_25
11. Ivanitsky, G.; Nedbaylo, A.; Konyk, A.; Tselen, B.Ya.; Gozhenko, L. Modeling cavitation reactors: a unified approach. *Proc. XVII Int. Conf. on Improving processes and equipment of food and chemical industries ICPA*, Odessa national academy of food technologies, 3–8 September **2018**, 84–89. https://card-file.ontu.edu.ua/items/481a5626-aad3-4743-957e-f2a987c16b91
12. Brennen, C.E. Cavitation and Bubble Dynamics; Cambridge University Press: Cambridge, **2013**; pp. 249. https://doi.org/10.1017/CBO9781107338760
13. Herbert, E.; Balibar, S.; Caupin, F. Cavitation pressure in water. *Phys. Rev. E*. **2006**, *74*, 041603, 1–22. https://doi.org/10.1103/PhysRevE.74.041603
14. Winnick, J.; Cho. S.J. Erratum: *PVT* Behavior of Water at Negative Pressures. *J. Chem. Phys*. **1972**, *57*(2), 1018. https://doi.org/10.1063/1.1678289
15. Huang, H.S.; Guell, D.L.; Winnick, J. *PVT* behavior of water at negative pressures: Capillary tube deformation effects. *J. Chem. Phys*. **1973**, *59*(11), 6191–6192. https://doi.org/10.1063/1.1679997

APTEFF, Vol. 54, 1-335 (2023)
DOI: https://doi.org/10.2298/APT2354245K

UDC: 504.05+615.9:632.95:547.236]:004.8
BIBLID: 1450-7188 (2023) 54, 245-253

Original scientific paper

# ARTIFICIAL INTELLIGENCE IN PREDICTION OF ECOTOXICITY OF A SERIES OF *s*-TRIAZINE COMPOUNDS AS POTENTIAL PESTICIDES

*Milica KARADŽIĆ BANJAC, Strahinja KOVAČEVIĆ*, Lidija JEVRIĆ,*
*Sanja PODUNAVAC-KUZMANOVIĆ*

Department of Applied and Engineering Chemistry, Faculty of Technology Novi Sad, University of Novi Sad,
Bulevar cara Lazara 1, 21000 Novi Sad, Serbia

**Received: 16 July 2023** **Revised: 23 August 2023** **Accepted: 04 September 2023**

*The elevated levels of pesticides and their residues occur in the environment lately due to increased usage of different agrochemicals. These pesticide residuals enter the human body through water and food. Nowadays different statistics and artificial intelligence tools are employed in order to solve different problems in agricultural science. Artificial neural networks (ANNs) have shown up as a convenient tool in establishing the non-linear mathematical relationships. The ecotoxicity of studied s-triazine pesticides was expressed as acute algae toxicity (AAT) and modeled by the ANN approach. Prior to applying feedforward multilayer perceptron (MLP) neural network with Broyden-Fletcher-Goldfarb-Shanno (BFGS) learning algorithm. The ANN modeling resulted in two networks with the best statistical performance. An excellent correlation was obtained between experimentally observed data and acute algae toxicity predicted data with correlation coefficient higher than 0.9342. Additionally, global sensitivity analysis (GSA) was conducted in order to estimate the influence of all molecular descriptors in the input layer on the networks performance.*

**Keywords**: ecotoxicity, pesticides, artificial neural networks, triazines.

## INTRODUCTION

As one of the commonly used pesticides in agriculture nowadays symmetric triazines (*s*-triazines) occur due to their well-known and proven activity (1, 2). These molecules are frequently studied since they can be considered as pesticides (3), herbicides (4) and antifungal agents (5). The use of *s*-triazine based herbicides was approved in 1957 when simazine was introduced as commercial product (1). *s*-Triazine ring has a very good possibility to form the non-covalent bonds which has a very important role in expression of the biological activity of compounds. This is important for the understanding of the degradation, metabolism and elimination of the *s*-triazine from living organisms and from the environment. Triazine compounds are extensively used as broad-spectrum herbicides since they provide disruption of electron transfer in photosynthesis and in that way disable weed growth and development. Since the human population is growing it is necessary to provide enough food that leads to the additional pesticide use in order to limit and control weed and to avoid wastage of unnecessary resource (water, light, nutrients, space etc.). Nevertheless, this additional pesticide use brings with it a negative side, an abuse of pesticide utilization and harmful effects to the nature and human health (6). Used pesticides and their residue express high toxicity in water, soil and crops (7). Ecotoxicity impact has a great roll

---

* Corresponding author: Strahinja KOVAČEVIĆ, Department of Applied and Engineering Chemistry, Faculty of Technology Novi Sad, University of Novi Sad, Bulevar cara Lazara 1, 21000 Novi Sad, Serbia, e-mail: strahko@uns.ac.rs

speaking of the life cycle assessment of some pesticide. Ecotoxicity of different triazine based herbicides and their residues is well investigated and it attracts a lot of attention of researchers. The impact of triazine based herbicides and their residues was investigated regarding earthworm *Eisenia fetida* (8), photobacteria *Vibrio qinghaiensis* sp. (9), midge *Chironomus tentans* (10), zebrafish embryos (*Danio rerio*) (11) and phytoplankton (12).

Nowadays, different chemometric methods are employed in modeling of *Daphnia magna* toxicity of agrochemicals (13), toxicity assessment of atrazine and related triazine compounds in the microtox assay study (14) and triazine herbicides risk management strategies on environmental and human health aspects study (15). New models to predict the acute and toxicities of representative species of aquatic environments were also published (16). One of the increasingly applied chemometric methods in the domain of agriculture is artificial intelligence regression tool – artificial neural networks (ANNs) that is employed when the non-linear complex relationships between variables occur. The basis of ANNs and its architecture is a biological neuron structure and function. ANNs were constructed and developed based on the brain structure so they can learn, manage data and recognize patterns. The efficacy and usefulness in prediction using ANNs has been proven in numerous scientific studies concerning herbicides (17-19). Built ANN regression model will generalize the relationship between one or more dependent and independent variables but it will not give a specific mathematical function. In ANNs several linked layers of artificial neurons occur– input, one or more hidden and output (20).

In this paper, the ANNs were used for the purpose of predicting the ecotoxicity of a series of *s*-triazine compounds that can be used as potential pesticides. Chosen ecotoxicity for the prediction was acute algae toxicity (AAT) and it was predicted based on the three molecular descriptors: CrippenLogP, Autocorrelation Descriptor Mass (ATSm4) and McGowanVolume. The ANN modeling resulted in two statistically significant and meaningful models that were externally validated. Global sensitivity analysis (GSA) was conducted in order to estimate the significance of the input variables and their interactions influencing the models outputs.

## MATERIAL AND METHODS

### THE SERIES OF THE STUDIED *S*-TRIAZINE DERIVATIVES

The analyzed data set included 21 *s*-triazine derivatives whose IUPAC names are listed in Table 1. The analyzed compounds have been synthesized at the Faculty of Technology and Metallurgy, University of Belgrade, according to the procedure described in literature (21, 22).

**Table 1.** The IUPAC names of the analyzed compounds

| Compound | IUPAC name |
|---|---|
| **1** | 6-chloro-$N^2$,$N^4$-dipropyl-1,3,5-triazine-2,4-diamine |
| **2** | 6-chloro-$N^2$,$N^4$-bis(propan-2-yl)-1,3,5-triazine-2,4-diamine (propazine) |
| **3** | $N^2$,$N^4$-bis(butan-2-yl)-6-chloro-1,3,5-triazine-2,4-diamine |
| **4** | 6-chloro-$N^2$,$N^4$-bis(2-methylpropyl)-1,3,5-triazine-2,4-diamine |

**Table 1.** Continuation

| Compound | IUPAC name |
|---|---|
| **5** | 6-chloro-$N^2$,$N^4$-dicyclopentyl-1,3,5-triazine-2,4-diamine |
| **6** | 6-chloro-$N^2$,$N^4$-dicyclohexyl-1,3,5-triazine-2,4-diamine |
| **7** | 6-chloro-$N^2$,$N^4$-dicycloheptyl-1,3,5-triazine-2,4-diamine |
| **8** | 6-chloro-$N^2$,$N^4$-dicyclooctyl-1,3,5-triazine-2,4-diamine |
| **9** | 6-chloro-$N^2$,$N^4$-bis(1-phenylethyl)-1,3,5-triazine-2,4-diamine |
| **10** | 6-chloro-$N^2$,$N^4$-bis(1-(p-tolyl)ethyl)-1,3,5-triazine-2,4-diamine |
| **11** | 6-chloro-$N^2$,$N^4$-bis(1-(4-chlorophenyl)ethyl)-1,3,5-triazine-2,4-diamine |
| **12** | $N^2$,$N^4$-bis(1-(4-bromophenyl)ethyl)-6-chloro-1,3,5-triazine-2,4-diamine |
| **13** | 6-chloro-$N^2$,$N^4$-dicyclohexyl-$N^2$,$N^4$-dimethyl-1,3,5-triazine-2,4-diamine |
| **14** | 6-chloro-$N^2$,$N^4$-dicyclohexyl-$N^2$-phenyl-1,3,5-triazine-2,4-diamine |
| **15** | 6-chloro-$N^2$,$N^4$-dicyclohexyl-$N^2$,$N^4$-diphenyl-1,3,5-triazine-2,4-diamine |
| **16** | 6-chloro-$N^2$,$N^4$-bis(1-methylcyclopentyl)-1,3,5-triazine-2,4-diamine |
| **17** | 6-chloro-$N^2$,$N^4$-bis(1-methylcyclohexyl)-1,3,5-triazine-2,4-diamine |
| **18** | 6-chloro-$N^2$,$N^{4-}$bis(1-methylcycloheptyl)-1,3,5-triazine-2,4-diamine |
| **19** | 4,6-dichloro-*N*-(1-methylcyclopentyl)-1,3,5-triazin-2-amine |
| **20** | 4,6-dichloro-*N*-(1-methylcyclohexyl)-1,3,5-triazin-2-amine |
| **21** | 4,6-dichloro-*N*-(1-methylcycloheptyl)-1,3,5-triazin-2-amine |

## THE ECOTOXICITY DATA AND THE INPUT PARAMETERS

The data used for the ANN modeling are shown in Table 2. From the pool of calculated descriptors, three of them were selected for further analysis using appropriate descriptor selection procedure. The stepwise selection (SS) method was applied as the first step of variable selection (23). Acute algae toxicity (AAT) was calculated using PreADMET online program (24) and transformed into its logarithmic form for the following ANN modeling. PaDEL-descriptor was used two-dimensional structures of molecules for CrippenLogP, Autocorrelation Descriptor Mass (ATSm4) and McGowanVolume calculation (25, 26). The calculated values ranged from 1.643 (compound **2**) to 3.128 (compound **15**) for -logAAT, from 2.976 (compound **2**) to 9.331 (compound **15**) for CrippenLogP, from 22.732 (compound **2**) to 68.007 (compound **12**) for ATSm4 and from 1.675 (compound **19**) to 3.604 (compound **15**) for McGowanVolume.

**Table 2.** The ecotoxicology data (-logAAT) and molecular descriptors used for the ANN modeling

| Compound | -logAAT | CrippenLogP | ATSm4 | McGowanVolume |
|---|---|---|---|---|
| **1** | 1.736 | 2.979 | 23.064 | 1.761 |
| **2** | 1.643 | 2.976 | 22.732 | 1.760 |
| **3** | 1.928 | 3.756 | 27.064 | 2.042 |
| **4** | 1.953 | 3.471 | 25.396 | 2.042 |
| **5** | 2.019 | 4.044 | 27.396 | 2.107 |

DOI: https://doi.org/10.2298/APT2354245K
BIBLID: 1450-7188 (2023) 54, 245-253

**Table 2.** Continuation

| Compound | -logAAT | CrippenLogP | ATSm4 | McGowanVolume |
|---|---|---|---|---|
| **6** | 2.320 | 4.825 | 33.396 | 2.389 |
| **7** | 2.616 | 5.605 | 41.396 | 2.670 |
| **8** | 2.872 | 6.385 | 43.396 | 2.952 |
| **9** | 2.183 | 4.999 | 41.396 | 2.694 |
| **10** | 2.677 | 5.055 | 45.396 | 2.976 |
| **11** | 2.966 | 6.306 | 53.203 | 2.939 |
| **12** | 3.128 | 6.524 | 68.007 | 3.044 |
| **13** | 2.325 | 4.873 | 42.061 | 2.670 |
| **14** | 2.660 | 7.078 | 47.061 | 2.996 |
| **15** | 3.244 | 9.331 | 60.726 | 3.604 |
| **16** | 2.156 | 4.825 | 33.396 | 2.389 |
| **17** | 2.490 | 5.605 | 39.396 | 2.670 |
| **18** | 2.819 | 6.385 | 47.396 | 2.952 |
| **19** | 1.750 | 3.328 | 27.303 | 1.675 |
| **20** | 1.865 | 3.718 | 30.303 | 1.815 |
| **21** | 1.977 | 4.108 | 34.303 | 1.956 |

### THE ANN MODELING PROCEDURE

To obtain the realistic and reliable output using ANN, the data set comprising of 21 compounds was randomly divided into training (13 compounds), validation (2 compounds), test (2 compounds) and external (4 compounds) data set. In this way the best network configuration can be found. For ANN modeling procedure Statistica software was used (27). These data were processed and optimal structure of ANN was searched using feedforward multilayer perceptron (MLP) neural network with Broyden-Fletcher-Goldfarb-Shanno (BFGS) learning algorithm. ANN models were formed with 2000 networks that were trained for each combination of variables, while the number of hidden neurons varied from 2 to 200. As the activation functions of hidden and output layers the following ones were used: logistic (Lgt), hyperbolic tangent (Tahn), exponential (Exp) and identity function (Idn). After the ANN modeling process output data were compared and correlated with the experimentally obtained values and statistically evaluated.

## RESULTS AND DISCUSSION

### THE TRAINING AND PERFORMANCE OF THE ANNS

From 20 trained networks, the best 3 were selected based on their statistical parameters that are presented in Table 3. Regarding the optimal architecture of established ANNs, ANN1 has 3 input variables, 8 hidden neurons and one output variable (3-8-1), while ANN2 has 3 input variables, 7 hidden neurons and one output variable (3-7-1). Three molecular descriptors (CrippenLogP, ATSm4 and McGowanVolume) were selected as the most important contributors to the acute algae toxicity of the studied *s*-triazine pesticides.

For ANN1 the correlation coefficients for training, test and validation set ranged from 0.9608 to 1.0000, while training, test and validation root mean square error ranged from 0.0000 to 0.0093. High values of the correlation coefficient (R) for training, test and validation set confirm validity of the ANNs, as well as low values of the root mean square error (RMSE). Numbers 9 and 11 placed at the training algorithm represent the number of the training cycles that gave the optimal network architecture. In both ANNs hidden and output activation functions were logistic and hyperbolic tangent, respectively.

**Table 3.** The characteristics of the trained ANNs

| **Net. name** | ANN1: MLP 3-8-1 | ANN2: MLP 3-7-1 |
|---|---|---|
| $\mathbf{R_{calib}}$ | 0.9608 | 0.9766 |
| $\mathbf{R_{test}}$ | 1.0000 | 1.0000 |
| $\mathbf{R_{valid}}$ | 1.0000 | 1.0000 |
| $\mathbf{RMSE_{calib}}$ | 0.0093 | 0.0056 |
| $\mathbf{RMSE_{test}}$ | 0.0082 | 0.0056 |
| $\mathbf{RMSE_{valid}}$ | 0.0000 | 0.0012 |
| **Training algorithm** | BFGS 9 | BFGS 11 |
| **Hidden activation** | Lgt | Tanh |
| **Output activation** | Lgt | Tanh |

In Table 4 predicted -logAAT values and residuals obtained with both ANNs are presented. Since the absolute maximum values of residuals are 0.270 for ANN1 and 0.264 for ANN2 it can be concluded that there is a close agreement between the experimentally obtained and estimated acute algae toxicity data. Also it can be concluded that the established neural networks have an excellent predictive power and very high accuracy in the considered range of the -logAAT values.

**Table 4.** The outputs (predicted values) and residuals of the obtained ANNs

| **Compounds** | **Set** | **ANN1 (MLP 3-8-1) Output** | **ANN1 (MLP 3-8-1) Residuals** | **ANN2 (MLP 3-7-1) Output** | **ANN2 (MLP 3-7-1) Residuals** |
|---|---|---|---|---|---|
| **1** | Train | 1.782 | -0.046 | 1.698 | 0.038 |
| **2** | Train | 1.780 | -0.137 | 1.703 | -0.060 |
| **4** | Train | 1.845 | 0.108 | 1.870 | 0.083 |
| **5** | Train | 1.916 | 0.103 | 2.039 | -0.020 |
| **6** | Train | 2.171 | 0.149 | 2.247 | 0.074 |
| **7** | Train | 2.528 | 0.088 | 2.525 | 0.091 |
| **8** | Test | 2.739 | 0.134 | 2.777 | 0.096 |
| **9** | Train | 2.453 | -0.270 | 2.347 | -0.163 |
| **11** | Test | 2.845 | 0.122 | 2.851 | 0.115 |
| **12** | Train | 2.993 | 0.135 | 3.035 | 0.093 |
| **13** | Train | 2.439 | -0.114 | 2.302 | 0.023 |
| **14** | Train | 2.854 | -0.194 | 2.924 | -0.264 |
| **15** | Train | 3.095 | 0.149 | 3.174 | 0.070 |
| **16** | Train | 2.171 | -0.014 | 2.247 | -0.090 |
| **17** | Validation | 2.493 | -0.003 | 2.517 | -0.028 |

**Table 4.** Continuation

| Compounds | Set | ANN1 (MLP 3-8-1) Output | ANN1 (MLP 3-8-1) Residuals | ANN2 (MLP 3-7-1) Output | ANN2 (MLP 3-7-1) Residuals |
|---|---|---|---|---|---|
| **19** | Train | 1.805 | -0.056 | 1.728 | 0.022 |
| **21** | Validation | 1.967 | 0.010 | 1.914 | 0.063 |
| **3** | *External* | 1.878 | 0.051 | 1.937 | -0.008 |
| **10** | *External* | 2.625 | 0.052 | 2.470 | 0.207 |
| **18** | *External* | 2.789 | 0.030 | 2.809 | 0.010 |
| **20** | *External* | 1.864 | 0.001 | 1.826 | 0.039 |

The relationships between experimentally observed and predicted -logAAT values for both ANNs are presented in Figure 1. These graphs indicate a very good fit between the experimentally observed and predicted data since there is a low scattering of the points around the linear relationship in both ANNs. The values of slope are significant (>0.8814), intercept is close to zero (<0.2697) and $R^2$ is higher than 0.9342 which also confirms a very good concurrence between the data for both networks.

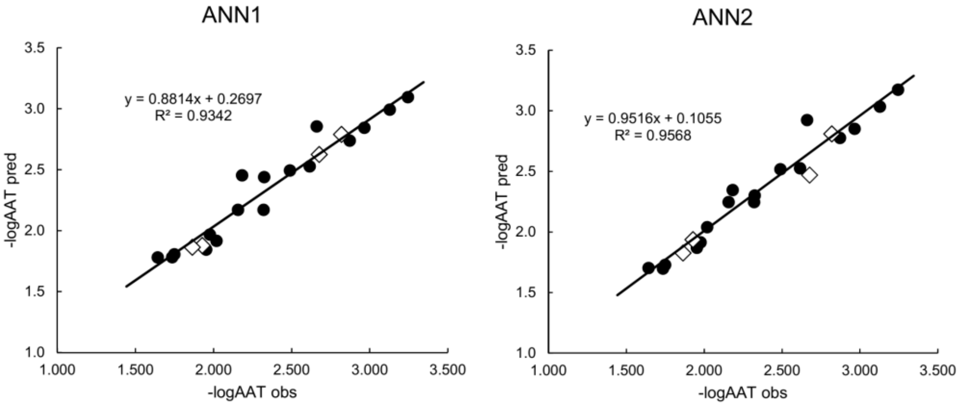

**Figure 1.** The relationships between experimentally observed and predicted –logAAT values modeled by ANN1 and ANN2 networks (circle – training set, square – external test set).

One of the ways to reveal the existence of the systematic error in development of the ANN models is plotting the residuals compared with predicted -logAAT values. So, the quality of the established networks was estimated by the analysis of residuals (Figure 2). The distribution of the residuals around the zero value on the y axis indicate the randomness of the prediction error of these two established models.

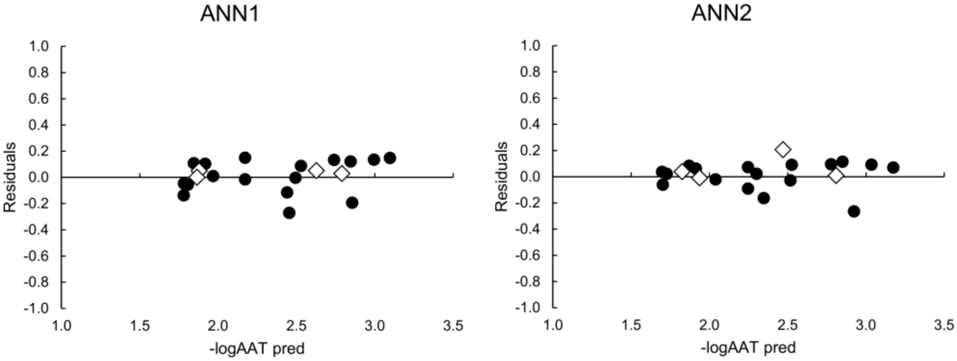

**Figure 2.** The distribution of the residuals for the ANN1 and ANN2 networks (circle – training set, square – external test set).

### The global sensitivity analysis

The influence of all molecular descriptors in the input layer on the variations is assessed by global sensitivity analysis (GSA). GSA coefficient explains the ratio between the network error when the observed variable is present in the ANN model and the network error when the observed variable is left out of it If GSA coefficient is equal to 1 or less it is a sure indicator that this variable should be left out from the model. The results of GSA for ANN1 and ANN2 networks are presented in Table 5. From these results can be seen that each variable has higher GSA coefficient than 1 which indicates the significance of the molecular descriptors, particularly the significance of CrippenLogP and ATSm4 descriptor.

**Table 5.** The GSA coefficients of the input parameters of the ANNs

| Networks | CrippenLogP | ATSm4 | McGowan_Volume |
|---|---|---|---|
| **ANN1** | 1.98 | 2.04 | 1.62 |
| **ANN2** | 14.34 | 3.99 | 1.41 |
| **Average** | 8.16 | 3.01 | 1.51 |

## CONCLUSION

In this paper the artificial neural networks modeling was applied as regression tool on the set of twenty one *s*-triazine pesticide. Targeted molecular descriptors CrippenLogP, ATSm4 and McGowanVolume were selected according the procedure as the most appropriate ones for ANN modeling. The presented results show that the ANN modeling can be used as a very useful tool for the prediction of the acute algae toxicity of the studied *s*-triazine derivatives. The constructed ANNs expressed excellent concurrence between the experimentally observed and predicted values of the acute algae toxicity. The validity of ANNs was confirmed by statistical parameters as well as through graphical presentation of experimentally observed *versus* predicted data and residual analysis. Global sensitivity analysis provided an insight into molecular descriptors model contribution. The conducted modeling of acute algae toxicity can contribute to the future *s*-triazine molecular design and their synthesis with aim of finding new similar pesticides with reference and attention to their ecotoxicity.

## Acknowledgements

The present research is financed in the framework of the project of Provincial Secretariat for Higher Education and Scientific Research of AP Vojvodina (Project: Molecular engineering and chemometric tools: Towards safer and greener future, No. 142-451-3095/ 2022-01/01). The authors thank Professors Dušan Antonović and Bratislav Jovanović from the Faculty of Technology and Metallurgy, University of Belgrade, for the synthesis of the studied triazines

## REFERENCES

1. LeBaron, H.M.; McFarland, J.E.; Burnside, O.C. The triazine herbicides: A milestone in the development of weed control technology. In *The triazine herbicides, 50 years revolutionizing agriculture*; LeBaron, H.M.; McFarland, J.E.; Burnside, O.C., Eds.; Elsevier: Amsterdam, 2008; pp 1-12.
2. Sharma, A.; Sheyi, R.; de la Torre, B.G.; El-Faham, A.; Albericio, F. *s*-Triazine: A privileged structure for drug discovery and bioconjugation. *Molecules*. **2021**, *26 (4)*, 864.
3. Gupta, A.K.S.; Bhattaharya, T.; Hajela, K.; Shankar, K.; Ahmad, S. Synthesis and pesticidal activities of some substituted 1,2,4-triazines. *Pest. Sci*. **1985**, *16 (1)*, 65-72.
4. Koizumi, K.; Kuboyama, N.; Tomono, K., Tanaka, A.; Ohkl, A.; Kohno, H.; Wakabayashi, K.; Böger, P. Novel 1,3,5-triazine derivatives with herbicidal activity. *Pest. Sci*. **1999**, *55 (6)*, 642-645.
5. Mekheimer, R.A.; Abuo-Rahma, G.E-D,; Abd-Elmonem, M.; Yahia, R.; Hisham, M.; Hayallah, A.M.; Mostafa, S.M.; Abo-Elsoud, F.A.; Sadek, K.U. New *s*-triazine/tetrazole conjugates as potent antifungal and antibacterial agents: Design, molecular docking and mechanistic study. *J. Mol. Struct*. **2022**, *1267*, 133615.
6. Narenderan, S.T.; Meyyanathan, S.N.; Babu, B. Review of pesticide residue analysis in fruits and vegetables. Pre-treatment, extraction and detection techniques. *Food Res. Int*. **2020**, *133*, 109141.
7. Su, R.; Li, D.; Wu, L.; Han, J.; Lian, W.; Wang, K.; Yang, H. Determination of triazine herbicides in juice samples by microwave-assisted ionic liquid/ionic liquid dispersive liquid–liquid microextraction coupled with high performance liquid chromatography. *J. Sep. Sci*. **2017**, *40 (14)*, 2950-2958.
8. Lydy, M.J.; Linck, S. L. Assessing the impact of triazine herbicides on organophosphate insecticide toxicity to the earthworm *Eisenia fetida*. *Arch. Environ. Con. Tox*. **2003**, *45*, 343-349.
9. Zhu, X-W.; Liu, S-S.; Ge, H-L.; L, Y. Comparison between the short-term and the long-term toxicity of six triazine herbicides on photobacteria Q67. *Water Res*. **2009**, *43*, 1731-1739.
10. Schuler, L.J.; Trimble, A.J.; Belden, J.B.; Lydy, M.J. Joint toxicity of triazine herbicides and organophosphate insecticides to the midge *Chironomus tentans*. *Arch. Environ. Contam. Toxicol*. **2005**, *49 (2)*, 173-177.
11. Adeyemi, J.A.; Martins-Junior, A.D.C.; Jr, F.B. Teratogenicity, genotoxicity and oxidative stress in zebrafish embryos (*Danio rerio*) co-exposed to arsenic and atrazine. *Comp. Biochem. Phys. C*. **2015**, *172-173*,7-12.

12. Yang, L.; Li, H.; Zhang, Y.; Jiao, N. Environmental risk assessment of triazine herbicides in the Bohai Sea and the Yellow Sea and their toxicity to phytoplankton at environmental concentrations. *Environ Int*. **2019**, *133*, 105175.
13. Khan, P.M.; Roy, K.; Benfenati, E. Chemometric modeling of *Daphnia magna* toxicity of agrochemicals. *Chemosphere*. **2019**, *224*, 470-479.
14. Tchounwou, P.B.; Wilson, B.; Ishaque, A.; Ransome, R.; Huang, M-J.; Leszczynski, J. Toxicity assessment of atrazine and related triazine compounds in the microtox assay, and computational modeling for their structure-activity relationship. *Int. J. Mol. Sci*. **2000**, *1 (4)*, 63-74.
15. Yao, T; Sun, P.; Zhao, W. Triazine herbicides risk management strategies on environmental and human health aspects using *in-silico* methods. *Int. J. Mol. Sci*. **2023**, *24 (6)*, 5691.
16. Toma, C.; Cappelli, C.I.; Manganaro, A.; Lombardo, A.; Arning, J.; Benfenati, E. New models to predict the acute and chronic toxicities of representative species of the main trophic levels of aquatic environments. *Molecules*. **2021**, *26 (22)*, 6983.
17. Esfandian, H.; Samadi-Maybodi, A.; Parvini, M.; Khoshandam, B. Development of a novel method for the removal of diazinon pesticide from aqueous solution and modeling by artificial neural networks (ANN). *J. Ind. Eng. Chem*. **2016**, 35, 295-308.
18. Hamadache, M.; Hanini, S.: Benkortbi, O.: Amrane, A.; Khaouane, L.; Moussa, C.S. Artificial neural network-based equation to predict the toxicity of herbicides on rats. *Chemometr. Intell. Lab*. **2016**, *154*, 7-15.
19. Silva, T.S.; de Freitas Souza, M.; da Silva Teófilo, T.M.; dos Santos, M.S.; Porto, M.A.F.; Souza, C.M.M.; dos Santos, J.B.; Silva, D.V. Use of neural networks to estimate the sorption and desorption coefficients of herbicides: A case study of diuron, hexazinone, and sulfometuron-methyl in Brazil. *Chemospehere*. **2019**, *236*, 124333.
20. Miller, J.N.; Miller, J.C. Statistics and Chemometrics for Analytical Chemistry, 6th edition. Pearson: Harlow, **2010**.
21. Bončić-Caričić, G.A.; Tadić, Ž.D.; Jeremić, D.S. Electron impact mass spectrometry of some 2,4,6-substituted *s*-triazines. Effect of the ring size. *Int. J. Mass Spectrom. Ion Phys.* **1983**, *47*, 451-454.
22. Antonović, D.; Bončić-Caričić, G.A. Gas chromatographic retention indices for *N*-substituted amino s-triazines on DB-1 and DB-5 capillary columns. *J. Serb. Chem. Soc.* **1994**, *59* (12), 993-996.
23. Kovačević, S.Z.; Podunavac-Kuzmanović, S.O.; Jevrić, L.R.; Djurendić, E.A.; Ajduković, J.J. Non-linear assessment of anticancer activity of 17-picolyl and 17-picolinylidene androstane derivatives – Chemometric guidelines for further syntheses. *Eur. J. Pharm. Sci*. **2014**, *62*, 58-266.
24. PreADMET program, https://preadmet.qsarhub.com/
25. Yap, C.W. PaDEL-descriptor: An open source software to calculate molecular descriptors and fingerprints. *J. Comput. Chem*. **2011**, *32 (7)*, 1466-1474.
26. PaDEL-descriptor, www.padel.nus.edu.sg/software/padeldescriptor
27. StatSoft Inc., 2300 East 14th Street, Tulsa, Oklahoma, USA, www.statsoft.com

APTEFF, Vol. 54, 1-335 (2023) UDC: 543.068:632.95:504.05+615.9
DOI: https://doi.org/10.2298/APT2354255K BIBLID: 1450-7188 (2023) 54, 255-264

Original scientific paper

# LINEAR QUANTITATIVE STRUCTURE-ECOTOXICITY RELATIONSHIP MODELING OF A SERIES OF SYMMETRICAL TRIAZINE DERIVATIVES BASED ON PHYSICOCHEMICAL PARAMETERS

*Strahinja KOVAČEVIĆ, Milica KARADŽIĆ BANJAC*, Lidija JEVRIĆ, Sanja PODUNAVAC-KUZMANOVIĆ*

Department of Applied and Engineering Chemistry, Faculty of Technology Novi Sad, University of Novi Sad,
Bulevar cara Lazara 1, 21000 Novi Sad, Serbia

**Received: 26 July 2023** **Revised: 25 August 2023** **Accepted: 04 September 2023**

*The present study reports the Quantitative Structure-Ecotoxicity Relationship (QSER) analysis of a series of 21 1,3,5-triazine derivatives based on multiple-linear regression (MLR) method. The ecotoxicity data were estimated by using in silico approach and included the following parameters: acute algae toxicity (AAT), acute daphnia toxicity (ADT), Daphnia Magna $LC_{50}$ 48h/EPA (DMepa) and Daphnia Magna $LC_{50}$ 48h/DEMETRA (DMdemetra). The ecotoxicity data were correlated with molecular descriptors selected by using the stepwise selection method. The considered molecular descriptors are lipophilicity descriptors (CrippenLogP, ALogp2), Autocorrelation Descriptor Mass (ATSm1, ATSm2, ATSm3, ATSm4), Autocorrelation Descriptor Charge (ATSc2), minimum E-states for (strong) hydrogen bond acceptors (minHBa), maximum E-states for (strong) hydrogen bond acceptors (maxHBa), second kappa shape index (Kier2), maximum atom-type E-State: ":N:" (maxaaN), sum of path lengths starting from nitrogens (WTPT-5) and McGowan characteristic volume (McGowan_Volume). The modeling resulted in four statistically valid MLR models. The models were validated by the internal and external validation approaches. The external validation confirmed high predictive ability of the established MLRs.*

**Keywords**: chemometrics, pesticides, toxicity, QSAR, molecular modeling.

## INTRODUCTION

The wide spectrum of crop pests (bacteria, fungi, viruses, insects) requires a wide range of crop protection methods. Biotic factors reduce crop yields by up to 35% (1). The application of various chemicals (pesticides) for this purpose is most common, however brings certain environmental risks. The estimation of the influence of compounds on the environment can be estimated by using *in silico* or *in vitro/in vivo* methods. *In silico* methods imply the application of previously established mathematical models (quantitative structure-activity relationship – QSAR) (2-4) in prediction of various environmental factors, including toxicity towards aquatic organisms, biodegradability estimation, bioconcentration factors, etc. Some QSAR models have been developed for the prediction of the reproductive toxicity induced in *Folsomia candida*, a species of springtail from the *Isotomidae* family (5).

Some QSARs were modelled for classification for prediction of toxicity of a huge set of pesticides based on several classification algorithms, including linear and quadratic discriminant analysis, nearest mean classifier, K-nearest neighbors classification, etc (6). QSAR

---

* Corresponding author: Milica KARADŽIĆ BANJAC, Department of Applied and Engineering Chemistry, Faculty of Technology Novi Sad, University of Novi Sad, Bulevar cara Lazara 1, 21000 Novi Sad, Serbia, e-mail: mkaradza@uns.ac.rs

modeling based on the regression approaches, such as univariate linear regression (ULR), multiple linear regression (MLR), partial least squares regression (PLSR), principal component regression (PCR), artificial neural networks (ANNs) regression, is more common and provides mathematical models for estimation of the biological activity of compounds (7-10).

Triazines are one of the most common group of compounds that have found the application in agriculture as pesticides (mostly as herbicides) (1). Some new perspectives regarding the QSAR and molecular docking modeling of triazine compounds pointed out that some of non-commercial triazine molecules could be a base for development of new pesticide formulae (11). Also, there are some extensive works that dealt with the lipophilicity estimation and chromatographic behavior determination of triazine derivatives (12-14). Lipophilicity is one of the most important molecular features (physicochemical parameters) that can affect the distribution of the molecules in biological systems and environment. It has a crucial role in absorption, distribution, metabolism and excretion of compounds. Other important group of descriptors is the molecular topology descriptors that are the numerical quantifiers of molecular topology based on a graph representation of the compound. They are relevant in drug discovery and synthesis of new biologically active compounds as much as lipophilicity descriptors.

The present study is focused on the development of linear QSAR models for prediction of *in silico* ecotoxicity of a class of *s*-triazine derivatives that includes twenty-one compounds. These derivatives possess halogen, alkyl, cycloalkyl and aryl substituents. The linear modeling is a first step of QSAR modeling since the linear models are usually the easiest for interpretation and application. Univariate and multivariate QSAR modeling was applied so the appropriate molecular descriptors are selected based on which selected ecotoxicity parameters were predicted: acute algae toxicity, acute daphnia toxicity, *Daphnia magna* $LC_{50}$ 48h/EPA and *Daphnia magna* $LC_{50}$ 48h. The present analysis is the first step in development of so-called local QSARs of ecotoxicity of the series of *s*-triazine derivatives.

## MATERIAL AND METHODS

### THE SERIES OF *S*-TRIAZINE DERIVATIVES

The series of the studied *s*-triazine derivatives have been synthesized at the Faculty of Technology and Metallurgy, University of Belgrade, based on the procedure described earlier (15, 16). Their molecular structures are given in Figure 1. The analyzed series includes 6-chloro-$N^2$,$N^4$-, 6-dichloro-*N*- and 6-chloro-$N^2$,$N^4$-bis(1-methylcyclopentyl)- derivatives. The compounds **1-4** and **19-21** are the smallest compounds in the series, while the other compounds possess quite bulky substituents.

### *In silico* models of ecotoxicity data and calculation of molecular descriptors

The estimation of the ecotoxicity data, including acute algae toxicity (AAT) and acute daphnia toxicity (ADT) was carried out by PreADMET online program (17), whilst the estimation of *Daphnia Magna* $LC_{50}$ *48h/EPA (DMepa)* and *Daphnia Magna* $LC_{50}$ *48h/DEMETRA* (DMdemetra), was carried out by using the VegaNIC application (18). DMepa (version 1.0.6) was estimated by the QSAR model based on multiple linear regression. The original model was developed by US EPA inside the T.E.S.T. software. DMdemetra (version 1.0.3-DEV) considers an acute toxicity for Water Flea (*Daphnia magna*) for pesticides ($LC_{50}$ 48-hours exposure) and it was estimated based on a model which was built as a hybrid model upon two ANNs and a PLS model (DEMETRA project, http://www.demetra-tox.net).

The molecular descriptors were calculated by using PaDEL program (19) based on 2D molecular structures. The set of the calculated descriptors includes: lipophilicity descriptors (CrippenLogP, ALogp2), Autocorrelation Descriptor Mass (ATSm1, ATSm2, ATSm3, ATSm4), Autocorrelation Descriptor Charge (ATSc2), minimum E-states for (strong) hydrogen bond acceptors (minHBa), maximum E-states for (strong) hydrogen bond acceptors (maxHBa), second kappa shape index (Kier2), maximum atom-type E-State: ":N:" (maxaaN), sum of path lengths starting from nitrogens (WTPT-5) and McGowan characteristic volume (McGowan_Volume).

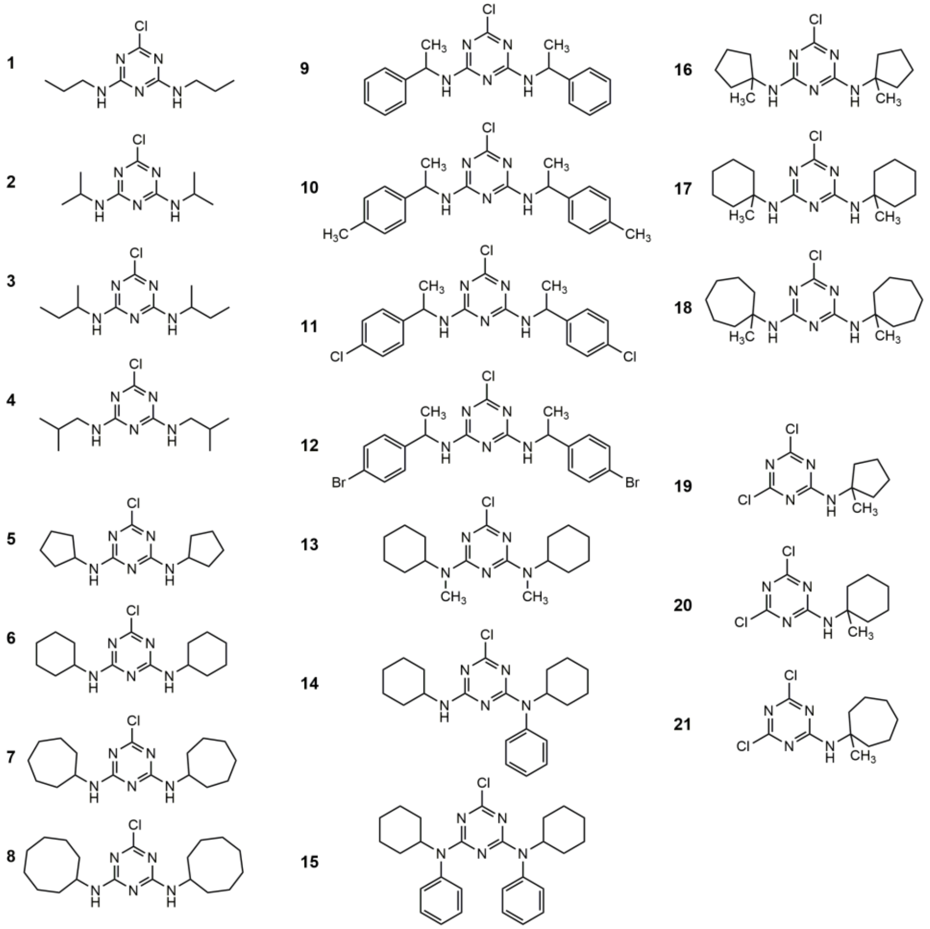

**Figure 1.** The molecular structures of the analyzed *s*-triazine derivatives

UDC: 543.068:632.95:504.05+615.9
BIBLID: 1450-7188 (2023) 54, 255-264

### QUANTITATIVE STRUCTURE-ECOTOXICITY RELATIONSHIP (QSER) MODELING

The QSER modeling was performed in NCSS 2023 program (20). The QSER modeling was based on MLR models. The selection of the most suitable descriptors for the MLR models was carried out by stepwise selection procedure with forward selection method. Minimum root mean square error (RMSE) change was set at 0.015 with maximum iterations of 20. The best MLR models were selected based on their statistical and prediction performance. The models were validated by the internal and external validation procedures. The validation parameters were the following: determination coefficient ($R^2$), adjusted determination coefficient ($R^2_{adj}$), leave-one-out (LOO) cross-validation determination coefficient ($R^2_{cv}$), Fischer's test ($F$), mean square error ($MSE$) and determination coefficient of external test set ($R^2_{ext}$). The external validation was done by using the external test set which was formed based on four randomly selected compounds (the compounds **3**, **10**, **18** and **20**). Also, the predictive power of the models was validated by comparing the observed and predicted values and by the residual's distribution.

## RESULTS AND DISCUSSION

### THE ESTIMATION OF ECOTOXICITY OF *S*-TRIAZINE DERIVATIVES AND SELECTION OF MOLECULAR DESCRIPTORS

A significant threat to the environment and human health comes from triazine derivatives that slowly degrade and accumulate in soil (21). In the present study, the estimation of their ecotoxicity, expressed as -logAAT, -logADT, DMepa and DMdemetra parameters, was carried out by *in silico* approach. The obtained results are presented in Table 1. The calculated *in silico* data were used as dependent variables in the QSER modeling. The originally calculated AAT and ADT values were mathematically transformed in the logarithmic values prior to the modeling. Their logarithmic values are given in Table 1 together with non-transformed (original) DMepa and DMdemetra parameters.

**Table 1.** The ecotoxicity data of the studied *s*-triazines obtained by *in silico* methods

| Compound | -logAAT | -logADT | DMepa | DMdemetra |
|---|---|---|---|---|
| **1** | 1.736 | 0.817 | 3.710 | 4.440 |
| **2** | 1.643 | 0.883 | 3.740 | 4.410 |
| **3** | 1.928 | 1.125 | 3.830 | 4.530 |
| **4** | 1.953 | 0.896 | 3.780 | 4.640 |
| **5** | 2.019 | 1.228 | 3.880 | 5.730 |
| **6** | 2.320 | 1.684 | 4.080 | 5.640 |
| **7** | 2.616 | 2.146 | 4.300 | 5.890 |
| **8** | 2.872 | 2.480 | 4.480 | 6.180 |
| **9** | 2.183 | 2.055 | 4.880 | 5.930 |
| **10** | 2.677 | 2.460 | 5.120 | 6.180 |
| **11** | 2.966 | 2.753 | 5.180 | 6.260 |
| **12** | 3.128 | 2.948 | 6.120 | 6.650 |

**Table 1.** Continuation

| Compound | -logAAT | -logADT | DMepa | DMdemetra |
|---|---|---|---|---|
| **13** | 2.325 | 1.904 | 3.650 | 8.240 |
| **14** | 2.660 | 2.366 | 5.030 | 7.190 |
| **15** | 3.244 | 3.006 | 5.150 | 8.740 |
| **16** | 2.156 | 1.370 | 4.600 | 5.640 |
| **17** | 2.490 | 1.833 | 4.800 | 5.540 |
| **18** | 2.819 | 2.299 | 5.020 | 5.800 |
| **19** | 1.750 | 0.989 | 3.990 | 5.160 |
| **20** | 1.865 | 1.214 | 4.050 | 5.070 |
| **21** | 1.977 | 1.442 | 4.140 | 5.120 |

The values of the calculated physicochemical molecular descriptors are presented in Table 2.

**Table 2.** The values of molecular descriptors used as independent variables present in the MLR models

| Compound | CrippenLogP | ALogp2 | ATSm1 | ATSm2 | ATSm3 | ATSm4 | ATSc2 | minHBa | maxHBa | Kier2 | maxaaN | WTPT-5 | McGowan_Volume |
|---|---|---|---|---|---|---|---|---|---|---|---|---|---|
| **1** | 2.979 | 0.983 | 24.513 | 18.614 | 25.737 | 23.064 | -0.367 | 0.664 | 3.176 | 7.302 | 4.290 | 15.190 | 1.761 |
| **2** | 2.976 | 0.191 | 24.513 | 18.614 | 28.069 | 22.732 | -0.360 | 0.646 | 3.183 | 5.915 | 4.296 | 15.055 | 1.760 |
| **3** | 3.756 | 1.026 | 26.513 | 30.614 | 30.069 | 27.064 | -0.360 | 0.646 | 3.288 | 7.438 | 4.391 | 15.195 | 2.042 |
| **4** | 3.471 | 0.394 | 26.513 | 20.614 | 29.737 | 25.396 | -0.367 | 0.650 | 3.237 | 7.438 | 4.359 | 15.228 | 2.042 |
| **5** | 4.044 | 8.679 | 28.513 | 20.614 | 36.069 | 27.396 | -0.360 | 0.678 | 3.471 | 6.635 | 4.542 | 15.495 | 2.107 |
| **6** | 4.825 | 12.404 | 30.513 | 24.614 | 38.069 | 33.396 | -0.360 | 0.674 | 3.523 | 8.022 | 4.604 | 15.554 | 2.389 |
| **7** | 5.605 | 16.794 | 32.513 | 26.614 | 40.069 | 41.396 | -0.360 | 0.670 | 3.576 | 9.475 | 4.665 | 15.584 | 2.670 |
| **8** | 6.385 | 21.846 | 34.513 | 28.614 | 42.069 | 43.396 | -0.360 | 0.667 | 3.613 | 10.983 | 4.712 | 15.599 | 2.952 |
| **9** | 4.999 | 0.291 | 34.513 | 30.614 | 44.069 | 41.396 | -0.360 | 0.574 | 3.376 | 9.796 | 4.546 | 15.386 | 2.694 |
| **10** | 5.055 | 0.554 | 36.513 | 21.233 | 48.069 | 45.396 | -0.360 | 0.570 | 3.403 | 10.156 | 4.581 | 15.389 | 2.976 |
| **11** | 6.306 | 0.901 | 51.939 | 30.614 | 55.876 | 53.203 | -0.385 | 0.580 | 3.422 | 10.156 | 4.598 | 15.389 | 2.939 |
| **12** | 6.524 | 1.533 | 123.029 | 32.614 | 70.680 | 68.007 | -0.376 | 0.585 | 3.430 | 10.156 | 4.604 | 15.389 | 3.044 |
| **13** | 4.873 | 6.003 | 32.513 | 36.517 | 42.069 | 42.061 | -0.422 | 0.677 | 2.310 | 8.393 | 4.840 | 15.873 | 2.670 |
| **14** | 7.078 | 9.538 | 36.513 | 43.919 | 48.402 | 47.061 | -0.382 | 0.630 | 3.609 | 10.156 | 4.898 | 16.096 | 2.996 |
| **15** | 9.331 | 7.048 | 42.513 | 28.946 | 58.734 | 60.726 | -0.404 | 0.585 | 2.403 | 12.301 | 5.193 | 16.636 | 3.604 |
| **16** | 4.825 | 0.131 | 30.513 | 33.780 | 42.402 | 33.396 | -0.355 | 0.656 | 3.560 | 6.246 | 4.633 | 15.397 | 2.389 |
| **17** | 5.605 | 0.879 | 32.513 | 40.946 | 44.402 | 39.396 | -0.355 | 0.652 | 3.612 | 7.486 | 4.694 | 15.442 | 2.670 |
| **18** | 6.385 | 2.291 | 34.513 | 22.233 | 46.402 | 47.396 | -0.355 | 0.648 | 3.665 | 8.792 | 4.755 | 15.464 | 2.952 |
| **19** | 3.328 | 0.072 | 31.866 | 26.614 | 35.068 | 27.303 | -0.342 | 0.724 | 3.489 | 4.473 | 4.408 | 12.070 | 1.675 |
| **20** | 3.718 | 0.000 | 32.866 | 23.233 | 36.068 | 30.303 | -0.342 | 0.722 | 3.529 | 5.104 | 4.439 | 12.092 | 1.815 |
| **21** | 4.108 | 0.094 | 33.866 | 28.614 | 37.068 | 34.303 | -0.342 | 0.720 | 3.569 | 5.760 | 4.469 | 12.103 | 1.956 |

Calculated descriptors were submitted to the stepwise selection procedure in order to select the most suitable descriptors as independent variables that are highly correlated with the dependent variables. In this procedure the following descriptors were selected: McGowan_Volume, ALogp2, ATSc2, ATSm1, ATSm3, ATSm4, maxaaN, maxHBa, minHBa and WTPT-5. Selection of the descriptors was limited respecting the Topliss-Costello rule so the ratio of the number of compounds and the number of selected descriptors a

UDC: 543.068:632.95:504.05+615.9
BIBLID: 1450-7188 (2023) 54, 255-264

model is equal or less than five. In the present MLR modeling, the maximum number of descriptors in the models was three.

## QSER MODELING AND VALIDATION OF THE MODELS

One MLR model was established for each ecotoxicity parameter. The MLR modeling resulted in the following mathematical (QSER) models with satisfactory statistical characteristics and predictive performance:

**MLR1:** $-\log AAT = -0.4073 + 0.9109 \cdot \text{McGowan\_Volume} + 0.7626 \cdot \text{minHBa}$ (1)
**MLR2:** $-\log ADT = -0.4319 + 0.0616 \cdot \text{ATSm4} + 0.0168 \cdot \text{ALogp2} - 0.0065 \cdot \text{ATSm1}$ (2)
**MLR3:** $\text{DMepa} = 3.4354 + 0.0464 \cdot \text{ATSm3} + 0.5036 \cdot \text{maxHBa} - 4.0556 \cdot \text{minHBa}$ (3)
**MLR4:** $\text{DMdemetra} = -19.1280 + 3.9168 \cdot \text{maxaaN} - 26.6333 \cdot \text{ATSc2} - 0.1823 \cdot \text{WTPT-5}$ (4)

The statistical parameters of the presented QSERs are presented in Table 3. All of the established models fulfill the criteria for statistical quality, however their quality is different. The model MLR2 has the highest determination coefficient and adjusted determination coefficient, however it has the lowest cross-validation determination coefficient. The best fitting of the data of this model is confirmed by the highest *F*-test value. This model is also described by the lowest *MSE* value and it fits the external data set satisfactorily. Considering the determination coefficients ($R^2$ and $R^2_{adj}$) and *F*-test, the model MLR1 has the lowest performance. However, this model best fits the external data set (the highest $R^2_{ext}$). The MLR4 model has the highest *MSE* and the lowest determination coefficient of external test set meaning that this model has the poorest predictive performance among all models.

**Table 3.** The statistical parameters of the MLR models

| Parameter | MLR1 | MLR2 | MLR3 | MLR4 |
|---|---|---|---|---|
| $R^2$ | 0.9066 | 0.9821 | 0.9643 | 0.9576 |
| $R^2_{adj}$ | 0.8932 | 0.9780 | 0.9561 | 0.9478 |
| $R^2_{cv}$ | 0.8486 | 0.7213 | 0.9250 | 0.9344 |
| $F$ | 67.9 | 238.1 | 117.0 | 97.9 |
| $MSE$ | 0.0264 | 0.0118 | 0.0204 | 0.0760 |
| $R^2_{ext}$ | 0.9966 | 0.9582 | 0.9813 | 0.6572 |

The comparison between the observed and predicted data for all established models are presented in Figure 1. The graphs include the training and external test set.

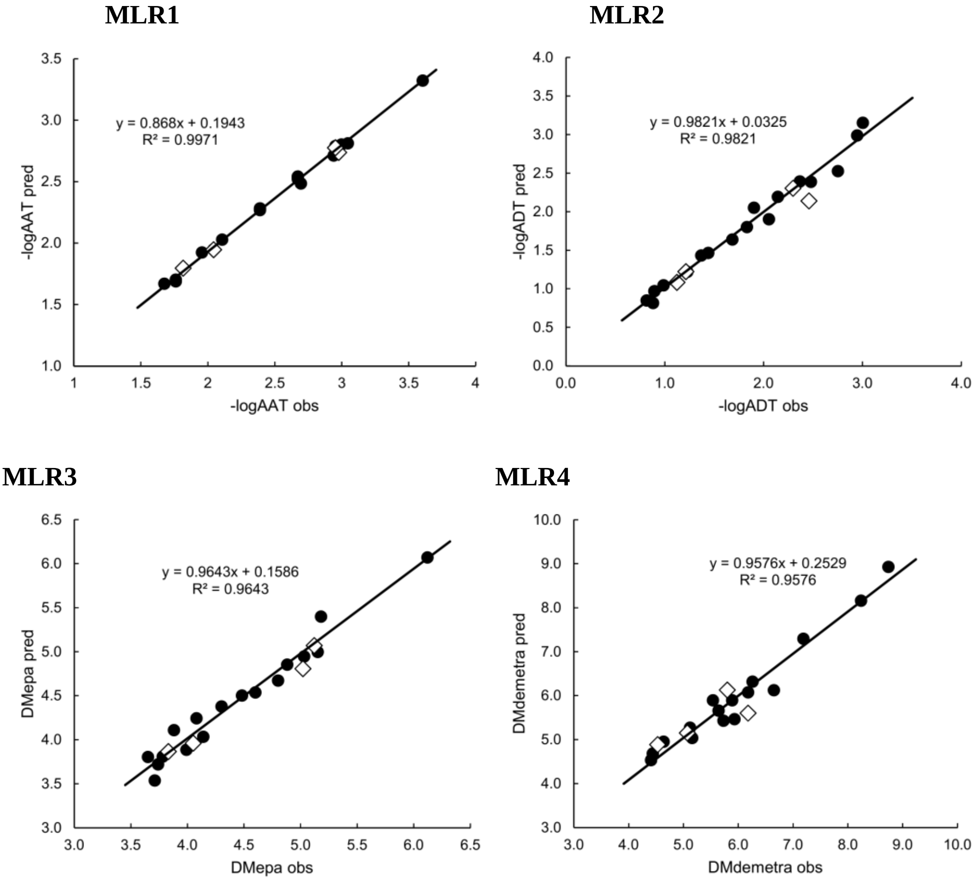

**Figure 1.** The relationships between observed (obs) and predicted (pred) ecotoxicity data for the obtained MLR models (● - training set, ◇ - external test set)

The comparison of the observed and predicted data can indicate how the data are correlated. Ideal case means that the determination coefficient and the slope are equal to 1, whilst the intercept is equal to 0 (the case when $y = x$). Taking into account the aforementioned criteria, the MLR2 has the slope closest to 1 and the intercept closest to zero. However, it can be said that all of the established models correlate the data well.

In order to gain an overview which model makes the highest or the lowest differences between the observed and predicted parameters (residuals), the comparison of the predicted data and residuals was carried out in the residuals distribution analysis. The corresponding graphs for each MLR model are presented in Figure 2.

Figure 2 indicates the randomness of the distribution of the residuals along the $y = 0$ axis. Considering the values of the distribution coefficients, which are very close to zero as it is shown on each graph in Figure 2, it can be concluded that the distribution of the residuals is unpredictable. The slopes and intercepts are close to zero as well. The randomness of both observed and predicted data is noticeable.

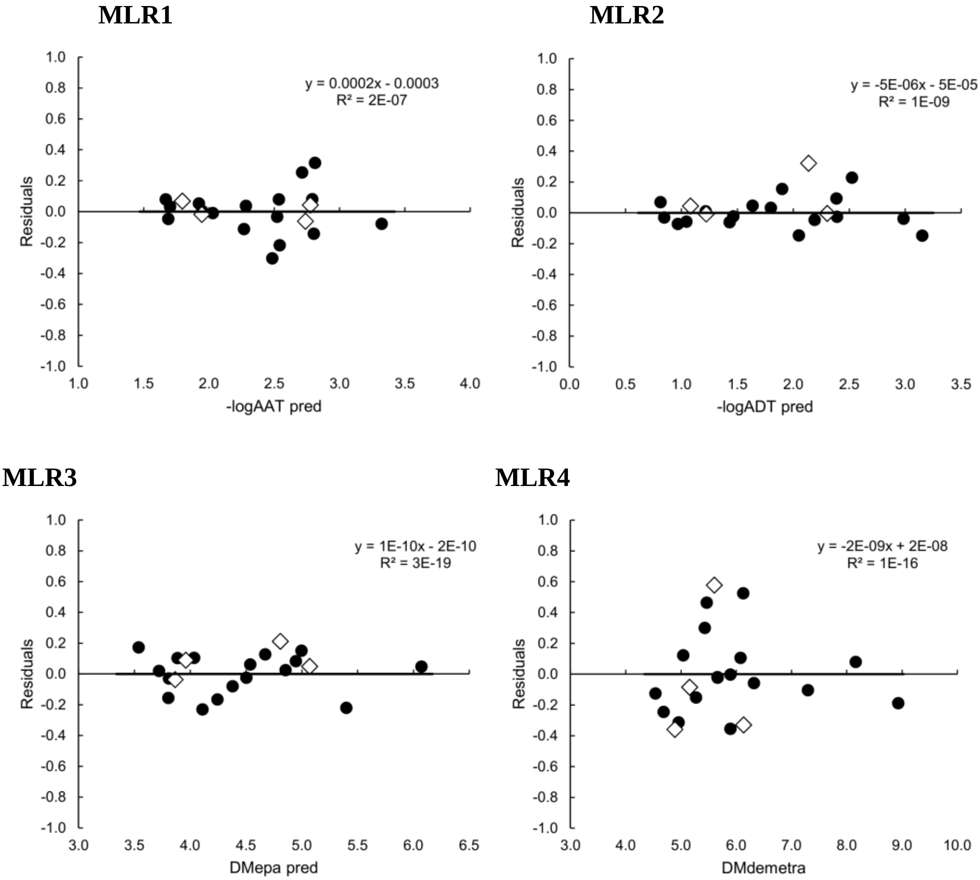

**Figure 2.** The distribution of the residuals for the obtained MLR models

Figure 2 indicates the randomness of the distribution of the residuals along the *y* = 0 axis. Considering the values of the distribution coefficients, which are very close to zero as it is shown on each graph in Figure 2, it can be concluded that the distribution of the residuals is unpredictable. The slopes and intercepts are close to zero as well. The randomness of both observed and predicted data is noticeable. The absolute amplitude of the residuals is the lowest for MLR3 model (around 0.2), whilst the highest is in MLR4 where the highest residual value is noticeable for a compound from the external test set (around 0.6). In the MLR1 and MLR3 models the data from the external data set are incorporated very well in the data from the training set which means that their residuals amplitudes are lower than the residuals amplitudes of the data from the training set. In the MLR2 model, one point form the external data set has higher residual amplitude than the other data (around 0.3).

Generally speaking, all the established MLR models have quite good predictive power with acceptable prediction error, which was confirmed by both the internal and external validation procedures.

Besides their very good predictive ability, the established MLR-QSER models have the importance in estimation of the influence of particular molecular features on the ecotoxicity parameters (-logAAT, -logADT, DMepa and DMdemetra). The lipophilicity parameter, atom type electrotopological state, autocorrelation and weighted path descriptors were shown to be the best predictors of the selected ecotoxicity parameters.

The obtained models have the limited applicability domain. They are aimed to the compounds structurally similar to the compounds used in both the training and external data sets. Also, the applicability domain covers the range of the descriptors values present in each model (the descriptors values are given in Table 2).

## CONCLUSION

In the present study, the ecotoxicity parameters of the set of twenty-one triazine derivatives was modelled by multiple linear regression approach. The established quantitative structure-ecotoxicity relationship models correlate some lipophilicity, atom type electrotopological state, autocorrelation and weighted path descriptors with acute algae toxicity, acute daphnia toxicity, *Daphnia magna* $LC_{50}$ 48h/EPA and *Daphnia magna* $LC_{50}$ 48h. The obtained MLR-QSER models were validated by internal leave-one-out cross-validation approach and the external validation by using the external data set. Besides, the models were validated by the comparison of the observed and predicted data, as well as by the residuals distribution analysis. All the validation procedures confirmed high statistical quality and prediction ability of the models. The applicability domain of the models was defined based on the structural similarity to compounds used in the data set and based on the range of the molecular descriptors present in the models. The MLR-QSER models pointed out the significance of particular molecular features, such as lipophilicity and molecular topology, in the ecotoxicity of the studied series of *s*-triazine derivatives including 6-chloro-$N^2$,$N^4$-, 6-dichloro-*N*- and 6-chloro-$N^2$,$N^4$-bis(1-methylcyclopentyl)- derivatives.

### Acknowledgement

The present research is financed in the framework of the project of Provincial Secretariat for Higher Education and Scientific Research of AP Vojvodina (Project: Molecular engineering and chemometric tools: Towards safer and greener future, No. 142-451-3095/2022-01/01). The authors thank Professors Dušan Antonović and Bratislav Jovanović from the Faculty of Technology and Metallurgy, University of Belgrade, for the synthesis of the studied triazines.

## REFERENCES

1. Matolcsy, G.; Nádasy, M.; Andriska, V. *Pesticide Chemistry;* Akadémia Kiadó: Budapest, 1988; pp 15.
2. Giner, B.; Lafuente, C.; Lapeña, D.; Errazquin, D.; Lomba, L. QSAR study for predicting the ecotoxicity of NADES towards Aliivibrio fischeri. Exploring the use of mixing rules. *Ecotoxicol. Environ. Saf.* **2020**, *191*, 110004.

3. Yang, L.; Wang, Y.; Hao, W.; Chang, J.; Pan, Y.; Li, J.; Wang, H. Modeling pesticides toxicity to Sheepshead minnow using QSAR. *Ecotoxicol. Environ. Saf.* **2020**, *193*, 110352.
4. Khan, K.; Baderna, D.; Cappelli, C.; Toma, C.; Lombardo, A.; Roy, K.; Benfenati, E. Ecotoxicological QSAR modeling of organic compounds against fish: Application of fragment based descriptors in feature analysis. *Aquat. Toxicol.* **2019**, *212*, 162-174.
5. Lavado, G. J.; Baderna, D.; Carnesecchi, E,; Toropova, A. P.; Toropov, A. A.; Dorne, J. L. C. M.; Benfenati, E. QSAR models for soil ecotoxicity: Development and validation of models to predict reproductive toxicity of organic chemicals in the collembola *Folsomia candida*. *J Hazard Mater* **2022**, *423*, 127236.
6. Mazzatorta, P.; Benfenati, E.; Lorenzini, P.; Vighi, M. QSAR in Ecotoxicity: An Overview of Modern Classification Techniques. *J. Chem. Inf. Comput. Sci.* **2004**, *44* (1), 105-112.
7. Ciura, K.; Belka, M.; Kawczak, P.; Bączek, T.; Markuszewski, M. J.; Nowakowska, J. Combined computational-experimental approach to predict blood-brain barrier (BBB) permeation based on "green" salting-out thin layer chromatography supported by simple molecular descriptors. *J Pharm Biomed Anal* **2017**, *143*, 214-221.
8. Chakravarti, S. K.; Alla, S. R.M. Descriptor Free QSAR Modeling Using Deep Learning With Long Short-Term Memory Neural Networks. *Front. Artif. Intell*. **2019**, *2*, 17.
9. Stanton, D. T. QSAR and QSPR model interpretation using partial least squares (PLS) analysis. *Curr Comput Aided Drug Des*. **2012**, *8*(2), 107-127.
10. Saxena, A.K.; Prathipati, P. Comparison of MLR, PLS and GA-MLR in QSAR analysis. *SAR QSAR Environ Res*. **2003**, *14*(5-6), 433-445.
11. Salaković, B.; Kovačević, S.; Karadžić Banjac, M.; Podunavac-Kuzmanović, S.; Jevrić, L.; Pajčin, I.; Grahovac, J. New Perspective on Comparative Chemometric and Molecular Modeling of Antifungal Activity and Herbicidal Potential of Alkyl and Cycloalkyl s-Triazine Derivatives. *Processes* **2023**, *11*, 358.
12. Perišić-Janjić, N.; Jovanović, B.Ž.; Janjić, N.J.; Rajković, O.S.; Antonović, D.G. Study of the Retention Behavior of Newly Synthesized s-Triazine Derivatives in RP TLC Systems, and the Lipophilicity of the Compounds. *JPC-J Planar Chromat* **2003**, *16*, 425-432.
13. Janicka, M.; Kwietniewski, L.; Perišić-Janjić, N. Determination of Retention Factors of s-Triazines Homologous Series in Water Using a Numerical Method Basing on Ościk's Equation. *Chromatographia* **2006**, *63, 87-93.*
14. Milošević, N.; Janjić, N.; Milić, N.; Milanović, M.; Popović, J.; Antonović, D. Pharmacokinetics and Toxicity Predictors of New s-Triazines, herbicide Candidates, in Correlation with Chromatographic Retention Constants. *J. Agric. Food Chem*. **2014**, *62*, 8579-8585.
15. Bončić-Caričić, G.A.; Tadić, Ž.D.; Jeremić, D.S. Electron impact mass spectrometry of some 2,4,6-substituted s-triazines. Effect of the ring size. *Int. J. Mass Spectrom. Ion Phys.* **1983**, *47*, 451-454.
16. Antonović, D.; Bončić-Caričić, G.A. Gas chromatographic retention indices for *N*-substituted amino s-triazines on DB-1 and DB-5 capillary columns. *J. Serb. Chem. Soc.* **1994**, *59* (12), 993-996.
17. PreADMET program, https://preadmet.qsarhub.com/
18. VegaNIC application, Laboratory of Environmental Chemistry and Toxicology of Mario Negri Institute of Pharmacological Research, http://vega-qsar.eu.
19. Yap, C.W. PaDEL-descriptor: An open source software to calculate molecular descriptors and fingerprints. *J. Comput. Chem.* **2011**, *32* (7), 1466-1474.
20. NCSS 2023 Statistical Software (2023). NCSS, LLC. Kaysville, Utah, USA, ncss.com/software/ncss.
21. Rajendran, K.; Pujari, L.; Ethiraj, K. Biodegradation and Bioremediation of S-Triazine Herbicides. In: *Environmental Biotechnology Vol. 3. Environmental Chemistry for a Sustainable World, vol 50*. Gothandam, K.M.; Ranjan, S.; Dasgupta, N.; Lichtfouse, E., Eds.; Springer: Cham, 2021; pp 31-54.

APTEFF, Vol. 54, 1-335 (2023)
DOI: https://doi.org/10.2298/APT2354265D
UDC: 664.231:66-911.48
BIBLID: 1450-7188 (2023) 54, 265-275

Original scientific paper

# COMPARATIVE ANALYSIS OF THE GELLING, RETROGRADING AND RHEOLOGICAL PROPERTIES OF EMMER STARCH COMPARED TO OTHER CEREAL STARCHES

*Mina M. DZHIVODEROVA-ZARCHEVA[1]*, Vesela N. SHOPSKA[2], Georgi A. KOSTOV[2], Rositsa S. DENKOVA-KOSTOVA[3]*

[1] Department of Technology of tobacco, sugar, and plant essential oils, Technological Faculty, University of food technology, Plovdiv, Bulgaria
[2] Department of Technology of Wine and Beer, Technological Faculty, University of food technology, Plovdiv, Bulgaria
[3] Department of Biochemistry and Molecular Biology, Technological Faculty, University of food technology, Plovdiv, Bulgaria

**Received: 03 August 2023** **Revised: 28 August 2023** **Accepted: 04 September 2023**

*In today's dynamic development of food technologies it becomes necessary to study alternative sources of starch to replace the traditionally used ones. Characteristics such as granule size, gelling properties, retrogradation and rheology are fundamental for the selection of starch in the food industry. The aim of the present study is to investigate the possibilities for application of an emmer starch in food industry by comparing its main properties with two other cereal starches, isolated from rice and wheat. The results showed that the emmer starch had a similar granule size and structure, with increased amylose content as the wheat starch. This was also the reason for the similar gelling and retrograde properties as wheat starch. In terms of retrogradation, the highest results showed emmer starch and the lowest - rice starch. Emmer starch had the lowest onset temperature of gelatinization, and the peak temperature of gelatinization was 76.3 °C. The starch gel obtained with emmer starch has the lowest viscosity but the most shear resistance compared to that with wheat and rice starch.*

**Keywords**: emmer, cereal starches, gelatinization, retrogradation, rheological properties.

## INTRODUCTION

Starch is the main polysaccharide synthesized and accumulated in green plants and is a semi-crystalline polymeric form consisting of two D-glucose polymers: amylose and amylopectin. Amylose is characterized by long linear chains of α-(1→4) glycosidic linkages with relatively few α-(1→6) linked branches, whereas amylopectin is a highly branched molecule with fewer α-(1→4) glycosidic linkages per glucose molecule and more often α-(1→6) branches (1-5).

Starch is a very important biopolymer with wide application in human life. It is a major part of our diet, with two-thirds of the amount produced being used in the food industry (6). There starch performs various functions as a thickener, binder, disintegrant, stabilizer, texture modifier, gelling and bulking agent, useful in the preservation of canned and frozen foods, in the formulation of syrups, essences and beverages, in confectionery and baking, cakes and sweets (7). The physicochemical properties of starch, including its morphological characteristics, crystallization and thermal properties, swelling indices, and pasting characteristics, establish the variety of applications of starch in the food and non-food indus-

---

* Corresponding author: Mina M. Dzhivoderova-Zarcheva, University of food technology, Faculty of Technology, Department of Technology of tobacco, sugar, and plant essential oils, e-mail: mina_dj@abv.bg

tries (8-11). The quality characteristics of products containing starch are the result of the gelatinization and retrogradation properties of starch (11, 12). Gelatinization of starch occurs at high temperature in the presence of sufficient water. It is an irreversible phase transition process initiated by starch hydration and swelling (11, 13). Gelatinization of starch is a process in which it loses the natural order and crystalline structure of the granules and becomes amorphous. The key rheological properties of starch include pasting properties, starch paste viscosity, and starch gel rheological characteristics (14). Retrogradation is a recrystallization process in which disaggregated molecules of the two constituent polymers in gelatinized starches reassociate to form ordered structures (11, 12). The study of starch retrogradation over time influences the long-term development of the gelled starch structure (15).

Starch isolated from different genotypes and botanical sources with suitable characteristics is attracting increasing attention in the food industry because it does not require chemical or genetic modification (16-18). As a whole, cereals are the main raw material used for the isolation and extraction of starch. The method of isolation of cereal starch is mainly influenced by the solubility of the protein, the level of protein-starch interaction, and the characteristics of the starch granules (19, 20).

Emmer wheat today is a minor cereal crop that needs to be redeveloped due to the nutritional value of its grain. It is particularly valued for its high starch content and the lack of a gluten structure (21-24). Attention to emmer wheat has been renewed by the growing demand for traditional products, the search for species suitable for cultivation in marginal areas and the need to preserve genetic diversity. Emmer wheat is a rural cereal crop that adapts to soils that are poor in nutrients and is resistant to extreme climatic conditions (cold and hot climates), drought and humidity, which is why it is mainly grown in the hills and low mountain areas. (25). Emmer and einkorn are also considered more disease resistant than modern wheats. Certain cultivars have been identified as sources of resistance against fungal diseases, including powdery mildew, stem rust, yellow and leaf rust, brown spot, septoria spot, heads and fusarium (26, 27).

The morphology and physicochemical properties of new types of starches should be investigated to explore their potential applications while investigating their most suitable usability as a food additive (18, 19). Therefore, the aim of the present study is to compare the gelation, retrogradation and rheological characteristics of alkaline isolated emmer starch to other two starches, isolated from rice and wheat, in order to find an application of this novel starch in food industry.

## EXPERIMENTAL

### MATERIALS

### Emmer starch

Emmer is a precursor to wheat, but it does not create a gluten structure (28), which is why we have turned to a different technology than wheat starch.

Due to the lack in the scientific literature of a specific technological scheme for obtaining starch from emmer, as well as the close chemical composition of emmer and rice seeds, a technology for the production of rice starch by alkaline milling (29) was used with some modifications in the purification steps described in previous research. After further microscopic observation of the starch molecules, no change in their structure was detected (30). The isolated starch had a protein content of 4.8±0.12% and a moisture content of 10.43±0.05%.

### Grain starches for comparison

Wheat and rice grain starch with protein content (1±0.01% and 0.5±0.00%, respectively) and moisture content (13.27±0.13% and 11.78±0.08%, respectively) was purchased from the market.

## METHODS

### Digital images of starch granules

Starch granule size was measured with an analysis software program microscopic images, UTHSCSA ImageTools – Version 3.0, at 40x magnification. Digital images were captured with a Boeco microscope (Germany), Video camera ocular 5MP, USB 2.0 and Scope Photo program.

### Determination of amylose content

A standard spectrophotometric method with a defatting procedure by methanol and with calibration amylose solutions (ISO 6647-1:2020) was used, and the samples were analyzed at Spekol 11, Carl-Zeiss.

### Determination of gelatinization of native starch

The native starch analyzed was mixed with distilled water in ration 1:2. The weighed starch samples are placed in an empty vessel. The vessels are hermetically sealed by a Netzsch press. A differential scanning calorimeter (DSC 204 F1 Phoenix®) was used for the analysis. Blowing is performed with argon. The starch gelatinization process is investigated by heating in a calorimeter at a temperature increase of 10 °C/min. The gelling capacity of native starch has been measured in the temperature range of 25 to 90 °C.

### Retrogradation properties

Starch suspension in water (2%, w/w) was heated at 85 °C for 30 minutes in a temperature-controlled water bath. The starch sample was stored for 24, 48, and 120 hours at 4 °C. Syneresis was measured as % amount of liquid released after centrifugation at 5000 rpm for 15 minutes.

$$S = \left(\frac{F_1}{F_0}\right) \times 100 \qquad [1]$$

where S - syneresis of the sample, %; $F_0$ – used sample, g; $F_1$ - the amount of liquid released after centrifugation, g.

### Rheological measurements

The 2 % w/w starch-aqueous suspension was prepared for 30 minutes at 80 °C. The samples were placed at 8±1 °C for 24 hours and then allowed to temper for 15 minutes. Rheological characteristics were determined using a Rheotest-2 rotational viscometer (Rheotest Medingen GmbH, Medingen, Germany), operating at 25 °C within the shear rate range from 0.17 to 72.9 $s^{-1}$. The dynamic viscosity ($\eta$) was calculated using the formula:

$$\eta = \frac{\tau}{D} \qquad [2]$$

where $\tau$ is the shear stress, Pa; D is the shear rate, $s^{-1}$.

$$\tau = \tau_0 + k.D^n \qquad [3]$$

where $\tau_0$ – is the yield stress, Pa; k – is the consistency coefficient, Pa·s; n – is the flow behavior index.

### Statistics

All results were expressed as the mean ±standard deviation (SD). The experimental data were subjected to analysis of variance, at the confidence level of $p = 0.05$, using ANOVA.

## RESULTS and DISCUSSION

### DIGITAL IMAGES OF STARCH GRANULES

Different botanical sources have different microstructures and morphologies of starch granules, which also affect their properties (31-34). A comparison was made between microscope photos (Figure 1).

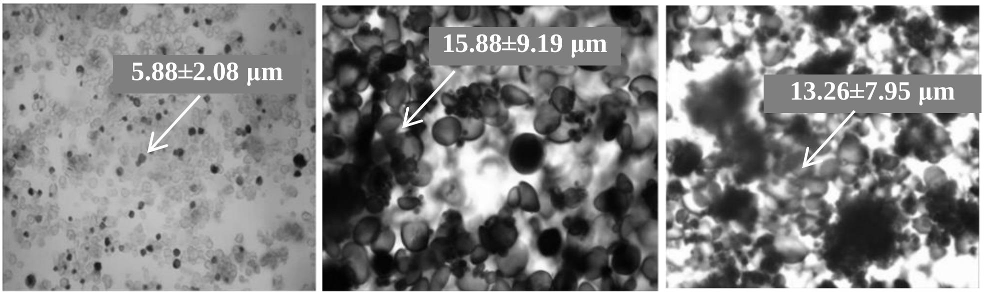

(A) (B) (C)

**Figure 1.** Microscope images of rice (A), wheat (B) and emmer (C) starch granules.

Obviously, there is a difference between the size of starch grains of wheat and rice, which will affect the gelling properties. Rice starch granules had the smallest size (5.88±2.08 μm), which confirmed the results, published by Shi et al. (34). The granule size of emmer starch (13.26±7.95 μm) is comparable to the wheat starch granules (15.88±9.19 μm). The microscopic images showed no deterioration of the structure. The starch granules of emmer (ancient wheat), like wheat, are oval and lenticular in shape, with granule sizes (10–40 μm) and smaller starch granules (<10 μm) (35). There is a difference in the color of the starch granules after iodine treatment of emmer and wheat, which is an indicator of the difference in composition (36). Rice granules are colored red-brown due to the absence of amylose (1.34±0.01%). Wheat and emmer starch granules are colored blue with clearly defined darker colored rings caused by the presence of amylose, wheat starch with amylose content 21.66±0.05% and emmer starch with 10.90±0.06% amylose, confirmed by other authors (37).

### Determination of gelatinization of native emmer starch

The results of the starch gelatinization using Differential Scanning Calorimetry (DSC) are presented in Figure 2.

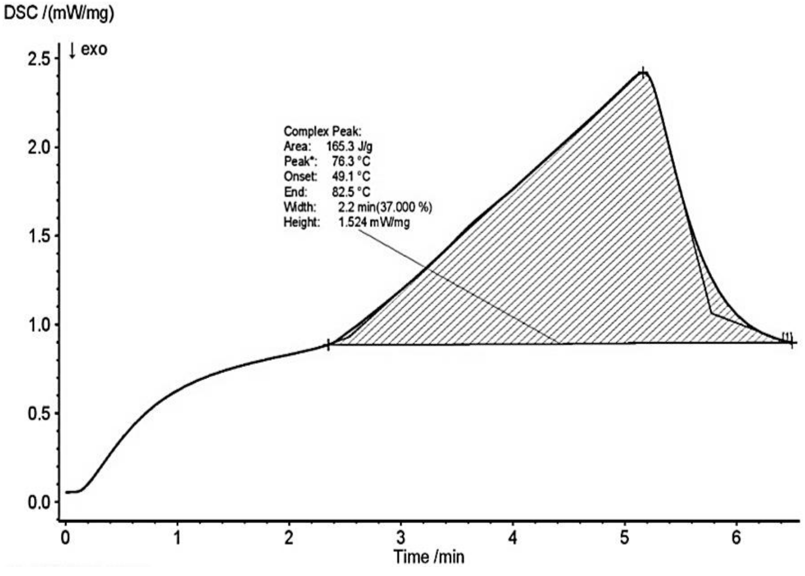

**Figure 2.** Gelatinization of native emmer starch in a temperature range from 25 to 90 °C.

There is enough information in the literature about the gelling properties of wheat and rice starch (29). The results for starch gelatinization of emmer (determined experimentally), wheat and rice (taken from the literature data) are presented in Table 1. The comparison was made on the basis of previous studies, using the same method for the analysis of rice and wheat starch samples (38).

UDC: 664.231:66-911.48
BIBLID: 1450-7188 (2023) 54, 265-275

Original scientific paper

**Table 1.** Starch gelatinization parameters

| | Wheat starch (38) | Rice starch (38) | Emmer starch |
|---|---|---|---|
| Onset temperature of gelatinization, °C | 65.8 | 63.6 | 49.1 |
| Peak temperature of gelatinization, °C | 71.2 | 71.0 | 76.3 |
| End temperature of gelatinization, °C | 79.1 | 81.4 | 82.5 |
| Enthalpy of gelatinization, J/g | 3.588 | 2.463 | 165.3 |

The data in Table 1 shows that the gelatinization temperature of emmer starch is close to that of wheat starch and rice starch, except for onset temperature of gelatinization, which is lower compared to the other two types of starch.

The significant difference in the values of enthalpies of gelatinization of the wheat and emmer starches cannot be taken as decisive (39). The detection of changes in enthalpy during DSC scans depends on many factors, including scanning rate, moisture content, degree of starch granule hydration and equipment sensitivity. Moreover, when samples are subjected to a progressively increasing heat treatment during “direct scanning”, it is impossible to detect precisely what enthalpic changes occur at specific temperatures (40).

## Retrogradation properties

One of the main indicators characterizing the starch properties of starch is retrogradation. It influences the choice of starch in the production of specific food products.

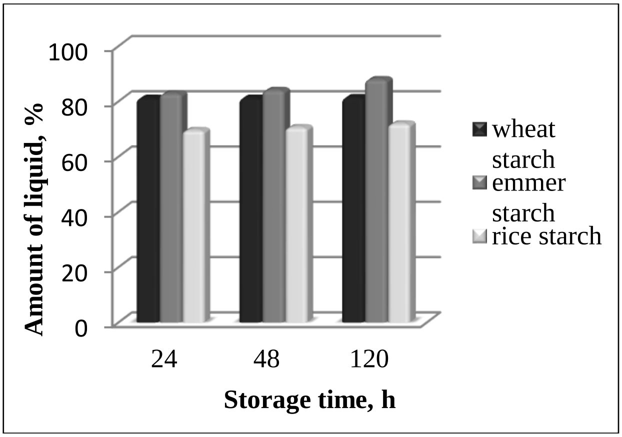

**Figure 3.** Retrogradation properties of rice, wheat and emmer starch.

Figure 3 represents the amount of supernatant after centrifugation of the starch suspension stored at 4 °C for 24, 48 and 120 hours, respectively. It can be summarized that the lowest resistance to retrogradation was observed for emmer starch, followed by wheat starch and rice starch. It could be explained by the higher amylose content in emmer and wheat starches (Figure 1). Retrogradation occurs more easily with amylose because it is a less unbranched molecule than amylopectin (41). The increase in storage time resulted in higher amount of released water, which is due to retrogradation. The biggest difference was reported for emmer starch (5.137 %), followed by rice starch (2.368 %) and with the smallest changes was wheat starch (0.213 %).

### Comparison between the rheological properties of emmer, wheat and rice

The obtained starch-aqueous suspension was analyzed on a rheoviscometer, and the rheological characteristics and viscosity are presented in Figure 4.

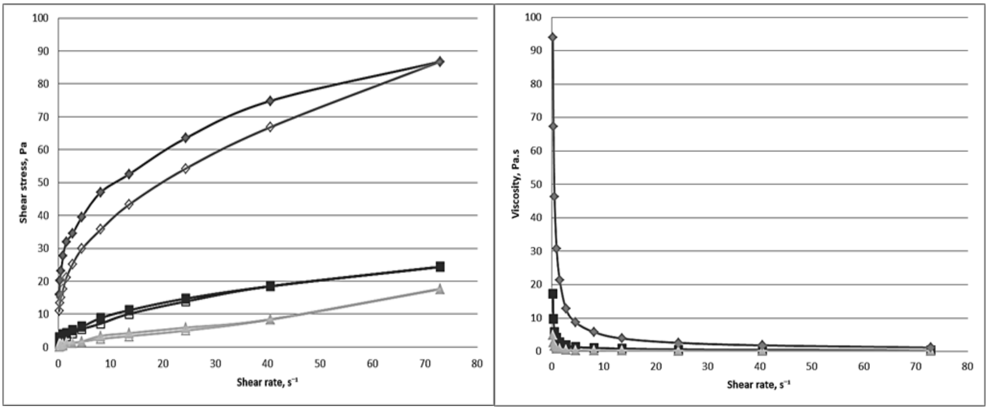

(A) (B)

**Figure 4.** Flow curves of ♦, ◊ - rice, ■, □ – wheat and ▲, Δ- emmer starch suspensions (A) and changes in the apparent viscosity (B).

The flow properties are an important characteristic for all foods products, and it is essential information to the economic design of the most suitable food process equipment and operation that can be selected (42). Rheological properties of starch gels were studied at 25 °C. The rheograms of the analyzed samples were shown in Figure 4 (A). The shape of these curves showed non-Newtonian, shear thinning flow with tendency to yield stress. The highest values of shear stress were showed by starch gel with rice starch. Shear-thinning behavior, i.e., decreased in viscosity with increasing shear rate was a common phenomenon (43). At higher shear rates, individual starch granules can be deformed.

The most important characteristic of starch gels is its viscosity. Viscosity is also defined as the main rheological property of starch products (44, 45) The viscosity values of the samples as a function of the shear rate in an interval of variation of 0.17 to 72.9 $s^{-1}$ were shown in Figure 4. (B).

The initial viscosity of the samples was different, but the rice starch gel showed the highest viscosity. The initial viscosity of the wheat and emmer starch gel was close. The shear rate increased from 0.17 to 72.9 $s^{-1}$, and the viscosity of the starch gels decreased.

These facts showed that the starch gels were non-Newtonian fluids, and their viscosity variations were closely. These samples had pseudoplastic properties because they flow with applying the external impact.

The power law model parameters for the samples and the coefficients of determination ($R^2$) are shown in Table 2.

Flow curves for all the systems presented narrow hysteresis loops indicating rather changes in the structure of the samples on the shear applied.

The power law model parameters for the samples are given in Table 2, along with correlation coefficient ($R^2$). The multiple correlation coefficients, $R^2$, reported in Table 2 informed about, generally, very good fitting of the Herschel–Bulkley model, which is widely used in the analysis of various food systems (46). The coefficients of determination ($R^2$) obtained were high and varied from 0,906±0,05 to 0,9957±0,06 typical for the Herschel–Bulkley models.

**Table 2.** Parameters of Herschel–Bulkley models for flow curves of the systems

| Type of Starch | $\tau_0$ | K | n | $R^2$ | $\tau_0$ | K | n | $R^2$ | Hysteresis loop area [Pa. $s^{-1}$] |
|---|---|---|---|---|---|---|---|---|---|
| | Upward curve | | | | Downward curve | | | | |
| Emmer | 0.5±0.05 | 1.197±0.06 | 0.5038±0.03 | 0.9060±0.05 | 0.1±0.01 | 0.737±0.04 | 0.6504±0.03 | 0.9773±0.05 | 2.9436±0.15 |
| Rice | 13.3±0.68 | 27.245±1.36 | 0.2671±0.01 | 0.9957±0.06 | 8.7±0.43 | 18.869±0.94 | 0.3335±0.01 | 0.9945±0.06 | 945.5764±47.27 |
| Wheat | 2.3±0.12 | 4.194±0.21 | 0.3751±0.02 | 0.9609±0.04 | 0.1±0.00 | 2.155±0.1 | 0.5855±0.03 | 0.9903±0.07 | 51.5432±2.58 |

The consistency coefficient (K) and flow behavior index (n), obtained by fitting of the power law and Herschel–Bulkley models to the experimental shear stress-shear rate data are given in Table 2. Yield stress is an important characteristic indicates the stress at which a material will begin to deform plastically. High values of yield stress, $\tau_0$, from the Herschel–Bulkley model, pointed to a high stability of the structure of the samples (47). The power law equation was found to be an adequate model to describe the flow behaviour of the samples in this study. Viscosity functions data showed that all of the systems under examination were Non-Newtonian fluids, since the values for flow behaviour indices, n, were below 1, which was indicative of the pseudoplastic (shear thinning) nature (46-48). The yield stress ($\tau_0$) of the samples was from 0.1 to 13.3 (Pa). Rice starch gel had the highest value of $\tau_0$. These results show that the high stability of structure have rice starch gel (49). The flow behaviour indices (n) are between 0,2671±0,01 and 0,6504±0,03 for the Herschel–Bulkley model. The smaller n values determine the greater departure from the Newtonian behaviour (50).

Consistency coefficient, K, from the Herschel–Bulkley model can also be used as a criterion of viscosity. It was from 0,737±0,04 to 27,245±1,36 (Pa). So, the highest viscosity showed the rice starch gel and the lowest – the emmer.

The hysteresis loop area data showed that the narrowest loops were found for the emmer starch gel. Thus, the emmer starch gel structure was the strongest and the most shear-resistant. It can be summarized that the rheological properties of emmer and wheat starch gels were almost similar.

UDC: 664.231:66-911.48
BIBLID: 1450-7188 (2023) 54, 265-275

Original scientific paper

## CONCLUSIONS

Gelling, retrograde and rheological properties of emmer starch were analyzed and compared with those of rice and wheat starch. Apparently, the higher amylose content of emmer and wheat starch is the main reason for their higher retrograde properties (81.4% for wheat and 87.9% for emmer starch at 120 hours of storage, respectively). Emmer starch shows the lowest onset gelatinization temperature, lowest viscosity and smallest thixotropic area. The results show that Emmer starch and wheat starch have similar properties and can be used interchangeably.

## REFERENCES

1. Apriyanto, A.; Compart, J.; Fettke, J. A review of starch, a unique biopolymer – Structure, metabolism and in planta modifications. *Plant Science*. **2022**, *318*, 111223.
2. Huang, L.; Tan, H.; Zhang, Ch.; Li, Q.; Liu Q. Starch biosynthesis in cereal endosperms: An updated review over the last decade. *Plant communication*s. **2021**, *2* (5), 100237.
3. Bertoft, E. Understanding Starch Structure: Recent Progress. *Agronomy*. **2017**, *7* (3), 56.
4. Cornejo-Ramírez, Y. I.; Oliviert Martínez-Cruz, O.; Del Toro-Sánchez, C.L.; Wong-Corral, F.J.; Borboa-Flores, J.; CincoMoroyoqui, F. J. The structural characteristics of starches and their functional properties. *CyTA - Journal of Food*. **2018**, *16* (1), 1003-1017.
5. Seung, D. Amylose in starch: towards an understanding of biosynthesis, structure and function. *New Phytologist*. **2020**, *228* (5), 1490-1504.
6. Junejo, S.A.; Flanagan, B.M.; Zhang, B.; Dhital, S. Starch structure and nutritional functionality – Past revelations and future prospects. *Carbohydrate Polymers*. **2022**, *277*, 118837.
7. Himashree, P.; Sengar, A.S.; Sunil, C.K. Food thickening agents: Sources, chemistry, properties and applications - A review. International Journal of Gastronomy and Food Science. 2022, 27, 100468.
8. Li, H.; Wang, R.; Zhang, Q.; Li, G.; Shan, Y.; Ding, S. Morphological, structural, and physicochemical properties of starch isolated from different lily cultivars grown in China. *International Journal of Food Properties*. **2019,** *22* (1), 737-757.
9. Bustillos-Rodríguez, J.C.; Tirado-Gallegos, J.M.; Ordóñez-García, M.; Zamudio-Flores, P.B.; Ornelas-Paz, J.J.; Acosta-Muñiz, C.H.; Gallegos-Morales, G.; Páramo-Calderón, D.E.; Rios-Velasco, C. Physicochemical, thermal and rheological properties of three native corn starches. *Food Sci. Technol*. **2019**, *39* (1), 149-157.
10. Govindaraju, J.-M.I.; Chakraborty, I.; Baruah, V.J.; Sarmah, B.; Mahato, K.K.; Mazumder, N. Structure and Morphological Properties of Starch Macromolecule Using Biophysical Techniques. *Starch*. **2021**, *73* (1-2), 2000030.
11. Yan, W; Yin, L.; Zhang, M.; Zhang, M.; Jia, X. Gelatinization, Retrogradation and Gel Properties of Wheat Starch–Wheat Bran Arabinoxylan Complexes. *Gels*. **2021**, *7* (4), 200.
12. Liu, X.; Huang, S.; Chao, Ch.; Yu, J.; Copeland, L.; Wang, Sh. Changes of starch during thermal processing of foods: Current status and future directions. *Trends in Food Science & Technology*. **2022**, *119*, 320-337.
13. Jin, N.; Kong, D.; Wang, H. Effects of temperature and time on gelatinization of corn starch employing gradient isothermal heating program of rapid visco analyzer. *Journal of food process engineering*. **2019**, *42* (7), e13264.
14. Li, Ch. Recent progress in understanding starch gelatinization - An important property determining food quality. *Carbohydrate Polymers*. **2022**, *293*, 119735.
15. Chang, Q.; Zheng, B.; Zhang, Y.; Zeng, H. A comprehensive review of the factors influencing the formation of retrograded starch. *International Journal of Biological Macromolecules*. **2021**, *186*, 163-173.

16. Makroo, H.A.; Naqash, S.; Saxena, J.; Sharma, S.; Majid, D.; Dar, B.N. Recovery and characteristics of starches from unconventional sources and their potential applications: A review. *Appl. Food Res.* **2021**, *1* (1), 100001.
17. Ren, Y.; Yuan, T. Z.; Chigwedere, C. M.; Ai, Y. A current review of structure, functional properties, and industrial applications of pulse starches for value-added utilization. *Compr. Rev. Food Sci. Food Saf.* **2021**, *20* (3): 3061-3092,
18. Halal, E.; Sh, L.M.; Kringel, D. H.; Zavareze, E. da R.; Dias, A.R.G. Methods for Extracting Cereal Starches from Different Sources: A Review. *Starch*. **2019**, *71* (11-12), 1900128
19. Zhang, R.; Ma, S.; Li, L.; Zhang, M.; Tian, Sh.; Wang, D.; Liu, K.; Liu, H.; Zhu, W.; Wang, X. Comprehensive utilization of corn starch processing by-products: A review. *Grain Oil Sci. Technol.* **2021**, *4* (3), 89-107.
20. Geisslitz, S.; Wieser, H.; Scherf, K.A.; Koehler, P. Gluten protein composition and aggregation properties as predictors for brad volume of common wheat, spelt, durum wheat, emmer and einkorn. *J. Cereal Sci.* **2018**, *83*, 204–212.
21. Lacko-Bartosova, M.; Konvalina, P.; Lacko-Bartošová, L.; Štěrba, Z. Quality evaluation of emmer wheat genotypes based on rheological and Mixolab parameters. *Czech J. Food Sci.* **2019**, *37* (3), 192-198.
22. Ullah, S.; Bramley, H.; Mahmood, T.; Trethowan, R. The impact of emmer genetic diversity on grain protein content and test weight of hexaploid wheat under high temperature stress. *J. Cereal Sci.* **2020**, *95*, 103052.
23. Lacolla, G.; Rinaldi, M.; Savino, M.; Russo, M.; Caranfa, D.; Cucci, G. Effects of organic fertilization from wet olive pomace on emmer wheat (Triticum dicoccum Shrank) grain yield and composition. *J. Cereal Sci.* **2021**, *102*, 103369.
24. Christopher, A.; Sarkar, D.; Zwinger, S.; Shetty, K. Ethnic food perspective of North Dakota Common Emmer Wheat and relevance for health benefit targeting type 2 diabetes. *Journal of Ethnic Food*, **2018**, 5, 66-74.
25. Góral, T.; Ochodzki, P. Fusarium head blight resistance and mycotoxin profiles of four Triticum species genotypes. *Phytopathol. Mediterr*. **2017**, *56*, 175–186.
26. Bencze, S.; Makádi, M.; Aranyos, T. J.; Földi, M.; Hertelendy, P.; Mikó, P.; Bosi, S.; Negri, L.; Drexler, D. Re-Introduction of Ancient Wheat Cultivars into Organic Agriculture—Emmer and Einkorn Cultivation Experiences under Marginal Conditions. *Sustainability*. **2020**, *12*, 1584.
27. Das, S.; Chatterjee, A.; Pal, T.K. Organic farming in India: a vision towards a healthy nation. *Food Qual. Saf.* **2020**, *4* (2), 69–76.
28. Lacko-Bartosova, M.; Konvalina, P.; Lacko-Bartošová, L.; Štěrba, Z. Quality evaluation of emmer wheat genotypes based on rheological and Mixolab parameters. *Czech J. Food Sci.*, **2019**, *37* (3), 192-198.
29. BeMiller, J.; Whistler, R., Starch: Chemistry and Technology, Third Edition, Academic Press is an imprint of Elsevier, 2009, pp 573-574, 305, 453.
30. Dzhivoderova-Zarcheva, M.; Dobrev, G.; Shopska, V.; Merdzhanov, P.; Kostov, G.; Stoyanova, A.; Denkova-Kostova, R. Emmer starch isolation by alkaline protease digestion of wet-milled seeds. *Food Science and Applied Biotechnology (In press)*.
31. Saari, H.; Rayner, M.; Wahlgren, M. Effects of starch granules differing in size and morphology from different botanical sources and their mixtures on the characteristics of Pickering emulsions. *Food Hydrocolloids*, **2019**, *89*, 844-855.
32. Liu, W.; Zhao, R.; Liu, Q.; Zhang, L.; Li, Q.; Hu, X.; Hu, H. Relationship among gelatinization, retrogradation behavior, and impedance characteristics of potato starch. *Int. J. Biol. Macromol.* **2023**, *227*, 354-364.
33. Zhang, X.; Shen, Q.; Yang, Y.; Zhang, F.; Wang, C.; Liu, Z.; Zhao, Q.; Wang, X.; Diao, X.; Cheng, R. Structural, functional and mechanistic insights uncover the role of starch in foxtail millet cultivars with different congee-making quality. *International Journal of Biol. Macromol.* **2023**, *242* (3), 125107.

34. Shi, S.; Pan, K.; Yu, M.; Li, L.; Tang, J.; Cheng, B.; Liu, J.; Cao, C.; Jiang, Y. Differences in starch multi-layer structure, pasting, and rice eating quality between fresh rice and 7 years stored rice. *Curr. Res. Food Sci. Food Saf*. **2022**, *5*, 1379–1385.
35. Chakraborty, I.; Pallen, S.; Shetty, Y.; Roy, N.; Mazumder, N. Advanced microscopy techniques for revealing molecular structure of starch granules. *Biophys. Rev.* **2020**, *12*, 105–122
36. Pesek, S.; Lehene, M.; Brânzanic, A.M.V.; Silaghi-Dumitrescu, R. On the Origin of the Blue Color in The Iodine/Iodide/Starch Supramolecular Complex. *Molecules*. **2022**, *27* (24), 8974.
37. Shang, J.; Zhao, B.; Liu, C.; Li, L.; Hong, J.; Liu, M.; Zhang, X.; Lei, Y.; Zheng, X. Impact of wheat starch granule size on viscoelastic behaviors of noodle dough sheet and the underlying mechanism. *Food Hydrocolloids*. **2023**, *134*, 108111.
38. Dzhivoderova, M.M.: Dzhivoderova, M.M. Technological research on starch and starch hydrolysates. Ph.D. Thesis, University of Food Technology, December 2016.
39. Chakraborty, I.; Pooja, N.; Mal, S.S.; Paul, U.C.; Rahman, Md.H.; Mazumder, N. An Insight into the Gelatinization Properties Influencing the Modified Starches Used in Food Industry: A review. *Food Bioprocess Technol*. **2022**, *15*, 1195–1223.
40. Ratnayake, W.S.; Otani, C.; Jackson, D.S. DSC enthalpic transitions during starch gelatinization in excess water, dilute sodium chloride, and dilute sucrose solutions. *J. Sci. Food Agric.* **2009**, *89* (12), 2156–2164.
41. Kong, F.; Singh, R.P. Chemical Deterioration and Physical Instability of Foods and Beverages. *In The Stability and Shelf Life of Food (Second Edition)*, Woodhead Publishing Series in Food Science, Technology and Nutrition, 2016; pp 43-76.
42. Chen, J.; Rosenthal, A. Food texture and structure, Modifying Food Texture. *In Volume 1: Novel Ingredients and Processing Techniques*; Woodhead Publishing Series in Food Science, Technology and Nutrition, 2015; pp 3-24.
43. Himashree, P.; Sengar, A.S.; Sunil C.K. Food thickening agents: Sources, chemistry, properties and applications - A review. *International Journal of Gastronomy and Food Science*. **2022**, *27*, 100468.
44. Santamaria, M.; Garzon, R.; Moreira, R.; Rosell, C.M. Estimation of viscosity and hydrolysis kinetics of corn starch gels based on microstructural features using a simplified model. *Carbohydrate Polymers*. **2021**, *273*, 118549.
45. Santamaria, M.; Montes, L.; Garzon, R.; Moreira, R.; Rosell, C.M. Unraveling the impact of viscosity and starch type on the in vitro starch digestibility of different gels. *Food Funct.* **2022**,*13*, 7582-7590.
46. Magnon, E.; Cayeux, E. Precise Method to Estimate the Herschel-Bulkley Parameters from Pipe Rheometer Measurements. *Fluids*. **2021**, *6*, 157.
47. Taibi, H.; Messelmi F. Effect of yield stress on the behavior of rigid zones during the laminar flow of Herschel-Bulkley fluid. *Alexandria Eng. J.* **2018**, *57* (2), 1109-1115.
48. Ansari, S.; Rashid, M.A.I.; Waghmare, P.R.; Nobes, D.S. Measurement of the fow behavior index of Newtonian and shear-thinning fuids via analysis of the fow velocity characteristics in a mini-channel. *SN Appl. Sci*. **2020**, *2*, 1787.
49. Lenci, A.; Chiapponi, L. An Experimental Setup to Investigate Non-Newtonian Fluid Flow in Variable Aperture Channels. *Water*, **2020**, *12* (5), 1284.
50. Leye, M.; Amoo, R.; Fagbenle, L. Overview of non-Newtonian boundary layer flows and heat transfer. *In Applications of Heat, Mass and Fluid Boundary Layers*, Woodhead Publishing Series in Energy, 2020; pp 413-435.

APTEFF, Vol. 54, 1-335 (2023)
DOI: https://doi.org/10.2298/APT2354277P

UDC: 549.516:544.526.5
BIBLID: 1450-7188 (2023) 54, 277-299

Review paper

# A REVIEW ON NON-METAL AND METAL DOPED ZNO: FUNDAMENTAL PROPERTIES AND APPLICATIONS

*Preeti M. PATIL*[1,2], *Basavaraja SANNAKKI*[2], *Shridhar N. MATHAD*[3]*,
*E. VEENA*[4], *Sheela GANDAD*[4]

[1] Government First Grade College, Haliyal, India
[2] Department of Physics Gulbarga University Kalaburgi-585106, India
[3] Department of Physics, KLE Institute of Technology, Hubballi 580030, India
[4] Department of Physics, P. C. Jabin Science College, Hubballi, India

**Received: 14 May 2023** **Revised: 18 September 2023** **Accepted: 20 September 2023**

*Several non-metal and metal doped ZnO nanoparticles were produced by a variety of routes, including Sol-gel, hydrothermal, and combustion methods. The methods of synthesis, characterization, and applications of these nanoparticles were surveyed and summarised in this review. This study will improve our understanding of developments in doped ZnO and assist in the creation of new ZnO-based materials with improved structural, photocatalytic, and antimicrobial properties.*

**Keywords**: Metal oxide, doped, photocatalyst, antibacterial, dye degradation.

## INTRODUCTION

Recently zinc oxide (ZnO) nanocrystals have evolved as one of the most potential research materials due to its unique properties and mesmerizing applications. Zinc oxide is an inexpensive material, biodegradable and has a fairly low toxicity, which makes it an appropriate candidate for biomedical studies (1-3). ZnO is N- type semiconductor having a wide band gap of nearly 3.37 eV at 300K, high exciton binding energy of approximately 60 meV, and a hexagonal unit cell with lattice constants of a = b = 0.325 nm, c = 0.521 nm (4). ZnO nanocrystals have drawn a lot of interest because they can exhibit novel optical, electrical, chemical, and mechanical properties when compared to their bulk form (5,6). Because of their outstanding optoelectronic properties, piezoelectric properties, pyroelectric characteristics, non-toxicity, natural abundance, ZnO nanocrystals are used in solar cells (7-9), LED’s (10), thermoelectrics (11), photocatalysis (12), sensors (13), bioapplications (14, 15), cosmetic and dermatological products (2, 16-23). Due to its antimicrobial and deodorising qualities, ZnO has also been used as an additive in paints, ceramics, plastic, ointments, sealant pigment, rubber, cotton fabric and food packaging (19–22). Many different morphologies of ZnO, including nanowires, nanobelts, nanorods, and many others, have been reported to demonstrate its adaptability for use in a variety of applications (24–40). Many synthesis methods are developed, and they can be divided into physical, chemical, and biological methods (green route). Though compared to other synthesis techniques, chemical synthesis techniques are less expensive, faster, and produce pure crystals with a higher yield and stability (41). However, they also seem to be harmful to the environment. When reaction conditions (precursor and their concentrations, solvent type, surfactant concentrations, and temperature) in a specific synthesis route are controlled, it is possible to alter the size and morphology of ZnO nanostructures (42).

---

* Corresponding author: Shridhar N. MATHAD, Department of Physics, KLE Institute of Technology, Hubballi 580030, India. E-mail: physicssiddu@gmail.com

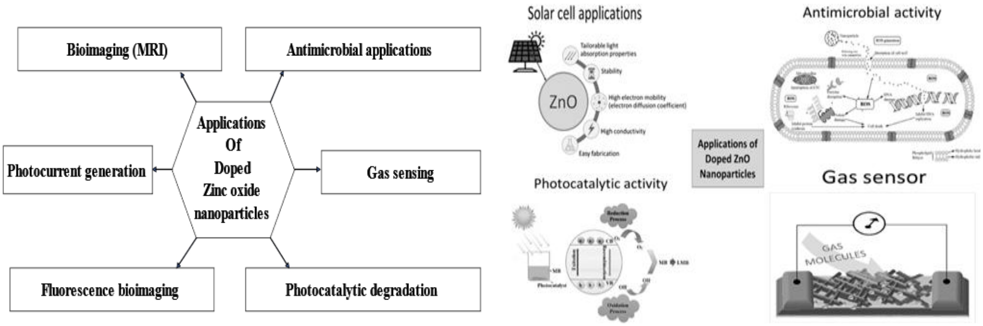

**Figure 1.** Applications of doped ZnO Nanoparticles

Literature study reveals that undoped ZnO nanocrystals have been synthesized using various solution-based techniques like polyol process (43-52), chemical co-precipitation (53,54), colloidal synthesis (55), solvothermal method (56), hydrothermal approaches (57), sol-gel technique (58), and electrochemical synthesis (59). Over the last decade, there has been a growing interest in developing doped zinc oxides to improve its electrical and optical properties (60-64). Despite the significance of doped zinc oxide nanoparticles, there are still few reports of a reliable synthesis. This is largely because colloidal nanoparticle stabilisation is challenging, and doping makes the problem even worse. Higher surface energy typically relates to lower surface area (65). Doping frequently induces additional surface vacancies and defects that make the surface more receptive and unstable, leading to changes in shape and homogeneity as well as problems with aggregation (66) Given these factors, it is important to concentrate on and master the technique for producing trustworthy doped zinc oxide nanoparticles. In this review we concentrate on earlier research findings on the synthesis, properties and applications of doped zinc oxide nanoparticles. The consequences of doping on the enhancement of visible-light absorption and corresponding improvements in properties and their impacts on focussed applications will also be considered, as outlined in Fig 3. The study focussed herein should impart a good foundation for the development of new semiconducting nanoparticle architectures for emerging and future applications.

## METHODS OF NANOPARTICLES SYNTHESIS

There are two main techniques of synthesis of nanoparticles: Top-down and Bottom-Up as shown in Fig 2. In a bottom-up approach, tiny atomic building blocks are linked together to form nanoparticles, whereas in a top-down approach, the bulk material is broken down into nanosized particles. The bottom-up technique is a better option as the products have high purity, have narrow particle size distribution and are homogeneous. Top-down techniques have a number of drawbacks including crystal flaws, the need for high reaction temperatures, the formation of metal oxides, inhomogeneous products, contamination, a broad size distribution, and imperfections in surface structure. Numerous physical and chemical processes are used in the top-down method to produce nanoparticles.

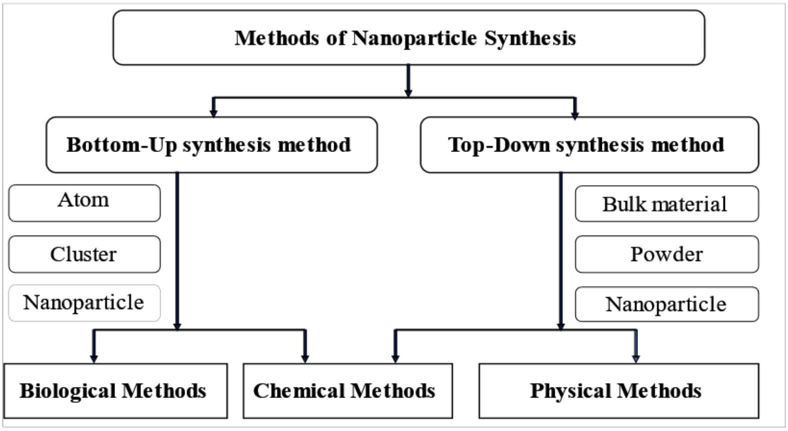

**Figure 2.** Methods of synthesis of Nanoparticles.

## SYNTHESIS OF DOPED ZINC OXIDE NANOPARTICLES

In the synthesis of zinc oxide nanoparticles, acetate, nitrate and chloride salts of zinc are commonly used zinc precursors (67-71). These salts are readily soluble in most of the solvents (water (72, 73), ethanol (74) and methanol (75)) used in this kind of reaction. The typical options for the dopant precursor are chlorides (67), nitrates (76, 77), and acetates (78) of the corresponding dopant elements.

### Solvothermal

This process involves thoroughly mixing and stirring precursors with end product stoichiometry in organic solvents (benzyl alcohol). The mixture is then placed in a sealed autoclave and heated for a period of time at a temperature between 100 °C and 250 °C. Chemical reagent dissolution and product crystallization are made easier by the temperature and pressure conditions. The mixture is centrifuged, washed, and dried after cooling to room temperature. For the synthesis of binary, ternary, and doped metal oxide nanoparticles, nonaqueous solvothermal techniques have become increasingly popular (79, 80). Size and shape can be controlled effectively with solvothermal technology (79-81).

### Co-precipitation

Co-precipitation is one of the of the simplest, cost effective, and highly efficient process used for the synthesis of doped zinc oxide nanoparticles. The precursors were mixed in a stoichiometric ratio and magnetically stirred with sodium hydroxide solution for 30 minutes. This mixture is held at steady temperature of 60 °C for 5 hrs until precipitate is formed. Solution is allowed to cool at room temp, and precipitates were collected by centrifugation.

The resulting precipitate was dried in an incubator at 80 °C for 24 hrs to remove moisture and annealed at 300 °C for 5 hrs (82, 83).

## Hydrothermal

This synthesis technique is simple and convenient method that imparts good control over homogeneity, composition, size, phase, and morphology (84-86). In this process the precursors undergo heterogeneous reactions in solvent like water under high temperature and pressure to dissolve the recrystallized materials insoluble under normal conditions. The metal oxide is produced during this process, which is typically carried out below 300 °C and can be thought of as an electrostatic reaction between metal ions and hydroxyl ions (84, 85). Hydrothermal technique is favourable over standard solution-based methods owing to high temperatures in a closed vessel, mainly a Teflon-lined autoclave inside a stainless-steel reactor which aid in the formation of crystalline nanoparticles.

## Solid state

Nano powders of oxides of zinc and dopant metal were mixed in a stoichiometric proportion in the existence of sodium hydroxide that acts as a fuel. After measuring out the specific ingredient in the proportions calculated to yield 5 g of powder, the mixture was thoroughly homogenized. The resulting slurry was then dried in an oven set to 100 °C. The powder was thoroughly ground in a mortar for 2 hours before being added to an aluminium crucible and heated for 5 hours at 700 °C. The resultant powder was ground for 15 minutes (87).

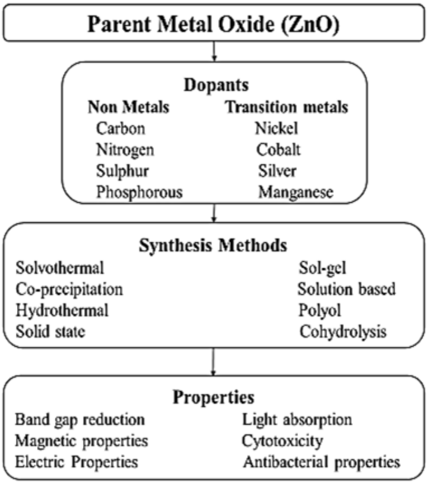

**Figure 3.** An outline of synthesis methods and focussed properties of Zinc oxide nanoparticles

## Sol-Gel

Sol gel synthesis is a facile, affordable, scalable, and low-temperature method. The sol-gel method begins with a homogeneous solution of the precursors; a coordinating agent (ethylene glycol) added to the solution produces a sol, after the solution condenses to form a gel, the solvent is dried to create the nanoparticles (88, 89). This method is particularly well suited for producing doped zinc oxide nanoparticles with good control over size and shape, and it can produce crystalline nanoparticles using ambient temperatures for sol and gel preparation (88). To increase the crystallinity of the resulting nanoparticles, the majority of these processes seek for an additional calcination step (90-92).

### Solution based

In solution-based processes, the synthesized doped zinc oxide nanoparticles possess improved phase purity, uniform size distribution, higher surface area, and a shorter reaction time. In sonochemical processes, a stream of amplified ultrasonic vibrations is applied to the solution of the precursors, which breaks the chemical bonds between the compounds. The solution experiences alternate compression and relaxation as the ultrasound waves pass through it. As a result, acoustic cavitation begins i.e., bubbles start to form, grow, and implosively collapse in the liquid, Additionally, the pressure change produces microscopic bubbles that violently implode, causing shock waves to emerge within the gas phase of the collapsing bubbles. The result of millions of bubbles collapsing at once releases an excessive amount of energy into the solution. At the localized cavitational implosion hotspots, transient temperature of around 5000 K, pressure of around 1800 atm, and cooling rate above 1010 K/s have been observed. The formation and crystallization of the obtained products are found to be impacted by the excessively high rate of cooling. This technique has been used to create a variety of metal oxides nanomaterials, and it has been found to improve the photocatalytic abilities and change the magnetism of specific nanoparticles (93, 94).

### Polyol

Another effective technique for controlled synthesis of nanoparticles is the polyol method, which uses ethylene glycol and its derivatives as the solvent. Additional flexibility is provided by the sheer quantity of polyols that are readily available, each of which has a different molecular weight and boiling point, with solubility in water for most common precursors (95). Furthermore, synthesis temperatures between 200 and 320 °C can be reached without the use of autoclaves.

### Cohydrolysis

High purity nano powders of the precursors were immersed into distilled water and treated ultrasonically for 10 mins (96, 97). Then a small quantity of acetic acid was added to the solution which promotes the hydrolysis reaction between the nano powders and $H_2O$. Hydrolysis is achieved at 60 °C for 24 hrs to carry out the precipitation of doped zinc hydroxide gel. The resulting gel was precipitated as ZnO powder which is filtered and subsequently dried in an oven. Following this the precipitated powders are sintered at 300 °C.

### Characterization methods

The method of X-Ray diffraction helps to understand the crystallite profile of the synthesized sample. Surface morphology, grain size and grain shape of the samples are determined using scanning electron microscopy (98), Transmission electron microscopy and

Field Emission Scanning Electron Microscopy. XRD is sometimes replaced by Scanning electron microscopy when the size of the nanoparticles synthesized is very small (99, 100). Estimation of magnetic properties of the powder samples were carried out by using vibrating sample magnetometer (VSM) (101-103). Optical measurements were executed by using UV-visible spectrometer. The doping effect on the structure of the ZnO nanoparticles has been analysed by using Photo luminous spectral analysis (104-106).

## SYNTHESIS AND STRUCTURAL STUDIES

### Non-metal doped ZnO

The synthesis of uniform nitrogen-doped ZnO nanoparticles is quite challenging. It is observed that majority of N-doped ZnO research reports include films rather than colloidal nanoparticles (107, 108). There are very few reports that reveal the ability to form nonaggregate N-doped ZnO NPs (109-113). Macias-Sánchez et al. (109) mixed the precursors zinc acetate and urea together with ammonium hydroxide as the nitrogen source to produced N-doped zinc oxide nanoparticles. Further heating at 400 °C for 5 h in presence of air, a mixed cluster of N-doped zinc oxide nanorods and nano spheres with an average size around 80−100 nm were produced. Nitrogen doping reduces the crystallite size suggesting increase in lattice strain. Zhang et al. (110) obtained an equivalent outcome using similar technique that involved carbon instead of nitrogen doping. C-doped zinc oxide nanoparticles were produced by grinding zinc acetate with urea in a mortar and then annealing at 450 °C. Pure zinc oxide particles show nanorod morphology, but after C doping, size slowly decreases to yield nanospheres for up to 50 wt % C doped samples. It is observed that the crystallite size of nearly 50 nm remained proportionally constant up to 20% C-doping; but, a steady decrease from 33 nm to 12 nm for 30% and 40% doped sample were observed respectively. This technique also holds good for large scale industrial synthesis.

S-doped ZnO with the hexagonal wurtzite structure can be efficiently synthesized by using mechanochemical method followed by hydrothermal (114). In the hydrothermally produced Ag/S co-doped ZnO, it was observed that silver acts as a good substitute and reduces the generation of interstitial Zn and O vacancies while sulphur increases the solubility of silver in the co-doped samples (115).

It is evident that the change in molar concentration of dopants influences both product formation and the structure of the nanoparticles. ZnO hexagonal wurtzite structure is formed only at lower S content, whereas at the higher S content a mixture of ZnS, S, $Zn_2(OH)_2SO_4$, $ZnSO_3$ and $ZnSO_4$ is obtained. The sulphur concentration not only influence the structure and the phase but also remarkably influences the crystal size and the lattice strain (114, 116-121). In view of this the crystallite size shrink and the lattice strain firstly increases and after that reduces as the S content is increased continuously (117, 122, 123).

Phosphorous doped zinc oxide with different concentration of phosphorous were synthesized by sol-gel technique. Zinc acetate dehydrate is melted in methanol by continuous stirring for 10 minutes at room temperature. P-dopant precursor like ammonium dihydrogen phosphate with various concentrations ranging from 0 to 5% were added with continuous magnetic stirring up till the total dissolution of the precursors. Later, the resulting solution was put in an autoclave adding ethanol for drying in the supercritical state (124). P-doped ZnO holds polycrystalline hexagonal wurtzite structure with varying crystallite size between 22-40 nm with varying doping concentrations (125).

Review paper

## Properties and applications of non-metal doped ZnO

Non-metal doping in ZnO can activate visible-light absorption, thereby enhancing its photocatalytic efficiency, by reducing the electron-hole recombination and hence proves beneficial for the advancements in solar cells and cleaning of the environment (126-128).

In non-metal doped ZnO, carbon and nitrogen are the dominant non-metal dopants. Zhang et al. (129) noticed a significant decrease in the band gap energy upon C-doping. Zhang observed that the highest overall visible-light absorption was for 30% C-doped sample, displaying nearly thrice the absorption compared to the undoped zinc oxide nanoparticles. Increase in the carbon content shows morphological changes from nanorods to nanospheres and the band gap is monotonically reduced from 3.19 to 2.72 eV for C-doping up to 40%. Usually, nanorod morphology displays a longer lifetime for photogenerated charge carriers. Zhang et al. established that the photoluminescence (PL) intensity lowered gradually upon C-doping, which implies that the nanospheres had a lesser rate of recombination than the nanorods. Subsequently owing to these two factors, nanospheres with greater C-doping percentage (59%) showed better photocatalytic activity compared to 10% C-doped nanorods. Analogous study of $TiO_2$ nanorods by Zhang et al. (130) and Lee et al. (90) implies that doping percentage is a more significant factor than morphology for photocatalytic enhancement. Nitrogen dopant is found to be effective in reducing the bandgap of zinc oxide from 3.06 to 2.87 eV and was found beneficial in herbicide degradation (109) Kale et al. (111) in his investigation observed that N-doping in porous ZnO nanocomposites would not only decrease the bandgap of ZnO from 3.14 to 2.97 eV, but also add an absorption tail up to 700 nm, implying the shifting of band gap towards the visible-light region. The N-doped sample showed almost an eightfold increment in photocatalytic activity compared to undoped ZnO.

In Sulphur doped ZnO, SEM images with lower magnification shows spherical morphology whereas with higher magnification show rectangle and square shape morphology. It is observed that lower sulphur doping effectively reduces the band gap energy compared to higher S-doping. Ohno T. et al. (131), confirmed using DRS analysis that in sulphur doped ZnO the electron capture increases on irradiation of visible light absorption. Guozhen et al. (116) showed that S-doping not only increases the electron mobility, but also enhances the feasible recombination rate upon photo light irradiation. In addition to this, S-doped photocatalysts proves beneficial in promoting solar energy for the removal of hazardous organic materials (114).

The structural analysis of P-doped ZnO suggests a hexagonal wurtzite structure with grain size changing from 22 - 40 nm (125, 132, 133). TEM study reveals that with increase in P-doping, size of the crystallite enhances and the crystal modifies from hexagonal to spherical shape. The optical investigation detects the existence of the intense absorption in the UV range and prominent reflectance in the visible and IR region, as is in agreement with the common behaviour of ZnO nanoparticles. Ghoul et al. (134) estimated the band gap energies lying between 3.31 and 3.27eV with increase in P doping from 2% to 8%. Siva et al. (135) emphasized that doping of Phosphorous into ZnO nanorods cause variation in UV emissions but does not alter visible and near infrared emissions which proves beneficial for various optoelectronic and biological applications.

DOI: https://doi.org/10.2298/APT2354277P
BIBLID: 1450-7188 (2023) 54, 277-299

**Table 1**. Synthesis techniques and morphology of non-metal doped ZnO

| Dopant | Precursors | Synthesis method | Morphology/ Particle size | Binding energy eV | Ref |
|---|---|---|---|---|---|
| S | Thiourea (0.25 g & 0.5g) and ZnO | Solid State Reaction | Rectangle and square shape | 3.07-3.09eV | (140) |
| N | Guanidine nitrate and ZnO | Microemulsion method | Spherical/Particle size ~15-60nm | 2.40eV | (143) |
| P | Zinc acetate dihydrate, methanol, ammonium dihydrogen phosphate (P at wt 2, 4, 6, 8 %) | Sol-Gel Method | Hexagonal to spherical/ Particle size ~22-40nm | 3.31-3.27eV | (134) |
| S | Zinc acetate dihydrate, Zinc nitrate, Thiourea | Hydrothermal | Nanowires and nanostars with hexagon cross-section | 3.37eV | (121) |
| N | ZnO, $HNO_3$, ethanol | Solvothermal | Nanorod and nanosphere/ Particle size ~5–20 μm | 3.13-3.17eV | (141) |
| C | $Zn(Ac)_2.2H_2O$, GO | Coprecipitation | Sandwich structure / Particle size ~5–14 nm | 3.26-3.31eV | (142) |
| C | Zinc acetate and urea | Solid state reaction | Nanorods, nanospheres/ Particle size ~200 nm | 3.19-2.72eV | (110) |
| C | Zinc nitrate hexahydrate, cyclohexane, butanol, CTAB | Microemulsion method | Irregular/ Particle size ~20-70 nm | 2.69-2.88eV | (144) |

## Synthesis of metal doped ZnO

Transition metals like Nickel, Cobalt, Manganese and Silver can be doped into ZnO by the process of cohydrolysis of acetates of zinc and dopant metals using sodium hydroxide. Achouri and co-authors (68) successfully synthesized manganese doped zinc oxide by the co-hydrolysis of acetates of zinc and magnesium succeeded by hydrothermal treatment at 160 °C for 24 h. Using this method doping of 1-7% is achieved with consistent hexagonal ZnO wurtzite structure.

Mn-doped ZnO nanoparticles appear slightly smaller than the undoped counterpart which is mainly due to inhibition of growth from the presence of dopant ions in the reaction medium. Just in the same manner Ullah et al. (136) co-hydrolysed acetates of zinc and magnesium to produce Magnesium doped zinc oxide nanoparticles. Both the groups used alcoholic solutions to avoid formation of ZnOH (68, 136). By hydrolysing zinc acetate in the presence of cobalt chloride, Jacob et al. (137) were able to successfully synthesise Co-doped zinc oxide with 4% doping. The nanoparticles produced here have a 40–50 nm particle size and exhibit a hexagonal wurtzite structure. In the presence of diethylene glycol (DEG) and oleic acid (OA) as a surfactant, cobalt doped ZnO up to 10% doping was produced by microwave-assisted thermal decomposition of Co(II) acetylacetonate and zinc acetate dihydrate. This study produced nanocrystals with an average size between 8.9 and 9.9 nm (138). Zinc nitrate precursor along with nitrate salts of dopant element produced doped zinc oxide nanoparticle (69). Nigussie et al. (71) prepared Ag-doped ZnO nanoparticles by sol-gel technique using silver nitrate and zinc nitrate. Rathika A. et al. (139) synthesized Ag /

ZnO NP's by combustion method using zinc nitrate, glycine and citric acid as pioneer materials and silver nitrate as doping source. Synthesized nanoparticles have the typical hexagonal zincite structure and average crystalline size of the particles is 74 nm.

**Table 2.** Optical properties and applications of non-metal doped ZnO

| Dopant | Precursors | Synthesis method | Optical property/Application | Ref |
|---|---|---|---|---|
| S | Thiourea (0.25 g & 0.5g) and ZnO | Solid State Reaction | Absorption in visible region/ Dye sensitized Solar cell application | (140) |
| N | Guanidine nitrate and ZnO | Microemulsion method | Absorption tail until700 nm/ Dye degradation | (143) |
| P | Zinc acetate dihydrate, methanol, ammonium dihydrogen phosphate P at wt 2, 4, 6, 8%) | Sol-Gel Method | Absorption in UV region 300-400nm | (134) |
| S | Zinc acetate dihydrate,<br>Zinc nitrate,<br>Thiourea | Hydrothermal | Emission peak near 517nm/ Visible light emitting devices | (121) |
| N | ZnO, $HNO_3$, ethanol | Solvothermal | Broad tail from approximately 400 nm to 750 nm/ photocatalyst in remediation of water polluted | (141) |
| C | $Zn(Ac)_2 \cdot 2H_2O$, GO | Coprecipitation | Photodegradation of organic pollutant in water | (142) |
| C | Zinc acetate and urea | Solid state reaction | Absorption band until 600 nm/ dye degradation | (110) |
| C | Zinc nitrate hexahydrate, cyclohexane, butanol, CTAB | Microemulsion method | Absorption peak at 616nm/ dye degradation | (144) |

By using chemical co-precipitation and using zinc sulphate, nickel sulphate, sodium hydroxide, and ethylene glycol as a capping agent, Chauhan J. et al. (148) were able to produce Ni-doped zinc oxide. The synthesised sample exhibits crystalline wurtzite structure, with grain size increasing with increasing Ni-doping, roughly ranging between 19 and 30 nm. In another approach using coprecipitation method Zinc acetate dihydrate, nickel hexahydrate, sodium hydroxide and deionized water were employed (146). Synthesized Ni-doped ZnO shows hexagonal cubic structure with particle size calculations performed by Debye Scherrer method (25-29 nm), Williams-Hall (UDM) method (51-63 nm), and Halder-Wagner method (42-47 nm). Average particle size and strain size obtained by Halder-Wagner method (42-47 nm) are very suitable as observed in the study. Iqbal A. and others (147) synthesized Ni / ZnO using wet chemical method utilising zinc nitrate and nickel nitrate solutions, with doping from 2% to 14%. Ni/ ZnO nano catalysts exhibits hexagonal wurtzite crystalline structure with particle size decreasing with increasing Ni impurity. It is also observed that increasing the impurity content shifts the absorption band towards lower wavelength region. Pal B. et al. (148) has reported on the room temperature ferromagnetism in the 3% to 5% Nickel doped ZnO synthesized by ball milling technique. Higher milling time for 3% Ni doped ZnO shows single phase crystalline wurtzite structure with average particle size of approximately 30–40 nm. For the ball milling technique 3% doping is most favourable as for higher concentrations (5.7%) appearance of secondary phases are observed.

## Properties and applications of metal doped ZnO nanoparticles

Zinc oxide nanoparticles possess a bandgap of 3.37 eV which can be improved by the doping process, to extend the activity of ZnO to the visible region. Amongst the doped ZnO nanoparticles, Co-doped zinc oxide nanoparticles produced by Jacob et al. (137) show most favourable visible -light absorption. Cobalt doping shows new peaks in the 563, 610, and 657 nm regions which correlates to d-d transitions of $Co^{2+}$ ions in tetrahedral coordination. Owing to these peaks, strongest visible-light absorption was observed for 2% doped sample.

Higher doping concentrations of Co began to cause an overall reduction in absorption across all wavelengths, though the UV region's absorption remained unchanged from that of undoped ZnO. Similarly, the bandgap initially decreased after Co-doping at 1% and 2% but increased again for samples with high Co-doping levels (3% and 4%). The quantum efficiency and photocurrent studies also showed a similar pattern of growth and decline with doping percentage. Under the various visible light lasers employed, the 2% Co-doped zinc oxide sample showed the best photocurrent performance. Bilecka et al. (149) noted comparable spectral characteristics in Co-doped ZnO nanoparticles. Their nanoparticles, however, were considerably smaller (approximately 10 nm) than those created by Jacob et al. (143), (40-50nm) and displayed Curie-Weiss magnetic behaviour as well as a gradual increase in absorption with Co-doping percentages up to 30%. Co doped nanoparticles synthesized by Jyotsna et al. (150) using chemical co-precipitation method with 3% mole concentration showed an average size of 17 nm and optical band gap between 2.65-3.02eV. Average strain is found to increases as the particle size decreases. In their study, David et al. (138), demonstrated the viability of using colloidal solutions of cobalt doped zinc oxide nanoparticles produced by microwave-assisted reaction in diethylene glycol in optoelectronic devices, most commonly in hybrid polymer light emitting diodes. The Fe-, Ni-, and Mn-doped ZnO nanoparticles displayed magnetic behaviour in addition to strong visible light absorption, but the precise UV–vis spectra for these substances were not provided. Spintronics can make use of such dilute magnetic semiconductors to enable improved electrical and photonic devices. According to Achouri et al. (68), 7% Mn-doped porous zinc oxide nanoparticles had a nearly four-fold increase in visible light absorption over undoped ZnO and a gradually decreasing bandgap from 3.06 to 2.84 eV.

**Table 3**. Synthesis techniques and morphology of metal doped ZnO

| **Dopant** | **Precursors** | **Synthesis method** | **Morphology/ Particle size** | **Binding energy gap eV** | **Ref** |
|---|---|---|---|---|---|
| Ni | Zinc sulphate heptahydrate, Nickel nitrite hexahydrate, Sodium hydroxide | Coprecipitation | Square and Rectangular/ Particle size ~4.17-7.59 nm | 1.46 eV | (151) |
| Ni | Zinc acetate dihydrate, Nickel chloride hexahydrate, diammonium oxalate and ethanol | Solvothermal | Nanorods/ Particle size~5.19 -8.51 nm | 1.47eV | (151) |
| Ni | Zinc oxide nanopowder, Nickel powder | Mechanical ball milling | Nanospheres / Particle size~30-40nm | 3.26 eV | (148) |
| Co | Zinc acetate dihydrate, Cobalt acetylacetonate, DEG and Oleic acid | Polyol method | Particle size ~8.9-9.9nm | 2.97-2.79 eV | (138) |
| Mn | Zinc acetate, manganese acetate, ammonia | Coprecipitation | Seed like structure/ Particle size ~17.5 nm | 2.737 eV | (161) |
| Mn | Zinc nitrate hexahydrate ($Zn(NO_3)_2 \cdot 6H_2O$) and Manganese nitrate hexahydrate ($Mn(NO_3)_2 \cdot 6H_2O$) | Sol Gel Technique | Spherical shape/ Particle size ~42nm | 2.33 eV | (162) |
| Mn | $Zn(OAc)_2 \cdot 2H_2O$, $Mn(OAc)_2 \cdot 4H_2O$, NaOH and Ethanol | Solvothermal | Nanospheres/ Particle size~21nm | 2.83 eV | (68) |
| Ag | Silver nitrate ($AgNO_3$), Zinc nitrate ($ZnNO_3$), | Sol-Gel | Irregular | - | (71) |
| Ag | Zinc nitrate hexahydrate ($Zn(NO_3)_2 \cdot 6H_2O$), and Silver nitrate ($AgNO_3$) | Solution combustion technique | Nano platelet/ Particle size~22-32nm | 3.22 - 3.42 eV | (163) |
| Ag | Zinc nitrate $Zn(NO_3)_2 \cdot 6H_2O$, Silver nitrate ($AgNO_3$ ) | Combustion | Spherical/ Particle size 74nm | 3.08eV | (139) |
| Co | Zinc acetate di-hydrate ($Zn(CH_3COO)_2 \cdot 2H_2O$), Cobalt chloride ($CoCl_2$), Sodium hydroxide (NaOH) | Coprecipitation | Nano spheres/ Particle size 40-50 nm | 2.8eV | (137) |
| Co | Zn acetate, Co acetate, oleic acid | Microwave assisted | Irregular/ Particle size ~10nm | - | (149) |

However, the 3% doped sample showed the most photocatalytic activity when exposed to solar light, and this activity decreased as the doping percentage increased. However, $Mn^{2+}$ ions will act as recombination centres when in excess, which could be a possible explanation for the observed trend. The $Mn^{2+}$ ions initially act as electron-trap centres, reducing recombination and enhancing interfacial charge transfer. According to research by Ullah et al. (137), $Mn^{2+}$-doped zinc oxide nanoparticles exhibit significantly higher overall absorption than undoped zinc oxide, with absorption extending well into the visible spectrum up to 650 nm. Their research suggested that Mn-doped ZnO absorbs more visible light than Al- and Cu-doped ZnO, which can be attributed to the material's higher defect density. Doped ZnO nanoparticles performed worse than undoped ZnO nanoparticles when used for the photocatalytic degradation of dyes in the UV region, but they performed 50 times better under visible light.

Shahid et al. (151) synthesised Ni-doped ZnO using Co-precipitation and solvo-thermal methods. The average particle diameter of Ni-doped ZnO synthesized by coprecipitation method and solvothermal method was found to be 6.32 nm and 7.17 nm respectively. The findings also demonstrate that the band gap values of the sample made using the solvothermal method are marginally higher than those of the sample made using the co-precipitation method. Zinc oxide nanoparticles that have been doped with nickel exhibit higher optical activity than undoped ZnO nanoparticles. The created particles exhibit potent antibacterial qualities. When compared to Gram (-) bacteria, their activity was found to be more promising. The created nanoparticles have the potential to be used in solar cell applications and as a future antibacterial agent. According to a study by Pal et al. (152), for 3% Ni-doped ZnO, the lattice parameters a, c, and the cell volume v decrease with doping because $Ni^{2+}$ has an ionic radius of 0.55 A while $Zn^{2+}$ has an ionic radius of 0.60 A. The spherical shape of Ni-doped ZnO NPs is achieved with an average particle size of 30–40 nm. Hysteresis loop is observed in room-temperature magnetic measurements, with saturation magnetization (Ms) of 1.6-2.56 (emu/g) and coercive field (Hc) of 260 Oe. Micro-Raman studies show additional Raman modes at 547 and 574 $cm^{-1}$ in addition to the peak of pure ZnO at 437 $cm^{-1}$(154, 155). Peak at 574 $cm^{-1}$ in Co-, Al-, and Ce-doped ZnO was also observed by Wang et al. (153) and Cheng et al. (156).

UV-vis absorption measurements and photoluminescence (PL) spectra show some alteration to the band edge emission and absorption properties, respectively. According to Chauhan et al. (145), the average Ni-doped ZnO grain size is about 22 nm, and the average strain is 0.004059, as determined by the slope of the W-H plot. An optical band gap of 3.02 eV was determined using PL spectra, and PL spectra demonstrate a blue shift in peak wavelength from undoped to doped ZnO. Using a refluxed chemical method, Snehal S et al. (157) synthesised Ag-doped ZnO with a doping percentage of 0 to 5 wt%. According to the study, the optical band gap of 3.17 eV for crystallites with an average size ranges from 20 to 25 nm and have granular morphology. When ZnO is doped with 2% Ag, the microstrain rises to 0.1041 from 0.0841 for pure ZnO. The dye degradation experiment demonstrates that photocatalytic efficiency rises with increasing Ag doping amounts up to 5 weight percent. Under visible light irradiation, Ag-doped ZnO produced via a straightforward chemical process is effective in treating contaminated water released from industries including textile, dyeing, pharmaceutical, paper, and other organic waste producing industries. Ag-doped zinc oxide nanoparticles were also used in antibacterial studies (71). The slightly red shifted band edge (>400 nm) of Ag-doped zinc oxide is most likely caused by the silver plasmonic peak at 420 nm. ZnO nanoparticles out performed $TiO_2$ nanoparticles in terms of antibacterial activity, and this pattern was also true for Ag-doped ZnO and $TiO_2$ nanoparticles, which both outperformed the corresponding undoped metal oxide nanoparticles. Ag-ZnO nanoparticles were demonstrated by Rathika A. et al. (139) as a photo-catalyst to break down impurities in the presence of UV light. In comparison to pure ZnO nanoparticles, Ag-doped ZnO nanoparticles demonstrated higher photocatalytic efficiency. Using the sol-gel method, Janković S. et al. (158) synthesised Ag-doped ZnO. Because there are precursors, the synthesised particle does not have a single phase. Nanorods with an average size of 6 nm are visible in SEM images of Ag-doped ZnO; these nanorods are used in a variety of optical and electrical device industries. Ni, Co, Fe, and Cu are transition metal dopants that not only improve ZnO's resistance but also the sensing response. Additionally, the dopants lower the sensor's operating temperature and increase its selectivity, stability, and quick response to the target gas (159, 160).

**Table 4.** Optical properties and applications of metal doped ZnO

| Dopant | Precursors | Synthesis method | Optical property/ Application | Ref |
|---|---|---|---|---|
| Ni | Zinc sulphate heptahydrate, nickel nitrite hexahydrate, sodium hydroxide | Coprecipitation | Solar cell applications and antibacterial agent | (151) |
| Ni | Zinc acetate dihydrate, nickel chloride hexahydrate, diammonium oxalate and ethanol | Solvothermal | Solar cell applications and antibacterial agent | (151) |
| Ni | Zinc oxide nanopowder, Nickel powder | Mechanical ball milling | Absorption tail is blue shifted/<br>Spintronic devices | (148) |
| Co | Zinc acetate dihydrate, Cobalt acetylacetonate, DEG and Oleic acid | Polyol method | Absorption tail between 350 to 450nm/<br>Optoelectronic devices. | (138) |
| Mn | Zinc acetate, manganese acetate, ammonia | Coprecipitation | Cosmetic, nutraceutical pharmaceutical industries | (161) |
| Mn | Zinc nitrate hexahydrate ($Zn(NO_3)_2{\cdot}6H_2O$) and Manganese nitrate hexahydrate ($Mn(NO_3)_2{\cdot}6H_2O$) | Sol-Gel Technique | Dye degradation | (162) |
| Mn | $Zn(OAc)2{\cdot}2H_2O$, $Mn(OAc)_2{\cdot}4H_2O$, NaOH and Ethanol | Solvothermal | Broad absorption tail until 800 nm/<br>Dye degradation | (68) |
| Ag | Silver nitrate ($AgNO_3$), Zinc nitrate ($ZnNO_3$), | Sol-Gel | Band edge narrowing to 450 nm/<br>antibacterial | (71) |
| Ag | Zinc nitrate hexahydrate ($Zn(NO_3)_2{\cdot}6H_2O$, and silver nitrate ($AgNO_3$) | Solution combustion technique | Dye degradation and antimicrobial performance. | (163) |
| Ag | Zinc nitrate ($Zn(NO_3)_2{\cdot}6H_2O$), Silver nitrate ($AgNO_3$) | Combustion | UV-visible absorption peaks at 370 nm/<br>dye degradation | (139) |
| Co | Zinc acetate di-hydrate ($Zn(CH_3COO)_2{\cdot}2H_2O$), cobalt chloride ($CoCl_2$), sodium hydroxide (NaOH) | Coprecipitation | Broad absorption peaks 500-700nm/<br>Photodetectors, photocurrent generation | (137) |
| Co | Zn acetate, Co acetate, oleic acid | Microwave assisted | Broad absorption peaks 500-700nm/<br>Magnetic semiconductors | (149) |

## SUMMARY

This review has taken into account a lot of pertinent research on the synthesis and uses of metal and non-metal doped zinc oxide nanoparticles. Doping changes the properties of ZnO nanoparticles and improves their suitability for use in a variety of applications, including gas sensing, photocatalysis, optoelectronics, and antimicrobial activity. Mostly, ZnO NPs have been doped with different elements, including non-metals and metals, using wet chemical techniques based on sol-gel, hydrothermal routes, and combustion methods. Numerous variables affect the selection criteria for a dopant. For reducing the bandgap of zinc oxide while maintaining morphological consistency, non-metals have shown to be practical dopants. However, both as monodopants and as codopants, metal dopants result in stronger visible light absorption; non-metal dopant effects are also improved when codoped with metals. The use of a multidoped antimicrobial agent that combines metal and non-metal components could represent a crucial advance in the elimination of highly resistant microorganisms. The most widely used non-metal dopants to encourage visible light absorption and photocatalytic activity are nitrogen, sulphur, carbon, and phosphorous. When introduced into ZnO, nitrogen, sulphur and carbon dopants reduce electron-hole recombination and shift the absorption in the UV-visible range by decreasing the band gap, which enhances their antimicrobial activity. S-doped photocatalysts are discovered to be extremely beneficial for promoting solar energy for the removal of dangerous organic materials. Applications for phosphorus doped ZnO nanorods range from biological to optoelectronic devices. Transition metal dopants in ZnO nanoparticles for photocatalysis include nickel, cobalt, silver, and manganese. Along with structural similarity resulting in fewer defects, doping with relatively electron-rich metals is preferred for electrical applications because it increases the Fermi level, resulting in higher conduction. Co, Ni, and Mn are very effective against a variety of microbe strains. Doping ZnO NPs with transition metals is another potent method for acquiring new bioimaging capabilities, and it has been used to great effect in magnetic resonance imaging applications. There are currently numerous opportunities for the synthesis of novel doped metal oxide nanoparticle systems that combine different dopants in order to increase the visible-light activity and produce additional properties like magnetism.

## REFERENCES

1. Akhtar, M.J.; Ahamed, M.; Kumar, S.; Khan, M.M.; Ahmad, J.; Alrokayan, S.A. Zinc oxide nanoparticles selectively induce apoptosis in human cancer cells through reactive oxygen species. *Int. J. Nanomed.* **2012**, *7*, 845.
2. Mirzaei, H.; Darroudi, M. Zinc oxide nanoparticles: Biological synthesis and biomedical applications, *Ceram. Int*. **2017**, *43*, 907-914.
3. Zhang, Y.; Nayak, T.R.; Hong, H.; Cai, W.; Biomedical applications of zinc oxide nanomaterials, *Curr. Mol. Med.*, **2013**, *13*, 1633-1645.
4. Özgür, Ü.; Alivov, Y.I.; Liu, C.; Teke, A.; Reshchikov, M.A.; Doğan, S.; Avrutin, V.; Cho, S.-J.; Morkoç, H. A comprehensive review of ZnO materials and devices, *J. Appl. Phys.* **2005**, *98* (4), 041301. https://dx.doi.org/10.1063/1.1992666.
5. Wang, J.; Chen, R.; Xiang, L.;Komarneni, S. Synthesis, properties and applications of ZnO nanomaterials with oxygen vacancies: a review, *Ceram. Int.* **2018**, *44* (7), 7357–7377. https://dx.doi.org/10.1016/j.ceramint.2018.02.013.
6. Ong, C.B.; Ng, L.Y.; Mohammad, A.W. A review of ZnO nanoparticles as solar photocatalysts: synthesis, mechanisms and applications, *Renew. Sustain. Energy Rev.* **2018**, *81*, 536–551 https://dx.doi.org/10.1016/j.rser.2017.08.020.
7. Law, M.; Greene, L.E.; Johnson, J.C.; Saykally, R.; Yang, P.; Nanowire dye-sensitized solar cells, *Nat. Mater.***2005,** *4*, 455. https://dx.doi.org/10.1038/nmat1387.
8. Hosni, M.; Kusumawati, Y.; Farhat, S.; Jouini, N.;Pauporté, T. Effects of oxide nanoparticle size and shape on electronic structure, charge transport, and recombination in dye-sensitized solar cell photoelectrodes, *J. Phys. Chem.* C. **2014**, *118* (30), 16791–16798 https://dx.doi.org/10.1021/jp412772b.
9. Zheng, Y.-Z.; Tao, X.; Hou, Q.; Wang, D.-T.; Zhou, W.-L.; Chen, J.-F. Iodine-doped ZnO nanocrystalline aggregates for improved dye-sensitized solar cells, *Chem. Mater.* **2011**, *23* (1), 3–5. https://dx.doi.org/10.1021/cm101525p.

10. Kwak, J.; Bae, W.K.; Lee, D.; Park, I.; Lim, J.; Park, M.; Cho, H.; Woo, H.; Yoon, D.Y.; Char, K.; Lee, S.; Lee, C. Bright and efficient full-color colloidal quantum dot lightemitting diodes using an inverted device structure, *Nano Lett.* **2012**, *12* (5), 2362–2366. https://dx.doi.org/10.1021/nl3003254.
11. Jood, P.; Mehta, R.J.; Zhang, Y.; Peleckis, G., Wang, X.; Siegel, R.W.; Borca-Tasciuc, T.; Dou, S.X.; Ramanath, G. Al-doped zinc oxide nanocomposites with enhanced thermoelectric properties, *Nano Lett.* **2011,** *11* (10), 4337–4342. https://dx.doi.org/10.1021/nl202439h.
12. McLaren, A.; Valdes-Solis, T.; Li, G.; Tsang, S.C.; Shape and size effects of ZnO nanocrystals on photocatalytic activity, *J. Am. Chem. Soc.* **2009**, *131* (35), 12540–12541. https://dx.doi.org/10.1021/ja9052703.
13. Liu, B.; Xu, J.; Ran, S.; Wang, Z.; Chen, D.; Shen, G.; High-performance photodetectors, photocatalysts, and gas sensors based on polyol reflux synthesized porous ZnO nanosheets, *Cryst. Eng. Comm.* **2012**, *14* (14), 4582–4588. https://dx.doi.org/10. 1039/C2CE25278C.
14. Jia, Z.; Misra, R.D.K. Tunable ZnO quantum dots for bioimaging: synthesis and photoluminescence, *Mater. Technol.* **2013**, *28* (4), 221–227. https://dx.doi.org/10.1179/1753555713Y. 0000000061.
15. Tang, X.; Choo, E.S.G.; Li, L.; Ding, J.; Xue, J.; One-pot synthesis of water-stable ZnO nanoparticles via a polyol hydrolysis route and their cell labeling applications, *Langmuir,* **2009**, *25* (9), 5271–5275. https://dx.doi.org/10.1021/la900374b.
16. Janotti, A.; Van de Walle, C.G. Fundamentals of zinc oxide as a semiconductor, *Rep. Prog. Phys*. **2009**, *72*,126501.
17. Zhang, Y.; Nayak, T. R.; Hong, H.; Cai, W. Biomedical applications of zinc oxide nanomaterials, *Curr. Mol. Med*., **2013**, *13*, 1633-1645.
18. Ali, R.N.; Diao, K.; Naz, H.; Cui, X.; Xiang, B.; Synthesis, characterization, and applications of zinc oxide nanoparticles and nanorods in acetone gas detection, *Mater. Res. Express*, **2017**, *4*, 095015.
19. Li, Q.; Chen, S.L.; Jiang, W.C. Durability of nano ZnO antibacterial cotton fabric to sweat, *J. Appl. Polym. Sci.* **2007**, *103*, 412-416.
20. Padmavathy, N.; Vijayaraghavan, R. Enhanced bioactivity of ZnO nanoparticles - an antimicrobial study, *Sci. Technol. Adv. Mater.* **2008**, *9*, 035004.
21. Peng, Z.; Dai, G.; Chen, P.; Zhang, Q.; Wan, Q.; Zou, B. Synthesis, characterization and optical properties of star-like ZnO nanostructures, *Mater. Lett*. **2010**, *64*, 898-900.
22. Widiyastuti, W.; Maula, I.; Nurtono, T.; Taufany, F.; Machmudah, S.; Winardi, S.; Panatarani, C. Preparation of zinc oxide/silica nanocomposite particles via consecutive sol–gel and flame-assisted spray-drying methods, *Chem. Eng. J.* **2014**, *254*, 252-258.
23. Harding, F. Breast cancer: cause, prevention, cure, *Tekline publishing*, **2006**.
24. Zang, Z.; Zeng, X.; Du, J.; Wang, M.; Tang, X. Femtosecond laser direct writing of microholes on roughened ZnO for output power enhancement of InGaN light-emitting diodes, *Opt. Lett.* **2016**, *41*, 3463-3466.
25. Zang, Z.; Tang, X. Enhanced fluorescence imaging performance of hydrophobic colloidal ZnO nanoparticles by a facile method, *J. Alloys Compd*. **2015**, *619*, 98-101.
26. Zang, Z.; Wen, M.; Chen, W.; Zeng, Y.; Zu, Z.; Zeng, X.; Tang, X. Strong yellow emission of ZnO hollow nanospheres fabricated using polystyrene spheres as templates, *Mater. Des.* **2015**, *84*, 418-421.
27. Akhavan, O.; Ghaderi, E. Enhancement of antibacterial properties of Ag nanorods by electric field, *Sci. Technol. Adv. Mater*. **2009**, *10*, 015003.
28. Vijayan, T.A.; Chandramohan, R.; Valanarasu, S.; Thirumalai, J.; Venkateswaran, S.; Mahalingam, T.; Srikumar, S.R. Optimization of growth conditions of ZnO nano thin films by chemical double dip technique, *Sci. Technol. Adv. Mater.*, **2008**, *9*, 035007.
29. Hughes, G.; McLean, N. Zinc oxide tape: a useful dressing for the recalcitrant finger-tip and soft-tissue injury, *Emer. Med. J.*, **1988**, *5*, 223-227.

30. Kim, S.Y.; Jeong, S.H.; Lee, E.Y.; Park, Y.-H.; Bae, H.C.; Jang, Y.S.; Maeng, E.H.; Kim, M.-K.; Son, S.W. Skin absorption potential of ZnO nanoparticles, *J. Toxicol. Environ. Health Sci*. **2011**, *3*, 258-261.
31. Lin, L.L.; Nufer, K.L.; Tomihara, S.; Prow, T.W. Non-invasive nanoparticle imaging technologies for cosmetic and skin care products, *Cosmet*. **2015**, *2*, 196-210.
32. Madhu, R.; Veeramani, V.; Chen, S.-M.; Veerakumar, P.; Liu, S.-B.; Miyamoto, N. Functional porous carbon–ZnO nanocomposites for high-performance biosensors and energy storage applications, *Phys. Chem. Chem. Phys.*, **2016**, *18*, 16466-16475.
33. Wang, J.; Sun, X.W.; Wei, A.; Lei, Y.; Cai, X.; Li, C.M.; Dong, Z.L. Zinc oxide nanocomb biosensor for glucose detection, *Appl. Phys. Lett*., **2006**, *88*, 233106.
34. Zhou, Q.; Wen, J.; Zhao, P.; Anderson, W.; Synthesis of vertically-aligned zinc oxide nanowires and their application as a photocatalyst, *Nanomater.* **2017,** *7,* 9.
35. Wang, Z.L.; Nanostructures of zinc oxide, *Mater. Today*, **2004**, 7, 26-33.
36. Wen, X.; Fang, Y.; Pang, Q.; Yang, C.; Wang, J.; Ge, W.; Wong, K.S.; Yang, S. ZnO nanobelt arrays grown directly from and on zinc substrates: synthesis, characterization, and applications, *J. Phy. Chem*. B, **2005**, *109*, 15303-15308.
37. Li, L.; Meng, G.; Wang, H.; Zhai, T.; Fang, X.; Gautam, U.K.; Fang, X.; Bando, Y.; Golberg, D.; High-yield synthesis of single-crystalline zinc oxide nanobelts and their applications in novel Schottky solar cells, *Chem. Commun.,* **2011**, *47* 8247-8249.
38. Jafari, F.;Kodabakhshi, S.; Shirazi, S.G. Zinc oxide nanorods: a new application as a powerful catalyst for the green one-pot synthesis of new warfarin analogs, *RSC Adv*. **2014**, *4*, 48095-48100.
39. Saoud, K., Alsoubaihi, R.; Bensalah, N.; Bora, T.; Bertino, M.; Dutta, J. Synthesis of supported silver nano-spheres on zinc oxide nanorods for visible light photocatalytic applications, *Mater. Res. Bull.*, **2015**, *63*, 134-140.
40. Khalafi, T.;Buazar, F.;Ghanemi, K.Phycosynthesis and Enhanced Photocatalytic Activity of Zinc Oxide Nanoparticles Toward Organosulfur Pollutants. *Sci. Rep.***2019**, 9, article No. 6866. doi:10.1038/s41598-019-43368-3.
41. Kalpana, V.N.; Rajeswari, V.D. A review on green synthesis, biomedical applications, and toxicity studies of ZnO NPs. *Bioinorg. Chem. Appls.* **2018**, 1-12, https://doi.org/10.1155/2018/3569758.
42. Chu, H.O.; Wang, Q. Shi, Y-J.; Song, S.; Liu, W.; Zhou, S.; Gibson, D.; Alajlani, Y.; Li. C. Structural, optical properties and optical modelling of hydrothermal chemical growth derived ZnO nanowires. *Trans. Nonferrous Met. Soc.* China **2020**, *30*, 191-199, https://doi.org/10.1016/S1003-6326(19)65191-5
43. Hosni, M.; Kusumawati, Y.; Farhat, S.; Jouini, N.; Pauporté, T. Effects of oxide nanoparticle size and shape on electronic structure, charge transport, and recombination in dye-sensitized solar cell photoelectrodes, *J. Phys. Chem*. C. **2014**, *118* (30), 16791–16798 https://dx.doi.org/10.1021/jp412772b.
44. Liu, B.; Xu, J.; Ran, S.; Wang, Z.; Chen, D.; Shen, G. High-performance photodetectors, photocatalysts, and gas sensors based on polyol reflux synthesized porous ZnO nanosheets, *Cryst. Eng. Comm.* **2012**, *14* (14), 4582-4588. https://dx.doi.org/10.1039/C2CE25278C.
45. Zhao, L.-H.; Sun, S.-Q. Synthesis of water-soluble ZnO nanocrystals with strong blue emission via a polyol hydrolysis route, *Cryst. Eng. Comm.* **2011**, *13* (6), 1864–1869. https://dx.doi.org/10.1039/C0CE00548G.
46. Anžlovar, A.; Kogej, K.; Orel, Z.C.; Žigon, M.; Impact of inorganic hydroxides on ZnO nanoparticle formation and morphology, *Cryst. Growth Des*. **2014**, *14* (9), 4262–4269 https://dx.doi.org/10.1021/cg401870e.
47. Trenque, S.; Mornet, E.; Duguet, M.; Gaudon, New insights into crystallite size and cell parameters correlation for ZnO nanoparticles obtained from polyol-mediated synthesis, *Inorg. Chem*. **2013**, *52* (21), 12811–12817. https://dx.doi.org/10.1021/ ic402152f.

48. Wang, M.; Li, A.-D.; Kong, J.-Z.; Gong, Y.-P.; Zhao, C.; Tang, Y.-F.; Wu, D. Fabrication and characterization of ZnO nano-clips by the polyol-mediated process, *Nanoscale Res. Lett.* **2018**, *13* (1), 47. https://dx.doi.org/10.1186/s11671-018-2458-9.
49. Feldmann, C. Polyol-mediated synthesis of nanoscale functional materials, *Solid State Sci.* **2005**, *7* (7), 868–873. https://dx.doi.org/10.1016/j.solidstatesciences. 2005.01.018.
50. Lee, S.; Jeong, S.; Kim, D.; Hwang, S.; Jeon, M.; Moon, J. ZnO nanoparticles with controlled shapes and sizes prepared using a simple polyol synthesis, *Superlattice. Microst.* **2008,** *43* (4), 330–339. https://dx.doi.org/10.1016/j.spmi.2008.01.004.
51. Chieng, B.W.; Loo, Y.Y.; Synthesis of ZnO nanoparticles by modified polyol method, *Mater. Lett.* **2012,** *73*, 78–82. https://dx.doi.org/10.1016/j.matlet.2012.01.004.
52. Alves, T.E.P.; Kolodziej, C.; Burda, C.; Franco, A. Effect of particle shape and size on the morphology and optical properties of zinc oxide synthesized by the polyol method, *Mater. Des.* **2018**, *146*, 125–133. https://dx.doi.org/10.1016/j.matdes. 2018.03.013.
53. Yogamalar, R.; Anitha, S.; Srinivasan, R.; Vinu, A.; Ariga, K.; Bose, A.C. An investigation on co-precipitation derived ZnO nanospheres, *J. Nanosci. Nanotechnol.* **2009**, *9* (10), 5966–5972. https://dx.doi.org/10.1166/jnn.2009.1289.
54. Andelman, T.; Gong, Y.; Polking, M.; Yin, M.; Kuskovsky, I.; Neumark, G.; O'Brien, S. Morphological control and photoluminescence of zinc oxide nanocrystals, *J. Phys. Chem.* B. **2005**, *109* (30), 14314–14318. https://dx.doi.org/10.1021/jp050540o.
55. Hodges, J.M.; Fenton, J.L.; Gray, J.L.; Schaak, R.E. Colloidal ZnO and Zn1-xCoxO tetrapod nanocrystals with tunable arm lengths, *Nanoscale*. **2015**, *7* (40), 16671–16676. https://dx.doi.org/10.1039/C5NR04425A.
56. Zheng, Y.; Chen, C.; Zhan, Y.; Lin, X.; Zheng, Q.; Wei, K.; Zhu, J.; Zhu,Y. Luminescence and photocatalytic activity of ZnO nanocrystals: correlation between structure and property, *Inorg. Chem*. **2007**, *46* (16), 6675–6682. https://dx.doi.org/10.1021/ ic062394m.
57. Sridev, D.; Rajendran, K.V. Synthesis and optical characteristics of ZnO nanocrystals, *Bull. Mater. Sci.* **2009**, *32* (2), 165–168. https://dx.doi.org/10.1007/s12034-009- 0025-9.
58. Rani, S.; Suri, P.; Shishodia, P.K.; Mehra, R.M.; Synthesis of nanocrystalline ZnO powder via sol-gel route for dye-sensitized solar cells, *Sol. Energy Mater. Sol. Cells.* **2008**, *92* (12), 1639–1645. https://dx.doi.org/10.1016/j.solmat.2008.07.015.
59. Inamdar, D.Y.; Vaidya, S.R.; Mahamuni, S. On the photoluminescence emission of ZnO nanocrystals, *J. Exp. Nanosci.* **2014**, *9* (5), 533–540. https://dx.doi.org/10.1080/17458080.2012. 676678.
60. Kwon, H.J.; Shin, K.; Soh, M.; Chang, H.; Kim, J.; Lee, J.; Ko, G.; Kim, B.H.; Kim, D.; Hyeon,T. Large-Scale Synthesis and Medical Applications of Uniform-Sized Metal Oxide Nanoparticles, *Adv. Mater.* **2018,** *30,* 1704290.
61. Prakash, J.; Kumar, P.; Harris, R.; Swart, C.; Neethling, J.; van Vuuren, A.J.; Swart, H.; Synthesis, characterization and multifunctional properties of plasmonic Ag–TiO2 nanocomposites, *Nanotechnol.* **2016**, *27,* 355707.
62. Nair, K.K.; Kumar, P.; Kumar, V.; Harris, R.; Kroon, R.; Viljoen, B.; Shumbula, P.; Mlambo, M.; Swart, H.; Synthesis and evaluation of optical and antimicrobial properties of Ag-SnO2 nanocomposites, *Physica B: Condens. Matter.* **2018,** *535,* 338-343.
63. Prakash, J.; Sun, S.; Swart, H.C.; Gupta, R.K.; Noble metals-TiO2 nanocomposites: From fundamental mechanisms to photocatalysis, surface enhanced Raman scattering and antibacterial applications, *Applied Materials Today,* **2018**, *11,* 82-135.
64. Prakash, J.; Pivin, J.; Swart, H.; Noble metal nanoparticles embedding into polymeric materials: from fundamentals to applications, *Adv. Colloid Interface Sci*. **2015**, *226,* 187-202.
65. Baer, D. R.; Engelhard, M. H.; Johnson, G. E.; Laskin, J.; Lai, J.; Mueller, K.; Munusamy, P.; Thevuthasan, S.; Wang, H.; Washton, N.; Elder, A.; Baisch, B. L.; Karakoti, A.; Kuchibhatla, S. V. N. T.; Moon, D. Surface Characterization of Nanomaterials and Nanoparticles: Important Needs and Challenging Opportunities. *J. Vac. Sci. Technol*. A. **2013**, *31*, 50820−50820.

66. García-Mota, M.; Vojvodic, A.; Abild-Pedersen, F.; Nørskov, J. K. Electronic Origin of the Surface Reactivity of Transition-Metal Doped TiO2 (110). *J. Phys. Chem*. C. **2013**, *117*, 460−465.
67. Pradeev, R.; Sadaiyandi, K.; Kennedy, A.; Sagadevan, S.; Chowdhury, Z. Z.; Johan, M. R. B.; Aziz, F. A.; Rafique, R. F.; Thamiz Selvi, R.; Rathina bala, R. Influence of Mg Doping on ZnO Nanoparticles for Enhanced Photocatalytic Evaluation and Antibacterial Analysis. *Nanoscale Res. Lett.* **2018**, *13*, 229.
68. Achouri, F.; Corbel, S.; Balan, L.; Mozet, K.; Girot, E.; Medjahdi, G.; Said, M. B.; Ghrabi, A.; Schneider, R. Porous Mn doped ZnO Nanoparticles for Enhanced Solar and Visible Light Photocatalysis. *Mater. Des.* **2016**, *101*, 309−316.
69. Han, L.; Wang, D.; Lu, Y.; Jiang, T.; Liu, B.; Lin, Y. VisibleLight-Assisted HCHO Gas Sensing Based on Fe-Doped Flowerlike ZnO at Room Temperature. *J. Phys. Chem*. C **2011**, *115*, 22939-22944.
70. Jacob, A. A.; Balakrishnan, L.; Shambavi, K.; Alex, Z. C. MultiBand Visible Photoresponse Study of Co2+ Doped ZnO Nanoparticles. *RSC Adv.* **2017**, *7*, 39657−39665.
71. Nigussie, G. Y.; Tesfamariam, G. M.; Tegegne, B. M.; Weldemichel, Y. A.; Gebreab, T. W.; Gebrehiwot, D. G.; Gebremichel, G. E. Antibacterial Activity of Ag-Doped TiO2 and Ag-Doped ZnO Nanoparticles. *Int. J. Photoenergy.* **2018**, 5927485.
72. Abinaya, C.; Marikkannan, M.; Manikandan, M.; Mayandi, J.; Suresh, P.; Shanmugaiah, V.; Ekstrum. C.; Pearce, J.M. Structural and optical characterization and efficacy of hydrothermal synthesized Cu and Ag doped zinc oxide nanoplate bactericides. *Mater Chem Phys.* **2016**, *184*, 172–182. doi: 10.1016/j.matchemphys.2016.09.039.
73. Sharma, N.; Jandaik, S.; Kumar, S.; Chitkara, M.; Sandhu, I.S. Synthesis, characterisation and antimicrobial activity of manganese- and iron-doped zinc oxide nanoparticles. *J. Exp Nanosci.* **2016**, *11*, 54–71. doi: 10.1080/17458080.2015.1025302.
74. Liu, Y.; Ai, K.; Yuan, Q.; Lu, L. Fluorescence-enhanced gadolinium-doped zinc oxide quantum dots for magnetic resonance and fluorescence imaging. *Biomaterials***.** **2011**, *32*, 1185–1192. doi: 10.1016/j.biomaterials.2010.10.022.
75. Ghaemi, B.; Mashinchian, O.; Mousavi, T.; Karimi, R.; Kharrazi, S.; Amani, A. Harnessing the Cancer Radiation Therapy by Lanthanide-Doped Zinc Oxide Based Theranostic Nanoparticles. *ACS Appl Mater Interfaces.* **2016**, *8*, 3123–3134. doi: 10.1021/acsami.5b10056.
76. Sharma, N.; Kumar, J.; Thakur, S.; Sharma, S.; Shrivastava, V. Antibacterial study of silver doped zinc oxide nanoparticles against *Staphylococcus aureus* and *Bacillus subtilis*. *Drug Invent Today.* **2013**, 5, 50–54. doi: 10.1016/j.dit.2013.03.007.
77. Chandrasekaran, K.; Varaprasad, K.; Venugopal, S.K.; Arun, L.; Hameed, A.S.H. Synergistic Antibacterial Effect of the Magnesium-Doped ZnO Nanoparticles with Chloramphenicol. *BioNanoScience.* **2020**, *10*, 106–111. doi: 10.1007/s12668-019-00696-y.
78. Martínez Julca, M.A.; Rivera, I.; Perales-Pérez, O.; Bailón S.; Pérez M. Li-Doped ZnO Nanoparticles as Novel Direct Generator of Singlet Oxygen for Potential Photodynamic Therapy Applications. *MRS Proc.* **2015**, 1784:mrss15-2136565. doi: 10.1557/opl.2015.625.
79. Djerdj, I.; Arcon, D.; Jagličič, Z.; Niederberger, M. Nonaqueous´ Synthesis of Metal Oxide Nanoparticles: Short Review and Doped Titanium Dioxide as Case Study for the Preparation of Transition Metal-Doped Oxide Nanoparticles. *J. Solid State Chem.***2008**, *181*, 1571−1581.
80. Pinna, N.; Garnweitner, G.; Antonietti, M.; Niederberger, M. Non-Aqueous Synthesis of High-Purity Metal Oxide Nanopowders Using an Ether Elimination Process. *Adv. Mater.* **2004**, *16*, 2196-2200.
81. Stefik, M.; Heiligtag, F. J.; Niederberger, M.; Gratzel, M. Improved Nonaqueous Synthesis of TiO2 for Dye-Sensitized Solar Cells. *ACS Nano.* **2013**, *7*, 8981−8989.
82. Ravichandran, A.T.; Karthick, R. Enhanced photoluminescence, structural, morphological and antimicrobial efficacy of Co-doped ZnO nanoparticles prepared by Co-precipitation method. *Results Mater.* **2020**, *5*, 100072. doi: 10.1016/j.rinma.2020.100072.

83. Liu, Y.; Zhu, S.; Gu, Z.; Chen, C.; Zhao, Y. Toxicity of manufactured nanomaterials, *Particuology,* **2022**, *69*, 31–48. doi: 10.1016/j.partic.2021.11.007.
84. Hayashi, H.; Hakuta, Y. Hydrothermal Synthesis of Metal Oxide Nanoparticles in Supercritical Water. *Mater.* **2010**, *3*, 3794−3817.
85. Gan, Y. X.; Jayatissa, A. H.; Yu, Z.; Chen, X.; Li, M. Hydrothermal Synthesis of Nanomaterials. *J. Nanomater.* **2020**, *2020*, 8917013.
86. Mirzaei, A.; Neri, G. Microwave-Assisted Synthesis of Metal Oxide Nanostructures for Gas Sensing Application: *A Review. Sens. Actuators,* B. **2016**, *237*, 749−775.
87. Divya, N.K.; Pradyumnan, P.P. Solid state synthesis of erbium doped ZnO with excellent photocatalytic activity and enhanced visible light emission, *Mater. Sci. Semicond. Process*., **2016**, *41*, 428–435.
88. Gupta, S.; Tripathi, M. A Review on the Synthesis of TiO2 Nanoparticles by Solution Route. *Open Chem*. **2012**, *10*, 279−294.
89. Rajput, N. Methods of Preparation of Nanoparticles − A Review. *IJAET.* **2015**, *7*, 1806−1811.
90. Lee, M.; Yun, H. J.; Yu, S.; Yi, J. Enhancement in Photocatalytic Oxygen Evolution via Water Oxidation under Visible Light on Nitrogen-Doped TiO2 Nanorods with Dominant Reactive {102} Facets. *Catal. Commun.* **2014**, *43*, 11−15.
91. Wu, Z.; Dong, F.; Zhao, W.; Wang, H.; Liu, Y.; Guan, B. The Fabrication and Characterization of Novel Carbon Doped TiO2 Nanotubes, Nanowires and Nanorods with High Visible Light Photocatalytic Activity. *Nanotechnol.* **2009**, *20*, 235701.
92. Kim, S.; Hwang, S.-J.; Choi, W. Visible Light Active PlatinumIon-Doped TiO2 Photocatalyst. *J. Phys. Chem.* B. **2005**, *109*, 24260− 24267.
93. Bang JH, Suslick KS. Applications of Ultrasound to the Synthesis of Nanostructured Materials. *Adv Mater.* **2010**, *22*, 1039–1059. doi: 10.1002/adma.200904093.
94. Karunakaran, C.; Gomathisankar, P.; Manikandan, G. Preparation and characterization of antimicrobial Ce-doped ZnO nanoparticles for photocatalytic detoxification of cyanide. *Mater Chem Phys.* **2010**, *123*, 585–594. doi: 10.1016/j.matchemphys.2010.05.019.
95. Dong, H.; Chen, Y. C.; Feldmann, C. Polyol Synthesis of Nanoparticles: Status and Options Regarding Metals, Oxides, Chalcogenides, and Non-Metal Elements. *Green Chem.* **2015**, *17*, 4107−4132.
96. Han, B.S.; Uhm, Y.R.; Kim, G.M.; Rhee, C.K. Novel synthesis of nanorod ZnO and Fe doped ZnO by the hydrolysis of metal powders, *J. Nanosci. Nanotechnol.* **2007**, *7*(11), 4158-4160.
97. Han, B.S.; Uhm, Y.R.; Rhee, C.K. Synthesis of nanoflower and rod of ZnO by a surfactant free and low temperature method, *Surf. Rev. Lett*., **2010**, *17*(2), 173-176.
98. Fafal, T.; Taştan, P.; Tüzün, B. S.; Ozyazici, M.; Kivcak, B. Synthesis, characterization and studies on antioxidant activity of silver nanoparticles using *Asphodelus aestivus* Brot. aerial part extract, *S. Afr. J. Bot.*, **2017**, *112*, 346–353.
99. X-Ray Diffraction Analysis: An Overview, **2021**. https://www.sciencedirect.com/topics/engineering/ x-ray-diffraction-analysis.
100. Sagadevan, S.; Podder, J.; Das, I. Synthesis and characterization of cobalt ferrite (CoFe2O4) nanoparticles prepared by hydrothermal method. *Springer proc.*Phys. **2017**, *189*, 145-152. https://doi.org/10.1007/978-3-319-44890-9_14.
101. Foner, S. Versatile and Sensitive Vibrating-Sample Magnetometer. *Rev. Sci. Instrum.* **1959**, *30* (7), 548–557. Bibcode:1959RScI...30..548F. doi:10.1063/1.1716679.
102. Van Oosterhout, G.W. A rapid method for measuring coercive force and other ferromagnetic properties of very small samples. *Appl. Sci. Res*. **1957**, B6, 101-104. https://doi.org/10.1007/BF02920365
103. Flanders, P.J. *IEEE Special Publication*, Conference on Magnetism and Magnetic Materials. American Institute of Electrical Engineers, New York. 1957, **T-91**, 315–317.
104. Tebyetekerwa, M.; Zhang, J.; Xu, Z.; Truong, T.N.; Yin, Z.; Lu, Y.; Ramakrishna, S.; Macdonald, D.; Nguyen, Hieu T. Mechanisms and Applications of Steady-State Photolumines-

cence Spectroscopy in Two-Dimensional Transition-Metal Dichalcogenides. *ACS Nano.* **2020**, *14* (11), 14579 14604. doi:10.1021/acsnano.0c08668.PMID33155803.S2CID 226269683.

105. IUPAC, Compendium of Chemical Terminology, 2nd ed. (the "Gold Book") (**1997**). Online corrected version: (2006–) "photochemistry".
106. Hayes, G.R.; Deveaud, B. Is Luminescence from Quantum Wells Due to Excitons?. *Physica Status Solidi* A. **2002**, *190*(3), 637–640. doi:10.1002/1521-396X(200204)190:3<637::AID-PSSA637>3.0.CO;2-7.
107. Pathak, T. K.; Kumar, V.; Purohit, L. P. High Quality Nitrogen-Doped Zinc Oxide Thin Films Grown on ITO by Sol−Gel Method. *Phys. E.* **2015**, *74*, 551−555.
108. Ng, Z.-N.; Chan, K.-Y.; Muslimin, S.; Knipp, D. P-Type Characteristic of Nitrogen-Doped ZnO Films. *J. Electron. Mater.* **2018**, *47*, 5607−5613.
109. Macías-Sanchez, J. J.; Hinojosa-Reyes, L.; Caballero-Quintero,´ A.; de la Cruz, W.; Ruiz-Ruiz, E.; Hernandez-Ramírez, A.; Guzma´ n-Mar, J. L. Synthesis of Nitrogen-Doped ZnO by Sol−Gel Method: Characterization and its Application on Visible Photocatalytic Degradation of 2,4-D and Picloram Herbicides. *Photochem. Photobiol. Sci.* **2015**, *14*, 536−542.
110. Zhang, X.; Qin, J.; Hao, R.; Wang, L.; Shen, X.; Yu, R.; Limpanart, S.; Ma, M.; Liu, R. Carbon-Doped ZnO Nanostructures: Facile Synthesis and Visible Light Photocatalytic Applications. *J. Phys. Chem.* C. **2015**, *119*, 20544−20554.
111. Kale, G.; Arbuj, S.; Kawade, U.; Rane, S.; Ambekar, J.; Kale, B. Synthesis of Porous Nitrogen Doped Zinc Oxide Nanostructures using a Novel Paper Mediated Template Method and their Photocatalytic Study for Dye Degradation under Natural Sunlight. *Mater. Chem. Front.* **2018**, 2, 163−170.
112. Yi-Hao, T.; Hang, Z.; Yin, W.; Ming-Hui, D.; Guo, J.; Bin, Z. Facile Fabrication of Nitrogen-Doped Zinc Oxide Nanoparticles with Enhanced Photocatalytic Performance. *Micro Nano Lett.* **2015**, *10*, 432−434.
113. Chavillon, B.; Cario, L.; Renaud, A.; Tessier, F.; Chevire, F.;´ Boujtita, M.; Pellegrin, Y.; Blart, E.; Smeigh, A.; Hammarström, L.; Odobel, F.; Jobic, S. P-Type Nitrogen-Doped ZnO Nanoparticles Stable under Ambient Conditions. *J. Am. Chem. Soc.* **2012**, *134*, 464−470.
114. Patil, A. B.; Patil, K. R.; Pardeshi, S. K. Ecofriendly synthesis and solar photocatalytic activity of S-doped ZnO. *J. Hazard. Mater.* **2010**, *183*(1–3), 315–323.
115. Yan, Y.; Al-Jassim, M. M.; Wei, S. H. Doping of ZnO by group-IB elements. *Appl. Phys. Lett*. **2006**, *89* (18), 181912.
116. Shen, G.; Cho, J.H.; Yoo. J. K.; Yi. G. C.; Lee. C. J. Synthesis and optical properties of S-doped ZnO nanostructures: nanonails and nanowires. *J. Phys. Chem.* B, **2005**, *109*(12), 5491–5496.
117. Xie, X. Y.; Zhan. P.; Li, L. Y.; Zhou, D.J; Guo, D.Y.; Meng, J.X.; Bai, Y.; Zheng, W.J. Synthesis of S-doped ZnO by the interaction of sulfur with zinc salt in PEG200. *J. Alloys Compd.*, **2015**, *644*, 383–389.
118. Darzi, S. J.; Mahjoub, A.; Bayat, A. Sulfur modified ZnO nanorod as a high performance photocatalyst for degradation of Congored azo dye. *Int. J. Nano Dimens*., **2015**, *6*(4), 425–431.
119. Cruz-Vázquez, C.; Rocha-Alonzo, F.; Burruel-Ibarra, S.E.; Inoue, M.; Bernal, R. Fabrication and characterization of sulfur doped zinc oxide thin films. *Superficies Vacio*, **2001**, *13*, 89–91.
120. Poongodi, G.; Mohan Kumar, R.; Jayavel, R. Influence of S doping on structural, optical and visible light photocatalytic activity of ZnO thin films. *Ceram. Int.* **2014**, *40*(9), 14733–14740.
121. Cho, J.; Lin, Q.; Yang, S.; Simmons, J. G.; Cheng, Y.; Lin, E.; Yang, J.; Foreman, J. V.; Everitt H. O.; Yang, W.; Kim, J.; Liu, J. Sulfur-doped zinc oxide (ZnO) nanostars: Synthesis and simulation of growth mechanism. *NanoResearch*, **2012**, *5*(1), 20–26.
122. Yang, J.; Xu, C.; Ye, T.; Wang, Y.; Meng, D. Synthesis of S-doped hierarchical ZnO nanostructures via hydrothermal method and their optical properties. *J. Mater. Sci.: Materials in Electronics*, **2017**, *28*(2), 1785–1792.

123. Babikier, M.; Wang, D.; Wang, J.; Li, Q.; Sun, J.; Yan, Y.; Yu, Q.; Jiao, S. Fabrication and properties of sulfur (S)-doped ZnO nanorods. *J. Mater. Sci.*: *Materials in Electronics*, **2014**, *25*(1), 157–162.
124. Ghoul, J. El. Synthesis of vanadium doped ZnO nanoparticles by sol–gel method and its characterization *J Mater Sci*: *Mater. Electron.* **2016,** *27*, 2159-2165. https://doi.org/10.1007/s10854-015-4006-z.
125. Ghoul, J. El.; Barthou, C.; Mir, L.El. Synthesis by sol–gel process, structural and optical properties of nanoparticles of zinc oxide doped vanadium. *Superlattices and Microstruct*. **2012,** *51,* 942-951. https://doi.org/10.1016/j.spmi.2012.03.013.
126. Kerli, S.; Alver, U.; Yaykasli, H.; Avar, B.; Tanriverdi, A.; Kursun, C. Synthesis of Fluorine Doped Zinc Oxide Particles by Hydrothermal Method. *Asian J. Chem*. **2013**, *25*(13), 7539-7542. http://dx.doi.org/10.14233/ajchem.2013.15092.
127. Serpone, N. Is the Bandgap of Pristine TiO2 Narrowed by Anion- and Cation-Doping of Titanium Dioxide in SecondGeneration Photocatalysts? *J. Phys. Chem.* B. **2006**, *110*, 24287− 24293.
128. Carrettin, S.; Hao, Y.; Aguilar-Guerrero, V.; Gates, B. C.; Trasobares, S.; Calvino, J. J.; Corma, A. Increasing the Number of Oxygen Vacancies on TiO2 by Doping with Iron Increases the Activity of Supported Gold for CO Oxidation. *Chem. - Eur. J.,* **2007**, *13*, 7771−7779.
129. Zhang, X.; Qin, J.; Hao, R.; Wang, L.; Shen, X.; Yu, R.; Limpanart, S.; Ma, M.; Liu, R. Carbon-Doped ZnO Nanostructures: Facile Synthesis and Visible Light Photocatalytic Applications. *J. Phys. Chem.* C. **2015**, *119*, 20544−20554.
130. Zhang, Y.; Xing, Z.; Liu, X.; Li, Z.; Wu, X.; Jiang, J.; Li, M.; Zhu, Q.; Zhou, W. Ti3+ Self-Doped Blue TiO2(B) Single-Crystalline Nanorods for Efficient Solar-Driven Photocatalytic Performance. *ACS Appl. Mater. Interfaces.* **2016**, *8*, 26851−26859.
131. Ohno, T.; Akiyoshi, M.; Umebayashi, T.; Asai, K.; Mitsui, T.; Matsumura, M. Preparation of S doped TiO2 photocatalysts and their photocatalytic activities under visible light. *Appl. Catal., A: General*. **2004**, *265*(1), 115–121.
132. Ghoul, J.El.; Barthou, C.; Saadoun, M.; Mir, L.El. Synthesis and optical characterization of SiO2/Zn2SiO4:Mn nanocomposite. *Physica B: Condensed Matter,* **2010,** *405*(2), 597-601. https://doi.org/10.1016/j.physb.2009.09.072
133. Prajapati, C.S.; Sahay, P.P. Influence of In doping on the structural, optical and acetone sensing properties of ZnO nanoparticulate thin films. *Mater. Sci. Semicond. Process* **2013**, *16*(1), 200-210. https://doi.org/10.1016/j.mssp.2012.04.015
134. Ghoul, J. El.; Abdel, All. N. Synthesis and characterizations of phosphorus doped ZnO nanoparticles. *J. Opt. Biomed. Maters, **2022**, 14*(3), 137 – 144.
135. Siva, V., Park, K., Kim, M. S., Kim, Y. J., Lee, G. J., Kim, M. J., & Song, Y. M., "Mapping the structural, electrical, and optical properties of hydrothermally grown phosphorus-doped ZnO nanorods for optoelectronic device applications". *Nanoscale Res. Lett.* **2019**, *14,* 1-9. https://doi.org/10.1186/s11671-019-2920-3
136. Ullah, R.; Dutta, J. Photocatalytic Degradation of Organic Dyes with Manganese-Doped ZnO Nanoparticles. *J. Hazard. Mater*. **2008**, *156*, 194−200.
137. Jacob, A. A.; Balakrishnan, L.; Shambavi, K.; Alex, Z. C. MultiBand Visible Photoresponse Study of Co2+ Doped ZnO Nanoparticles. *RSC Adv.* **2017**, *7*, 39657−39665.
138. Skoda, D.; Urbanek, P.; Sevcik, J.; Munster, L.; Nadazdy, V.; Cullen, D.A.; Bazant, P.; Antos, J.; Kuritka, I. Colloidal cobalt-doped ZnO nanoparticles by microwave-assisted synthesis and their utilization in thin composite layers with MEHPPV as an electroluminescent material for polymer light emitting diodes. *Org. Electron*., **2018**, *59*, 337-348 https://doi.org/10.1016/j.orgel.2018.05.037
139. Rathika, A.; Irine T.M. Synthesis of silver (ag) doped zinc oxide (zno) nanoparticles as efficient photocatalytic activity for degradation methylene blue dye. *J Adv Sci Res.* **2022,** *13 (2)*, 129-135. https://doi.org/10.55218/JASR.202200000.

140. Jothi Ramalingam, R.; Arun, K.; Shukla, K.; Kombaiah, J.; Vijaya, J.; Tawfeek, A. M. Synthesis, characterization and optical properties of sulfur and fluorine doped ZnO nanostructures for visible light utilized catalysis. *Optik.* **2017**, *148*, 325-331. https://doi.org/10.1016/j.ijleo.2017.08.129.
141. Wu, C.; Zhang, Y. C.; Huang, Q. Solvothermal synthesis of N-doped ZnO microcrystals from commercial ZnO powder with visible light-driven photocatalytic activity. *Mater. Lett.*, **2014**, *119*, 104–106.
142. Fu, D.; Han, G.; Chang, Y.; Dong, J. The synthesis and properties of ZnO–graphene nano hybrid for photodegradation of organic pollutant in water.*Mater. Chem. Phys*. **2012**, *132*(2–3), 673–681.
143. Lavand, A.B.; Malghe,Y.S. Synthesis, characterization and visible light photocatalytic activity of nitrogen-doped zinc oxide nanospheres. *J. Asian Ceram Soc.* **2015,** *3* (3), 305-310. https://doi.org/10.1016/j.jascer.2015.06.002.
144. Lavand, A.B.; Malghe, Y.S. Synthesis, Characterization, and Visible Light Photocatalytic Activity of Nanosized Carbon Doped Zinc Oxide. *Int. J. Photochem.* **2015**, *2015*, 790153. http://dx.doi.org/10.1155/2015/790153.
145. Chauhan, J.; Shrivastav, N.; Dugaya, A.; Pandey, D. Synthesis and Characterization of Ni and Cu Doped ZnO. *J. Nanomed. Nanotechnol.* **2017**, *8*(2), 1000429. doi: 10.4172/2157-7439.1000429.
146. Destalina, D.; Mujtahid, F.; Mutmainna, I.; Tahir, D.; Gareso, P. L. The Structure Study of Nickel Doped Zinc Oxide Nanoparticles Synthesized by Coprecipitation Method. *Indonesian Phy. Review*, **2022**, 5 (3), 188-196.
147. Ahmad, I.; Aslam, M.; Jabeen,U.; Zafar, M.N.; Malghani, M.N.K.; Alwadai N.; Alshammari, F.H.; Almuslem, A.S.; Ullah, Z. ZnO and Ni-doped ZnO photocatalysts: Synthesis, characterization and improved visible light driven photocatalytic degradation of methylene blue. *Inorganica Chimica Acta,* **2022**, 121167. https://doi.org/10.1016/j.ica.2022.121167
148. Pal, B.; Sarkar, D.; Giri, P. K. Structural, optical and magnetic properties of Ni doped ZnO nanoparticles: Correlation of magnetic moment with defect density. *Appl. Surf. Sci*. **2015**, *356*, 804–811. https://doi.org/10.1016/j.apsusc.2015.08.163.
149. Bilecka, I.; Luo, L.; Djerdj, I.; Rossell, M. D.; Jagodić, M.; Jagličić, Z.; Masubuchi, Y.; Kikkawa, S.; Niederberger, M. Microwave-Assisted Nonaqueous Sol-Gel Chemistry for Highly Concentrated ZnO-Based Magnetic Semiconductor Nanocrystals. *J. Phys. Chem. C*, **2011**, *115*, 1484−1495.
150. Chauhan, J.; Mehto, V. R.; Singh, S. Synthesis and Characterization of Pure and Co doped Zinc oxide. *Glob J Nano.* **2017**, *1* (2), 555558. DOI: 10.19080/GJN.2017.01.555558.
151. Shahid, S.; Sher, M.M. Solvothermal synthesis and biological activity of ni-doped zinc oxide nanoparticles. *PAP-WCTIE*, **2017**, *33*, 240-246. DOI: 10.17261/Pressacademia.2017.595.
152. Shannon, R.D. Revised effective ionic radii and systematic studies of interatomic distances in halides and chalcogenides. *Acta Crystallogr. Sect. A.* **1976**, *32*, 751–767. https://doi.org/10.1107/ S0567739476001551.
153. Wang, J.B.; Huang, G.J.; Zhong, X.L.; Sun, L.Z.; Zhou, Y.C; Liu, E.H. Raman scattering and high temperature ferromagnetism of Mn-doped ZnO nanoparticles. *Appl. Phys. Lett.* **2006**, *88* (25), 252502. https://doi.org/10.1063/1.2208564
154. Alaria, J.; Bieber, H.; Colis, S.; Schmerber, G.; Dinia, A. Absence of ferromagnetism in Al-doped $Zn_{0.9}$ $Co_{0.10}O$ diluted magnetic semiconductors. *Appl. Phys. Lett.* **2006**, *88* (11), 112503. https://doi.org/10.1063/1.2186079
155. Chen, Z.-Y.; Chen, Z.Q.; Zou, B.; Zhao, X.G.; Tang, Z.; Wang, S.J. Defect mediated ferromagnetism in Ni-doped ZnO nanocrystals evidenced by positron annihilation spectroscopy. *J. Appl. Phys.* **2012**, *112* (8), 083905. https://doi.org/10.1063/1.4759136
156. Cheng, B.; Xiao, Y.; Wu, G.; Zhang, L. The vibrational properties of one-dimensional ZnO:Ce nanostructures. *Appl. Phys. Lett*. **2004**, *84* (3), 416–418. https://doi.org/10.1063/1.1639131

157. Wagh, S. S.; Jagtap, C. V.; Kadam, V. S.; Shaikh, S. F.; Ubaidullah, M.; Bidhan, P.; Salunkhe D. B.; Patil, R.S. Silver Doped Zinc Oxide Nanoparticles Synthesized for Photocatalysis Application. *ES Energy Environ*., **2022**, *17*, 94-105. https://dx.doi.org/10.30919/esee8e720.
158. Janković, S.; Milisavić, D.; Okolić, T.; Jelić, D. Synthesis of ZnO-Ag nanoparticles by sol-gel method, *Contemp. Mater.* **2019**, *10* (1). DOI 10.7251/COMEN1901022J
159. Bhati, V.S.; Ranwa, S.; Fanetti, M.; Valant, M.; Kumar, M. Efficient hydrogen sensor based on Ni-Doped ZnO nanostructures by RF sputtering. *Sens. Actuators, B.* **2018a**, *255*, 588–597.
160. Bhati, V.S.; Ranwa, S.; Rajamani, S.; Kumari, K.; Raliya, R.; Biswas, P.; Kumar, M. Improved sensitivity with low limit of detection of a hydrogen gas sensor based on rGO-Loaded Ni-Doped ZnO nanostructures. *ACS Appl. Mater. Interfaces,* **2018b,** *10-13*, 11116–11124.
161. Khan, S. A.; Shahid, S.; Bashir, W.; Kanwal, S.; Iqbal, A. Synthesis, characterization and evaluation of biological activities of manganese-doped zinc oxide nanoparticles. *Trop. J. Pharm. Res.* **2017**, *16*(10), 2331-2339. https://doi.org/10.4314/tjpr.v16i10.4.
162. Velavan, R.; Balakrishnan, G.; Batoo, K. M.; Raslan, E.H. Synthesis and Characterization of Pure and Manganese (Mn) Doped Zinc Oxide (ZnO) Nanocrystallites for Photocatalytic Applications. *J. Civil Environ. Eng.* **2021**, *11* (8).
163. Jongprateep, O.; Meesombad, K.; Techapiesancharoenkij, R.; Surawathanawises, K.; Siwayaprahm, P.; Watthanarat, P. Influences of chemical composition, microstructure and bandgap energy on photocatalytic and antimicrobial activities of ZnO and Ag-doped ZnO by solution combustion technique. *J. Met., Mater. Miner.* **2019**, *29* (1), 78-85.

APTEFF, Vol. 54, 1-335 (2023)
DOI: https://doi.org/10.2298/APT2354301R
UDC: 634.711:664.037.5]:547.973:579.64
BIBLID: 1450-7188 (2023) 54, 301-311

Original scientific paper

# ANALYSIS OF ANTHOCYANINS CONTENT AND MICROBIOLOGICAL QUALITY CONTROL IN FRESH AND FROZEN RASPBERRY FRUIT

*Dobrila G. RANDJELOVIĆ*, Svetlana Z. BOGDANOVIĆ, Ivana D. ZLATKOVIĆ, Saša D. PETROVIĆ*

Toplica academy of Applied Studies, Department of Agricultural and Technological Studies, Prokuplje, Serbia

**Received: 06 July 2023** **Revised: 16 September 2023** **Accepted: 18 September 2023**

*Raspberry (Rubus idaeus L.) is a plant from the rose family and the most important berry-type fruit in our country. The most significant sorts of raspberries grown in Serbia are the red sorts, namely Willamette, Meeker, Gradina, Malling exploit and Skina. Raspberry fruit may be used either fresh or as a raw material in food industry, for the production of fruit juice, nectar, syrup, concentrate, dried and frozen fruit. The goal of this paper is to determine pH, titratable acidity (as citric acid), soluble solids, concentration of anthocyanins, vitamin C and total polyphenols, and to perform sensory analysis and microbiological quality control in both fresh and frozen fruit. pH value was measured with pH-meter. The concentration of acids was determined by the volumetric method, by titration with NaOH. The dry matter was measured by a refractometer. The concentration of anthocyanins was determined by the spectrophotometry method. The concentration of vitamin C was determined using the volumetric method. The concentration of polyphenol compounds was determined according to the Singleton method. The microbiological methods of detection and counting microorganisms were performed according to ISO standards. The results of this study have shown that both fresh and frozen raspberries are a good source of anthocyanins, indicating that their consumption is favorable for human health and that they may be useful in the production of functional food. The microbiological analyses have shown the absence of L. monocytogenes and Salmonella spp., while the concentration of Enterobacteriaceae and E. coli was below 10 cfu/g in both fresh and frozen raspberry fruit.*

**Keywords**: *Rubus ideus* L., chemical analysis, polyphenols, vitamin C.

## INTRODUCTION

Due to the high concentration of nutrients, fruits and vegetables represent a primary food source for humans. Their consumption is connected to enormous benefits for human health and is associated with decreased risk of many chronic diseases. Berries are important in human diet. Whether they are consumed fresh or processed, they are an important source of nutrients. They contain minerals, sugars, vitamins, organic acids, dietary fiber, and, due to high potential for the improvement of human health, attract much attention from scientists (1). In our country, one of the most important berry fruits is raspberry (*Rubus ideus* L.). Raspberry is a plant from the *Rosaceae* family farmed as a perpetual crop. There are over 1200 varieties of red, black and purple raspberries worldwide, but only red varieties are produced in Serbia (2, 3). Raspberry fruit may be used both fresh and as a raw material in food industry, for preparing fruit juice, nectar, syrup, concentrate, dried and frozen fruit. In the Republic of Serbia, there are 15,200 ha of raspberry crops, with tendency of increase. The largest areas under raspberry crop are situated in Central Serbia, and raspberries are the

---

* Corresponding author: Dobrila G. RANDJELOVIĆ, Toplica academy of Applied Studies, Department of Agricultural and Technological Studies, Prokuplje, Serbia, e-mail: dobrilarandjelovic74@gmail.com

most important export product of our country (4). According to the data issued by the Statistical Office of the Republic of Serbia, the production of raspberries achieved in the Republic of Serbia in 2022 was 4% higher than in 2021 (5). The consumers are attracted to raspberry fruit because of its pleasant aroma and hue, high nutritive value and low caloric value, with health advantages represented by a high concentration of antioxidants (6). The antioxidants are reductive agents limiting oxidative damage to biological structures through removal of free radicals. When they are added to lipids or lipid-containing foods, their shelf life may be prolonged by slowing down the processes of lipid peroxidation (7). Raspberry has a much greater anti-oxidative capacity than other fruits and vegetables (8). Many scientific papers prove the antioxidant properties of raspberries and their extracts (9, 10), as well as their beneficial impact on human health (11, 12). Due to all this, raspberries, as well as other berries can be used as the component of functional food and various diets (13,14). Most of the anti-oxidative components in raspberries belong to anthocyanins, compounds that provide its attractive intense color (15). Concentration of anthocyanins in raspberry fruit is highly dependent on the variety. General order of concentrations would be cyanidin-3-sophoroside > cyanidin-3-glucosylrutinoside > cyanidin-3-glucoside > cyanidin-3-rutinoside > all pelargonidin glucosides combined, where cyanidin-3-sophoroside was predominant in all the studied varieties of raspberry (16). Due to their anti-cancer, anti-inflammatory and anti-oxidative properties, anthocyanins are significantly contributing to health protection (17). Stability of anthocyanins depends on numerous factors, including: storage temperature, enzymes, pH, oxygen concentration, light, structure and concentration of biologically active compounds (flavonoids, minerals and proteins) (18). There are some studies suggesting that freezing during the processing of raspberry fruit may slightly decrease the antioxidant potential (19). Therefore, our studies included analysis of anthocyanins both in fresh and frozen raspberry fruit, after 48 hours of storage. Apart from the content of anthocyanins, other properties analyzed included the pH value, titratable acidity (as citric acid), soluble solids, vitamin C and total polyphenols, that represent extremely important components of the raspberry fruit (20). Considering the enormous importance of the microbiological control of fresh products, one of the objectives of this paper was to carry out the microbiological testing of the fresh and frozen raspberry fruit.

## EXPERIMENTAL

Fruits of two varieties (Willamette and Polka) of raspberry (*Rubus idaeus* L.) were collected at plantations in the vicinity of Prokuplje (Toplica District). The plantations are located in the continental climate zone at 450 meters above sea level. The conditions for including individual fruit in the sample included the appropriate phenotype without any damage caused by handling or disease, as well as the physiological maturity determined by size and color. The samples were picked randomly in the morning hours, in the middle of the ripening season (July 2021). Handpicked fruit was packed into polyethylene containers which were then packed in ice-cooled Styrofoam boxes and transported to a laboratory for further analysis. The fruits intended for freezing were frozen in the continual tunnel Frigoscandia for 7-10 minutes, with the tunnelair temperature of -30°C to -35°C and the speed of air current of 4-7 m/s, so the temperature of -18°C is achieved and stabilized in the thermal center of the fruit.

This paper presents the results of analyses of dry matter, pH value, the concentration of acids (as citric acid), the concentration of vitamin C, of anthocyanins, of total polyphenols, as well as the sensory analysis and the microbiological quality analysis of fresh and frozen raspberry fruit. All the analyses were performed in the laboratory of Agriculture and Food College of Applied Studies in Prokuplje. 30 sets of samples were used for each variety. Macerated fresh and defrosted raspberries were used as samples for determining the concentration of dry matter, using the refractometry method Abbe refractometer (21).

The original solution was prepared by weighing 25 g of a homogenized sample of fresh or defrosted raspberry fruit in a laboratory beaker using an analytical scale, adding 50 $cm^3$ of hot distilled water and stirring vigorously with a glass rod while heating it in a water bath for 30 minutes. After cooling, the contents of the beaker were transferred to a normal 250 $cm^3$ container, topping it with distilled water up to the line, and then filtered. The pH value and total acidity were determined from the filtrate (21).

The pH value was determined with a pH meter (InoLab WTW, Germany), using the sufficient the volume of the original solution to immerse the electrode (22).

The original solution is also used to determine the content of total acids by acid titration with a standard sodium hydroxide solution with a concentration of 0.1 mol/dm3 in the presence of the phenolphthalein indicator. The result is expressed in % as citric acid (22).

## CONCENTRATION OF VITAMIN C

The concentration of vitamin C was determined using the volumetric method according to Tilmans, based on the reduction of vitamin C with 2,6-dichlorphenol-indophenol. 20 g of a homogeneous sample is extracted with 0.2% acetic acid with the addition of quartz sand. The filtered extract is titrated with a 2,6-dichlorphenol-indophenol solution with the concentration of 0,001 $mol/dm^3$, until a stable reddish hue appears. The vitamin C content is expressed as mg/100 g (21).

## CONCENTRATIONS OF ANTHOCYANINS

The concentrations of anthocyanins was determined by spectrophotometry (23) using the pH-differential method devised by Fuleki and Francis (24). The spectrometer Jenway UV-VIS 6305 was used in this study. The homogenized sample of 1 g was extracted with 0.1% HCl in methanol. The extraction was performed within 24 hours at 0°C. The resulting filtrate was used for analysis. The absorbances of raspberry extracts were measured at 510 and 700 nm in 0.025 M potassium chloride buffer (pH 1.0) and 0.4 M sodium acetate buffer (pH 4.5). Anthocyanin content is expressed as mg equivalent of cyanidin 3-glucoside per 100 g.

## TOTAL PHENOLIC CONTENT

Polyphenol compounds were determined according to the method by Singleton (25), using the Folin–Ciocalteu reagent. 2 g of the homogenized sample was extracted for one hour with 80% ethanol. Distilled water and Folin-Ciocalteu reagent were added to the filtrate, followed by 20% $Na_2CO_3$ after 5 minutes. Absorbance was measured at a wavelength of 765 nm. The spectrometer Jenway UV-VIS 6305 was used in this study. The calibration curve of standard solutions of gallic acid was used to determine total polyphenols (mg of gallic acid/100 g of sample).

### SENSORY ANALYSIS

One of the methods of sensory analysis is the point system, where the samples were graded by five persons. Different quality criteria were graded with a different number of points so the total score has a maximum of 20 points: color (1-5), smell (1-4), taste (1-4) and condition and visual properties of fruits (1-7). The results are shown as the mean value ± standard deviation (14).

### MICROBIOLOGICAL ANALYSIS

The microbiological analysis included classic microbiological methods for detection and counting in order to determine the presence of *Salmonella spp.* (SRPS EN ISO 6579:2017) (26), *Listeria monocitogenes* (SRPS EN ISO 11290-1:2017) (27), *Escherichia coli* (SRPS EN ISO 16649-1:2018) (28) and Enterobacteriaceae (SRPS ISO 21528-2:2017) (29) in fresh and frozen fruits of both varieties.

### STATISTICAL ANALYSIS

The statistical data processing was performed using the ANOVA program, a part of the SPSS v20 software package, as well as the PERMANOVA program in the R-u v4.0.3 software package (30). All measurements were carried out in triplicate, and presented as mean ± SD.

## RESULTS AND DISCUSSION

The results of the chemical analysis of fresh and frozen raspberry fruit of Willamette and Polka varieties are presented in Table 1.

The statistical analysis of the data confirmed the normality of the data, justifying thus the use of parametric tests (t test and ANOVA). Using a student's t test for two independent samples, two subsamples of raspberries, fresh and frozen fruit, were compared in relation to the average values of the parameters.

According to the results presented in Table 1, there were statistically significant differences in the average pH and acidity values between frozen and fresh raspberries. The pH values were higher in fresh raspberries, while the acidity was higher in frozen raspberries.

The influence of the process of freezing and the fruit variety on the chemical characteristics of raspberries was investigated by the two-factor analysis of variance. The existence of a significant effect of interaction of these two factors was observed in the average pH value. With the Willamette variety, the difference between the frozen and the fresh fruit was significantly greater than with the Polka variety. The same results were obtained during the acidity test. When it comes to dry matter testing, the only statistical significance was found between the different varieties.

**Table 1**. Chemical analysis of fresh and frozen raspberry fruit of Willamette and Polka varieties.

| **Tested parameters** | **pH** | | **Titratable acidity (total acidity as citric %)** | | **Dry matter (%)** | |
|---|---|---|---|---|---|---|
| Raspberry sample | Willamette | Polka | Willamette | Polka | Willamette | Polka |
| Fresh fruit | 3.36 ± 0.18 | 3.22 ± 0.08 | 1.17 ± 0.06 | 1.80 ± 0.04 | 10.96 ± 0.18 | 12.36 ± 0.35 |
| Frozen fruit | 2.29 ± 0.02 | 2.52 ± 0.06 | 2.03 ± 0.12 | 2.25 ± 0.05 | 10.60 ± 0.57 | 12.30 ± 0.27 |
| Significance of freezing | **0.000** | | **0.000** | | 0.224 | |
| Significance of the varieties | 0.354 | | **0.000** | | **0.000** | |
| Significance of the interaction of the two factors (fruit varieties and freezing) | **0.001** | | **0.000** | | 0.380 | |

$p < 0.001$ – tested parametres are statistically significantly different

This paper presents results of a comparative analysis of fresh and frozen raspberry fruit of Willamette and Polka varieties from the Toplica region. The chemical composition of studied varieties, both in fresh and frozen state, indicates variability between varieties (Table 1). As expected, pH value of fruit is lower in frozen state for both varieties, while difference between fresh fruit of different varieties is negligible. In fresh fruit of studied varieties acidity is lower than in frozen fruit, matching the change of pH values. Our results are consistent with the results by Žlabur *et al.* 2021 (31). The recorded values of acidity (as citric acid) of fresh fruit are matching the reference data (32, 33). During the freezing process, due to the formation of ice crystals, there is a deformation of the cell structure and an increase in the concentration of dissolved substances that do not freeze at low temperatures. With this increase in concentration, a change in pH values occurs (3).

Contents of dry matter matched the previously reported values for fresh and frozen fruit of the same variety (6). The results for Polka variety showed higher value of dry matter. Percentage of dry matter is lower than the reference data for both varieties (6). The difference in chemical composition may be significant depending on factors connected to production and the varieties, as well as the conditions after the fruit was harvested (34, 35).

Concentration of anthocyanins (mg/100g), total polyphenols (mg GAE/100g) and vitamin C (mg/100g) in fresh and frozen fruit of selected varieties of raspberry are presented in Table 2.

Based on the obtained results, it was determined that there are statistically significant differences in anthocyanins average values between frozen and fresh raspberries. The anthocyanins, total polyphenols and vitamin C values are higher in fresh than in frozen fruit.

As for the average concentration of anthocyanins, there is a statistically significant difference between fresh and frozen fruits, and between the two analyzed varieties, Polka and Willamette. The same results were obtained when examinin the total concentration of polyphenols, as well as the concentration of vitamin C.

UDC: 634.711:664.037.5]:547.973:579.64
BIBLID: 1450-7188 (2023) 54, 301-311

Original scientific paper

**Table 2.** Concentration of anthocyanins, total polyphenols and vitamin C in fresh and frozen raspberry varieties.

| **Tested parameters** | **Anthocyans (mg/100g)** | | **Total polyphenols (mg GAE/100g)** | | **Vitamin C (mg/100g)** | |
|---|---|---|---|---|---|---|
| Raspberry sample | Willamette | Polka | Willamette | Polka | Willamette | Polka |
| Fresh fruit | 57.98±0.20 | 53.28 ± 0.38 | 251.16±0.76 | 372.16±0.19 | 40.62 ± 0.48 | 55.06±0.09 |
| Frozen fruit | 39.60±0.14 | 47.46 ± 0.43 | 210.92±0.90 | 301.04±0.09 | 31.96 ± 0.36 | 40.20±0.76 |
| Significance of freezing | **0.000** | | **0.000** | | **0.000** | |
| Significance of the varieties | **0.000** | | **0.000** | | **0.000** | |
| Significance of the interaction of the two factors (fruit varieties and freezing) | **0.000** | | **0.000** | | **0.000** | |

$p < 0.001$ – tested parameters are statistically significantly different

There are significant differences in anthocyanin concentrations in fresh and frozen fruit. In fresh fruit, the concentration of anthocyanin was higher in the Willamette variety (57.93 mg/100g) than in the fresh fruit of the Polka variety (53.34 mg/100g). In frozen fruit, the concentration of anthocyanins was higher in the Polka variety (47.53 mg/100g). Our results match the literature values, which have shown that in the fresh state, the Willamette variety has a higher concentration of total anthocyanins in comparison to the Polka variety (36, 6). The lower concentration of total anthocyanins in frozen state might be attributed to changes in pH values and the temperature at which the food is processed (37). According to a study by Miletić *et al.* (38), the Willamette variety contents a much higher concentration of anthocyanins in frozen fruit (87.04 ± 10.09 mg/100g). The difference in concentration of anthocyanins may be explained by the differences in geographic area, agro-ecological conditions and the year of harvest. The comparative analysis of the vitamin C concentration matches the literature data, where it ranges from 19.4 mg/100g to 73.8 mg/100g (33, 34). According to the results of our study, the Polka variety contents more vitamin C than the Willamette, both in fresh and frozen state. The Willamette was classified as a variety with moderate concentration of vitamin C (30-50 mg/100g), while the Polka was classified as a variety with a high concentration of vitamin C (>50 mg/100g) (39). According to the classification by Vasco *et al.* (39), both varieties belong to the category of moderate concentration of polyphenols (100 – 500 mg GAE/100 mg). The results of our study showed a significantly higher concentration of total polyphenols in the Polka variety (372.21 mg GAE/ 100g) compared with the Willamette variety (251.35 mg GAE/ 100g) in fresh fruit, while lower concentrations of polyphenols were recorded in frozen fruit.

The research conducted by De Ancos *et al.* (20), has shown that the total content of polyphenols remained essentially unchanged even after 12 months of storage of frozen fruit, while the concentration of ascorbic acid significantly decreased.

Using the Mann-Whitney's U-test for two independent samples, the two subsamples of raspberries, fresh and frozen, were compared in relation to their sensory characteristics.

Statistically significant differences were observed in relation to the color, condition and appearance of the fruit. Higher values were recorded for fresh raspberries.

The results of the sensory analysis have shown that the Willamette variety scored the best results both in fresh and frozen state (Figure 1). According to the graders, the fruit has sweet taste, red color, and the smell and the shape typical for a raspberry, while the Polka variety in fresh state showed better characteristics taste-wise.

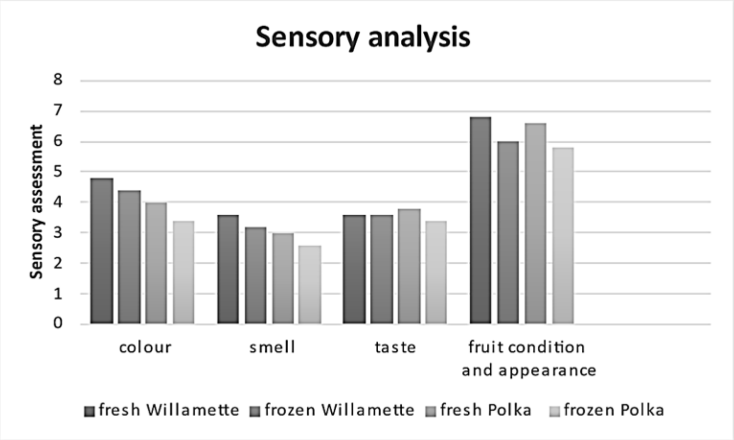

**Figure 1**. Results of the sensory analysis of fresh and frozen raspberry fruit of Willamette and Polka varieties.

The results have shown that the Wilamette variety, both in fresh and frozen state, has better organoleptic characteristics compared to the Polka variety. The sensory characteristics of both varieties appeared to be better in the fresh state, compared to the frozen. In the sensory analysis of several varieties of raspberry from Bosanska Krupa, the Polka variety was established as the variety with the best characteristics (6). Pritts (40) even recommended the Polka variety in comparison with all others for the consumption in fresh state. The differences in organoleptic characteristics may be attributed to different geographic areas. Stevanović *et al.* (41) determined that the process of freezing has significant impact on the sensory characteristics of the Willamette variety. As for the Spanish varieties, the process of freezing and storage of frozen fruit does not seem to have any significant impact on the colour and the taste of the fruit (42). As there is a scarcity of literature data on sensory analysis of raspberry fruit, it was not possible to make more detailed comparisons.

The main reason for short shelf life of fresh raspberries is the development of microorganisms on their surface. Therefore microbiological tests according to ISO standards were performed in order to determine the presence of bacteria causing food spoilage. The results have shown lower incidence of Enterobacteriaceae and *E. coli* (<10 cfu/g), as well as complete absence of *Salmonella spp.* and *L. monocytogenes* (Table 2).

**Table 3.** Results of microbiological analyses of fresh and frozen raspberry fruit from varieties Willamette and Polka.

| Microorganisms | Limit values (cfu/g) | | Code of method | Determined value | | | |
|---|---|---|---|---|---|---|---|
| | M[a] | M[b] | | Fresh Willamette | Frozen Willamette | Fresh Polka | Frozen Polka |
| ***Salmonella spp.*** | Should be absent in 25g | | SRPS EN ISO 6579-1:2017 | No presence detected in any of the samples | | | |
| **Enterobacteriaceae** | 10 cfu/g | | SRPS EN ISO 21528-2:2017 | < 10 cfu/g in all samples | | | |
| ***L. monocytogenes*** | Should be absent in 25g | | SRPS EN ISO 11290-1:2017 | No presence detected in any of the samples | | | |
| ***E. coli*** | $10^2$cfu/g | $10^3$cfu/g | SRPS EN ISO 16649-1:2018 | < 10 cfu/g in all samples | | | |

[a]m - lower limit value of the tested microorganisms; [b]M - upper limit value of the tested microorganisms

The microbiological control of raw materials is one of the most important factors for achieving a high-quality final product (43). Therefore, one of the goals of this paper includes microbiological characterization of raw materials. Fresh fruit is often considered a good transmitter of coliform bacteria such as *E. coli* and *Salmonella spp*., as they are present in the irrigation water and manure (44). As there is no legislative framework that would regulate microbiological quality control of raw materials derived from berries, the available information is scarce, and therefore it is difficult to compare the results. In our study none of the samples showed presence of *Salmonella spp*. and *L. monocytogenes*, while *E. coli* and Enterobacteriaceae were recorded at <10 cfu/g. These results indicate high sanitary standards of fresh and frozen raspberry fruit and adequate hygienic conditions during handling, collecting and storage of fresh and frozen raspberry fruit (45). Several available referenced studies are matching our results. In the study by Oliveira (43), none of the samples exceeded the limits of hygiene criteria determined by the Commission (EC) No. 2073/2005 for fruit and vegetables. *L. monocitogenes* was isolated in two studies on strawberries (46, 47) where the detection of *L. monocitogenes* was reported as sporadic. *L. monocitogenes* is a bacterium with high importance for hygiene, due to its wide distribution in natural environment and therefore easy contamination of fruit and vegetables (43). This study did not include enumeration of yeasts and moulds, and as they are highly important for food production, our future research will be directed to the study of these organisms.

## CONCLUSION

This type of research is highly significant due to large areas under raspberry crops in Serbia and its importance in the food industry. Raspberry fruit bruises easily and the quality may quickly change, so they may be stored only for a short amount of time. On the other hand, raspberry fruit is highly suitable for freezing and, as such, it represents our most important fruit product and one of the most demanded export products of our agriculture. Studies on the produce quality should always include frozen fruit as well.

Our research has shown that the content of anthocyanin, total polyphenols and vitamin C content of differs significantly in fresh and frozen fruit. Although the Willamette variety has a higher concentration of anthocyanins in the fresh state (Willamette 57.98 ± 0.20 mg/100g; Polka 53.28 ± 0.38 mg/100g), the results showed that the Polka variety in the frozen state has a higher concentration of anthocyanins (Polka 47.46 ± 0.43 mg/100g; Willamette 39.60 ± 0.14 mg/100g), vitamin C (Polka 40.20 ± 0.76 mg/100g; Willamette 31.96 ± 0.36 mg/100g) and total polyphenols (Polka 301.04 ± 0.09 mg GAE/100 mg; Willamette 210.92 ± 0.90 mg GAE/100 mg). On the other hand, Willamette showed better sensory characteristics in the frozen state. Although they belong to foods easily prone to spoilage, both varieties have proven to be microbiologically safe, both in fresh and frozen state.

The future research should be directed towards the analysis of the content of individual anthocyanins and their change during long-term storage.

## REFERENCES

1. Koraqi, H.; Durmishi, N.; Rizani, K.L.; Rizani, S. Chemical composition and nutritional value of raspberry fruit (*Rubus idaeus* L.). UBT International Conference. **2019**, 397.
2. Keserović, Z. Small scale production of fruit and grapes. Faculty of Agriculture, University of Novi Sad, Serbia. **2008** (In Serbian).
3. Vračar, Lj. Technology of freezing fruit. Faculty of Technology, University of Novi Sad, Serbia. **2012** (In Serbian).
4. Gulan, B. Pogled na maline u svetu i Srbiji. https://www.makroekonomija.org/0-branislav-gulan/pogled-na-maline-u-svetu-i-srbiji2/; (accessed on 7 November 2022).
5. Statistical Office of the Republic of Serbia Official Page https://www.stat.gov.rs/sr-latn/vesti/statisticalrelease/?p=8841&a=13&s=1301; (accessed on 7 November 2022).
6. Alibabić, V.; Skender, A.; Bajramović, M.; Šeritović, E.; Bajrić, E. Evaluation of morphological, chemical and sensory characteristics of raspberry cultivars grown in Bosnia and Herzegovina. *Turk. J. Agric. For*. **2018**, *42*, 67-74.
7. Eberhardt, M.V.; Lee C.Y.; Liu, R.H. Antioxidant activity of fresh apples. *Nature*. **2000**, *405*, 903-4.
8. Beekwilder, J.; Hall, R.D.; de Vos, C.H. Identification and dietary relevance of antioxidants from raspberry. *BioFactors*. **2005**, *23*, 97-205.
9. Stajčić, S.; Tepić, A.; Đilas, S.; Šumić, Z.; Čanadanović Brunet J.; Ćetković, G.; Vulić, J.; Tumbas, V. Chemical composition and antioxidant activity of berry fruits. *Acta Period. Technol*. **2012**, *43*, 93-105.
10. Ilhami, G., Fevzi, T, Ramazan, C., Mine, B., Ahmet, C.G.; Ummugulsum, E. Pomological Features, Nutritional Quality, Polyphenol Content Analysis, and Antioxidant Properties of Domesticated and 3 Wild Ecotype Forms of Raspberries (Rubus idaeus L.). *J. Food Sci*. **2011**, *76* (4), 585–593.
11. Freeman, B.M.B.; Sandhu, K.A.; Edirisinghe, I. Red Raspberries and Their Bioactive Polyphenols: Cardiometabolic and Neuronal Health Links. American Society for Nutrition. *Adv Nutr*. **2016,** *7* (1), 44–65.
12. Seeram, N.P.; Adams, L.S., Zhang, Y.; Lee, R.; Sand, D.; Scheuller, H.S.; Heber, D. Blackberry, black raspberry, blueberry, cranberry, red raspberry, and strawberry extracts inhibit growth and stimulate apoptosis of human cancer cells in vitro. *J. Agric. Food Chem*. 54 (2006) 9329-9339.
13. Konić-Ristić, A.; Šavikin, K.; Zdunić, G.; Janković, T.; Juranić, Z.; Menković, N.; Stanković, I. Biological activity and chemical composition of different berry juices, *Food Chem*. **2011**, 125, 1412–1417.

14. Hancock RD, McDougall GJ, Stewart D. Berry fruit as ‘superfood’: hope or hype. *Biologist.* **2007**, *54* (2), 73–79.
15. Da Silva, F.L.; Escribano-Bailon, M.T.; Perez Alonso, J.J.; Rivas-Gonzalo, J.C.; Santos-Buelga, C. Anthocyanin pigments in strawberry. *LWT Food Sci Techn*. **2007**, *40*, 374-382.
16. Rao, A.B.; Snyder, D.M. Raspberries in human health: A Review. *J. Agric. Food Chem*. **2010**, *58* (7), 3871-3883.
17. Kong, J.; Chia, L.; Goh, N.; Chia, T.; Brouillard, R. Analysis and biological activities of anthocyanins. *Phytochemistry*. **2003**, *64,* 923-933.
18. Rein, M. Copigmentation reactions and color stability of berry anthocyanins. PhD Thesis, University of Helsinki, Department of Applied Chemistry and Microbiology, Food Chemistry Division. **2005**.
19. Pichler, A. Influence of different additives and storage on quality, rheological and thermophysical properties of raspberry cream filling. PhD Thesis, Josip Juraj Strossmayer University, Osijek. Croatia. **2011**.
20. De Ancos, B.; González E.M.; Cano, M.P. Ellagic Acid, Vitamin C, and Total Phenolic Contents and Radical Scavenging Capacity Affected by Freezing and Frozen Storage in Raspberry Fruit. J. *Agric. Food Chem*. **2000**, *48,* 4565-4570.
21. Vracar, Lj. Manual concerning quality control of fresh and processed fruit, vegetables and mushrooms and non-alcoholic beverages. Faculty of Technology, University of Novi Sad. Serbia**.** **2001**. ISBN 86-80995-33-9 (In Serbian).
22. Pravilnik o metodama uzimanja uzoraka i vršenja hemijskih i fizičkih analiza radi kontrole kvaliteta proizvoda od voća i povrća, Službeni list SFRJ 29/83.
23. Giusti, M.M.; Wrolstad, R.E. Characterizacion and Measurment of Anthocyanins by UV-Visible Spectroscopy. In: Current Protocols in Food Analytical Chemistry, John Wiley & Sons. **2001,** Unit F1.2.1-13.
24. Fuleki, T.; Francis, F.J. Quantitative methods for anthocyanins. 1. Extraction and determinaton of total anthocyanin in cranberries. *J. Food Sci*. **1968**, *33* (1), 72–77.
25. Singleton, V.L.; Orthofer, R.; Lamuela-Raventos, R.M. Analysis of total phenols and other oxidation substrates and antioxidants by means of Folin-Ciocalteu reagent. *Methods Enzymol*. **1999**, *299*,152-178.
26. International Organization for Standardization (SRPS EN ISO 6579-1) Microbiology of the food chain – Horizontal method for the detection, enumeration and serotyping of *Salmonella* - Part 1: Detection of *Salmonella spp*, **2017**.
27. International Organization for Standardization (SRPS EN ISO 11290-2) Microbiology of the food chain – Horizontal method for the detection and enumeration of *Listeria monocytogenes* and of *Listeria spp*. **2017**.
28. International Organization for Standardization (SRPS ISO 16649-1:2018) Microbiology of the food chain -- Horizontal method for the enumeration of beta-glucuronidase-positive Escherichia coli Colony-count technique at 44 degrees C using membranes and 5-bromo-4-chloro-3-indolyl beta-D-glucuronide, **2018**.
29. International Organization for Standardization (SRPS EN ISO 21528-2) Microbiology of the food chain – Horizontal method for the detection and enumeration of Enterobacteriaceae - Part 2: Colonycount technique, **2017**.
30. Johnson, R.A.; Wichern, D.W. Applied Multivariate Statistical Analysis, Pearson Prentice Hall, **2007**.
31. Žlabur, J.Š.; Mikulec, N.; Doždor, L.; Duralija, B.; Galić, A.; Voća, S. Preservation of Biologically Active Compounds and Nutritional Potential of Quick-Frozen Berry Fruits of the Genus Rubus. *Processes*, **2021**, *9* (11), 1940.
32. Nikolić, M.; Radović, A.; Fotrić, M.; Milivojević, J.; Nikolić, D. Pomological properties of promising Raspberry seedlings with yellow fruit. *Genetika*. **2009**, *41*, 255-262.

UDC: 634.711:664.037.5]:547.973:579.64
BIBLID: 1450-7188 (2023) 54, 301-311

Original scientific paper

33. Orzeł, A.; Król-Dyrek, K.; Kostecka-Gugala, A., Wyżgolik, G. Evaluation of vegetative growth and fruit chemistry of some raspberry and blackberry cultivars grown in southern Poland. *Acta Hort.* **2016**, *1133*, 371-378.
34. Lewandowski, M.; Żurawicz, E., Pruski, K. Effects of the growing season extension on Polish primocane fruiting raspberry cultivars. *Hort Sci*. **2015**, *42*, 203-208.
35. Talcott, S.T. Chemical components of berry fruits. Edited by Zhao Y. Berry Fruit: Value-Added Products for Health Promotion. Taylor & Francis Group. New York, NY, USA, **2007**, pp 51-73.
36. Ivanović, M.; Pavlović, A.; Mitić, M.; Pecev-Marinković, E.; Krstić J, Mrmošanin, J. Determination of total and individual anthocyanins in raspberries grown in South Serbia, In: Zbornik radova. XXI Savetovanje o biotehnologiji sa međunarodnim učešćem, Čačak, Srbija, **2016**, pp. 263-267.
37. Tepić, A. Coloured substances in fruits and vegetables**.** Faculty of Technology, University of Novi Sad, Serbia. **2012**. ISBN 978-86-6253-008-0 (In Serbian).
38. Miletić, N.; Leposavić, A.; Popović, B.; Mitrović, O.; Kandić, M. Chemical and antioxidant properties of fully matured raspberry fruits (*Rubus idaeus* L.) picked in different moments of harvesting season. *Acta Hortic*. **2015**, *1099*, 211-218.
39. Vasco, C.; Ruales, J.; Kamal-Eldin, A. Total phenolic compounds and antioxidant capacities of major fruits from Ecuador. *Food Chem*. **2008**, *111*, 816-823.
40. Pritts, M.P. Winter raspberry production in a greenhouse. *Fruit Notes*. **2000**, *65*, 20-21.
41. Stevanović, S.M.; Petrović, T.S.; Marković, D.D.; Milovančević, U.M.; Stevanović Urošević, T.M.; Kozarski, M.S. Changes of Quality and Free Radical Scavenging Activity of Strawberry and Raspberry Frozen under Different Conditions. *J. food process. and preserv*. **2021**, *46* (10), e15981.
42. De Ancos, B.; Ibanez, E.; Reglero, G.; Pilar Cano, M. Frozen storage effects on anthocyanins and volatile compounds of raspberry fruit. *J. Agric. Food Chem.* **2000**, *48*, 873-879.
43. Oliveira, M.; Rodrigues, C.M.; Teixeira, P. Microbiological quality of raw berries and their products: A focus on foodborne pathogens. *Heliyon*, **2019**, *5* (12), e02992.
44. Gagliardi, J.; Karns J. Leaching of *Escherichia coli* O157:H7 in Diverse Soils under Various Agricultural Management Practices. *Appl. Environ. Microbiol*. **2000**, *66* (3), 877-883.
45. Thang, K.; Au, K.; Rakovski, C.; Prakash A. Effect of phytosanitary irradiation and methyl bromide fumigation on the physical, sensory, and microbiological quality of blueberries and sweet cherries. *J. Sci. Food Agric*. **2016**, *96*: 4382–4389.
46. Johannessen, G.S.; Loncarevic, S.; Kruse H. Bacteriological analysis of fresh produce in Norway. *Int. J. Food Microbiol.* **2002**, *77*, 199–204.
47. Dziedzinska, R.; Vasickova, P.; Hrdy, J.; Slany, M.; Babak, V.; Moravkova, M. Foodborne Bacterial, Viral, and Protozoan Pathogens in Field and Market Strawberries and Environment of Strawberry Farms. *J. Food Sci*. **2018,** *83*(12), 3069-3075.

APTEFF, Vol. 54, 1-335 (2023) UDC: 534.12+678.7:66.067.2]:577.112
DOI: https://doi.org/10.2298/APT2354313M BIBLID: 1450-7188 (2023) 54, 313-324

Original research paper

# MEMBRANES MODIFIED WITH RIGID POLYMER FOR PROCESSING SOLUTIONS OF VEGETABLE PROTEINS

*L.C.A. MOLINA[1], G.A.V. MAGALHÃES -GHIOTTO[1], L. NICHI[1], Yuliya S. DZYAZKO[2]*, R. BERGAMASCO[1]*

[1] Department of Chemical Engineering, State University of Maringa, Av. Colombo, 5790, Maringa, Parana 87020-900, Brazil
[2] V.I. Vernadskii Institute of General & Inorganic Chemistry of the NAS of Ukraine, Palladin Ave. 32/34, Kyiv, 03142, Ukraine

**Received: 01 August 2023 Revised: 19 September 2023 Accepted: 20 September 2023**

*Baromembrane separation is attractive for food industry since it provides no destruction of organic substances. The aim of this study is purposeful formation of the rejection ability of macroporous polymer membranes simultaneously with their resistance against compression for juice clarification and protein fractionalization. This problem is solved by modifying of asymmetric polymer microfiltration membrane with polymethyl methacrilate (PMMA), the content of this rigid modifier was varied from 15 to 80 mass %. Morphology of composite membranes was investigated with SEM method, water test was performed. Based on obtained results, the modifying mechanism was proposed: (I) blockage membrane pores with PMMA particles, (II) stretching pore walls caused by mechanical action of embedded particles, (III) screening pores of both active layer and support with modifier particle located on the outer surface, The optimal PMMA amount in the membranes was found to be up to 20 %. Depending on the modifier content, selectivity of the membranes towards vegetable albumin, which was extracted from Moringa oleifera seeds, reaches 30-91 %. Thus, the membranes can be used for the purposeful separation of the large protein particles from smaller fractions, which can be used as nutritional supplements due to their better digestibility.*

**Keywords**: membrane filtration, polymer membrane, polymethyl methacrylate, vegetable proteins, albumin.

## INTRODUCTION

Nowadays tubular polymer microfiltration membranes, which are produced from elastic polymers like polyamide (1) or polyvinylidene fluoride (2), become widespread. This is due to a possibility to regulate the separation efficiency by a control of tube length without manufacture of a new membrane module. In the case of planar membranes, each or other efficiency requires different membrane modules, since a possibility to increase pressure is limited. However, the application of polymer tubular membranes is complicated by stretching elastic polymers affected by pressure. The polymer deformation makes difficult the operating membrane modules.

The solution of this problem can be modifying elastic membrane with rigid polymer. As a rule, these polymers are hydrophobic – it is necessary to control their content in a matrix to avoid deterioration of its functional properties. In order to expand the application field of microfiltration membranes, a modifier has to improve their selectivity. Commonly microfil-

---

* Corresponding author: V.I. Vernadskii Institute of General & Inorganic Chemistry of the NAS of Ukraine, Palladin Ave. 32/34, Kyiv, 03142, Ukraine. E-mail: dzyazko@gmail.com

APTEFF, Vol. 54, 1-335 (2023)
DOI: https://doi.org/10.2298/APT2354313M
UDC: 534.12+678.7:66.067.2]:577.112
BIBLID: 1450-7188 (2023) 54, 313-324

tration membranes modified with polymers show rejection of colloidal particles (3). As a result, they can be used for processing liquid feedstock and wastes of food and beverage industry. These membranes (polymer, inorganic or polymer-inorganic) are applied to concentrating proteins from skim milk (4), milky whey (5), corn distillery (6), spent brewer's yeast (7) and potato juice (8), clarification of sugar cane juice (9). Nowadays obtaining concentrate of aminoacids and proteins from nuts (*Cola acuminata*, *Garcinia kola*, *Anacardium occidentale*, i.e. cashew (10), *Moringa oleifera* (11) are in a focus of attention due to their worth as nutritional supplements. For both animal (12) and vegetable (13) proteins, smaller particles are more digestible than larger ones. In order to solve the problem of protein fractionation, the rejection ability of membranes can be varied.

The aim of this study is a purposeful formation of the rejection ability of macroporous polymer membranes simultaneously with their resistance against compression for juice clarification and protein fractionation. This problem is supposed to be solved by modifying microfiltration membrane with rigid polymethylacrilate (PMMA). This approach can be used in a future for the additional introduction of highly hydrophilic components into the membrane (inorganic ion-exchanger, graphene oxide etc.) in order to prevent their leakage under pressure conditions.

In this study, asymmetric membrane was taken as a model object since it contains pores in a wide diapason of size. As expected, PMMA localization in different regions of a membrane is strongly affected by the precipitation conditions. Asymmetric membrane is an attractive object for investigations, since purposeful formation of the modifier in pores of one or other size is possible. In other words, composite materials with different separation properties can be obtained using only one type of membrane and one modifier.

## Experimental

### MATERIALS

PMMA and polyvinylpyrollidone (PVP) were purshased from Sigma, chloroform was supplied by Nuclear company (Brazil). Albumun produced in the State University of Maringa (Brazil) from the seeds of *Moringa oleifera* (14) was used for investigations. Earlier the proteins extracts were used as coagulant for water treatment (15), and also to water decolorization (16).

Planar membranes (UNIFIL, Brazil) were used for modifying as model objects. Microfiltration membranes (47 mm of a diameter) were made of cellulose acetate.

### MODIFYING OF MEMBRANES AND INVESTIGATIONS OF THEIR MORPHOLOGY

Before the modifying, the membranes were dried at 45 °C and weighted. Polymethylmetacrilate (PMMA, 350 kDa) was dissolved in chloroform. The solution concentration (%) was: 1, 3. 7, 10 and 15. The solution sample (0.5 cm$^3$) was inserted into the active layer of the membrane, the composite was dried at 40 °C down to the constant mass. Then the membranes were cleaned at 40 kHz in water using an Ultracleaner-1400 A ultrasonic bath. The membranes were modified 1 time. This series of samples was marked as PMMA-1.1, PMMA-1.3 etc.

The procedure was also repeated 3 and 7 times, when the solution concentration was 1%. The membranes were labelled as PMMA-3.1 and PMMA-7.1. The amount of embedded modifier was determined as a difference of masses between the composite and pristine membranes. Morphology of the membranes was studied with a SEM-Quanta FEG-250 scanning electron microscope (SEM Quanta 250 FEI Company, the Netherlands). Preliminarily the membranes were coated with an ultrathin gold film using a BAL-TEC - Sample Coater (BAL-TEC, USA).

## WATER TEST

The materials were tested using a HP4750 Sterlitech™ dead-end filtration system (Sterlitech, USA). The effective area of the membrane was $9.08\times10^{-4}$ m$^2$. Pressure (from 0.5 to 2 bar) was provided with a controlled flow of nitrogen. Filtration was performed under 25 °C. Cumulative volume ($V$) of water at the cell outlet was monitored, the dependencies of volume on time ($\tau$) were plotted. The flux ($J$) through compressed membranes was found from the slope of linear regions of the $V{-}\tau$ curves:

$$J = \frac{dV}{d\tau}\frac{1}{A} \qquad [1]$$

where $A$ is the effective area of membranes. Normally the flux obeys Darcy law (17):

$$J = \frac{\Delta P}{\mu R_m} \qquad 2]$$

where $\mu$ is the dynamic viscosity, $R_m$ is the hydrodynamic resistance of membrane, $\Delta P$ is the pressure drop.

After the water test, the membrane was weighted immediately. The volume of water in the membrane was calculated from the values of mass growth and water density. This volume corresponds to the volume of pores, which are responsible for the water transport, porosity ($\varepsilon$) was calculated via:

$$\varepsilon = \frac{V_p}{V_m} \qquad [3]$$

where $V_p$ and $V_m$ are the volumes of pores and membranes. The radius of pores ($r$) was estimated using Hagen-Poiseuille equation for cylindrical voids (17):

$$r = \sqrt{\frac{8\mu t\Delta x J}{\varepsilon\Delta P}} \qquad [4]$$

Here $t$ is the tortuosity coefficient (as supposed, $t$ = 1 for filtration membranes), $\Delta x$ is the membrane thickness. Modified Hagen-Poiseuille equation (Guerout-Elford-Ferry equation) can be also applied (17):

$$r = \sqrt{\frac{8\mu\Delta x(2.9-1.75\varepsilon)J}{\varepsilon\Delta P}} \qquad [5]$$

### SOLUTION FILTRATION

The concentration of aqueous PVP and albumin solutions was 1 g·dm$^{-3}$, filtration was carried out at 1 bar and ambient temperature. In order to minimize fouling, the filtration process was carried out during 15 min. The content of PVP in the solution was estimated as a chemical oxygen demand (COD), its value was controlled using a TOC analyzer (Shimadzu, TOC-L series). The content of albumin was determined similarly to the gravimetric method for cheese whey, which also contain proteins (18). Briefly: 5 cm$^3$ of the solution was inserted into weighted ceramic crucible, the liquid was evaporated et 50 °C. Then the temperature was increased up to 100 °C, the crucible with the sample was kept during 2 h under these conditions, cooled down to room temperature and weighted again.

## RESULTS AND DISCUSSION

### PMMA CONTENT IN MEMBRANES

Modifying of membranes with PMMA causes an increase of their mass due to the polymer deposition, which can occur both on the outer surface and inside pores. The modifier precipitates from the side of active layer (i.e. the face side of the membrane) and macroporous support (bottom side). The largest amount of polymer (about 80 mass %) is precipitated, when the polymer concentration exceeds 3% (Table 1). Less sufficient deposition is realized, when the solution of minimal concentration is used several times. When the PMMA concentration is higher than 7 %, no sufficient increase of the polymer amount in the membrane was found. Moreover, the content of polymer slightly decreases, when 15% solution was used for modifying. Multiple procedure of PMMA insertion leads to a gradual growth of the modifier in the membrane (from 18 to 22%).

**Table 1.** Water test for the membranes containing different PMMA amount

| **Membrane** | **Increase of mass, %** | $d(b - b_{const})/d\tau$, **m$^3$ s$^{-1}$** | $b_0 - b_{const}$, **m$^3$ s$^{-1}$** | **Porosity** | **Pore size, nm** | |
|---|---|---|---|---|---|---|
| | | | | | Hagen Poiseuille equation | Modified Hagen-Poiseuille equation |
| Pristine | – | $6.33\times10^{-10}$ | $3.20\times10^{-9}$ | 0.62 | 33 | 45 |
| PMMA-1.1 | 14 | $1.78\times10^{-10}$ | $4.30\times10^{-9}$ | 0.50 | 24 | 34 |
| PMMA-3.1 | 17 | $1.16\times10^{-10}$ | $5.22\times10^{-9}$ | 0.46 | 21 | 30 |
| PMMA-7.1 | 23 | $2.10\times10^{-11}$ | $8.41\times10^{-10}$ | 0.49 | 63 | 88 |
| PMMA-1.3 | 15 | $5.17\times10^{-11}$ | $1.55\times10^{-9}$ | 0.38 | 36 | 54 |
| PMMA-1.7 | 78 | $4.00\times10^{-11}$ | $1.80\times10^{-9}$ | 0.34 | 37 | 57 |
| PMMA-1.10 | 79 | $5.34\times10^{-11}$ | $1.33\times10^{-9}$ | 0.28 | 42 | 65 |
| PMMA-1.15 | 72 | $2.66\times10^{-11}$ | $1.45\times10^{-9}$ | 0.30 | 18 | 28 |

## MORPHOLOGY OF MEMBRANES

Figs. 1a-d illustrate SEM images of membranes. Pristine membrane is asymmetric: the face side contains pore of different size. Pores of ≈400 nm 1 μm dominate, larger pores are also seen. Polymer globules (≈ 2.5 μm) are present on the surface of active layer. The bottom side, i.e. support, is more loosening. Here pores, a size of which is 4 μm, are dominating, voids of ≈10 μm are also observed. A thickness of the membrane is 93 μm, the active layer is about 10 of a height.

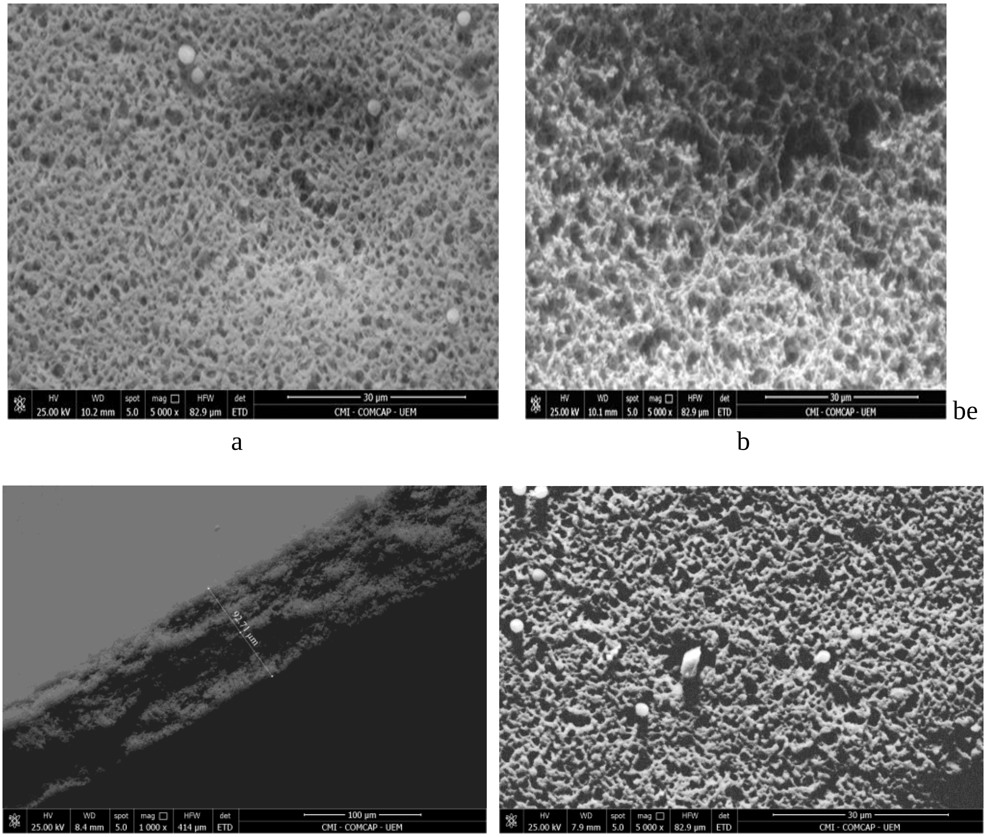

be

a b

c d

**Figure 1.** SEM images of pristine (a-c) and modified (d) membranes. Active layer (a, d), support (b) and cross-section (c) are represented.

Elongated particles of PMMA are visible on the face side of composite membrane, their thickness is 1-3 μm (indeed, no screening of polysulfone globules is observed). This type of particles can be deposited inside a support and also in the largest pores of active layer. Thinner particles (several hundred nanometers) are also seen on the outer surface of membrane, they can be localized also in active layer. The particles are entangled with "poles" forming a network with holes of micron size.

In fact, polymer form a film on the surface of face and bottom side, it can be visually observed. The film contains cracks, a sizes of which is up to ≈100 μm and even larger. It means, the pores of the modifier on the outer surface cannot affect rejection ability of the membrane. It should be noted strong adhesion of PMMA to the membrane surface, since the outer film is not removed under the influence of ultrasound.

## WATER TEST. MEMBRANE COMPRESSION. POROSITY

The PMMA particles deposited in various regions of membranes (active layer or support) provide their different rejection ability. Other modifier function is to provide rigidity of the polymer matrix. Fig. 2a illustrates the volume of water through the membranes as a function of time. Just after the beginning filtration, the $V\!-\!\tau$ curves are not linear due to the membrane compression. When the membranes are compressed, the curves are linear. It this case, the $V\!-\!\tau$ dependence is fitted with polynomial function:

$$V = a + b\tau \qquad [6]$$

Here $a$ and $b$ are the empirical parameters, linearity means the constancy of $b$ value, i.e. $b=b_{const}$. The time, when the $b$ parameter reaches constancy, characterizes the membrane resistance against compression. Figs. 2b and 2c show a change of this parameter over the time of water filtration, the $b$ values were normalized to $b_{const}$ for all membranes. Zero value of the $b\text{-}b_{const}$ parameter means the constant flux and no compression. This steady state is reached in 50 min for the pristine and PMMA-1.15 samples. In the case of PMMA-1.1 – PMMA-1.10 series, the time of steady state is shorter (25-35 min). This period also decreases for other series of membranes within the order: PMMA-1.1<PMMA-7.1<PMMA-3.1< pristine membrane. It means, the insertion of rigid polymer into membranes provides their resistance against compression.

Next parameter, which characterises the resistance of membranes against compression, is the $db/dt$ parameter (or $d(b\text{-}b_{const})/d\tau$), this is a second derivative of the $V\!-\!\tau$ function. The initial parameter of $b_0\text{-}b_{const}$ that corresponds to $\tau$=0 characterizes the degree of membrane compression. The effective data of $d(b\text{-}b_{const})/d\tau$ are given in Table 1. This parameter reduces in the order PMMA-7.1< PMMA-3.1< PMMA-1.1, this is in agreement with the modifier amount. The same phenomenon was found for the PMMA-1.1 – PMMA-1.7 series. Among the PMMA-1.7, PMMA-1.10, and PMMA-1.15 samples, the PMMA-1.10 membrane shows the largest $d(b\text{-}b_{const})/d\tau$ value. This can be caused by competitive factors: stretching of walls of membrane pores affected by rigid PMMA particles as well as partial PMMA deposition on the outer surface (stronger compactness) and filling pores with PMMA on the other hand (weaker compactness). These reasons evidently provide fluctuations of the $b_0\text{-}b_{const}$ parameter. The membranes, in which the modifier content exceeds 20%, show the strongest resistance against compression.

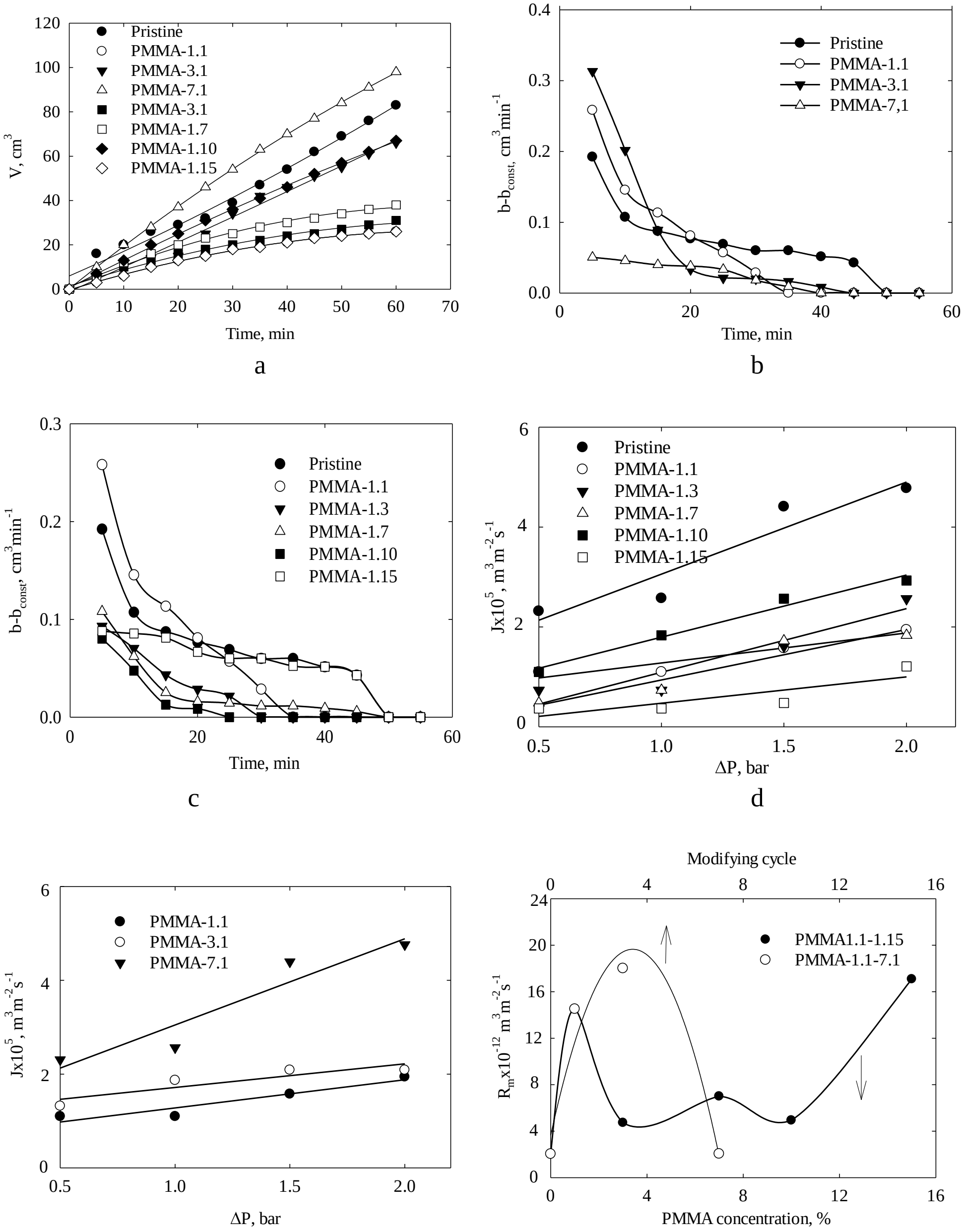

a b c d e f

**Figure 2.** Cumulative volume of water through membranes (a), the parameter of $b_0$-$b_{const}$ (b, c) as functions of filtration time; water flux as a function of pressure drop (d, e); hydrodynamic resistance of membranes obtained under different conditions.

The membranes are asymmetric, i.e. the filtration rate is determined by the pores of both active layer and support. Moreover, the thickness of these membrane constituents is not taken into consideration. It means, equations [4] and [5] give only effective values.

Figs. 2d,e illustrate the fluxes under steady state as functions of pressure drop ($\Delta P$). Linearity of the $J$-$\Delta P$ dependence means stability of the polymer modifier incorporated to the membranes. In other words, the dependence is in accordance with Darcy law. Hydrodynamic resistance is plotted in Fig. 2f *vs* concentration of the PMMA solution for modifying, and also *vs* the modifying cycle. The highest $R_m$ values comparing with pristine membrane were obtained for the PMMA-1.1, PMMA-3.1 and PMMA-1.15 samples.

Multiple modifying increases resistance (transition from PMMA-1.1 to PMMA-3.1) and then reduces it (compare PMMA-3.1 and PMMA-7.1. In the last case, the resistance is close to that for the pristine membrane. Regarding the PMMA-1.1- PMMA-1.15 series, the samples containing the smallest and highest amount of modifier demonstrate the highest $R_m$ magnitudes.

A change of the hydrodynamic resistance of modified membranes can be determined by: (I) blockage membrane pores with PMMA particles, (II) stretching pore walls, (III) screening pores of both active layer and support with modifier particle located on the outer surface. The blockage mechanism is supported by a decrease of porosity with a growth of the modifier content. As opposite to ion exchange polymers containing inorganic ion-exchanger like zirconium hydrophosphate, where modifier particles act as additional osmotic centres (19, 20) due to strong dissociation of functional groups (21), stretching the membrane pores is caused by mechanical impact of embedded particles. This mechanism is valid for the PMMA-7.1 and PMMA 1.3-1.10 samples, since the effective diameter of pores is larger comparing with pristine membrane (see Table 1). Stretching is possible due to formation of large particle under high PMMA concentration of the polymer solution. Indeed, an increase of concentration provides aggregation of macromolecules. It should be noted that no separation of PMMA into high- and low molecular weight layers occurs in chloroform (the Huggins parameter of the Flory-Huggins equation is equal to zero (22)). At last, screening outer membrane surface with the modifier particles prevails, when the solution of the highest PMMA concentration is used for modifying. The method of multiple modifying is similar to increase of polymer concentration, since early deposited PMMA is partially dissolved in chloroform and reprecipitated further.

Blockage and screening outer surface of the membrane depress water transport, stretching of pores increase water flux. Due to these competitive factors, the curves of Fig. 2f show extremes.

## FILTRATION OF PVP SOLUTION AND PROTEIN SOLUTION

Fig. 3a illustrates permeate flux through different membranes over albumin and PVP filtration. The curves show extremes: they are antibatic to those of Fig. 2f. Selectivity towards linear PVP macromolecules is 2-4%. This is due to the unwinding of the coil of macromolecules caused by pressure (17). Alternately, selectivity towards albumin strongly depends on the modifier content in membranes (Fig. 3b). The maximum is reached for the PMMA-1.3 sample (91 %), the membrane containing the lowest PVP amount (PMMA-1.1) shows minimal selectivity (≈30%). It is logically to assume precipitation of modifier particles in active layer, which is responsible for rejection. From this point of view, aggregation of PMMA macromolecules in the solution, concentration of which is higher than 3 %, limits their penetration into active layer. As a result, the particles are precipitated mainly on outer surface. During multiple insertion of the modifier, earlier deposited particles are dissolved in chloroform increasing solution concentration and enhancing aggregate formation. Thus, smaller particles are washed out active layer and redeposited in the membrane support. Aggregates can also stretch pores deteriorating rejection.

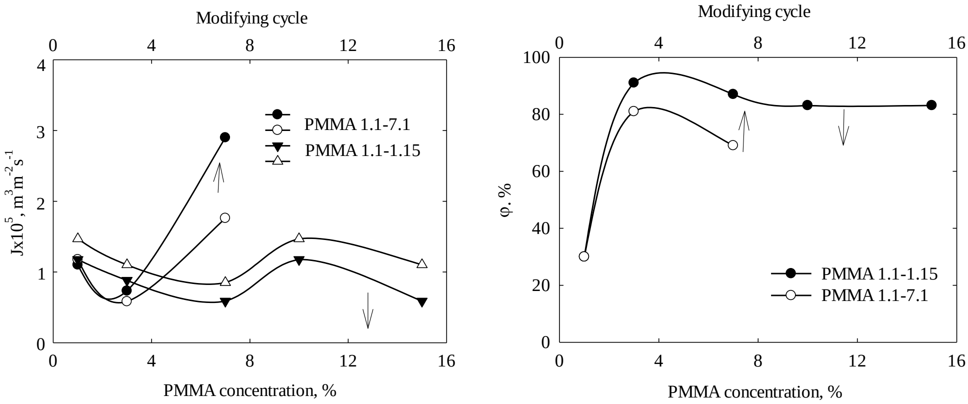

a b

**Figure 3.** Permeate flux (a) and selectivity (b) for different membranes over PVP (a, dark symbols) and albumin filtration (a: white symbols, b: dark and white symbols).

It should be noted that albumin obtained from seeds of *Moringa oleifera* contains mainly small particles. The fraction of <0,9 kDa dominates (61.58 %). Other fractions are 0.9-12.4 kDa (29.46%), 29-66 kDa (7.07 %), >66 kDa (1.89%) (14). The PMMA-1.1-1.7 and PMMA-3.1 membranes possess selectivity from 30-91%. After water evaporation, small fractions in permeate can be used as a food supplement. The concentrate of larger fractions are recommended for water treatment similarly to (15, 16).

Among commercial ultrafiltration membranes for the recovery of plant or fungi proteins or peptides, the PMMA-1.3 sample possesses an optimal combination of high selectivity and fast permeate transport (Table 2). For instance, rather high selectivity (80-90 %) was found for the membrane, which was applied to the recovery of proteins from the coconut milk. However, the rate of filtration is much slower.

**Table 2.** Membrane performance for the recovery of plant and fungi proteins

| **Membrane, membrane module** | **Source of proteins** | **Flux, m$^3$ m$^{-2}$ s$^{-1}$ (Pressure, bar)** | **Selectivity, %** | **Ref.** |
|---|---|---|---|---|
| Ceramic, cross-flow | Spent brewer yeast | $1.4\times10^{-7}$–$1.4\times10^{-5}$ | 0-70 depending on molecular mass | (7) |

**Table 2.** Continuation

| Membrane, membrane module | Source of proteins | Flux, m$^3$ m$^{-2}$ s$^{-1}$ (Pressure, bar) | Selectivity, % | Ref. |
|---|---|---|---|---|
| Polyethersulfon, polyvinylidenefluoride, cellulose, cross-flow | Potato juice | $8\times10^{-7}$–$2.7\times10^{-5}$ | No information | (8) |
| Polyethersulfone (5-300 kDa), dead-end | Coconate milk | 1×10-6 - 5×10-6 (2-4) | 80-90 | (23) |
| Polyethersulfone (100 kDa), cross-flow | Potato juice | $2.5\times10^{-6}$–$7\times10^{-5}$ (1.4) | 10 | (24) |
| Polyethersulfone (100 kDa), dead-end | Potato juice | $2\times10^{-5}$–$6\times10^{-5}$ (3) | 12-35 | (25) |
| Polyethersulfon, cellulose (30 kDa), dead-end | Spent brewer yeast | $5.5\times10^{-6}$–$4.4\times10^{-5}$ | 58-77 | (26) |
| Polysulfon, cross-flow | Soy protein isolate | No information (0.6) | 28-38 | (27) |
| PMMA-1.3 sample | Albumin from *Moringa oleifera* seeds | $1.2\times10^{-5}$(1) | 91 | This work |

## CONCLUSIONS

For simultaneous formation of rejection properties towards colloidal particles and stability against compression, asymmetric flexible polymer microfiltration membranes were modified with different amounts of rigid PMMA. Based on the SEM data and water test, the modifying mechanism was proposed: (I) blockage membrane pores with PMMA particles, (II) stretching pore walls caused by mechanical action of embedded particles, (III) screening pores of both active layer and support with modifier particle located on the outer surface. The (I) way dominates under low PMMA content in membranes (up to 20 %), this is suitable for asymmetric membranes. When the content is higher, the ways (II) and (III) prevail. From the practical point of view, the (I) direction is preferable, since it allows us control selectivity within rather large diapason. For albumin, which was obtained from the seeds of *Moringa oleifera*, selectivity of the membranes is varied from 30 to 91 %. Thus, the membranes can be applied for the purposeful separation of the large protein particles from smaller fractions, which can be used as nutritional supplements due to their better digestibility.

Since PMMA is hydrophobic polymer, additional insertion of hydrophilizing agents (hydrophilic polymers, inorganic ion-exchangers, graphene oxide) is recommended. This is a subject of further investigations.

### Acknowledgements

The work was supported by a project entitled "Development of membranes of poly (lactic acid) PLA produced in 3D printer and application for the removal of emerging contaminants" supported by an Araucaria foundation (Brazil).

## REFERENCES

1. Ang, M.B.M.Y.; Marquez, J.A.D.; Lin, C.-C.; Yang, H.-L.; Wang, Y.-S.; Huang, S.-H.; Tsai, H.-A.; Lee, K.-R. Modifying the surface of active polyamide layer in thin-film composite tubular membranes with polyethylene glycol for improved separation and antifouling. *J. Taiwan Inst. Chem. Eng.* **2022**, *131*, 104157.
2. Wang, X.; Xiao, C.; Liu, H.; Chen, M.; Xu, H.; Luo, W.; Zhang, F. Robust functionalization of underwater superoleophobic PVDF-HFP tubular nanofiber membranes and applications for continuous dye degradation and oil/water separation. *J. Membr. Sci.* **2020**, *596*, 117583.
3. Wang, X.; Zeng, B.; Chen, T.; Liu, X.; Wu, T.; Shen, H.; Luo, W.; Yuan, C.; Xu, Y.; Chen, G.; Dai, L. Polyethersulfone microfiltration membrane modified by an amphiphilic dithiolane-containing copolymer for improving anti-protein-fouling performance and rejection of nanoparticles. *Polym. Adv. Technol.* **2020**, *31* (11), 2816-2826.
4. Ng, K.S.Y.; Dunstan, D.E.; Martin, G.J.O. Influence of processing temperature on flux decline during skim milk ultrafiltration. *Sep. Purif. Technol*. **2018**, *195*, 322-331.
5. Kudelko, K.O.; Rozhdestvenska, L.M.; Verbytska, A.A.; Borysenko, Yu.V.; Borsukov, V.Z. Microfiltration membranes modified with hydrated zirconium dioxide containing carbon nanodots. *Technologies and Engineering. Chemical and Biopharmaceutical Technologies.* **2022**, (5), 43-55.
6. Zmievskii, Yu.; Rozhdestvenska, L.; Dzyazko, Yu.; Kornienko L.; Myronchuk, V.; Bildukevich, A.; Ukrainetz, A. Organic-inorganic materials for baromembrane separation. *Springer Proc. Phys.* **2017**, *196*, 675–686.
7. Marson, G.V.; Lacour, S.; Hubinger, M.D.; Belleville, M.-P. Serial fractionation of spent brewer's yeast protein hydrolysate by ultrafiltration: A peptide-rich product with low RNA content. *J. Food Eng*. **2022**, *312*, 110737.
8. Zwijnenberg, H.J.; Kemperman, A.J.B.; Boerrigter, M.B.; Lotz, M.; Dijksterhuis, J.F.; Poulsen, P. E.; Koops, G.-H. Native protein recovery from potato fruit juice by ultrafiltration. *Desalination.* **2002**, *144* (1-3), 331-334.
9. Rozhdestvenska, L.M.; V’yunov, O.I.; Ponomarova, L.N.; Bilduykevich, A.V.; Plisko, T.V.; Zmievskii, Y.G.; Ivchenko, V.D. Modification of ultrafiltration polymeric membranes with dispersed oxide nanoparticles. *Vopr. Khim. Khim. Tekhnol.* **2020**, *3*, 154-161.
10. Adeyeye, E.I.; Asaolu, S.S.; Aluko, A. O. Amino acid composition of two masticatory nuts (Cola acuminata and Garcinia kola) and a snack nut (Anacardium occidentale). *Int. J. Food Sci. Nutr.* **2007**, *58* (4), 241-249
11. Aderinola, T.A.; Lawal, O.E.; Oluwajuyitan, T.D. Assessment of nutritional and microbiological properties of biscuit supplemented with Moringa oleifera seed protein concentrate. *Journal of Food Engineering and Technology.* **2020**, *9* (1), 22-29.
12. Li, L.; Liu, Y.; Zou, X.; He, J.; Xu, X.; Zhou, G.; Li, C. In vitro protein digestibility of pork products is affected by the method of processing. *Food Res. Int.* **2017**, *82*, 88-94.
13. Byars, J.A.; Singh, M.; Kenar, J.A.; Felker, F.C.; Winkler-Moser, J.K. Effect of particle size and processing method on starch and protein digestibility of navy bean flour. *Cereal Chem*. **2021**, *98* (4), 829-839.
14. Baptista, A.T.A.; Silva, M.O.; Gomes, R.A.; Bergamasco, R.; Vieira, M.F.; Vieira, A.M.S. Protein fractionation of seeds of Moringa oleifera lam and its application in superficial water treatment. *Sep. Purif. Technol.* **2017**, *180*, 114–124.
15. Reck, I.M.; Paixão, R.M.; Baptista, A.T.A.; Bergamasco, R.; Vieira, M.F.; Vieira, A.M.S. Application of magnetic coagulant based on fractionated protein of *Moringa oleifera* Lam. seeds for aqueous solutions treatment containing synthetic dyes. *Environ. Sci. Pollut. Res*. **2020**, *27*, 12192–12201.
16. Reck, I.M.; Baptista, A.T.A.; Paixão, R.M.; Bergamasco, R.; Vieira, M.F.; Vieira, A.M.S. Protein fractionation of Moringa oleifera Lam. seeds and functionalization with magnetic particles for the

treatment of reactive black 5 solution. *The Canadian Journal of Chemical Engineering*. **2019**, *97* (8), 2309-2317.

17. Mulder, M. *Basic principles of membrane technology*; Kluwer Academic Publisher, Dordrecht, Boston, London, 1996; pp 564.
18. Marshall, R. *Standards Methods for the examination of dairy products, 16th edition*; American Public Health Association, Washington, 1992; pp 546.
19. Dzyazko, Y.S.; Ponomareva, L.N.; Volfkovich, Y.M.; Sosenkin, V.E. Effect of the porous structure of polymer on the kinetics of $Ni^{2+}$ exchange on hybrid inorganic-organic ionites. *Russ. J. Phys. Chem. A.* **2012**, *86* (6), 913–919.
20. Dzyazko, Y.S.; Ponomareva, L.N. ; Volfkovich, Y.M.; Sosenkin, V.E.; Belyakov, V.N. Conducting properties of a gel ionite modified with zirconium hydrophosphate nanoparticles. *Russ. J. Electrochem*. **2013**, *49*(3), 209–215.
21. Dzyazko, Y.S.; Trachevskii, V.V.; Rozhdestvenskaya, L.M.; Vasilyuk, S.L.; Belyakov, V.N. Interaction of sorbed Ni(II) ions with amorphous zirconium hydrogen phosphate. *Russ. J. Phys. Chem. A*. **2013**, *87*(5), 840–845.
22. Bellenger, V.; Kaltenecker-CommerCon, J.; Verdu, J. Interactions of solvents with poly(methyl methacrylate). *Polymer*. **1997**, *38*(16), 41785-4184.
23. Vijayasanthi, J.; Adsare, S.R.; Lamdande, A.G.; Naik, A.; Raghavarao, K. S. M. S., Prabhakar G. Recovery of proteins from coconut milk whey employing ultrafiltration and spray drying. *J. Food Sci. Technol*. **2020**, *57*(1):22–31.
24. Schmidtm J.M.; Greve-Poulsen, M.; Damgaard, H.; Hammershøj, M., Larsen, L.B. Effect of membrane material on the separation of proteins and polyphenol oxidase in ultrafiltration of potato fruit juice. *Food Bioprocess Technol.* **2016**, *9*, 822–829.
25. Zhu, Z.; Yuan, F.; Xu, Z.; Wang, W.; Di, X.; Barba, F.J., Shen, W.; Koubaa, M. Stirring-assisted dead-end ultrafiltration for protein and polyphenol recovery from purple sweet potato juices: Filtration behavior investigation and HPLC-DAD-ESI-MS2 profiling. *Sep. Purif. Technol.* **2016**, *169*, 25–32.
26. Marson, G.B.; Pereira, D.T.V.; Costa Machado, M.T.; Martínez, J.; Belleville, M.-P.; Dupas Hubinger, M. Ultrafiltration performance of spent brewer's yeast protein hydrolysate: Impact of pH and membrane material on fouling. *J. Food Eng*. **2021**, *302*, 110569.
27. Ranamukhaarachchi, S.; Meissner, L., Moresoli, C. Production of antioxidant soy protein hydrolysates by sequential ultrafiltration and nanofiltration. *J. Membrane Sci*. **2013**, *429*, 81-87.

APTEFF, Vol. 54, 1-335 (2023)
DOI: https://doi.org/10.2298/APT2354325D

UDC: 577.15:577.86]:628.4.042
BIBLID: 1450-7188 (2023) 54, 325-335

Original research paper

# *Bacillus* spp. ENZYMATIC ACTIVITY TO SUPPORT CIRCULAR ECONOMY

*Tatjana D. DUJKOVIĆ*, Ivana S. PAJČIN, Vanja R. VLAJKOV, Jovana A. GRAHOVAC*

*University of Novi Sad, Faculty of Technology Novi Sad, Bulevar cara Lazara 1, 21000 Novi Sad, Serbia*

**Received: 01 August 2023** **Revised: 14 September 2023** **Accepted: 18 September 2023**

*Agricultural and industrial waste represents the most abundant renewable resource in the biosphere and is readily available in substantial quantities. Recently, there has been a growing focus on harnessing the potential of these types of waste as raw materials for producing value-added products, such as microbial enzymes, using solid-state or submerged fermentation systems. Among all the bacterial genera utilized in the production of industrially important enzymes, the Bacillus genus stands out as the most extensively employed for this purpose. In this study, the production of various enzymes such as protease, pectinase, cellulase, xylanase, lipase, and gelatinase was evaluated using the different Bacillus strains isolated from vegetables' rhizosphere. The growth zones and halos were observed to determine production of the following enzymes: cellulases, proteases, pectinases, xylanases, gelatinases and lipases, confirming the breakdown of complex substrates in the medium. Bacillus Pap 3 exhibited the highest EAI (enzymatic activity index) value (4.00) for pectinase activity, indicating its remarkable extracellular level of pectinase performance. The highest enzymatic activity in terms of halo zone diameters was achieved in the case of cellulases and xylanases production by the isolates Mah 1a and Mah 1b. Further research would be directed towards the production of the tested enzymes by Bacillus spp. on the waste streams of food and agroindustry, but also towards the utilization of the proven enzymatic activity to obtain other microbial value-added products to develop viable bioprocess solutions usable in the circular economy context.*

**Keywords**: cellulases, xylanases, proteases/gelatinases, pectinases, lipases.

## INTRODUCTION

Recently, the concept of a 'circular economy' involving the utilization of organic waste from one industry as a raw material for another, has gained much popularity. This approach is based on the principle of sustainable development known as the '5Rs' (reduce, recycle, reuse, recover, and restore) and replaces the traditional linear economy (make-use-throw) with a more efficient circular one (1). With the advent of industrialization and modernization, the food and agro-industrial sectors have undergone significant transformations, resulting in a substantial increase in the production of agro-industrial, mostly food waste (2). Considering that disposal of this waste causes serious health and environmental problems, great efforts have been focused on harnessing the potential of these types of waste as raw materials for production of the value-added products, such as microbial enzymes (3).

Agricultural waste is generated in millions of tons annually worldwide and its inadequate management and disposal have detrimental effects on the environment, leading to ecosystem damage. Agro-waste as lignocellulosic biomass is mostly composed of cellulose as a backbone, with hemicellulose and lignin as other vital carbonaceous fractions (2). The use of microorganisms or microbial enzymes for pre-treating lignocellulosic materials has

---

* Corresponding author: Tatjana D. DUJKOVIĆ, University of Novi Sad, Faculty of Technology Novi Sad, Bulevar cara Lazara 1, 21000 Novi Sad, Serbia. E-mail: tatjana.dujkovic@uns.ac.rs

attracted significant interest from the industry primarily due to the promising outcomes of applying lignocellulosic biomass in the production of bioethanol through enzymatic hydrolysis. This sustainable approach presents an alternative to fossil fuels, making it a compelling option for the industry to explore further (4). Besides this utilization of lignocellulosic biomass, these polymers have been investigated as prospective substrates for the production of many value-added products such as additives, organic acids, pesticides, enzymes, pharmaceuticals, fertilizers, and detergents among others (5 - 8).

Fruit and vegetable waste is generated at various stages of the food supply chain spanning from the farm to the consumer's plate, including production, processing, packaging, handling, storage, and transportation. Moreover, this waste frequently arises as food products do not meet market requirements due to microbial attack, discoloration, and a number of biochemical reactions which involve enzymes, antioxidants, phenolic chemicals, and oxidation (9). Considering that pectin is one of the major polysaccharides in the plant cell wall, pectinases have a significant role in the treatment of fruit and vegetable wastes (10).

Meat, poultry, and egg processing industry represent a huge segment of the food chain (2). Meat industry waste generally comprising feathers, hair, skin, horn, hooves, blood, bones, etc. could cause severe environmental impacts if released untreated into the environment. Hence, these types of waste are treated by the different treatment approaches, such as physicochemical treatment, biological treatment, advanced oxidation, or combined processes. Taking into account that this waste is rich in proteins and organic matter (carbon, nitrogen, and phosphorus), it could be used as a substrate for the production of valuable microbial products, with the necessity of enzymatic activity by the applied microorganisms to break down and utilize the aforementioned complex and mostly proteinaceous substrates (11). Previous research has demonstrated the practicality of utilizing slaughterhouse waste for various purposes, such as animal fodder production (12), biogas production (13), enzyme production (14), fertilizers production (15), etc.

The edible oil industry generates waste at different stages of the refining process, such as degumming, neutralization, bleaching, deodorization, oxidative and hydrolytic rancidity. Hydrolytic rancidity occurs as a result of lipid oxidation, aging, moisture, oxygen presence, and the effluent discharged from the industry contains significant amounts of fatty acids, carbohydrates, and proteins (16). Waste cooking oil is an oil-based substance that arises from repeated deep-oil/fat frying processes, rendering the oil/fat unsuitable for human consumption. This unsuitability is attributed to the formation of polar compounds, such as free short-chain fatty acids, mono- and di-glycerides, aldehydes, ketones, polymers, cyclic, and aromatic compounds. Industrial edible oil waste is a low-cost substrate for microbial lipid synthesis that can be produced through co-fermentation with food waste, with the necessity to apply lipase treatment for release of fatty acids (17).

Enzymes are naturally produced by all living organisms, but microbial enzymes offer several advantages over those derived from plant or animal sources. Microbial enzymes stand out due to their diverse range of catalytic activities, cost-effectiveness, and relatively higher stability, followed by wider availability, less production resource requirements and non-competitivity with the food chain. A wide variety of microorganisms, including bacteria, yeast, and fungi, are capable of producing different types of enzymes, such as proteases, lipases, and more, which hold significant biotechnological interest in various industries like food processing, detergent manufacturing, textile industry, pharmaceuticals production, medical therapy, and others (18). Among all the bacterial genera utilized in the

DOI: https://doi.org/10.2298/APT2354325D BIBLID: 1450-7188 (2023) 54, 325-335

production of industrially important enzymes, the *Bacillus* genus stands out as the most widely utilized for this purpose. *Bacillus* species are highly valued for their contribution as sources of antibiotics, enzymes, insecticides, and vitamins (19). They have been the primary workhorse among industrial microorganisms, playing crucial roles in industrial biotechnology. *Bacillus* strains are highly suitable for industrial applications due to their rapid growth rates, leading to shorter fermentation cycles, their ability to secrete proteins into the extracellular medium, and their GRAS (Generally Recognized As Safe) status by the United States Food and Drug Administration, such as *Bacillus subtilis* and *Bacillus licheniformis* (20). In this study, the possibility of production enzymes such as cellulases, xylanases, pectinases, proteases, gelatinases and lipases by different *Bacillus* isolates was investigated, to explore the feasibility of biotechnological enzyme production using different carbohydrate, protein, and lipid wastes as substrates.

## EXPERIMENTAL

### MICROORGANISMS AND CULTIVATION CONDITIONS

Microorganisms used in this study were the following *Bacillus* strains: *Bacillus* sp. Mah 1a, *Bacillus* sp. Mah 1b, *Bacillus* sp. Pap 3 and *Bacillus* sp. Kup 4, which were previously isolated from the rhizosphere of green beans, pepper, and cabbage, respectively, by using the selective medium HiCrome *Bacillus* agar (HiMedia Laboratories, India). The following isolation procedure was applied: 1 g of soil sample was resuspended in 9 mL of sterile saline, subjected to heat treatment (100 °C, 8 min) in water bath (JSWB-30T, JSR, Korea), serially diluted (10 and 100 fold) and placed on a surface of the selective medium (100 μL), followed by incubation at 28 °C for 48 h and selection of single colonies. The selection of colonies followed by the incubation procedure was repeated until visually pure cultures were obtained. The isolated strains have been kept on nutrient agar slant (4 °C) in fridge.

Cultivation of the *Bacillus* isolates was carried out in nutrient broth (HiMedia Laboratories, India) on a rotary shaker (KS 4000i control, Ika® Werke, Germany) at 28°C and 170 rpm, under spontaneous aeration for 48 h to reach the exponential growth phase. This inoculum was used for inoculation of the solid media used for enzymatic activity screening, as described below.

### SCREENING OF ENZYMATIC ACTIVITY

Enzyme activity screening of *Bacillus* spp. was performed by cultivating isolates on semi-solid media containing substrates for targeted enzyme activity. Mediums were sterilized by autoclaving (121 °C, 2.1 bar, 20 min) and then poured into Petri plates. After inoculation of the prepared plates using 1 μL of the cultivation broth, incubation was carried out at 28 °C for 7 days. The evaluation of the enzymatic activity was performed based on the appearance of the biomass growth and clear (halo) zone around it, with or without adding an appropriate solution of reagents/indicators for halo zones visualization.

The enzymatic activity index was calculated according to the following equation:

$$EAI = \frac{diameter\ of\ halo\ zone}{diameter\ of\ biomass\ growth} \qquad [1]$$

### PROTEASE ACTIVITY SCREENING

The proteolytic activity of the *Bacillus* isolates was assayed using the modified skim milk agar. The medium composition included (g/L): skim milk 28, tryptone 5, yeast extract 2.5, glucose 1, agar 15. The pH value of the medium was adjusted to 7.00±0.02 before adding agar (21).

### PECTINASE ACTIVITY SCREENING

The pectinase activity of the *Bacillus* isolates was assayed using the medium of the following composition (g/L): $NaNO_3$ 1, KCl 1, $K_2HPO_4$ 1, $MgSO_4\cdot 7H_2O$ 1, yeast extract 0.5, pectin 10, agar 15. The pH value of the medium was adjusted to 7.00 ± 0.02 before adding agar (22).

### CELLULASE AND XYLANASE ACTIVITY SCREENING

The cellulase and xylanase activity of the *Bacillus* isolates was assayed using the media of the same composition, except the substrate: $NaNO_3$ 1 g/L, KCl 1 g/L, $K_2HPO_4$ 1 g/L, $MgSO_4\cdot 1,_2O$ 1 g/L, yeast extract 0.5 g/L, glucose 1 g/L, CMC (carboxymethyl cellulose) or xylan 5 g/L, agar 17 g/L. For better visualization of the clear zones around microbial growth, after incubation the Petri dishes were poured over using the Congo red solution (0.5% (w/v), 15 min) (21).

### LIPASE ACTIVITY SCREENING

The lipase activity of the *Bacillus* isolates was assayed using the following medium (g/L): $MgSO_4\cdot 7H_2O$ 1.24, yeast extract 3, peptone 5, tributyrin 2.5, $CaCl_2$ 0.28, agar 20 (23).

### GELATINASE ACTIVITY SCREENING

For determination of gelatinase activity of the *Bacillus* isolates 20 mL of 8% gelatin solution and 250 mL of nutrient agar (HiMedia Laboratories, India) were prepared. They were sterilized separately in the autoclave at a temperature of 121 °C and a pressure of 2.1 bar (20 min). These two solutions were then mixed and added to Petri plates. After incubation, the media were poured using the Frazier reagent (15% (w/v) $HgCl_2$ in 2 N HCl) for better visualization of the clear zones around microbial growth (24).

### EXPERIMENTAL DATA ANALYSIS

The statistical data analysis was performed using ANOVA (analysis of variance) and Duncan's multiple range test in the Statistica 13.2 software (Dell, TX, USA), with all tests performed at the significance level of 0.05 (95%).

## RESULTS AND DISCUSSION

Cultivation of the selected *Bacillus* isolates was performed to determine the potential of these bacteria for enzyme production. The production of various enzymes such as proteases, pectinases, cellulases, xylanases, lipases, and gelatinases was evaluated using the different substrates. Figures 1, 2, and 3 illustrate the results of enzymatic activity screening, providing information on the diameters of the halo zones around the colonies and the growth diameter on media containing the target enzyme substrate. Additionally, the extracellular enzymatic activity index (EAI) is presented, representing the ratio of the enzymatic activity directly associated with the production of extracellular enzymes. Both the growth and halo zones were observed on each of the substrates for determining the production of the following enzymes: cellulases, proteases, pectinases, xylanases, and gelatinases, which confirmed the decomposition of the complex substrates in the media. The difference was observed in the case of the lipid substrate, i.e. lipase activity, where only *Bacillus* spp. growth occurred without visible halo zones.

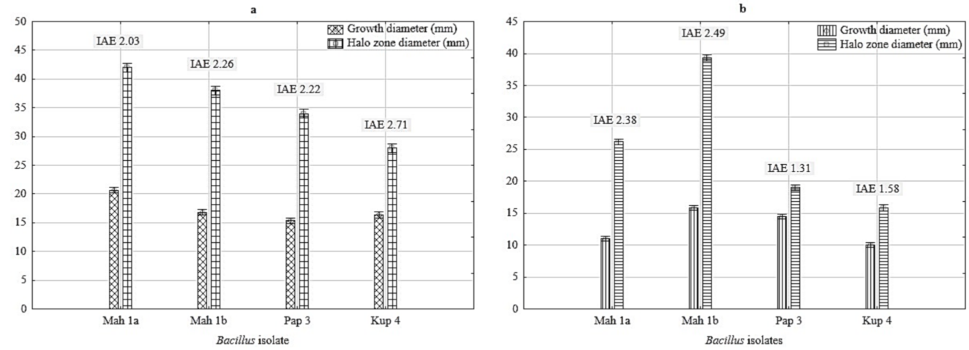

**Figure 1.** Screening of cellulase (a) and xylanase (b) activity of the *Bacillus* spp. isolates

Cellulases hydrolyze the 1,4-β-D-glycosidic linkages in cellulose and play a crucial role in nature by recycling the most abundant component of plant biomass (4). Cellulases consist of a group of three enzymes (β-glucosidases, endoglucanases, and exoglucanases) that synergistically hydrolyze cellulose into soluble sugars and glucose (25). According to Gaur and Tiwari, halo zones greater than 10 mm in diameter indicate significant cellulolytic activity, consequently placing *Bacillus* isolates used in this study in the group of highly efficient cellulase producers with a hydrolysis zone diameter ranging from 28 to 42 mm (25). The highest cellulase activity was observed using the strains *Bacillus* sp. Mah 1a, with the halo zone diameter over 40 mm (Figure 1a). Balla et al. have isolated 398 strains from various environments, where 26 of them, belonging to *Bacillus* genus, expressed cellulase activity, with the EAI varying from 0.34 to 5.2, where the strains used in this study fall in the middle of the aforementioned range in terms of the extracellular cellulase activity with EAI values around 2 (4). Previous studies successfully proved the possibility of cellulase production by *Bacillus* isolates on waste office paper (26), coconut coir waste (27), and wheat and rice straw (28).

Considering that xylan covers 33% of the total lignocellulosic biomass on a global level, xylanases are one of the key enzymes for the conversion of lignocellulose into fermentable sugars (29). *Bacillus pumilus* and *Bacillus subtilis* were identified as good xylanase producers in the study by Ammoneh et al. (30). Among 41 isolates of *Bacillus subtilis* in the study by Ariaeenejad et al. (31) clear zones larger than 35 mm was observed in 28 of them and were selected for further studies. In the study by Tamariz-Angeles et al. , 12 strains identified as members of the *Bacillus licheniformis* species and two *Bacillus subtilis* strains have shown enzymatic activity with clear zones of diameters up to 5 mm (32). The possibility of production of xylanases on agricultural waste was investigated in a study conducted by Irdawaty et al. in which the straw-based substrate showed the highest average of enzymatic activity (33). High xylanase activity was also proved on oat flour, wheat bran, and corn cobs (34). In the present study diameters of halo zones were 26.16, 39.33, 19, and 15.83 for *Bacillus* sp. Mah 1a, *Bacillus* sp. Mah 1b, *Bacillus* sp. Pap 3 and *Bacillus* sp. Kup 4, respectively (Figure 1b).

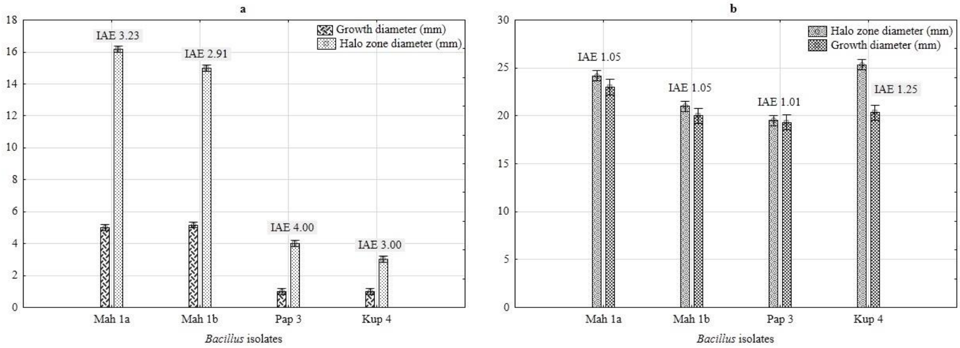

**Figure 2.** Screening of pectinase (a) and protease (b) activity of the *Bacillus* spp. isolates

Pectinases hydrolyze pectic compounds linked by α-1,4-glycosidic bonds and esterified with methyl groups (35). The pectinolytic activity of these enzymes plays a significant role in decomposing plant material, especially in the case of fruit and vegetable residues rich in pectin. By breaking down pectic substances pectinase facilitate the recycling of carbon compounds in the biosphere, contributing to the natural nutrient cycling process (36). In a study by Oumer et al. *Bacillus* isolates derived from coffee pulp demonstrated extracellular pectinase activity index values ranging from 2.0 to 4.7 (37). Out of 65 isolates from the rhizosphere of the medical plant *Andrographis paniculata* Nees, the highest pectinolytic activity was achieved by *Bacillus* isolates with a hydrolysis zone diameter ranging from 25 to 29 mm (38). According to Kavuthodi and Sebastian pineapple stems can be successfully employed in the production of pectinase using *Bacillus subtilis* BKDS1 (10). The usage of cassava wastes as a substrate for pectinase production by *Bacillus* isolate and optimization of cultivation conditions was investigated in the study by Mukesh Kumar et al. (39). Investigated strains *Bacillus* sp. Mah 1a, *Bacillus* sp. Mah 1b, *Bacillus* sp. Pap 3, and *Bacillus* sp. Kup 4 showed a high pectinase activity index with values 3.23, 2.91, 4, and 3 respectively (Figure 2a). The highest value of the halo zone was observed for the isolate *Bacillus* sp. Mah 1a (17 mm).

Proteases are enzymes that hydrolyze peptide bonds between amino acid groups of proteins, offering significant potential for applications in various industries such as detergent, leather, food, pharmaceuticals, and beverages (40). Protease activity was evaluated in the study by Suberu et al., where among 48 *Bacillus* isolates from the soil, 10 were identified as potential protease producers with a diameter of hydrolysis zone between 33 and 49 mm (20). *Bacillus subtilis* S1 and *Bacillus amyloliquefaciens* KSM12 were selected as the best protease producers based on the halo zones that were 22 and 19 mm (41). Proteases play a significant role in the lysis of the cell wall of phytopathogenic fungi because chitin and/or fibrils of β-glucan are embedded into the protein matrix (42). In the study conducted by Khan et al., proteases production by *Bacillus* species was investigated as an additional biocontrol mechanism supporting the suppression of *F. oxysporum* f. sp. c*onglutinans*, *F. oxysporum* f. sp. *matthioli*, and *F. solani* (43). It was determined that *Bacillus* species have the ability to produce proteases on various wastes such as *Imperata cylindrica* grass and potato peel (44), slaughterhouse effluent (11), the groundnut oil cake and cabbage leaf (45), fish waste homogenate (46), etc. In the present study the highest extracellular protease activity was observed for the isolate *Bacillus* sp. Kup 4. with EAI value 1.25 (Figure 2b).

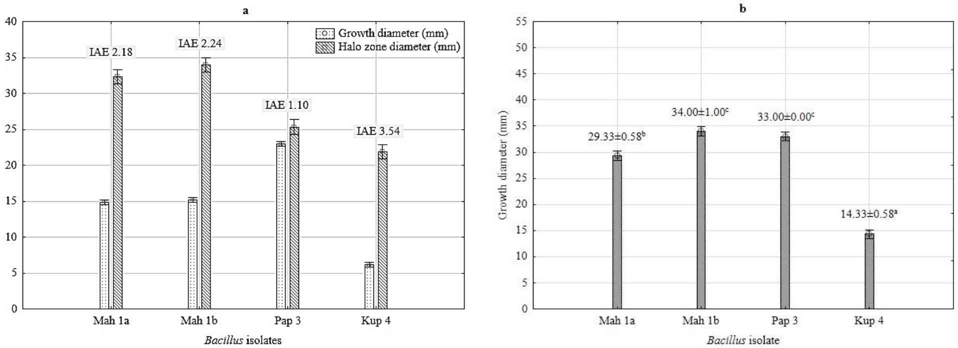

*Different letter designations next to the growth diameter indicate different homogenous groups of isolates concerning enzymatic activity as the dependent variable.

**Figure 3.** Screening of gelatinase (a) and lipase (b) activity of the *Bacillus* spp. isolates

Gelatinase is one type of diverse group of proteolytic enzymes, an extracellular metallo-endopeptidase or metalloproteinase which can hydrolyze gelatin and other compounds such as pheromone, collagen, casein, and fibrinogen (47). According to Joseph et al. (18), optimized conditions for maximum production of gelatinases by *Bacillus* species are pH 7, temperature 40 °C, and incubation time 48 h. In the study published by Mekonnen et al., gelatinases were produced by *Bacillus* isolate in solid-state fermentation using wheat bran as a substrate (48). In the present study, the gelatinase enzymatic activity index ranged from 1.10 to 3.54, with the best result achieved by *Bacillus* sp. Kup 4 (Figure 3a).

Lipases catalyze the hydrolysis of ester bonds in fats and oils into glycerol and free fatty acids at the oil-water interface. These enzymes are commonly used in the food industry, pulp and paper processes, the medical field, and as cleaning agents (23). *Bacillus licheniformis* A7 (GenBank accesion number: KC310458) was determined to be the best lipase producer on media with waste frying oil in a concentration of 40 mL/L (49). Mazhar et al. have investigated the ability of *Bacillus* isolates to produce lipases on low-cost agro-industrial waste such as soybean meal, sunflower meal, wheat bran, oat bran, rice bran, and sugar cane bagasse, as well as peels of different fruits, including banana, orange, watermelon, and melon as a carbon source (50). Although in this work clear zones on the lipid substrate were not observed, a significant number of papers prove the lipid activity of *Bacillus* species and their ability to survive on oil-contaminated soil (23, 51, 52). Figure 3b shows the growth diameters of *Bacillus* spp. isolates on lipid substrate, where the highest growth diameter was observed in the case of the isolate *Bacillus* sp. Mah 1b. Using Duncan's test of multiple comparisons, isolates of *Bacillus* sp. Mah 1b and *Bacillus* sp. Pap 3 are included in the same homogenous group of higher lipase activity, while the remaining two isolates differ significantly in terms of lipolytic activity.

In this study, the highest EAI value (4.00), indicating the highest level of extracellular pectinase activity, was achieved by *Bacillus* sp. Pap 3. Conversely, the lowest extracellular enzymatic activity was observed for protease activity in the same isolate. The highest overall enzymatic activity was observed in cellulases and xylanases. *Bacillus* sp. Mah 1a and *Bacillus* sp. Mah 1b exhibited the largest halo zone diameters and displayed the highest enzymatic activity for cellulases and xylanases, as well as for other tested enzymes, except for protease activity. In the case of protease activity, *Bacillus* sp. Kup 4 demonstrated the highest enzymatic activity.

## CONCLUSION

The results of this study have shown a significant potential of the isolated *Bacillus* strains in the production of various enzymes, which further enables their cultivation on diverse agro-industrial waste materials. Growth zones and halos were observed for each substrate to determine the production of the following enzymes: cellulases, proteases, pectinases, xylanases and gelatinases, confirming the breakdown of complex substrates in the medium. Comparing to the available literature data, *Bacillus* strains used in this study show moderate to high level of enzymatic activity, with additional advantage considering the multienzymatic activity for each investigated strain. The following steps will include screening of the enzymatic activity of the isolated strains using various waste substrates to define their potential to be used in treatment of agro-industrial effluents to obtain a wide range of microbial value-added products. This effort aligns with the broader goal of promoting the principles of the circular economy.

## Acknowledgements

This study was supported by the Autonomous Province of Vojvodina - Provincial Secretariat for Higher Education and Scientific Research - project 142-451-3187/2022-01/01 “Development of industrial symbiosis in the AP Vojvodina through valorization of fruit processing by-products using green technologies”.

## REFERENCES

1. Rojas, L. F.; Zapata, P.; Ruiz-Tirado, L. Agro-industrial waste enzymes: Perspectives in circular economy. *Current Opinion in Green and Sustainable Chemistry*, **2022**, *34*, 100585.
2. Sharma, V.; Tsai, M. L.; Nargotra, P.; Chen, C. W.; Kuo, C. H.; Sun, P. P.; Dong, C. D. Agro-industrial food waste as a low-cost substrate for sustainable production of industrial enzymes: a critical review. *Catalysts*, **2022**, *12* (11), 1373.

3. Devi, S.; Dwivedi, D.; Bhatt, A. K. Utilization of Agroresidues for the Production of Xylanase by *Bacillus safensis* XPS7 and Optimization of Production Parameters. *Fermentation*, **2022**, *8* (5), 221.
4. Balla, A.; Silini, A.; Cherif-Silini, H.; Bouket, A. C.; Boudechicha, A.; Luptakova, L.; Alenezi, F. N.; Belbahri, L. Screening of Cellulolytic Bacteria from Various Ecosystems and Their Cellulases Production under Multi-Stress Conditions. *Catalysts*, **2022**, *12*, 769.
5. Nargotra, P.; Sharma, V.; Sharma, S.; Kapoor, N.; Bajaj, B. K. Development of consolidated bioprocess for biofuel-ethanol production from ultrasound-assisted deep eutectic solvent pretreated *Parthenium hysterophorus* biomass. *Biomass Conversion and Biorefinery*, **2020**, 1-16.
6. Sharma, S.; Sharma, V.; Nargotra, P.; Bajaj, B.K. Bioprocess Development for Production of a Process-Apt Xylanase with Multifaceted Application Potential for a Range of Industrial Processes. *SN Appl. Sci.* **2020**, *2*, 739.
7. El-Shishtawy, R.M.; Mohamed, S.A.; Asiri, A.M.; Abu-Bakr, M.G.; Ibrahim, I.H.; Al-Talhi, H.A. Saccharification and hydrolytic enzyme production of alkali pre-treated wheat bran by *Trichoderma virens* under solid state fermentation. *BMC Biotech.* **2015**, *15* (1), 37.
8. Gunny, A. A. N.; Arbain, D.; Nashef, E. M.; Jamal, P. Applicability evaluation of Deep Eutectic Solvents-Cellulase system for lignocellulose hydrolysis. *Bioresource technology* **2015**, *181*, 297-302.
9. Ji, C.; Kong, C. X.; Mei, Z. L.; & Li, J. A review of the anaerobic digestion of fruit and vegetable waste. *Applied biochemistry and biotechnology*, **2017**, *183* (3), 906-922.
10. Kavuthodi, B.; Sebastian, D. Biotechnological valorization of pineapple stem for pectinase production by Bacillus subtilis BKDS1: Media formulation and statistical optimization for submerged fermentation. *Biocatalysis and agricultural biotechnology*, **2018**, *16*, 715-722.
11. Ramakodi, M. P.; Santhosh, N.; Pragadeesh, T.; Mohan, S. V.; Basha, S. Production of protease enzyme from slaughterhouse effluent: an approach to generate value-added products from waste. *Bioresource Technology Reports*, **2020**, *12*, 100552.
12. Gómez-Juárez, C.; Castellanos, R.; Ponce-Noyola, T.; Calderón, V.; Figueroa, J. Protein recovery from slaughterhouse wastes. *Bioresource Technology*, **1999**, *70* (2), 129-133.
13. Afazeli, H.; Jafari, A.; Rafiee, S.; Nosrati, M. An investigation of biogas production potential from livestock and slaughterhouse wastes. *Renewable and Sustainable Energy Reviews*, **2014**, *34*, 380-386.
14. Ben Rebah, F.; Miled, N. Fish processing wastes for microbial enzyme production: a review. *3 Biotech.* **2013**, *3*, 255-265.
15. Zwetsloot, M. J.; Lehmann, J.; Solomon, D. Recycling slaughterhouse waste into fertilizer: how do pyrolysis temperature and biomass additions affect phosphorus availability and chemistry?. *Journal of the Science of Food and Agriculture*, **2015**, *95* (2), 281-288.
16. Okino-Delgado, C.H.; Prado, D.Z.D.; Facanali, R.; Marques, M.M.O.; Nascimento, A.S.; Fernandes, C.J.D.C.; Zambuzzi W.F.; Fleuri, L. F. Bioremediation of cooking oil waste using lipases from wastes. *PLoS One*, **2017**, *12* (10), e0186246.
17. Sharma, P.; Gaur, V. K.; Kim, S. H.; Pandey, A. Microbial strategies for bio-transforming food waste into resources. *Bioresource technology*, **2020**, *299*, 122580.
18. Joseph, J.; Sasidharan, H.; Chithira, O. S. Isolation, production and characterisation of novel gelatinase enzyme from *Bacillus* spp. *Int. J. Sci. Res. in Biological Sciences*, **2018.** Vol, *5* (6).
19. Dave, B. R.; Parmar, P.; Sudhir, A.; Panchal, K.; Subramanian, R. B. Optimization of process parameters for cellulase production by *Bacillus licheniformis* MTCC 429 using RSM and molecular characterization of cellulase gene. *J Bioprocess Biotech.* **2015**, *5* (3), 1000212.
20. Suberu, Y.; Akande, I.; Samuel, T.; Lawal, A.; Olaniran, A. Optimization of Protease Production in Indigenous Bacillus Species Isolated from Soil Samples in Lagos, Nigeria Using Response Surface Methodology. *Biocatal. Agric. Biotechnol.* **2019**, *18*, 101011.

21. Syed-Ab-Rahman, S. F.; Carvalhais, L. C.; Chua, E.; Xiao, Y.; Wass, T. J.; Schenk, P. M. Identification of soil bacterial isolates suppressing different *Phytophthora* spp. and promoting plant growth. *Frontiers in Plant Science*, **2018**, *9*, 1502.
22. Mohandas, A.; Raveendran, S.; Parameswaran, B.; Abraham, A.; Athira, R. S.; Mathew, A. K.; Pandey, A. Production of pectinase from *Bacillus sonorensis* MPTD1. *Food technology and biotechnology*, **2018**, *56*(1), 110.
23. Lee, L. P.; Karbul, H. M.; Citartan, M.; Gopinath, S. C.; Lakshmipriya, T.; Tang, T. H. Lipase-secreting *Bacillus* species in an oil-contaminated habitat: promising strains to alleviate oil pollution. *BioMed research international*, **2015**, *2015*, 820575.
24. Bose, A.; Chawdhary, V.; Keharia, H.; Subramanian, R. B. Production and characterization of a solvent-tolerant protease from a novel marine isolate *Bacillus tequilensis* P15. *Annals of microbiology*, **2014**, *64*, 343-354.
25. Gaur, R.; Tiwari, S. Isolation, production, purification and characterization of an organic-solvent-thermostable alkalophilic cellulase from *Bacillus vallismortis* RG-07. *BMC Biotechnol.* **2015**, *15*, 19.
26. Nair, A. S.; Al-Battashi, H.; Al-Akzawi, A.; Annamalai, N.; Gujarathi, A.; Al-Bahry, S., Dhillon G. S; Sivakumar, N. Waste office paper: a potential feedstock for cellulase production by a novel strain *Bacillus velezensis* ASN1. *Waste management*, **2018**, *79*, 491-500.
27. Poddar, B.; Manthanvar, R.; Chandak, A. Production of Cellulase from Coconut coir Waste by *Bacillus Subtilis* Under Solid State Fermentation. *Int J Recent Sci Res.*, **2017**, 8 (7), 18139-18142.
28. Acharya, S.; Chaudhary, A. Optimization of fermentation conditions for cellulases production by *Bacillus licheniformis* MVS1 and *Bacillus* sp. MVS3 isolated from Indian hot spring. *Brazilian Archives of Biology and Technology*, **2012**, *55*, 497-503.
29. Vlajkov, V.; Pajčin, I.; Vučetić, S.; Anđelić, S.; Loc, M.; Grahovac, M.; Grahovac, J. *Bacillus*-Loaded Biochar as Soil Amendment for Improved Germination of Maize Seeds. *Plants*, **2023**, *12*, 1024.
30. Ammoneh, H.; Harba, M.; Akeed, Y.; Al-Halabi, M.; Bakri, Y. Isolation and Identification of Local *Bacillus* Isolates for Xylanase Biosynthesis. *Iran. J. Microbiol.* **2014**, *6*, 127–132.
31. Ariaeenejad, S.; Mousivand, M.; Dezfouli, P.M.; Hashemi, M.; Kavousi, K.; Salekdeh, G.H.A. Computational method for prediction of xylanase enzymes activity in strains of *Bacillus subtilis* based on pseudo amino acid composition features. *PLoS ONE*, **2018**, *13* (10), e0205796.
32. Tamariz-Angeles, C.; Lázaro-Palomino, J.; Olivera-Gonzales, P.; Castañeda-Barreto, A.; Villena, G.K. Isolation of Thermotolerant *Bacillus Subtilis* DCH4 From The Chancos Hot Spring (Carhuaz, Peru) With Potential To Degrade Agricultural Lignocellulosic Residues. *Peruv. J. Biol.* **2020**, *27*, 67–78.
33. Irdawati, I.; Sofiyyana, A.; Advinda, L.; Fiffendy, M.; Salvia, S.; Syamsuardi, S.; Agustien, A.; Rilda Y. Yahya, Y. Optimization of Agricultural Waste Substrate as an Alternative Medium for Xylan in Producing Xylanase Enzymes by Thermophilic Bacteria. *Journal of Physics: Conference Series*, **2021**, *1940*, 012052.
34. Shete H. G. Utilization of Agro-waste Residues for Xylanase Production Using Thermoalkalistable *Bacillus* Isolates. *World Journal of Environmental Biosciences*, **2014**, *3* (1), 69-76.
35. Alqahtani, Y. S.; More, S. S.; R., K.; Shaikh, I.A.; K.J., A.; More, V.S.; Niyonzima, F.N.; Muddapur, U.M.; Khan, A.A. Production and Purification of Pectinase from *Bacillus subtilis* 15A-B92 and Its Biotechnological Applications. *Molecules*, **2022**, *27*, 4195.
36. Vlajkov, V.; Pajčin, I.; Loc, M.; Budakov, D.; Dodić, J.; Grahovac, M.; Grahovac, J. The Effect of Cultivation Conditions on Antifungal and Maize Seed Germination Activity of *Bacillus*-Based Biocontrol Agent. *Bioengineering*, **2022**, *9*, 797.
37. Oumer, O.J.; Abate, D. Screening and Molecular Identification of Pectinase Producing Microbes from Coffee Pulp. *Biomed. Res. Int.* **2018**, e2961767.

38. Kabir, M.S.; Tasmim, T. Isolation of Pectinase Producing Bacteria from the Rhizosphere of *Andrographis paniculata* Nees and 16S RRNA Gene Sequence Comparison of Some Potential Strains. *Adv. Microbiol.* **2019**, *9*, 1–13.
39. Mukeshkumar D. J.; Saranya G. M.; Suresh, K.; Andal Priyadharshini, D.; Rajakumar, R.; Kalaichelvan P.T. Production and Optimization of Pectinase from *Bacillus* sp. MFW7 using Cassava Waste. *Asian Journal of Plant Science & Research,* **2012**, *2* (3), 369-375
40. Alnahdi, H.S. Isolation and Screening of Extracellular Proteases Produced by New Isolated *Bacillus* Sp. *J. Appl. Pharm. Sci.* **2012**, *2*, 71–74.
41. Hashmi, S.; Iqbal, S.; Ahmed, I.; Janjua, H.A. Production, optimization, and partial purification of alkali-thermotolerant proteases from newly isolated *Bacillus subtilis* S1 and *Bacillus amyloliquefaciens* KSM12. *Processes*, **2022**, *10*, 1050.
42. Khan, N.; Martínez-Hidalgo, P.; Ice, T.A.; Maymon, M.; Humm, E.A.; Nejat, N.; Sanders, E.R.; Kaplan, D.; Hirsch, A.M. Antifungal Activity of *Bacillus* Species against Fusarium and Analysis of the Potential Mechanisms Used in Biocontrol. *Front. Microbiol.* **2018**, *9*, 2363.
43. Rz, S. Hydrolytic Enzymes of Rhizospheric Microbes in Crop Protection. *MOJ Cell Sci. Rep.* **2016**, *3*, 135–136.
44. Mukherjee, A. K.; Adhikari, H.; Rai, S. K. Production of alkaline protease by a thermophilic *Bacillus subtilis* under solid-state fermentation (SSF) condition using Imperata cylindrica grass and potato peel as low-cost medium: characterization and application of enzyme in detergent formulation. *Biochemical Engineering Journal* **2008**, *39* (2), 353-361.
45. Sathishkumar, R.; Ananthan, G.; Arun, J. Production, purification and characterization of alkaline protease by ascidian associated *Bacillus subtilis* GA CAS8 using agricultural wastes. *Biocatalysis and Agricultural Biotechnology,* **2015**, *4* (2), 214-220.
46. Kumari, P. S.; Reshma, R. Effect of Alkaline Protease Produced from Fish Waste as Substrate by *Bacillus clausii* on Destaining of Blood Stained Fabric. *Journal of Tropical Life Science* **2021**, *11* (1).
47. Balan, S. S.; Nethaji, R.; Sankar, S.; Jayalakshmi, S. Production of gelatinase enzyme from *Bacillus* spp isolated from the sediment sample of Porto Novo Coastal sites. *Asian Pacific Journal of Tropical Biomedicine*, **2012**, *2*(3), S1811-S1816.
48. Mekonnen, M.; Girma, S.; Atnafu, A. Hydrolysis of gelatin from animal hoof using bacterial gelatinase, Ph.D Thesis, Addis Abeba University, **2018**.
49. Tuysuz, E.; Baltaci, M.O., Ozkan, H.; Taskin, M.; Adiguzel, A. Lipase production from thermophilic bacteria using waste frying oil as substrate. *Teknik Bilimler Dergisi*, **2019**, *9* (3), 23-27.
50. Mazhar, H.; Abbas, N.; Hussain, Z.; Sohail, A.; Ali, S. S. Extracellular lipase production from *Bacillus subtilis* using agro-industrial waste and fruit peels. *Punjab Univ. J. Zool*. **2016**, 31 (2), 261-267.
51. Treichel, H.; De Oliveira, D.; Mazutti, M. A.; Di Luccio, M.; Oliveira, J. V. A review on microbial lipases production. *Food and bioprocess technology,* **2010**, *3*, 182-196.
52. Ilesanmi, O. I.; Adekunle, A. E.; Omolaiye, J. A.; Olorode, E. M.; Ogunkanmi, A. L.. Isolation, optimization and molecular characterization of lipase producing bacteria from contaminated soil. *Scientific African*, **2020**, *8*, e00279.

## INSTRUCTION FOR MANUSCRIPT PREPARATION

***Acta Periodica Technologica*** publishes reviews and scientific papers covering all branches of food, chemical, biochemical, and pharmaceutical technologies, as well as process engineering and related scientific fields.

***Acta Periodica Technologica*** is published in English. The journal may include supplements from congresses, meetings or symposiums.

### SUBMISSION OF PAPERS

All correspondence, including submission of the manuscript, notification of the Editor's decision and requests for revision, takes place by e-mail apteff@tf.uns.ac.rs or apteff.tf.uns@gmail.com.

**Authors are expected to propose the category of manuscript (review or original scientific paper) and three potential reviewers.** Reviewers should be experts in the field of the paper, and not associated with the institution with which the authors are affiliated. The final choice of referees will remain entirely with the Editor. Also, optionally, the authors should state any person that is not desired as a reviewer.

**Submission of paper implies that:**

- it is prepared according to this Instructions,
- it has not been published previously (except in the form of an abstract or as a whole in the proceedings of papers of a scientific meeting, or as part of a published lecture or academic thesis),
- it is not under consideration for publication elsewhere, and
- it will not be published elsewhere in the same form, in English or any other language, without the written consent of the publisher.

### PREPARATION OF MANUSCRIPT

**Language:** Manuscript should be written in English.

**Typing:** Manuscript must be written in Word with a font size 10 pt., 1.5 lines spaced, with 2.5 cm margins, on A4 pages (maximum 15 pages for scientific papers and 25 pages for review papers). All lines of the manuscript should be numbered restarting on each page. Also, all pages must be numbered. Tables, figures and schemes must be imported into the text. Abbreviations and symbols-notation should be explained at first appearing, or on a separate list at the end of the manuscript.

**General format.** The manuscript should contain the following in this order: Title page, ABSTRACT and KEYWORDS, INTRODUCTION, EXPERIMENTAL, RESULTS and DISCUSSION, CONCLUSIONS, ACKNOWLEDGEMENTS and REFERENCES.

**Title page:** On the first page should be the title without symbols, formulae or abbreviations (capital bold letters). The title should be concise and explanatory of the content of the paper. Full name (name, initial and surname) of authors (without degrees, professional or official titles) should be given under the title, written in italic. Clearly indicate (with an asterisk) who is responsible for correspondence at all stages of refereeing and publication. Ensure that e-mail address and the full postal address are provided. Affiliation of authors should be given after the author's name. Indicate all affiliations with the superscript number immediately after authors name and in front of the appropriate address. If the paper was given, wholly or in part, at a scientific meeting, this should be stated in a footnote on the title page.

**Abstract** of the paper (100-250 words, written in italic) should be given under the title and authors. Abstracts should contain the aim of investigated work, methods, results and conclusion.

**Keywords** (normal letters, max. 5 keywords) should be listed afterward.

**Introduction** should state previous relevant work with appropriate references, the problem investigated and the aim of work.

**Experimental.** The materials and methods used should be stated clearly in sufficient detail to permit the work to be repeated by others. Only new techniques should be described in detail; known methods must have adequate references.

**Results and Discussion**. Results should be presented concisely, with tables or illustrations for clarity. The significance of the findings should be discussed without repetition of the material in the Introduction. The adequate number of illustrations, graphs and chemical formulae used must be kept on a minimum.

**Conclusions.** This section should present the main conclusions of the study. Also, conclusions should indicate the significance of contribution and application possibilities of the obtained results.

**Acknowledgements:** These should be kept to a minimum.

**References** cited should be indicated in the text using Arabic numerals in round brackets ( ), in the order of appearing. All publications cited in the text should be presented in a list of references given on a separate page. Abbreviations of journal titles should be given according to the Chemical Abstracts Service (CASSI Search Tool; http://cassi.cas.org). The list of references should be presented according to the *ACS citation style* and their appearance in the text. Give names of all authors (do not use „et. al.“), with their initials after respective surnames. Include article titles in journals. The abbreviated titles should be followed by the year (**bold**), volume (*italic*), number (in round brackets if exists), and first and last page numbers.

**Examples:**

***Journals:*** Pascual, E.C.; Goodman, B.A; Yeretzian, C. Characterisation of Free Radicals in Solubile Coffee by Electron Paramagnetic Resonance Spectroscopy. *J. Agric. Food Chem.* **2002,** *50* (21), 6114-6122.

***Books:*** Morris, R. *The Last Sorcerers: The Path from Alchemy to the Periodic Table;* Joseph Henry Press: Washington, DC, 2003; pp 145-158.

***Book with more chapters:*** Puls, J.; Saake, B. Industrially Isolated Hemicelluloses. In *Hemicelluloses: Science and Technology;* Gatenholm, P., Tenkanen, M., Eds.; ACS Symposium Series 864; American Chemical Society: Washington, DC, 2004; pp 24-37.

***Book of Abstracts:*** Noe, W.; Howaldt, M.; Ulber, R.; Scheper, T. Immunobase elution assay for process control, 8th European Congress on Biotechnology, Budapest, 17-21 August 1997, Book of Abstracts WE 163, p. 246.

***Thesis:*** Linstead, J.B.: Linstead, J.B. Effects of adding natural antioxidants on colour stability of paprika. Ph.D. (or M.S.) Thesis, University of Glasgow, November 2006.

***Patent:*** Lenssen, K. C.; Jantscheff, P.; Kiedrowski, G.; Massing, U. Cationic Lipids with Serine Backbone for Transfecting Biological Molecules. Eur. Pat. Appl. 1457483, 2004.

***Unpublished data:*** Should be cited with one of the following comments: *in press*, *unpublished work* or *personal communication*.

***Online citations:*** Should include the author, title, website and date of access.

Example: Wright, N.A. The Standing of UK Histopathology Research 1997-2002.
http://pathsoc.org.uk (accessed 7 October 2004).

**Chemical nomenclature and units.** Authors are requested to use SI units and chemical nomenclature following the rules of Chemical Abstracts whenever possible.

**Tables.** Each Table is numbered with an Arabic numeral, followed by the title (**Table 1.** The result...). The table width must be 12.5 cm max.

**Figures.** Each drawing or figure should also be numbered with Arabic numerals followed by the title (**Figure 1.** Chromatogram of...).

Schemes and figures must be submitted as separate files in their original extension (xls, xlsx, vdr, cdr, wmf, tiff, bmp, jpg).

**Formulae and Equations.** Type formulas and mathematical equations clearly, accurately placing superscripts and subscripts. Equations should be indicated in the text using Arabic numerals in square brackets [ ].

**Review process.** All papers submitted to the journal will be reviewed by at least two independent referees who will be asked to complete the refereeing job within 2-4 weeks. The final decision on publication will be made by the Editorial Board. Manuscripts may be sent back to authors for revision if necessary. Revised manuscript submissions should be made as soon as possible (within 2 weeks) after the receipt of the referees' comments.

**Proofs.** The corresponding author will receive via email an uncorrected proof of the manuscript. This proof should only be used to check for spelling errors in the manuscript. After receiving the email with uncorrected proof, authors have 48 hours to submit a list of corrections. Another alternative is to mark changes to the pdf file with sticky note option and return it to the Editor’s office.

**Author service.** For inquiries relating to the submission of the manuscript, please send an email to the Editor’s office (apteff@tf.uns.ac.rs or apteff.tf.uns@gmail.com). Postal address: *Acta Periodica Technologica*, Editorial Board, Bulevar cara Lazara 1, 21000 Novi Sad, Serbia.

**THIS ISSUE OF ACTA PERIODICA TECHNOLOGICA**
**IS FINANCIALLY SUPPORTED BY:**

***Ministry of Science, Technological Development and Innovations***
***of Republic of Serbia***

## FORMER EDITORS-IN-CHIEF

## Editorial:

University of Novi Sad, Faculty of Technology Novi Sad,
Bulevar Cara Lazara 1, 21000 Novi Sad, Serbia

Phone: +381 21 485 3693
Fax: +381 21 450 413
e-mail: apteff@tf.uns.ac.rs, apteff.tf.uns@gmail.com

Prepress: Branislav S. Bastaja

Printed by: BIROGRAF COMP DOO BEOGRAD,
Atanasija Pulje 22, Beograd (Zemun), Serbia

Copies: 200